SYNTHETIC FRC GROUND SLABS SUBJECTED TO A CENTRAL CONCENTRATED FORCE

DOCTORAL DISSERTATION IN THE DISCIPLINE OF CIVIL ENGINEERING, GEODESY, AND TRANSPORT

AUTHOR Julia BLAZY

SUPERVISOR Professor Łukasz DROBIEC, DSc, PhD, CEng.

| I dedicate this doctoral dissertation to my family, my friends, and all those we support, encouragement, and contributions have made this work poss I am deeply grateful to each of | ible. |
|--|-------|
| | |
| Niniejszą rozprawę doktorską dedykuję mojej rodzinie, przyjaciołom wszystkim tym, których wsparcie, życzliwość i wkład pozwoliły na jej realize | |
| Każdemu z Was jestem bardzo wdzięc | |
| | |

CONTENTS

| 1. | INTROD | OUCTION | 11 |
|----|--------------------|---|-----|
| 2. | MOTIVA | ATION AND THESES | 13 |
| | | ground and Motivation | |
| | | tives and Theses | |
| | | ations | |
| | 2.4. Scope | | 17 |
| 3. | EVALŪA | ATION OF THE STATE OF KNOWLEDGE | 19 |
| | | uction | |
| | | etical models | |
| | | roduction | |
| | | eoretical models for FRC | |
| | | eoretical models for ground slabs | |
| | 3.2.3.1 | Westergaard approach | |
| | 3.2.3.2 | Falkner et al. approach | |
| | 3.2.3.3 | Shentu et al. approach | |
| | 3.2.3.4 | Meyerhof-Losberg approach | |
| | | eoretical models for punching shear | |
| | | nmary | |
| | | ards | |
| | | roduction | |
| | | ndards for testing FRC | |
| | 3.3.2.1 | Uniaxial tensile tests | |
| | 3.3.2.2 | Splitting tensile tests | |
| | 3.3.2.3 | ndards for designing FRC | |
| | 3.3.3.1 | RILEM TC 162-TDF | |
| | 3.3.3.2 | Model Code 2010 | |
| | 3.3.3.3 | PN-EN 1992-1-1:2024 Annex L | |
| | | ndards for designing ground slabs | |
| | | ndards for punching shear design | |
| | 3.3.5.1 | PN-EN 1992-1-1:2008 | |
| | 3.3.5.2 | PN-EN 1992-1-1:2024-05 | |
| | 3.3.5.3 | Technical Report 34 | |
| | 3.3.5.4 | Model Code 2010 | |
| | | nmary | |
| | | ng studies | |
| | • | nthetic fiber reinforced concrete | |
| | 3.4.1.1 | Introduction | |
| | 3.4.1.2 3.4.1.3 | Mix design Workability | |
| | 3.4.1.3 | Crack limitation | |
| | 3.4.1.4 | Elasticity modulus | |
| | 3.4.1.6 | Compressive strength | |
| | 3.4.1.7 | Flexural tensile strength | |
| | 3.4.1.8 | Fracture energy, energy absorption, toughness | |
| | 3.4.1.9 | Splitting tensile strength. | |
| | | Shrinkage | |
| | 3.4.1.11 | Impact resistance | 106 |

| | 3.4.1.12 | Spalling and temperature resistance | 107 |
|----|--------------|--|-----|
| | 3.4.1.13 | Freeze-thaw resistance | 108 |
| | 3.4.1.14 | Abrasion resistance | 109 |
| | 3.4.1.15 | Water absorption, porosity, air content | 110 |
| | 3.4.1.16 | Sustainability and economics | 111 |
| | 3.4.1.17 | Summary | 113 |
| | 3.4.2. Lar | ge-scale research on centrally loaded ground slabs | 115 |
| | 3.4.2.1 | | |
| | 3.4.2.2 | Alani et al. research | |
| | 3.4.2.3 | Elsaigh research | |
| | 3.4.2.4 | Roesler et al. research | |
| | 3.4.2.5 | Bischoff et al. research | |
| | 3.4.2.6 | Shi et al. research | |
| | 3.4.2.7 | Sucharda et al. research. | |
| | 3.4.2.8 | Manfredi et al. research. | 139 |
| | 3.4.2.9 | Summary | 143 |
| | 3.5. Practic | ce | |
| | | rch gap and significance | |
| 1 | | RCH PROGRAM | |
| 4 | | | |
| | | uction | |
| | | ials and mix design | |
| | - | e preparation | |
| | | odology | |
| | 4.4.1. Ma | terial characteristics | 158 |
| | 4.4.1.1 | Fresh concrete properties | 158 |
| | 4.4.1.2 | Compressive strength tests | 159 |
| | 4.4.1.3 | Modulus of elasticity tests | 160 |
| | 4.4.1.4 | Splitting strength tests | |
| | 4.4.1.5 | Flexural strength tests | 162 |
| | 4.4.2. Lar | ge-scale slab tests | 164 |
| | 4.4.2.1 | Testing schedule | 164 |
| | 4.4.2.2 | Slab samples | 165 |
| | 4.4.2.3 | Ground conditions | 168 |
| | 4.4.2.4 | Measuring methods and testing setup | 176 |
| 5. | . RESULT | S | |
| | | ial characteristics | |
| | | sh concrete properties | |
| | | | |
| | | mpressive strength tests | |
| | | dulus of elasticity tests | |
| | - | itting tensile tests | |
| | | xural tensile strength tests | |
| | 5.1.6. Sur | nmary | 206 |
| | 5.1.6.1 | Influence of fiber addition | |
| | 5.1.6.2 | Influence of fiber dosage | |
| | 5.1.6.3 | Influence of fiber type | 208 |
| | 5.2. Large- | -scale slab tests | 208 |
| | 5.2.1. Sla | bs FF 2 – type 6 | 211 |
| | 5.2.1.1 | Load-deflection response | |
| | 5.2.1.2 | Crack morphology | |
| | 5.2.1.3 | Deflection profiles | |
| | 5.2.1.4 | Punching cone characteristics | |
| | 5.2.1.5 | Influence of ground support | |
| | | Provisions for further tests | |
| | | | |

| API | PENDIX : | B. Literature review on large-scale ground slab testing | 371 |
|-----|----------------------|---|-----|
| APl | PENDIX . | A. Literature review on the influence of macro SyFs | 367 |
| 10. | | GRAPHY | |
| 9. | FURTH | ER RESEARCH AREAS | 347 |
| 8. | FINAL (| CONCLUSIONS AND RECOMMENDATIONS | |
| 7. | DISCUS | | |
| 6. | .9. Synth | esis and conclusions of the analytical analysis | 327 |
| 6. | .8. Analy | tical model validation | 324 |
| 6. | | id-supported slab with linear edge support | |
| | | y supported slab | |
| | | ntribution of fibers and ground in transferring punching shear load | |
| | | oment and punching shear capacity calculations | |
| | | ical Report 34 – Meyerhof-Losberg approach and Eurocode 2 | |
| | | u et al. approach | |
| 6. | | er et al. approach | |
| | | rgaard approach | |
| 6. | | uction | |
| 6. | | ΓICAL ANALYSIS | |
| 5. | .3. Synth | esis and conclusions of the research program | |
| | 5.2.8.3 | Influence of fiber type | |
| | 5.2.8.2 | Influence of fiber dosage | |
| | 5.2.8.1 | Influence of fiber addition. | |
| | | nmary | |
| | | shrod results | |
| | 5.2.6.4 | Punching cone characteristics | |
| | 5.2.6.3 | Deflection profiles | |
| | 5.2.6.2 | Crack morphology | |
| | | bs PD_3 – type 5 Load-deflection response | |
| | 5.2.5.4 5.2.6 Slo | Punching cone characteristics | |
| | 5.2.5.3 | Deflection profiles | |
| | 5.2.5.2 | Crack morphology | |
| | 5.2.5.1 | Load-deflection response | |
| | | bs PD_2 – type 4 | |
| | 5.2.4.4 | Punching cone characteristics | |
| | 5.2.4.3 | Deflection profiles | |
| | 5.2.4.2 | Crack morphology. | |
| | 5.2.4.1 | Load-deflection response | |
| | | bs PM 3 – type 3 | |
| | 5.2.3.4 | Punching cone characteristics | |
| | 5.2.3.3 | Deflection profiles | |
| | 5.2.3.2 | Crack morphology | |
| | 5.2.3. Sia | Load-deflection response | |
| | | bs PM_2 – type 2 | |
| | 5.2.2.3 5.2.2.4 | Deflection profiles Punching cone characteristics | |
| | 5.2.2.2 | Crack morphology | |
| | 5.2.2.1 | Load-deflection response | |
| | | bs PC – type 1 | |
| | | | |

LIST OF BASIC SYMBOLS

Latin upper case letters

 loading area, \boldsymbol{A}

 $CMOD_i$ - crack mouth opening displacement corresponding to 0.5, 1.5, 2.5,

3.5 mm, where i = 1, 2, 3, 4, respectively,

CTOD crack tip opening displacement, E_c concrete modulus of elasticity,

- concrete initial secant modulus of elasticity from drilled core samples, $E_{c0,core}$

- concrete stabilized secant modulus of elasticity from drilled core $E_{cs.core}$

samples,

- fiber modulus of elasticity, E_f

- primary static deformation modulus of soil, E_{v1} E_{ν^2} secondary static deformation modulus of soil,

- dynamic deformation modulus of soil, E_{vd}

Fforce,

 F_{cr1} - experimentally obtained first cracking force,

- experimentally obtained secondary cracking force, F_{cr2}

- experimentally obtained maximum force, F_{max} F_p - experimentally obtained punching shear force,

- experimentally obtained ultimate force, F_u

 fracture energy, G_F

 deformation index of soil, I_0

- negative (hogging) resistance moment of the slab, M_n - positive (sagging) resistance moment of the slab, M_p

concentrated force,

pcal load-bearing capacity calculated according to the analytical model,

pcal,val - validated load-bearing capacity calculated according to the analytical

model,

 $P_{cr.W}$ - load-bearing capacity according to the Westergaard approach,

concrete, fiber contribution in punching shear load-bearing capacity of $P_{p,c}, P_{p,f}$

the ground slab, respectively,

 $P_{p,g}$ or R_p – ground contribution in punching shear load-bearing capacity of the ground slab,

maximum punching shear load-bearing capacity at the face of the loaded $P_{p,max}$ or

 $V_{R max}$

 load-bearing capacity according to the Falkner et al. approach, $P_{u.F}$

 $P_{u,i}$, $P_{u,e}$, – load-bearing capacity according to the Meyerhof-Losberg approach for

internal, edge, corner concentrated loading, respectively, $P_{u.c}$

- load-bearing capacity according to the Shentu et al. approach, $P_{u.S}$

 R_e fracture toughness index, V_E - applied punching shear force,

- reduced applied punching shear force, $V_{E.red}$

- nominal fiber volume content,

 $V_{R,c}$ – punching shear load-bearing capacity without punching shear

reinforcement at the control section considered,

 $V_{R,f}$ – additional punching shear load-bearing capacity resulting from the

presence of fibers in concrete at the control section considered,

 W_0 – concrete toughness, W_{el} – elastic section modulus.

Latin lower case letters

a – distance of the critical control section from the loading area,

 a_r – equivalent radius of contact area of the load,

b – width.

 b_r – equivalent radius of pressure distribution,

d – effective slab depth,

 d_f – fiber diameter,

 f_c – concrete compressive strength,

 $f_{c,core}$ — concrete compressive strength of drilled core samples, $f_{c,cube}$ — concrete compressive strength of cast cube samples,

 f_{ct} – concrete uniaxial tensile strength,

 f_{eq} — concrete equivalent flexural tensile strength, f_{Fts} — concrete serviceability residual tensile strength,

 f_{Ftu} – concrete ultimate residual tensile strength,

 $f_{ct,L}$ – concrete limit of proportionality, f_{fl} or $f_{ct,fl}$ – concrete flexural tensile strength,

 f_{ft} – fiber tensile strength,

 $f_{R,j}$ — concrete residual flexural tensile strength corresponding to $CMOD = CMOD_j$ or $\delta = \delta_j$, where j = 1, 2, 3, 4, respectively,

 $CMOD = CMOD_j$ of $0 = 0_j$, where j = 1, 2, 3, 4, respect

 f_{spl} – concrete splitting tensile strength,

 $f_{spl,core}$ – concrete splitting tensile strength from drilled core samples,

h – slab thickness,

 h_{sp} — distance between the tip of the notch and the bottom of the specimen,

k – modulus of subgrade reaction,
 l – slab radius of relative stiffness,

 l_f – fiber length,

m – bending moment,
 t – baseplate thickness,

 u_0 - length of the perimeter of the loaded area, u_1 - length of the critical control perimeter,

ubase – punching cone base perimeter,

- equivalent critical control perimeter of the punching cone,

 v_E – applied punching shear stress,

v_f - additional shear strength resulting from the presence of fibers in concrete,

 v_{max} — concrete maximum shear strength at the face of the loaded area, v_{min} — concrete minimum shear strength at the control section considered, $v_{R,c}$ — concrete punching shear resistance without punching sh

reinforcement at the control section considered,

w – crack width opening,

wf - fiber content in units of weight in 1 m³,
 racking leg base or column side dimension.

Greek upper case letters

 ΔV_{Ed} — net upward force within the control perimeter considered, resultant soil resistance.

Greek smaller case letters

 α – parameter, β – parameter, δ – deflection,

 $\delta_{central}$ – deflection at the center,

 κ_G – factor accounting for size effect,

 κ_O – factor accounting for fiber orientation,

 ρ_f — density of fiber material,

 σ_i , σ_e , σ_c - stresses under internal, edge, corner concentrated loading, respectively,

 σ_{rl} – axial tensile strength at the tip of the crack,

 σ_{r4} – axial tensile strength at the tension face (the opening of the crack),

 θ – inclination angle of the punching cone,

 ϕ – diameter,

 γ_c — material partial safety factor for concrete,

 γ_{fc} — material partial safety factor for fiber reinforced concrete,

— material partial safety factor for steel fiber reinforced concrete,

v – concrete Poisson's ratio.

1. INTRODUCTION

Civil engineering is inherently interdisciplinary. It encompasses not only design and construction but also maintenance, renovation, and eventual demolition of structures [1]–[3]. Furthermore, it encompasses a wide range of subdisciplines, including structural, construction process, materials, mechanical, transportation, geotechnical, surveying, and environmental engineering, among others. When examining the field of structural engineering more closely, it becomes evident that it can be subdivided into various categories, such as building and engineering construction, industrial buildings, as well as roads, railways, and bridges. It is uncommon for a project to require expertise solely from one discipline or field; rather, civil engineers must possess a comprehensive understanding of materials, construction techniques, load transfer mechanisms, and supporting conditions.

The subject of the synthetic fiber reinforced concrete (SyFRC) ground slabs subjected to centrally loaded concentrated force exemplifies this interdisciplinarity. Specifically, due to its association not only with structural engineering but also with materials, construction technology, and geotechnical engineering. Consequently, addressing this topic necessitates a broader knowledge base, which ultimately benefits a wider group of civil engineers. Given that ground-supported slabs in industrial halls are the most prevalent application area for fiber reinforcement, it is essential to understand their role, potential, limitations, and the challenges that arise from incorporating synthetic fibers (SyFs) into the concrete mixture. The adoption of fiber reinforcement in slab construction has become widespread for several reasons, including ease of construction, potential labor and cost savings, reduced construction time, increased resistance to cracking, and enhanced durability and strength. However, despite the growing knowledge and experience, SyFRC continues to provoke skepticism among investors, designers, and contractors, resulting in a limited range of applications [4]. This may also be due to the limited attention given specifically to SyFs in existing design codes and standards since they typically focus on steel fibers (SFs) and steel fiber reinforced concrete (SFRC) [5]–[8]. It also appears that the issue of concentrated loads and the resulting risk of the punching shear failure in ground-supported slabs is still insufficiently explored, especially when these slabs are made of fiber reinforced concrete (FRC). This underscores the ongoing need for further research in this area. In response to this demand, the author of this dissertation undertaken a study on SyFRC ground slabs centrally loaded by a concentrated force, focusing specifically on their punching shear behavior.

2. MOTIVATION AND THESES

2.1. Background and Motivation

FRC is a composite material consisting of concrete and reinforcing fibers. The concept is not novel, as historical evidence indicates that ancient civilizations such as Babylonia and Egypt utilized natural materials, such as reeds, to reinforce clay structures. Furthermore, historically, straw was employed to enhance the strength of bricks, while horsehair was incorporated into plaster for similar purposes. The practical utilization of fibers in concrete as a form of dispersed reinforcement has been prevalent since the 1960s [9], leading to comprehensive studies on their influence on concrete performance. Nevertheless, despite the growing knowledge and experience in this field, FRC are still approached with great doubt and caution, which strongly limits its broader acceptance. Common concerns include the uniform distribution of fibers within the concrete matrix [10], their actual effects on the physical and mechanical properties of concrete, and their potential use as a substitute for traditional steel reinforcement bars. To systemize existing knowledge, various standards and guidelines for the testing and designing FRC have been published, although these documents are predominantly dedicated to SFRC. Availability of data and recommendations concerning the SyFs contribution in the load-bearing capacity of structural elements is significantly limited. Usually, the standards and guidelines primarily developed for SFRC are adopted for concretes with SyFs.

The majority of studies have concentrated on evaluating the properties of SyFs and their influence on concrete using small-sized samples. Numerous experiments have been conducted on cubes, cylinders, beams, and other small-scale specimens to assess the effects of fibers on parameters such as density, thermal properties, electrical conductivity, workability, porosity, absorbability, and various other physical properties. Additionally, studies have investigated mechanical properties including the modulus of elasticity, compressive, tensile, flexural, and splitting strength as well as toughness, abrasion,

impact, and shrinkage resistance. Conversely, there is limited research dedicated to structural testing using full- or semi-full-scale samples. Such tests are particularly valuable as they provide a broader and more realistic understanding of the behavior of structural elements, providing crucial insights into their mechanical performance. Moreover, research involving large-scale samples has the potential to significantly influence existing design codes and guidelines. It remains an open question whether the results derived from small-scale tests accurately and reliably reflect the behavior of structural elements. Furthermore, research on FRC elements has primarily focused on the testing of beams and slabs, with ground slabs being studied less frequently, despite their position as one of the principal applications of FRC. The primary objective of large-scale tests on ground slabs has typically been to evaluate their flexural load-bearing capacity and overall mechanical behavior. In industrial applications, one of the principal design loads anticipated for ground slabs is the point load generated by racking and forklifts, which can lead to punching shear failure (Fig. 2.1) [11]. Despite its practical importance, this failure mode remains insufficiently investigated, as relatively few studies have examined the structural response of slabs subjected to concentrated loads. The existing research has concentrated on plain concrete (PC) slabs or slabs with traditional bar or mesh reinforcement. There is still a lack of a sufficient amount of comprehensive research on FRC ground-supported slabs, specifically those incorporating SyFs. Given that ground slabs are typically not reinforced against punching failure, it is often recommended to enhance the slab's thickness or to upgrade the concrete class in cases where there is insufficient punching shear load-bearing capacity [12]. Consequently, the concept of utilizing fiber reinforcement to enhance this capacity in ground slabs seems to be promising. Concluding, the influence of fibers on aspects such as load-bearing capacity, failure modes, crack propagation, and deformations require further research and analysis. Moreover, the existing standards and guidelines do not provide unambiguous provisions regarding the determination of the critical control section position and punching shear capacity of SyFRC ground slabs. Additionally, uncertainties remain regarding the influence of the supporting ground on the slab's structural response. Numerous studies indicate that the punching shear capacity of slabs tested on real subgrades is substantially greater than that of slabs evaluated on simulated subsoil. Unfortunately, a significant number of tests are conducted on simulated subgrades, including springs, insulation materials, and line supports [13], due to challenges in achieving realistic ground supporting conditions.



Fig. 2.1 Industrial floor subjected to loading from storage racking

2.2. Objectives and Theses

To address the identified research gap, the author of this dissertation conducted a comprehensive experimental campaign on SyFRC ground-supported slabs subjected to centrally applied concentrated loads. The outcomes of this study have the potential to influence future design standards and construction practices for SyFRC ground slabs, while also contribute to a deeper understanding of their punching shear behavior. The specific objectives that guided the research presented in this dissertation are summarized in Table 2.1. Furthermore, five research theses have been formulated based on the objectives and scope of this doctoral study (Table 2.2). They reflect the assumed structural behavior and performance of SyFRC ground-supported slabs under concentrated loading conditions, as well as the expected applicability of used experimental and analytical methods.

Table 2.1 Objectives of the doctoral dissertation

| No. | Objectives |
|-----|---|
| 1. | Comprehensive review and critical analysis of selected theoretical and analytical models, existing standards, and guidelines as well as performed experimental investigations on the effect of SyFs inclusion in concrete, testing and design methods of SyFRC focusing particularly on ground slabs and punching shear capacity. |
| 2. | Execution of an experimental campaign on small-scale specimens to determine the influence of SyFs addition, type, and dosage on selected physical and mechanical properties of concrete, including workability, modulus of elasticity, compressive, flexural, and splitting tensile strength as well as fracture energy. |
| 3. | Development and design of a testing setup and adequate experimental methodology to investigate the punching shear behavior of semi-full scale ground slab samples. |
| 4. | Assessment of structural behavior differences between centrally loaded unsupported slabs and ground-supported slabs. |
| 5. | Comparative analysis of flexural cracking loads, punching shear load capacity, crack morphology, deflections, and location of the critical control section of PC and SyFRC ground slabs, considering various SyFs types and dosages. Identification and characterization of failure stages and mechanisms of SyFRC ground-supported slabs under concentrated central loads. |
| 6. | Validation of the accuracy and predictivity of selected analytical models through comparison with experimental results. Conducting analytical analyses to quantify the contribution of SyFs to punching shear load-bearing capacity and support conditions to flexural cracking loads. |
| 7. | Formulation of practical design recommendations, including methods to incorporate SyFs contribution in punching shear capacity calculations and determination of critical control section location for SyFRC ground-supported slabs. |

Table 2.2 Theses of the doctoral dissertation

| No. | Theses |
|-----|--|
| 1. | The structural response of SyFRC ground-supported slabs under central concentrated loading |
| | can be reliably predicted based on the results obtained from small-scale beam specimens. |
| 2. | The structural behavior of SyFRC ground-supported slabs under central concentrated loading |
| | differs substantially from that of unsupported slabs, particularly in terms of load-bearing |
| | capacity and failure mechanisms. |
| 3. | The addition of SyFs improves the post-cracking behavior and results in more ductile failure |
| | modes in slabs compared to PC ground-supported slabs. |
| 4. | The inclusion and increased dosage of SyFs enhance the punching shear load-bearing capacity |
| | of the ground-supported slabs and increase the critical control perimeter. |
| 5. | The type of SyFs has influence on both the punching shear load-bearing capacity and the length |
| | of the critical control perimeter of the ground-supported slabs. |

2.3. Limitations

Being aware of the inherent complexity and numerous uncertainties associated with punching shear behavior in SyFRC ground slabs, the scope of this dissertation has been consciously constrained. Specifically, the investigation is limited to ground-supported slabs composed of two material types: PC and SyFRC, excluding the influence of traditional steel bar and mesh reinforcement, shrinkage reinforcement, or combined reinforcement systems. Furthermore, the study focuses on only five distinct SyFRC

types, varying in fiber type and dosage. Consequently, the findings may not be representative of all commercially available SyFs or dosage variations. The experimental campaign addresses solely a single static loading condition, namely, a concentrated load applied at the slab center. Loading at other locations, such as edges and corners, along with different loading types including multiple point loads, line loads, and uniformly distributed loads has not been examined. Additionally, the experimental results are also based on specific slab geometry of limited dimensions which may not fully represent the in situ ground slabs. Furthermore, the slab support conditions were limited to a single type of subgrade material, uniformly compacted across all samples. Alternative support configurations, including varied soil types or compaction levels, were not considered. As a result, the variability in load types, slab dimensions, and subgrade conditions, is not fully accounted for, possibly limiting the generalizability of the conclusions. In the analytical analysis, only selected theoretical methods were studied and compared, which may influence the completeness of the comparative assessment. Lastly, the study does not include numerical modeling, which could provide more detailed insight into stress distribution, load-bearing capacity, deflection, crack propagation, and slab-soil interaction. Acknowledging the limitations of the dissertation scope defines the boundaries of the current study and highlights key areas for future research.

2.4. Scope

The scope of the dissertation includes a comprehensive literature review, a small-scale and large-scale experimental campaign, as well as analytical analyses, all aimed at achieving the defined objectives and validating the formulated theses. The dissertation is structured into ten chapters, each addressing specific topics.

Chapter 1 introduces the subject of SyFRC ground-supported slabs.

Chapter 2 provides the overall context of the dissertation, outlining the motivation, objectives, theses, and limitations of the conducted experimental and analytical studies.

Chapter 3 presents a detailed literature review, covering theoretical models as well as testing and designing methods for FRC, alongside experimental results on the influence of macro SyFs on various concrete properties. Additionally, it reviews analytical approaches for assessing the capacity of ground-supported concrete slabs and addresses the topic of punching shear with particular focus on the determination of the

critical control section location. The chapter further examines existing studies on ground-supported slabs, emphasizing research related to SyFRC slabs and their punching shear behavior. The literature review also coveres a practical perspective on ground-supported slabs in industrial floors. Finally, it identifies the research gaps addressed in this dissertation.

Chapter 4 describes the experimental campaign involving SyFRC mixtures with different fiber types and dosages, along with a PC reference mix. It details the material characterization tests for both fresh and hardened concrete properties. Furthermore, the chapter outlines the design, setup, and testing methodology for large-scale ground slab experiments, including testing schedule, sample preparation, subbase conditions, load application, and measurement techniques.

Chapter 5 presents the experimental results from material tests, covering workability, modulus of elasticity, compressive, flexural, and splitting tensile strength. It also reports on the structural behavior of unsupported and ground-supported slabs subjected to central concentrated loading, including load-deflection responses, recorded flexural cracking forces, punching shear capacities, deflection profiles, crack morphology, and characteristics of punching cones. The chapter concludes with a discussion and comparison of results, highlighting the effects of SyFs addition, dosage, and type.

Chapter 6 compares the experimental findings with selected theoretical models proposed by Westergaard, Falkner et al., Shentu et al., and Meyerhof-Losberg to evaluate their accuracy and predictivity. Additionally, calculations of moment and punching shear capacity are performed following Technical Report 34. The chapter also investigates the contribution of SyFs and ground on the slabs' punching shear capacity as well as the influence of different support conditions on the flexural cracking capacity. Finally, the procedure for validating the analytical models is presented.

Chapter 7 discusses the main findings from experimental campaign and analytical studies, along with their comparative analysis with the literature review, focusing on the impact of fiber addition, dosage, and type on the punching shear behavior of SyFRC ground slabs. Additionally, the chapter presents a critical reflection on the conducted research and analyses, outlining both its strengths and limitations.

Chapter 8 presents the final conclusions and design recommendations, including methods to incorporate the contribution of SyFs in punching shear capacity calculations and determination of critical control section location for SyFRC ground-supported slabs.

Chapter 9 highlights the potential and necessity for further research, identifying key areas for future investigation.

Chapter 10 contains the bibliography.

3. EVALUATION OF THE STATE OF KNOWLEDGE

3.1. Introduction

This chapter provides an extensive review of the existing literature related to the subject of this dissertation. It aims to evaluate the current state of knowledge, identify key findings, and highlight research gaps that require further investigation. The theoretical models, available standards, and existing studies concerning influence of SyFs, testing, and designing of FRC structural elements, focusing on SyFRC ground slabs and punching shear performance are discussed. Furthermore, the review addresses the practical aspects of ground slabs of industrial floors, with particular attention to common types of damages and their causes. The goal of this comprehensive literature review is to set the foundation for the subsequent experimental campaign and analytical analysis.

3.2. Theoretical models

3.2.1. Introduction

The aim of this chapter is to present the theoretical background concerning the behavior of fibers in concrete, with particular emphasis on the fiber-bridging mechanism and the tensile stress-crack opening relationship. In addition, selected analytical approaches for the capacity assessment of ground-supported concrete slabs are reviewed, with a focus on their underlying assumptions and applicability to FRC. Finally, the chapter addresses the complex phenomenon of punching shear in ground slabs, with particular attention given to the determination of the critical control perimeter.

3.2.2. Theoretical models for FRC

Fibers are usually considered as a dispersed reinforcement of concrete which properly incorporated enhance the material's post-cracking behavior, toughness, and crack control ability. The fundamental mechanisms governing fiber behavior in concrete are illustrated in Fig. 3.1a. In the uncracked state (7), fibers remain inactive and do not contribute to the mechanical response. As microcracks begin to form within the concrete matrix (6), and subsequently connect into macrocracks (3), the embedded fibers become active by bridging the cracks and enabling the transfer of tensile stresses across the crack faces. This crack-bridging mechanism distinguishes FRC from conventional concrete, which typically exhibits a sudden drop in tensile resistance immediately after the initiation of the first crack. Additionally, fibers play a critical role in arresting or slowing the propagation of crack tips (5). However, an inadequate mix design or poor fiber-matrix bond can lead to premature fiber debonding (4). Depending on the strength of the matrix and the tensile strength of the fibers, two failure mechanisms may occur: fiber pull-out (2), when the bond strength is insufficient, or fiber rupture (1), when the tensile strength of the fibers is exceeded. Fig. 3.1b presents the typical fracture zones identified in FRC. Namely, a micro and macrocracking development zone, bridging and branching zone where both aggregates and fibers contribute to tensile stress transfer, and traction-free zone, where complete crack opening occurs and no further stresses can be transmitted across the crack.

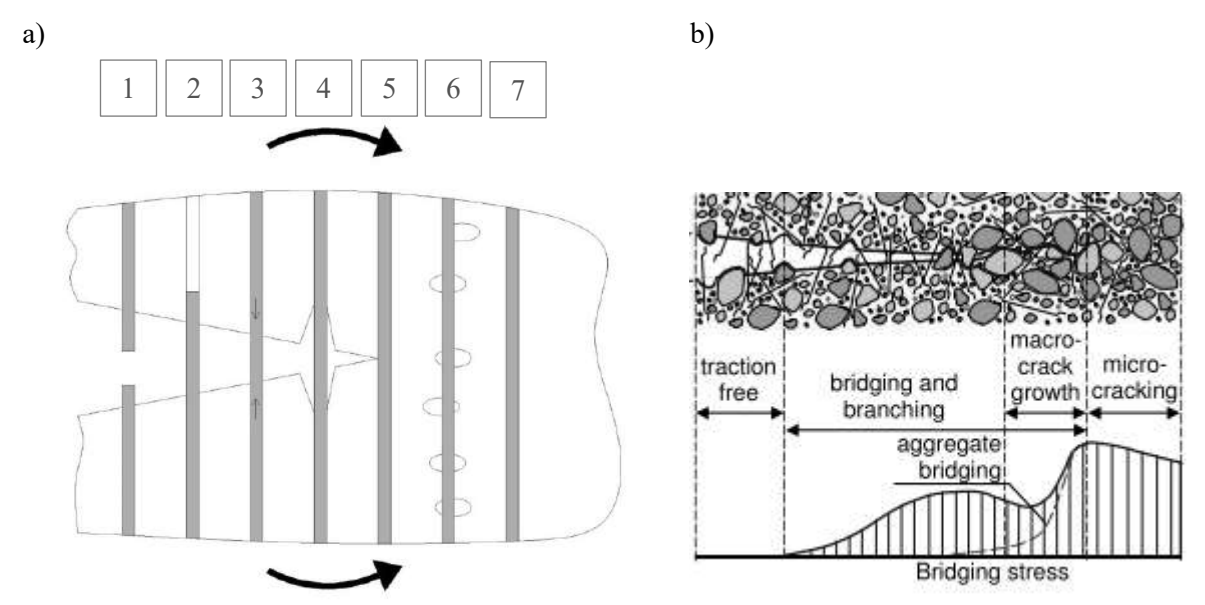


Fig. 3.1 Fiber behavior in concrete: a) 1 – fiber rupture, 2 – fiber pull-out, 3 – fiber bridging a macrocrack, 4 – matrix/fiber debonding, 5 – fiber counteracting crack propagation, 6 – fiber bridging a microcrack, 7 – inactive fiber, b) development of bridging stresses in fracture zones [14]

Depending on the material, type, dosage, and distribution of fibers, as well as the properties of the concrete matrix, FRC may exhibit either strain-hardening or strain-softening behavior, as illustrated in Fig. 3.2. Strain-hardening refers to the phase following initial cracking where the tensile load capacity continues to increase. In this phase, the structural element maintains its stability and continues to carry increasing loads despite the presence of cracks. This behavior is typically associated with the development of multiple fine cracks (microcracking) and is characteristic for concretes with higher fiber dosages. Once the material reaches its ultimate tensile strength and crack localization occurs, the tensile load begins to decrease. Despite this reduction, the element retains the residual load-bearing capacity even as crack width increases what is known as a strain-softening behavior.

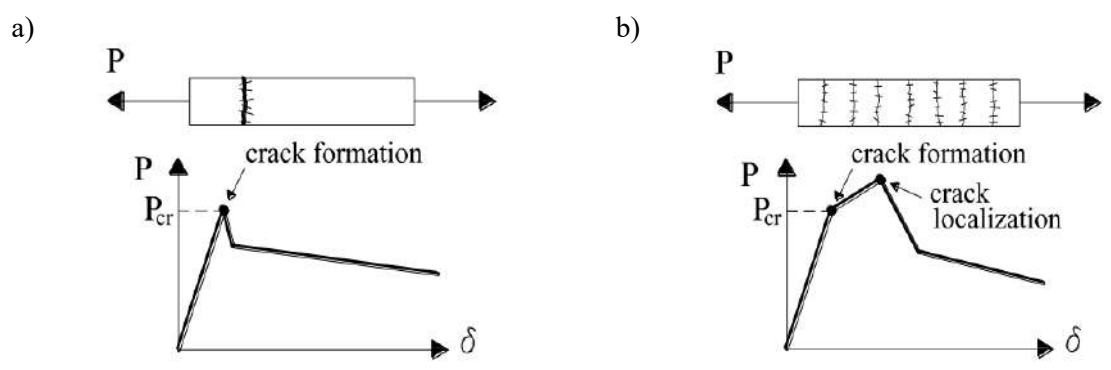


Fig. 3.2 FRC under uniaxial tension: a) strain-softening, b) strain-hardening behavior [15]

The concrete tensile behavior is described using the tensile stress-crack opening relationship, which forms a basis for cohesive crack models i.e. the fictitious crack model originally proposed by Hillerborg [16] and Hillerborg et al. [17] as well as the crack band model developed by Bazant et al. [18]. In the fictitious crack model, the principals parameters include the concrete tensile strength f_{ct} , modulus of elasticity E_c , fracture energy G_F , and the shape of the tensile stress-crack opening σ -w curve (Fig. 3.3). In case of PC, which is a brittle material, the σ -w shape does not vary significantly, therefore it is usually sufficient for engineering purposes to determine only the f_{ct} and G_F as well as adopt an appropriate σ -w curve. The G_F can be determined experimentally, analytically using simplified assumptions or based on other recommendations that can be found in standards and literature. In case of FRC the total fracture energy G_{FFRC} is composed of fracture energy of PC matrix (G_F) and the additional fracture energy resulting from the fiber bridging (G_{Ff}). Consequently, the shape of the σ -w curve can vary widely depending on the material, type, dosage, and orientation of fibers, concrete quality, and bonding strength. In order to comprehensively characterize the tensile behavior of FRC the experimental determination of the σ -w relationship is required.

However, due to the complexity and the challenges associated with direct uniaxial tensile tests, indirect methods are commonly employed such as flexural tests or splitting tensile tests typically followed by inverse analysis to estimate the tensile behavior [19]–[21]. Given that the shape of σ -w curve may be complex, analytical, and numerical analyses often require simplifications to enable practical implementation. Depending on the curve's shape, intended purpose of the analysis, and the assumed constitutive model, the σ -w relationship can be idealized as linear, bilinear, multi-, or polylinear, polynomial, or exponential.

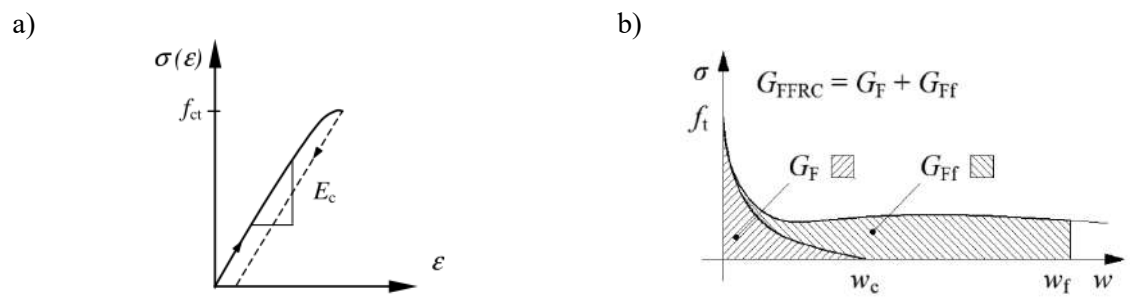


Fig. 3.3 Fictious crack model: a) stress-strain curve [14], b) stress-crack opening curve for FRC [22]

3.2.3. Theoretical models for ground slabs

3.2.3.1 Westergaard approach

The Westergaard model was developed around 1925 and formally published in 1926 [23]. It is based on the principles of elastic theory and incorporates the Winkler model for the design of concrete pavements. In this analytical approach, the infinite or semi- infinite slab is idealized as a homogenous, isotropic, and linearly elastic solid of constant thickness, fully supported by the underlying subgrade. The subgrade reaction is modeled as a system of independent, vertical, linearly elastic springs, with the magnitude of the reaction force being directly proportional to the deflection of the slab. The applied load is idealized as a uniformly distributed pressure over a small circular contact area. A key parameter in the model is the radius of relative stiffness *l*, which serves as an indication of the slab's flexural rigidity in relation to the supporting subgrade. It is important to note that the Westergaard model assumes purely elastic material behavior and therefore does not account for the post-cracking tensile capacity characteristic of FRC. The model provides analytical expressions to estimate the stress and deflection for three loading cases: interior loading, edge loading, and corner loading. Following its initial publication, the original equations proposed by Westergaard were

subsequently modified by Westergaard himself and other researchers. Today, the revised formulations, presented as equations (3.1)-(3.3), are widely used for evaluating the stress response under specific loading configurations. Additionally, the Westergaard approach has been supplemented with design charts and tabulated values to facilitate practical application. However, despite its widespread adoption, it has been consistently reported in the literature [24] that the failure loads observed in experimental tests are typically 3.0 to 4.5 times higher than those predicted by the Westergaard model, highlighting the conservative nature of the theoretical assumptions.

For an internal load:

$$\sigma_i = \frac{0.275P}{h^2} \cdot (1+v) \cdot \left[\log \left(\frac{E_{cm}h^3}{kb_r^4} \right) - 0.436 \right]$$
 (3.1)

For an edge load:

$$\sigma_e = \frac{0.529P}{h^2} \cdot (1 + 0.54v) \cdot \left[\log \left(\frac{E_{cm}h^3}{kb_r^4} \right) + \log \left(\frac{0.1b_r}{1 - v^2} \right) - 1.08 \right]$$
 (3.2)

For a corner load:

$$\sigma_c = \frac{3P}{h^2} \cdot \left[1 - \frac{12 \cdot 10^4 \cdot (1 - v^2) \cdot k}{E_{cm} h^3} \right]^{0.3} \cdot \left(0.1 a_r \sqrt{2} \right)^{1.2}$$
 (3.3)

where:

 σ_i , σ_e , and σ_c – stresses under internal, edge, and corner concentrated loading, respectively [N/mm²],

P – concentrated load [N],

h – slab thickness [mm],

v – concrete Poisson's ratio [-],

 E_{cm} – concrete modulus of elasticity [N/mm²],

k – modulus of subgrade reaction [N/mm³],

 b_r – equivalent radius of pressure distribution according to equation (3.4) or (3.5) [mm], a_r – radius of contact area of the load [mm].

For $a_r < 1.724h$

$$b_r = \sqrt{1.6a_r^2 + h^2} - 0.675h \tag{3.4}$$

For $a_r > 1.724h$

$$b_r = a_r \tag{3.5}$$

3.2.3.2 Falkner et al. approach

The Falkner et al. model was developed around 1995 based on a 3D Finite Element Model (FEM). This model enables the calculation of the maximum load-bearing capacity of centrally loaded rectangular or square slab with finite dimensions, as defined by equation (3.6). Similar to the Westergaard approach, it assumes the full contact between the slab and the ground and adopts the Winkler subgrade model, representing the subbase as a system of independent vertical elastic springs. However, in contrast to Westergaard's purely elastic approach, the Falkner et al. model is based on the plastic theory. Namely, it considers two critical conditions: the initial cracking load, corresponding to the initiation of tensile cracking as defined in Westergaard's formulation, and the ultimate load, which accounts for the slab's residual strength after cracking. By incorporating the post-cracking behavior of the material, particularly relevant in the case of FRC, the model provides a more realistic estimation of slab load-bearing capacity. Nevertheless, a limitation of the model is its applicability solely to centrally applied loads since it does not address edge or corner loading configurations. The assumed failure mechanism, which involves radial cracking and plastic hinging in the slab, is illustrated Fig. 3.4. As can be seen, the load-deflection curve can be divided into three distinct regions. The first region corresponds to the uncracked state of the slab and is characterized by linear elastic behavior prior to cracking. In the second region, primary radial cracks initiate at the center of the slab, directly beneath the applied load, and progressively propagate toward the edges. This stage marks the transition from elastic to inelastic behavior. Finally, the third region represents the plastic phase, during which moment redistribution occurs as yield lines develop throughout the slab. This phase continues until the ultimate failure of the structure.

For an internal load:

$$P_u = P_W \cdot \left[1 + \left(\frac{k}{E_{cm} h^3} \right)^{0.25} \cdot W \cdot \frac{\sqrt{A}}{h} \right] \cdot \left[1 + \frac{R_e}{100} \right]$$
 (3.6)

where:

 P_u – ultimate load-bearing capacity [N],

 P_W – first cracking load from Westergaard model [N],

k – modulus of subgrade reaction [N/mm³],

 E_{cm} – concrete modulus of elasticity [N/mm²],

h – slab thickness [mm],

W – slab width [mm],

 $A - \text{load area } [\text{mm}^2],$

 R_e – fracture toughness index obtained from the four-point bending test according to JSCE-SF4 standard [25] [%].

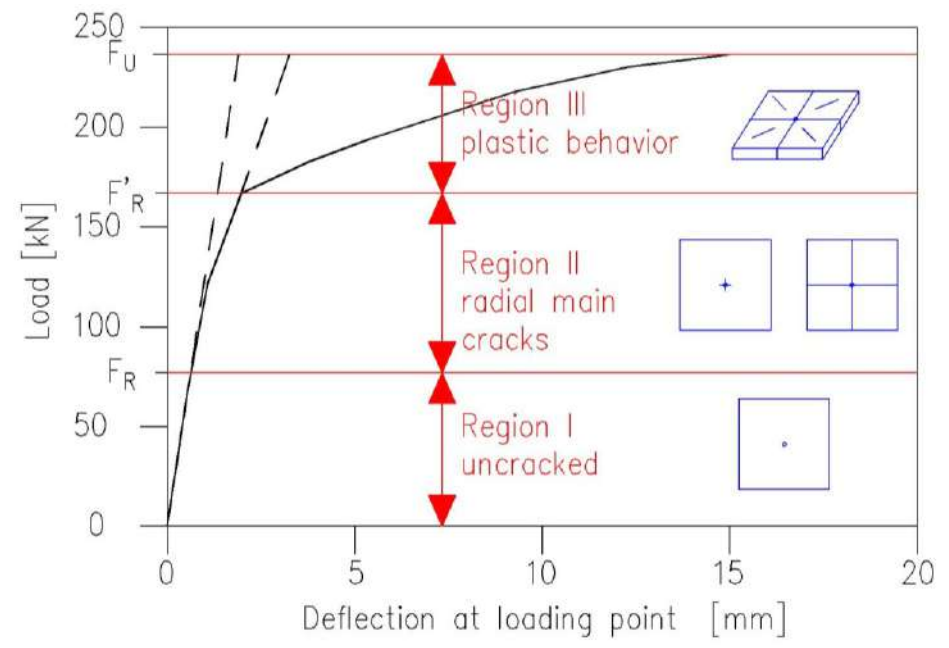


Fig. 3.4 Failure mechanism assumed in the Falkner et al. approach [26]

3.2.3.3 Shentu et al. approach

The model proposed by Shentu et al. (1997) [27], developed based on FEM analysis, enables the calculation of the load-bearing capacity of a centrally loaded slab, where the concentrated force is uniformly distributed over a small circular area, as expressed by equation (3.7). However, this approach does not consider edge or corner loading conditions, which are critical for comprehensive slab design. The infinite slab is idealized as a circular slab, horizontally restrained but free to move vertically. The model also accounts for the horizontal thrusts that are typically present in the slab. As for the subgrade, the Winkler foundation model is adopted. Additionally, the Shentu et al. model requires knowledge of the uniaxial tensile strength of concrete, a mechanical property that is difficult to determine accurately and typically necessitates complex experimental procedures.

For an internal load:

$$P_u = 1.72 \cdot \left[\left(\frac{ka_r}{E_{cm}} \right) \cdot 10^4 + 3.6 \right] \cdot f_{ct} \cdot h^2$$
 (3.7)

where:

 P_u – ultimate load-bearing capacity [N], k – modulus of subgrade reaction [N/mm³], a_r – radius of contact area of the load [mm], E_{cm} – concrete modulus of elasticity [N/mm²], f_{ct} – concrete uniaxial tensile strength [N/mm²], h – slab thickness [mm].

3.2.3.4 Meyerhof-Losberg approach

The Meyerhof-Losberg theory was developed in the early 1960s and allows for calculating the load-bearing capacity of ground slabs subjected to concentrated central, edge, and corner loading. Furthermore, it is applicable not only to single point loads but also to two- and four-point loads, line loads, and uniformly distributed loads acting on the slab. However, it does not provide information on slab deflections. In this approach, slab design for flexure at the ultimate limit state is based on yield line theory and plastic analysis. Namely, this method assumes that once the slab reaches its load-carrying capacity, plastic hinges form along predefined failure lines, enabling moment redistribution up to collapse. A crucial design requirement for ground-supported slabs is to prevent the formation of cracks on the upper surface, which may indicate serviceability failure or durability concerns. Therefore, the bending moment along hogging yield lines (negative moment) is limited to the concrete cracking moment [28]. On the other hand, the bending moment along sagging yield lines (positive moment) can be considered as the full plastic or residual post-cracking moment capacity [28]. In terms of failure mechanism, the Meyerhof-Losberg theory predicts a fan-type failure pattern. It is assumed to occur in large slabs supported by a linear-elastic subgrade (Winkler model) in full contact with the slab bottom. As the applied load increases, the flexural stresses at the bottom of the slab gradually approaches the concrete's flexural strength. Once this limit is reached, plastic behavior initiates, and radial cracks begin to form at the bottom of the slab due to positive tangential moments (Fig. 3.5). With continued loading, moment redistribution takes place within the slab, preventing any further increase in positive moments. Consequently, negative circumferential moments develop at a certain radial distance from the point of load application. When these negative moments exceed the slab's negative moment capacity, calculated based on PC section properties, tensile cracking appears at the top surface of the slab (Fig. 3.5). The ultimate capacity is considered to be reached when a circular crack is observed on the top surface.

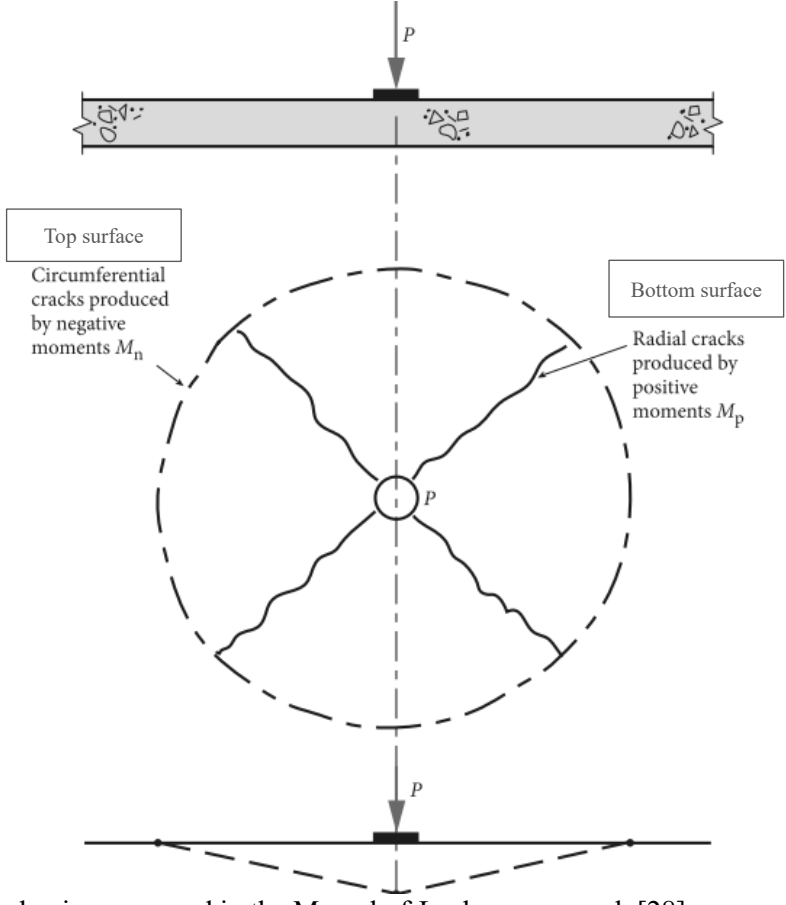


Fig. 3.5 Failure mechanism assumed in the Meyerhof-Losberg approach [28]

The following equations (3.8)-(3.20) present the calculation procedure for determining the maximum allowed concentrated load applied at the center, edge, and corner of an FRC slab, in accordance with the Meyerhof-Losberg approach. It must be mentioned that the linear interpolation of the a_r/l value within the range of 0 to 0.2 is permitted, as a reasonable agreement between theoretical predictions and experimental results has been demonstrated according to [28].

For an internal load:

$$a_r/l = 0$$

$$P_{u,0,i} = 2\pi \cdot (M_{un} + M_{up}) \tag{3.8}$$

 $a_r/l \ge 0.2$

$$P_{u,0.2,i} = 4\pi \cdot \frac{M_{un} + M_{up}}{1 - \frac{a_r}{3l}}$$
(3.9)

For an edge load:

$$a_r/l=0$$

$$P_{u,0,e} = \pi \cdot \frac{M_{un} + M_{up}}{2} + 2M_{un} \tag{3.10}$$

 $a_r/l \ge 0.2$

$$P_{u,0.2,e} = \frac{\pi \cdot \left(M_{un} + M_{up}\right) + 4M_{un}}{1 - \frac{2a_r}{3I}}$$
(3.11)

For a corner load:

 $a_r/l = 0$

$$P_{u,0,c} = 2M_{un} (3.12)$$

 $a_r/l \geq 0.2$

$$P_{u,0.2,c} = \frac{4M_{un}}{1 - \frac{a_r}{l}} \tag{3.13}$$

where:

 $P_{u,0,i}$ and $P_{u,0,2,i}$ – maximum single point load acting in the center of the slab calculated for a_r/l equals to 0 and 0.2, respectively [N],

 $P_{u,0,e}$ and $P_{u,0,2,e}$ – maximum single point load acting on the edge of the slab calculated for a_r/l equals to 0 and 0.2, respectively [N],

 $P_{u,0,c}$ and $P_{u,0,2,c}$ – maximum single point load acting in the corner of the slab calculated for a_r/l equals to 0 and 0.2, respectively [N],

 a_r – equivalent radius of contact area of the load (see Fig. 3.6) according to equation (3.14) [mm],

l – radius of relative stiffness according to equation (3.15) [mm],

 M_{un} – ultimate negative (hogging) resistance moment of the slab assumed to be that of the plain unreinforced concrete according to equation (3.16) [Nmm/mm],

 M_{up} – ultimate positive (sagging) resistance moment of the slab assumed to be that of the reinforced concrete according to equation (3.18) [Nmm/mm].

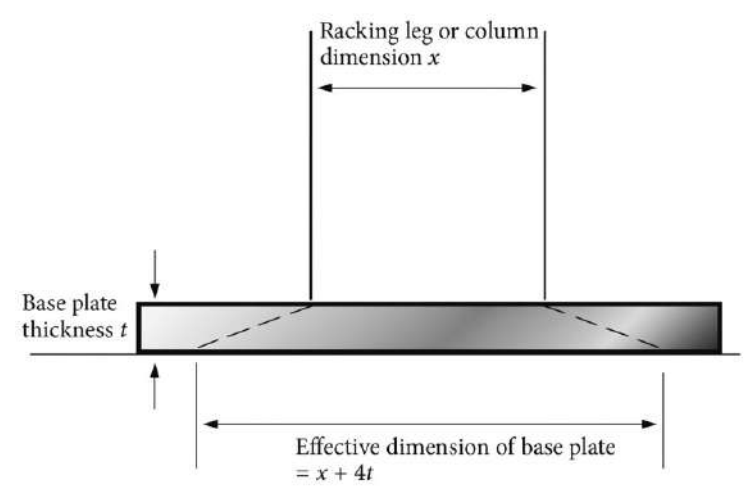


Fig. 3.6 Calculation of the effective dimension of the racking leg or column with a baseplate [28]

$$a_r = \sqrt{\frac{(x+4t)^2}{\pi}} \tag{3.14}$$

where:

x – racking leg base or column side dimension [mm],

t – baseplate thickness [mm].

$$l = \left(\frac{E_{cm} \cdot h^3}{12 \cdot (1 - v^2) \cdot k}\right)^{0.25} \tag{3.15}$$

where:

 E_{cm} – concrete modulus of elasticity [N/mm²],

h – slab thickness [mm],

v – concrete Poisson's ratio [-],

k – modulus of subgrade reaction [N/mm³].

$$M_{un} = \frac{f_{ctk,fl}}{\gamma_c} \cdot \frac{h^2}{6} \tag{3.16}$$

where:

 $f_{ctk,fl}$ – characteristic concrete flexural tensile strength according to equation (3.17) [N/mm²],

 γ_c – partial safety factor for concrete = 1.5 [-],

h – slab thickness [mm].

$$f_{ctk,fl} = f_{ctm} \cdot \left(1.6 - \frac{h}{1000}\right)$$
 (3.17)

where:

 f_{ctm} – mean concrete uniaxial tensile strength [N/mm²],

h – slab thickness [mm].

$$M_{up} = \frac{h^2}{\gamma_{fc}} \cdot (0.29\sigma_{r4} + 0.16\sigma_{r1}) \tag{3.18}$$

where:

h – slab thickness [mm],

 γ_{fc} – partial safety factor for FRC = 1.5 [-],

 σ_{rl} – mean axial tensile strength at the tip of the crack according to equation (3.19) $[N/mm^2]$,

 σ_{r4} – mean axial tensile strength at the tension face (the opening of the crack) according to equation (3.20) [N/mm²].

$$\sigma_{r1} = 0.45 f_{R,1}$$
 (3.19)
 $\sigma_{r4} = 0.37 f_{R,4}$ (3.20)

$$\sigma_{r4} = 0.37 f_{R.4} \tag{3.20}$$

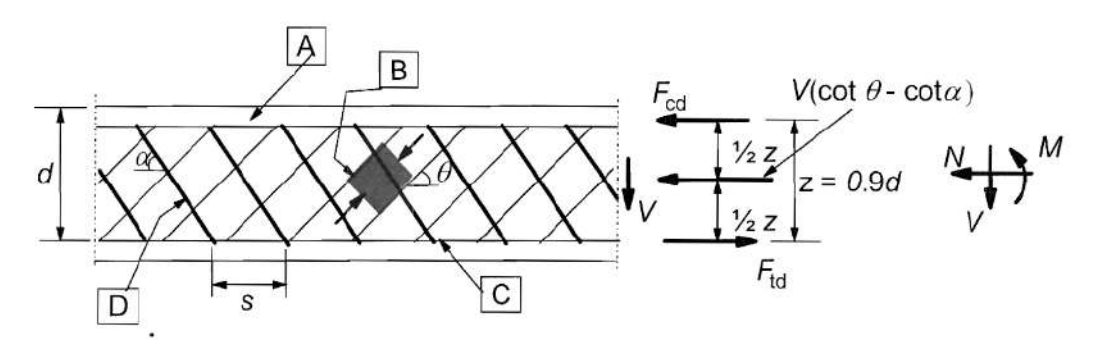
where:

 $f_{R,I}$ and $f_{R,4}$ – concrete residual flexural tensile strength at the crack mouth opening displacement CMOD = 0.5 mm and 3.5 mm, respectively defined from the three-point bending test according to PN-EN 14651 standard [29] [N/mm²].

One of the main differences between the Westergaard and Meyerhof-Losberg theories lies in the accounting of post-cracking behavior, particularly relevant for FRC slabs. While the Westergaard model is based on purely elastic assumptions and does not consider residual strength, the Meyerhof-Losberg model assumes the formation of plastic hinges at cracking locations, which enables plastic redistribution. This mechanism reflects the capacity of FRC slabs to continue carrying load even after cracking due to the bridging effect of fibers. Consequently, the Meyerhof-Losberg approach allows for a more realistic estimation of the ultimate load-bearing capacity of FRC ground-supported slabs. It is noteworthy that, according to findings reported in the literature [24], the ultimate loads predicted using the Meyerhof-Losberg model are typically about twice as high as those estimated by the Westergaard theory. However, they still remain approximately 1.5 to 2.0 times lower than the ultimate loads observed in experimental studies, highlighting the conservative nature of the model. Nevertheless, it is widely adopted for the design of both PC and FRC ground slabs, for instance in Technical Report 34 (TR34) [28].

3.2.4. Theoretical models for punching shear

The design of members subjected to shear is typically based on the truss model, also referred to as the strut-and-tie model, which is illustrated in Fig. 3.7. In this model, the internal force distribution is idealized by compressive struts and tensile ties, inclined at angles θ and α , respectively. The shear resistance of an unreinforced element is governed primarily by the capacity of the compression struts. Consequently, the accurate determination of the angle θ is critical for reliable shear design. However, identifying an appropriate value for θ remains a significant challenge, particularly in ground-supported elements, due to the additional contribution of the subgrade in transferring loads and soil-structure interaction.



A - compression chord, B - struts, C - tensile chord, D - shear reinforcement Fig. 3.7 Truss model for members subjected to shear according to PN-EN 1992-1-1:2008 [30]

Punching shear may occur when a slab or foundation is subjected to significant concentrated force or reaction acting over a relatively small area. Specifically, punching results from a localized shear failure in the vicinity of the loaded zone. Although it is analyzed similarly to standard shear, the correct identification of the shear perimeter is essential. In the design, the location of the critical control perimeter is closely related to the value of the inclination angle of the diagonal crack θ (Fig. 3.8). Its position depends, among other factors, on element's geometry, reinforcement, material properties, as well as loading conditions, including the shape, dimensions, and position of the loaded area on the slab surface. In thicker slabs, the critical crack typically forms at an angle θ between 40° and 60° , whereas in thinner slabs, this angle decreases to approximately 20° - 30° [31]. The distance from the edge of the loaded zone to the location of the critical control section, measured at an effective slab depth d, is denoted as a. It is worth mentioning that for FRC slabs d is typically taken as d = 0.75h, where h is the slab thickness (Fig. 3.8). Another key parameter in punching shear analysis is the length of the critical control perimeter, denoted as u and illustrated in Fig. 3.8.

In industrial ground-supported slabs, concentrated loads from racking systems and forklift operations represent one of the primary design considerations due to their potential to induce punching shear failure. Namely, forces transmitted through the legs of high-storage racks can reach magnitudes of up to 250 kN and when applied over relatively small contact areas, they may create a risk of exceeding the punching shear load-bearing capacity of the slab. In order to increase this capacity, the designers usually increase slab thickness, concrete compressive strength, dimensions of the loading

element (e.g., column cross-section or racking leg area), baseplate thickness, or/and the modulus of subgrade reaction. Ground-supported slabs are typically not reinforced with conventional punching shear reinforcement. Unlike columns in flat slabs, where the location of concentrated loads is predetermined, predicting the exact placement of racking legs or protecting entire vehicle aisles is often impossible. As a result, the contribution of distributed fiber reinforcement in the punching shear capacity of ground-supported slabs emerges as a promising field of application. However, despite the growing use of FRC in ground slabs, questions still arise regarding the influence of fibers on the cracking and load-bearing capacity, deformation characteristics, crack morphology, and failure mechanisms of slabs subjected to concentrated loading. It is also important to emphasize that the punching behavior of ground-supported slabs differs fundamentally from that of flat slabs due to the interaction with the subgrade, which contributes to the overall structural response.

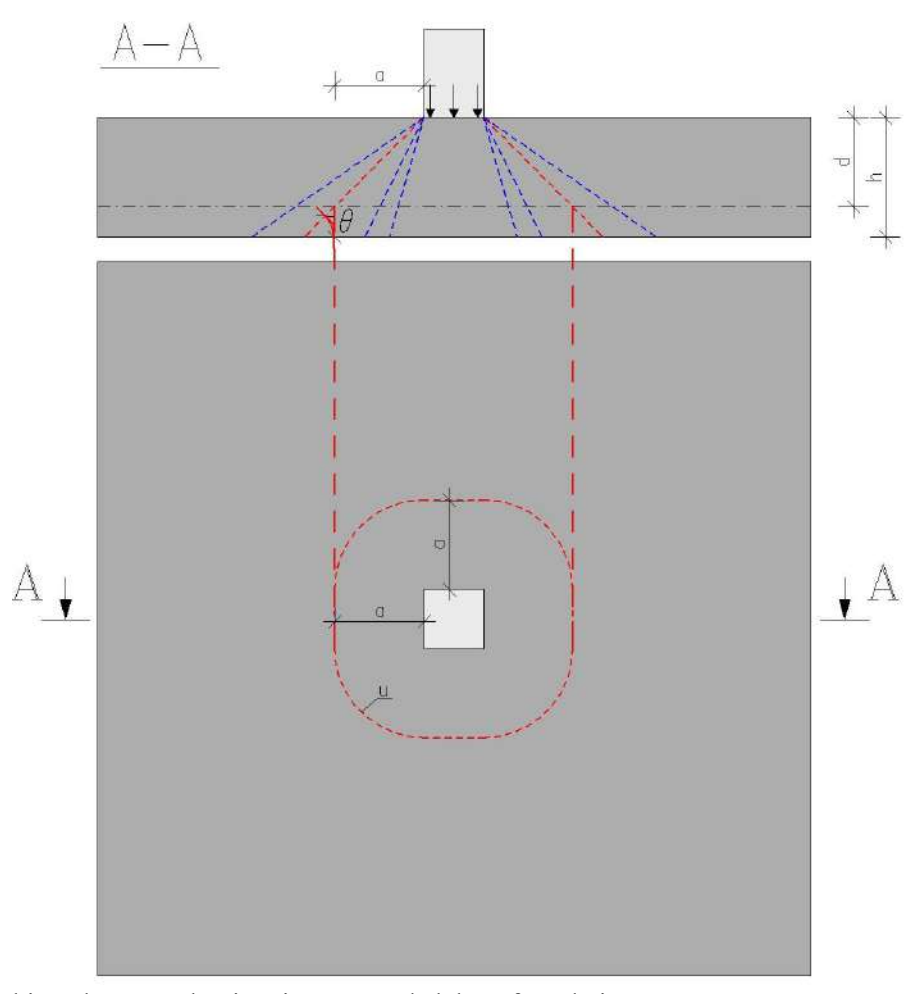


Fig. 3.8 Punching shear mechanism in a ground slab or foundation

In terms of design procedures, most standards and guidelines require verification of punching shear capacity both at the face of the loaded area and along a defined critical control perimeter. One of the most discussed aspects in the design of ground-supported slabs and foundations is the determination of the location of this critical control section. According to the former Polish standard PN-B-03264:2002 [32], the control perimeter was assumed at a distance of a = 1.0d from the edge of the loaded area, corresponding to a diagonal crack inclination angle θ of 45°. In contrast, PN-EN 1992-1-1:2008 [30] recommends assessing punching shear iteratively within a distance of 2.0d from the loaded area, since concentrated forces in ground-supported slabs are counteracted by significant soil pressure (as noted in clauses 6.4.2(2) and 6.4.4(2) of [30]). The most recent version of Eurocode 2, PN-EN 1992-1-1:2024 [33], defines the critical control section at a fixed distance of a = 0.5d from the loaded area, representing a significant modification compared to the earlier recommendations provided in [30]. Meanwhile, the TR34 guideline [28] adopts a critical control perimeter position at exactly a = 2.0dfrom the periphery of the loaded area, for which $\theta = 26.6^{\circ}$. As can be seen, the provisions for critical control section position adopted by various standards and design guidelines are inconsistent and may lead to confusion. Difficulties in adopting a fixed value of a result from the presence of ground support. Specifically, in elements subjected to high opposing pressure, the limiting shear strength v_{Rd} increases as the critical control perimeter approaches the edge of the loaded area (Fig. 3.9). However, the reduced punching shear force $V_{Ed,red}$, acting on the element, also increases. Namely, it depends on the base area of the theoretical punching cone, which affects the net soil capacity ΔV_{Ed} . In other words, the portion of the load acting within the critical control perimeter ΔV_{Ed} contributes to the capacity of the structural element since it may be subtracted when evaluating the permissible punching shear stress v_{Ed} , reflecting the favorable effect of soil support (Fig. 3.9). To summarize, as the distance a between the critical control section and the edge of the loaded area decreases the punching shear capacity $V_{Rd,c}$ along the considered control perimeter increases but also the acting reduced punching shear force $V_{Ed,red}$ increases, due to a smaller net upward soil reaction ΔV_{Ed} (i.e., a smaller area over which the soil force is subtracted). As a result, identifying a single definitive position of the critical control section becomes challenging. Consequently, it seems that it is necessary to evaluate multiple potential control perimeters and determine the one that corresponds to the highest ratio of applied shear stress to limiting shear strength v_{Ed}/v_{Rd} . If the condition $v_{Ed} \le v_{Rd}$ is not satisfied for even one of the considered control sections, then the ground-supported slab is considered to have insufficient punching shear load-bearing capacity.

```
For concentric loading the net applied force is V_{\rm Ed,red} = V_{\rm Ed} - \Delta V_{\rm Ed} where: V_{\rm Ed} \quad \text{is the applied shear force} \Delta V_{\rm Ed} \quad \text{is the net upward force within the control perimeter considered i.e. upward pressure from soil minus self weight of base.} v_{\rm Ed} = V_{\rm Ed,red}/ud v_{\rm Rd} = C_{\rm Rd,c} k (100 \, \rho f_{\rm ck})^{1/3} \times 2d \, l \, a \geq v_{\rm min} \times 2d \, a
```

Fig. 3.9 Determination of the limiting shear stress v_{Rd} and the permissible punching shear stress v_{Ed} according to PN-EN 1992-1-1:2008 [30]

To further clarify the punching shear phenomenon in ground-supported structures, the study conducted by Goldyn [31] is presented. In this work, the punching shear resistance of foundation was analyzed by considering control perimeters located at distances ranging from a = 0 to 2d from the edge of the column. Fig. 3.10a illustrates the relationship between the applied shear stresses v_{Ed} and the limiting shear strength v_{Rd} , expressed as a function of the a/d ratio. In all evaluated sections, the condition $v_{Ed} \le v_{Rd}$ was satisfied, leading to the conclusion that the punching shear capacity of the analyzed foundation was adequate. The maximum value of the ratio v_{Ed}/v_{Rd} was found to be 0.927, occurring at a control perimeter located at a = 1.25d from the column edge. Furthermore, the study examined the influence of subgrade stiffness by considering various Winkler coefficients: C = 25, 50, and 200 MPa/m. Fig. 3.10b presents the relationship between soil stiffness and the position of the critical control section, for which v_{Ed}/v_{Rd} reached its maximum value. It was observed that increasing soil stiffness resulted in the critical control perimeter shifting closer to the loaded area. Specifically, increasing the Winkler coefficient from 50 to 200 MPa/m reduced the distance of the critical control section from 1.35d to 1.20d. It was explained by the changes in the soil reaction distribution in the vicinity of the column. Goldyn emphasized that the impact of varying soil parameters may differ depending on the considered example. Therefore, when determining the reduced punching shear force $V_{Ed,red}$, the actual distribution of soil resistance beneath the element should be accurately taken into account [31].

Moreover, Nepelski [34] addressed the problem of determining the location of the critical control perimeter in the calculation of foundation punching shear capacity in accordance with PN-EN 1992-1-1:2008. His conclusions were consistent with those drawn by Gołdyn. Specifically, the graphs illustrating the relationship between the ratio v_{Ed}/v_{Rd} and a/d, developed for foundations with varying geometries, exhibited a parabolic shape (Fig. 3.11a). The curves reached their peak values at distances ranging from 0.55d to 1.40d, corresponding to critical diagonal crack inclinations θ between 35° and 61°. It is also noteworthy that in none of the analyzed cases, the maximum

utilization of punching shear capacity occurred at a distance of 2d from the loaded area. Furthermore, Nepelski demonstrated that as the net stresses beneath the foundation increased, the location of the most critical control section shifted closer to the column (Fig. 3.11b).

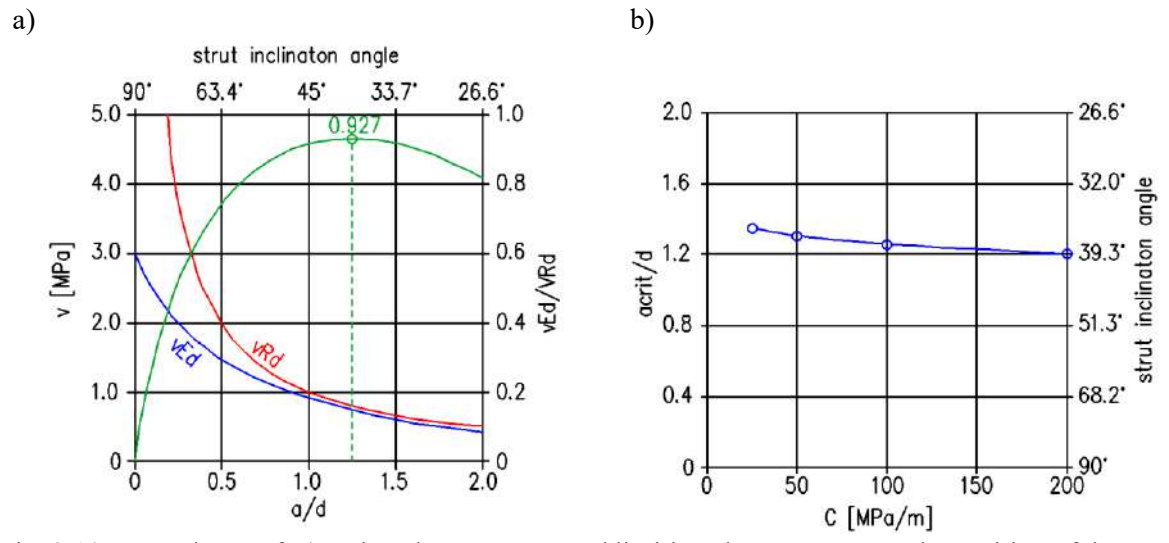


Fig. 3.10 Dependence of: a) acting shear stresses and limiting shear stresses on the position of the control perimeter, b) the position of the critical control perimeter on the soil stiffness under the foundation [31]

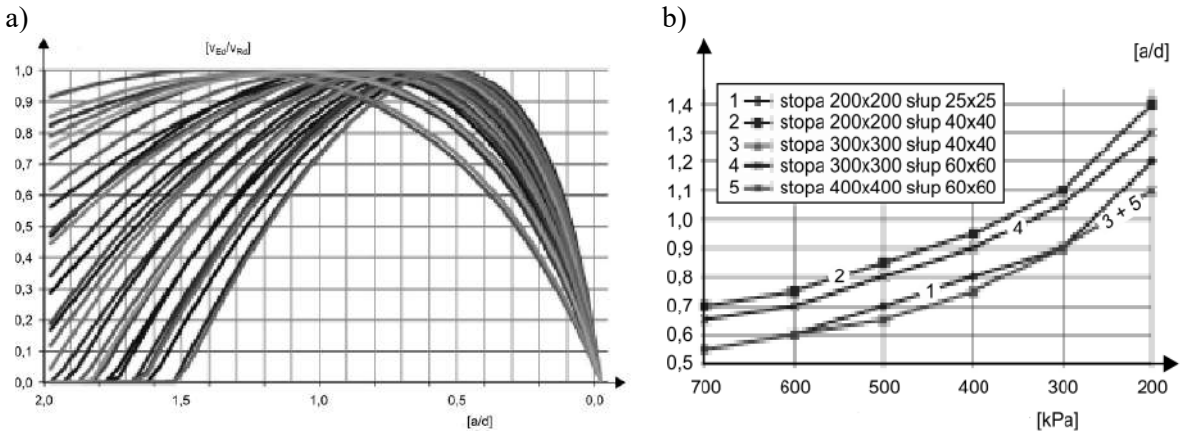


Fig. 3.11 a) Usage of punching shear capacity depending on the position of the control perimeter, b) distance of the critical control perimeter depending on the net stresses under the foundation (1 – foundation 200 x 200 cm, column 25 x 25 cm; 2 – foundation 200 x 200 cm, column 40 x 40 cm; 3 – foundation 300 x 300 cm, column 40 x 40 cm; 4 – foundation 300 x 300 cm, column 60 x 60 cm; 5 – foundation 400 x 400 cm, column 60 x 60 cm) [34]

In conclusion, numerous experimental, analytical, and numerical studies on ground-supported structures [31], [34]–[36] have shown that assuming the critical control perimeter at a usually assumed distance a = 2.0d often resulted in the overestimated punching shear capacities. Consequently, it has been concluded that the most accurate approach involves considering multiple potential control perimeters located between the edge of the contact area and 2.0d, with possible diagonal crack

inclination angles θ ranging approximately from 26.6° to 90°. Given that the iterative procedure for determining a is time-consuming and computationally demanding, some simplified methods have been proposed in the literature as alternative approaches. One such method, developed by the European Concrete Platform ASBL [37], is based on a performed comprehensive parametric study and presented in the form of design charts (Fig. 3.12). This graphical approach is primarily intended for foundation elements, as it is based on their typical geometrical configurations where the slab length-to-column width ratio (l/c) does not exceed value of 10. In contrast, ground-supported slabs often exhibit significantly higher l/c ratios, placing them usually outside the applicable range of these charts. Bonić et al. [12] concluded that the results obtained from the design charts were consistent with those derived through iterative calculations, confirming the applicability and accuracy of ASBL proposition.

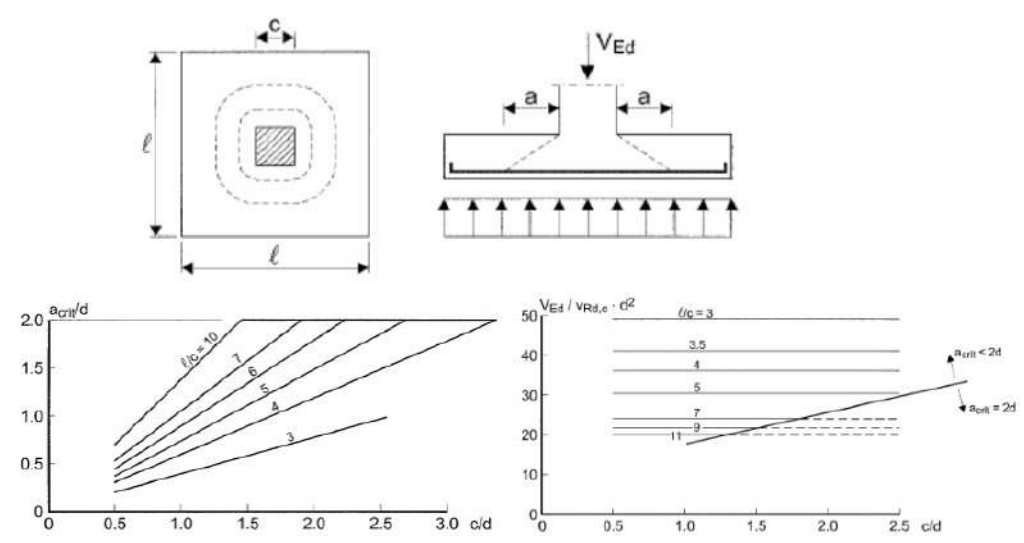


Fig. 3.12 Determination of the critical control section location and punching shear capacity according to the European Concrete Platform ASBL approach [37]

In a related study, Knauff and Knyziak [35] proposed other simplified method for verifying the punching shear load-bearing capacity. Their approach provides a direct procedure to identify the location of the critical control perimeter without requiring multiple iterations (Fig. 3.13). The publication [35] includes detailed algorithms, graphical tools, and illustrative examples to facilitate the implementation of the method. It also emphasizes its applicability to both slabs and foundations, provided that the critical control perimeter remains within the boundaries of the structural element. Importantly, the method complies with the PN-EN 1992-1-1 standard [30].

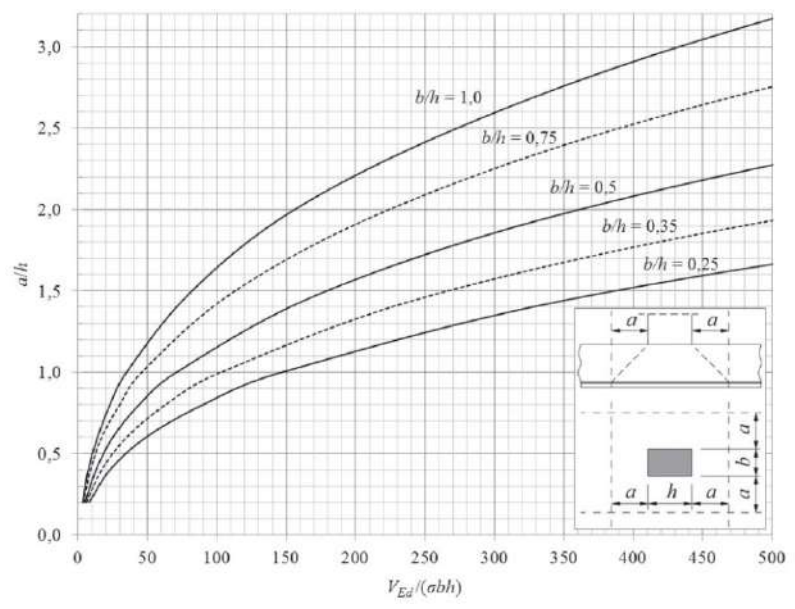


Fig. 3.13 Determination of the critical control section location according to the method proposed by Knauff and Knyziak [35]

3.2.5. Summary

The post-cracking strength of FRC, resulting from fibers bridging cracks and transferring tensile stresses across the crack faces, is the key mechanism that distinguishes FRC from conventional concrete which exhibits a sudden loss of tensile resistance after cracking. Therefore, an accurate representation of FRC's tensile behavior is essential for reliable structural assessment. Specifically, experimental tests are conducted to determine the relationship between tensile stress and crack opening. The resulting curves are then simplified according to the adopted constitutive laws and used in analytical and numerical calculations of FRC elements. Regarding the design of ground-supported slabs under concentrated loads, several analytical models have been selected for review. Namely, the assumptions, predicted failure loads, and expected failure mechanisms of Westergaard, Falkner et al., Shentu et al., and Meyerhof-Losberg approaches were discussed. It was also concluded that the experimentally obtained failure loads of tested FRC ground-supported slabs, as reported in the literature, are typically much higher, ranging from 3.0 to 4.5 times greater than those predicted by Westergaard's theory, and 1.5 to 2.0 times higher than those calculated using the Meyerhof-Losberg approach. This may be explained by the fact that not all of these analytical models consider the post-cracking behavior of FRC and the additional capacity provided by the inclusion of fibers in concrete. Moreover, most of them assume slabs of infinite dimensions, which differ significantly from the finite sizes of the tested specimens. Finally, the discussed approaches include simplifications and assumptions

that enable easier calculations while ensuring a conservative design approach what can lead to the capacity underestimation. When designing industrial ground-supported slabs, it is also necessary to verify their punching shear capacity in cases where concentrated forces are expected. In such calculations, the assumed location of the critical control perimeter plays a crucial role. Key parameters include the distance a from the loaded area to the critical control section, and the inclination angle θ of diagonal shear cracks. Moreover, due to the additional response of the subbase, punching shear capacity in ground slabs should be analyzed separately from that in flat slabs. It has been concluded that assuming a fixed value of a may result in either an overestimation or underestimation of the punching shear capacity. Therefore, the most appropriate approach is to consider multiple potential critical control sections located between the perimeter of the loaded area and a distance of a = 2d, with possible inclination angles θ ranging from 26.6° to 90°. This is because a smaller distance a leads to a higher calculated punching shear capacity, but also to a higher acting shear force, as less ground area contributes to load resistance. Consequently, the critical control section corresponding to the highest ratio of acting to allowable shear stress should be identified. Since the iterative procedure to find this ratio may be time-consuming, the literature provides simplified methods, often in the form of diagrams or formulas, to determine the location of the critical control section. However, these methods are generally developed for foundations, with relatively fewer solutions available for slabs on ground.

3.3. Standards

3.3.1. Introduction

Despite growing knowledge and experience, FRC continues to raise concerns among designers, and its range of applications remains relatively limited, particularly in the case of SyFRC. To systematize existing knowledge, several standards and guidelines have been developed, addressing both testing methods and structural design using FRC. In addition, a few guidelines specifically focused on FRC ground slabs are available in the literature, as this represents one of the primary areas of fiber application. This chapter reviews selected standards for testing and designing FRC, with particular emphasis on the design of ground-supported slabs against punching shear failure, which is the primary topic addressed in this dissertation.

3.3.2. Standards for testing FRC

The assessment of the basic mechanical properties of FRC, such as compressive strength and modulus of elasticity, is conducted in the same manner as for conventional PC. These properties are typically evaluated in accordance with PN-EN 206 [38], PN-EN 12390-3 [39], and related standards. In general, the compressive behavior of FRC closely resembles that of PC, as the presence of fibers has a relatively minor influence on compressive strength (Fig. 3.14).

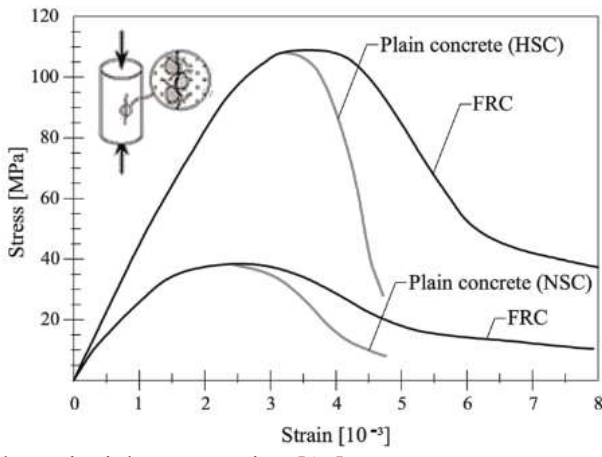


Fig. 3.14 PC and FRC under uniaxial compression [15]

On the other hand, the tensile behavior represents a key aspect of FRC, as it is characterized by a ductile response in the post-elastic deformation range (Fig. 3.15). Consequently, the post-cracking tensile capacity, commonly referred to as the residual or equivalent tensile strength, must be determined. For this purpose, several experimental methodologies are available and standardized. The uniaxial tensile test provides a direct measurement of the tensile strength of concrete. However, it is generally not recommended for standard evaluation of new mixtures, due to its complexity in both execution and interpretation. The test requires rigorous control of loading conditions, elimination of eccentricities, and the precise preparation of specimens. Moreover, the relatively small size of typically used samples can result in an insufficient number of fibers intersecting the critical crack plane, as well as fiber orientation effects related to the casting process. As an alternative, bending tests are often employed to evaluate the tensile behavior of FRC indirectly [40]. These tests result in load-deflection curves, which can be used to derive stress-crack width relationships through inverse analysis. Flexural tensile tests are generally easier to perform and less time-consuming than direct tensile tests. Standard configurations include three-point or four-point bending tests on notched or unnotched prismatic beams. However, it should

be noted that in such tests significant amount of elastic energy is stored in the beam samples, which may influence the results. Additional indirect methods for assessing FRC tensile strength include splitting tensile tests, such as the Brazilian test, Wedge Splitting Test, Double Wedge Splitting Test, and the Montevideo test. It is important to note that not all of these methods are standardized, nor are they commonly incorporated into design procedures for FRC structural elements. In the following chapters, selected testing methodologies suitable for characterizing the tensile behavior of FRC will be presented and discussed in detail.

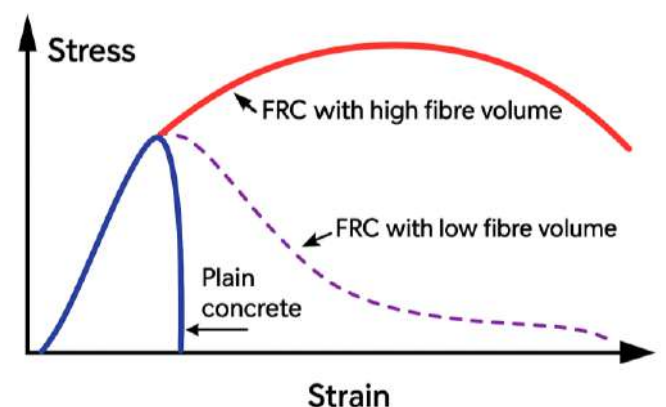


Fig. 3.15 Comparison of stress-strain response of PC and FRC [41]

3.3.2.1 Uniaxial tensile tests

One of the most widely adopted methodologies for uniaxial direct tensile testing is described by the Japan Society of Civil Engineers (JSCE) in [42]. Testing Method 2 is specifically designed for High Performance Fiber Reinforced Cement Composites characterized by multiple fine cracking behavior. In this procedure, dog-bone-shaped specimens with dimensions shown in Fig. 3.16a are used. It should be noted that the recommended specimen dimensions apply to samples whose minimum size is at least twice the maximum aggregate size and at least equal to the fiber length. For specimens outside these criteria, dimensions must be individually determined. Furthermore, the recommendations in [42] indicate that the size effect is negligible for specimen thicknesses ranging from 13 to 50 mm. Prior to testing, the specimen is secured between two grips shaped to fit the sample, ensuring that the tensile load is applied precisely along the specimen's central axis. Two linear variable differential transformers (LVDTs), attached to an aluminum jig or a similar holder, measure the elongation of the specimen. Throughout the test, the applied force and the corresponding displacement, measured between the reference points, are continuously recorded (Fig. 3.17).

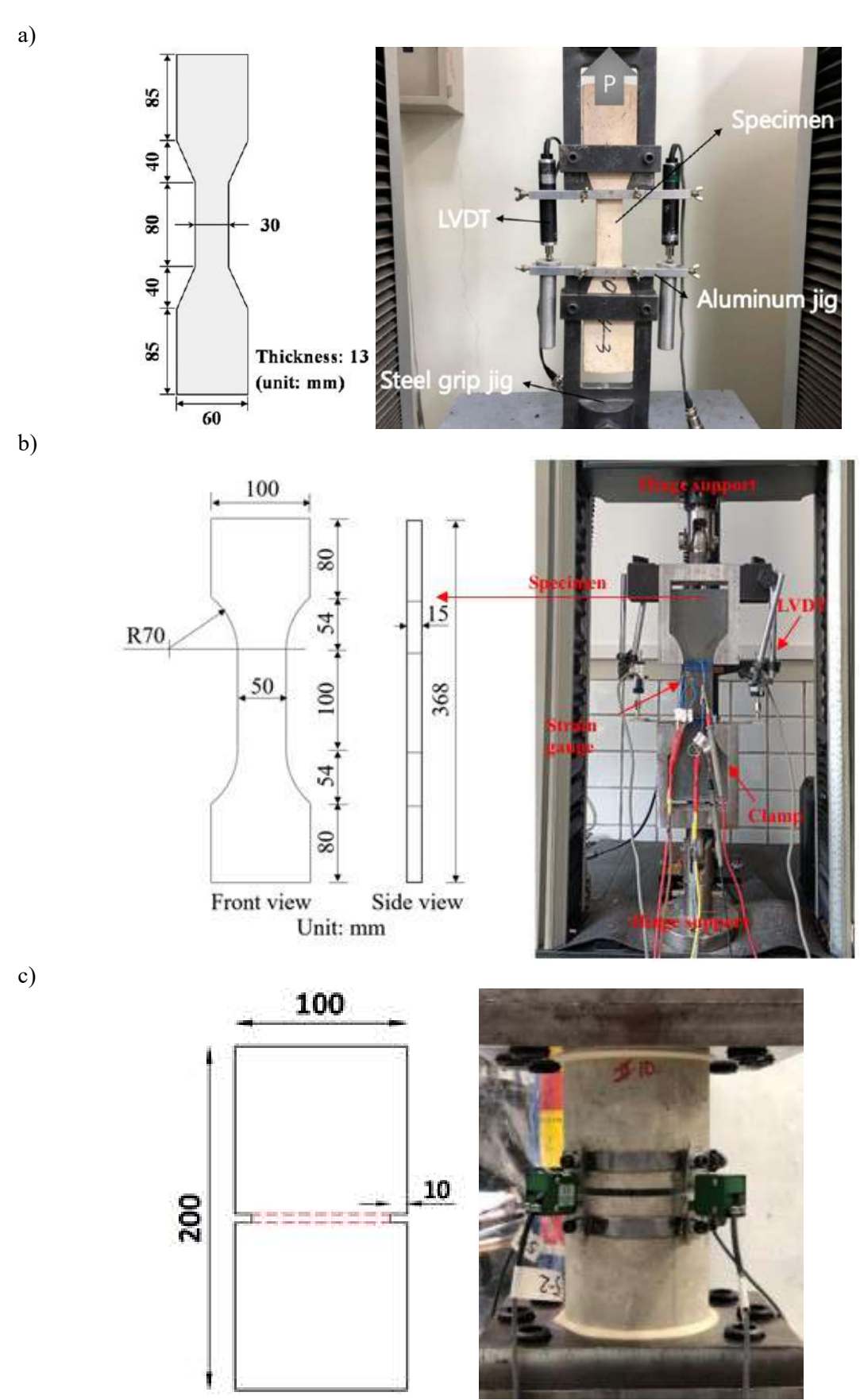


Fig. 3.16 Uniaxial tensile tests on: a) dog-bone samples [43], b) dog-bone samples [44], c) cylinders with a groove [45]

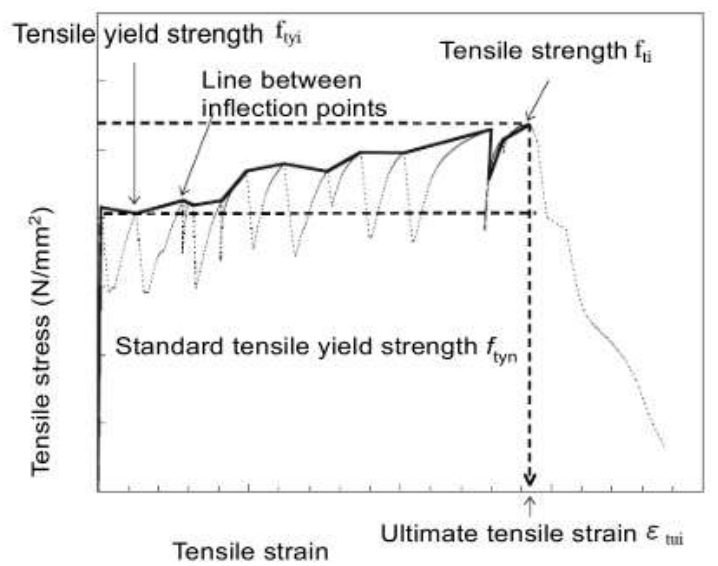


Fig. 3.17 Graph obtained from the uniaxial tensile tests performed according to [42]

Following the methodology outlined in [42], tensile yield strength, maximum stress in the strain-hardening region, tensile strength, and ultimate tensile strain can be calculated using equations (3.21), (3.22), (3.23) and (3.24), respectively. Finally, it is important to emphasize that the test results are valid only if the fracture occurs within the measured gauge length.

$$f_{tyi} = \frac{F_{ty}}{A_0} \tag{3.21}$$

where:

 f_{tyi} – concrete tensile yield strength [N/mm²],

 F_{ty} – load at the yield point [N],

 A_0 – initial sectional area of sample test zone [mm²].

$$f_{pshi} = \frac{F_{psh}}{A_0} \tag{3.22}$$

where:

 f_{pshi} – maximum stress in the strain-hardening region [N/mm²],

 F_{psh} – maximum load in the strain region between yield and softening starting point [N], A_0 – initial sectional area of the sample test zone [mm²].

$$f_{ti} = \frac{F_t}{A_0} \tag{3.23}$$

 f_{ti} – concrete tensile strength [N/mm²],

 F_t – maximum load [N],

 A_0 – initial sectional area of the sample test zone [mm²].

$$\varepsilon_{tui} = \frac{l_u - l_0}{l_0} \cdot 100 \tag{3.24}$$

where:

 ε_{tui} – ultimate tensile strain [%],

 l_u – reference point distance at the ultimate point [mm],

 l_0 – original reference point distance [mm].

A similar methodology for uniaxial tensile testing is proposed in the Chinese Standard GB/T 50081-2019 [46], which is dedicated to conventional concrete, and in CECS 13-2009 [47], which focuses specifically on FRC. In both standards, dog-bone-shaped specimens, with slightly modified dimensions compared to those in [42], are tested using a similar setup. In the study presented in [44], in addition to LVDTs, strain gauges were installed in both the longitudinal and transverse directions to measure tensile strains and determine Poisson's ratio (Fig. 3.16b). In the literature, methodologies for performing uniaxial direct tensile tests on concrete specimens extracted from existing structures have also been proposed. For instance, Nilimaa and Nilforoush [45] describe a method employing cylindrical specimens with a circumferential groove positioned at mid-height, intended to ensure crack initiation and propagation in a predefined region. Crack opening measurement devices are mounted on four orthogonal sides around the groove, using two steel belts fixed above and below the grooved section to facilitate installation. Additionally, the flat ends of the cylinder are adhesively bonded to steel plates, which are subsequently fastened to the testing machine. The specimen dimensions and test configuration are illustrated in Fig. 3.16c. The test provides the load-crack width relationship, from which key tensile properties can be derived. These include the maximum tensile strength, the maximum crack width (defined as the crack width corresponding to zero stress), and the associated deformations. Furthermore, the fracture energy can be determined as the area under the stress-crack width curve.

3.3.2.2 Splitting tensile tests

One of the most widely recognized methods for evaluating splitting tensile strength is the Brazilian splitting test, as described in ASTM C496-96 [48] and PN-EN 12390-06 [49]. In this procedure, a cylindrical or prismatic specimen is subjected to a compressive load applied over a narrow contact strip along its longitudinal axis (Fig. 3.18), generating tensile stresses perpendicular to the loading plane. Failure occurs when these transverse tensile stresses exceed the tensile strength of concrete at the center of the sample (Fig. 3.19). The splitting tensile strength of a cylindrical concrete specimen is determined using equation (3.25). It is worth noting that this method can be applied to both cast and core-drilled specimens. According to PN-EN 1992-1-1:2008 [30], the axial tensile strength f_{ct} may be estimated from the splitting tensile strength f_{spl} , using the relation $f_{ct} = 0.9 f_{spl}$ (formula (3.3) in [30]).

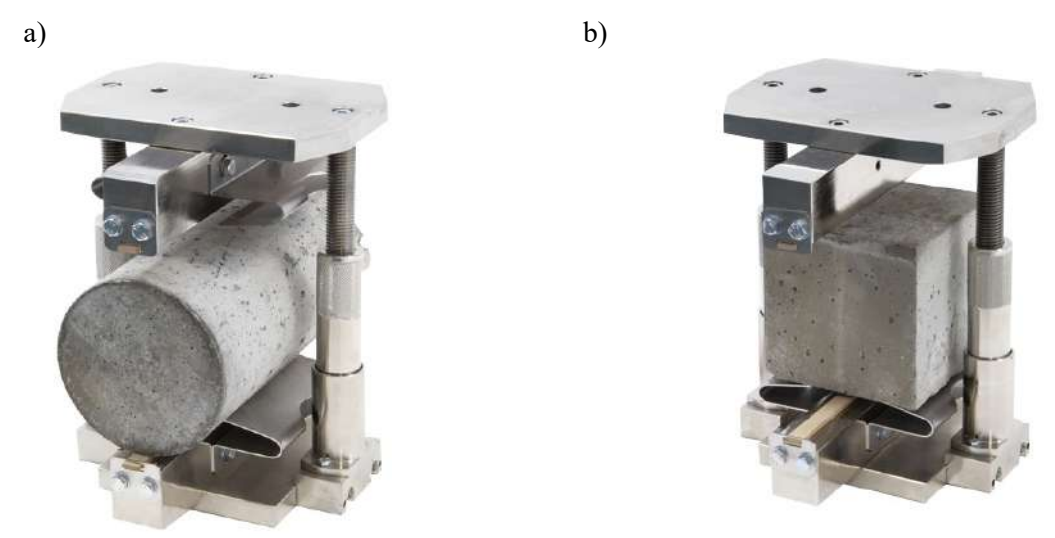


Fig. 3.18 Brazilian splitting tensile tests on: a) cylindrical sample, b) cubic sample [50]

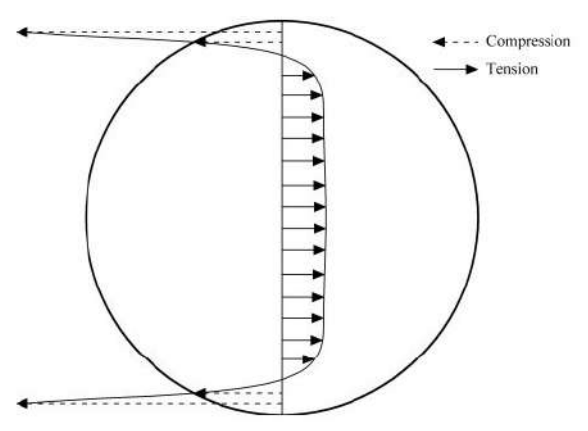


Fig. 3.19 Stress distribution along the loading axis of a cylindrical sample during a Brazilian splitting tensile test [51]

$$f_{spl} = \frac{2F}{\pi L d} \tag{3.25}$$

 f_{spl} – concrete splitting tensile strength [N/mm²],

F – maximum vertical load [N],

L – length of the sample's line of contact [mm],

d – diameter of the sample [mm].

Another widely recognized method for characterizing the tensile behavior of concrete is the Wedge Splitting Test (WST), originally patented and thoroughly described by Linsbauer and Tschegg [52]-[54], and further examined by other researchers [52]–[54]. The test setup and the force arrangement during the experiment are illustrated in Fig. 3.20a and Fig. 3.20b, respectively. To further simplify the methodology of the WST, Segura-Castillo et al. introduced a modified approach known as the Montevideo Test (MVDT) [55], [56]. In this variant, the number of cuts in the specimen is reduced to a single notch, and the three-part loading assembly of the traditional WST (i.e., the wedge, wedge-loading fixture, and load transmission plates with roller bearings) is replaced by a solid wedge with a simplified geometry and reduced dimensions compared to the original setup (Fig. 3.20c and Fig. 3.20d). The author of this dissertation successfully conducted MVDT experiments on SyFRC specimens, the results of which are described in [57]–[60]. One of the key findings from these studies was the determination of a load correlation coefficient, $k_{MVDT} = 1.5$, enabling the conversion of MVDT results into equivalent values obtained from the three-point bending test. Both WST and MVDT are considered stable and relatively straightforward testing methods, which can be executed using standard testing machines under displacement-controlled conditions. The specimens are typically compact, including standard cubes, cylinders, or core-drilled samples [61]. Moreover, a significant advantage of these tests is the stable crack propagation, attributed to the low amount of stored elastic energy and the presence of a compressive stress field ahead of the crack tip [20]. Additionally, the influence of the specimen's self-weight is negligible due to its minimal effect on the measured response [20]. Finally, WST and MVDT methods can be considered compact alternatives to the three-point bending test what is illustrated in Fig. 3.21a. As a replacement for the uniaxial tensile test, Prisco et al. proposed the Double Edge Wedge Splitting Test (DEWST) [62], depicted in Fig. 3.21b. In DEWST, a vertical load is applied through two steel rods placed in triangular notches

with inclined faces (Fig. 3.20e), effectively diverting the compressive stress trajectories away from the plane of symmetry (Fig. 3.20f). However, it is important to account for the relatively small thickness of DEWST specimens, as it may influence fiber distribution and consequently the results.

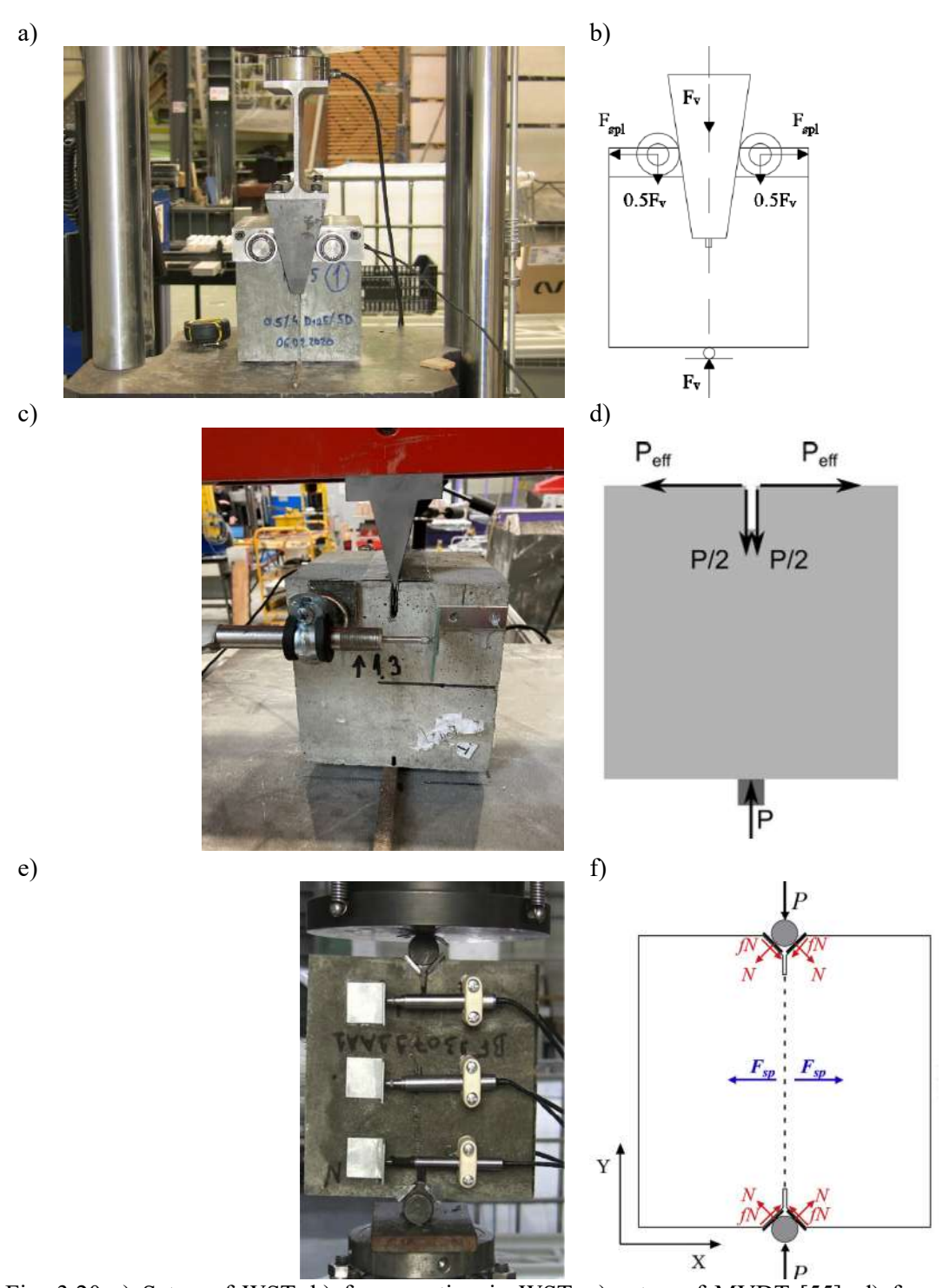


Fig. 3.20 a) Setup of WST, b) forces acting in WST, c) setup of MVDT [55], d) forces acting in MVDT [55], e) setup of DEWST [63], f) forces acting in DEWST [63]

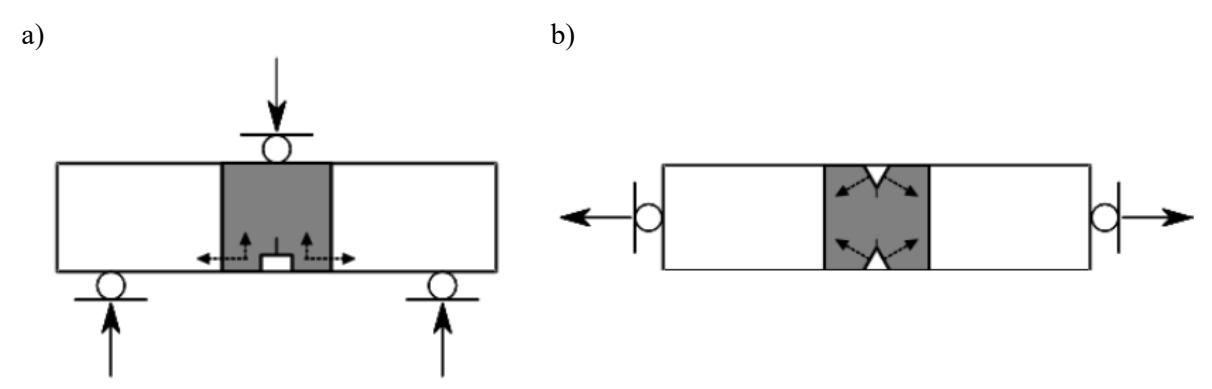


Fig. 3.21 a) WST and MVDT as a compact three-point bending test, b) DEWST as a compact uniaxial tensile test [62]

All three presented splitting tensile tests: WST, MVDT, and DEWST allow for the indirect determination of concrete tensile strength. However, when using equation (3.26), it must be emphasized that the splitting force (F_{spl} , P_{eff} or F_{sp} as referred to in Fig. 3.20) is not equal to the vertical force (F_v or P) applied through the wedge or the rod. This difference results from the influence of specimen geometry, the inclination angle of the wedge, and the friction coefficient between the wedge or rod and the concrete specimen.

$$f_{spl} = \frac{F_{spl}}{bh_{sp}} \tag{3.26}$$

where:

 f_{spl} – concrete splitting tensile strength [N/mm²],

 F_{spl} – maximum splitting force [N],

b – width/thickness of the sample [mm],

 h_{sp} – distance between the tip of the notch and the bottom of the specimen or distance between the tips of the notches of the specimen [mm].

3.3.2.3 Flexural tensile tests

Standard PN-EN 12390-05

Standard PN-EN 12390-5:2019 [64] defines a testing procedure for determining the maximum flexural strength of concrete. This method is intended for concretes without fibers and therefore does not include provisions for characterizing post-cracking behavior. The testing setup, illustrated in Fig. 3.22, represents a four-point bending test (4PBT), consisting of two supporting rollers and two loading rollers. The span between the rollers is equal to d, which corresponds to the specimen width. The samples are required to be unnotched prisms, however, the standard also permits the testing of sawn

beams. During testing, the load shall be applied with a constant rate of stress increase ranging between 0.04 MPa/s and 0.06 MPa/s. Upon reaching the maximum load, the test is terminated, and the maximum flexural strength is calculated according to equation (3.27).

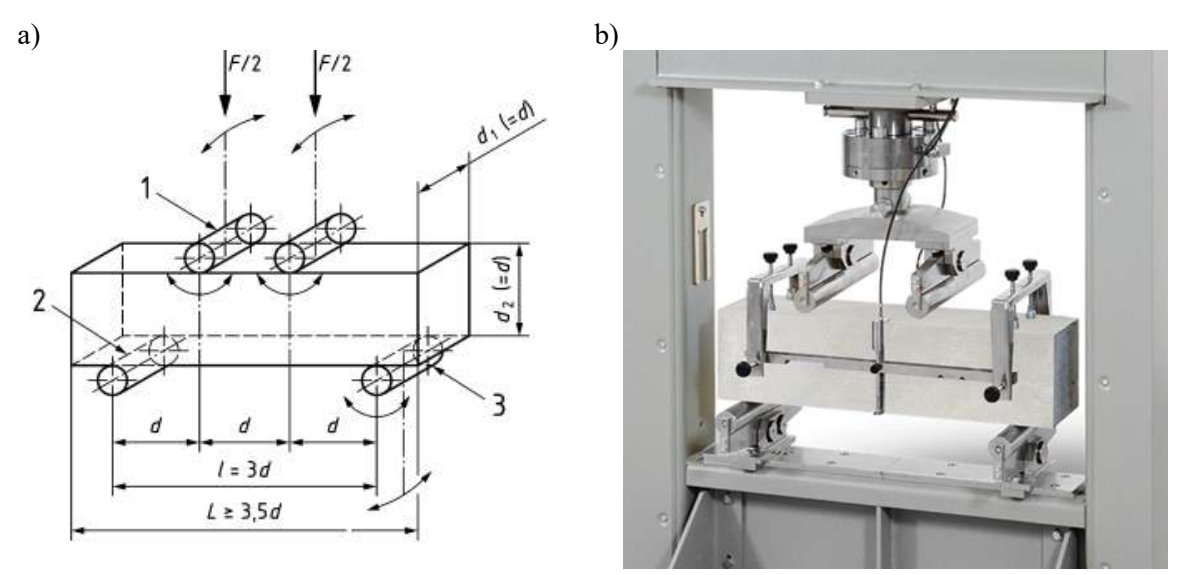


Fig. 3.22 a) Setup for 4PBT according to PN-EN 12390-5:2019 [64], b) 4PBT on the unnotched beam sample [65]

$$f_{cf} = \frac{F \cdot l}{d_1 \cdot d_2^2} \tag{3.27}$$

where:

 f_{cf} – concrete maximum flexural strength [N/mm²],

F – maximum load [N],

l – distance between the supporting rollers [mm],

 d_1 and d_2 –lateral dimensions of the sample [mm].

Standard PN-EN 14651

Standard PN-EN 14651 [29] specifies a testing method for concrete reinforced with metallic fibers up to 60 mm in length, as well as with combinations of metallic fibers with other fiber types. This method enables the determination of the limit of proportionality (LOP) and residual flexural tensile strengths based on the three-point bending test (3PBT) conducted on notched beam specimens. The test specimens should have nominal dimensions of 150 mm in width and depth, with a length ranging from 550 to 700 mm. To create the notch, the prism is rotated 90° about its longitudinal axis and then sawed across its entire width at the midspan, so that the top surface during

casting becomes the side surface during testing. The notch dimensions must not exceed 5 mm in width and 25 mm in depth. In the tests, the prism specimens should be positioned between the support rollers and accurately centered to ensure that the applied load (F) is introduced at the midspan, as illustrated in Fig. 3.23. When the crack mouth opening displacement (CMOD, see Fig. 3.24) is measured, a clip gauge is installed at the mid-width of the bottom surface of the specimen (Fig. 3.23). Alternatively, when deflection (δ) is monitored, a dedicated rigid frame is attached to the specimen to facilitate the mounting of LVDTs. When the testing machine operates under CMOD-controlled conditions, the crack mouth opening displacement should increase at a constant rate of 0.05 mm/min up to a CMOD value of 0.1 mm, and subsequently at a rate of 0.2 mm/min. The test may be terminated once a CMOD value exceeding 4 mm is recorded. It is worth noting that, alternatively, the displacement rate may be controlled based on midspan δ instead of CMOD. In such cases, the CMOD values must be converted to their δ equivalents. For this purpose, standard PN-EN 14651 [29] provides equation (3.28), which defines the relationship between CMOD and δ .

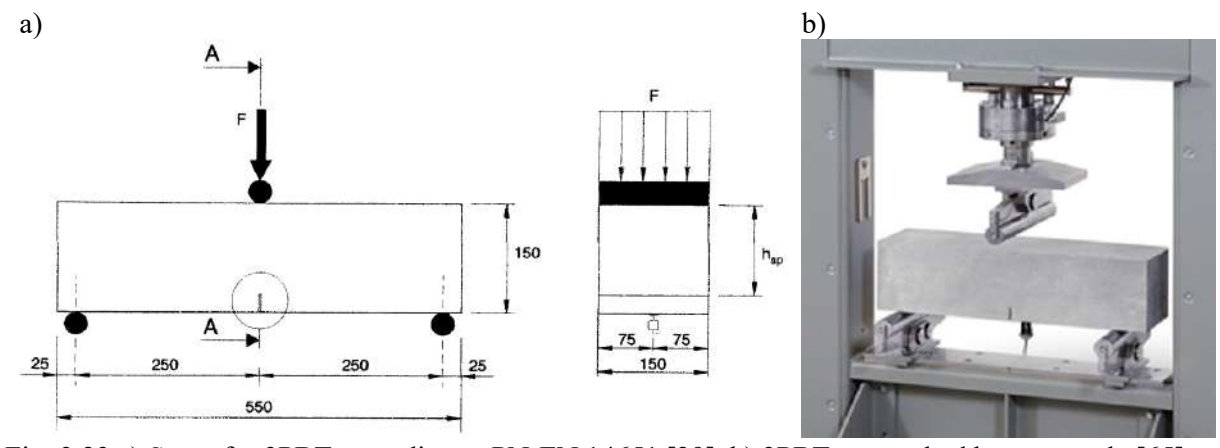
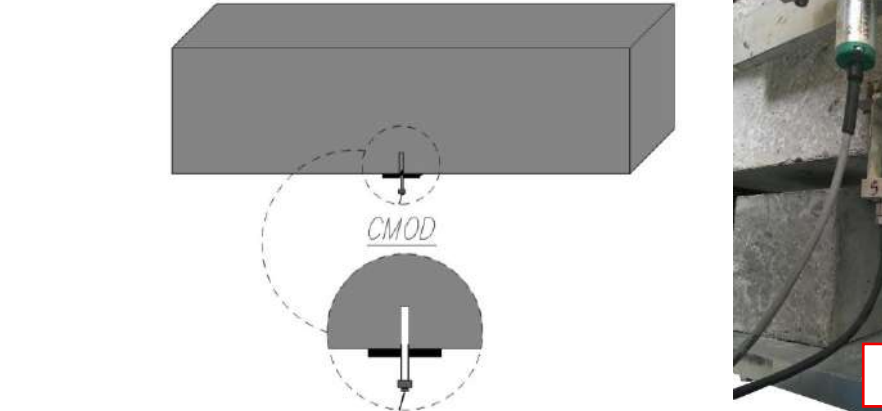
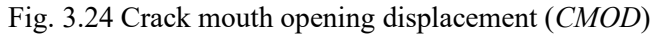


Fig. 3.23 a) Setup for 3PBT according to PN-EN 14651 [29], b) 3PBT on notched beam sample [65]







$$\delta = 0.85CMOD + 0.04 \tag{3.28}$$

 δ – deflection [mm],

CMOD – crack mouth opening displacement [mm].

The flexural tensile behavior of FRC is characterized based on the F-CMOD (Fig. 3.25) or F- δ response obtained during 3PBT. The limit of proportionality ($f_{ct,L}$) corresponds to the load F_L , while the residual flexural tensile strengths $(f_{R,j})$ are determined based on loads F_1 , F_2 , F_3 , and F_4 , corresponding with CMOD values of 0.5 mm, 1.5 mm, 2.5 mm, and 3.5 mm, respectively. When F- δ is used, F_1 , F_2 , F_3 , and F_4 corresponds to $\delta_1 = 0.47$ mm, $\delta_2 = 1.32$ mm, $\delta_3 = 2.17$ mm, and $\delta_4 = 3.02$ mm, in accordance with equation (3.28). The values of $f_{ct,L}$ and $f_{R,j}$ are calculated using equations (3.29) and (3.30), respectively.

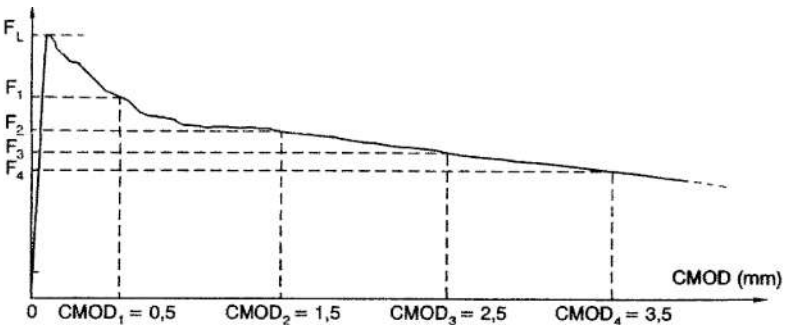


Fig. 3.25 F-CMOD diagram from 3PBT according to PN-EN 14651 [29]

$$f_{ct,L}^{f} = \frac{3F_L l}{2bh_{sp}^2}$$

$$f_{R,j} = \frac{3F_j l}{2bh_{sp}^2}$$
(3.29)

$$f_{R,j} = \frac{3F_j l^2}{2bh_{\rm SD}^2} \tag{3.30}$$

where:

 $f_{ct,L}$ – concrete limit of proportionality [N/mm²],

 $f_{R,j}$ – concrete residual flexural tensile strength corresponding to $CMOD = CMOD_j$ or $\delta = \delta_i \ (j = 1, 2, 3, 4) \ [\text{N/mm}^2],$

 F_L – load corresponding to the limit of proportionality [N],

 F_i – load corresponding to $CMOD = CMOD_i$ or $\delta = \delta_i$ (i = 1, 2, 3, 4) [N],

l – distance between the supporting rollers [mm],

b – width of the sample [mm],

 h_{sp} – distance between the tip of the notch and the top of the specimen [mm].

Standard RILEM TC 162-TDF

RILEM TC 162-TDF [66] describes testing and design methodologies for SFRC, based on the σ - ε (stress-strain) approach, which follows the same principles as those applied in conventional reinforced concrete design. The proposed methodology is applicable to SFRC with compressive strengths up to class C50/60. Although SFs may also be incorporated into high strength concrete, particular attention must be paid to ensure that fiber fracture does not occur in a brittle manner prior to fiber pull-out. The guideline emphasizes that the provided design approach is intended for cases where SFs are used for structural purposes. Consequently, it explicitly states that the methodology is not suitable for elements such as slabs on ground. In such applications, fibers are not considered as a structural reinforcement but are instead intended to improve properties such as shrinkage control, abrasion resistance, or impact resistance [66].

RILEM TC 162-TDF [66] also proposes the indirect determination of tensile strength by conducting the 3PBT on notched beams. The testing procedure closely follows the methodology described in PN-EN 14651 [29]. Both the maximum and residual flexural tensile strengths are derived from F-CMOD (Fig. 3.26) or F- δ curves, based on the previously discussed equations (3.29) and (3.30). Moreover, RILEM TC 162-TDF [66] classifies the SFRC using the residual strength class FL expressed as $FL_{0.5}/FL_{3.5}$. The first parameter, $FL_{0.5}$, is obtained by rounding down the residual flexural tensile strength $FL_{0.5}$ to the nearest multiple of 0.5 MPa and may range from 1 MPa to 6 MPa. The second parameter, $FL_{3.5}$, is determined by rounding down $f_{R,4}$ to the nearest multiple of 0.5 MPa, and may range from 0 MPa to 4 MPa. These two parameters represent the minimum guaranteed characteristic values of residual flexural tensile strength at CMOD of 0.5 mm and 3.5 mm, respectively.

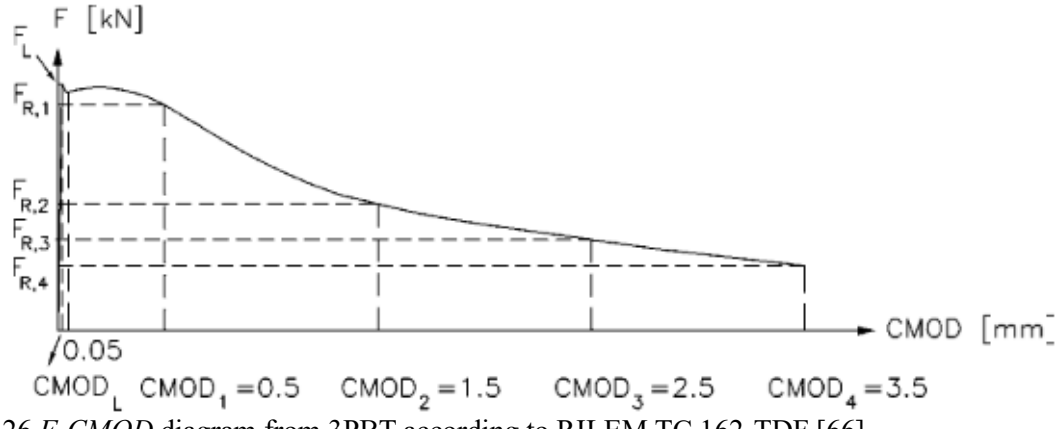


Fig. 3.26 F-CMOD diagram from 3PBT according to RILEM TC 162-TDF [66]

It is also interesting to note that according to the older version of RILEM TC 162-TDF [67], SFRC behavior was also characterized based on the 3PBT on notched beams, however, equivalent flexural tensile strengths were determined using equation (3.31) and (3.32).

$$f_{eq,2} = \frac{3}{2} \frac{D_{BZ,2}^f}{0.5} \frac{l}{bh_{sp}^2}$$

$$f_{eq,3} = \frac{3}{2} \frac{D_{BZ,3}^f}{2.5} \frac{l}{bh_{sp}^2}$$
(3.31)

$$f_{eq,3} = \frac{3}{2} \frac{D_{BZ,3}^f}{2.5} \frac{l}{bh_{sp}^2}$$
 (3.32)

where:

 $f_{eq,2}$ and $f_{eq,3}$ – concrete equivalent tensile flexural strength corresponding to $D^f_{BZ,2}$ and $D^{f}_{BZ,3}$, respectively [N/mm²],

 $D^f_{BZ,2}$ and $D^f_{BZ,3}$ – area under the F- δ curve representing the contribution of fibers to the energy absorption capacity, see Fig. 3.27 [N/mm],

l – distance between the supporting rollers [mm],

b – width of the sample [mm],

 h_{sp} – distance between the tip of the notch and the top of the specimen [mm].

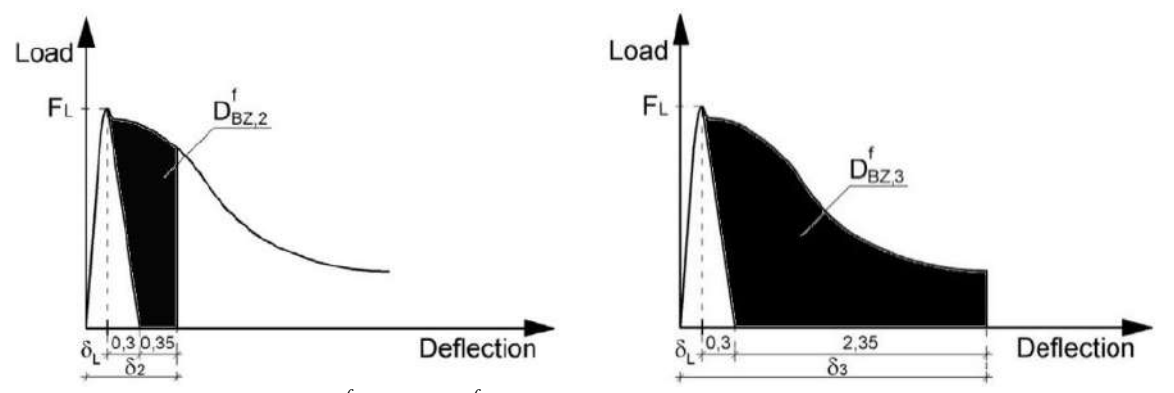


Fig. 3.27 Determination of $D^f_{BZ,2}$ and $D^f_{BZ,3}$ areas to calculate $f_{eq,2}$ and $f_{eq,3}$, respectively according to RILEM TC 162-TDF [66]

Standard JSCE-SF4

The Japanese standard JSCE-SF4 [25] provides a methodology for evaluating the maximum flexural tensile strength (f_b) , equivalent flexural tensile strength (f_{eq}) , and flexural toughness (T_b) of SFRC using 4PBT conducted on unnotched beams. According to the standard, if the SFs are shorter than 40 mm, the beam width and height should both be 100 mm. For fibers exceeding 40 mm in length, the recommended cross-sectional dimensions are 150 x 150 mm. The beam length should be at least 80 mm greater than three times the height of the specimen. The test setup described in

JSCE-SF4 [25] is presented in Fig. 3.28. Specimens must be positioned in the testing machine such that the side surfaces during casting become the top and bottom surfaces during the test. The span length should be three times the height of the specimen, and the distance between the loading and support rollers corresponds to one-third of the span length. During testing, the F- δ curve is recorded. Deflections are measured using LVDTs, which are mounted by screws to a dedicated steel or aluminum bar. This bar may be affixed to the specimen using adhesive. The standard permits deflection measurements at either the loading points or the midspan, however, for more accurate evaluation of flexural toughness, the first arrangement is recommended. Regarding the load, it should be applied at a constant rate of stress increase of 0.06 ± 0.04 MPa/s until the maximum load is reached. If deflection is recorded beyond the peak load, the loading rate should be adjusted such that the deflection increases at a constant rate within the range of $^{1}/_{1500}$ to $^{1}/_{3000}$ of the span per minute. Finally, from the F- δ curve, the values of f_b and f_{eq} can be calculated by equations (3.33) and (3.34), respectively.

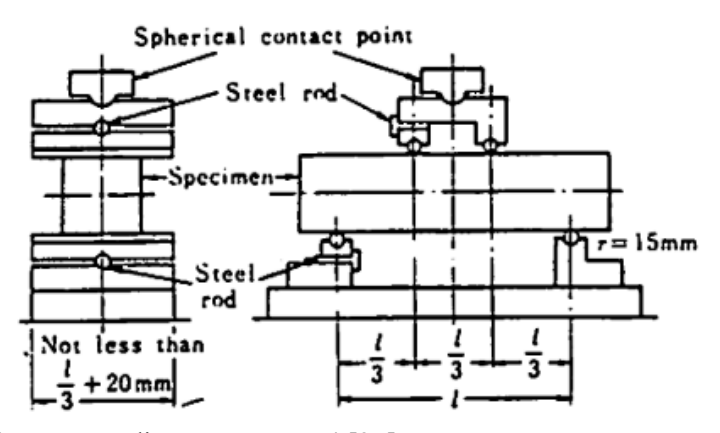


Fig. 3.28 Setup for 4PBT according to JSCE-SF4 [25]

$$f_b = \frac{Fl}{bh^2} \tag{3.33}$$

where:

 f_b – concrete maximum flexural tensile strength [N/mm²],

F – maximum load indicated by the testing machine [N],

l – span between the bottom supports [mm],

b – width of the sample [mm],

h – height of the sample [mm].

$$f_{eq} = \frac{T_b l}{\delta_{tb} b h^2} \tag{3.34}$$

 f_{eq} – concrete equivalent flexural tensile strength/flexural toughness factor [N/mm²],

 T_b – flexural toughness, as work required to obtain a beam deflection equals to $^{1}/_{150}$ of l, see Fig. 3.29 [Nmm],

l – span between the bottom supports [mm],

 δ_{tb} – deflection equals to $^{1}/_{150}$ of l [mm],

b – width of the sample [mm],

h – height of the sample [mm].

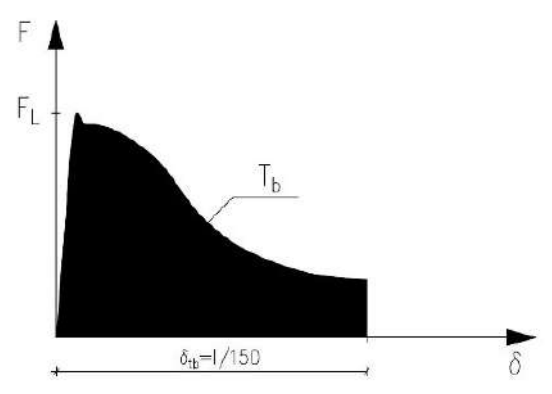


Fig. 3.29 Determination of T_b area to calculate f_{eq} according to JSCE-SF4 [25]

It is noteworthy that the f_{eq} value is used in the calculation of the fracture toughness index R_e , as defined in equation (3.35). This index appears in several design guidelines for FRC. Incorporating it into design calculations enables consideration of the additional load-bearing capacity provided by the incorporation of fibers in the concrete mixture. For instance, the third edition of TR34 [68], permits the inclusion of beneficial fiber reinforcement effects in the calculation of the maximum allowable positive (upper) bending moment, M_p . However, the standard requires that the R_e value must be no less than 0.30 for such consideration to be valid.

$$R_e = \frac{f_{eq}}{f_{ctm.fl}} \cdot 100\% \tag{3.35}$$

where:

 R_e – fracture toughness index [%],

 f_{eq} – concrete equivalent flexural tensile strength/flexural toughness factor [N/mm²], $f_{ctm,fl}$ – concrete mean flexural tensile strength [N/mm²].

Empirical equations

In certain cases, direct experimental determination of the flexural tensile strength may not be possible. Therefore, a number of empirical equations have been developed to estimate this mechanical property indirectly, typically based on available compressive or axial tensile strength data. RILEM TC 162-TDF [66] presents equations (3.36)-(3.39), thanks to which the flexural tensile strength may be estimated indirectly based on the compressive strength of cylindrical specimens. Exemplary values of SFRC flexural and tensile strengths derived through these formulas are presented in Table 3.1.

$$f_{fctm,ax} = 0.3 \cdot (f_{fck})^{\frac{2}{3}}$$
 (3.36)

$$f_{fctk,ax} = 0.7 \cdot f_{fctm,ax} \tag{3.37}$$

$$f_{fct,ax} = 0.6 \cdot f_{fct,fl} \tag{3.38}$$

$$f_{fctk,fl} = 0.7 \cdot f_{fctm,fl} \tag{3.39}$$

where:

 $f_{fctm,ax}$ – mean value of SFRC tensile strength [N/mm²],

 f_{fck} – characteristic value of SFRC compressive strength [N/mm²],

f_{fctk,ax} – characteristic value of SFRC tensile strength [N/mm²],

 $f_{fct,ax}$ – value of SFRC tensile strength from tested sample [N/mm²],

f_{fct,fl} – value of SFRC flexural tensile strength from tested sample [N/mm²],

f_{fctk,fl} – characteristic value of SFRC flexural tensile strength [N/mm²],

f_{fctm,fl} – mean value of SFRC flexural tensile strength [N/mm²].

Table 3.1 Values of SFRC strength for selected strength classes

| Strength class of SFRC | C20/25 | C25/30 | C30/37 | C35/45 | C40/50 |
|------------------------|--------|--------|--------|--------|--------|
| f_{fck} | 20 | 25 | 30 | 35 | 40 |
| $f_{fctm,ax}$ | 2.2 | 2.6 | 2.9 | 3.2 | 3.5 |
| f _{fctk,ax} | 1.5 | 1.8 | 2.0 | 2.2 | 2.5 |
| $f_{fctm,fl}$ | 3.7 | 4.3 | 4.8 | 5.3 | 5.8 |
| $f_{fctk,fl}$ | 2.6 | 3.0 | 3.4 | 3.7 | 4.1 |

Additionally, PN-EN 1992-1-1:2008 [30] provides an equation (3.40) for estimating the flexural tensile strength of concrete (f_{fl}) based on the axial tensile strength and the depth of the structural element depth. However, it must be mentioned that the standard [30] does not explicitly indicate whether this formulation is applicable to FRC elements.

$$f_{fl} = max \left\{ \left(1.6 - \frac{h}{1000} \right) \cdot f_{ct} \right. \tag{3.40}$$

 f_{fl} – concrete flexural tensile strength [N/mm²],

h – depth of the structural element cross-section [mm],

 f_{ct} – concrete axial tensile strength following Table 3.1 in [30] equals to $0.3f_c^{2/3}$ [N/mm²],

 f_c – concrete compressive strength [N/mm²].

Furthermore, the literature presents several empirical expressions for determining the f_{fl} , including FRC. For example, Légeron and Paultre [69] proposed equation (3.41), which estimates the f_{fl} of SFRC based on the compressive strength of concrete (f_c) and a coefficient λ . Nevertheless, this equation has been subject to criticism, as it considers only f_c while neglecting other influential parameters such as fiber material, geometry, and volume content. An alternative formulation was proposed by Glinicki [9], [70], specifically developed for concretes containing SFs. Equation (3.42) incorporates both the fiber volume fraction (V_f) and geometric properties of the fibers. In a similar manner, Swamy and Mangat [71] introduced equation (3.43), which relates the f_{fl} of SFRC not only to the mechanical characteristics of metallic fibers but also to the flexural tensile strength of corresponding PC. Considering the above, it is evident that the majority of available empirical equations are dedicated to SFRC. The author of this dissertation proposed a new formulation in [72], expressed as equation (3.44), specifically intended for SyFRC. It was demonstrated that it provides reliable estimates of f_{fl} for concretes reinforced with SyFs of slenderness less than 200 and $V_f \le 1.0\%$.

$$f_{fl} = \lambda_{\sqrt{f_c^2}}^3 \tag{3.41}$$

$$f_{fl} = \lambda_{\sqrt{f_c^2}}^{3}$$

$$f_{fl} = 0.73 + 8.061 \cdot V_f \frac{l_f}{d_f}$$
(3.41)

$$f_{fl} = 0.97 \cdot f_{fl}^{pc} (1 - V_f) + 3.41 \cdot V_f \frac{l_f}{d_f}$$
(3.43)

$$f_{fl} = f_{fl}^{pc} (1 - V_f) + 0.7 \cdot V_f \frac{l_f}{d_f}$$
 (3.44)

where:

 f_{fl} – concrete flexural tensile strength [N/mm²],

 λ – coefficient ranging from 0.35 to 0.65, with a common assumption of 0.50 [-],

 f_c – concrete compressive strength [N/mm²],

 V_f – nominal fiber volume content [-],

 l_f and d_f – fiber length and diameter, respectively [mm],

f_{fl}^{pc} – plain concrete flexural tensile strength [N/mm²].

3.3.3. Standards for designing FRC

3.3.3.1 RILEM TC 162-TDF

RILEM TC 162-TDF [66] outlines a comprehensive design methodology for SFRC, describing the testing of material properties, evaluation of structural performance under ultimate and serviceability limit states (ULS and SLS, respectively), and specific detailing provisions. Additionally, the document provides analytical expressions and design tables for calculating crack widths, taking into account factors such as exposure class and type of reinforcement. It also includes explicit recommendations for shear design and the specification of minimum reinforcement to ensure both structural integrity and durability. In ULS design, several fundamental assumptions are adopted to accurately reflect the mechanical behavior of SFRC. Firstly, cross-sections are assumed to remain plain in accordance with Bernoulli's hypothesis. Then, the internal stresses within SFRC elements subjected to combined tension and compression are determined based on the material's constitutive σ - ε relationship, as illustrated in Fig. 3.30. The maximum compressive strain is limited to -2% for elements under pure compression and to -3.5% for members not entirely in compression. In elements combining fibers with conventional reinforcement, the strain at the level of the reinforcement is further restricted to 25%. To maintain adequate fiber anchorage and ensure structural integrity, the maximum deformation in ULS is limited to 3.5 mm. Additionally, for certain environmental exposure classes, if the calculated crack width exceeds 0.2 mm, the structural contribution of fibers located near the surface must be reduced in ULS design. In such cases, the effective height of the cracked zone is decreased by 10 mm. It is important to note that this adjustment does not apply for SLS verifications.

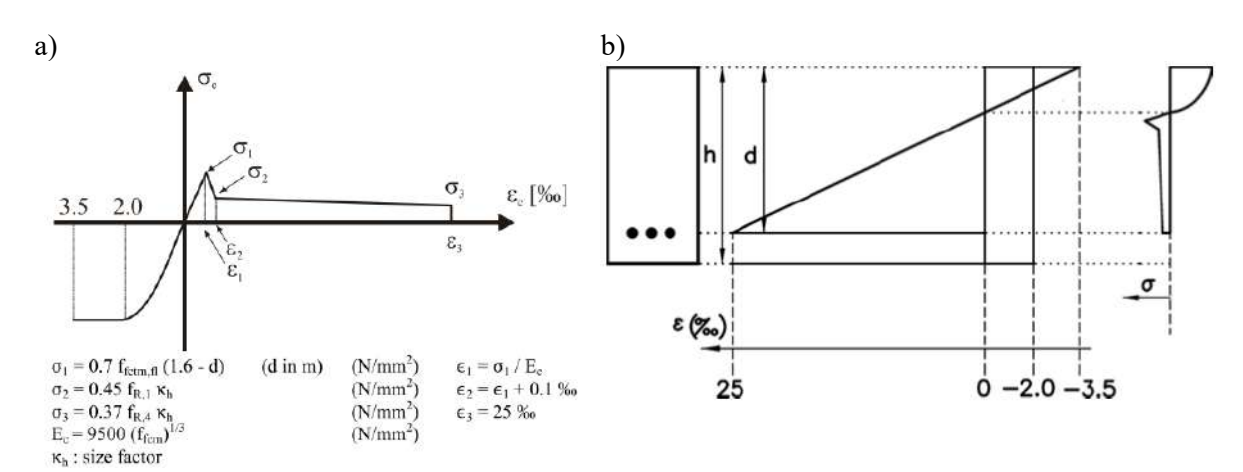


Fig. 3.30 a) Stress-strain diagram, b) stress and strain distribution according to RILEM TC 162-TDF [66]

In RILEM TC 162-TDF [66], shear design provisions apply exclusively to beams and plates that incorporate conventional flexural reinforcement, such as bars or welded meshes, including prestressed elements. The standard explicitly states that the contribution of SFs to shear load-bearing capacity must not be considered in cases where no longitudinal reinforcement or compression zone is present. Within the ULS design provisions, the total shear capacity is determined by summing the individual contributions of the concrete, shear reinforcement (stirrups), and SFs. The additional shear strength provided by presence of fibers in concrete is calculated using equation (3.45). Furthermore, the guideline specifies that the use of minimum shear reinforcement may not be required in members with SFs, provided that $f_{Rk,4}$ of at least 1 N/mm² is achieved in 3PBT according to [66].

$$\tau_{fd} = 0.12 \cdot f_{Rk,4} \tag{3.45}$$

where:

 τ_{fd} – design value of the additional shear strength resulting from the presence of SFs in concrete [N/mm²],

 $f_{Rk,4}$ – concrete characteristic residual flexural tensile strength at $CMOD_4 = 3.5$ mm determined according to [66] [N/mm²].

3.3.3.2 Model Code 2010

The Model Code 2010 (MC2010) [15] serves as a comprehensive guide for the design of concrete structures and includes a dedicated section on FRC. Chapter 5.6 addresses key aspects such as material properties, testing procedures, constitutive models, and safety factors associated with FRC. However, the document explicitly states that the presented provisions are not intended for fibers exhibiting a Young's modulus that is sensitive to time-dependent or thermo-hygrometric effects. Moreover, the guidelines are primarily based on experience with SFRC. Additionally, to allow for a partial or complete substitution of conventional reinforcement at the ULS using fibers, the following conditions must be satisfied: $f_{Rk,1}/f_{Ctk,L} > 0.4$ and $f_{Rk,3}/f_{Rk,1} > 0.5$. These residual flexural tensile strengths are determined using the 3PBT as defined in PN-EN 14651 [29]. According to MC2010 [15], two simplified constitutive stress-crack opening (σ -w) relationships may be adopted for FRC: a rigid-plastic model and a linear model with either post-cracking softening or hardening behavior, as illustrated in Fig. 3.31a and Fig. 3.31b, respectively. In the rigid-plastic approach, the compressive

force is assumed to be concentrated in the top fiber of the section. In contrast, the linear model assumes that the compressive stress resultant is applied on the extrados chord, while the tensile response of the section is modelled as rigid-linear [15].

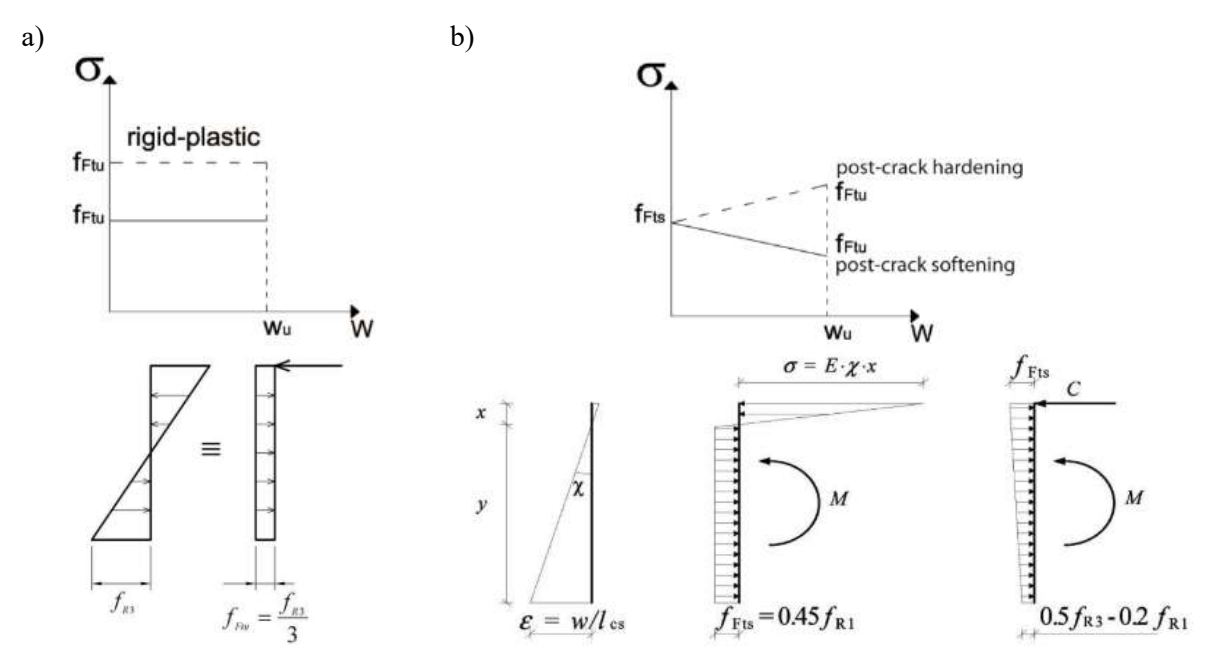


Fig. 3.31 Simplified post-cracking constitutive laws for: a) rigid-plastic model, b) liner model, where continuous and dashed lines refer to softening and hardening behavior, respectively according to Model Code 2010 [15]

The characteristic value of the ultimate residual tensile strength (f_{Ftuk}) for FRC is determined differently depending on the assumed constitutive model. Specifically, for the rigid-plastic model (Fig. 3.31a), f_{Ftuk} is calculated using equation (3.46), whereas for the linear post-cracking model (Fig. 3.31b), it is derived from equation (3.47) based on Fig. 3.32. The ultimate crack opening (w_u) in the rigid-plastic and linear model are assumed to be 2.5 mm and 1.5 mm, respectively. The contribution of fibers to the structural resistance is then calculated based on the design value of the ultimate residual tensile strength (f_{Ftud}), which is obtained by dividing the characteristic value f_{Ftuk} by the partial safety factor for materials, taken as 1.5, in accordance with Chapter 5.6.6 of MC2010 [15].

$$f_{Ftuk} = \frac{f_{Rk,3}}{3} \tag{3.46}$$

where:

 f_{Ftuk} – characteristic value of the ultimate residual tensile strength for FRC [N/mm²], $f_{Rk,3}$ – characteristic residual flexural tensile strength at $CMOD_3 = 2.5$ mm determined according to PN-EN 14651 [29] [N/mm²].

$$f_{Ftuk} = f_{Ftsk} - \frac{w_u}{CMOD_3} \left(f_{Ftsk} - 0.5 f_{Rk,3} + 0.2 f_{Rk,1} \right) \ge 0 \tag{3.47}$$

 f_{Ftsk} – characteristics value of the serviceability residual tensile strength for FRC equals to $0.45f_{Rk,1}$ [N/mm²],

 w_u – maximum crack opening accepted in the structural design, usually taken as 1.5 mm [mm],

CMOD₃ – crack mouth opening displacement corresponding to 2.5 mm according to PN-EN 14651 [29] [mm],

 $f_{Rk,1}$ and $f_{Rk,3}$ – characteristic residual flexural tensile strength at $CMOD_1 = 0.5$ mm and 2.5 mm, respectively determined according to PN-EN 14651 [29] [N/mm²].

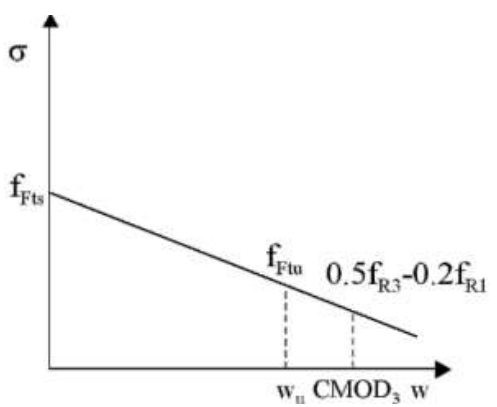


Fig. 3.32 Linear post-cracking constitutive law according to Model Code 2010 [15]

3.3.3.3 PN-EN 1992-1-1:2024 Annex L

Annex L of PN-EN 1992-1-1:2024 [33] introduces supplementary provisions for the design of SFRC structures. These guidelines apply to structural elements with or without traditional reinforcing bars, and those incorporating either pre-tensioned or post-tensioned tendons. It provides the classification of SFRC based on the results of flexural tests conducted in accordance with PN-EN 14651 standard [29]. Specifically, it defines residual strength classes (SC) based on the $f_{Rk,1}$, with designated values of 1.0, 1.5, 2.0, 2.5, 3.0, 3.5, 4.0, 4.5, 5.0, 6.0, 7.0, and 8.0 MPa. Additionally, ductility classes, denoted by letters from a to e, are established from the ratio $f_{Rk,3}/f_{Rk,1}$. Table 3.2 summarizes the performance classes for SFRC. It should also be noted that this classification system is consistent with the post-cracking classification of FRC presented in MC2010 [15]. With respect to the $f_{Rk,1}$ and $f_{Rk,3}$, it is also important to highlight their relevance to SLS and ULS, respectively. Moreover, an increase in $f_{Rk,1}$ contributes to

enhanced structural stiffness, whereas a higher value of $f_{Rk,3}$ directly correlates with increased load-bearing capacity. Finally, to appropriately account for the beneficial contribution of SFs in the design of concrete elements, the condition expressed by equation (3.48) must be fulfilled.

Table 3.2 Performance classes for SFRC according to PN-EN 1992-1-1:2024 Annex L [33]

| Ductility | | | | Analytical | | | | | | | | | |
|-----------|-----|-----|-----|------------|-----|-----|-----|-----|-----|---------------|-----|------|----------------------|
| classes | 1.0 | 1.5 | 2.0 | 2.5 | 3.0 | 3.5 | 4.0 | 4.5 | 5.0 | 0 6.0 7.0 8.0 | | 8.0 | formulae |
| а | 0.5 | 0.8 | 1.0 | 1.3 | 1.5 | 1.8 | 2.0 | 2.3 | 2.5 | 3.0 | 3.5 | 4.0 | $f_{Rk,3} \ge 0.5SC$ |
| b | 0.7 | 1.1 | 1.4 | 1.8 | 2.1 | 2.5 | 2.8 | 3.2 | 3.5 | 4.2 | 4.9 | 5.6 | $f_{Rk,3} \ge 0.7SC$ |
| С | 0.9 | 1.4 | 1.8 | 2.3 | 2.7 | 3.2 | 3.6 | 4.1 | 4.5 | 5.4 | 6.3 | 7.2 | $f_{Rk,3} \ge 0.9SC$ |
| d | 1.1 | 1.7 | 2.2 | 2.8 | 3.3 | 3.9 | 4.4 | 5.0 | 5.5 | 6.6 | 7.7 | 8.8 | $f_{Rk,3} \ge 1.1SC$ |
| e | 1.3 | 2.0 | 2.6 | 3.3 | 3.9 | 4.6 | 5.2 | 5.9 | 6.5 | 7.8 | 9.1 | 10.4 | $f_{Rk,3} \ge 1.3SC$ |

$$\frac{f_{Rk,1}}{f_{ctk,0.05}} \ge 0.5\tag{3.48}$$

where:

 $f_{Rk,1}$ – characteristic residual flexural tensile strength corresponding to $CMOD_1 = 0.5 \text{ mm}$ determined according to PN-EN 14651 [29] [N/mm²],

 $f_{ctk,0,05}$ – 5% quantile of the distribution of the characteristic concrete uniaxial tensile strength [N/mm²].

The σ - ε constitutive model proposed in Annex L of PN-EN 1992-1-1:2024 [33] for structural analysis is illustrated in Fig. 3.33. However, for the design of members subjected to bending with or without axial force at the ULS, simplified stress distributions across the cross-section may also be employed according to Fig. 3.34. Specifically, the rigid-plastic approach (Fig. 3.34a) is applicable to members subjected to flexure with or without axial compression and is recommended for ductility classes a, b, and c (as defined in Table 3.2). Alternatively, a bilinear residual tensile stress distribution may be adopted (Fig. 3.34b), providing a more detailed representation of the post-cracking behavior.

To characterize the stress distribution within the SFRC cross-section according to [33], the effective residual flexural tensile strengths: $f_{Ftu,ef}$, $f_{Ftl,ef} = f_{Fts,ef}$, and $f_{Ft3,ef}$ should be calculated using equations (3.49), (3.50), and (3.51), respectively. The corresponding design values: f_{Ftud} , $f_{Ftld} = f_{Ftsd}$, and f_{Ft3d} are obtained by dividing the effective strengths by the material partial safety factor equals to 1.5, as specified in Chapter 4.3.3 of PN-EN 1992-1-1:2024 [33]. Finally, the design value f_{Ftud} is used to determine the additional load-bearing capacity provided by the fibers in structural elements.

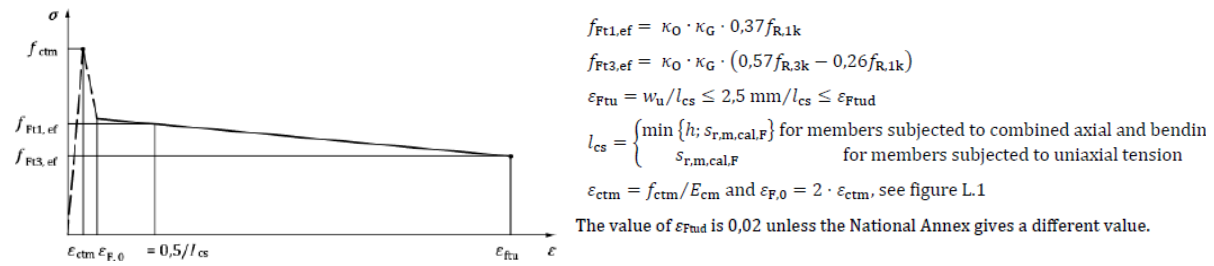


Fig. 3.33 Constitutive law for SFRC in uniaxial tension according to PN-EN 1992-1-1:2024 Annex L [33]

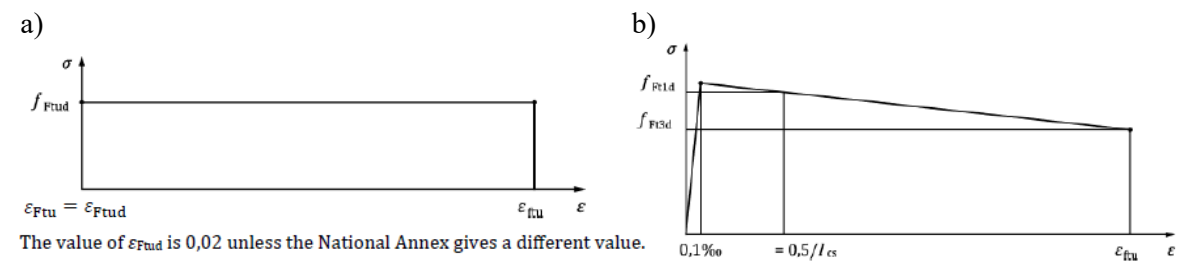


Fig. 3.34 Simplified stress distributions for SFRC: a) plastic, b) bilinear distribution according to PN-EN 1992-1-1:2024 Annex L [33]

$$f_{Ftu,ef} = \kappa_O \cdot \kappa_G \cdot 0.33 \cdot f_{Rk,3} \tag{3.49}$$

$$f_{Ft1,ef} = f_{Fts,ef} = \kappa_O \cdot \kappa_G \cdot 0.37 \cdot f_{Rk,1} \tag{3.50}$$

$$f_{Ft3.ef} = \kappa_0 \cdot \kappa_G \cdot (0.57 \cdot f_{Rk,3} - 0.26 \cdot f_{Rk,1})$$
 (3.51)

 $f_{Ftu,ef}$ – effective residual tensile strength of SFRC for given crack width accounting for fiber orientation and volume effect [N/mm²],

 $f_{Fts,ef}$ – effective residual tensile strength of SFRC for crack widths at the serviceability limit state accounting for fiber orientation [N/mm²],

 $f_{Ft1,ef}$ and $f_{Ft3,ef}$ – effective residual tensile strength of SFRC for crack width = 0.5 mm and 2.5 mm, respectively accounting for fiber orientation [N/mm²],

 κ_O – factor accounting for fiber orientation, should be taken as 0.5 unless otherwise specified in Annex L or verified by testing, however for bending moments, shear and punching shear forces, and torsion in slabs and beams made of concrete with consistency classes S2-S5 in accordance with PN-EN 206 [38], κ_O = 1,0 may be used [-],

 κ_G – factor accounting for size effect on the coefficient of variation equals to $1.0+0.5A_{ct} \le 1.5$, where A_{ct} is the area of the tension zone (in m²) of the cross-section involved in the failure of the equilibrium system [-],

 $f_{Rk,I}$ – characteristic residual flexural tensile strength corresponding to $CMOD_I = 0.5$ mm, representing the residual strength class [N/mm²],

 $f_{Rk,3}$ – characteristic residual flexural tensile strength corresponding to $CMOD_3 = 2.5$ mm, representing the performance class [N/mm²].

3.3.4. Standards for designing ground slabs

Although concrete ground slabs are extensively used in practice, there is currently no unified standard governing their design [73]–[75]. Moreover, existing guidelines adopt varying methodologies and design approaches, which often leads to inconsistency and confusion. Specifically, some documents are adapted from road pavement design and rely on empirical tables or design charts, while others are based on building design principles, treating the slab as a reinforced or unreinforced concrete element [73]. The design of ground-supported slabs is inherently complex and must address not only the provisions for calculation of load-bearing capacity, effective crack control, and long-term durability, but also considers the advanced materials such as FRC and the interaction between the slab and its supporting subgrade. Table 3.3 presents a comparative overview of four commonly used design guidelines for concrete ground slabs: Technical Report 34 [28], Concrete Hardstanding Design Guidance [76], Heavy Duty Pavements [77], and ACI 360R-10 standard [78]. The comparison includes the scope of application of each guideline, the adopted structural design principles, the types of loads considered and the manner in which slab-subgrade interaction are accounted for. Attention is also given to fiber reinforcement and whether its contribution is recognized in structural calculations. In addition, the guidelines are evaluated with respect to punching shear verification procedures, the use and magnitude of safety factors, and the complexity of the proposed design methodology.

Table 3.3 Comparison of standards and guidelines for the design of ground-supported slabs

| Feature | Technical Report 34 [28] | Concrete Hardstanding Design Guidance [76] | Heavy Duty Pavements [77] | ACI 360R-10: Design of Slabs-on-Ground [78] |
|---------|--|--|---|---|
| Scope | Primarily for ground-supported internal industrial floors, especially in warehouses. Not intended for external pavements, docks, container parks, or traditional elevated floors in buildings. | Designed for indoor and outdoor pavements subjected to heavy loads from vehicles and forklift traffic in industrial, commercial, and warehousing buildings. Not intended for very heavy container handling vehicles. | Specifically for pavements in highways, ports, and heavy-traffic industries. Covers traffic loads like cargo transport and ship loading, and static loads from shipping containers. | Dedicated to designing unreinforced, reinforced, or post-tensioned concrete slabs on ground. Not specifically intended for roadway and airport pavements, parking lots, or mat foundations. |

| Feature | Technical Report 34 [28] | Concrete Hardstanding Design Guidance [76] | Heavy Duty Pavements [77] | ACI 360R-10: Design of Slabs-on-Ground [78] |
|-------------------|---|---|---|---|
| Design principles | Uses analytical equations based on Westergaard and Meyerhof approaches. Complies with Eurocode principles. Provides procedures for calculating bending moments, punching shear, and dowel capacity. | Design procedures are based on empirical methods. Pavements are classified by foundation conditions, traffic intensity, reinforcement type, and concrete class. Tables are used to determine required slab thickness depending on the pavement class (Fig. 3.35). | Uses design charts and tables to determine the equivalent thickness of C _{8/10} material based on single equivalent wheel load (SEWL) and number of load passes over the design life (Fig. 3.36a). SEWL is calculated by multiplying the static wheel load by dynamic factors such as braking, cornering, acceleration, and surface unevenness. Material Equivalence Factors (MEF) then relate the required slab thickness for C _{8/10} to other materials (Fig. 3.36b). The method is calibrated using FEM analysis. | Presents various thickness design methods: PCA, WRI, and COE. PCA and WRI only consider interior live loads, while COE addresses loads at slab edges or joints. The PCA method (Fig. 3.37) is based on Pickett's approach, the WRI method (Fig. 3.38) uses a discrete element computer model, and the COE method (Fig. 3.39) relies on Westergaard's edge stress formula. |
| Loads | Covers single point, multiple point, line, and uniformly distributed loads. Evaluates multiple load locations and allows simultaneous load combinations. Includes loads from warehouses equipment (static loads: racking and live storage systems, mezzanines; dynamic loads: pallet, reach, and counterbalance trucks, front and side stackers, and stacker cranes). | Considers loads from heavy goods vehicles and forklift traffic, excluding very heavy container handling equipment. Traffic is quantified using the cumulative vehicle damage factor (VDF), expressed in millions of standard axles (msa), based on the number of vehicles and their axle loads. | Provides detailed analysis of loads from highway vehicles, containers, lane channelization, trucks, reach stackers, straddle carriers, side and front lift trucks, yard gantry cranes, tractor-trailer systems, and mobile cranes. Includes proximity factors for adjacent tires. | Covers concentrated, line and strip, distributed, construction, environmental, and unusual loads. Considers diverse load locations, including materials stored directly on slabs, storage rack loads, and static and dynamic equipment and vehicle loads. Also accounts for roof loads transferred via dual-purpose rack systems. |

| Feature | Technical Report 34 [28] | Concrete Hardstanding Design Guidance [76] | Heavy Duty Pavements [77] | ACI 360R-10: Design of Slabs-on-Ground [78] |
|----------------|---|--|---|---|
| Safety factors | Applies material partial safety factors of 1.5 for concrete and FRC, and 1.15 for steel reinforcement. Load partial safety factors include 1.2 for defined racking, 1.6 for dynamic loads, and 1.5 for other loads. Dynamic effects from braking and cornering are also considered. | Does not mention safety factors. However, in areas with frequent vehicle traffic and no load transfer, slab thickness should be increased by 25% to account for edge loading. | Dynamic factors are included in calculating the SEWL value. Two condition factors are applied based on material condition and maximum localized rutting or settlement. A material safety factor of 1.5 is used in developing the design charts. | Considers safety factors varying by load type: 1.7 to 2.0 for moving wheels and concentrated loads (rack, post), 1.7 for line and strip loads, and between 1.4 and 2.0 for construction loads. |
| Punching shear | Punching shear capacity is determined in accordance with PN-EN 1992-1-1:2008 [30]. Shear resistance must be checked both at the face and at the critical control perimeter located 2.0d from the contact area. | States that punching shear failures have not occurred in slabs thicker than 200 mm and thus recommends a minimum slab thickness of 200 mm, otherwise, separate calculations are required. | Does not address punching shear. | Does not provide calculation procedures for punching shear resistance. Only mentions that shear stresses at bearing plates should be checked. |
| Subgrade | Considers subgrade effects using a modulus of subgrade reaction, assuming that it behaves as an elastic medium. Allows reduction of design forces by accounting for loads within the punching shear perimeter applied directly to the subgrade. Soil investigations should follow Eurocode 7 recommendations. | Divides foundations into classes based on subbase composition, compaction, and thickness. Describes test methods for subgrade surface modulus characterization, including CBR (California Bearing Ratio) and LWD (Light Weight Deflectometer). Foundation Class 2 (unbound) and Class 3 (bound) are commonly used. | Introduces four foundation classes based on half-space stiffness, composition, compaction, and subbase thickness. Offers accurate methods to assess supporting materials, including cement-bound, hydraulic, bitumen-bound, unbound materials, concrete, and concrete block paving. Describes testing procedures for subgrade surface modulus characterization (e.g., CBR). | PCA, WRI, and COE design charts account for the modulus of subgrade reaction's influence on required slab thickness. They assume continuous ground support and uniform subgrade modulus. Discusses subgrade classification and estimation methods for subgrade modulus, such as plate load field tests and CBR. |

| Feature | Technical Report 34 [28] | Concrete Hardstanding Design Guidance [76] | Heavy Duty Pavements [77] | ACI 360R-10: Design of Slabs-on-Ground [78] |
|------------|---|---|--|--|
| Fibers | Provides a straightforward method to calculate the effect of SFs and SyFs using residual flexural tensile strengths from experimental tests. Includes calculation procedures for concrete reinforced with fibers alone and with combined fibers and steel bars reinforcement. | Does not consider fiber reinforcement and the additional strength attributed to fibers presence in the concrete. When fibers are used, following the manufacturer's recommendations is advised. | Considers the effect of SFs at dosages of 20, 30, and 40 kg/m ³ . Fiber amount influences the MEF, enabling a reduction in required slab thickness. | Discusses polymeric and steel fibers. In thickness design methods (PCA, WRI, COE), fibers are considered only for serviceability design. In elastic and yield line design (based on Meyerhof's work), fibers' effect is represented by equivalent flexural strength. |
| Difficulty | Most demanding and time-consuming, however very comprehensive. The most accurate for FRC. Aligned with Eurocode standards. | Simplest and fastest to use. | Requires effort and time but allows quick switching between different materials using the MEF value. | The time and effort required vary depending on the selected design method, with tabular methods significantly improving efficiency. |

| | | | | | | C | oncre | te sla | b thic | Concrete slab thickness (mm) | | | | | | | | | | | | | | |
|------------------|------------------------|---|-----|-----|-----|-----|-------|--------|--------|------------------------------|-----|-----|-------|-----|-----|-----|--|--|--|--|--|--|--|--|
| | Concrete | Designated Concrete to BS8500 Part 1 Table A.15 | | | | | | | | | | | | | | | | | | | | | | |
| Traffic Class | Class | PAV1(I) | | | | | | | PAV2 | ř | | R | 40/50 | XF | | | | | | | | | | |
| Class | Reinforcement Class | RO | R1 | R2 | R3 | R4 | RO | R1 | R2 | R3 | R4 | RO | R1 | R2 | R3 | R4 | | | | | | | | |
| | Foundation Class | V | V | V | V | V | V | V | V | V | V | V | V | V | V | V | | | | | | | | |
| ті | F2 | 205 | 205 | 190 | 175 | 175 | 185 | 185 | 175 | 175 | 175 | 175 | 175 | 175 | 175 | 175 | | | | | | | | |
| | F3 | 185 | 185 | 180 | 165 | 150 | 175 | 175 | 165 | 155 | 150 | 150 | 150 | 150 | 150 | 150 | | | | | | | | |
| 2200 | F2 | 235 | 235 | 220 | 205 | 180 | 210 | 210 | 200 | 185 | 175 | 190 | 190 | 180 | 175 | 175 | | | | | | | | |
| Т2 | F3 | 215 | 215 | 205 | 190 | 165 | 200 | 200 | 190 | 175 | 155 | 175 | 175 | 170 | 155 | 150 | | | | | | | | |
| 2002 | F2 | 255 | 255 | 240 | 220 | 195 | 230 | 230 | 215 | 200 | 175 | 205 | 205 | 195 | 180 | 175 | | | | | | | | |
| ТЗ | F3 | 230 | 230 | 225 | 205 | 180 | 215 | 215 | 205 | 190 | 170 | 190 | 190 | 185 | 170 | 150 | | | | | | | | |
| 100000 | F2 | 270 | 270 | 255 | 235 | 205 | 240 | 240 | 230 | 215 | 185 | 220 | 220 | 210 | 190 | 175 | | | | | | | | |
| T4 | F3 | 245 | 245 | 235 | 220 | 190 | 225 | 225 | 220 | 205 | 180 | 200 | 200 | 195 | 180 | 155 | | | | | | | | |

Fig. 3.35 Concrete slab thickness design according to Concrete Hardstanding Design Guidance [76]

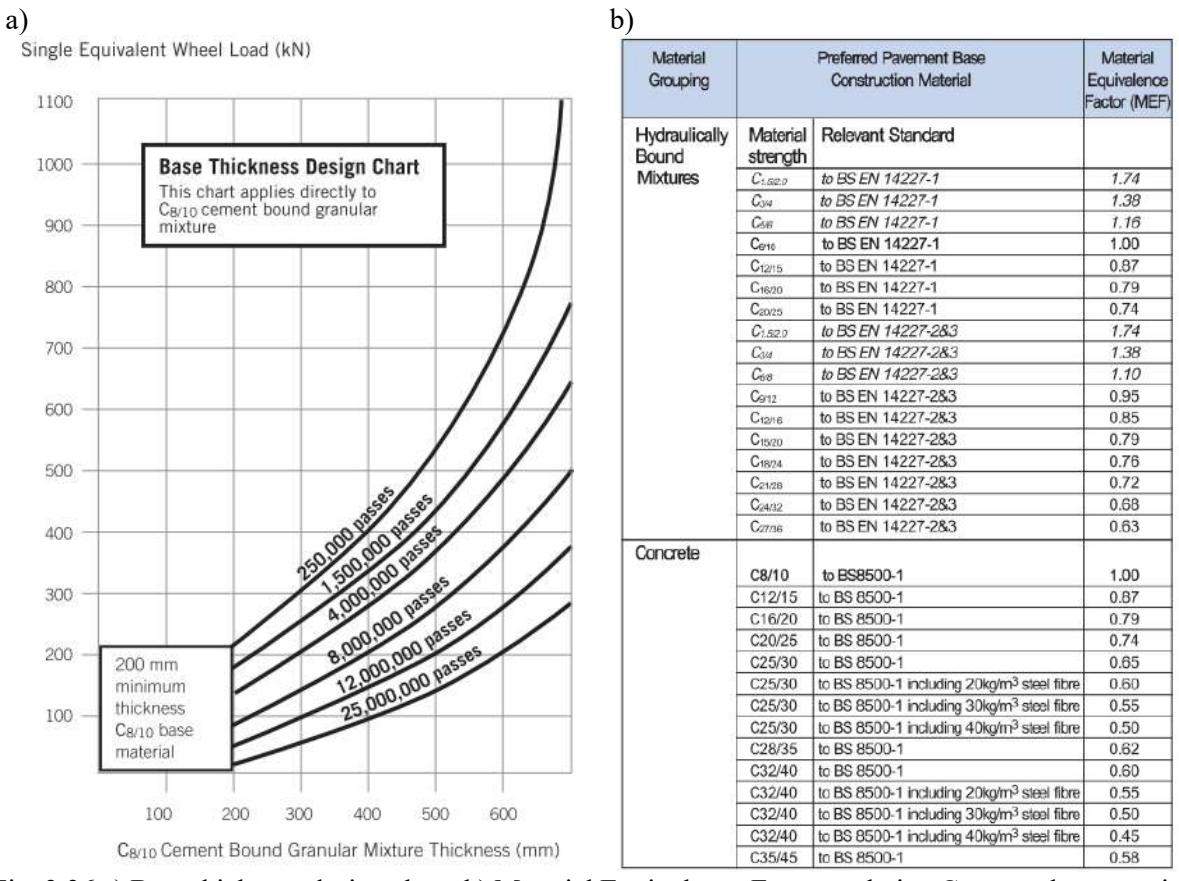


Fig. 3.36 a) Base thickness design chart, b) Material Equivalence Factors relating $C_{8/10}$ to other materials according to Heavy Duty Pavements [77]

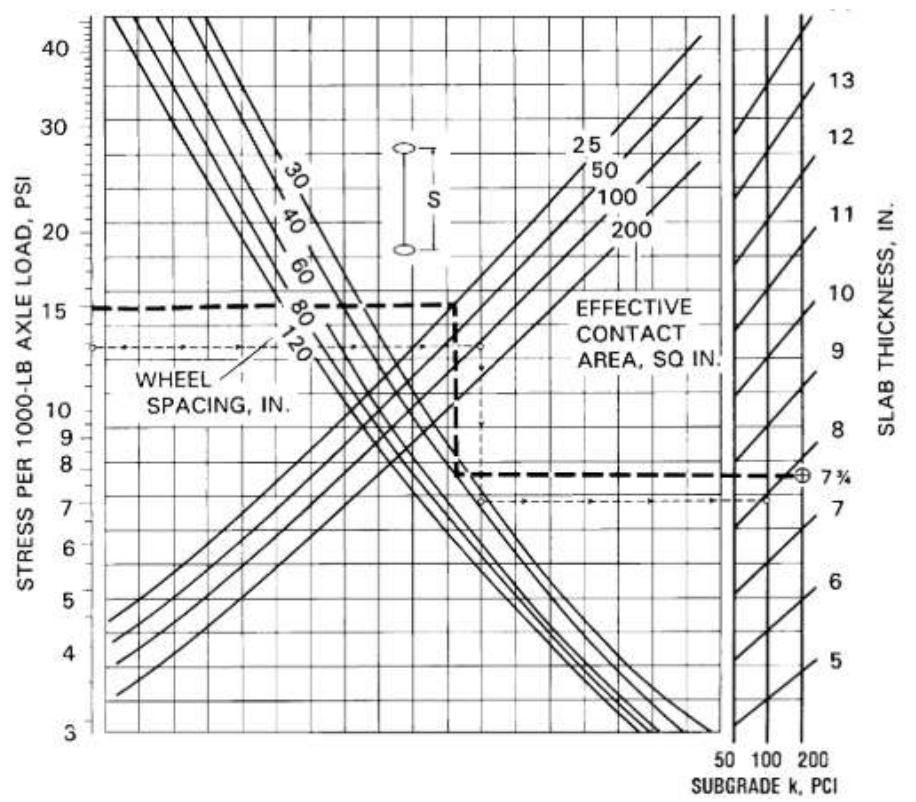


Fig. 3.37 PCA design chart for axles with single wheels according to ACI 360R-10 [78]

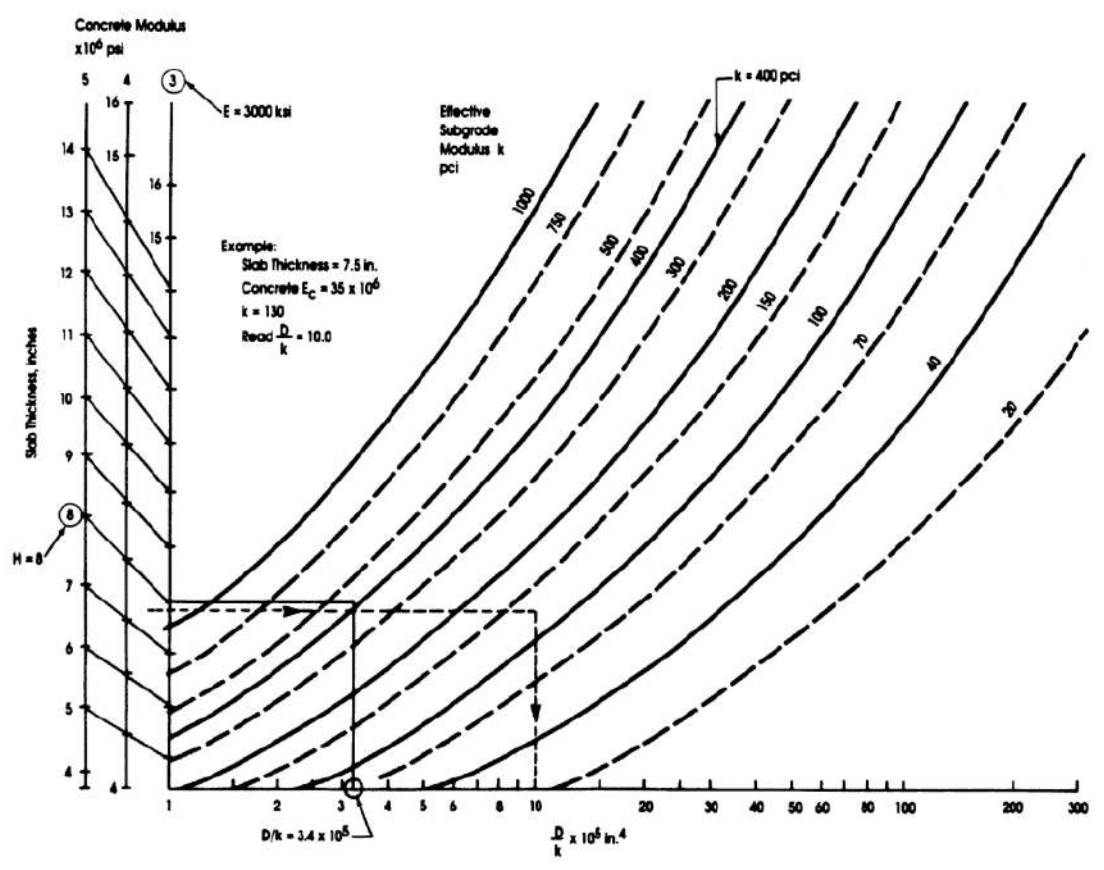


Fig. 3.38 Subgrade and slab stiffness relationship chart used in WRI design procedure according to ACI 360R-10 [78]

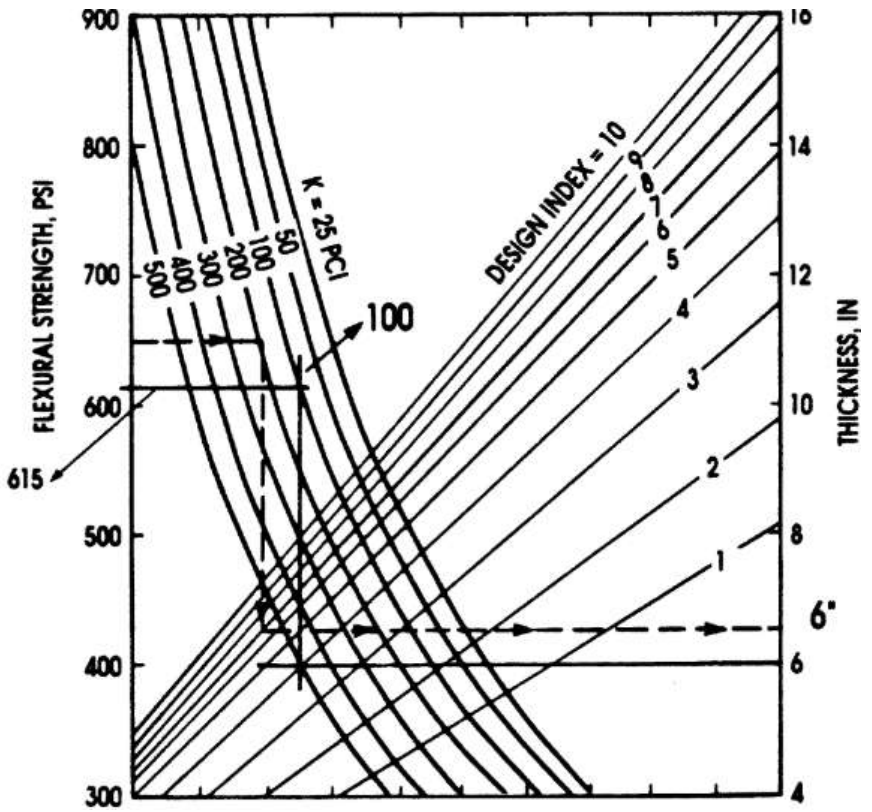


Fig. 3.39 COE curves for determining concrete floor thickness using design index according to ACI 360R-10 [78]

A comparative overview highlighted the key similarities and differences between the four considered design guidelines (Table 3.3). Among them, ACI 360R-10 [78] offers the broadest perspective, providing an extensive selection of design concepts and methodologies applicable to a wide range of ground-supported slab. In contrast, the remaining handbooks employ more specialized methodologies, emphasizing particular applications and corresponding design procedures. TR34 [28] offers a comprehensive design framework specifically dedicated for industrial floors, with detailed provisions for FRC and full alignment with Eurocode standards. Moreover, it provides precise and rigorous calculation methods for punching shear capacity, following the recommendations of PN-EN 1992-1-1:2008 [30]. In contrast, the Heavy Duty Pavements guidelines [77] is intended for heavy industrial applications, placing particular emphasis on thickness design based on the equivalent wheel load and material substitution approach. The Concrete Hardstanding Design Handbook [76], meanwhile, serves as a more general guide, featuring simplified design tables but with limited applicability to extreme loading conditions and FRC slabs. Although it specifies a minimum slab thickness of 200 mm and recognizes the need for punching shear capacity design, it lacks detailed calculation provisions in this regard. Considering these differences, the analytical study presented in this dissertation adopts the TR34 [28], as it comprehensively addresses the key phenomena relevant to the design of SyFRC ground-supported slabs, including both bending and punching capacity calculations.

3.3.5. Standards for punching shear design

3.3.5.1 PN-EN 1992-1-1:2008

The first condition (I) that must be verified in accordance with to PN-EN 1992-1-1:2008 [30] when calculating punching shear capacity is defined by equation (3.52). Specifically, at the control perimeter located directly at the column face or at the edge of the loaded area u_0 , the maximum punching shear stress v_{Ed} must not exceed the maximum punching shear resistance, denoted as $v_{Rd,max}$.

$$(I) v_{Ed} \le v_{Rd,max} (3.52)$$

where:

 v_{Ed} – design value of the applied shear stress at the face of the loaded area according to equation (3.60) [N/mm²],

 $v_{Rd,max}$ – design value of the maximum shear strength of concrete at the face of the loaded area according to equation (3.53) [N/mm²].

$$v_{Rd,max} = 0.5 \cdot v \cdot f_{cd} \tag{3.53}$$

where:

v – strength reduction factor for concrete cracked in shear according to equation (3.54) [-],

 f_{cd} – design value of concrete compressive strength [N/mm²].

$$v = 0.6 \cdot \left(1 - \frac{f_{ck}}{250}\right) \tag{3.54}$$

where:

 f_{ck} – characteristic value of concrete compressive strength [N/mm²].

The second condition (II) that must be verified is defined by equation (3.55). It specifies that punching shear reinforcement is not required if the maximum punching shear stress v_{Ed} is lower than the punching shear resistance $v_{Rd,c}$ of an element without shear reinforcement, evaluated at the face of the critical control section. According to PN-EN 1992-1-1:2008 [30], in the case of ground-supported slabs, the critical control section should be located within a distance of 2d from the edge of the loaded area, due to the counteracting effect of high ground pressure (clauses 6.4.2(2) and 6.4.4(2) in [30]). Consequently, determining the location of the critical control section requires an iterative procedure. Specifically, the critical control section should be positioned where the ratio of v_{Ed}/v_{Rd} reaches its maximum value.

$$(II) v_{Ed} \le v_{Rd,c} (3.55)$$

where:

 v_{Ed} – design value of the applied shear stress at the face of the critical control section according to equation (3.60) [N/mm²],

 $v_{Rd,c}$ – design value of the punching shear strength of concrete element without shear reinforcement at the face of the critical control section according to equation (3.56) [N/mm²].

$$v_{Rd,c} = max \begin{cases} C_{Rd,c} \cdot k \cdot (100 \cdot \rho_l \cdot f_{ck})^{\frac{1}{3}} \cdot \frac{2d}{a} \\ v_{min} \cdot \frac{2d}{a} \end{cases}$$
(3.56)

 $C_{Rd,c}$ – coefficient, may be found in National Annex, recommended value is $0.18/\gamma_c$ [-], γ_c – material partial safety factor for concrete = 1.5, in Polish National Annex = 1.4 [-], k – coefficient taking into consideration size/scale effect according to equation (3.57) [-], ρ_l – reinforcement ratio for longitudinal reinforcement according to equation (3.58) [-], f_{ck} – characteristic value of concrete compressive strength [N/mm²],

d – effective slab depth [mm],

a – distance from the loaded area to the control section considered [mm],

 v_{min} – minimum shear strength of concrete at the face of the critical control section according to equation (3.59) [N/mm²].

$$k = 1 + \left(\frac{200}{d}\right)^{0.5} \le 2.0\tag{3.57}$$

where:

d – effective slab depth in mm [mm].

$$\rho_l = \sqrt{\rho_{ly} \cdot \rho_{lz}} \le 0.02 \tag{3.58}$$

where:

 ρ_{ly} and ρ_{lz} – degree of primary reinforcement related to the bonded tension steel in y- and z- directions, respectively [-].

$$v_{min} = 0.035 \cdot k^{1.5} \cdot f_{ck}^{0.5} \tag{3.59}$$

where:

k – coefficient taking into consideration size/scale effect according to equation (3.57) [-], f_{ck} – characteristic value of concrete compressive strength [N/mm²].

In conclusion, when no longitudinal reinforcement is provided, the first term in equation (3.56) is equal to 0, and $v_{Rd,c}$ depends solely on the concrete compressive strength, the effective depth of the slab, and the assumed critical control perimeter. Furthermore, PN-EN 1992-1-1:2008 [30] does not provide a specific formulation for

calculating the punching shear resistance of FRC elements. As a result, FRC ground slabs without conventional reinforcement are treated as unreinforced concrete members in design calculations. However, the revised version of the Eurocode 2, PN-EN 1992-1-1:2024-05 [33], explicitly accounts for the presence of fibers and their contribution to the structural performance of concrete elements.

It should also be noted that PN-EN 1992-1-1:2008 [30], based on extensive experimental investigations and practical observations, accounts for the eccentricity of concentrated loading. This eccentricity arises from structural factors such as the presence of bending moments acting in combination with axial forces at the column base and/or head, as well as from geometric imperfections. Its influence is incorporated through the application of the coefficient β in equation (3.60). Moreover, for elements supported directly on the ground, where concentrated forces are counteracted by high subgrade pressure, the portion of the load transmitted within the critical control perimeter contributes to the punching shear capacity and may be subtracted from the total applied punching force. Consequently, a reduced value of applied shear force is adopted when calculating the punching shear stresses acting on the element, as defined in equation (3.60).

$$v_{Ed} = \beta \frac{V_{Ed,red}}{ud} \tag{3.60}$$

where:

 v_{Ed} – design value of the applied shear stress along the control section considered [N/mm²],

 β – coefficient taking into account the eccentricity of acting force (clause 6.4.3(3-6) in [30]), for centrically loaded elements equals to 1.0 [-],

 $V_{Ed,red}$ – design value of the reduced applied shear force according to equation (3.61) [N], u – length of the considered control perimeter [mm],

d – effective slab depth [mm].

$$V_{Ed,red} = V_{Ed} - \Delta V_{Ed} \tag{3.61}$$

where:

 V_{Ed} – design value of the applied shear force [N],

 ΔV_{Ed} – design value of the net upward force within the control perimeter considered i.e., upward pressure from soil minus self weight of base according to equation (3.62) [N].

$$\Delta V_{Ed} = A_{\sigma} \cdot \sigma_n \tag{3.62}$$

 A_{σ} – area within the considered control perimeter [mm²],

 σ_n – effective soil pressure (without the influence of the self weight of the footing/slab) within the considered control perimeter [N/mm²].

Finally, it is worth noting that several studies have indicated that the reinforcement ratio and concrete strength do not influence punching shear resistance to the same extent as assumed in PN-EN 1992-1-1:2008 [30]. Specifically, in equation (3.56), the influence of both parameters is represented by the same exponent (1/3). However, research findings suggest that the effect of reinforcement ratio is less significant than that of concrete compressive strength in determining punching shear capacity. Bonić et al. [12], for example, proposed that the reinforcement ratio should be considered with an exponent of 0.25, while the concrete compressive strength should be assigned an exponent of 0.50. Similar conclusions were drawn in studies conducted by Hallgren et al. and Braestrup et al. [79]. As can be observed, the method for assessing punching shear capacity continues to raise considerable doubts and remains a topic of ongoing discussions.

3.3.5.2 PN-EN 1992-1-1:2024-05

The updated version of Eurocode 2, PN-EN 1992-1-1:2024-05 [33], introduces a revised procedure for verifying punching shear capacity, which, although based on the same fundamental assumptions, includes several significant modifications when compared to the earlier edition, PN-EN 1992-1-1:2008 [30]. One notable change concerns the minimum punching shear resistance $\tau_{Rdc,min}$. Specifically, if the condition (I), expressed by equation (3.63), is satisfied along the critical control perimeter, a detailed verification of punching shear capacity may be omitted. This highlights a further distinction between the two versions of the code. Namely, in the earlier edition [30], the critical control section was defined at a distance of 2*d* from the loaded area, whereas in the revised version [33], this distance has been reduced to $0.5d_v$.

(I)
$$\tau_{Ed} \le \tau_{Rdc,min} \tag{3.63}$$

 τ_{Ed} – design value of the applied punching shear stress at the face of the critical control section according to equation (3.64) [N/mm²],

 $\tau_{Rdc,min}$ – design value of the minimum punching shear stress resistance according to equation (3.65) [N/mm²].

$$\tau_{Ed} = \beta_e \frac{V_{Ed}}{b_{0.5} d_v} \tag{3.64}$$

where:

 β_e – coefficient accounting for concentrations of the shear forces, may be adopted according to Table 8.3 of PN-EN 1992-1-1:2024-05 [33] [-],

 V_{Ed} – design value of the applied shear force at the face of the critical control section (in case of foundation and ground slabs without shear reinforcement the soil reaction may be deducted from the shear force up to a distance of $0.67d_v$ from the face of loaded area) [N],

 $b_{0.5}$ – length of the critical control perimeter assumed at a distance $0.5d_v$ from the loaded area [mm],

 d_v – shear-resisting effective slab depth [mm].

$$\tau_{Rdc,min} = \frac{11}{\gamma_v} \cdot \sqrt{\frac{f_{ck}}{f_{yd}} \cdot \frac{d_{dg}}{d}}$$
 (3.65)

where:

 γ_v – material partial safety factor for shear and punching resistance without shear reinforcement dependent on the design situations according to Table 4.3 or Table A.1 and Table A.2 of PN-EN 1992-1-1:2024-05 [33] [-],

 f_{ck} – characteristic value of concrete compressive strength [N/mm²],

 f_{yd} – design value of the flexural reinforcement yield strength [N/mm²],

 d_{dg} – size parameter characterizing the failure zone roughness, accounts for the concrete type and its aggregate properties, may be assumed as 16 mm + $D_{lower} \le 40$ mm for concrete $f_{ck} \le 60$ MPa or 16 mm + D_{lower} ($60/f_{ck}$) $^2 \le 40$ for concrete $f_{ck} > 60$ MPa [mm], D_{lower} – the smallest value of the upper sieve size D in aggregate for the coarsest fraction of aggregates in the concrete permitted by the PN-EN 206 [38] [mm],

d – effective slab depth [mm].

Subsequently, the second condition (IIa) must be verified to determine whether punching shear reinforcement can be omitted. This is achieved by satisfying equation (3.66) along the critical control perimeter $b_{0.5}$, located at a distance of $0.5d_v$ from the loaded area.

(IIa)
$$\tau_{Ed} \le \tau_{Rd,c} \tag{3.66}$$

where:

 τ_{Ed} – design value of the applied punching shear stress at the face of the critical control section according to equation (3.64) [N/mm²],

 $\tau_{Rd,c}$ – design value of the punching shear strength of concrete element without shear reinforcement at the face of the critical control section according to equation (3.67) [N/mm²].

$$\tau_{Rd,c} = min \begin{cases} \frac{0.60}{\gamma_v} \cdot k_{pb} \cdot \left(100 \cdot \rho_l \cdot f_{ck} \cdot \frac{d_{dg}}{d_v}\right)^{\frac{1}{3}} \\ \frac{0.5}{\gamma_v} \cdot \sqrt{f_{ck}} \end{cases}$$
(3.67)

where:

 γ_{ν} – material partial safety factor for shear and punching resistance without shear reinforcement dependent on the design situations according to Table 4.3 or Table A.1 and Table A.2 of PN-EN 1992-1-1:2024-05 [33] [-],

 k_{pb} – punching shear gradient enhancement coefficient according to equation (3.68) [-], ρ_l – reinforcement ratio for longitudinal reinforcement according to equation (3.58) [-], f_{ck} – characteristic value of concrete compressive strength [N/mm²],

 d_{dg} – size parameter characterizing the failure zone roughness, accounts for the concrete type and its aggregate properties, may be assumed as 16 mm + $D_{lower} \le 40$ mm for concrete $f_{ck} \le 60$ MPa or 16 mm + D_{lower} ($60/f_{ck}$)² ≤ 40 for concrete $f_{ck} > 60$ MPa [mm], D_{lower} – the smallest value of the upper sieve size D in aggregate for the coarsest fraction of aggregates in the concrete permitted by the PN-EN 206 [38] [mm],

 d_v – shear-resisting effective slab depth [mm].

$$1.0 \le k_{pb} = 3.6 \sqrt{1 - \frac{b_0}{b_{0.5}}} \le 2.5 \tag{3.68}$$

where:

 b_0 – length of the perimeter at the face of the loaded area [mm],

 $b_{0.5}$ – length of the critical control perimeter assumed at a distance $0.5d_v$ from the loaded area [mm].

It is noteworthy that the design provisions outlined in PN-EN 1992-1-1:2024-05 [33] take into account the use of new materials, such as FRC. Specifically, Annex L is dedicated to the design of concrete structures incorporating fiber reinforcement, however, its scope is limited exclusively to SFs and does not include provisions for SyFRC. Furthermore, it is explicitly stated that ground-supported slabs are not intended to be designed in accordance with the rules of Annex L [33], as such elements are not considered essential to the overall structural stability. Instead, the document advises that alternative design recommendations should be followed to address the specific requirements of this application. Nevertheless, the fundamental rules for ULS design with respect to shear strength and punching shear capacity are discussed below.

In particular, punching shear reinforcement is not required in regions of SFRC elements with flexural reinforcement where condition (IIb), as expressed by equation (3.69), is satisfied.

(IIb)
$$\tau_{Ed} \le \tau_{Rd,cF} \tag{3.69}$$

where:

 τ_{Ed} – design value of the applied punching shear stress at the face of the critical control section according to equation (3.64) [N/mm²],

 $\tau_{Rd,cF}$ – design value of the punching shear strength of SFRC element (with flexural reinforcement) without shear reinforcement at the face of the critical control section according to equation (3.70) [N/mm²].

$$\tau_{Rd,cF} = \eta_c \cdot \tau_{Rd,c} + \eta_F \cdot f_{Ftud} \ge \eta_c \cdot \tau_{Rdc,min} + f_{Ftud}$$
 (3.70)

where:

 η_c – strength reduction coefficient for shear resistance equal to $\tau_{Rd,c}/\tau_{Ed} \le 1.0$ [-],

 $\tau_{Rd,c}$ – design value of the punching shear strength of concrete element without shear reinforcement at the face of the critical control section according to equation (3.67) [N/mm²],

$$\eta_F = 0.4$$
 [-],

 f_{Ftud} – design residual tensile strength of SFRC for given crack width accounting for

fiber orientation and volume effect according to equation (3.71) [N/mm²], $\tau_{Rdc,min}$ – design value of the minimum punching shear stress resistance according to equation (3.65) [N/mm²].

$$f_{Ftud} = \frac{f_{Ftu,ef}}{\gamma_{SF}} \tag{3.71}$$

where:

 $f_{Ftu,ef}$ – effective residual tensile strength of SFRC for given crack width accounting for fiber orientation and volume effect according to equation (3.49) [N/mm²], γ_{SF} – material partial safety factor for SFRC [-].

For lightly reinforced SFRC without longitudinal reinforcement, the design value of the punching shear strength should be calculated according to equation (3.72).

$$\tau_{Rd,cF} = f_{Ftud} \tag{3.72}$$

where:

 $\tau_{Rd,cF}$ – design value of the punching shear strength of SFRC element (without flexural reinforcement) without shear reinforcement at the face of the critical control section [N/mm²],

 f_{Ftud} – design residual tensile strength of SFRC for given crack width accounting for fiber orientation and volume effect according to equation (3.71) [N/mm²].

It is also noted that the shear reinforcement in slabs may be fully replaced by SFs if equation (3.73) is fulfilled, which after simplification results in equation (3.74).

$$\frac{f_{Ftu,ef}}{f_{yk}} \ge \rho_{w,min}$$

$$f_{Ftu,ef} \ge 0.08 \cdot \sqrt{f_{ck}}$$
(3.73)

$$f_{Ftu,ef} \ge 0.08 \cdot \sqrt{f_{ck}} \tag{3.74}$$

where:

 $f_{Ftu,ef}$ – effective residual tensile strength of SFRC for given crack width accounting for fiber orientation and volume effect according to equation (3.49) [N/mm²],

 f_{yd} – design value of the flexural reinforcement yield strength [N/mm²],

 $\rho_{w,min}$ – minimum reinforcement ratio equals to $0.08 f_{ck}^{1/2}/f_{yk}$ [-],

 f_{ck} – characteristic value of concrete compressive strength [N/mm²].

3.3.5.3 Technical Report 34

In the currently adopted 4th edition of TR34 [28], the punching shear capacity of ground-supported slabs is determined in accordance with PN-EN 1992-1-1:2008 [30]. Specifically, two conditions (I) and (II) must be satisfied. Firstly, according to equation (3.75), the concentrated force acting on the slab must not exceed the maximum punching shear capacity of the concrete at the face of the loaded area. Secondly, equation (3.76) limits the concentrated force to the maximum punching shear capacity at the critical control section. One of the key differences between the provisions of PN-EN 1992-1-1:2008 [30] and TR34 [28] lies in the assumption of the critical control section. In TR34 [28], this section is located at a fixed distance of 2*d* from the loaded area, whereas in [30], its position must be determined iteratively within a range of up to 2*d*.

$$(I) P_{n,max} \ge P (3.75)$$

where:

 $P_{p,max}$ – punching shear load-bearing capacity at the face of the loaded area according to equation (3.77) [N],

P – applied punching shear force [N].

(II)
$$P_p \ge P \tag{3.76}$$

where:

 P_p – punching shear load-bearing capacity at the face of the critical control section according to equation (3.80) [N],

P – applied punching shear force [N].

$$P_{n,max} = v_{max} \cdot u_0 \cdot d \tag{3.77}$$

where:

 v_{max} – maximum shear strength of concrete at the face of the loaded area according to equation (3.78) [N/mm²],

 u_0 – length of the perimeter of the loaded area based on the effective dimensions of the baseplate according to equation (3.83), (3.85), or (3.87) depending on the load location [mm],

d – effective slab depth, for PC and FRC = 0.75h, where h is a slab thickness [mm].

$$v_{max} = 0.5 \cdot k_2 \cdot f_{cd} \tag{3.78}$$

 k_2 – strength reduction factor for concrete cracked in shear according to equation (3.79) [-],

 f_{cd} – design value of concrete compressive strength [N/mm²].

$$k_2 = 0.6 \cdot \left(1 - \frac{f_{ck}}{250}\right) \tag{3.79}$$

where:

 f_{ck} – characteristic value of concrete compressive strength [MPa].

$$P_p = v_{Rd,c,min} \cdot u_1 \cdot d \tag{3.80}$$

where:

 $v_{Rd,c,min}$ – minimum shear strength of concrete at the face of the critical control section according to equation (3.81) [N/mm²],

 u_I – length of the critical control perimeter at a distance 2d from the loaded area according to equation (3.84), (3.86), or (3.88) depending on the load location [mm], d – effective slab depth, for PC and FRC = 0.75h, where h is a slab thickness [mm].

$$v_{Rd,c,min} = 0.035 \cdot k_s^{1.5} \cdot f_{ck}^{0.5}$$
 (3.81)

where:

 k_s – coefficient taking into consideration size/scale effect according to equation (3.82) [-],

 f_{ck} – characteristic value of concrete compressive strength [N/mm²].

$$k_s = 1 + \left(\frac{200}{d}\right)^{0.5} \le 2.0\tag{3.82}$$

where:

d – effective slab depth, for PC and FRC = 0.75h, where h is a slab thickness [mm].

The aforementioned perimeters of the loaded area u_0 and the critical control section u_1 vary depending on the load position, whether internal, edge, or corner. For an internal load applied through a square baseplate, the perimeters $u_{0,i}$ and $u_{1,i}$ are determined using

equations (3.83) and (3.84), respectively. In the case of an edge load, $u_{0,e}$ and $u_{1,e}$ are calculated according to equations (3.85) and (3.86). Finally, for a corner load, the corresponding perimeters $u_{0,c}$ and $u_{1,c}$ are derived from equations (3.87) and (3.88), respectively.

$$u_{0,i} = 4(x+4t) (3.83)$$

$$u_{0,i} = 4(x+4t)$$
 (3.83)
 $u_{1,i} = 4(x+4t) + 4d\pi$ (3.84)

$$u_{0,e} = 3(x+4t) (3.85)$$

$$u_{1,e} = 3(x+4t) + 2d\pi (3.86)$$

$$u_{0,c} = 2(x+4t) (3.87)$$

$$u_{1,c} = 2(x+4t) + d\pi ag{3.88}$$

where:

 $u_{0,i}$, $u_{0,e}$, and $u_{0,c}$ – length of the perimeter of the loaded area based on the effective dimensions of the baseplate for the internal, edge, and corner load, respectively [mm], $u_{1,i}$, $u_{1,e}$, and $u_{1,c}$ – length of the critical control perimeter at a distance 2d from the loaded area for the internal, edge, and corner load, respectively [mm],

x – racking leg base or column dimensions [mm],

t – thickness of the baseplate [mm],

d – effective slab depth, for PC and FRC = 0.75h, where h is a slab thickness [mm].

TR34 [28] states that, according to RILEM guidance [66], the presence of SFs can enhance the shear capacity of a concrete element, however, this improvement is typically observed when conventional reinforcement is also present. Some studies on slabs reinforced solely with SFs have reported an increase in punching shear capacity. Nevertheless, it is emphasized that these results are often qualitative and based on fiber dosages higher than those typically used in ground slabs. Due to the limited number of research papers providing relevant data, TR34 [28] recommends following the RILEM TC 162-TDF guidelines [66], however with certain exceptions. Specifically, the guideline advises applying a 50% reduction to the RILEM value, regardless of whether traditional reinforcement is present. Furthermore, RILEM [66] proposes that the increase in shear strength equals 0.12 times the residual flexural tensile strength $f_{Rk,4}$ corresponding to a $\delta = 3$ mm or CMOD = 3.5 mm, as expressed in equation (3.45). In contrast, TR34 [16] considers the mean value of all residual flexural tensile strengths $(f_{R,1}, f_{R,2}, f_{R,3}, \text{ and } f_{R,4})$. Finally, the formula proposed by TR34 [28], presented in equation (3.89), is stated to apply to concretes reinforced with both SFs and macro SyFs.

$$v_f = \frac{0.12 \cdot \left(\frac{f_{R,1} + f_{R,2} + f_{R,3} + f_{R,4}}{4}\right)}{2} \tag{3.89}$$

 v_f – additional shear strength resulting from the presence of fibers in concrete [N/mm²], $f_{R,j}$ – residual flexural tensile strength corresponding to $CMOD = CMOD_j$ or $\delta = \delta_j$ (j = 1, 2, 3, 4) obtained from the 3PBT according to PN-EN 14651 [29] [N/mm²].

It can be noted that in the previous version of TR34 [68], the test described in standard JSCE-SF4 [25] was conducted to characterize the equivalent flexural tensile strength f_{eq} . The testing procedure is discussed in detail in Chapter 3.3.2.3. Consequently, the additional shear strength attributable to the presence of SyFs in the concrete was characterized using the fracture toughness index R_e , as expressed in equation (3.90).

$$v_f = 0.12 \cdot R_e \cdot f_{ctk,fl} \tag{3.90}$$

where:

 v_f – additional shear strength resulting from the presence of fibers in concrete [N/mm²], R_e – fracture toughness index according to equation (3.35) obtained from the 4PBT according to JSCE-SF4 [25] [%],

 $f_{ctk,fl}$ – concrete characteristic flexural tensile strength according to equation (3.17) [N/mm²].

Consequently, the total punching shear capacity of ground-supported slab, incorporating the additional resistance provided by the presence of fibers in concrete, can be calculated using equation (3.91).

$$P_p = (v_{Rd,c,min} + v_f) \cdot u_1 \cdot d \tag{3.91}$$

where:

 P_p – punching shear load-bearing capacity at the face of the critical control section [N], $v_{Rd,c,min}$ – minimum shear strength of concrete at the face of the critical control section according to equation (3.81) [N/mm²],

 v_f – additional shear strength resulting from the presence of fibers in concrete according to equation (3.89) or (3.90) [N/mm²],

 u_1 – length of the critical control perimeter at a distance 2d from the loaded area according to equation (3.84), (3.86), or (3.88) depending on the load location [mm],

d – effective slab depth, for PC and FRC = 0.75h, where h is a slab thickness [mm].

The TR34 guideline [28] addresses also the issue of slab-soil interaction. Specifically, when a slab is in contact with the ground, a portion of the applied load is transferred directly to the subbase. As a result, the effective force acting on the slab may be reduced by accounting for the ground reaction. The area considered for determining the reduced force corresponds to the region within the punching shear critical control perimeter, located at a distance of 2d from the loaded area. TR34 [28] proposes methods for calculating the ground reaction and, consequently, the reduced punching force. For internal and edge concentrated loads, the ground reaction is calculated according to equations (3.92) and (3.93), respectively. For corner loading, the contribution of the subgrade to load transfer is not taken into account.

$$R_{cp,i} = 1.4 \cdot \left(\frac{d}{l}\right)^2 \cdot P \tag{3.92}$$

$$R_{cp,i} = 1.4 \cdot \left(\frac{d}{l}\right)^{2} \cdot P$$

$$R_{cp,e} = 2.4 \cdot \left(\frac{d}{l}\right)^{2} \cdot P$$
(3.92)

where:

 $R_{cp,i}$ and $R_{cp,e}$ – ground reaction resulting from an internal and edge point load [N], d – effective slab depth, for PC and FRC = 0.75h, where h is a slab thickness [mm], l – radius of relative stiffness according to equation (3.15) [mm], P – applied punching shear force [N].

Furthermore, TR34 [28] states that when a concentrated load is applied through a stiff bearing, the increase in the length of the critical control perimeter and the alteration of the ground pressure distribution can be taken into account. Although a comprehensive analysis of the resulting increase in ground reaction can be complex, a simplified procedure may be applied when the ratio a_r/l is less than 0.2. To avoid the potentially unconservative assumption that the peak pressure at the perimeter of the stiff bearing equals the peak pressure directly beneath the point load, the ground pressure under the bearing plate is neglected in the calculations. A detailed derivation of the equations for punching shear load reduction is provided in Appendix F of the TR34 guideline [28]. For internal and edge point loads applied through a stiff bearing with $a_r/l < 0.2$, the ground reactions are calculated according to equations (3.94) and (3.95), respectively.

$$R_{cp,i} = 1.4 \cdot \left(\frac{d}{l}\right)^2 \cdot P + 0.47 \cdot (x_b + y_b) \cdot \frac{d \cdot P}{l^2}$$
 (3.94)

$$R_{cp,e} = 2.4 \cdot \left(\frac{d}{l}\right)^2 \cdot P + 0.80 \cdot (x_b + 2y_b) \cdot \frac{d \cdot P}{l^2}$$
 (3.95)

 $R_{cp,i}$ and $R_{cp,e}$ – ground reaction resulting from an internal and edge point load applied through a stiff bearing, where a/l < 0.2 [N],

d – effective slab depth, for PC and FRC = 0.75h, where h is a slab thickness [mm],

l – radius of relative stiffness according to equation (3.15) [mm],

P – applied punching shear force [N],

 x_b and y_b – effective dimensions of the stiff bearing plate, look Chapter 7.8.1 in the TR34 [28] [mm].

Finally, the ground reaction can then be deducted from the imposed punching shear load according to equation (3.96).

$$P - R_{cp} \le P_p \tag{3.96}$$

where:

P – applied punching shear force [N],

 R_{cp} – ground reaction resulting from the point load according to equation (3.92), (3.93), (3.94), or (3.95) depending on the load location and presence of stiff bearing plate [N], P_p – punching shear load-bearing capacity at the face of the critical control section [N].

3.3.5.4 Model Code 2010

In MC2010 [80], the calculation of punching shear capacity is based on the critical shear crack theory [81]. With respect to control perimeters, the critical control perimeter b_1 is typically assumed at a distance of $0.5d_v$ from the loaded area, whereas the shear-resisting control perimeter b_0 accounts for the non-uniform distribution of shear stresses along b_1 . According to [80], the design punching shear capacity of concrete $V_{Rd,c}$ must satisfy condition (Ia), as defined by equation (3.97). It is also worth noting that for ground-supported slabs and footings, the design punching shear force V_{Ed} is equal to the support reaction reduced by the soil pressure acting within the critical control perimeter b_1 .

$$V_{Ed} \le V_{Rd,c} \tag{3.97}$$

 V_{Ed} – design value of the applied punching shear force [N],

 $V_{Rd,c}$ – design value of the punching shear force of concrete element without shear reinforcement along the shear-resisting control perimeter according to equation (3.98) [N].

$$V_{Rd,c} = k_{\psi} \cdot \frac{\sqrt{f_{ck}}}{\gamma_c} \cdot b_0 d_v \tag{3.98}$$

where:

 k_{ψ} – parameter depending on the slab deformations (rotations) according to equation (3.99) [-],

 f_{ck} – characteristic value of concrete compressive strength [N/mm²],

 γ_c – material partial safety factor for concrete [-],

 b_0 – shear-resisting control perimeter according to equation (3.101) [mm],

 d_v – shear-resisting effective slab depth [mm].

$$k_{\psi} = \frac{1}{1.5 + 0.9k_{dq}\psi d} \le 0.6 \tag{3.99}$$

where:

 k_{dg} – parameter depending on the aggregate size, if the maximum aggregate diameter $d_g \ge 16$ mm can be taken as 1.0, otherwise according to equation (3.100) [-],

 ψ – parameter depending on the slab rotation around the supported/loaded area according to equation (3.102), (3.103), or (3.104) depending on the Level of Approximation [-],

d – effective slab depth [mm].

$$k_{dg} = \frac{32}{16 + d_a} \ge 0.75 \tag{3.100}$$

where:

 d_g – maximum aggregate diameter [mm].

$$b_0 = k_e \cdot b_{1,red} \tag{3.101}$$

 k_e – coefficient of eccentricity, for the inner, edge, and corner location of the load can be usually taken as 0.90, 0.70, and 0.65, respectively, otherwise see Chapter 7.3.5.2(4) in the MC2010 [80] [-],

 $b_{1,red}$ – reduced critical control perimeter, usually can be taken as b_1 , otherwise see Chapter 7.3.5.2(4) in the MC2010 [80] [mm].

The MC2010 [80] introduces the idea of Levels of Approximation (LoA) from I to IV. The higher LoA, the higher accuracy of calculations but also greater time required for the analysis. The choice of LoA influences the calculation method of parameter ψ which reflects the slab rotation around the supported/loaded area. Level I of Approximation (LoA I) is dedicated for preliminary estimations, including regular flat slabs designed according to the elastic analysis with no notable internal force redistribution. In this level, the full utilization of the flexural reinforcement ($m_{Ed} = m_{Rd}$) is assumed. Moreover, large crack widths and large slab rotations are presumed. The distance r_s can be usually taken as 0.22L, where L is the slab span. The parameter ψ is calculated according to equation (3.102). Then, Level II of Approximation (LoA II) is assumed for regular flat slabs when the notable bending moment redistribution is expected. The bending moment m_{Ed} is calculated depending on the reinforcement direction and the support type. The distance r_s can be taken as that for LoA I. The parameter ψ is calculated according to equation (3.103). Regarding Level III of Approximation (LoA III), it is used for irregular slabs and when higher precision of the calculations is required when comparing with LoA I and II. Moreover, the calculations of r_s and m_{Ed} are performed according to the linear elastic (uncracked) model. The parameter ψ is calculated according to equation (3.104). Finally, Level IV of Approximation (LoA IV) is limited only to the unusual cases. The slab rotation is defined by the nonlinear analysis.

LoAI
$$\psi = 1.5 \cdot \frac{r_s}{d} \cdot \frac{f_{yd}}{E_s}$$
 (3.102)

LoA II
$$\psi = 1.5 \cdot \frac{r_s}{d} \cdot \frac{f_{yd}}{E_s} \cdot \left(\frac{m_{Ed}}{m_{Rd}}\right)^{1.5}$$
 (3.103)

LoA III
$$\psi = 1.2 \cdot \frac{r_s}{d} \cdot \frac{f_{yd}}{E_s} \cdot \left(\frac{m_{Ed}}{m_{Rd}}\right)^{1.5}$$
 (3.104)

 r_s – distance between the support axis and the zero radial bending moment [mm],

d – effective slab depth [mm],

 f_{yd} – design value of the flexural reinforcement yield strength [N/mm²],

 E_s – Young's modulus of the flexural reinforcement [N/mm²],

 m_{Ed} – average moment per unit length for calculation of the flexural reinforcement in the support strip depending on the considered direction, see Chapter 7.3.5.4 in the MC2010 [80] [Nmm],

 m_{Rd} – design average flexural strength per unit length in the support strip depending on the considered direction, see Chapter 7.7.3.5 in the MC2010 [80] [Nmm].

Additionally, the second condition (II), expressed by equation (3.105), must also be satisfied, as the maximum punching shear capacity is limited by the potential crushing of concrete struts in the supported/loaded area.

$$(II) V_{Ed} \le V_{Rd,max} (3.105)$$

where:

 V_{Ed} – design value of the applied punching shear force [N],

 $V_{Rd,max}$ – design value of the maximum punching shear force of concrete along the shear-resisting control perimeter according to equation (3.106) [N].

$$V_{Rd,max} = k_{sys} k_{\psi} \cdot \frac{\sqrt{f_{ck}}}{\gamma_c} \cdot b_0 d_v \le \frac{\sqrt{f_{ck}}}{\gamma_c} \cdot b_0 d_v$$
 (3.106)

where:

 k_{sys} – coefficient depending on the performance of punching shear reinforcing systems, in absence of other data and ensuring that the reinforcement is detailed according to the MC2010 [80] requirements, a value 2.0 can be assumed [-],

 k_{ψ} – parameter depending on the slab deformations (rotations) according to equation (3.99) [-],

 f_{ck} – characteristic value of concrete compressive strength [N/mm²],

 γ_c – material partial safety factor for concrete [-],

 b_{θ} – shear-resisting control perimeter according to equation (3.101) [mm],

 d_v – shear-resisting effective slab depth [mm].

Regarding FRC slabs, the MC2010 [80] provides the equation (3.107) for punching shear capacity verification. In particular, the guideline accounts for the additional shear capacity contributed by the presence of fibers. Consequently, the design punching shear capacity of FRC slab without shear reinforcement must satisfy condition (Ib).

(Ib)
$$V_{Ed} \le V_{Rd,c} + V_{Rd,f}$$
 (3.107)

where:

 V_{Ed} – design value of the applied punching shear force [N],

 $V_{Rd,c}$ – design value of the punching shear force of concrete element without shear reinforcement along the shear-resisting control perimeter according to equation (3.98) [N],

 $V_{Rd,f}$ – design value of the additional punching shear force of resulting from inclusion of fibers to concrete along the shear-resisting control perimeter according to equation (3.108) [N].

$$V_{Rd,f} = \frac{f_{Ftuk}}{\gamma_{fc}} b_0 d_v \tag{3.108}$$

where:

 f_{Ftuk} – characteristic value of the ultimate residual tensile strength for FRC, calculated taking into account $w_u = 1.5$ mm, where w_u is a maximum crack opening accepted in the structural design [N/mm²],

 γ_{fc} – material partial safety factor for FRC [-],

 b_0 – shear-resisting control perimeter according to equation (3.101) [mm],

 d_v – shear-resisting effective slab depth [mm].

More detailed information regarding designing of FRC can be found in Fib Bulletin 105 [82] which is fully dedicated to the fiber reinforcement. It must be also mentioned that in 2020 the International Federation for Structural Concrete published updated version of the Model Code [83]. However, due to lack of access to this standard, it was not discussed as part of this dissertation.

3.3.6. Summary

One of the key aspects of FRC characterization is the assessment of its post-cracking behavior, particularly residual tensile strength, and toughness. Table 3.4 summarizes the most commonly used standardized methods for evaluating the tensile performance of FRC. It is evident that these methods have been primarily developed for concretes reinforced with SFs, with none specifically addressed to testing SyFRC. Moreover, proposed methods most commonly aim at the indirect determination of the tensile strength of concrete, typically through flexural or splitting tensile tests. This is primarily attributed to the relative simplicity and practicality of performing these tests in comparison to uniaxial tensile strength measurements.

Table 3.4 Standardized FRC testing methods for characterizing tensile behavior

| Standard | Fibers | Description | Result |
|---------------------------------|------------------|--|--|
| JSCE Recommendations [42] | Not specified | Uniaxial tensile test of dog-bone samples | f_{tyi} – tensile yield strength f_{pshi} – maximum stress in the strain-hardening region f_{ti} – tensile strength ε_{tui} – ultimate tensile strain |
| ASTM C496-96 [48] | Not specified | Splitting tensile test of cylinders | f_{spl} – splitting tensile strength |
| EN 12390-06 [49] | Not specified | Splitting tensile test of cylinders or cubes | f_{spl} – splitting tensile strength |
| EN 12390-05 [64] | Not specified | 4PBT of unnotched prism samples | f_{cf} – maximum flexural concrete strength |
| EN 14651 [29] | Steel | 3PBT of notched prism samples | $f_{ct,L}$ – limit of proportionality $f_{R,j}$ – residual flexural tensile strength |
| RILEM TC 162-TDF [66] | Metallic | 3PBT of notched prism samples | $f_{ct,L}$ – limit of proportionality $f_{R,j}$ – residual flexural tensile strength $f_{eq,2}$, $f_{eq,2}$ – equivalent tensile flexural strength |
| JSCE-SF4 [25] | Steel | 4PBT of unnotched prism samples | f_b – maximum flexural tensile strength f_{eq} – equivalent flexural tensile strength |
| ASTM C1018-97 [84] | Not specified | 4PBT of unnotched prism samples | I_5 , I_{10} , I_{30} – toughness indices $R_{20,10}$, $R_{30,10}$ – residual strength factors |
| ASTM C1609-05 [85] | Not specified | 4PBT of unnotched prism samples | MOR – modulus of rupture/maximum equivalent flexural tensile strength f^{D}_{150} , f^{D}_{600} – residual flexural tensile strength T^{D}_{150} – toughness $R^{D}_{T, 150}$ – equivalent flexural strength ratio |
| ASTM C1550-20 [86] | Not specified | Centrally loaded round panel | W – toughness at 5, 10, 20, or 40 mm deflection |
| EN 14488-5:2006 [87] | Not specified | Centrally loaded square plate | Toughness at 25 mm deflection |

In addition, most widely recognized design standards and guidelines for FRC structures predominantly address SFRC, while significantly less attention has been given to SyFRC. Additionally, although concrete ground slabs are widely used, there is no unified standard governing their design. Namely, various guidelines employ different design methods what may lead to confusion and unclarity. Furthermore, the available calculation procedures provide little to no guidance on the use of fibers and their influence on the load-bearing capacity of ground-supported slabs. In addition, the theoretical assumptions typically rely on the application of linear elastic behavior of the concrete slab resting on an elastic subgrade, in accordance with Winkler's theory. However, these approaches significantly underestimate the load-bearing capacity of FRC ground slabs. In practice, the linear elastic model is even less suitable for FRC than for PC, as fibers become most effective after cracking occurs, when the concrete enters its nonlinear phase [88]. Consequently, guidelines based on yield line theory appear to be the most suitable for predicting the structural capacity of FRC ground-supported slabs. Furthermore, there are also discrepancies between standards regarding the requirements that FRC must meet in order for the fibers to be considered as structural reinforcement. Meeting these requirements is essential in order to include the additional load-bearing capacity provided by the fibers in design calculations.

Regarding the procedures for calculating ground slabs against punching shear failure (Table 3.5), they are usually dedicated to traditionally reinforced concrete slabs. The adaptation of those methods for FRC is commonly based on the inclusion in calculations the additional shear strength resulting from the presence of fibers in concrete. Nevertheless, some standards require the presence of conventional steel bars in order to consider the contribution of fibers to the overall slab capacity. Moreover, the fiber contribution to both flexural and punching shear capacity is calculated differently across various standards. Additionally, these provisions usually refer to elements with SFs, whereas even more conservative approaches are adopted for SyFRC due to the limited amount of available research on ground slabs with SyFs. Finally, one of the most significant differences between standards and guidelines in the calculation of the punching shear capacity is the assumed location of the critical control perimeter relative to the loaded area [89]. Namely, some standards suggest the specific value of a equals to 0.5d, 1.5d, or 2d, while others require the analytic and iterative determination of the a/d ratio (Table 3.6). In conclusion, there are still lingering questions and inaccuracies regarding such a particular and specific topic as punching shear capacity of SyFRC ground slabs.

Table 3.5 Punching shear design principles for FRC according to selected standards

| Standard | PN-EN 1992-1- 1:2008 [30] | PN-EN 1992-1- 1:2024 [33] | Model Code 2010 [80] | Technical Report 34 [28] |
|--|---|--|---|---|
| Verification of the punching shear capacity at the face of: | 1) loaded area; 2) critical control perimeter. | 1) critical control perimeter. | 1) critical control perimeter. | 1) loaded area, 2) critical control perimeter. |
| Critical control perimeter | a = 2d | a = 0.5d | a = 0.5d | a = 2d |
| Fiber contribution (equation and requirements) | Not considered. | Considered as $f_{Ftu,ef} = \kappa_0 \cdot \kappa_G \cdot 0.33 \cdot f_{Rk,3}$ for SFs with or without longitudinal reinforcement. | Considered as $f_{Ftuk} = f_{Ftsk} - \frac{w_u}{CMOD_3} (f_{Ftsk} - 0.5f_{Rk,3} + 0.2f_{Rk,1})$ for fibers (material not specified) with or without longitudinal reinforcement. | Considered as $v_f = 0.015 \cdot (f_{R,1} + f_{R,2} + f_{R,3} + f_{R,4})$ for SFs and macro SyFs, with or without longitudinal reinforcement. |
| Ground contribution | Considered since the net upward load within the critical control perimeter (ΔV_{Ed}) adds to the overall capacity and may be deducted from the acting punching force. | Considered since the soil reaction within the critical control perimeter (up to 0.67 <i>d</i>) adds to the overall capacity and may be deducted from the acting punching force. | Not mentioned. | Considered since the ground reaction (R_{cp}) adds to the overall capacity and may be deducted from the acting punching force; additionally, R_{cp} increases when punching force is applied through a stiff bearing. |

The performed literature review was also used to decide on the research methodology adopted in the dissertation for material characterization. Namely, the tests were conducted according to the PN-EN 206 [38], PN-EN 12390-13 [90], and regarding the tensile strength characteristic, using splitting and flexural tensile tests described in PN-EN 12390-06 [49] and PN-EN 14651 [29], respectively. Moreover in further analytical analysis, the TR34 guideline [28] is followed, since it covers most of the considered topics, namely flexural and punching shear design of slabs supported by the ground with the inclusion of macro SyFs and ground contribution. Finally, the additional shear strength resulting form the presence of SyFs in the concrete is evaluated by considering the formulas suggested in TR34 [28], PN-EN 1992-1-1:2024 [33], RILEM TC 162-TDF [66], and MC2010 [80].

Table 3.6 Recommended distance of a critical control perimeter relative to the loaded area, denoted as a, according to selected standards [28], [30], [33], [80], [91], [92]

| Standard | Picture | a = |
|---|--|------------------------------|
| PN-EN 1992-1- 1:2008 [30] | $\begin{array}{c ccccccccccccccccccccccccccccccccccc$ | Until 2 <i>d</i> (iterative) |
| PN-EN 1992-1- 1:2024- 05 [33] | b _{0,5} b ₀ | 0.5 <i>d</i> |
| Technical Report 34 [28] | $\begin{array}{c c} 2d \\ \hline \\ 2d \\ \hline \\ 2d \\ \hline \end{array}$ | 2d |
| Model Code 2010 [80] | 0,5 d _v 0,5 d _v 0,5 d _v 0,5 d _v slab edge | 0.5 <i>d</i> |
| ACI 318- 19 [91] | Critical section through slab shear reinforcement (first line of stirrup legs) Critical section through slab shear reinforcement (first line of stirrup legs) Slab edge Critical section through slab shear reinforcement (first line of stirrup legs) Slab edge Critical section through slab shear reinforcement (first line of stirrup legs) Slab edge Critical section through slab shear reinforcement (first line of stirrup legs) Slab edge Critical section through slab shear reinforcement (first line of stirrup legs) Slab edge Critical section through slab shear reinforcement (first line of stirrup legs) Slab edge All Plan Plan Plan Plan Plan | 0.5 <i>d</i> |
| BS 8110- 1:1997 [92] | Perimeter Perimeter l_p l_p l_p l_p l_p l_p The shear capacity is checked first on a perimeter 1.5 d from the face of the loaded area. | 1.5 <i>d</i> |

3.4. Existing studies

3.4.1. Synthetic fiber reinforced concrete

3.4.1.1 Introduction

The continuous advancement of concrete technology enables the individual design of its properties to meet specific performance requirements. Once considered a simple construction material, concrete has evolved into a complex solution, capable of being customized for diverse applications [93]. The selection of concrete type is primarily governed by its mechanical properties, such as compressive, tensile, and flexural strengths, as well as the modulus of elasticity and physical characteristics, including density, setting time, workability, and flowability. However, nowadays there is an increasing emphasis on the development of concrete responsible production and consumption as well as minimization of negative environmental impact. One of the solutions aligned with the principles of the sustainable development is the extension of structural service life and the reduction of maintenance costs [94]. Consequently, ensuring long-term durability has become a critical design criterion for the designed structures [95]. Achieving this goal requires careful and conscious choice of concrete composition. FRC is one of the materials capable of satisfying both mechanical and durability-related performance demands [96]. The incorporation of fibers into the concrete matrix enhances not only its strength characteristics but also contributes to the control of cracking by reducing both crack width and their number. Furthermore, due to the presence of fibers, concrete is not longer a brittle material but is able to transfer stresses even after cracking [97]-[99]. Additionally, SyFRC exhibit superior resistance to corrosion and oxidation compared to SFRC. This enhanced durability makes SyFRCs especially suitable for applications in aggressive environmental conditions, including industrial and marine fields of application [100]–[103].

A characterization of FRC requires the consideration of multiple parameters related to the fibers incorporated into the mix. These include the type of fiber material (e.g., monofilament, multifilament, fibrillated, straight, or shaped), geometric properties such as fiber length (l_f) , diameter (d_f) , and slenderness (l_f/d_f) . Mechanical properties of fiber, namely the fiber modulus of elasticity (E_f) and tensile strength (f_f) , must also be accounted for. Moreover, the nominal fiber dosage, expressed by equation (3.109), is a critical factor influencing the mechanical behavior of FRC.

$$V_f = \frac{w_f}{\rho_f} \cdot 100\% \tag{3.109}$$

 V_f – nominal fiber dosage [%], w_f – fiber content in units of weight in 1 m³ [kg/m³], ρ_f – density of fiber material [kg/m³].

Regarding the material type, fibers used in concrete can be categorized as metallic or non-metallic. The metallic group primarily consists of SFs, while the non-metallic category includes a wide range of materials such as synthetic, glass, carbon, basalt, and natural fibers. The variations in the performance of FRC are largely attributable to the specific properties of the fiber material. Since the present study focuses on SyFs, the subsequent discussion addresses only their influence on selected physical and mechanical properties of concrete. Additionally, PN-EN 14889-2 standard [104] classifies SyFs based on their physical form:

- Class Ia: microfibers: $d_f < 0.30$ mm: monofilament (nonstructural).
- Class Ib: microfibers: $d_f < 0.30$ mm: fibrillated (nonstructural).
- Class II: macrofibers: $d_f > 0.30$ mm (structural).

It is assumed that the structural fibers influence the load-bearing capacity of concrete elements and, under specific conditions, can serve as a partial or complete substitute for conventional reinforcement in the form of steel bars or meshes. In contrast, the primary role of microfibers is to control the initiation and propagation of microcracks by effectively bridging cracks. Given the scope of this dissertation, the discussion is restricted to macro SyFs. Table 3.7 presents examples of commercially available macro SyFs, detailing their physical and mechanical properties as well as the required dosage to achieve $f_{R,1} = 1.5$ MPa and $f_{R,4} = 1.0$ MPa corresponding with *CMOD* equals to 0.5 mm and 3.5 mm, respectively. Table A.1 in Appendix A summarizes the influence of macro SyFs dosage, material properties, and geometry on selected concrete properties, including slump, concrete modulus of elasticity E_c , compressive strength f_c , splitting tensile strength f_{spl} , flexural tensile strength f_{fl} , and toughness W_0 . The following subsections provide a detailed review of the effects of fiber incorporation on concrete properties, detailing the benefits, drawbacks, challenges, and additional requirements resulting from fiber integration.

Table 3.7 Examples of commercially available macro SyFs

| * | ny avanable maero byr s | |
|--|---|---|
| $l_f = 30 \text{ mm}, d_f = 0.77 \text{ mm}$ | $l_f = 39 \text{ mm}, d_f = 0.78 \text{ mm}$ | $l_f = 48 \text{ mm}, d_f = 0.93 \text{ mm}$ |
| f_{ft} = 400 MPa, E_f = 5.0 GPa Shape: monofilament, wavy Material: polyolefin | f_{ft} = 800 MPa, E_f = 7.1 GPa Shape: monofilament, wavy Material: polymer | f_{ft} = 560 MPa, E_f = 20.5 GPa Shape: monofilament, embossed |
| Dosage: 4.0 kg/m^3 to achieve $f_{R,l} = 1.5 \text{ MPa}$ and | Dosage: 3.3 kg/m^3 to achieve $f_{R,I} = 1.5 \text{ MPa}$ and | Material: polypropylene homopolymer and polyethylene |
| $f_{R,4} = 1.0 \text{ MPa}$ | $f_{R,4} = 1.0 \text{ MPa}$ | Dosage: 6.0 kg/m^3 to achieve $f_{R,I} = 1.5 \text{ MPa}$ and $f_{R,A} = 1.0 \text{ MPa}$ |
| *************************************** | | |
| l_f = 39 mm, d_f = 0.78 mm f_{ft} = 800 MPa, E_f = 7.1 GPa Shape: monofilament, wavy | l_f = 50 mm, d_f = 2.05 x 0.30 mm f_{ff} = 490 MPa, E_f = 4.0 GPa Shape: monofilament, flat | l_f = 30 mm, d_f = 0.70 mm f_{ff} = 500 MPa, E_f = 6.0 GPa Shape: monofilament, |
| Material: polymer with antistatic coat | Material: copolymer (polyolefin) | embossed Material: polyolefin |
| Dosage: 3.3 kg/m^3 to achieve $f_{R,1} = 1.5 \text{ MPa}$ and | Dosage: 4.0 kg/m^3 to achieve $f_{R,l} = 1.5 \text{ MPa}$ and | Dosage: 5.0 kg/m ³ to achieve $f_{R,I} = 1.5$ MPa and |
| $f_{R,4} = 1.0 \text{ MPa}$ | $f_{R,4} = 1.0 \text{ MPa}$ | $f_{R,4} = 1.0 \text{ MPa}$ |
| | | |
| $l_f = 50 \text{ mm}, d_f = 0.66 \text{ mm}$ $f_{ft} = 530 \text{ MPa}, E_f = 7.4 \text{ GPa}$ | $l_f = 54 \text{ mm}, d_f = 0.70 \text{ mm}$ $f_{ft} = 500 \text{ MPa}, E_f = 5.5 \text{ GPa}$ | l_f = 24 mm, d_f = not specified f_{ft} = 550-650 MPa, E_f = 4.8-5.9 |
| Shape: multifilament, twisted | Shape: multifilament, twisted | GPa Shanay multifilament, twisted |
| Material: polyolefin Dosage: 4.0 kg/m³ to achieve | Material: polyolefin Dosage: not specified | Shape: multifilament, twisted Material: polyolefin |
| $f_{R,I} = 1.5 \text{ MPa}$ and | | Dosage: 5.0 kg/m ³ to achieve |
| $f_{R,4} = 1.0 \text{ MPa}$ | | $f_{R,I} = 1.5 \text{ MPa}$ and $f_{R,4} = 1.0 \text{ MPa}$ |

3.4.1.2 Mix design

Designing the SyFRC mixture should address the following recommendations:

- The maximum aggregate size should be limited to 16 mm, or 8 mm for thin elements. Ideally, the maximum aggregate diameter should not exceed one-half to one-third of the maximum fiber length. Typically, fibers 2 to 4 times longer than the largest aggregate are employed [9].
- The fine aggregate content should be increased to provide uniform fiber distribution, while coarse aggregates amount should be limited to a maximum 55% of the total aggregate volume [105], [106].
- The water to cement ratio (w/c) must not exceed 0.55. It is also highly forbidden to adjust the consistency of the mixture by water addition.
- The use of an effective superplasticizer is essential to achieve the desired workability, otherwise, increased porosity, uneven fiber distribution, and fiber clumping may [105], [107], [108].
- The fibers should be added together with the aggregates, for example on the aggregate feeding conveyor, to facilitate fiber bundle separation during mixing. Fibers must not be added as the initial component of the concrete mixture.

In conclusion, it is essential to emphasize that when incorporating SyFs into the concrete mixture, special attention must be paid to achieving uniform fiber distribution and maintaining adequate workability in accordance with project requirements. Undoubtedly, the scattering in mechanical test results of FRC is partly attributed to inconsistent fiber dispersion within the concrete matrix [109]. In cases where the concrete mixture is not self-compacting or sufficiently flowable, vibration methods are commonly employed. However, it should be noted that compaction processes may induce specific fiber orientation. Namely, fibers tend to align perpendicular to the loading axis in cylindrical specimens and parallel in cubic specimens [110], as illustrated in Fig. 3.40. This should be considered when interpreting test results, as the preferred fiber orientation is perpendicular to the loading direction. Moreover, due to the low density of SyFs (0.90-0.91 g/cm³), they have a tendency to flow up toward the concrete surface during casting, resulting in non-uniform fiber distribution [100].

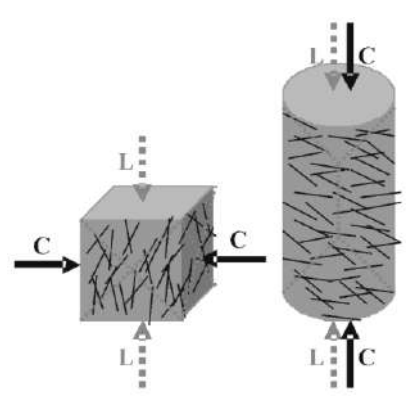


Fig. 3.40 Influence of casting and compaction direction (C) on fiber distribution relative to the loading direction in compressive strength tests (L) [110]

It should also be emphasized that improvements in mechanical properties generally increase with fiber content, but only up to an optimal threshold. Beyond this point, further increases in V_f may lead to negligible gains or even degradation of concrete performance. Numerous studies [111]–[114] support the concept of an optimally designed mix, where an appropriate fiber dosage is selected to achieve a balance between concrete workability and mechanical strength. In mix design, attention should be given not only to the fiber dosage but also to fiber geometry. The structural efficiency of fibers depends significantly on their bond strength with the concrete matrix [100]. A challenge in this regard is the inherently low hydrophilicity of SyFs, which can lead to bonding problems [100], [102], [103]. To enhance the mechanical interlock and fiber-matrix interaction, shaped fibers, such as crimped, twisted, sinusoidal, or wavy, are commonly employed to increase the effective contact surface area [115]. Additionally, the inclusion of supplementary cementitious materials such as zeolite or silica fume has been reported to improve the bond between fibers and the surrounding matrix as well as the bond between the cement paste and aggregates [116]. These considerations demonstrate that the design of FRC mixtures involves more complex criteria compared to PC, requiring careful optimization of both fiber-related and matrix-related parameters.

3.4.1.3 Workability

The workability of SyFRC is primarily influenced by fiber content, geometry, and dimensions [117]. Depending on the intended application, SyFs are typically used in dosages ranging from 1.5 to 9 kg/m³. However, when the fiber content exceeds approximately 2.5 kg/m³, adjustments to the concrete mixture composition are usually required to maintain adequate workability. Due to their high specific surface area,

intentionally increased to enhance bond performance, fibers demand more cement paste for proper coating. This leads to increased viscosity of the mix, which in turn results in reduced workability. In a study conducted by Altalabani et al. [118], although all polypropylene fiber reinforced concrete (PPFRC) mixtures satisfied the criteria for self-compacting concrete, they exhibited noticeably lower workability compared to the reference PC mix. Specifically, the inclusion of 0.44% and 0.66% macro polypropylene fibers (PPFs) reduced the slump flow diameter from 820 mm to 763 mm and 663 mm, respectively. Additional tests, including slump flow time, J-Ring passing height, and V-funnel flow time, further confirmed the presence and increased dosage of PPFs deteriorates the fresh concrete workability. Similar observations were made by Shi et al. [111], who found that in both C30 and C60 concrete mixes, each 0.3% increase in V_f reduced the slump by approximately 36 mm. When the fiber content reached 1%, the slump was reduced by about 110 mm compared to the control mix. Furthermore, Gencel et al. [119] conducted an extensive study on the influence of PPFs on concrete workability. As summarized in Table 3.8, the inclusion of fibers led to a reduction in slump flow and an increase in J-Ring passing height by 4.7-24.7% and 10.0-56.4%, respectively, depending on the mix composition and fiber content. Although no significant deterioration in compressive, splitting tensile, or flexural strength was observed in [119], it must be emphasized that the beneficial effects of fiber reinforcement can only be fully realized if adequate workability of the mixture is maintained.

Table 3.8 Results of slump flow and J-Ring passing height tests for concretes with different amount of macro PPFs according to the study by Gencel et al. [119]

| Fiber content | 0 kg/m^3 | 3 kg/m^3 | 6 kg/m ³ | 9 kg/m ³ | 12 kg/m ³ | | | |
|----------------------------|--------------------|--------------------|---------------------|---------------------|----------------------|--|--|--|
| Concrete series I | | | | | | | | |
| Slump flow [mm] | 730 | 685 (-6.2%) | 623 (-14.7%) | 586 (-19.7%) | 550 (-24.7%) | | | |
| J-Ring passing height [mm] | 10 | 11.0 (+10.0%) | 12.3 (+23.0%) | 13.8 (+38.0%) | 15.4 (+54.0%) | | | |
| | Concrete series II | | | | | | | |
| Slump flow [mm] | 750 | 715 (-4.7%) | 680 (-9.3%) | 615 (-18.0%) | 580 (-22.7%) | | | |
| J-Ring passing height [mm] | 9.4 | 10.7 (+13.8%) | 11.9 (+26.6%) | 12.5 (+33.0%) | 14.7 (+56.4%) | | | |

3.4.1.4 Crack limitation

The fundamental role of SyFs in concrete structures is schematically illustrated in Fig. 3.41. At the early stage, when concrete is in the plastic state, its low tensile strength and low Young's modulus allow plastic shrinkage stresses to exceed the material

strength. At this point, SyFs effectively counteract these stresses, reducing both the number and the width of shrinkage-induced cracks. As the concrete continues to set and transitions from the plastic to the hardened phase, its Young's modulus increases and eventually exceeds that of the SyFs. In this state, the fibers remain inactive until the tensile strength of the concrete is reached. Once cracking initiates, SyFs become fully engaged, acting as a three-dimensional reinforcement [120]. Their presence enables the bridging of both micro- and macro-cracks, thereby limiting their growth and propagation. Due to this bridging mechanism, FRC demonstrates significantly enhanced crack resistance compared to PC. Provided that appropriate design and performance criteria are met, FRC may serve as an effective alternative for traditional reinforcement in elements requiring enhanced crack width control, particularly in structures with high reinforcement ratios [33]. Moreover, the use of SyFs may allow for the partial or complete elimination of steel mesh dedicated to shrinkage control.

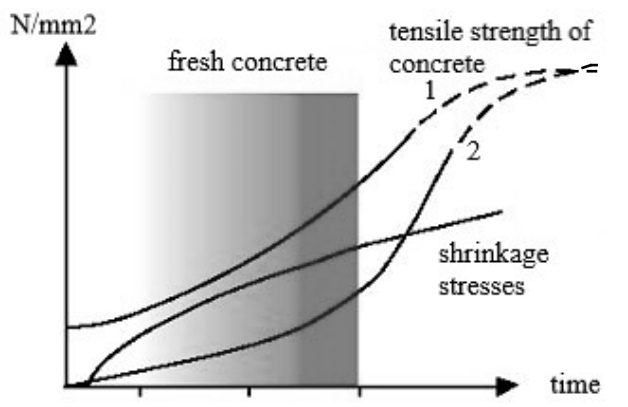


Fig. 3.41 Shrinkage stresses in concrete: 1 – with SyFs, 2 – without SyFs [121]

3.4.1.5 Elasticity modulus

The stiffness of SyFs is typically several times lower than that of the concrete matrix, which suggests that their incorporation does not exert a significant influence on the concrete modulus of elasticity. Nevertheless, selected studies investigating the effect of SyFs on E_c are presented herein. In the study by Altalabani et al. [118], E_c increased by a maximum of 0.318 GPa (approximately 1%) for mixtures containing 4 and 6 kg/m³ of PPFs ($l_f/d_f = 39/0.91$ mm) in comparison with PC. Fallah et al. [122] reported a progressive increase in E_c by 2.8%, 4.2%, 6.4%, 7.8%, and 8.2% for SyFRCs incorporating 0.25%, 0.50%, 0.75%, 1.00%, and 1.25% of macro PPFs ($l_f/d_f = 39/0.78$ mm), respectively. However, the influence of fiber incorporation is not always consistent or clearly defined. In the research conducted by Velasco et al. [123],

the addition of 0.25% PPFs to a C65 reference concrete resulted in an increase of E_c from 32.25 to 35.68 GPa (a 10.6% improvement). Further increase in fiber content to 0.50% led to a reduction in E_c to 32.48 GPa, showing only a marginal increase of 0.7% compared to the PC. For the C85 series, the addition of 0.25% PPFs resulted in a negligible 0.2% change in E_c , while 0.50% of fibers caused an 8.6% decrease. These findings highlight the concept of an optimal fiber dosage. In [112], the double increase of fiber dosage caused an 18% reduction in E_c for a concrete with polyolefin slightly coiled fibers ($I_f/d_f = 54/0.34$ mm), a 2.5% reduction for polystyrene hooked fibers ($I_f/d_f = 40/0.83$ mm), and a 2.9% increase for polymeric flat fibers. Detailed results are summarized in Table 3.9. Overall, both fiber dosage and fiber type influence the elastic modulus of concrete. In conclusion, based on the literature review, the effect of fiber incorporation on concrete's elasticity modulus is ambiguous, nevertheless small enough to be considered insignificant.

Table 3.9 Influence of fiber type and dosage on the modulus of elasticity and compressive strength of concrete according to the study by Buratti et al. [112]

| Fiber type | | | | | | |
|-----------------------------|------|------|------|------|------|------|
| Dosage [kg/m ³] | 2.0 | 4.8 | 5.0 | 10.0 | 2.0 | 4.8 |
| E_c [GPa] | 37.2 | 30.4 | 31.3 | 32.2 | 32.0 | 31.2 |
| fc,cube [MPa] | 50.2 | 42.8 | 40.9 | 42.1 | 41.4 | 44.6 |

3.4.1.6 Compressive strength

SyFRC is not typically associated with a substantial enhancement in compressive strength, as this parameter is primarily governed by the properties of the concrete matrix [100], [124], [125]. For example, in [126], the addition of 4, 6, and 8 kg/m³ of polyolefin fibers (l_f = 48 mm) resulted in only marginal improvements in f_c , amounting to 2.7%, 2.9%, and 3.3%, respectively. Wan Ibrahim et al. [105] investigated the compressive strength of concrete incorporating palm oil biomass clinker as a sand replacement. The specimens with 0.0%, 0.2%, 0.4%, and 0.6% of PPFs exhibited f_c values of 27.23, 27.40, 27.70, and 26.61 MPa, respectively. The initial strength increase followed by a decrease was attributed to the adverse impact of excessive fiber content on the cohesiveness of the concrete matrix. The optimal fiber dosage may vary depending on fiber type and concrete composition, as demonstrated in Table 3.9. This observation is consistent with the findings of Raviner et al. [127], who reported that the inclusion of 0.3% polymer fibers (l_f = 45 mm) resulted in the highest increase of compressive strength regardless

of the curing time. Specifically, the improvements in f_c at 7, 14, and 24 days were 6%, 10%, and 6%, respectively. Conversely, other studies have reported considerable reductions in f_c resulting from increased V_f . For instance, the addition of 0.8% modified olefin fibers led to a 26% decrease in f_c [106], while 1% of PPFs ($l_f/d_f = 50/0.5$ mm) reduced f_c by 16% [128]. Moreover, the study presented in [106] highlighted the role of fiber slenderness in compressive strength development. Specifically, an increase in l_f/d_f ratio was associated with a reduction in f_c at both 0.5% and 0.8% fiber dosages.

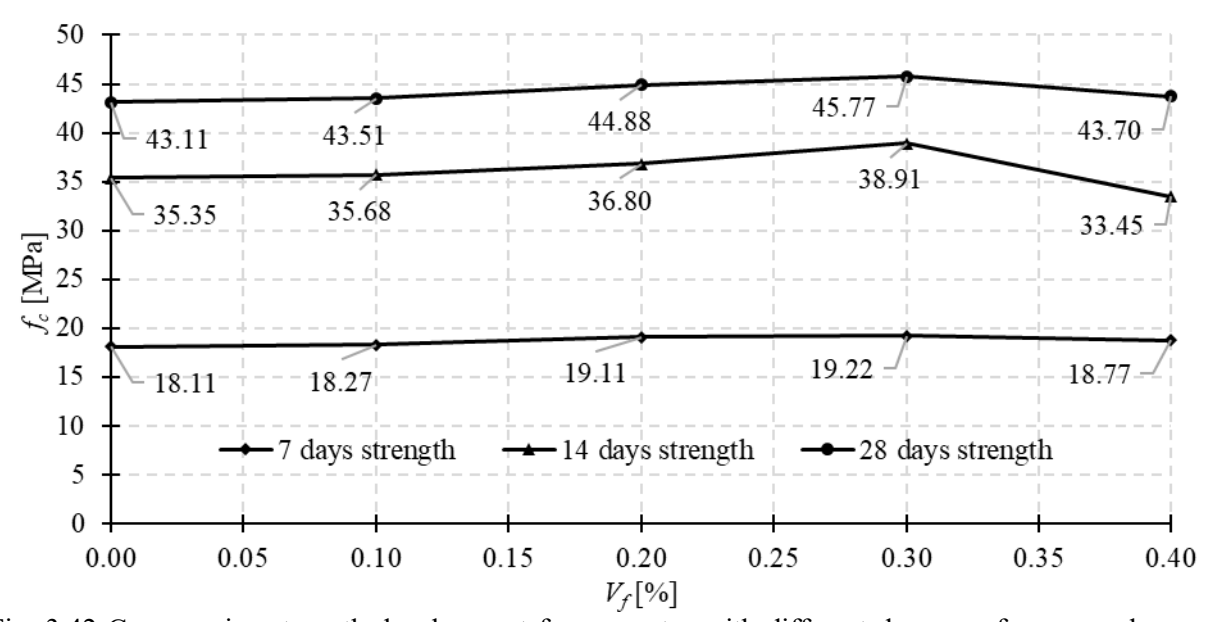


Fig. 3.42 Compressive strength development for concretes with different dosages of macro polymer fibers according to the study by Raviner et al. [127]

3.4.1.7 Flexural tensile strength

In the study by Gencel et al. [119], flexural tensile strength increased with higher fiber and cement contents. Specifically, the incorporation of 3 kg/m³ of PPFs resulted in a 59-65% improvement in strength, depending on the tested concrete. Similarly, Mashhadban et al. [129] reported f_{fl} enhancements of 24%, 27%, 29%, and 41% for SyFs dosages of 0.1%, 0.2%, 0.3%, and 0.4%, respectively ($l_f/d_f = 50/0.8$ mm). Sounthararajan et al. [130] also observed notable increases, with flexural tensile strengths of 5.04, 5.83, 6.56, and 7.92 MPa for $V_f = 0.0\%$, 0.1%, 0.2%, and 0.3% of PPFs ($l_f/d_f = 48/1.1 \times 0.6$ mm), corresponding to a 57% gain at the highest fiber dosage (Fig. 3.43). However, further increases in fiber content did not consistently lead to strength enhancement, as also shown in Fig. 3.43. Comparable findings were reported in [131], where the optimal SyFs dosage, resulted in 39% increase of f_{fl} compared to PC, was $V_f = 1.2\%$ ($l_f/d_f = 27/0.52$ mm). Higher dosages of 1.5% and 1.8% led to only 12%

or negligible improvements. In [132], f_{fl} increased with SyFs content ($l_f/d_f = 38/0.91$ mm), peaking at $V_f = 0.7\%$ with a value of 3.45 MPa, approximately 26% higher than the reference concrete. In contrast, Behfarnia et al. [126] reported only 1% and 4% gains for fiber dosages of 0.4% and 0.7%, respectively. Luna et al. [133] observed a maximum improvement of 6% at $V_f = 0.3\%$ using fibers with geometries of $l_f/d_f = 50/1.5 \times 0.5$ mm, $38/2.0 \times 0.5$ mm, and 50/0.66 mm, resulting in f_{fl} values of 4.345, 4.643, and 4.536 MPa, compared to 4.362 MPa for PC. A similar enhancement of 4% was reported in [105] for 0.4% SyFs ($l_f/d_f = 55/0.85$ mm). Conversely, some studies documented reductions in flexural tensile strength. In [118] and [134], f_{fl} decreased by 8% and 5%, respectively, following the addition of 0.2% of fibers. Such deterioration may result from reduced workability, insufficient compaction, uneven fiber distribution, fiber clustering, or poor fiber-matrix bonding. Nevertheless, assuming that the essential requirements for workability, uniform fiber dispersion, and adequate bond strength are met, the incorporation of SyFs into concrete can be expected to enhance its flexural tensile strength [135].

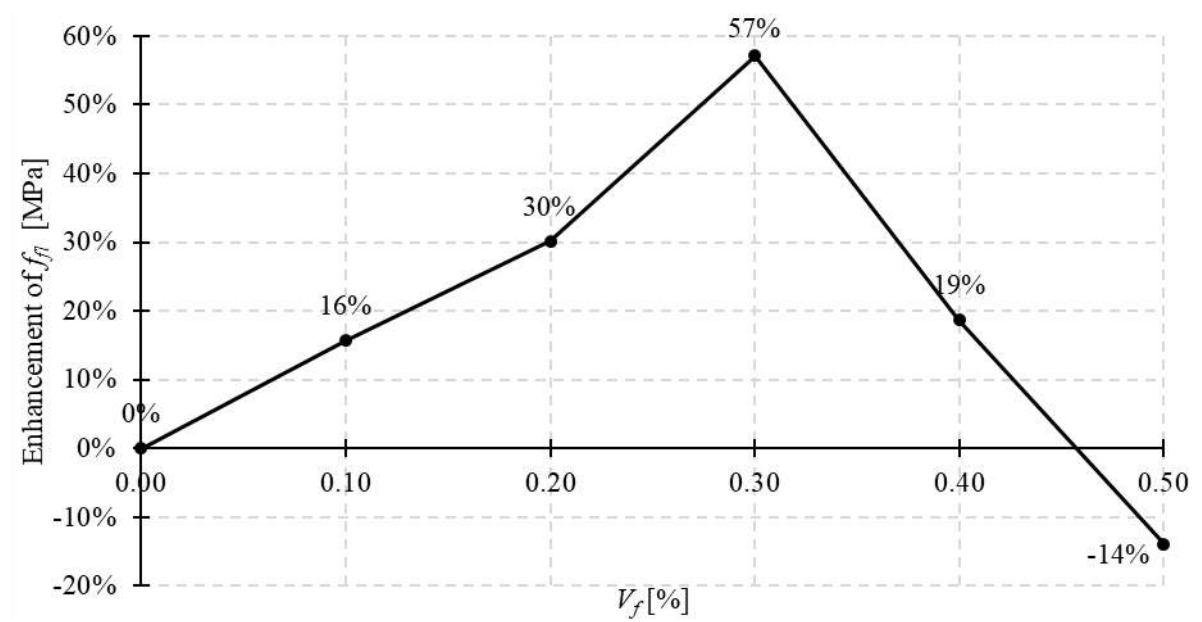


Fig. 3.43 Flexural tensile strength variation for concretes with different dosages of macro polymer fibers according to the study by Sounthararajan et al. [130]

3.4.1.8 Fracture energy, energy absorption, toughness

Fracture energy (G_F) quantifies the energy required to propagate a unit area of crack surface and serves as a measure of concrete resistance to crack growth [136]. It is typically determined as the ratio of the area under the F-w (where w denotes crack opening) or F-CMOD curve (referred to as the energy absorption W_0 or toughness) to

the cross-sectional area of the fractured element. In normal-weight concrete, G_F is primarily influenced by the w/c ratio, maximum aggregate size, curing conditions, and concrete age [15]. It is also affected by the geometry of the test specimen, particularly the ligament area above the crack or notch [15]. The incorporation of SyFs in concrete significantly enhances G_F , as SyFRC is capable of transferring internal stresses and maintaining structural integrity after cracking [137], [138]. Fibers bridge developing cracks, thereby promoting more ductile fracture behavior. Numerous experimental studies have confirmed the enhancing influence of SyFs on concrete fracture energy, energy absorption, and toughness. For example, Blazy et al. [72] evaluated G_F for concretes reinforced with three types of macro SyFs (PM, PD, and FF) at two dosages (2 and 3 kg/m³). The results demonstrated that the inclusion of fibers increased G_F by 16-19 times at 2 kg/m³ and by 20-22 times at 3 kg/m³, relative to PC, up to a CMOD of 3.5 mm (Fig. 3.44). Similarly, Altalabani et al. [118] reported an increase in toughness, and thus in G_F , from 17.84 Nm to 19.76 Nm when the fiber content was raised by 0.22%. In another study [139], an increase in V_f from 0.89% to 1.00% and then to 1.11% resulted in a minimum 20% improvement in W_0 , while lower fiber dosages led to negligible gains.

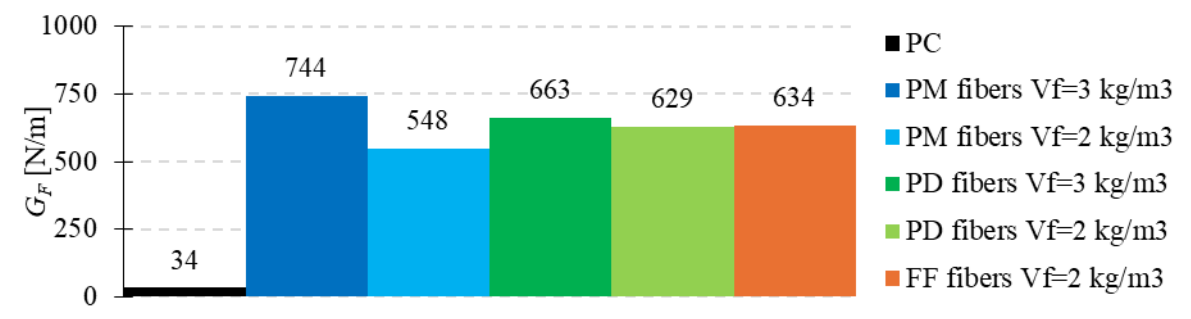


Fig. 3.44 Fracture energy for SyFRC with different fiber types and dosages according to the study by Blazy et al. [72]

According to the study by Hongbo et al. [106], the incorporation of macro SyFs into concrete enhanced energy absorption by 5.0 to 8.7 times, depending on fiber type and dosage. Moreover, the results showed that SyFs provided superior toughening effects compared to SFs, with SyFRC absorbing at least twice as much energy as SFRC for fiber dosages of approximately 4.5 or 7.2 kg/m³, versus 40 kg/m³ of SFs. Additionally, for SyFs with aspect ratios $l_f/d_f = 30$, 38, and 43, increasing V_f from 0.5% to 0.8% led to W_0 enhancements of 44%, 49%, and 46%, respectively. The analysis revealed a pronounced increase in energy absorption with the aspect ratio rising from 30 to 38, followed by a slight decline at a ratio of 43. Interestingly, Soutsos et al. [113] reported that SyFRC samples with fiber dosages of 4.6 kg/m³ (S 4.6) and 5.3 kg/m³ (S 5.3) achieved flexural toughness values of approximately 33 and 48 Nm, respectively, which

were comparable to SFRC samples containing 30 and 50 kg/m³ of 50 mm long SFs (Fig. 3.45). In conclusion, both the addition and increased dosage of macro SyFs enhanced the fracture energy, energy absorption, and toughness. However, fiber material, type, and geometry must also be considered, as they significantly affect these performance parameters.

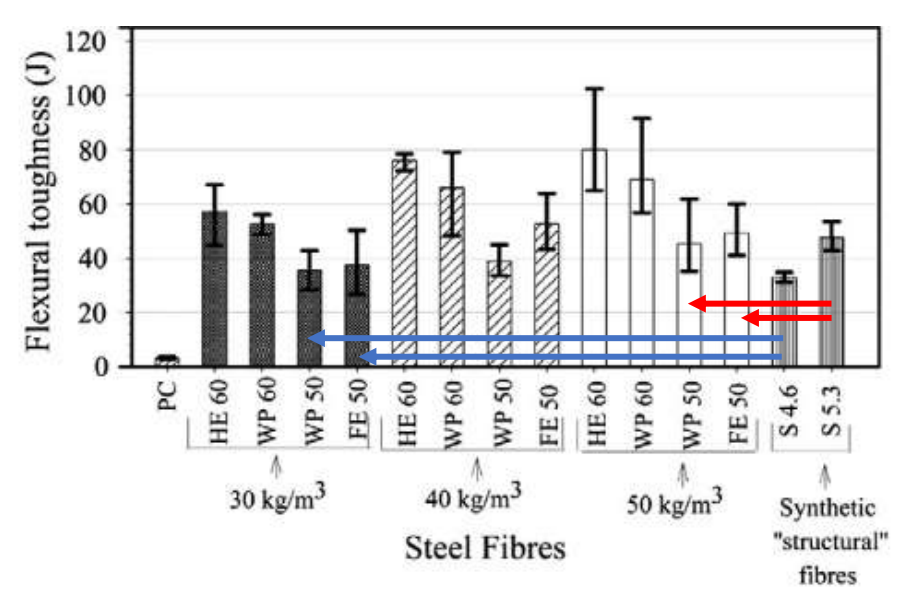


Fig. 3.45 Flexural toughness of PC, SFRC, and SyFRC according to the study by Soutsos et al. [113]

3.4.1.9 Splitting tensile strength

The enhancing effect of macro SyFs on the splitting tensile strength (f_{spl}) of concrete has been confirmed by many researchers [119], [140]–[143]. For instance, in [144], adding 4% of macro SyFs ($l_f/d_f = 50/1$ mm) increased f_{spl} by 65%, from 3.42 MPa to 5.63 MPa, however it significantly reduced the slump from 93 mm to 20 mm. Smaller dosages of 3, 6, and 9 kg/m³ of SyFs ($l_f/d_f = 60/1$ mm) led to f_{spl} improvements of 1, 3, and 8%, respectively [145]. Similar trends were observed in [126], where the use of 0.4-0.8% polyolefin macro fibers ($l_f = 48$ mm) resulted in 5-10% increases. The benefit of macro SyFs was also reported in [143], with the best performance observed in mixtures combining both macro and micro SyFs. Microfibers helped delay microcrack formation, while macro fibers controlled crack propagation. This synergistic effect was also noticed by Ghanem et al. [142], where hybrid mixes (M3, M5) outperformed mixture with only macro SyFs (M1) (Table 3.10). Nevertheless, the addition of 1% of multifilament macro SyFs increased f_{spl} significantly by 33% compared to PC. The differences in failure modes were also noticed, since specimen without fibers (M0) split completely due to testing, whereas SyFRC ones (M1-M7) maintained their integrity,

with M1 showing the most pronounced cracking (Fig. 3.46). It was also observed that specimen M0 developed a single crack, while M1-M7 cylinders exhibited multiple cracking. Finally, study [146] reported an enhancement of f_{spl} due to presence of SyFs, with the optimum $V_f = 3\%$. A further increase of V_f to 4% led to a reduction in strength, highlighting the importance of optimizing fiber content to achieve the best mechanical performance of SyFRC.

Table 3.10 Results of the splitting tensile tests according to the study by Ghanem et al. [142]

| Mix | V_f of macro SyFs $l_f/d_f = 54/0.34$ mm [%] | V_f of micro SyFs $l_f/d_f = 19/0.58$ mm [%] | V_f of micro SyFs $l_f/d_f = 19/0.048 \text{ mm } [\%]$ | f _{spl} [MPa] |
|-----|--|--|---|------------------------|
| M0 | 0.0 | 0.0 | 0.0 | 3.08 |
| M1 | 1.0 | 0.0 | 0.0 | 4.10 |
| M2 | 0.5 | 0.5 | 0.0 | 4.08 |
| M3 | 0.5 | 0.0 | 0.5 | 4.36 |
| M4 | 0.4 | 0.3 | 0.3 | 3.39 |
| M5 | 0.2 | 0.4 | 0.4 | 5.08 |
| M6 | 0.0 | 1.0 | 0.0 | 3.69 |
| M7 | 0.0 | 0.0 | 1.0 | 4.45 |



Fig. 3.46 Cylindrical samples after the splitting tensile tests according to the study by Ghanem et al.[142]

3.4.1.10 Shrinkage

In the fresh state, concrete has a low elastic modulus and strength, making it susceptible to stresses from plastic shrinkage resulting from water evaporation, especially in large, flat elements like slabs that are exposed to hot, dry, and windy conditions. It became increasingly popular to replace steel mesh reinforcement with macro SyFs, which also mitigate shrinkage cracking and effectively reduce the formation of plastic shrinkage cracks [100]. The study [147] describes the influence of SyFs geometry and dosage on the shrinkage cracking of cement-based composites. It was concluded that the effectiveness of fibers in resisting plastic shrinkage cracking was primarily influenced by their dosage rather than geometry, as shown in Fig. 3.47. Notably, for higher SyFs contents (above $V_f = 0.5\%$) a comparable level of the reduction in the plastic shrinkage crack area was observed for straight, crimped, and embossed fibers (Table 3.11). For dosages up to 0.25%, fiber geometry played a more significant role, with embossed fibers demonstrating superior resistance due to their enhanced interfacial bonding with the concrete matrix. Nevertheless, for all types of SyFs, an

increase of V_f was associated with a decrease in total plastic shrinkage crack area. Bertelsen et al. presented a comprehensive literature review [148] on the effect of fiber properties on the plastic shrinkage cracking. The enhancing influence was observed for fibers with smaller diameters, higher aspect ratios, greater fiber dosages, and improved bonding strength, while fiber length and modulus showed no clear correlation with surface cracking reduction. Drying shrinkage occurs when hardened concrete loses capillary water, and it becomes particularly pronounced under conditions of low relative humidity and elevated temperatures. The incorporation of macro SyFs into concrete is considered as advantageous for structural elements subjected to drying shrinkage. Specifically, in [149] the restrained drying shrinkage tests of SyFRC specimens revealed that the average maximum crack width was two times smaller (0.15 mm) than the one for PC samples (0.30 mm) at the 90th day. Moreover, the addition of 0.19% of SyFs delayed the crack formation. This is in agreement with the findings of Yousefieh et al. [150], where concrete samples with 0.1% polyolefin fibers exhibited average crack width, area, and length that were 45%, 14%, and 9% lower than those of PC, respectively.

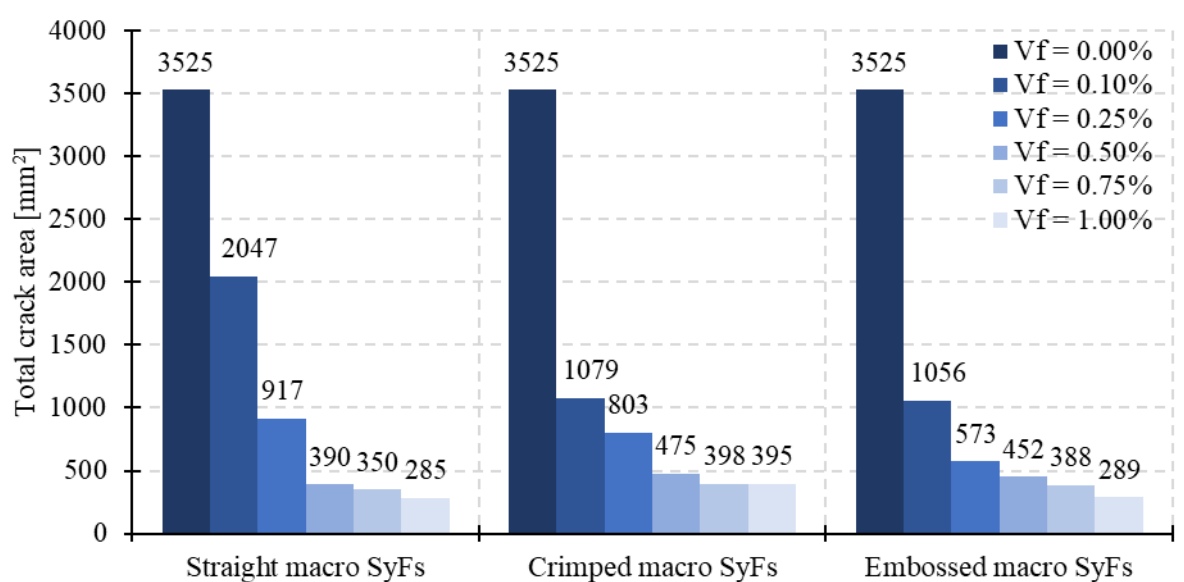


Fig. 3.47 Total plastic shrinkage crack area for straight, crimped, and macro SyFs depending on their volume content according to the study by Kim et al. [147]

Table 3.11 Total reduction in the plastic shrinkage crack area for straight, crimped, and macro SyFs depending on their volume content according to the study by Kim et al.[147]

| Fiber type/dosage | 0.00% | 0.10% | 0.25% | 0.50% | 0.75% | 1.00% |
|---------------------|-------|-------|-------|-------|-------|-------|
| Straight macro SyFs | 0% | -42% | -74% | -89% | -90% | -92% |
| Crimped macro SyFs | 0% | -69% | -77% | -87% | -89% | -89% |
| Embossed macro SyFs | 0% | -70% | -84% | -87% | -89% | -92% |

3.4.1.11 Impact resistance

Impact resistance is a critical property of concrete used in structural elements subjected to repeated dynamic loads or impacts from falling objects, such as industrial floors, pavements, and slabs. Since such elements are often reinforced with SyFs, the documented improvement in impact performance resulting from their addition is considered a significant benefit. Namly, Banthia et al. [151] conducted drop-weight tests on beam specimens to assess the effect of fiber addition and geometry, concluding that SyFs significantly improved impact resistance. Longer straight SyFs ($l_f/d_f = 38/0.63$ mm) outperformed shorter ones ($l_f/d_f = 25/0.38$ mm), while crimped fibers ($l_f/d_f = 30/0.76$ mm) provided superior energy absorption under impact loading. This was attributed to their increased pull-out resistance of crimped fibers compared to straight fibers. In follow-up tests on plates [152], SyFRC exhibited fracture energy absorption 1.23-1.84 times higher up to 5 mm deflection and 1.67-2.18 times higher up to 15 mm deflection compared to PC, depending on fiber type and dosage. Altalabani et al. [118] found that adding 0.44% macro SyFs ($l_f/d_f = 39/0.78$ mm) to 100 x 65 mm disc samples increased the impact energy at first crack and final failure by 36% and 169%, respectively. A further increase in fiber volume by 0.22% yielded only marginal improvements (3% and 6%, respectively), highlighting the importance of optimizing fiber content. Mindess et al. [153] reported that concrete with 0.5% of 37 mm fibrillated PPFs showed higher fracture energy and toughness than both normal and high-strength concrete without fibers. Similar improvements were observed in [154], where adding 0.1-0.3% of macro SyFs ($l_f = 50$ mm) increased the number of blows to failure by 3.0 to 5.0 times compared to PC. These findings align with [155], which recorded increases from 97 blows for PC to 494, 933, and 723 blows (i.e., 509%, 962%, and 745%) for SyFRC with 0.4%, 0.6%, and 0.8% fiber content, respectively. In [156] the impact resistance of various SyFs combinations with varying percentages were studied (Fig. 3.48). The number of blows to first crack and complete failure increased by approximately 2.5-2.7 and 3.1-3.6 times, respectively, compared to control samples. Among all tested samples, the hybrid blend with 0.5% of multifilament and 1% of monofilament fibers demonstrated the highest performance under impact loading, confirming the superiority of fiber hybridization over the use of a single fiber type. A comprehensive review of FRC impact resistance is provided by Yoo et al. [157].

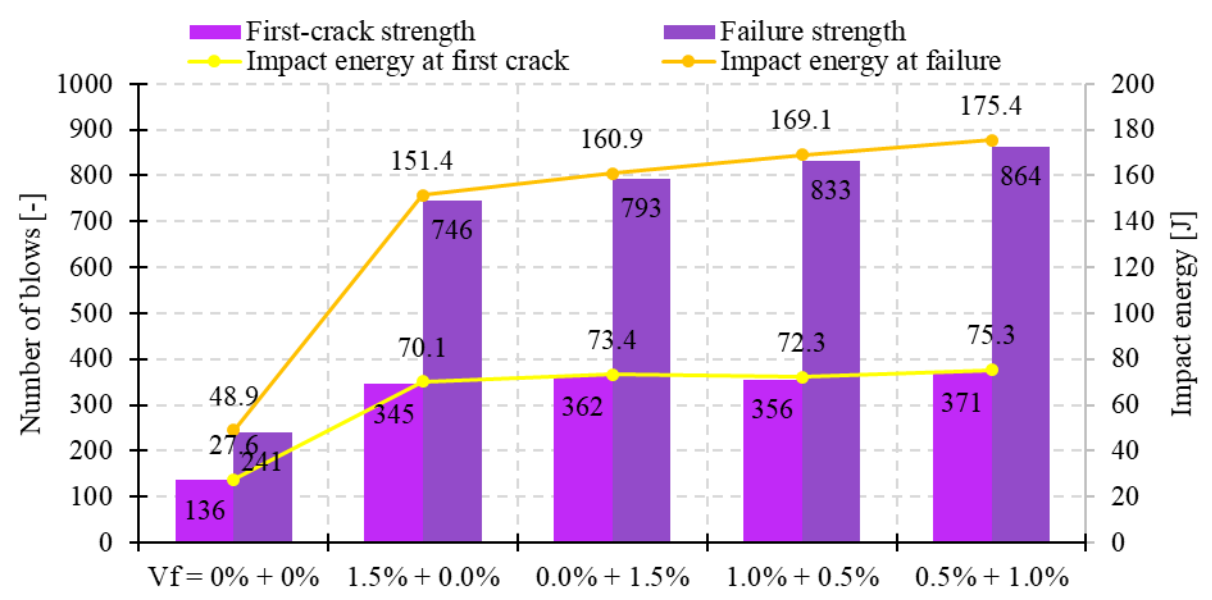


Fig. 3.48 Impact test results, where V_f = Type I (multifilament) + Type II (monofilament) SyFs, according to the study by Najaf et al. [156]

3.4.1.12 Spalling and temperature resistance

The addition of SyFs has been shown to significantly improve the spalling resistance of concrete when exposed to elevated temperatures, as illustrated in Fig. 3.49. SyFs begin to melt at approximately 160-170°C, creating voids and micro-channels within the concrete matrix that facilitate the release of vaporized water (Fig. 3.50). This mechanism reduces the internal pore pressure and thereby enhances the concrete's resistance to explosive spalling during fire exposure [158]. This effect was experimentally confirmed by Abdelalim et al. [159], where concrete samples containing PPFs demonstrated lower spalling than PC after being subjected to 800°C for 120 minutes. Similarly, Velasco et al. [123] observed that the inclusion of just 0.25% of SyFs ($l_f = 40$ mm) effectively prevented spalling in tested specimens. However, it was also reported that at 400°C, SyFRC experienced greater reductions in strength and stiffness compared to PC samples. At higher temperatures (650-900°C), the mechanical degradation was comparable across all specimens, regardless of fiber content. The decreased performance of SyFRC at moderate temperatures was attributed to the melting of SyFs. Further evidence is provided in [160], where the addition of 4 kg/m³ of macro SyFs ($l_f/d_f = 42/0.8$ mm) were found effective in enhancing spalling resistance for all tested concrete classes (C20/25, C30/37, C50/60). None of the SyFRC specimens experienced spalling up to 800°C, whereas PC samples of C30/37 and C50/60 experienced explosive failure at 500-800°C. Comprehensive reviews by So [161] and Mehrabi et al. [162] conclude that SyFs are the most effective type of fibers in reducing

spalling in concrete exposed to elevated temperatures. The addition of the fiber dosages in the range of 2-3 kg/m³ for optimal performance was recommended. Nonetheless, these studies also emphasize that despite improved spalling resistance, SyFRC still undergoes considerable losses in mechanical properties, particularly in modulus of elasticity and compressive strength, when exposed to high temperatures.

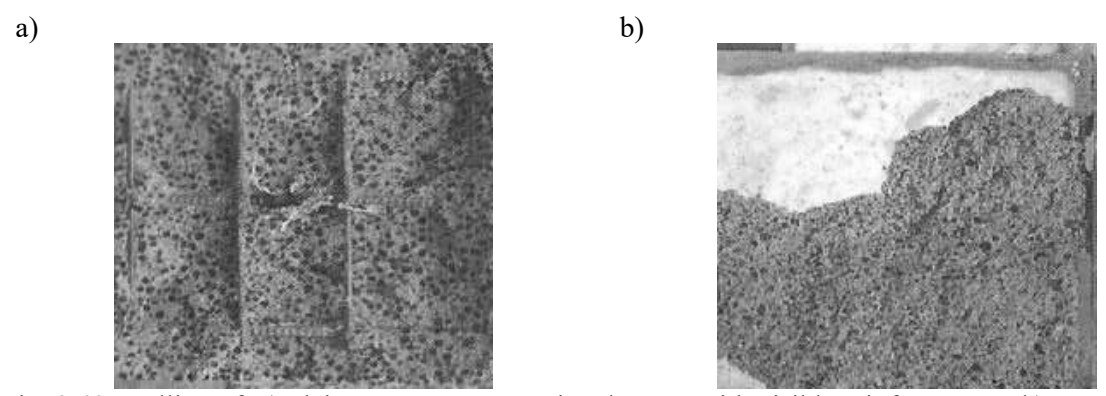


Fig. 3.49 Spalling of: a) plain concrete – extensive damage with visible reinforcement, b) concrete with 0.9 kg/m³ of SyFs – damage of the concrete cover [161], [163]

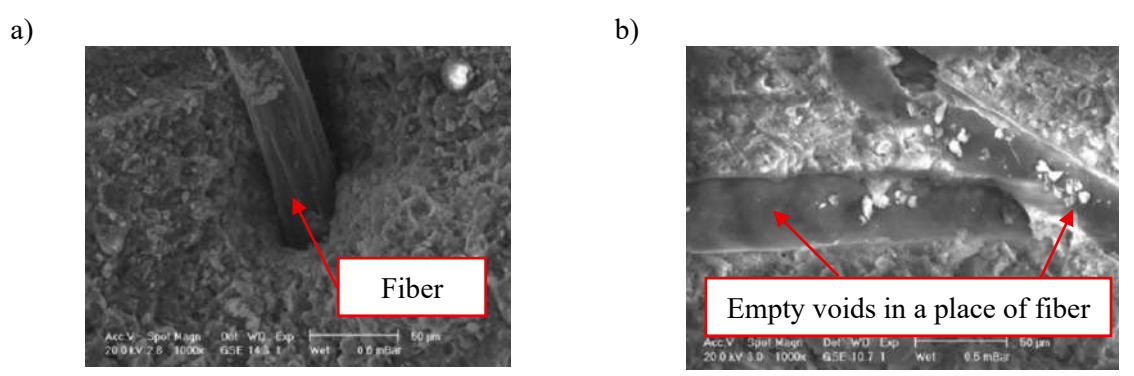


Fig. 3.50 Fracture surfaces of cement-based composites with SyFs: a) unheated, b) after exposure to 250° C [162], [164]

3.4.1.13 Freeze-thaw resistance

SyFs are widely adopted in structural elements exposed to water and aggressive environmental conditions, including industrial and marine atmospheres due to their resistance to corrosion. Additionally, such elements are frequently subjected to numerous freeze-thaw cycles resulting from temperature changes so their high durability and resistance is of particular importance. Bolat et al. [165] demonstrated that the inclusion of macro polyester ($l_f/d_f = 30x1/0.6$ mm) and PPFs ($l_f/d_f = 30x1/0.35$ mm) in 100 x 200 mm cylindrical specimens improved durability by enhancing resistance to freeze-thaw degradation. While the reference specimens failed after 270 cycles, the SyFRC exhibited deformation no earlier than after 300 cycles, with polyester fibers

providing superior performance compared to polypropylene. Similarly, Pietrzak et al. [166] observed a 20% compressive strength reduction in PC after frost-resistance trials, compared to only a 7% reduction in specimens containing 0.9 kg/m³ of 30-60 mm long SyFs. In another study, Chen et al. [167] studied C25, C30, and C35 type concretes with 0.5-1.5% of macro SyFs ($l_f/d_f = 30/1.24$ mm) over 28, 56, and 92 days of freeze-thaw cycles. The results indicated a significant improvement in freeze-thaw resistance up to $V_f = 1.0\%$, with performance declining beyond this dosage. Notably, a maximum increase of 72% in the resistance was reported for SyFRC after 92 days of testing compared to PC. Overall, SyFRC exhibits smaller reductions of strength and mass and can resist more freeze-thaw cycles than PC (Fig. 3.51). This improvement is usually attributed to the fiber ability of crack bridging, resulting in decreased number and width of cracks. Otherwise, cracks can function as pathways for water penetration, leading to freezing and expansion inside the concrete, ultimately causing its deterioration.

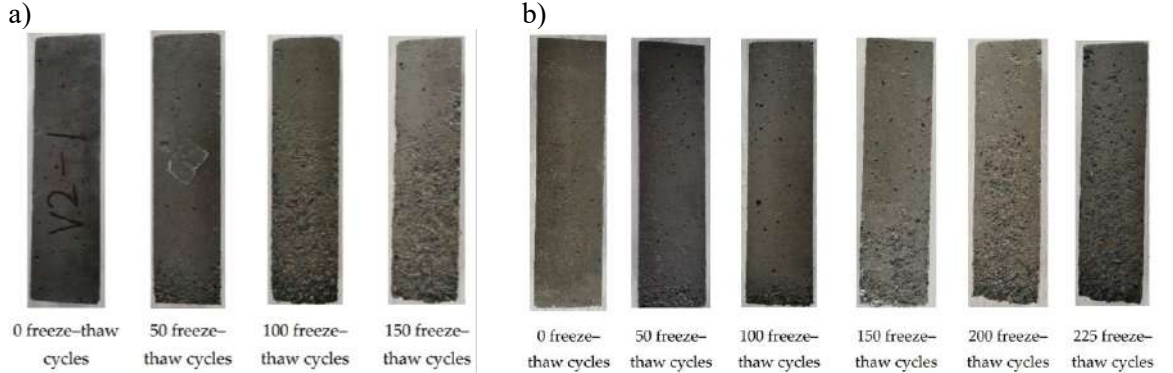


Fig. 3.51 Samples after freeze-thaw tests from: a) plain concrete, b) concrete with 0.9% of SyFs according to the study by Yuan et al. [168]

3.4.1.14 Abrasion resistance

Abrasion resistance is a relevant property for horizontal structural elements such as industrial floors, pavements, and slabs, which are often subjected to mechanical wear. Given that these elements are frequently reinforced with SyFs, the enhancement in abrasion performance associated with fiber incorporation, confirmed by numerous studies, is considered highly advantageous. In the study by Bolat et al. [165], the abrasion resistance of $100 \times 100 \text{ mm}$ cylindrical concrete specimens reinforced with 0.425% macro polyester fibers ($l_f/d_f = 30 \times 1/0.6 \text{ mm}$) was found to be almost 35% higher than that of PC. Similarly, Ridgley et al. [169] conducted a comprehensive experimental program to assess the abrasion performance of SyFRCs of different types. Their findings demonstrated that the inclusion of SyFs at a dosage of 0.2% led to a noticeable

improvement in abrasion resistance. Furthermore, flexible fibers exhibited lower average weight loss and wear depth compared to semi-rigid fibers. It was also observed that increasing fiber length correlated with lower abrasion resistance. Etli et al. [170] employed a rotating cutter apparatus to evaluate abrasion on 100 mm cubic samples and found that the addition of 3 and 4 kg/m³ of SyFs significantly reduced weight loss compared to control specimens. In another study, Alyousef [171] investigated the effect of waste macro SyFs ($l_f/d_f = 30/0.45$ mm) using a Bohme abrasion test. The results indicated a clear trend: as the fiber content increased, the abrasion volume loss decreased. Specifically, volume reductions of 5.4, 5.2, 4.9, 4.8, and 4.8 cm³/50 cm² were observed for $V_f = 0.2, 0.4, 0.6, 0.8,$ and 1.0%, respectively, compared to 5.5 cm³/50 cm² for PC. A similar enhancing effect was reported in [172] for waste macro SyFs with $l_f/d_f = 41.55/0.693$ mm. Additionally, it was noted that increasing the fiber amount led to greater fiber exposure on the sample surface (Fig. 3.52). This suggests that the fibers effectively limit the detachment of surface particles during abrasion, thereby reducing material loss. Unlike PC, the SyFRC matrix remains partially bonded due to the mechanical restraint provided by the fibers, resulting in the higher abrasion resistance.

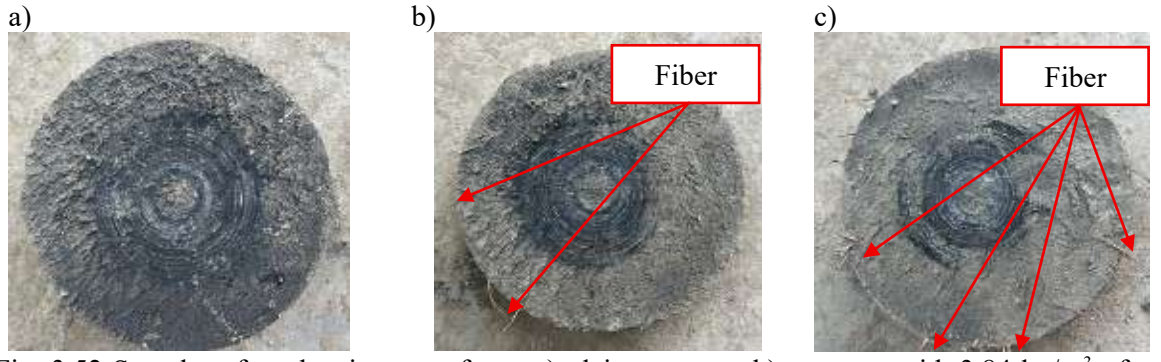


Fig. 3.52 Samples after abrasion tests from: a) plain concrete, b) concrete with 3.84 kg/m³ of waste macro SyFs, c) concrete with 7.68 kg/m³ of waste macro SyFs according to the study by Lee et al. [172]

3.4.1.15 Water absorption, porosity, air content

Table A.2 in Appendix A presents the effects of macro SyFs dosage, material properties, and geometry on selected concrete characteristics, including water absorption, porosity, and air content. In numerous studies, SyFRCs demonstrated lower water absorption compared to PC [173], which is primarily attributed to the crack-bridging capability of fibers that limits the formation and propagation of cracks, thereby reducing permeability. However, excessive fiber content or poor distribution may impair the workability of fresh concrete and adversely affect its absorbability. Bolat

et al. [165] reported that concrete samples incorporating PPFs ($l_f/d_f = 30 \times 1/0.35$ mm) exhibited approximately 24.7% lower water absorption, while those with macro polyester fibers ($l_f/d_f = 30 \times 1/0.6$ mm) showed a reduction of about 39.7% relative to the control mix. This improvement was likely due to the low density of SyFs, which, under the influence of vibration during placement, tended to migrate toward the upper layers of the specimen. This resulted in a non-uniform fiber distribution with a higher concentration near the surface, which effectively restricted surface cracking and improved concrete impermeability. Similarly, the study in [122] confirmed that the use of macro SyFs at dosages up to 1.25% led to reduced water absorption compared to PC. These results align with findings by Behfarnia et al. [126] and Ismail et al. [131], although the enhancement became less pronounced at higher fiber dosages. This is often explained by the tendency of fibers to agglomerate when overdosed, creating clusters and voids and thereby contributing to an increase in concrete absorption, porosity, and air content [122], [129]. In general, reduced water absorption is often accompanied by a decrease in porosity [122], [131]. However, with increasing fiber content, a rise in entrapped air has been documented. For instance, in [119], air content increased by approximately 10%, 18-22%, 28-33%, and 40-42% for $V_f = 0.33\%$, 0.67%, 1.00%, and 1.33%, respectively, depending on the mix composition compared to PC. In [174] it was reported that concrete reinforced with 60 mm long SyFs was characterized by 43% higher air content than with 48 mm fibers. This behavior may be influenced by the interaction between fibers and aggregates, which affects compaction efficiency and air entrapment [117]. Concluding, it is difficult to clearly determine whether the addition of macro SyFs results in an increase or decrease of concrete's absorption, porosity, and air content, as their strongly depend on various factors such as fiber geometry, dosage, distribution, mix composition, compaction method, and workability.

3.4.1.16 Sustainability and economics

Currently, sustainability and the use of environmentally friendly materials are widely discussed in the construction industry. Over the last century, the concentration of atmospheric carbon dioxide has increased by approximately 50% [175]. The cement and concrete sectors significantly contributes to this trend, accounting for about 8% of global CO₂ emissions and 2-3% of the world's annual energy consumption [176]. As a result, the construction sector faces a growing challenge: to develop concrete structures that meet environmental performance criteria while ensuring long service life. SyFRC, which offers enhanced durability, improved crack control, better corrosion resistance,

and reduced maintenance aligns with those requirements. Moreover, one of the significant benefits of SyFRC is its potential to improve the material mechanical properties and structural efficiency of concrete elements. The ability to reduce cross-sectional dimensions and increase joint spacing, thanks to limited cracking, supports material savings and sustainability.

Ozturk et al. [177] evaluated the environmental and cost impacts of incorporating 40 mm embossed PPFs in pavement concrete. While the addition of fibers led to increased material costs (by 13.9%, 51.3%, 85.5%, and 111.5% for $V_f = 0.25\%$, 0.50%, 0.75%, and 1.00%, respectively), it also enabled significant reductions in pavement thickness (by 5.2%, 9.6%, 14.0%, and 19.7%) and corresponding CO₂ emissions (by 8.3%, 9.9%, 11.6%, and 15.1%) compared to PC. These findings indicated that while higher fiber dosages increase initial material costs, they concurrently offer environmental benefits and structural optimization. The comparison of a concrete floor slab reinforced with 2.67 kg/m³ of macro SyFs and with traditional steel reinforcement consisting of ϕ 12.7 mm bars spaced at 300 mm was described in [178]. The SyFRC solution resulted in a carbon footprint of 20542 kg CO₂, compared to 46931 kg CO₂ generated by the conventionally reinforced slab. This corresponds to 1.47 kg CO₂/m² for a 200 mm thick SyFRC slab, compared to 3.36 kg CO₂/m² for the steel reinforced solution, demonstrating a 56% reduction in carbon emissions. Ali et al. [179] compared the environmental impact of producing different fiber types. Their findings showed that manufacturing of SyFs emits 30% and 9% less CO₂ than steel and glass fibers, respectively. Additionally, due to higher flexural and residual strength, SyFRC allowed for reduced pavement thickness by approximately 35 mm for $V_f = 0.5\%$ and 50 mm for $V_f = 1.0\%$ compared to PC. This reduction also led to total cost savings of 6% and 8% and carbon emission reductions of 13% and 18%, respectively. Yin et al. [100] reported that producing 17 kg of PPFs resulted in approximately 68 kg of CO₂-equivalent emissions, while manufacturing 156 kg of steel reinforcement generated around 536 kg CO₂-eq. In their study, a 100 mm thick footpath covering 43 m² required either three steel meshes (ϕ 7.6 mm steel bars spaced at 200 mm) or 17 kg of plastic fibers (4 kg/m³) to achieve equivalent reinforcement degree. From a cost perspective, fibers proved nearly twice as economical as steel mesh. Moreover, using SyFs simplifies construction, as they are added directly into the concrete mixture, eliminating the need for mesh placement, cutting, and tying, thereby also reducing labor and construction time. In another study [180], the use of SyFs enabled an 18% reduction in pavement thickness. Although the overall concrete mix cost (including mixing, transport, and placement) increased by 14% for normal strength and by 18% for high strength SyFRC, the cost per unit of flexural strength (USD/MPa) and per square meter (USD/m²) was comparable or even lower than for PC. The cost of SyFs varies depending on the type and manufacturer but generally ranges between 4€ and 10€ per kg. In contrast, 1 kg of steel fibers cost around 2-6€. However, due to much lower SyFs density, achieving a 1% volume fraction requires only approximately 9 kg/m³ of SyFs compared to 78 kg/m³ of steel fibers [179], [180]. Thus, even with higher unit prices, SyFs can be more cost-effective on a volume basis. Lastly, the environmental performance of SyFRC can be further improved through the use of recycled macro SyFs, whose effectiveness was confirmed in many studies [171], [172], [181], [182].

3.4.1.17 **Summary**

SyFRC is an advanced composite material developed to improve the brittle nature of conventional concrete by enhancing its ductility and overall durability. Table 3.12 presents the influence of SyFs on the selected concrete properties. Its primary advantage lies in its ability to control and limit cracking through three-dimensional reinforcement, allowing the concrete to transfer stresses, redistribute loads, and maintain structural integrity after cracking. Although SyFRC typically has a negligible effect on compressive strength, which is primarily dependent on the concrete matrix, and has an ambiguous or insignificant effect on the elasticity modulus, it offers substantial enhancements in other mechanical properties. These include improved flexural tensile strength, increased fracture energy, greater toughness, and enhanced splitting tensile strength. In terms of durability, SyFRC provides substantial benefits. It enhances resistance to impact, abrasion, and spalling by creating voids for vapor release. Additionally, it demonstrates improvements under freeze-thaw conditions and effectively mitigates both plastic and drying shrinkage cracking. The chemical resistance of SyFs, including their chemicals, chlorides, sulfates, and corrosion resistance, contributes to enhanced durability of SyFRC compared to traditionally reinforced concrete or steel fiber reinforced concrete. However, the effect of macro SyFs on properties such as water absorption, porosity, and air content can be inconsistent, influenced by multiple variables including fiber geometry, dosage, distribution, and the composition of the concrete mix. From both economic and environmental perspectives, SyFRC aligns well with the principles of sustainable development. It supports extended service life, reduced maintenance needs, and improved performance, all while lowering environmental impact. The carbon footprint of SyFs production is lower than that of steel or glass fibers [183]. Although initial fiber material costs may be higher, overall cost savings can be achieved through pavement thickness reduction, increased joint spacing, reduced CO₂ emissions, and simplified construction processes, thereby reducing labor and time. Achieving optimal SyFRC performance necessitates well-designed mix by limiting aggregate size, increasing fine aggregate content, and using an effective superplasticizer to ensure adequate workability and uniform fiber distribution. Selecting the appropriate fiber geometry and dosage is also essential, as excessive fiber content may lead to poor workability and deteriorated mechanical performance.

Many of the aforementioned benefits associated with the incorporation of macro SyFs into concrete are particularly advantageous for industrial floor applications. Such slabs are especially prone to shrinkage cracking, dynamic loading, abrasion, chemical exposure, and sometimes temperature variations. Moreover, in facilities where floors are frequently exposed to water, SyFs offer a distinct advantage over SFs due to their corrosion resistance. They also provide a safety benefit, as any fibers protruding from the slab surface do not pose an injury risk to people or devices, unlike SFs. Furthermore, long-term durability is often a critical requirement, since repairs of industrial floors can involve high costs and/or undesired work stoppages. Even a relatively low SyFs dosage of 2-3 kg/m 3 ($V_f = 0.22$ -0.33%) is considered beneficial, as it can improve concrete strength, enhance cracking resistance and post-cracking performance, as well as increase overall durability without significant deterioration of workability.

Table 3.12 Influence of SyFs on selected concrete properties

| Property | Influence |
|---|-----------|
| Workability | - |
| Crack limitation | ++ |
| Elasticity modulus | 0 |
| Compressive strength | 0 |
| Flexural tensile strength | + |
| Residual flexural tensile strength | ++ |
| Fracture energy, energy absorption, toughness | ++ |
| Splitting tensile strength | + |
| Shrinkage | ++ |
| Impact resistance | ++ |
| Spalling resistance | ++ |
| Freeze-thaw resistance | ++ |
| Abrasion resistance | ++ |
| Water absorption, porosity, air content | ± |
| Durability | ++ |
| Sustainability | + |
| Economic properties | + |

Note: 0 neutral, - negative, \pm difficult to assess, + positive, ++ very positive.

3.4.2. Large-scale research on centrally loaded ground slabs

3.4.2.1 Introduction

Large-scale studies are especially valuable because they provide a more realistic understanding of structural response of loaded element [184], [185]. Moreover, there are still lingering questions regarding whether the results obtained from small-scale tests accurately and reliably reflect the behavior of structural elements. Finally, existing research on SyFRC elements has so far mainly focused on testing beams, slabs, and less often ground slabs, despite the fact that the latter are one of the main applications of SyFs. This may be explained by the fact that such tests require a comprehensive knowledge and are not standardized. Moreover, since SyFs are usually used to limit shrinkage and minimize the number and width of cracks, their role in improving the mechanical performance of concrete is often disregarded in design, primarily due to their lower stiffness and strength compared to steel. However, when such studies are available, they have mostly focused on flexural behavior and moment load-bearing capabilities of ground slabs whereas one of the primary loads expected for industrial floors is the point load from racking and forklifts, which can lead to the punching shear failure. Finally, the majority of available research focuses on PC slabs without fibers, those reinforced with SFs or conventional steel meshes. Consequently, limited research discusses the punching shear behavior of ground slabs with SyFs subjected to concentrated loading. There is a lack of knowledge about the influence of SyFs on the load-bearing capacity, failure mode, crack propagation, deformations, and the location of the critical control perimeter of the ground slab. Moreover, there are also uncertainties related to the influence of the ground on the above-mentioned aspects.

An extensive literature review was conducted on experimental investigations of ground-supported concrete slabs subjected to concentrated loading. Seven experimental studies were selected for detailed analysis in order to understand the structural behavior of loaded ground slabs, demonstrate the influence of SyFs, and provide comparative results with other types of reinforcement. Each research was examined specifically in terms of its objectives, used materials, slab dimensions, support conditions, testing setup, and load application. Then the results were discussed, including cracking loads, ultimate capacities, deflections, crack morphology, and failure modes. The selected literature studies also examined the accuracy of current analytical models and design guidelines like TR34 and Eurocode 2 against experimental results. Finally, the aim of this extensive literature review was not only to determine the existing research gap, but also to analyze

the adopted testing methodologies and setups in order to establish key principles and recommendations to be followed when designing an experimental campaign on centrally loaded SyFRC ground slabs.

3.4.2.2 Alani et al. research

Alani et al. [186] conducted a comprehensive experimental investigation on a full-scale PC ground-supported slab subjected to concentrated loading applied at the center, edges, and corners. The objective of the study was to compare the experimental results with theoretical predictions based on the third edition of TR34 [68]. Furthermore, the study addressed the issue of edge and corner uplift observed in smaller slabs, suggesting that increasing the slab dimensions could overcome this phenomenon.

The test specimen was a PC slab of concrete class C32/40 with dimensions 150 x 6000 x 6000 mm. The slab was cast outdoors under a protective shelter. Subgrade preparation involved excavation, overturning, and reinstatement of the existing soil in order to ensure more compressible support conditions. Prior to casting, the subgrade stiffness was evaluated using the California Bearing Ratio (CBR) test, from which the subgrade reaction modulus *k* was determined, ranging from 44 to 55 MPa/m. An average value of 50 MPa/m was adopted for subsequent analytical calculations. A plastic membrane was placed on the subgrade before casting the slab using ready-mixed concrete delivered from an external batching plant. The experimental program comprised five loading scenarios: one central, two edge, and two corner positions performed on one PC slab (Fig. 3.53a). A 600 kN hydraulic jack applied the load through a 100 x 100 mm steel plate simulating a rack leg. The load was applied at a constant rate, and deflections were recorded using LVDTs, while crack initiation and propagation were monitored using acoustic emission sensors. Fig. 3.53b illustrates the test setup and Fig. 3.54 sensor arrangement for the centrally loaded case.

For the centrally loaded slab, no visible cracks appeared on the upper surface. Under edge loading, vertical cracks developed on the sides and widened with increasing load, followed by the formation of radial and/or circumferential cracks. In the corner loading scenarios, circumferential cracks developed initially, followed by the occurrence of radial cracks and vertical cracks on the slab's edge with further loading increase. In all cases, failure occurred due to punching. Table 3.13 summarizes the first cracking and failure loads. The results revealed that when the load was applied 150 mm and 300 mm from the slab edge, the failure loads were 15% and 8% lower, respectively, compared to the centrally loaded condition. In the corner loading cases, the ultimate load was

approximately 50% of that observed in the central loading scenario, confirming that slab corners are the most vulnerable regions and require special consideration during design.

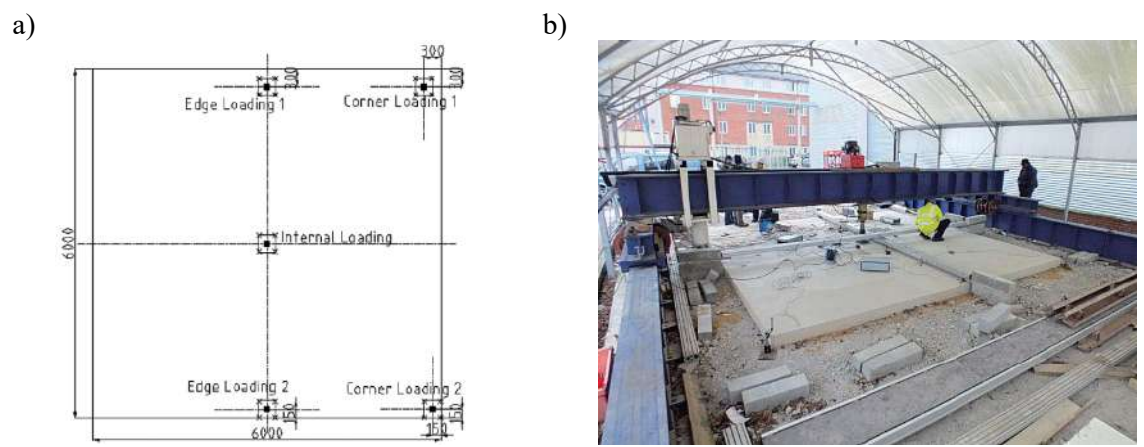


Fig. 3.53 a) Loading locations, b) testing setup for centrally loaded PC ground slab [186]

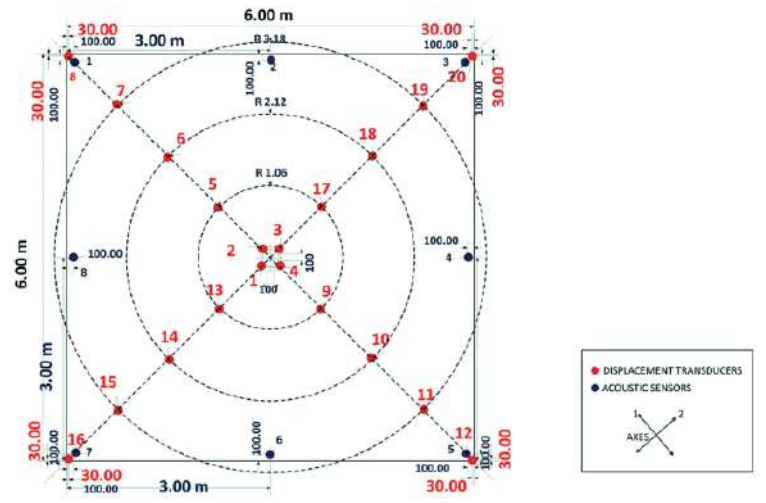


Fig. 3.54 Location of measurement devices on the centrally loaded PC ground slab [186]

Analytical calculations based on TR34 [68] were performed to predict bending and punching shear capacities for the five loading configurations (Table 3.13). According to TR34 calculations, punching shear failure was expected only for central loading; however, experimental results indicated that punching shear governed all loading scenarios. Furthermore, significant discrepancies were observed between theoretical predictions and experimental results. The measured failure loads were 1.3 to 2.0 times greater than those predicted for punching shear at the load plate perimeters. When comparing with calculated capacities at the critical control perimeter, the differences were even more pronounced. Unfortunately, the article did not specify whether the observed punching failure occurred along the loading face or the critical control perimeter. The study also concluded that testing larger slabs overcame the corner and edge uplift effects observed in smaller slabs.

Table 3.13 Results of experimentally obtained first cracking and failure loads and analytically calculated bending and punching load-bearing capacities for the tested PC ground slab [186]

| Load location | Center | Edge (150 mm) | Edge (300 mm) | Corner (150 mm) | Corner (350 mm) | | |
|-----------------------------------|-----------------------------|------------------|------------------|-----------------|-----------------|--|--|
| | Experimental results | | | | | | |
| First cracking load [kN] | - | 12.6 | 10.9 | 20.0 | 10.5 | | |
| Failure load (punching) [kN] | 479.0 | 407.0 | 443.0 | 192.0 | 262.3 | | |
| Theoretical results | | | | | | | |
| Bending capacity [kN] | 232.1 | 72.6 | 79.6 | 43.7 | 45.8 | | |
| Punching shear capacity [kN] | | | | | | | |
| - at the face of the loading area | 290.3 | 217.7 | 217.7 | 151.7 | 143.8 | | |
| - at the critical control section | 124.5 | 77.4 | 89.7 | 58.8 | 76.3 | | |

In continuation of this research, Alani et al. [187] conducted further testing on a SFRC ground slab incorporating 40 kg/m^3 of hooked-end fibers (l_f = 60 mm), under the same subgrade conditions and testing methodology as in the PC slab study [186]. Five loading positions were again examined to evaluate the influence of SFs inclusion on the load-bearing capacity, crack propagation, deflection behavior, and failure mode of the slab. Additionally, the experimental results were compared with those obtained for the PC ground slab, as well as with theoretical predictions calculated in accordance with TR34 [68].

In case of SFRC ground slab, similar crack patterns and failure modes were observed as in the PC slab, with all tests terminating in punching shear failure. Table 3.14 presents the results of the experimentally obtained first cracking and failure loads. Namely, when the load was placed 150 mm and 300 mm from the slab edge, the failure loads were 27% and 8% lower, respectively, than for the central loading. For corner loading at 150 mm and 300 mm from the edge, failure loads were 61% and 35% lower, respectively. According to TR34 [68], analytical calculations predicted punching shear failure for both central and edge loadings, but the tests demonstrated that corner loadings also led to punching failure. The experimental punching capacities were 24% to 57% higher than those calculated for the load plate perimeter, except for the 150 mm corner load case, where the experimental capacity was lower than predicted. When comparing with calculated capacities at the critical control perimeter, the differences were again even more pronounced. Unfortunately, the authors did not specify the location of the punching failure.

A comparison of PC and SFRC ground slab results revealed that first cracking loads were consistently higher for the SFRC slab for all loading scenarios. However, SFRC slabs showed superior failure capacity only for the corner loading at 300 mm. This suggests that while fiber inclusion improved cracking resistance, it did not significantly

enhance ultimate load-bearing capacity. On the other hand, TR34 [68] predicted that SFs should enhance bending capacity by 8-60% and punching shear capacity by 18-66%, however, this improvements were not reflected in the test results. Furthermore, the author of this dissertation raises concerns about the correctness of the theoretical bending capacity calculations for the PC slab in [186]. According to Sections 7.4 and 9.8.1 of TR34 [68], the positive bending moment capacity (M_p) for unreinforced concrete should be taken as 0 kNm/m. In the article [158], Alani et al. considered them equal to the values of the negative bending moment (M_n), leading to a substantial overestimation.

Table 3.14 Results of experimentally obtained first cracking and failure loads and analytically calculated bending and punching load-bearing capacities for the tested SFRC ground slab [187]

| Load location | Center | Edge (150 mm) | Edge (300 mm) | Corner (150 mm) | Corner (300 mm) | | | |
|-----------------------------------|-----------------------------|------------------|------------------|-----------------|-----------------|--|--|--|
| | Experimental results | | | | | | | |
| First cracking load [kN] | - | 180.0 | 300.0 | 60.0 | 160.0 | | | |
| Failure load (punching) [kN] | 480.0 | 350.7 | 443.0 | 187.0 | 310.0 | | | |
| Theoretical results | | | | | | | | |
| Bending capacity [kN] | 215.5 | 114.03 | 127.08 | 47.05 | 58.25 | | | |
| Punching shear capacity [kN] | | | | | | | | |
| - at the face of the loading area | 376.7 | 282.5 | 282.5 | 238.1 | 238.1 | | | |
| - at the critical control section | 163.7 | 106.0 | 106.0 | 73.3 | 96.6 | | | |

The third phase of the research, published in [188], investigated the performance of a ground slab reinforced with 7 kg/m³ of macro SyFs (l_f = 48 mm). The main objective of the study was to validate the analytical assumptions presented in TR34 [68] regarding the influence of SyFs on the structural performance of ground-supported slabs. Specifically, TR34 [12] suggests that SyFs contribute to enhanced ductility and provide a certain level of residual load-bearing capacity, however, their effectiveness is considered significantly lower compared to that of SFs. Furthermore, TR34 [12] does not allow for the inclusion of any additional shear resistance attributed to SyFs in the calculation of punching shear capacity, in contrast to the provisions made for SFs. The aim of this study was to experimentally verify the validity of this assumption. Again, the same ground conditions, testing methodology, and loading scenarios as in the previous studies [186], [187] were considered.

In case of SyFRC ground slab, similar crack patterns and failure modes were observed as in the PC and SFRC slab, with all slabs ultimately failing by punching shear. Experimental results (Fig. 3.55 and Table 3.15) showed that failure loads at corners 150 mm and 300 mm from the slab edge were 50% and 24% lower, respectively, than for the centrally loaded slab. For the edge load at 150 mm from the slab edge, the failure

load was 13% lower, whereas the edge load at 300 mm surprisingly produced a slightly higher (by 10 kN) failure load than the central load scenario.

Theoretical punching shear capacities calculated according to TR34 [68] are presented in Table 3.15. It appears that they were conducted taking into account the additional shear strength provided by the inclusion of SyFs in the concrete, using an equation applicable to SFRC. However, the Alani et al. do not provide detailed information on how the calculations were performed. Nevertheless, it was concluded that the experimental results exceeded the predicted ones by 24% to 93% for failure load at the load plate perimeter. Comparing SyFRC and PC slabs, the inclusion of SyFs improved tested punching failure loads by 2-42%, depending on load position. Theoretically, however, punching capacity should have been increased by 33-169%. This showed a discrepancy that can indicate the limitations and incorrectness of the design assumptions.

Furthermore, test results revealed that the SyFRC ground slab outperformed the SFRC slab in terms of ultimate capacity by 2-28%, contrary to expectations based on TR34 calculations [68]. Specifically, the theoretical punching shear capacities calculated at the face of the loading area were either only marginally higher (by 3%) or up to 19% lower for the SyFRC slab compared to the SFRC slab. As a consequence, Alani et al. highlighted that these findings require deeper investigation. Additionally, the results of this work raised doubts about the validity of the statement made in TR34 [68] regarding the marginal influence of SyFs on the load-bearing capacity of ground-supported slabs.

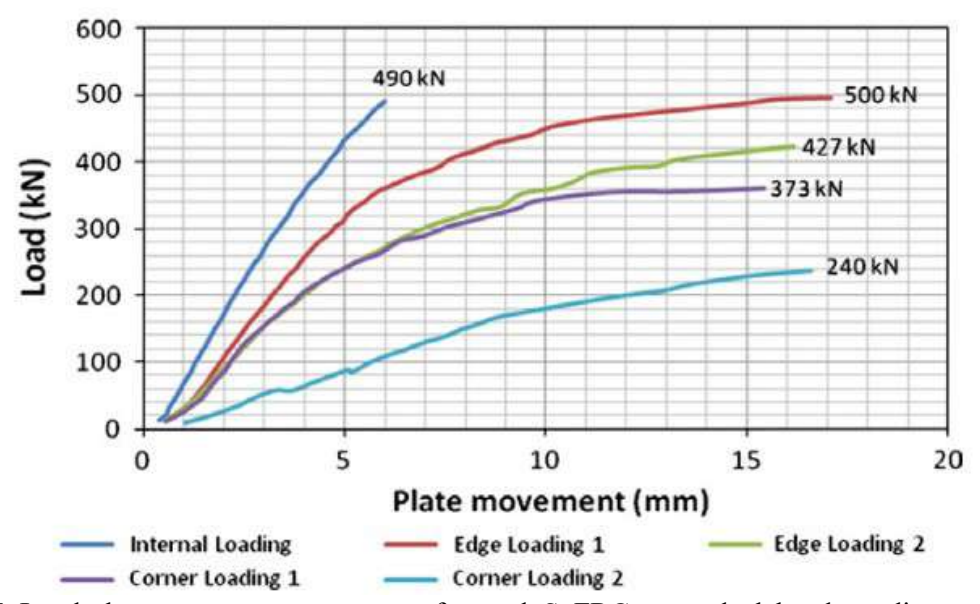


Fig. 3.55 Load-plate movement response of tested SyFRC ground slabs depending on the load location [188]

Table 3.15 Results of experimentally obtained first cracking and failure loads and analytically calculated bending and punching load-bearing capacities for the tested SyFRC ground slab [188]

| Load location | Center | Edge (150 mm) | Edge (300 mm) | Corner (150 mm) | Corner (300 mm) | | |
|-----------------------------------|----------------------|------------------|------------------|-----------------|-----------------|--|--|
| | Experimental results | | | | | | |
| First cracking load [kN] | - | 190.0 | 180.0 | 60.0 | 190.0 | | |
| Failure load (punching) [kN] | 490.0 | 427.0 | 500.0 | 240.0 | 373.0 | | |
| Theoretical results | | | | | | | |
| Bending capacity [kN] | 215.5 | 114.0 | 127.1 | 47.1 | 58.3 | | |
| Punching shear capacity [kN] | | | | | | | |
| - at the face of the loading area | 387.0 | 290.0 | 290.0 | 194.0 | 193.0 | | |

3.4.2.3 Elsaigh research

Elsaigh, in his master's dissertation [26], presented a comparative study on PC and SFRC ground slabs. The primary objective was to assess the impact of SFs on their structural performance. Additionally, theoretical load-bearing capacities and corresponding deflections were calculated using the Westergaard, Meyerhof, Falkner et al., and Shentu et al. analytical models and subsequently compared with experimental results.

The experimental campaign involved testing two types of full-scale slabs: one plain and one incorporating 15 kg/m³ of hooked-end SFs ($l_f/d_f = 80/1.33$ mm). To achieve similar load-bearing capacities, the SFRC slab thickness was reduced, resulting in 150 mm and 125 mm for PC and SFRC ground slabs, respectively. Both slabs had plan dimensions of 3000 x 3000 mm and were tested under four loading scenarios: center, edge, and two corner positions (Fig. 3.56). Loading was applied via a hydraulic twin jack using displacement control at 1.5 mm/min through a 50 x 100 x 100 mm loading plate (Fig. 3.57). Displacements were monitored using seven LVDTs mounted on a steel beam frame supported outside the slab area (Fig. 3.56). The slabs were supported on a 150 mm thick foamed concrete layer placed over a 1000 mm thick concrete floor (Fig. 3.57). The subgrade reaction modulus, determined by plate loading test, was k = 0.25 MPa/mm. Central loading tests were conducted 28 days post-casting, while edge and corner tests were conducted after 90 days.

The results (Table 3.16) show that the PC ground slabs exhibited slightly higher first-crack loads than the SFRC slabs: 3.8%, 1.7%, 4.7%, and 0.4% greater under center, edge, corner 150 mm, and corner 300 mm from edge loading, respectively. For maximum load-bearing capacity, PC slabs again outperformed SFRC slabs by 11.3% (center) and on average 5.6% (corners). Conversely, under edge loading, the SFRC slab demonstrated a 4.6% higher capacity than the reference sample. Despite these minor

differences, the overall load-bearing capacities of both types of slabs were considered comparable. Toughness factors were also similar, further supporting this conclusion. Regarding the deflection values, they were nearly identical, excluding the corner loading at 300 mm (Fig. 3.58). Failure modes differed depending on the loading scenarios: centrally, edge, and corner (150 mm) loaded slabs failed through punching shear, while the corner (300 mm) loading induced bending failure. The addition of SFs did not notably influence the failure modes; however, SFRC slabs retained post-failure integrity, whereas the PC slabs exhibited punching up to 10 mm into the subbase. Furthermore, the SFRC slabs demonstrated more effective load distribution across a larger area. Concluding, since the 16.6% reduction in slab thickness did not result in a significant decrease of load-bearing capacity, increase of deflection, or alteration of failure mode, it was confirmed that the addition of SFs allows for cross-section reduction without compromising structural performance.

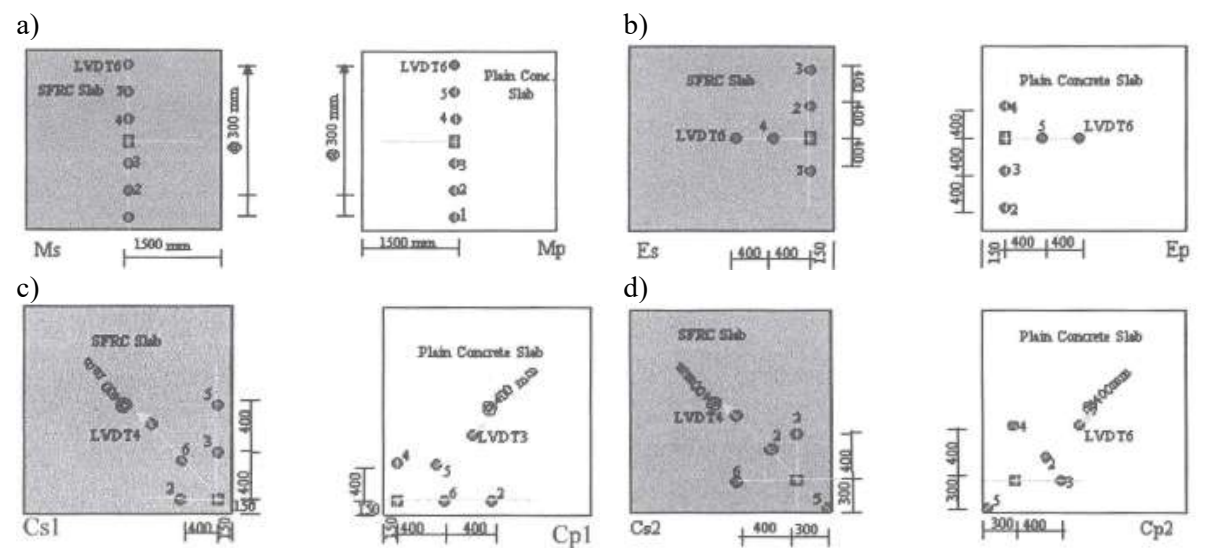
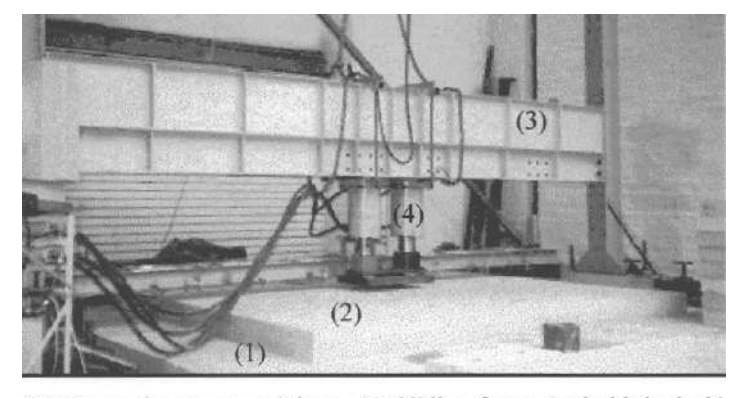


Fig. 3.56 Position of the load and LVDT measurement devices for PC and SFRC ground slabs subjected to: a) central, b) edge, c) corner 150 mm, d) corner 300 mm loading [26]



- (1) Foamed concrete sub base. (3) Sliding frame (to hold the jack)
- (2) Loaded slab.
- (4) Hydraulic twin jack.

Fig. 3.57 Testing setup for centrically loaded ground slabs [26]

Table 3.16 Experimental results from the PC and SFRC ground slab tests [26]

| Load location | Center | Edge | Corner (150 mm) | Corner (300 mm) | | | | |
|--------------------------------|----------------|-------|--------------------|-----------------|--|--|--|--|
| P | PC ground slab | | | | | | | |
| Load at first crack [kN] | 398.4 | 184.0 | 202.0 | 487.0 | | | | |
| Deflection at first crack [mm] | 1.36 | 6.50 | 6.70 | 14.60 | | | | |
| Load at failure [kN] | 731.0 | 513.0 | 437.5 | 598.0 | | | | |
| Deflection at failure [mm] | 3.94 | 13.60 | 14.60 | 17.23 | | | | |
| SFRC ground slab | | | | | | | | |
| Load at first crack [kN] | 383.8 | 181.0 | 193.0 | 485.0 | | | | |
| Deflection at first crack [mm] | 1.48 | 6.34 | 7.35 | 10.73 | | | | |
| Load at failure [kN] | 656.7 | 538.0 | 413.0 | 568.0 | | | | |
| Deflection at failure [mm] | 4.50 | 14.13 | 13.26 | 12.12 | | | | |

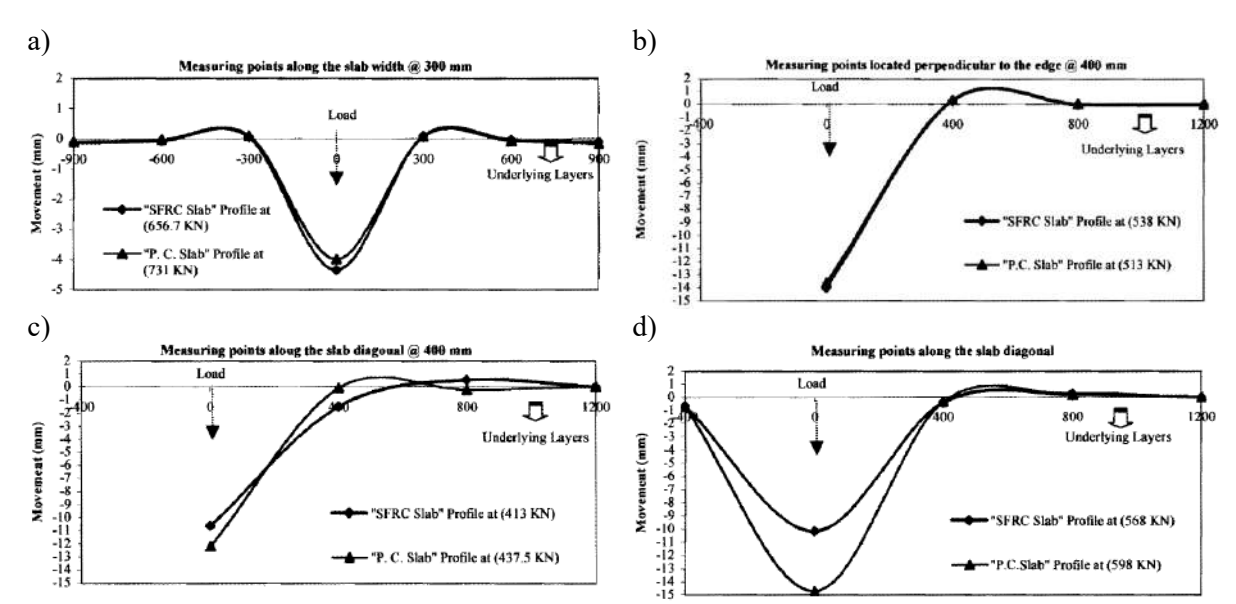


Fig. 3.58 Deflections of the PC and SFRC ground slabs subjected to: a) central, b) edge, c) corner 150 mm, d) corner 300 mm loading [26]

Elsaigh also conducted comparisons using analytical models by Westergaard, Meyerhof, Falkner et al., and Shentu et al. The Westergaard model significantly underestimated the experimental results: for SFRC ground slabs, the first-crack loads were approximately 510%, 375%, and 490% higher than predicted for center, edge, and corner loading, respectively; for PC samples, the discrepancies were 420%, 300%, and 400%. Furthermore, the deflections were underestimated using the Westergaard model. This was attributed to the model's assumption of an infinite slab of only elastic behavior. The Meyerhof model, despite accounting for elastic-plastic behavior, also showed large discrepancies. Experimental values exceeded theoretical predictions by 370% (interior), 485% (edge), and 560% (corner) for SFRC ground slabs, and by 520%, 560%, and 800%, respectively, for reference specimens. The Falkner et al. model produced comparatively closer results: experimental values for center loading exceeded theoretical ones by 66%

for SFRC and by 160% for PC ground slabs. Finally, the Shentu et al. model provided the best agreement. The predicted load for centrally loaded SFRC slab was only 27% lower than the experimental value, while the prediction for PC slab was 10% higher than the observed result. In summary, Elsaigh concluded that while the Westergaard and Meyerhof models significantly underestimated slab structural performance, the Falkner et al. and Shentu et al. approaches produced results closer to the experimental observations, with the latter offering the most accurate predictions among those considered.

3.4.2.4 Roesler et al. research

Roesler et al. [189], [190] investigated the structural response of PC and FRC ground slabs subjected to central loading, comparing the influence of macro SyFs and SFs at various dosages. Additionally, their research was extended to include experiments on SyFRC ground slabs subjected to edge loading [190]. The primary aim of these studies was to analyze differences in load-bearing capacity, deflection, and crack propagation in the tested slabs. The research also discusses various cracking loads, including tensile cracking, first and second flexural cracking, and ultimate (collapse) load. Furthermore, the study investigated if results from small-scale FRC beam tests can reliably predict the behavior of large-scale structural slabs.

Seven large-scale slabs (127 x 2200 x 2200 mm) were tested. Five were centrally loaded: one from PC, two with macro SyFs ($l_f/d_f = 40/0.44$ mm) at $V_f = 0.32\%$ and 0.48% (3.0 and 4.4 kg/m³, respectively), and two with SFs – hooked-end ($l_f/d_f = 60/0.92$ mm, $V_f = 0.35\% = 27.3 \text{ kg/m}^3$) and crimped $(l_f/d_f = 65/1.3 \text{ mm}, V_f = 0.50\% = 39 \text{ kg/s})$ fibers. Moreover, two additional slabs: one from PC and one with 0.48% of SyFs were loaded at the edge. The test setup is illustrated in Fig. 3.59. All slabs rested on a 200 mm thick of compacted low-plasticity clay within containment layer box (310 x 2440 x 5080 mm), with an average subgrade modulus reaction k = 0.103 MPa/mm. The authors stated that the variations in k were found to have minimal influence on load-bearing capacity. Loading was applied through a 25 x 203 x 203 mm steel plate using a 500 kN hydraulic actuator with a variable loading rate. Deflections were measured using 20 LVDTs positioned along axes, diagonals, and edges mounted on a frame supported outside the containment box (Fig. 3.60a). Moreover, strain gauges were used to record compressive strains at the top and tensile strains at the bottom of the slab near the loading area (Fig. 3.60b). Additional gauges on the slab surface captured strain evolution after flexural cracking. With no access to the underside of the slab, the strain gauges results were crucial for indicating the tensile cracking load which was defined as a point where the strains began to display nonlinear behavior.



Fig. 3.59 Testing setup for centrally loaded ground slabs [191]

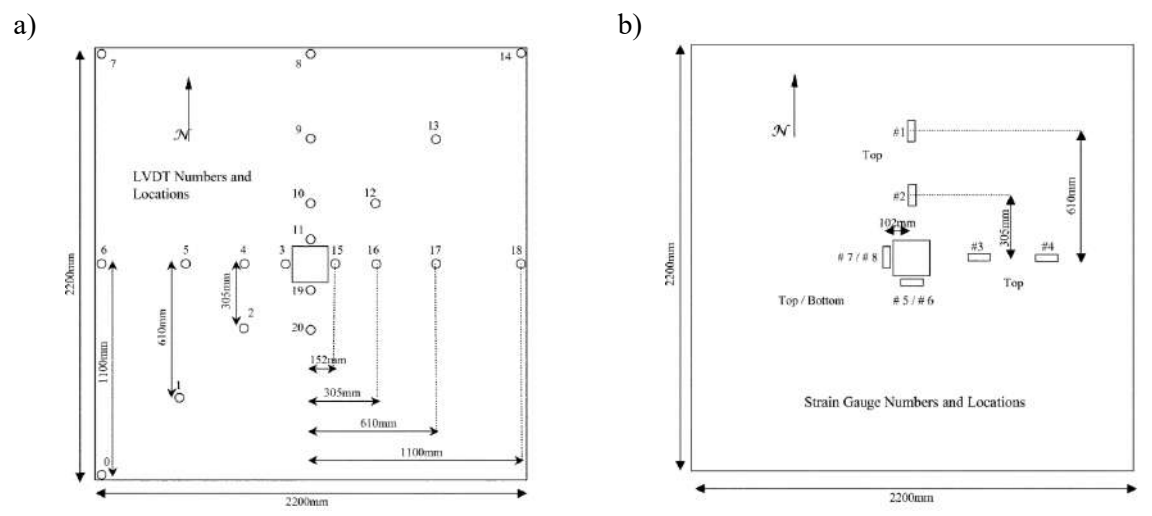


Fig. 3.60 Location of measurement devices for centrally loaded ground slabs: a) LVDTs, b) strain gauges [189]

The load-deflection response of the centrally loaded slabs is presented in Fig. 3.61a. Initially, the structural behavior of all slabs was similar, characterized by a linear relationship between applied load and deflection. Subsequently, the first flexural crack was formed, resulting in a significant reduction in stiffness and visible cracking near the slab edges. A secondary flexural crack then appeared, oriented approximately perpendicular to the first. These flexural cracks were typically initiated at the bottom surface of the slab near the loading area and propagated outward toward the edges and upward through the slab depth. The collapse load was defined as the peak load resisted by the slab, beyond which load capacity declined steadily with increasing deformation. This failure was visually indicated by either punching shear or the formation of

circumferential cracks at the top surface near the loading area, indicating that the slab's moment capacity had been reached. In the case of edge-loaded slabs, the first flexural crack also appeared at the edge, followed by a sudden drop only for PC ground slab, finally reaching their flexural capacity (Fig. 3.61b).

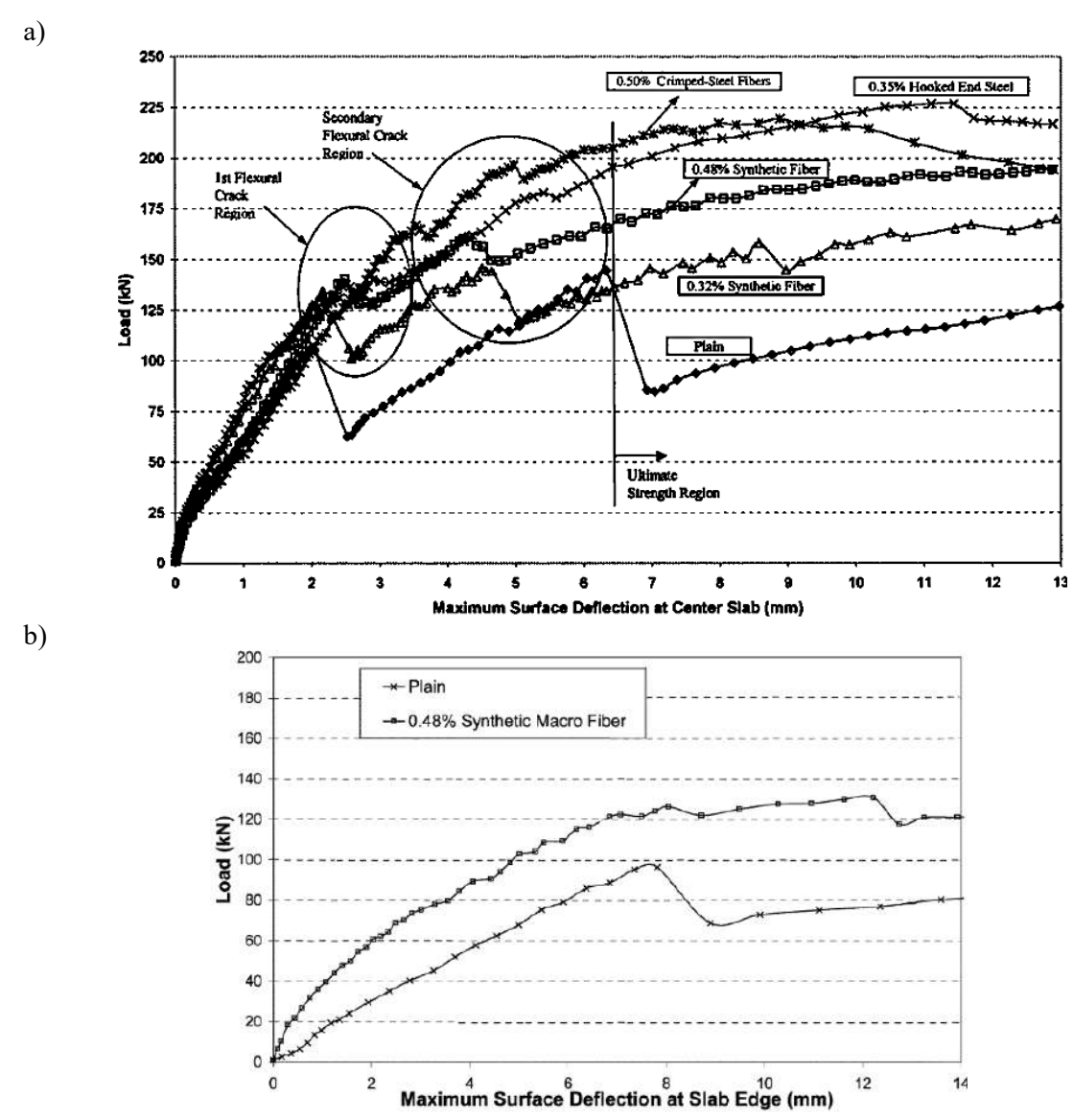


Fig. 3.61 Load-deflection response of tested ground slabs subjected to: a) central, b) edge loading [189], [190]

According to Table 3.17, the addition of fibers had negligible influence on the tensile cracking load for both centrally and edge-loaded slabs. In contrast, the presence of fibers significantly increased the first and second flexural cracking loads. Specifically, the inclusion of 0.32% and 0.48% of SyFs increased the first flexural cracking load by 25% and 32%, respectively. Hooked-end SFs at 0.35% dosage increased it by 31%, while crimped SFs at 0.50% dosage achieved the highest enhancement of 55% for centrally loaded slabs. The study also noted that SyFRC slabs and SFRC slabs with hooked-end

fibers exhibited comparable flexural cracking loads. For edge-loaded slabs, the addition of 0.48% of SyFs improved the first flexural cracking load of the PC slab by 28%. Regarding the second flexural cracking load, all slabs experienced higher loads than at first cracking. However, only in the case of the PC slab did the second flexural cracking load remain below the collapse load. It was also revealed that SyFRC ground slabs showed a smaller increase from first to second flexural cracking loads compared to SFRC slabs, yet all FRC samples demonstrated enhanced resistance to secondary cracking in comparison to PC. Moreover, the reduction in load-carrying capacities after both flexural cracking were significantly smaller for FRC slabs than for PC ground slabs. Fiber addition also notably enhanced the collapse load capacity. For centrally loaded slabs, the load increased by 29-44% in SyFRC and by 63-69% in SFRC slabs, depending on fiber type and dosage. For edge-loaded slabs with 0.48% of SyFs, collapse load was improved by 32%. Notably, SyFRC slabs with 0.48% of macrofibers achieved collapse loads only 13-17% lower than those of SFRC slabs. The study also found that the collapse capacity of edge-loaded slabs was 29% and 33% lower than that of centrally loaded PC and SyFRC slabs, respectively. Upon failure, PC slabs fractured into separate pieces, while slabs with fibers remained their structural integrity even under loads exceeding their ultimate capacity (Fig. 3.62).

Table 3.17 Results of cracking and collapse loads for tested ground slabs subjected to central and edge loading [189], [190]

| Fiber dosage | Tensile cracking load [kN] | First flexural load [kN] | Second flexural load [kN] | Collapse load [kN] | | |
|-------------------------|----------------------------|--------------------------|---------------------------|-----------------------|--|--|
| | Centr | al loading | | | | |
| None | 75 | 108 | 145 | 135 | | |
| 0.32% of SyFs | 75 | 135 | 148 | 174 | | |
| 0.48% of SyFs | 70 | 143 | 162 | 195 | | |
| 0.35% of hooked-end SFs | 70 | 141 | 185 | 228 | | |
| 0.50% of crimped SFs | 70 | 167 | 200 | 220 | | |
| Edge loading | | | | | | |
| None | 50 | 99 | - | 96 | | |
| 0.48% of SyFs | 55 | 127 | - | 131 | | |

The authors also observed that, following the formation of the first flexural crack, the centrally loaded PC slab began to lose contact with the subgrade at its edges and corners, with approximately 50% loss of contact occurring prior to reaching the second flexural cracking load. In contrast, slabs with fibers maintained full contact with the subgrade for a substantially longer duration. Specifically, the slab reinforced with 0.32% of SyFs preserved full contact up to the second flexural cracking load, while the slab with 0.48% of SyFs until the collapse load was reached. This prolonged slab-ground

contact enabled more effective load redistribution, contributing to the increased load-bearing capacity observed in FRC ground-supported slabs. Furthermore, the research revealed that the beam flexural strength, obtained from 4PBT, significantly underestimated the slab flexural strength for both plain and FRC slabs. Specifically, the ratio of slab to beam flexural strength was 1.4 for PC and 1.8 to 2.2 for FRC. On the other hand, it was confirmed that the fracture toughness index (R_e) could successfully predict the increase in flexural and ultimate capacity of the SyFRC ground slab. For instance, the slabs with 0.32% and 0.48% of SyFs showed flexural capacities 25% and 32% greater than PC slabs, respectively, correlating well with their R_e values of 24% and 39%.

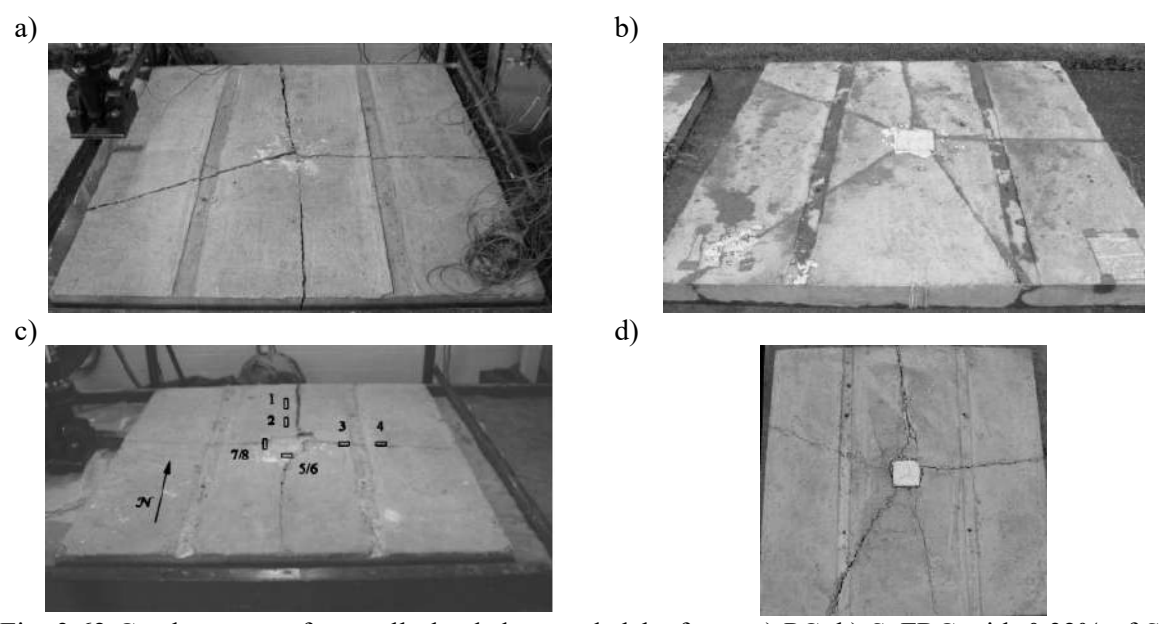


Fig. 3.62 Crack pattern of centrally loaded ground slabs from: a) PC, b) SyFRC with 0.32% of SyFs, c) SyFRC with 0.48% SyFs, d) SFRC with 0.35% hooked-end SFs [189], [191]

In summary, the addition of fibers, regardless of type or dosage, had minimal influence on tensile cracking load but significantly enhanced flexural cracking load, ultimate load-bearing capacity, ductility, and post-cracking behavior. The improved performance of FRC slabs also included better load distribution and prolonged maintaining of slab contact with the subgrade. Although SFRC ground slabs exhibited moderately superior performance compared to SyFRC slabs, the overall structural response of both material types was comparable, thereby validating the use of macro SyFs as effective secondary reinforcement in ground-supported slabs. The study also concluded that the fracture toughness index R_e , obtained from small-scale 4PBT of beams, reliably predicted the structural response of large-scale ground slabs.

3.4.2.5 Bischoff et al. research

Bischoff et al. [192] highlighted significant confusion and conflicting opinions regarding the effects of fibers on the behavior of concrete ground slabs. To address these uncertainties, the authors conducted an extensive experimental campaign on slabs on grade. Additionally, the possibility of replacing traditional reinforcement with dispersed fibers was assessed and the influence of subgrade stiffness was studied. The tested slabs measured 150 x 2500 x 2500 mm and included various reinforcement types: welded-wire reinforcement (WWR), steel fibers SFs ($l_f/d_f = 60/0.8$ mm), and fibrillated PPFs ($l_f = 51$ mm). Nine slabs were prepared: one plain concrete (PC) slab as a reference, two SFRC slabs with 10 kg/m³ of SFs, two SFRC slab with 30 kg/m³ of SFs, two polypropylene fiber reinforced concrete (PPFRC) slabs with 0.9 and 3.6 kg/m³ of PPFs, one slab with a single layer of WWR (ϕ 4.88 mm bars spaced at 152 mm, located 50 mm from the top surface), and one slab with two layers of WWR (ϕ 5.74 mm bars spaced at 152 mm, placed 50 mm from both top and bottom surfaces). Slabs with lower reinforcement levels were designed to provide a nominal reinforcement ratio of 0.1% by volume, while those with higher reinforcement levels provided a moderate reinforcement ratio of 0.4%. The slabs were tested under centrally applied load using a 100 x 100 mm bearing plate. Tests were conducted on both loose (k = 0.015 MPa/mm) and compacted (k = 0.075 MPa/mm) subgrades to assess the influence of soil stiffness.

Bischoff et al. described also the anticipated response of a slab-on-grade subjected to central loading (Fig. 3.63). Initially, the response of the slab is expected to be approximately linear, up to the point when the first crack forms in the center of the slab bottom surface. This moment corresponds to the cracking load (P_{cr}). Based on Westergaard's analytical approach, for a 150 mm thick slab with a compressive strength of 35 MPa and a subgrade stiffness of k = 0.015 MPa/mm, the P_{cr} was estimated to be approximately 45 kN. After this point, the load-deflection behavior begins to deviate from linearity due to crack propagation towards the slab edges. Nevertheless, the slab retains its load-carrying ability while cracking. This progression continues until the slab reaches its collapse load ($P_{collapse}$), usually 3-5 times greater than P_{cr} . The post-cracking performance depends significantly on the type and quantity of reinforcement incorporated into the slab. Failure load (P_f) of the slab is defined as the point at which it experiences a complete loss of load-bearing capacity.

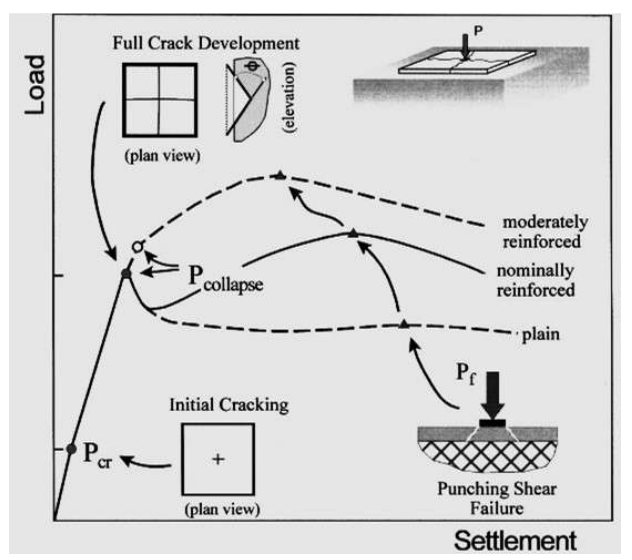


Fig. 3.63 Idealized model of the ground slab response subjected to central loading [192]

Fig. 3.64a presents the results from the tests of seven slabs supported by the loose subgrade and subjected to central concentrated force. Firstly, it was revealed that the flexural behavior observed in beam tests (Fig. 3.64b) correlated well with the performance of large-scale slabs, particularly in the post-cracking phase. It was also concluded that the Westergaard model underestimated the P_{cr} of the PC slab. Then, increasing reinforcement amount resulted in modest improvements in $P_{collapse}$, but more notably enhanced the post-cracking behavior. PPFRC slabs with a fiber dosage of 0.9 kg/m³ provided minimal performance enhancement and offered little structural benefit compared to the PC ground slab. The authors concluded that low dosage of PPFs should be used primarily for controlling plastic shrinkage cracking, not for structural reinforcement. For a higher dosage (3.6 kg/m³), PPFs led to improved structural performance compared to PC ground slabs, however also introducing some mixing challenges. Moreover, neither PPFs dosage resulted in a P_f exceeding $P_{collapse}$, in contrast to slabs reinforced with a single layer of WWR or 10 kg/m³ of SFs exhibited hardening behavior. The slab with 30 kg/m³ of SFs performed even better, and the slab with two layers of WWR demonstrated the best structural response. The enhanced performance of this slab was attributed primarily to the bottom reinforcement layer, which resisted the positive bending moments more effectively. Finally, the results showed that SFRC slabs achieved comparable load-bearing capacity to WWR reinforced slabs, suggesting that SFs are a viable alternative to traditional reinforcement in ground-supported slabs. Regarding failure modes, PPFRC slabs failed due to punching shear. In contrast, the slabs with one WWR layer or 10 kg/m³ of SFs showed cracking on their top surfaces, but only after unloading. Slabs with higher SFs content or two WWR layers did not show significant surface cracking. Additionally, all slabs experienced corner uplifting once the *Pcollapse* was achieved. This usually leads to a failure mechanism different from the one commonly encountered for slabs in situ. The authors emphasized that future experimental campaigns should include restraints against slab curling to more accurately reproduce field conditions. Finally, the study demonstrated the importance of good subgrade compaction. Fig. 3.65 presents the results of tests conducted on three SFRC slabs with varying reinforcement, each supported by either a loose or compacted subgrade, and subjected to a centrally applied concentrated load. It was concluded that properly compacted ground substantially improved slab performance. Moreover, the addition of 30 kg/m³ of SFs or one layer of WWR compensated for the poor ground conditions. In conclusion, SFs can effectively replace WWR in ground slabs, whereas low dosages of PPFs do not significantly enhance load-bearing capacity and should not be considered a substitute for conventional steel reinforcement. Higher dosages of PPFs can lead to modest improvements of slab structural performance compared to PC ground slabs. Both SFs and WWR were effective in compensating for inadequate subgrade support compaction.

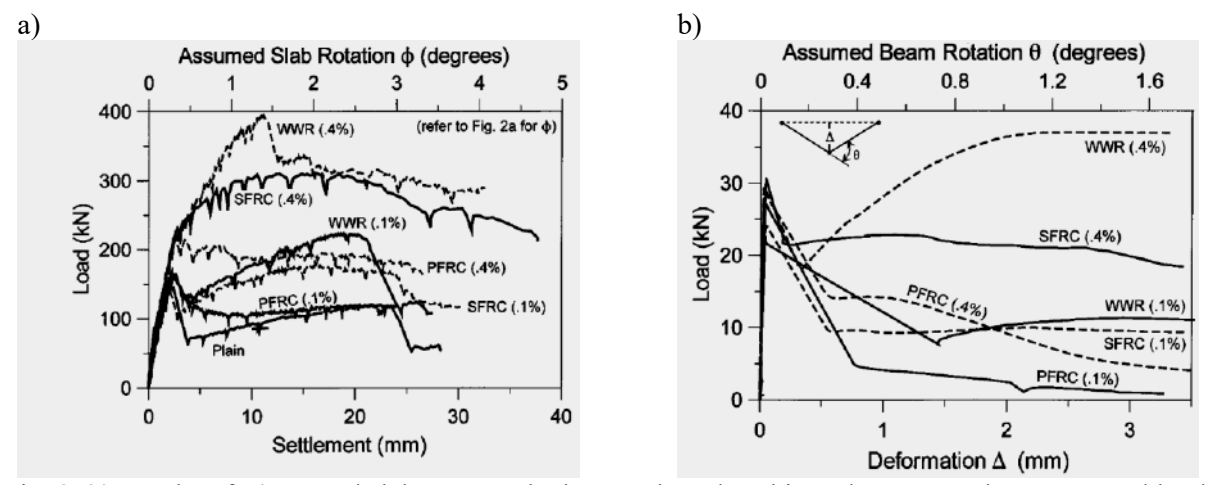


Fig. 3.64 Results of: a) ground slab tests on the loose subgrade subjected to a central concentrated load, b) flexural beam tests [192]

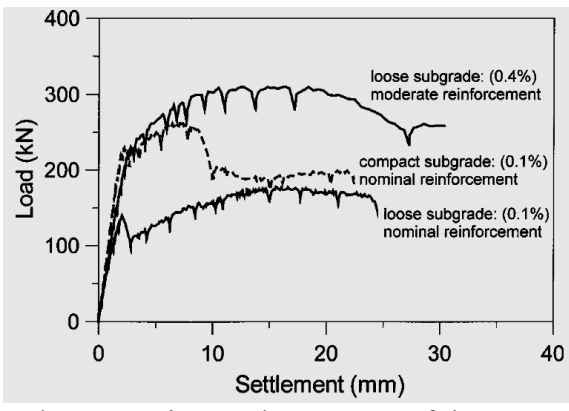


Fig. 3.65 Influence of subgrade compaction on the response of the SFRC ground slabs subjected to a central concentrated load [192]

3.4.2.6 Shi et al. research

Shi et al. [193] conducted a comparative experimental investigation into the structural performance of ground-supported concrete slabs and beams reinforced with PPFs, SFs, and conventional steel mesh. The primary objective was to evaluate the load-strain and load-deflection characteristics, deflection profiles, and crack propagation of variously reinforced ground slabs subjected to centrally applied concentrated loads. Additionally, experimental results were compared with analytical predictions based on the 3rd edition of TR34 guidelines [68].

The experimental program included four reinforced concrete slabs with dimensions of 120 mm thickness and 1800 x 1800 mm in plan. These comprised one PC slab, one slab reinforced with 6 kg/m³ of PPFs ($l_f/d_f = 50/0.6$ mm), one slab with 30 kg/m³ of SFs ($l_f/d_f = 50/0.3$ mm), and one slab incorporating a single layer of steel mesh reinforcement placed at the bottom (ϕ 6 mm bars spaced at 150 mm). In addition to the slabs, standard beams were prepared for 3PBT and 4PBT. The setup for ground slabs testing is shown in Fig. 3.66.

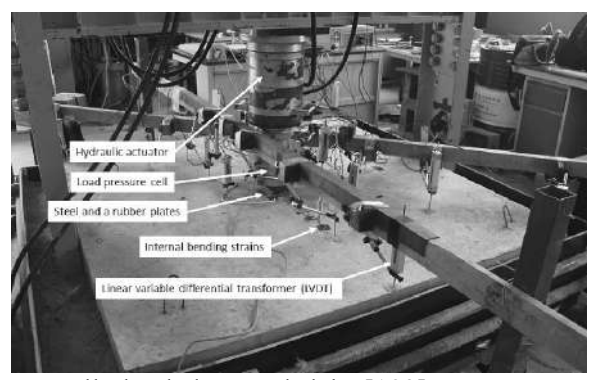


Fig. 3.66 Testing setup for centrally loaded ground slabs [193]

Each slab was placed on a sand-filled box measuring $400 \times 2100 \times 2100$ mm. Prior each testing, the subgrade was recompacted to ensure consistent support conditions. The subgrade stiffness was controlled using the plate bearing test and maintained at approximately k = 0.05 MPa/mm. A centrally applied load was introduced through a dual-plate setup comprising a 10 mm thick steel plate and a 5 mm thick rubber pad, both measuring 100×100 mm. The loading was applied using a 1000×100 kN hydraulic actuator under displacement control at a rate of 0.3 mm/min. The measuring instrumentation included 20×100 LVDTs mounted on an external frame placed on the laboratory floor and 8×100 strain gauges per slab to record deflections and internal strain distributions, respectively (Fig. 3.67). In the methodology, the tensile cracking load was identified as the point at which the load-strain response deviated from linearity. Then, the flexural cracking load

was determined at the turning point of the load-deflection curve, coinciding with significant changes in strain profiles and visible cracking. Finally, the ultimate capacity corresponded to punching shear failure or the development of circumferential top surface cracks.

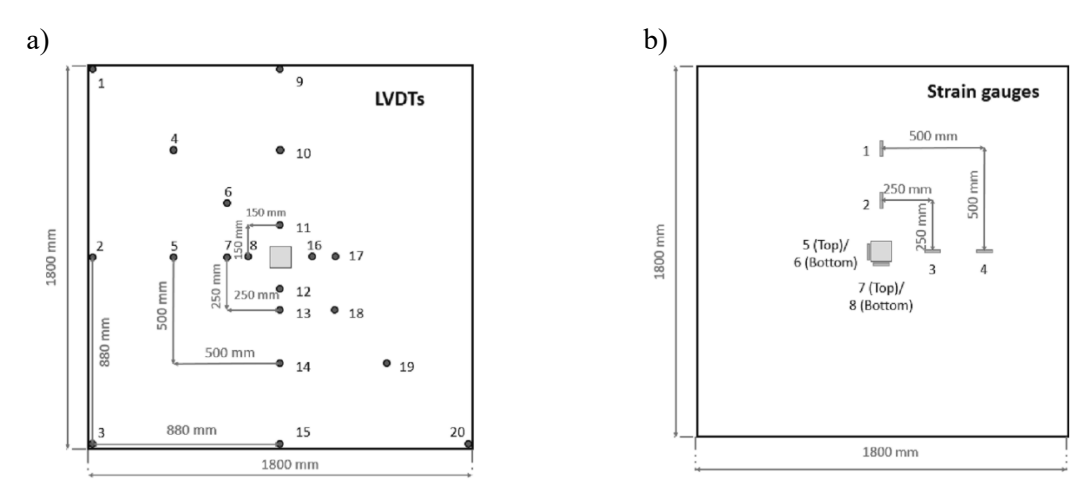


Fig. 3.67 Location of measurement devices for centrally loaded ground slabs: a) LVDTs, b) strain gauges [193]

The load-strain behavior of PC, PPFRC, SFRC, and steel mesh reinforced concrete (SMRC) ground slabs is presented in Fig. 3.68a. The PC slab exhibited a microcracking at approximately 25 kN, followed by macrocracking at 45 kN. PPFRC, SFRC, and SMRC slabs demonstrated macrocrack formation at approximately 50, 75, and 100 kN, respectively, whereas micro cracking points were not clearly observed. The minimal difference between PC and PPFRC in early loading stages was attributed to the relatively low stiffness of PPFs, making their contribution more apparent at higher strain levels. In contrast, SFs with their higher stiffness, substantially enhanced the tensile load capacity both prior to and after cracking. An interesting observation was that beyond macrocracking, the load-strain response of the SFRC slab exhibited a lower slope compared to PPFRC, indicating that PPFs may be more effective in resisting uplift deformation. This phenomenon was explained by the superior bonding strength and ductility of PPFs, which deform without causing concrete breakage unlike SFs. However, the authors acknowledged the need for further investigation to validate this conclusion. Nevertheless, both FRC ground slabs maintained load-carrying capacity after cracking, due to effective crack bridging. SMRC slab, in particular, showed substantial tensile strain increases post-cracking, and among all tested reinforcements, steel mesh was the most effective in resisting the applied loads. The analysis of load-deflection responses (Fig. 3.68b) showed that SMRC slabs achieved the highest flexural cracking load (122 kN), followed by SFRC (100 kN), PPFRC (87 kN), and PC (68 kN) ground slab.

Despite cracking, the PPFRC, SFRC, and SMRC slabs continued to carry increasing loads, demonstrating the contribution of reinforcement in the post-cracking phase. Interestingly, the post-cracking energy absorption of PPFRC slab was comparable to that of SFRC ground slab, despite significantly lower dosage and mechanical properties of PPFs. This contrasts with the results from standard beam bending tests, where SFRC generally outperformed PPFRC. For ground slabs, however, the post-cracking behaviors were found to be more comparable. Moreover, between deflections of 13 mm and 20 mm, PPFRC slab even outperformed SFRC slab in terms of load resistance. Additionally, while FRC beams exhibited flexural strengths similar to or only marginally higher than PC samples in standard bending tests, ground slabs showed a pronounced increase in flexural cracking loads when reinforced with fibers.

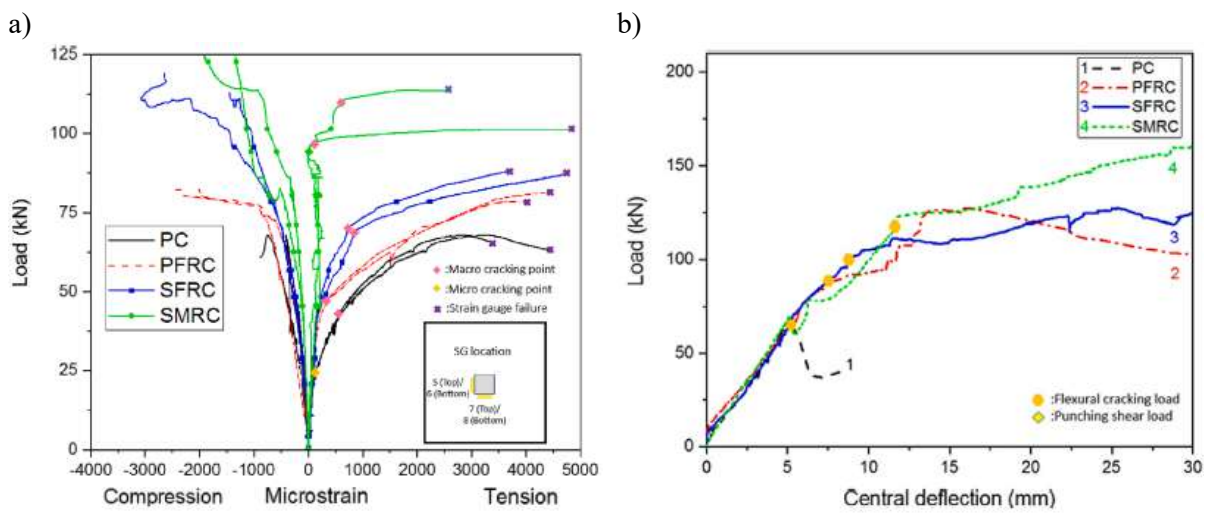


Fig. 3.68 Results from PC, PPFRC, SFRC, and SMRC ground slab tests: a) load-strain, b) load-deflection response [193]

In terms of deflection profiles, all tested slabs remained in full contact with the subgrade until the central deflection reached approximately 5 mm. Beyond this point, both PC and PPFRC slabs began to exhibit corner uplifting. Finally, when the deflection in the middle of the slab was equal to 15 and 20 mm, the SMRC and SFRC ground slabs were already deflected upward, respectively. This suggested that SFs and PPFs notably enhanced the deformation resistance of slabs under central loading when compared to the PC slab. Crack pattern analysis (Fig. 3.69) indicated that all slabs experienced similar radiating cracks starting from the center and propagating to the edges, with four primary cracks observed in the PC, PPFRC, and SMRC slabs, and five in the SFRC slab. Moreover, the PC slab exhibited a distinct punching shear failure as the applied load increased. In contrast, no clear evidence of punching shear was observed in the reinforced slabs, although circumferential cracks on the top surface were present.

Fig. 3.69 also presents a detailed view of the loading area, indicating that PPFs had minimal effect on the extent of top surface cracking, whereas SFs and steel mesh increased the distance between the central point and the outer edge of cracks by 220% and 280%, respectively.

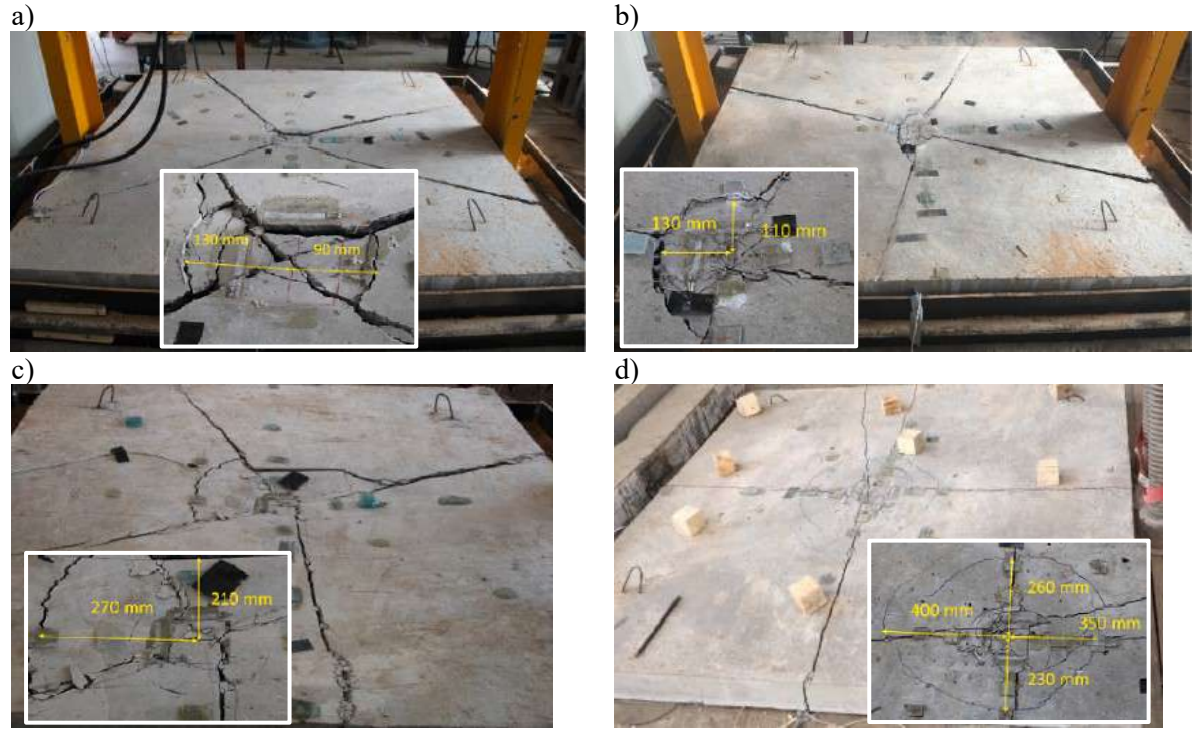


Fig. 3.69 Crack pattern of centrally loaded ground slabs from: a) PC, b) PPFRC, c) SFRC, d) SMRC [193]

Finally, the experimental results were compared with the analytical predictions obtained using the TR34 guideline [68]. It is important to note that in analytical calculations, the contribution of the subgrade reaction was not considered. As shown in Table 3.18, the experimentally obtained improvements attributed to fiber addition were significantly more pronounced in ground slabs than in beams, indicating that fibers have a greater influence in slab applications. The analytical model also predicted higher collapse loads than those observed in tests. Specifically, the analytical values were overestimated by approximately 12% for PC and SMRC ground slabs, 45% for the PPFRC slab, and 24% for the SFRC slab, potentially leading to unsafe design assumptions. Additionally, the punching shear capacity at the predefined critical control perimeter at a distance a = 2d from the loading area was calculated (Table 3.18). The increased shear resistance due to reinforcement addition was accounted for only SFRC and SMRC slabs. The authors highlighted that no guidelines exist for estimating the additional shear capacity contribution resulting from the presence of PPFs in concrete, limiting the accuracy of analytical predictions for PPFRC ground slab.

Table 3.18 Results from flexural beam tests and experimentally and analytically obtained collapse loads from ground slab tests [193]

| Ground slab type | PC | PPFRC | SFRC | SMRC |
|-------------------------------------|-------|--------------|---------------|---------------|
| Flexural strength from 3PBT [MPa] | 4.90 | 4.90 (1.00) | 5.00 (1.02) | - |
| Flexural strength from 4PBT [MPa] | 3.90 | 4.41 (1.13) | 4.90 (1.26) | - |
| Experimental collapse load [kN] | 68.0 | 87.0 (1.28) | 100.0 (1.47) | 122.0 (1.79) |
| Calculated collapse load [kN] | 76.0 | 126.0 (1.66) | 124.2 (1.63) | 136.3 (1.79) |
| Calcula./Experi. collapse load [-] | 1.12 | 1.45 | 1.24 | 1.12 |
| Calculated punching shear load [kN] | 96.16 | 96.16 (1.00) | 123.55 (1.28) | 200.29 (1.62) |

Note: In the brackets the normalized values against PC are presented.

Overall, the study demonstrated that fibers and steel mesh substantially improve the load-bearing capacity of ground-supported slabs, with flexural capacity increases of 28%, 47%, and 79% observed for PPFRC, SFRC, and SMRC slabs, respectively. Additionally, PPFs' favorable effect on the post-cracking phase and toughness of the ground slab compared to SFs was noted. However, the authors stated that PPFs did not influence the diameter of the circumferential top cracks, which appeared during testing, unlike SFs and steel mesh. Nevertheless, all types of reinforcement led to an improved deformation resistance of centrally loaded slabs compared to PC. Importantly, the mechanical behavior of FRC in beam tests was not representative of the performance in slab applications, reinforcing the need for large-scale slab testing. Finally, the TR34 [68] analytical model was found to overestimate the capacity of reinforced slabs.

3.4.2.7 Sucharda et al. research

The research discussed by Sucharda et al. in [36] focused on the punching shear response of a reinforced concrete ground-supported slab centrally loaded by a concentrated force. Additionally, the study aimed to validate the experimental results through analytical predictions based on PN-EN 1992-1-1:2006.

The tested slab had dimensions of $120 \times 1950 \times 2000$ mm and was cast using concrete class C16/20. Reinforcement consisted of a $\phi 8$ mm hand knotted steel mesh at the bottom of the slab with a spacing of 100 mm in both directions (Fig. 3.70). The load was applied centrally over a 200 x 200 mm area. The slab was supported over a 0.3 m thick compacted gravel layer (0/4 mm grading), which rested on a 5.0 m thick natural subsoil layer of loess loam. During the test, vertical displacements were recorded using 16 displacement sensors (LVDTs) mounted on an external frame outside the slab samples (Fig. 3.71a). The load was applied incrementally in 50 kN steps until the slab failed at a peak load of 344 kN due to punching shear. Post-failure inspection revealed a

non-symmetrical punching cone base at the bottom surface of the slab, with an average radius of 765 mm (Fig. 3.71b). Furthermore, as the applied load increased, the slab exhibited uneven settlements, attributed by the authors to the inhomogeneous subgrade and propagation of the concrete failure on one slab side. Corner uplift was also observed, and at the maximum load stage, the slab lost contact with the subgrade up to a distance of approximately 350 mm from the load application center.

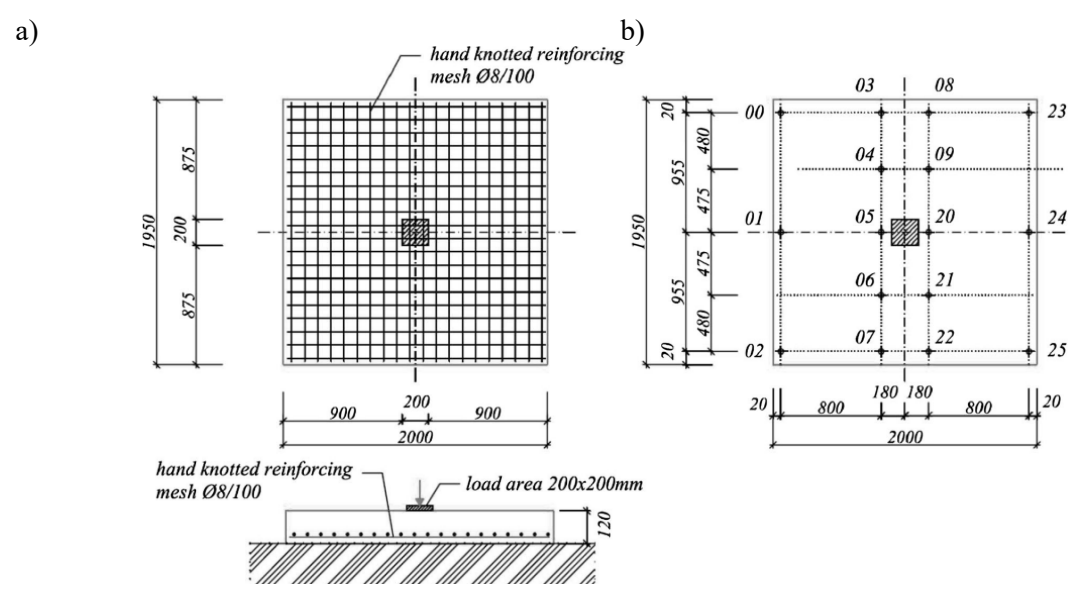


Fig. 3.70 a) Testing setup, b) LVDTs position for centrally loaded ground slab traditionally reinforced with steel mesh [36]

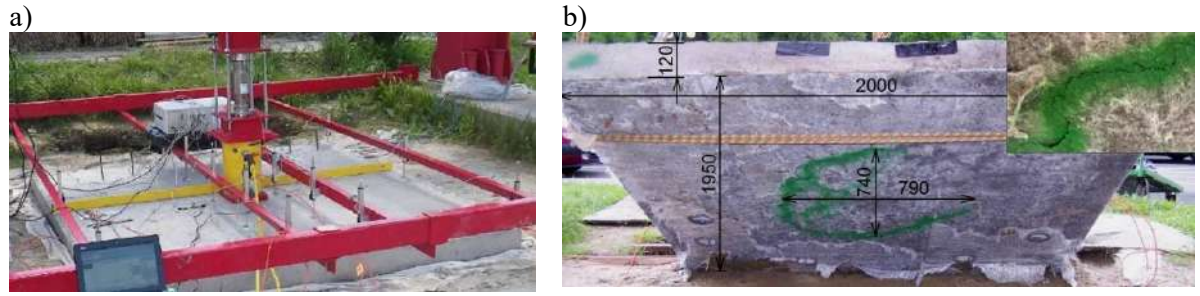


Fig. 3.71 a) Testing of centrally loaded ground slab, b) cracking pattern on the bottom surface of the slab (punching shear failure) [36]

Analytical punching shear calculations were carried out in accordance with PN-EN 1992-1-1:2006. Specifically, the shear capacity was evaluated at both the perimeter of the loaded area u_0 ($V_{R,max}$) and at the critical control perimeter u_1 ($V_{E,max}$) located up to a distance a = 2d from the edge of the loaded area. The calculations were performed for mean, characteristic, and design compressive strengths of concrete, resulting in predicted punching shear capacities of 177.42 kN, 139.77 kN, and 60.13 kN, respectively corresponding with critical control section at a distance a = 2d (Fig. 3.72). While the mean strength value was expected to align most closely with experimental

results, it was still significantly lower, approximately two times, than the experimentally observed punching load. It is important to note that these calculations assumed full contact between the slab and the subsoil across the entire slab area (3.90 m²), which did not reflect the actual conditions noted during testing. Due to the recorded corner uplift, the effective contact area was reduced to 3.52 m². Despite this discrepancy, the authors observed that the difference in predicted bearing capacity between full and partial subsoil contact conditions was negligible. However, they emphasized that the stress distribution beneath the slab was not uniform, highlighting that the presented calculations cannot be considered accurate. To further evaluate the accuracy of the Eurocode 2 approach, the slab was sectioned into eight segments post-testing. A the theoretical punching shear defined comparison between model PN-EN 1992-1-1:2006 and the experimental observations for the tested slab is presented in Fig. 3.73a. Measurements were taken to determine the actual location of the critical control section and the crack inclination angle θ at the reinforcement level d (Fig. 3.73b). It was found that the experimental distance a was equal to average 1.7d, rather than 2d predicted from analytical calculations. In conclusion, PN-EN 1992-1-1:2006 provided a conservative estimate of punching shear capacity of tested reinforced concrete ground-supported slab subjected to central, concentrated force. Moreover, the analytical model did not accurately predict the real punching shear response of the slab, specifically the location of the critical control section. These findings highlighted the necessity of incorporating more realistic analytical models for more accurate predictions of punching shear response of loaded ground slabs.



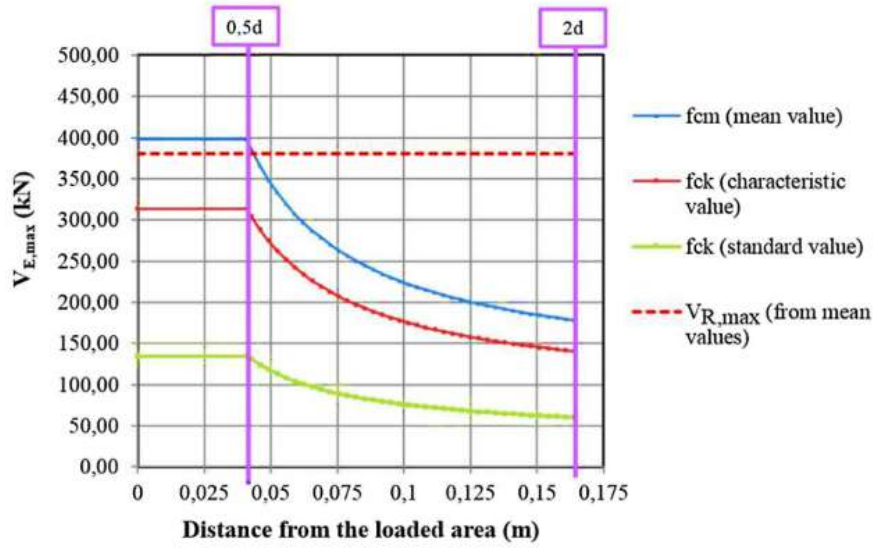


Fig. 3.72 Punching load-bearing capacity calculated according to PN-EN 1992-1-1:2006 for different positions of the critical control section [36]

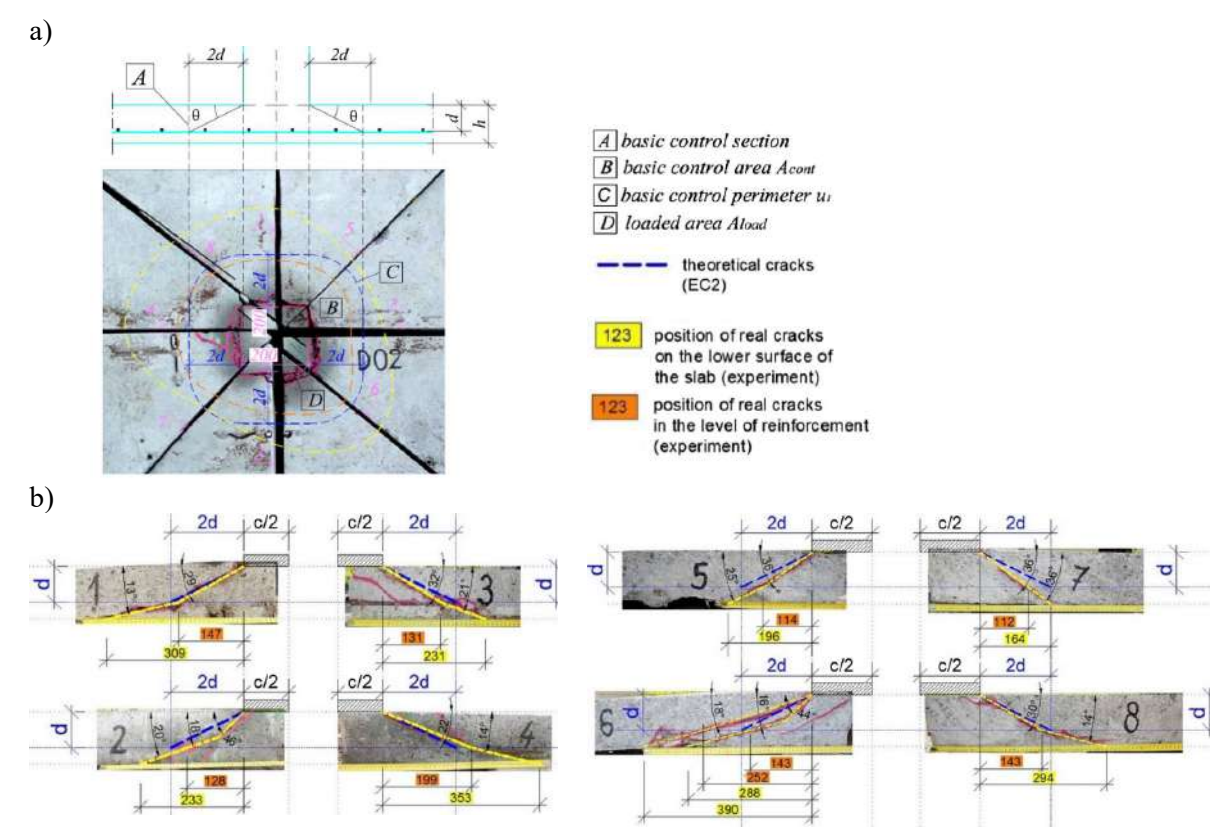


Fig. 3.73 Comparison of the theoretical model for punching shear according to PN-EN 1992-1-1:2006 with experimental results from ground slab test: a) bottom view, b) cross-sections of the slab [36]

3.4.2.8 Manfredi et al. research

Manfredi et al. [194] conducted an experimental investigation to evaluate the influence of SFs on the punching shear capacity of ground-supported concrete slabs subjected to a centrally applied single-point load. Additionally, the study aimed to compare the experimental results with predictions based on the TR34 guideline [28] and to develop a simplified mechanical model accounting for the all load-transfer mechanisms contributing to punching shear capacity.

The experimental program consisted of three concrete slabs reinforced with hookedend SFs ($l_f/d_f = 60/0.75$ mm) added at dosages of 20, 30, and 40 kg/m³. Each slab had dimensions of 120 x 2000 x 2000 mm and was supported on extruded polystyrene (XPS) insulation boards measuring 25 x 600 x 1200 mm. Compression testing of the XPS plates showed a subgrade reaction modulus of k = 0.0875 MPa/mm. The load was applied centrally through a rigid steel plate with dimensions 20 x 100 x 100 mm. To monitor deformations, ten LVDTs were installed to measure deflections in two orthogonal directions at distances of 10, 20, 35, 50, and 65 cm from the center of the slab along its symmetry axes. Additionally, the actuator transducer recorded central displacement. The test setup is illustrated in Fig. 3.74.

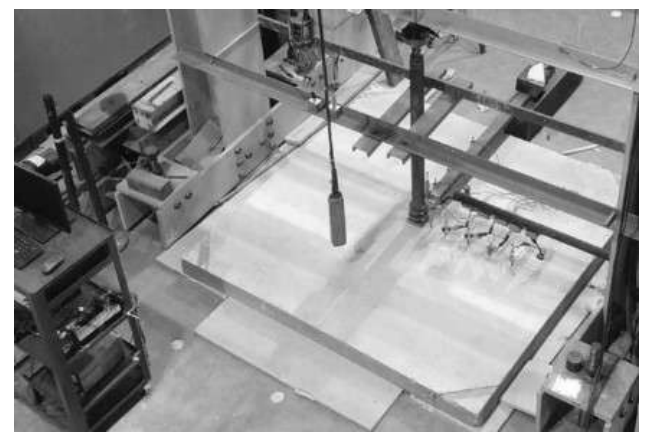


Fig. 3.74 Testing setup for centrally loaded SFRC ground slabs [194]

The results presented in Fig. 3.75 revealed that all SFRC ground slabs exhibited high ductility, attributed to the ability of the fibers to maintain structural integrity and enable load redistribution with increasing deflections. The slab containing 20 kg/m³ of fibers displayed a plateau in the load-deflection curve after reaching peak load, followed by a sudden drop. In contrast, slabs with 30 and 40 kg/m³ of fibers showed a more gradual increase to peak load, followed by a smoother decline. Moreover, both the first-crack load and the ultimate load capacity increased with fiber dosage. Namely, the maximum observed forces were 142 kN, 155 kN, and 175 kN for slabs with 20, 30, and 40 kg/m³ of SFs, respectively. At equivalent loading levels, slabs with higher fiber contents exhibited smaller deflections, indicating greater post-cracking stiffness. However, the elastic stiffness was found to be relatively unaffected by fiber dosage.

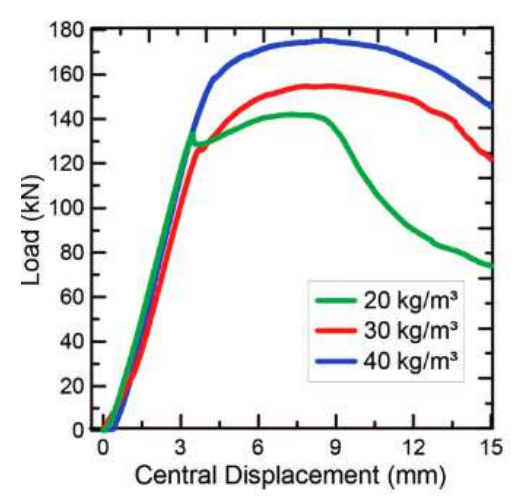


Fig. 3.75 Load-central displacement response of tested SFRC ground slabs [194]

All slabs developed radial cracks at the bottom surface (Fig. 3.76), while no circumferential cracks were observed on the top, confirming that failure occurred primarily through punching shear rather than bending. The central portion of each slab was punched downward, and circumferential cracks outlining the base of the punching

cone were visible at the slab bottom (Fig. 3.76). Slabs with higher fiber content exhibited narrower cracks, which were typically located at approximately 200 mm from the slab center, suggesting a critical control section location at a = 1.7d from the loading area.

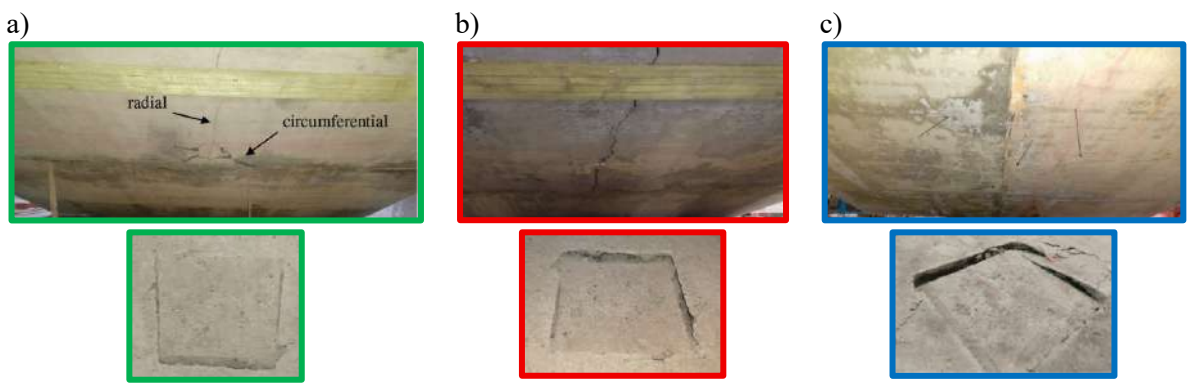


Fig. 3.76 Crack morphology on the bottom and top surface of tested SFRC ground slabs with: a) 20 kg/m^3 , b) 30 kg/m^3 , c) 40 kg/m^3 of SFs [194]

Measurements of central deflection obtained from the transducers were used to estimate the relative vertical displacement δ_{rel} and rotation ψ of the punching cone (Fig. 3.77a). Results indicated that increased fiber content reduced δ_{rel} while increasing ψ , suggesting that higher amounts of SFs more effectively hold the two portions of the slab together, leading to greater deformation of the punching cone.

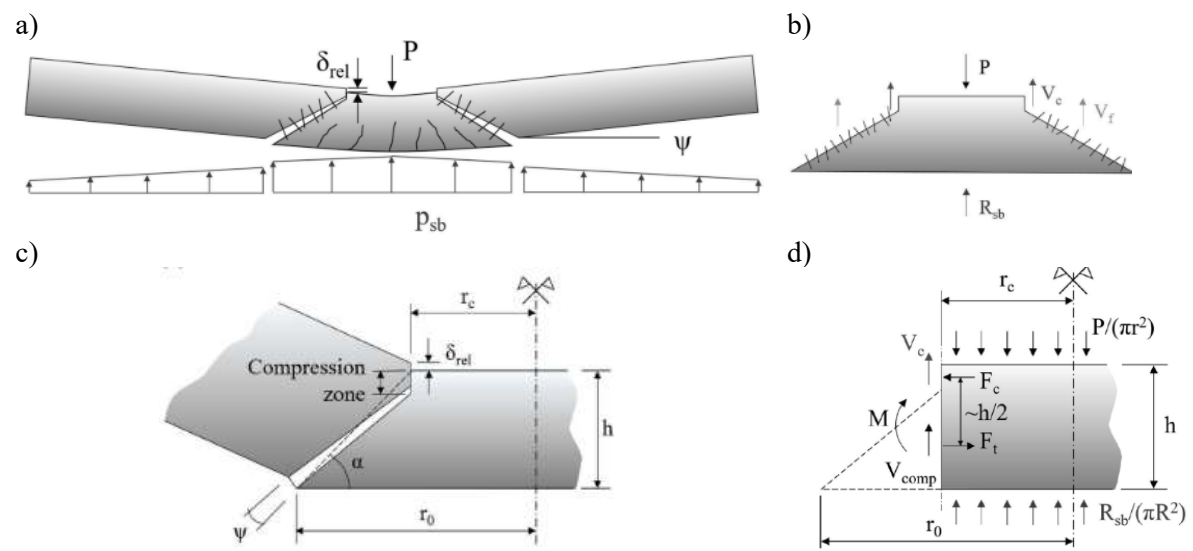


Fig. 3.77 Simplified punching shear mechanical model: a) slab subjected to a concentrated force, b) load-transfer mechanisms, c) crack kinematics, d) balance of forces of the central cylinder according to [194]

Analytical predictions of the punching shear capacity showed good agreement with experimental results. The calculated peak loads were 133 kN, 149 kN, and 159 kN for fiber dosages of 20, 30, and 40 kg/m³, respectively, underestimating the test results by

6.3%, 3.5%, and 9.2%. However, it was observed that the actual control perimeter during the tests differed in shape and was approximately 35% smaller than that prescribed in TR34 [28]. Analytical analysis also suggested that SFs contributed between 8.5% and 22% to the total punching shear capacity. The authors questioned the validity of these estimated contributions and proposed a mechanical model that accounted for the three main load transfer mechanisms: concrete, fibers, and subgrade reaction. As illustrated in Fig. 3.77b, the applied load P was assumed to be partially transferred directly to the subgrade (R_{sb}) , while the remainder was resisted through a critical shear crack by the compression zone (V_c) and the fibers (V_f) . The proposed model was based on several key assumptions. First, the contribution of concrete was attributed primarily to frictional resistance within a compression zone near the loading plate, as evidenced by the significant relative vertical displacement between the punching cone and the surrounding slab (Fig. 3.77c). The compression zone contribution V_c was determined from force equilibrium of the central cylindrical portion of the slab (Fig. 3.77d). Then, the subgrade reaction R_{sb} was estimated assuming a uniform pressure distribution beneath the punching cone, with the circular loading area rather than square. The subgrade contribution was also limited to 40% of the combined concrete and fiber capacity. Finally, the fiber contribution V_f was calculated as a remaining part from the total applied load P.

A summary of the contributions from each mechanism is provided in Table 3.19. Compared to the TR34 guideline [28], the proposed model predicted a subgrade contribution approximately four times greater. Likewise, the fibers were shown to resist a significantly higher load than assumed by TR34. Conversely, the resistance attributed to the concrete compression zone was notably lower than that preliminary predicted. According to the simplified model, the contributions to the total punching shear load-bearing capacity were approximately 30% from concrete, 30% from subgrade, and 40% from fibers. Recognizing the enhanced contribution of SFs to shear resistance, Manfredi et al. developed equations to estimate the additional shear strength attributed to the presence of fibers, derived from correlations with experimental data.

Table 3.19 Contribution of each load-transfer mechanism calculated according to the mechanical model proposed in [194]

| Resistance per | Ground slab with 20 | Ground slab with 30 | Ground slab with 40 |
|---------------------|---------------------|---------------------|---------------------|
| mechanism | kg/m³ of SFs | kg/m³ of SFs | kg/m³ of SFs |
| Ground R_b [kN] | 47.9 (33.7%) | 50.2 (32.5%) | 48.6 (27.8%) |
| Concrete V_c [kN] | 39.9 (28.1%) | 43.5 (28.1%) | 49.6 (28.3%) |
| Fiber $V_f[kN]$ | 54.2 (38.2%) | 50.9 (39.4%) | 76.8 (43.9%) |
| Total P [kN] | 142 (100%) | 155 (100%) | 175 (100%) |

3.4.2.9 Summary

A summary of the studies on large-scale ground-supported slabs subjected to a concentrated load, including those selected for the detailed analysis, is presented in Table B.1 in Appendix B. Furthermore, Table B.2 in Appendix B shows images of the testing setups and crack morphologies referenced in the other cited studies. Based on the comprehensive review of large-scale experimental studies on ground slabs, the following conclusions can be drawn:

- There are still lingering questions about whether results from beam flexural tests accurately and reliably reflect the behavior of large-scale structural ground slabs. Namely, several studies confirmed that experimental improvements from fiber addition were significantly more pronounced in ground slabs than would be expected based on beam test results. On the other hand, the toughness results from small-scale bending tests were found to predict large-scale FRC slab response more reliably than beam maximum flexural strength.
- SyFRC ground slabs showed enhanced performance regarding flexural cracking, punching, ultimate load capacity, deflection, load redistribution, ductility, and prolonged slab-ground contact compared to PC ground slabs, sometimes comparable with SFRC samples. This is an interesting point of view since many scientists doubt in the ability of SyFs to act effectively as a structural reinforcement, limiting their role to shrinkage control and crack bridging.
- Edge loading resulted in lower ultimate loads than central loading, whereas corners were consistently identified as the most vulnerable regions of the slab irrespectively on the ground slab reinforcement type.
- In the majority of cases, the centrally loaded ground-supported slabs failed due to punching shear or a combination of flexural and punching failure, regardless of the slab material: PC, SFRC, SyFRC or steel mesh reinforcement.
- The research findings reported in the literature review indicate that, for punching shear testing, large-scale centrally loaded ground-supported slabs with large dimensions can be effectively replaced by smaller slab segments whose side lengths correspond to the spacing between points of zero displacement.
- In tests of ground-supported slabs, LVDTs were typically used to measure

slab deflections and were mounted on steel frames positioned outside the slab area. They were commonly arranged along the slab's axes, diagonals, and edges (often in combination). In addition, strain gauges were used to record compressive and tensile strains, usually placed near the loading region, while acoustic sensors were positioned in areas where cracks were anticipated in order to monitor their initiation and propagation.

- Regardless of the casting method, whether the slab was cast in situ on natural ground or precast and subsequently placed on the testing setup, and irrespective of its dimensions, a similar crack morphology was observed. This typically included radial cracks on the bottom surface, circumferential cracks on the top surface, vertical cracks along the sides, and punching shear cracks. Radial cracks generally were initiated along the slab's symmetry axis, although deviations from this axis were generally noted. The distance between the central loading point and the circumferential cracks on the top surface appeared to depend on the type of reinforcement used in the slab. It should also be noted that smaller slabs were more susceptible to corner and edge uplift compared to larger slabs.
- The studies frequently highlight discrepancies between experimental results and theoretical predictions by TR34 guidelines regarding SyFs. TR34 suggests that SyFs' effectiveness is significantly lower than that of SFs. Moreover, TR34 does not allow for considering the additional shear resistance from SyFs in punching shear calculations. However, experimental results often challenge these assumptions, indicating greater punching capacities than analytically calculated. Furthermore, the improved slab capacity due to SyFs incorporation was evident under all loading scenarios, including central, edge, and corner positions. Nevertheless, the TR34 design provisions for moment capacity under corner loading do not permit this advantageous effect of fibers to be considered in the calculations.
- There is a limited number of studies on the effect of SyFs on the load-bearing capacity, deformations, crack propagation, and failure mode of ground-supported slabs centrally loaded by a concentrated force. To the best of the author's knowledge, there are no published studies dedicated to the punching shear behavior of such slabs that specifically investigate the influence of the addition, type, and dosage of SyFs on the punching cone characteristics.

3.5. Practice

FRC has been successfully used across a wide range of applications, including the precast concrete industry, roadways, pavements, bridge decks, infrastructure works, architectural and landscaping elements, shotcrete applications, as well as structural and decorative repairs [195]–[199]. Despite the continuous and substantial expansion of its application fields, industrial floors remain the primary use of FRC.

Industrial floors consist of several layers [200]. Typically, the topmost layer serves as the surface finish of the floor. Beneath it, the structural ground-supported concrete slab is placed over a slip layer, commonly made of polyethylene sheeting. This slip layer facilitates horizontal movements induced by concrete shrinkage, creep, and temperature variations, while also functioning as a waterproofing barrier that isolates the slab from the subgrade. The subgrade generally comprises an improved upper subbase layer with a minimum thickness of 10 cm, underlain by properly compacted in situ soil. Additionally, the inclusion of a lower subbase layer, typically around 30 cm thick, made of compacted, well-graded aggregate is considered beneficial. Each layer serves a distinct purpose, either in load transfer to the subgrade or in protecting it from external factors [201]. Regarding the thickness of ground-supported slabs, it is determined through calculations and depends on several factors, including the magnitude, type, area, and location of loads, concrete strength, as well as the characteristics and compaction of the subgrade (Table 3.20). Recommendations for the minimum slab thickness vary across different standards. For example, Technical Report 34 [28] suggests a minimum thickness of 150 mm, American guidelines specify a range of 127-152 mm depending on truck tire types, while Slovak design recommendations indicate values between 120 mm and 150 mm based on the concrete class [202]. In practice, ground-supported slabs typically have thicknesses ranging from approximately 150 mm to 300 mm [203]. The required concrete compressive strength for the load-bearing slab is selected according to the expected load and operational conditions. Generally, a minimum compressive strength corresponding to class C20/25 is specified. For heavily loaded floors, such as those subjected to frequent vehicular traffic, heavy goods transportation, and storage e.g. high-bay warehouses a minimum concrete strength class of C30/37 is recommended [202].

Table 3.20 Recommendations for concrete strength class and ground slab thickness depending on the acting loads [24]

| Maximum | Maximum design | | | Ground | slab thickr | ness [cm] |
|-----------------|---------------------------|----------|-------------|---------------|-----------------|----------------|
| design | concentrated load from | Concrete | w/c | Daily | traffic into | ensity |
| concentrated | racking legs in the | class | ratio | on | on slab surface | |
| wheel load [kN] | vehicle traffic zone [kN] | | | <i>n</i> ≤ 10 | <i>n</i> ≤ 50 | <i>n</i> ≤ 100 |
| 10 | 15 | C25/30 | \leq 0.55 | ≥ 16 | ≥ 16 | ≥ 18 |
| 20 | | | | ≥ 16 | ≥ 18 | ≥ 20 |
| 30 | 25 | C30/37 | \leq 0.50 | ≥ 16 | ≥ 18 | ≥ 20 |
| 40 | | | | ≥ 18 | ≥ 20 | ≥ 22 |
| 60 | 35 | | ≤ 0.45 | ≥ 20 | ≥ 22 | ≥ 24 |
| 80 | | | | ≥ 22 | ≥ 24 | ≥ 26 |
| 100 | 50 | C35/45 | | ≥ 24 | ≥ 26 | ≥ 28 |
| 120 | | | | ≥ 26 | ≥ 28 | ≥ 30 |
| 140 | | | ≤ 0.42 | ≥28 | ≥ 30 | ≥ 32 |

Ground-supported slabs must be designed to withstand both early-age shrinkage and, subsequently, significant operational loads resulting from vehicular traffic and storage of materials. Therefore, the floor must exhibit adequate load-bearing capacity to resist static point loads, uniformly distributed loads, as well as dynamic and cyclic loads, without undergoing excessive deflections, cracking, settlements, or joint deterioration. In certain applications, ground slabs are subject to additional performance requirements, which arise from the specific functions of the facility or the nature of the stored goods. These may include enhanced resistance to impact, abrasion, dust, and slip, as well as resistance to water, oils, acids, alkalis, and other chemically aggressive substances. In such cases, low water absorbability and chemical resistance may become a critical requirement. Furthermore, the slab must remain durable under temperatures changes, exhibiting freeze-thaw, fire, and spalling resistance. Additional requirements may concern adequate surface flatness and levelness, which are essential for the safe and efficient operations within the warehouse. The joint layout, including construction, contraction, and isolation joints, must also be carefully coordinated with the arrangement of racks and storage units. Otherwise, any unexpected surface irregularities may result in operational inefficiencies or lead to safety risks. Accordingly, the primary objectives in ground slab design are to ensure sufficient flexural and punching shear load-carrying capacity, effective crack control with minimized cracking risk, and overall durability and long-term performance. To meet these requirements, concrete slabs are typically reinforced with steel bars or welded wire mesh. These reinforcements are usually placed at mid-depth, near the bottom surface, or in two layers: near both the top and bottom surfaces, or at mid-depth and near the bottom surface [202] (Fig. 3.78). However, in recent years FRC has gained popularity, either as an addition or replacement for traditional reinforcement, due to its enhancing effects on concrete properties (see Chapter 3.4.1). The typical dosage of SFs ranges from $V_f = 0.25\%$ to 2.0%, with commonly used dosage between 20 and 40 kg/m³ [202]. Micro SyFs are primarily added to enhance resistance to early-age plastic shrinkage cracking, with typical V_f ranging from 0.6 to 1.0 kg/m³ [202]. Finally, macro SyFs, particularly suitable for ground slabs, where exposed SFs may corrode or pose an injury risk due to their sharp ends, are used in amounts ranging from 2 to 3 kg/m³ [202]. Furthermore, there is a growing trend toward the complete elimination of conventional reinforcement in ground-supported slabs motivated by the labor-intensive and time-consuming reinforcing work of steel bars or meshes. Moreover, traditional reinforcement mitigates surface cracking less effectively, as it is positioned at some distance from the slab surface. In contrast, fibers, when uniformly distributed throughout the slab, provide significantly improved crack control.

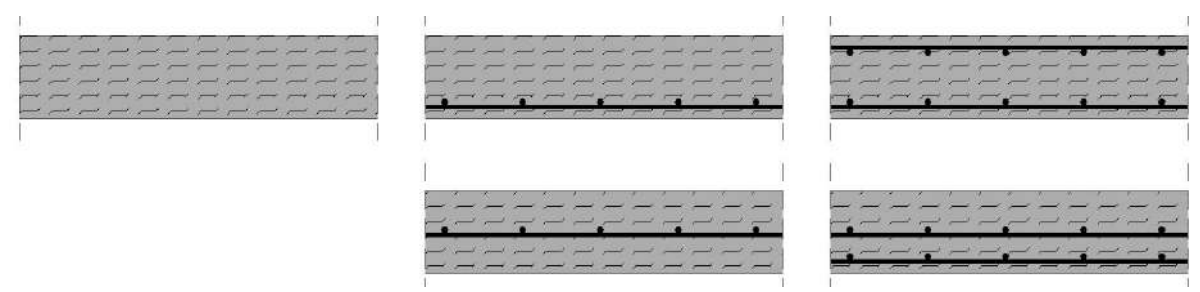


Fig. 3.78 Reinforcement of FRC ground-supported slabs [202]

Degradation of concrete ground slabs accounts for a significant portion of observed failures in industrial floors. Moreover, the deterioration of the surface layer is a direct consequence of underlying ground slab damage. However, surface defects can also initiate or accelerate the progressive degradation of the ground slab [203]. Despite the progress in design and construction practices as well as availability of dedicated guidelines for industrial floors, mistakes are still a frequent issue. It is estimated that over 50% of industrial floor failures are attributed to inadequate quality or improper preparation of the concrete ground slab [204]. An additional 25% result from inappropriate operational conditions, including premature use of the floor or applied loads that substantially exceed those considered in the design [204]. Typical forms of damages and defects in ground-supported slabs include full-depth cracking, map cracking (e.g. shrinkage-related), internal flaws (such as air voids, delamination, or foreign material inclusions), cracking from improper layout of saw-cut joints, joint damages, slab edge and corner curling, surface unevenness, and other various surface damages (e.g. dusting, abrasion, spalling, delamination, deformations, and pop-out

defects) (Fig. 3.79). The underlying causes of such damage can be broadly classified into structural, material, technological, and operational-related categories (Table 3.21). However, it is often challenging to identify a single, definitive cause, as damage typically results from a combination of multiple contributing factors. Among these, material- and technology-related errors are particularly common in leading to performance failures. The repairing methods of ground slabs of industrial floors depend on the type and extent of the damage. In most cases, the deterioration affects large surface areas, and their removal is frequently associated with high costs and may require taking the facility out of service for a certain period of time. The most commonly used methods for repairing cracks and other defects of ground slabs includes: crack injection and stitching, partial or complete replacement of the damaged part, repair of corners and edges, overlaying with a new concrete slab (topping), or even full ground slab replacement [203].



Fig. 3.79 Damages of industrial floors: a) full-depth cracking, b) edge cracking, c) corner cracking, d) map cracking, e) air voids in concrete drilled core samples, f) cracking due to improper layout of saw-cut joints, g) joint damage, h) slab curling, i) surface damages – delamination [203]

Table 3.21 Primary causes of industrial floor damages according to Hajduk's classification [204]

| Construction-related causes | Technological-related causes |
|--|---|
| - Insufficient investigation of the ground subsoil | - Uneven, improperly compacted subbase. |
| conditions. | - Not followed technological regimes during the |
| - Too weak parameters of the subsoil and | execution of industrial floor. |
| subbase under the ground slab. | - Faulty concrete transportation. |
| - Improperly selected floor layer system. | - Errors in reinforcement placement. |
| - Too low concrete strength. | - Use of mixture with defective composition or |
| - Insufficient ground slab thickness and | physical properties, not fulfilling the specified |
| reinforcement. | requirements. |
| - Errors in the design of joints. | - Improper method of concreting. |
| | - Insufficient concrete curing, not controlled |
| | shrinkage. |
| | - Errors in execution of joints. |
| | - Errors in execution of surface floor layers. |
| Material-related causes | Operational-related causes |
| - Inappropriately selected quality and quantity of | - Premature exploitation of the industrial floor. |
| concrete mixture compositions. | - Application of loads greater than those |
| - Presence of impurities in the concrete mixture. | assumed in the design. |
| - Use of aggregate susceptible to | - Change of operational conditions, inconsistent |
| alkali-aggregate reaction with cement. | with the original design. |
| - Use of inappropriate materials for filling joints. | - Improper method of floor cleaning. |

3.6. Research gap and significance

Based on comprehensive literature review, the research gaps have been identified.

- The majority of existing studies, design standards, and analytical models focus primarily on SFRC, resulting in a limited understanding of the behavior of SyFRC and a lack of dedicated provisions for its testing and design. Consequently, standards originally developed for SFRC are often applied to SyFRC, however with more conservative assumptions due to the insufficient amount of available research. This frequently leads to significant underestimations of the capacity of structural elements incorporating SyFs.
- Most studies are conducted on small-scale specimens, which do not always accurately capture the structural behavior of large-scale elements. As such, research involving full-scale or semi-full-scale specimens is of particular importance, since it provides a more realistic assessment of mechanical performance under actual loading conditions.
- Despite the widespread use of fiber reinforcement in ground-supported slabs, the increase in capacity associated with its presence is not consistently reflected in existing design recommendations. Specifically, in the context of

punching shear design, the current guidelines provide inconsistent instructions regarding the critical control section location and the method for incorporating the contribution of fibers to punching shear capacity. Moreover, there is a lack of research addressing the influence of SyFs' type and dosage on the punching shear behavior of ground slabs, particularly in relation to the maximum capacity and the characteristics of the punching cone shape.

These identified knowledge gaps highlight the need for further experimental research and the development of design recommendations for SyFRC ground-supported slabs, especially in the context of punching shear capacity evaluation. Addressing these understudied topics is essential to enhancing structural safety, optimizing material usage, and facilitating the broader acceptance of SyFRC in structural engineering practice. In response to the identified research needs, the author of this dissertation has developed a comprehensive experimental program of SyFRC ground-supported slabs subjected to centrally applied concentrated loading. The aim of this program is to fulfill the defined research objectives and to validate the theses presented in Chapter 2.2. Furthermore, the literature review provided the foundation for the design of experimental methodology, particularly with regard to the testing procedures for large-scale ground slab specimens.

4. RESEARCH PROGRAM

4.1. Introduction

The experimental campaign, designed to fulfill the defined research objectives and validate the proposed theses, focused on investigating the structural performance of SyFRC ground-supported slabs incorporating various types and dosages of SyFs. Specifically, the study examined the behavior of PC ground slabs, serving as a reference specimen, and five types of SyFRC slabs subjected to centrally applied concentrated loads. In addition to large-scale testing, a series of small-scale tests were conducted to characterize the material properties of both PC and SyFRC. These tests included assessments of workability, modulus of elasticity, compressive strength, splitting tensile strength, flexural tensile strength, and fracture energy. The primary aim was to evaluate the influence of SyFs inclusion, dosage, and type on selected physical and mechanical properties of concrete from standardized samples, as well as on the load-deflection response, crack morphology, and punching cone shape in large-scale slabs. Furthermore, the mechanical behavior of both unsupported and ground-supported slabs was investigated and analyzed to provide a comprehensive understanding of their structural performance under realistic loading conditions.

4.2. Materials and mix design

The research program comprised five SyFRC mixtures differing in fiber type and dosage, along with one reference mixture without fibers. Two fiber dosages were tested: 2 and 3 kg/m³, and three types of SyFs were used, denoted as PM, PD, and FF. The selection of fiber types and contents was based on manufacturer recommendations for industrial slab applications. The properties of the SyFs incorporated into the concrete mixtures are presented in Table 4.1. All fibers exhibited high chemical resistance, had a

relative density of 0.91 g/cm³, and a melting point in the range of 160-170°C. The fibers differed in geometry and form, for instance, PM and FF fibers were longer and slenderer than PD fibers. Finally, SyFs were introduced into the mix as bundles intended to disperse during mixing.

The concrete was designed to meet strength class C40/50 and consistency class F5 in accordance with PN-EN 206+A2:2021-08 [38]. This high performance specification was chosen to compensate for the anticipated reduction in workability resulting from fiber addition. Ordinary Portland Cement Type I of strength class 42.5 with high early strength (CEM I 42.5R) was used, along with a w/c ratio of 0.50. Tap water was used throughout the study. Fine aggregate consisted of sand with a particle size of 0/2 mm, while coarse aggregate was gravel with a maximum grain size of 8 mm. To ensure adequate workability, two types of chemical admixtures were incorporated into the mixes. The composition of all concrete mixtures is summarized in Table 4.2. Notably, the mixture design remained constant, with the only variable being the fiber volume content V_f .

Moreover, Fig. 4.1 presents the Declaration of Performance for the aggregates used as a subbase layer supporting the ground slabs during the large-scale tests. The ground support was constructed using limestone aggregates with a continuous grain size ranging from 0 to 31.5 mm and a light gray to yellowish color (Fig. 4.2). The aggregates were sourced from the Limestone Mine in Strzelce Opolskie and complied with the requirements of PN-EN 13242 [205] and PN-EN 13043 [206].

Table 4.1 Characterization of SyFs properties

| Property | PM | PD | FF | |
|-----------------------|-------------------------------------|------------------------|--|--|
| l_f | 54 mm | 48 mm | 54 mm/54 mm | |
| d_f | 0.45 mm | 0.60 mm | 0.45 mm/NS | |
| $l_{\it f}/d_{\it f}$ | 120 | 80 | 120/NS | |
| f_{ft} | 550-650 MPa | 500-580 MPa | 620-758 MPa | |
| E_f | 4.8-5.9 GPa | > 10 GPa | NS | |
| Form | extruded, twisted, multifilament | extruded, monofilament | hybrid: 95% twisted, multifilament/5% fibrillated | |
| Material | copolymer | polymer | copolymer/polypropylene | |
| Type | macrofibers | macrofibers | macrofibers/NS | |
| Picture | | | | |

Table 4.2 Concrete mixture composition [kg/m³]

| Composition | 1 (PC) | 2 (PM_2) | 3 (PM_3) | 4 (PD_2) | 5 (PD_3) | 6 (FF_2) |
|---------------------------------|--------|-----------|-----------|-----------|-----------|-----------|
| CEM I 42.5R | 400 | 400 | 400 | 400 | 400 | 400 |
| Sand 0/2 mm | 670 | 670 | 670 | 670 | 670 | 670 |
| Gravel 2/8 mm | 1012 | 1012 | 1012 | 1012 | 1012 | 1012 |
| Water | 200 | 200 | 200 | 200 | 200 | 200 |
| Masterglenium Sky 591 (BASF) | 2.12 | 2.12 | 2.12 | 2.12 | 2.12 | 2.12 |
| Masterpozzolith 501 HE (BASF) | 3.20 | 3.20 | 3.20 | 3.20 | 3.20 | 3.20 |
| Fiber type | - | PM | PM | PD | PD | FF |
| Fiber dosage | 0 (0%) | 2 (0.22%) | 3 (0.33%) | 2 (0.22%) | 3 (0.33%) | 2 (0.22%) |

DEKLARACJA WŁAŚCIWOŚCI UŻYTKOWYCH NR: GK/01/ Strzelce Opolskie / 2019 / 0/31,5 mm



- Niepowtarzalny kod identyfikacyjny typu wyrobu: PL6H Kruszywo 0/31,5 mm
- Zamierzone zastosowanie lub zastosowania;
 - W drogownictwie i innych robotach inżynieryjnych
- - Producent:
 Góraždže Cement SA ul. Cementowa 1, Chorula; 47-316 Góraždže, zakład produkcyjny: Kopalnia Wapienia Strzelce Opolskie, ul. Leśna 4

- Upoważniony przedstawiciel: Górażdże Kruszywa sp. z o.o. System (y) oceny i weryfikacji stałości właściwości użytkowych: system 4
- Norma zharmonizowana:
 "Kruszywa do niezwiązanych i hydraulicznie związanych materiałów stosowanych w obiektach budowlanych i budownictwie drogowym" PN-EN 13242:2004-A1:2010;
 "Kruszywa do niezwiązanych i powierzchniowych utrwaleń stosowanych na drogach, lotniskach i innych powierzchniach przeznaczonych do ruchu" PN-EN 13043:2004

 Jednostka notyfikowana: brak

 Deklarowane właściwości użytkowe:

| 9 | | Kategoria lub wartość deklarov | Zharmonizowana | | |
|--|----------------------------------|---|--|---|--|
| Podstawowe właściwości | Uwagi | EN 13043 | EN 13242 | dokumentacja techniczna | |
| Właściwości geometryczne | | | | | |
| Wymiar kruszywa, d/D | oznaczenie d/D | 0/3 | 1,5 | | |
| Uziarnienie | kategoria | G _A 85 G _A 90 | | PN-EN 13242:2004+A1:2010 | |
| Tolerancja uziarnienia | kategoria | | GT ₄ 25 | wg EN 13242:2002+A1:2007 | |
| Zawartość pyłów | kategoria - wart. deklarowana | · · · · · · · · · · · · · · · · · · · | f ₁₂ | "Kruszywa do niezwiązanyc i hydraulicznie związanych materiałów stosowanych | |
| Jakość pytów, MB _F | kategoria | MB _e 10 | NPD | w obiektoch budowlanych | |
| Wskaźnik piaskowy, SE | kategoria | >40 | >40 | i budownictwie drogowym* | |
| Kształt kruszywa grubego, SI | kategoria | SI ₂₅ | SI ₄₀ | | |
| Kształt kruszywa grubego, FI | kategoria | Flan | Flan | PN-EN 13043-2004 | |
| Zawartość ziarn o powierzchni przekruszonej i łam. | kategoria | C _{100/0} | Caora | wg EN 13043:2002/AC:2004 | |
| Właściwości fizyczne | | | | "Kruszywa do mieszanek | |
| Odporność na rozdrabnianie, LA | kategoria | LA ₁₅ | LA _{vs} | bitumicznych i powierzchniowych utrwaleń | |
| Odporność na ścieranie, (fr.10/14mm), Mpt | kategoria | Mpe 35 | Mor 35 | stosowanych na drogach, | |
| Gęstość ziarn, ρ _a , ρ _{rd} ,ρ _{sad} [Mg/m³] | wart. deklarowane | ρ _n =2,72±0,02 ρ _{rd} =2,65±0,02 ρ _{ssd} =2,68±0,02 | ρ _a =2,72±0,02 ρ _{ed} =2,65±0,02 ρ _{ad} =2,68±0,02 | lotniskach i innych powierzchniach przeznaczony | |
| Nasiąkliwość ziarn, WA ₂₄ | kategoria | 1.01%; WA ₂₄ 2 | 1.01% WA _M 2 | do ruchu" | |
| Odporność na polerowanie, PSV | kategoria | NPD | s. Edwardinates | 1 | |
| Odporność na ścieranie powierzchniowe, AAV | kategoria | NPD | | | |
| Odporność na ścieranie abrazyjne przez opony z kolcami kr. grubych | kategoria | NPD | | | |
| Przyczepność do spoiw bitumicznych | kategoria | NPD | | | |
| Odporność na szok termiczny | kategoria | NPD | | 1 | |
| Właściwości chemiczne | | * | | 1 | |
| Stałość objętości - skurcz przy wysychaniu | spełnia | NPD | Ĉ. | | |
| Chlorki | wart, deklarowana | NPD | | 1 | |
| Węglany wapnia (drobne do warstw ścieralnych naw. Betonowej) | kategoria | NPD | NPD | | |
| Siarczany rozpuszczalne w kwasie | kategoria | AS _{0,2} | AS _{0,2} | [| |
| Siarka całkowita | kategoria | Si | Sı | 1 | |
| Składniki, które wpływają na szybkość wiązania i twardnienia cementu /-zawartość humusu | spełnia | | barwa jaśniejsza od wzorca | | |
| Zawartość lekkich ziaren w kruszywie | kategoria | m _{LPC} 0,1 | ĝ | | |
| Substancje niebezpieczne, w szczególności: - promieniowanie radioaktywne* (finas , finas) | wart, deklarowane | f _{Imax} ≤ 1.0 i f _{Imax} ≤ 180 Bq/kg | | | |
| - uwalniane metale ciężkie** | wart. deklarowane | Cd<0,2 , Cr<0,5, Cu<0,5, Ni<0,5, Pb<0,5, Zn<2, Ba< 2 mg/[], As<0,1 [mg/l] | | 1 | |
| -uwalniane węglowodory aromatyczne | wart, deklarowana | NP | D |] | |
| Trwałość | | | To the second se | 1 | |
| Mrozoodporność kruszywa grubego | kategoria | F ₄ | F ₄ | 1 | |
| Mrozoodporność w obecności soli (F _{EC} i MS _{NR}) | kategoria | NPD | NPD |] | |
| "Zgorzei słoneczna" bazaltu | kategoria | NPD | | 1 | |

Fig. 4.1 Declaration of performance of aggregates supporting the ground slabs in large-scale tests



Fig. 4.2 Aggregates used to support the ground slabs in large-scale tests

4.3. Sample preparation

All six concrete mixtures were produced and delivered by the batching plant Górażdże Beton Sp. z o.o. to the laboratory of the Faculty of Civil Engineering at the Silesian University of Technology in Gliwice. It should be noted that the SyFs were transported to the plant separately prior to each mixing and dosed together with the aggregates on the aggregate feeder. This methodology, recommended by the fiber manufacturer, facilitates rapid and uniform fiber distribution in the concrete mix, while minimizing the risk of clustering and fiber balling.

The mixing and sample preparation process was conducted between December 2021 and June 2022. Exact dates are listed in Table 4.3. On average, one concrete type was produced per month to allow sufficient time for hardening and curing, and due to limitations in available formworks. For each of the six mixtures, the following specimens were prepared: three slabs measuring 200 x 1200 x 1200 mm for large-scale tests, three beams 150 x 150 x 550 mm for 3PBT, and six cubes 150 x 150 x 150 mm for compressive strength testing. A complete summary of the number and types of specimens is provided in Table 4.4. Immediately after casting, all samples were compacted using a needle vibrator to reduce entrapped air amount. For the slabs, four steel transport hooks were embedded at a distance of 30 cm from each slab's edge to facilitate lifting and transportation. All specimens were subsequently covered with plastic sheeting and regularly moistened to prevent surface drying and shrinkage cracking. After 7 days, the elements were demolded and stored in laboratory conditions until the testing day. In the case of beams designated for flexural testing, additional

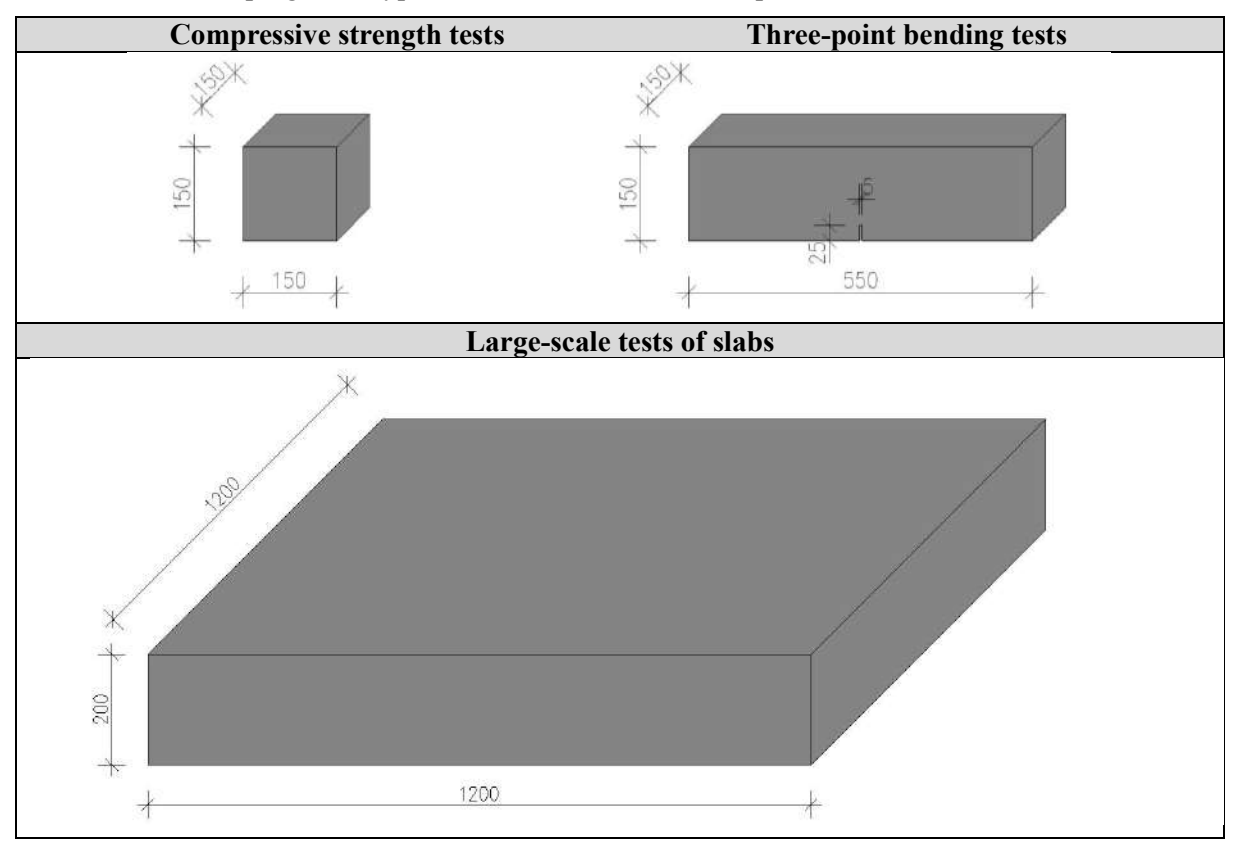
preparation was required. Specifically, a notch 5 mm wide and 25 mm deep was cut at mid-span along the full width of each beam using a diamond saw, in accordance with PN-EN 14651 [29]. The sample preparation process is illustrated in in Fig. 4.3, while Fig. 4.4 presents the slabs directly after concreting.

Following the slab tests, two cores of dimensions ϕ 94 x 188 mm (length to diameter ratio equals to 2) were drilled from each slab. The cores were typically drilled from uncracked slab edges to avoid damaged zones (Fig. 4.5). In total, 36 cores were collected: the first core from each slab was used to determine concrete compressive strength, while the second was used to evaluate the modulus of elasticity (Table 4.5). Subsequently, the second cores were sawn in half to produce two shorter cylinders with dimensions ϕ 94 x 94 mm, which were tested for splitting tensile strength (Table 4.5).

Table 4.3 Research program – concreting schedule and number of cast samples

| Type | Concreting date | Cubes | Beams | Slabs |
|----------|-----------------|-------|-------|-------|
| 1 (PC) | 14.12.2021 | 6 | 3 | 3 |
| 2 (PM_2) | 07.02.2022 | 6 | 3 | 3 |
| 3 (PM_3) | 10.03.2022 | 6 | 3 | 3 |
| 4 (PD_2) | 12.04.2022 | 6 | 3 | 3 |
| 5 (PD_3) | 17.05.2022 | 6 | 3 | 3 |
| 6 (FF_2) | 07.06.2022 | 6 | 3 | 3 |
| | Totally | 36 | 18 | 18 |

Table 4.4 Research program – type and dimensions of cast samples



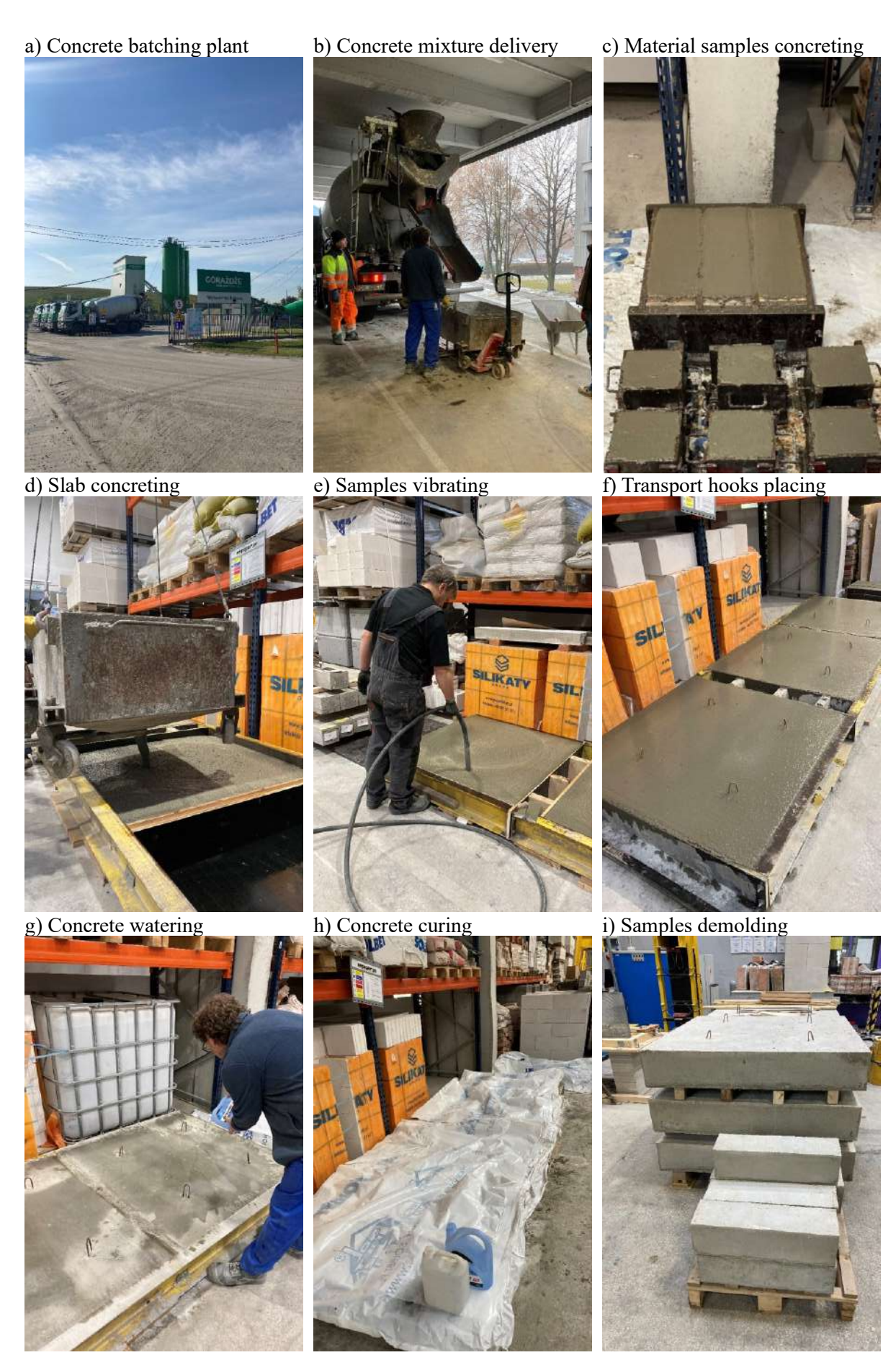


Fig. 4.3 Detailed procedure for the preparation of samples

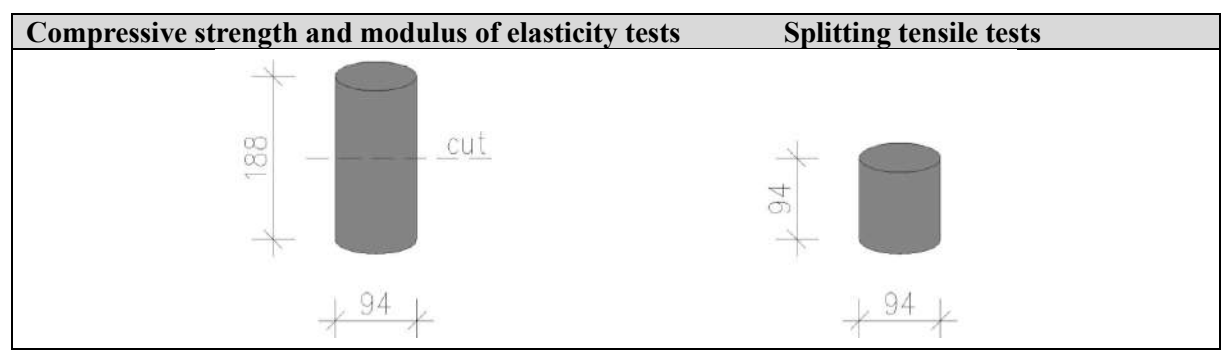


Fig. 4.4 Large-scale slab samples after concreting



Fig. 4.5 Tested slabs of type 2 with holes remaining from core drilling

Table 4.5 Research program – type and dimensions of drilled samples



4.4. Methodology

4.4.1. Material characteristics

The material characterization of the PC and SyFRCs involved the determination of basic physical properties, such as consistency, as well as key mechanical parameters, including modulus of elasticity, compressive strength, splitting tensile strength, and flexural tensile strength. Given the ductile nature of the investigated concretes, it was also necessary to evaluate their post-cracking behavior. For this purpose, 3PBTs were conducted, and the residual flexural tensile strengths were determined accordingly. It should be noted that uniaxial tensile strength tests were not performed due to their high complexity and limited availability of specialized equipment. Nevertheless, splitting tensile strength tests were conducted to provide a general assessment of the tensile performance of concrete with and without fiber reinforcement.

4.4.1.1 Fresh concrete properties

During the sample preparation, the properties of fresh concrete were monitored. The flow table test was conducted in accordance with PN-EN 12350-5 [207] to determine the flowability of the fresh concrete mixture and, consequently, to classify its consistency (Fig. 4.6a). The test involved measuring the spread of the concrete on a flat table. Firstly, the truncated cone mold was filled in two layers, each manually compacted using a wooden rod (Fig. 4.6b). After filling, the mold was carefully lifted, and the table was subjected to 15 cycles of lifting and free falling. Finally, two perpendicular diameters of the resulting slump spread were measured.

b)





Fig. 4.6 Flow table test: a) testing apparatus [208], b) filling the cone during the test

4.4.1.2 Compressive strength tests

The cast cubes (150 x 150 x 150 mm) and the drilled cores (ϕ 94 x 188 mm) were tested in compression in accordance with PN-EN 12390-3 [39], using a Form+Test Prüfsysteme machine of class 1 with a maximum capacity of 3000 kN (Fig. 4.7). Prior to testing, all specimens were measured and weighed. Subsequently, each sample was positioned between two steel bearing plates and subjected to a compressive load applied at a constant stress rate of 0.6 MPa/s until failure. The compressive strength of the concrete was then calculated for both cubes and cores (denoted as $f_{c,cube}$ and $f_{c,core}$, respectively, using the formula presented in standard [39] based on the recorded maximum load and specimen dimensions. In total, 36 cast cubes and 18 drilled cores were tested.

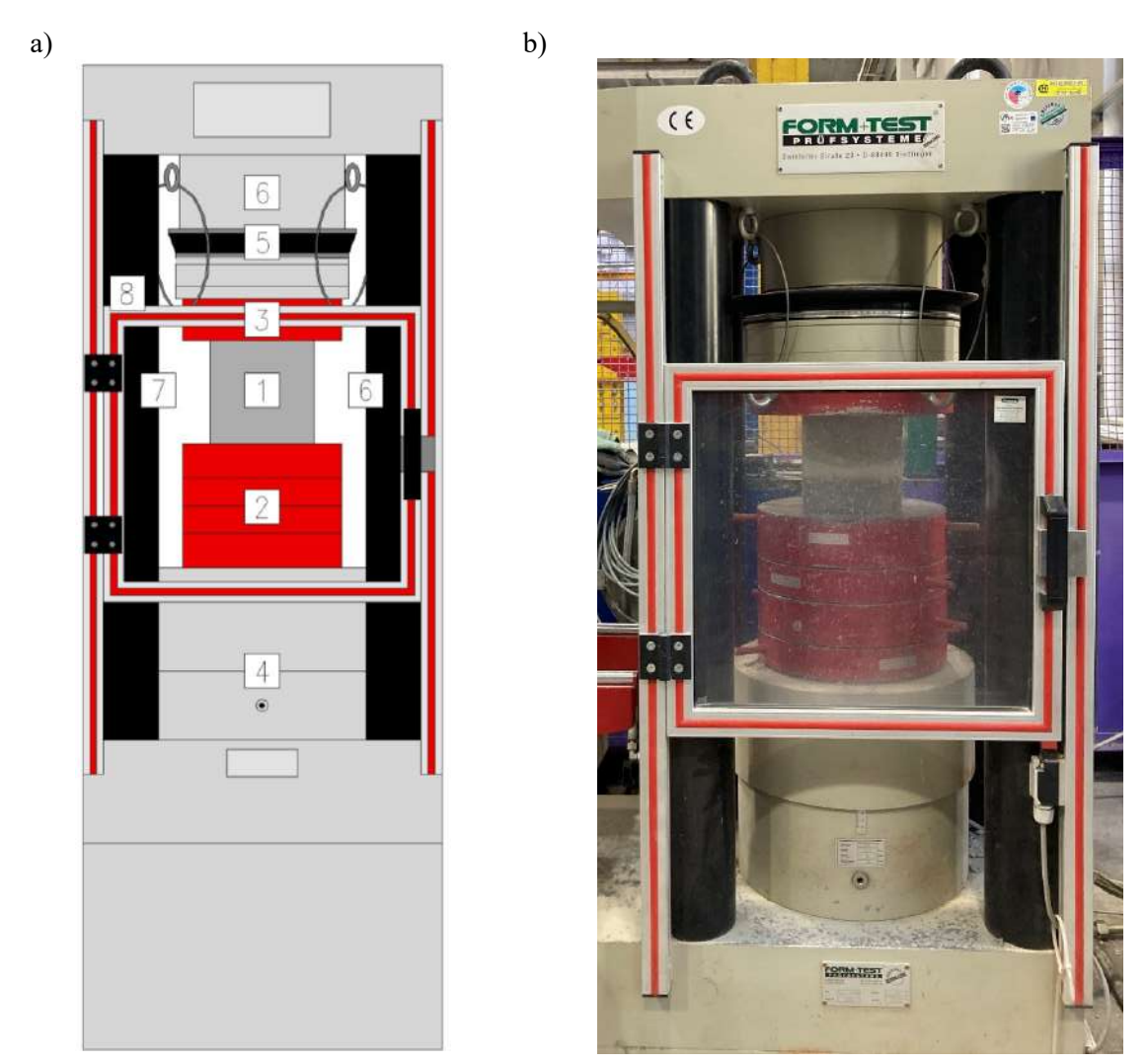


Fig. 4.7 Setup for compressive strength test: a) scheme: 1 – sample; 2 – bottom plate; 3 – upper plate; 4 – piston; 5 – hinge; 6 – load cell; 7 – column; 8 – safety window, b) view of the setup

4.4.1.3 Modulus of elasticity tests

The initial $E_{c0,core}$ and stabilized $E_{cs,core}$ modulus of elasticity of the drilled cores (ϕ 94 x 188 mm) were determined according to PN-EN 12390-13 Method A [90], which is also applicable to samples extracted from existing structures. Prior to testing, the samples were measured and weighed, and a frame with a reference base of 90 mm was attached to the mid-height section of each cylinder. This frame was equipped with two displacement gauges with measurement range ± 2.5 mm and accuracy of indications equals to ± 0.0125 mm (accuracy class 0.5%). They were positioned on opposite sides of the specimen at approximately one-quarter of the cylinder height measured from the bottom. The samples were then placed between the bearing plates of a Walter & Bai AG testing machine of class 1 with a 300 kN capacity (Fig. 4.8).

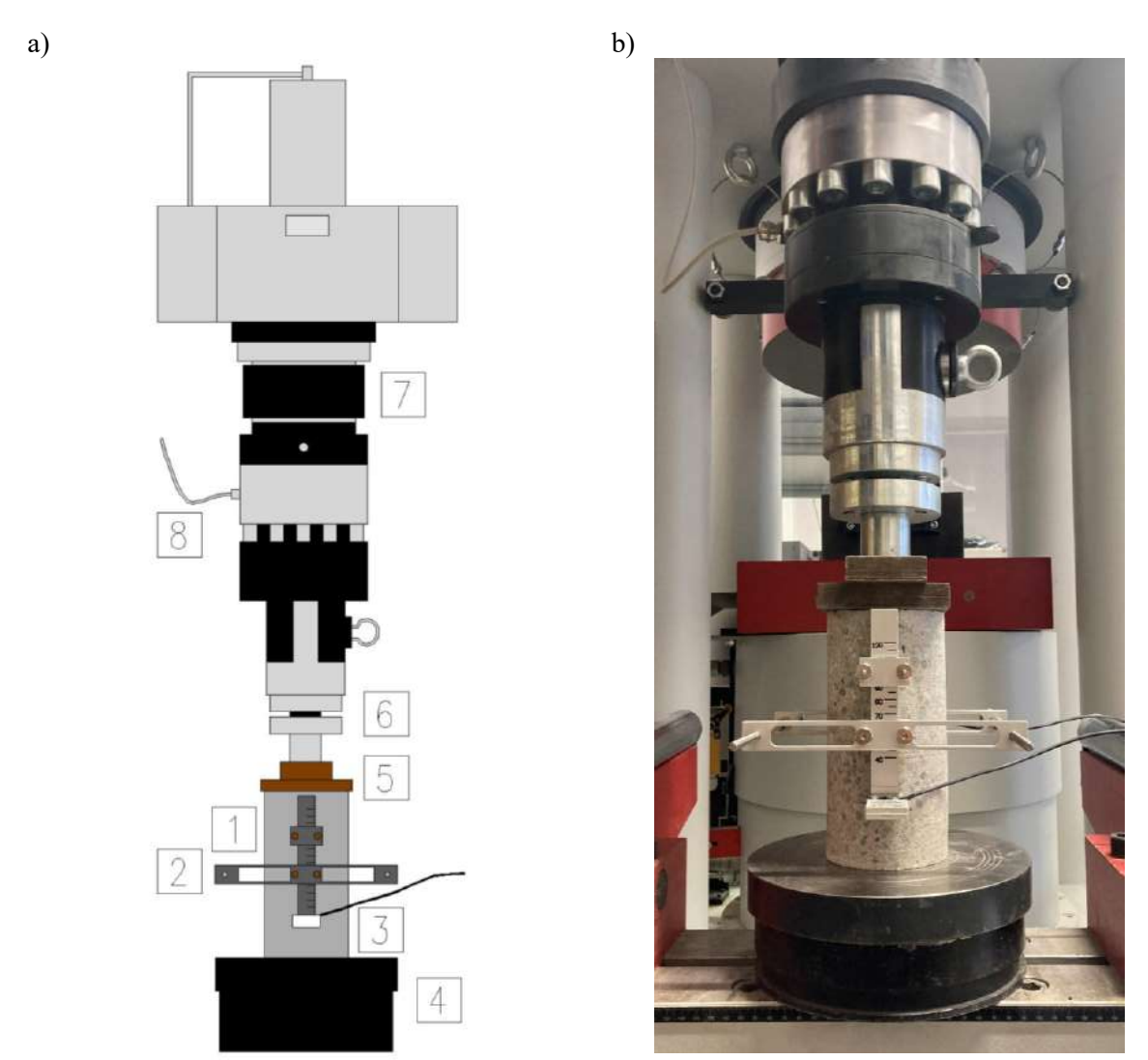


Fig. 4.8 Setup for elasticity modulus test: a) scheme: 1 - sample; 2 - frame with a reference base; 3 - displacement gauge; 4 - bottom plate; 5 - upper plate; 6 - hinge; 7 - load cell; 8 - actuator, b) view of the setup

The loading and unloading procedure for the determination of $E_{c0,core}$ and $E_{cs,core}$ followed the requirements specified in [90], illustrated in Fig. 4.9. Force and deformation data were recorded continuously until the test was terminated. Finally, the loading was stopped before sample failure, at approximately 33% of the compressive strength, to prevent damage to the steel frame. The values of $E_{c0,core}$ and $E_{cs,core}$ were calculated using formulas (2) and (3) from standard [90], based on the recorded data and specimen dimensions. In total, 18 drilled cores were tested.

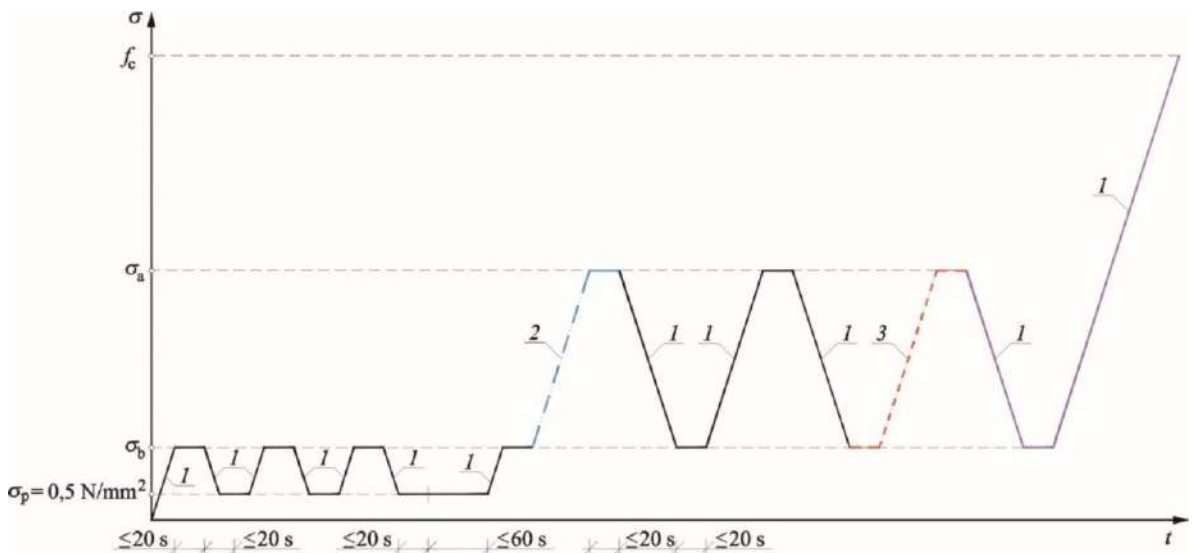


Fig. 4.9 Cycle for the determination of the initial and stabilized secant modulus of elasticity according to PN-EN 12390-13 Method A [90]: 1 – loading and unloading cycles, 2 – loading cycle for the determination of the initial secant modulus of elasticity, 3 – loading cycle for the determination of the stabilized secant modulus of elasticity, where σ – applies stress, σ_a – upper stress ($f_c/3$), σ_b – lower stress ($f_c/3$), σ_b – preload stress ($f_c/3$), $f_c/3$ 0. The cycle for the determination of the stabilized secant modulus of elasticity, where σ – applies stress, σ_a – upper stress ($f_c/3$), σ_b – lower stress ($f_c/3$), $f_c/3$ 0. The cycle for the determination of the stabilized secant modulus of elasticity, where σ – applies stress, σ_a – upper stress ($f_c/3$), σ_b – lower stress ($f_c/3$), $f_c/3$ 0. The cycle for the determination of the stabilized secant modulus of elasticity, where σ – applies stress, σ_a – upper stress ($f_c/3$), σ_b – lower stress ($f_c/3$), $f_c/3$ 0. The cycle for the determination of the stabilized secant modulus of elasticity, where σ – applies stress, σ_a – upper stress ($f_c/3$), σ_b – lower stress ($f_c/3$), $f_c/3$ 0. The cycle for the determination of the stabilized secant modulus of elasticity, where σ – applies stress, $f_c/3$ 0. The cycle for the determination of the stabilized secant modulus of elasticity, where σ – applies stress, $f_c/3$ 0. The cycle for the determination of the stabilized secant modulus of elasticity, $f_c/3$ 0. The cycle for the determination of the stabilized secant modulus of elasticity $f_c/3$ 0. The cycle for the determination of the stabilized secant modulus of elasticity $f_c/3$ 0. The cycle for the determination of the stabilized secant modulus of elasticity $f_c/3$ 0. The cycle for the determination of the stabilized secant modulus of elasticity $f_c/3$ 0. The cycle for the determination of the stabilized secant modulus of elasticity $f_c/3$ 0.

4.4.1.4 Splitting strength tests

The splitting tensile tests were performed on drilled cores (ϕ 94 x 94 mm) according to PN-EN 12390-6 standard [49], which is also discussed in Chapter 3.3.2.2 of this dissertation. It should be noted that the standard permits testing cores with a length to diameter ratio as low as 1, and a diameter of at least 75 mm. These requirements were fulfilled by the samples drilled from the tested slabs. Before the splitting tensile test, each sample was measured and weighed, and then centrally positioned in a U-Test Material Testing Equipment machine of class 1 with a capacity of 3000 kN (Fig. 4.10). Hardboard packing strips, with thickness, width, and length of 4 mm, 15 mm, and 300 mm respectively, were placed along the upper and bottom loading planes of the sample. The cores were loaded with a constant stress rate of 0.05 MPa/s until failure.

The splitting tensile strength, $f_{spl,core}$, was calculated using formula (2) from standard [49], based on the maximum load and specimen dimensions. Finally, the axial tensile strength f_{ct} was assumed equal to $0.9f_{spl,core}$ according to formula (3.3) from PN-EN 1992-1-1:2008 [30]. In total, 36 drilled cores were tested.

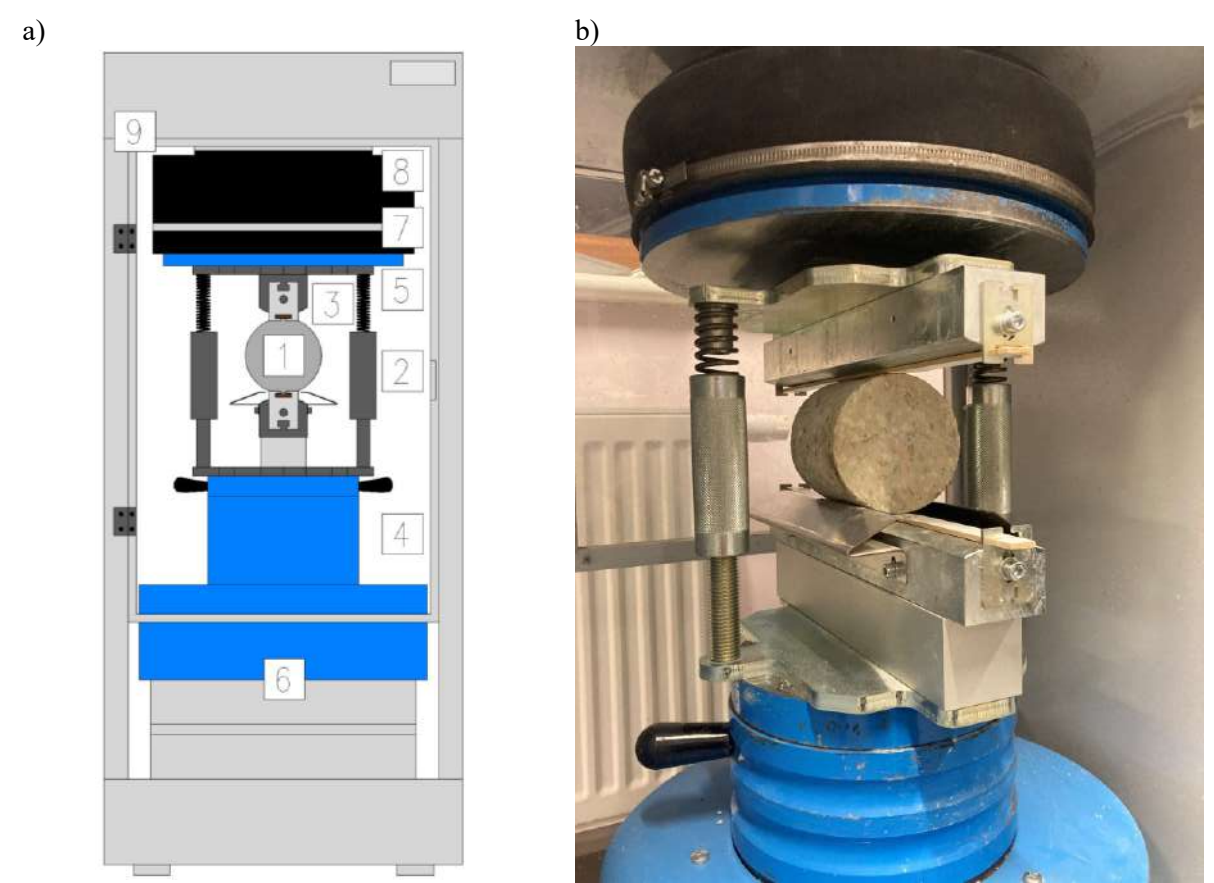


Fig. 4.10 Setup for splitting tensile test: a) scheme: 1 – sample; 2 – steel loading piece; 3 – hardboard packing strips; 4 – bottom plate; 5 – upper plate; 6 – piston; 7 – hinge; 8 – load cell; 9 – safety window, b) view of the setup

4.4.1.5 Flexural strength tests

The 3PBT of PC and SyFRC beams were conducted in accordance with PN-EN 14651 [29] to characterize their flexural tensile behavior. Due to the absence of a dedicated standard for non-metallic FRC, the standard intended for SFRC was applied. A detailed description of the flexural tensile strength test methodology according to [29] is provided in Chapter 3.3.2.3. Fig. 4.11 shows the test setup for the bending test, performed on a MATEST machine of class 1, model C090PN118, equipped with a Cyber-Plus Evolution progress control unit and a capacity of 200 kN. Before testing, the beams were measured and weighed, and then placed on two supporting rollers with a span length (l) of 500 mm. To measure beam deflection (δ), LVDTs were installed on

both sides via a rigid steel frame attached to the sample. The LVDT measurement range and accuracy of the indications were equal to ± 5 mm and ± 0.025 mm, respectively (accuracy class 0.5%). The average of the two LVDT readings was used for further analysis. Additionally, clip gauges were installed in the notch region to record crack mouth opening displacement (CMOD) and crack tip opening displacement (CTOD), as shown in Fig. 4.12. It is worth mentioning that small steel angles were glued to the beams prior to testing to facilitate accurate positioning of the LVDTs and clip gauges. The sample was loaded with a force (F) while increasing the δ at a rate of 0.05 mm/min until $\delta = 0.1$ mm, after which the rate was increased to a constant 0.2 mm/min until δ reached 5 mm, at which the test was terminated. During the 3PBT, the F-CMOD, F-CTOD, and F- δ curves were recorded. However, for the purposes of this doctoral study, only the first curve was considered for analysis. Based on these results, the limit of proportionality $f_{ct,L}$ (see equation (3.29) in Chapter 3.3.2.3) and residual flexural tensile: $f_{R,1}$, $f_{R,2}$, $f_{R,3}$, and $f_{R,4}$ (see equation (3.30) in Chapter 3.3.2.3) were calculated using the formulas provided in [29]. In total, 18 beams were tested. An example of the 3PBT setup for beam 2.2 is shown in Fig. 4.12. Furthermore, fracture energy G_F was determined from the 3PBT results as the area under the F-CMOD curve up to CMOD = 3.5 mm (Fig. 4.13). This value represents the work required to achieve a CMOD of 3.5 mm.

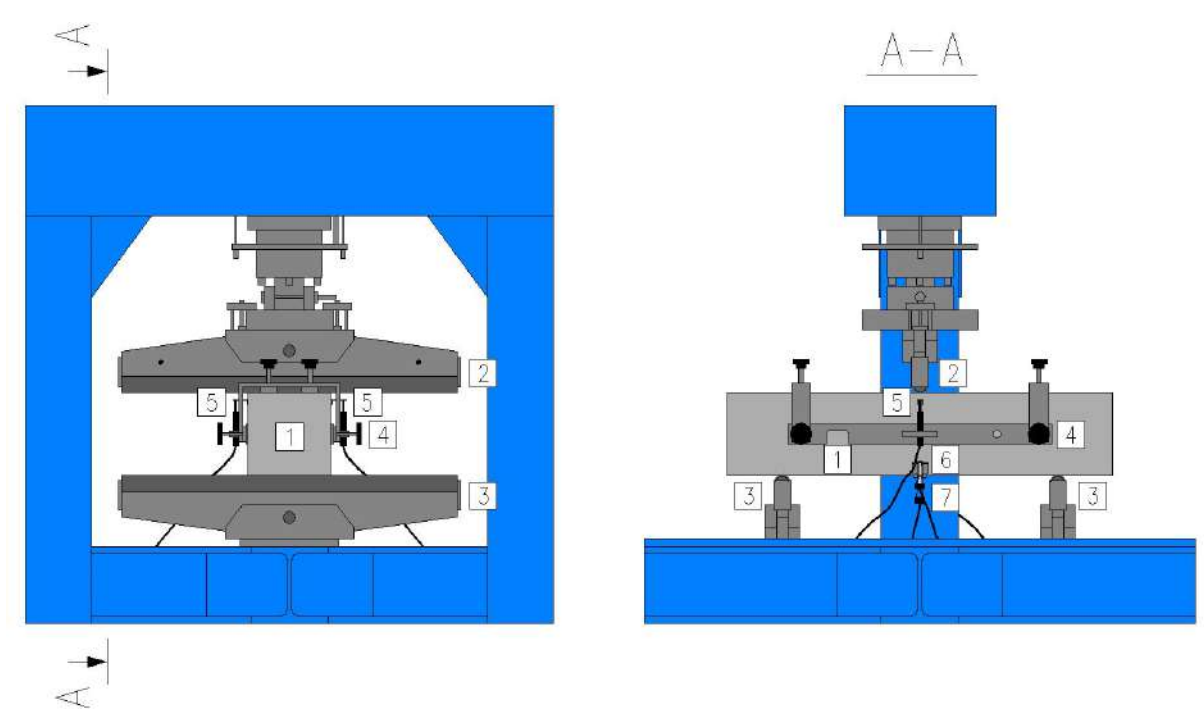


Fig. 4.11 Setup for 3PBT: 1 – sample, 2 – loading roller, 3 – supporting roller, 4 – rigid, steel frame to install LVDTs, 5 – LVDT to measure δ , 6 – clip gauge to measure CTOD, 7 – clip gauge to measure CTOD



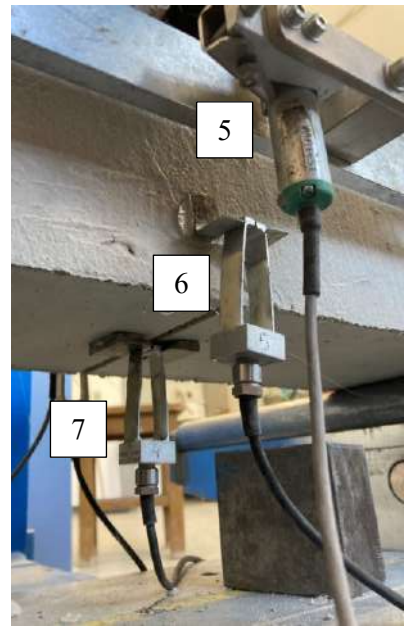


Fig. 4.12 View of the setup during the 3PBT with the location of measurement devices, where: 5 - LVDT to measure δ ; 6 - clip gauge to measure CTOD; 7 - clip gauge to measure CMOD

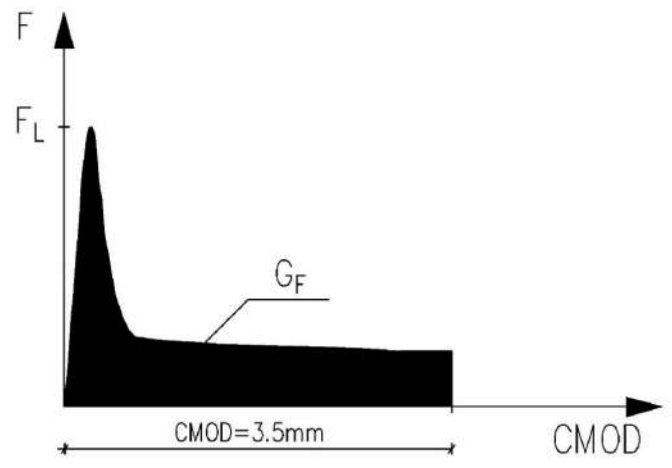


Fig. 4.13 Determination of the fracture energy G_F based on the 3PBT results

4.4.2. Large-scale slab tests

4.4.2.1 Testing schedule

The testing methodology for SyFRC ground-supported slabs subjected to centrally applied concentrated loads was developed based on an extensive literature review, with particular emphasis on previously conducted experimental studies and analytical investigations. To establish a timeline for the casting and testing of the slabs, the relevant dates were summarized in Table 4.6.

Table 4.6 Schedule of slab casting and testing

| Tyj | rpe Slab concreting date Slab testing date | | List of slabs in order of testing date | | |
|-----|--|------------|--|-----|------------|
| 1.1 | | | 20.12.2024 | 6.1 | 16.04.2024 |
| 1.2 | PC | 14.12.2021 | 22.01.2025 | 6.2 | 30.04.2024 |
| 1.3 | | | 27.01.2025 | 6.3 | 15.05.2024 |
| 2.1 | 2 | | 24.07.2024 | 2.1 | 24.07.2024 |
| 2.2 | PM | 07.02.2022 | 23.08.2024 | 2.2 | 23.08.2024 |
| 2.3 | ď | | 20.09.2024 | 2.3 | 20.09.2024 |
| 3.1 | 3 | | 25.10.2024 | 3.1 | 25.10.2024 |
| 3.2 | \square | 10.03.2022 | 31.10.2024 | 3.2 | 31.10.2024 |
| 3.3 | Ы | | 21.11.2024 | 3.3 | 21.11.2024 |
| 4.1 | 2 | | 06.02.2025 | 1.1 | 20.12.2024 |
| 4.2 | PD_ | 12.04.2022 | 10.02.2025 | 1.2 | 22.01.2025 |
| 4.3 | Ь | | 19.02.2025 | 1.3 | 27.01.2025 |
| 5.1 | 3 | | 26.02.2025 | 4.1 | 06.02.2025 |
| 5.2 | PD_ | 17.05.2022 | 28.02.2025 | 4.2 | 10.02.2025 |
| 5.3 | d | | 13.03.2025 | 4.3 | 19.02.2025 |
| 6.1 | 2 | | 16.04.2024 | 5.1 | 26.02.2025 |
| 6.2 | ا آتا | 07.06.2022 | 30.04.2024 | 5.2 | 28.02.2025 |
| 6.3 | H | | 15.05.2024 | 5.3 | 13.03.2025 |

4.4.2.2 Slab samples

Number of samples

In the experimental campaign, three slabs were cast for each concrete type 1-6 to enhance the representativeness of the results, resulting in a total of 18 large-scale samples. Firstly, a greater number of specimens helps minimize the influence of geometric deviations between individual slabs. Secondly, in case of FRC, the risk of non-uniform fiber distribution is inherent, thus, increasing the number of samples allows for result averaging, limiting the impact of local inconsistencies. Moreover, testing multiple specimens reduces the influence of potential technical problems that may occur during the experiment, such as setup inaccuracies as well as measuring device or actuator errors. Relying on a single sample would significantly increase the risk of above mentioned issues compromising the generalizability of the results. Finally, while many experimental studies identified in the literature review are based on single-specimen testing, the present study employs methodology that aimed to evaluate the repeatability and consistency of the obtained results.

Geometry

Slabs measuring 200 x 1200 x 1200 mm were prepared within the experimental campaign. It is worth mentioning that the slab thickness was assumed to represent real-scale slabs typically found in warehouses or parking lots subjected to medium loads (see Table 3.20). Moreover, according to Niezgodziński et al. [209], thin slabs are

defined by a thickness h that is small relative to the transverse dimensions, specifically when $h \le 0.2a$, where a is the width of the rectangular slab. In accordance with this criterion, the tested slabs can be classified as thin since h = 200 mm is less than 0.2a = 240 mm. Nevertheless, according to other existing provisions, the same slab can be classified as thick, what indicates that a straightforward classification is challenging [210]. Then, due to limitations related to testing space and laboratory facilities, slabs with smaller plan dimensions were tested compared to typical field-scale slabs, which commonly measure $4 \times 4 \text{ m}$ or $6 \times 6 \text{ m}$. This approach aligns with literature review, where slabs of reduced size were usually used for experimental investigation (see Table B.1 in Appendix B). Moreover, for characterizing the punching shear behavior of ground-supported slabs, it seems to be sufficient to test only the portion limited by the radius of relative stiffness l around the loading point, which corresponds to the area in contact with the ground (Fig. 4.14).

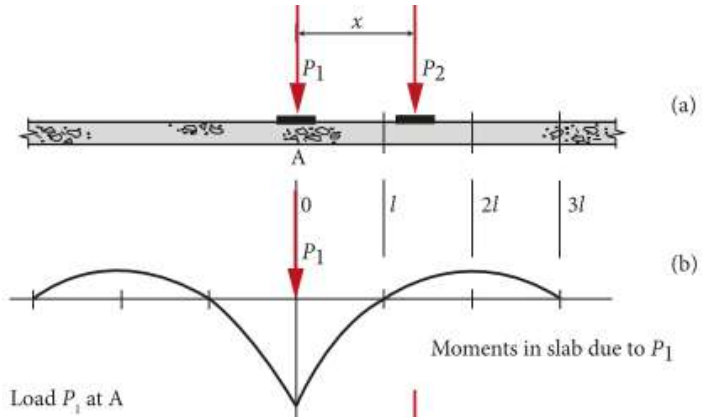


Fig. 4.14 Bending moments in ground slab subject to single concentrated load (l – radius of relative stiffness) [28]

Interestingly, Roesler et al. [211] selected the slab geometry based on locations, where bending moments were expected to reach a zero value. Furthermore, in Elsaigh's master's dissertation [26], the spacing between points of zero displacement was approximately 600 mm for both the PC slab (150 x 3000 x 3000 mm) and the SFRC ground slab (125 x 3000 x 3000 mm) as illustrated in Fig. 3.58. In the experimental study conducted by Shi et al. [193], this distance was around 1000 mm for PC and 1250 mm for SyFRC ground-supported slabs (120 x 1800 x 1800 mm). Similarly, Sucharda et al. [212] reported a spacing ranging from 1400 to 1800 mm for tested SFRC ground slabs (150 x 2000 x 2000 mm), depending on the applied SFs dosage. Furthermore, literature examples reviewed in Chapter 3.4.2 demonstrated that punching shear failure was concentrated within a relatively small area around the applied load, regardless of the overall sample geometry. Consequently, it was concluded that slabs

with smaller plan dimensions are suitable for describing punching shear behavior of centrally loaded ground-supported slabs, whereas larger slabs are generally preferred for evaluating flexural load-bearing characteristics. Analytical calculations, following TR34 [28] and equation (3.15), confirmed that for the assumed slab thickness (200 mm), the plan dimensions of the samples (1200 x 1200 mm) are greater than the distance between points of zero displacement. Namely, 2l ranges between 958 mm and 1072 mm depending on concrete strength and the modulus of subgrade reaction k.

Boundary conditions

In accordance with the adopted methodology, the slab width was limited to approximately 2l (Fig. 4.14) corresponding to the distance between point of zero displacement/bending moment. Consequently, to provide hinged support and allow slab rotation at these locations, steel rollers were installed along all four edges of the slab. At this point, it should also be taken into account that in in-situ ground-supported slabs or large-scale slab samples, membrane action may occur and influence the elements' structural response [213]. Namely, this action arises due to the presence of adjacent structural elements that stiffen the slab and restrain its lateral movement. Specifically, the application of a concentrated load induces in-plane forces within the slab depth (Fig. 4.15). With increasing vertical deformations, compressive membrane forces develop along a ring near the slab perimeter, provided that the perimeter is supported vertically and restrained against horizontal movement. Simultaneously, tensile membrane forces may form in the central zone of the slab. As a result, the presence of membrane action enhances the load-bearing capacity of the element. In the case of ground-supported slabs, this action is generated by the rigidity of the surrounding slab regions. However, simulating such conditions in conventional laboratory tests on isolated specimens is challenging. Moreover, reducing the slab dimensions inherently limits the development of membrane action compared to full-scale slabs in industrial floors.

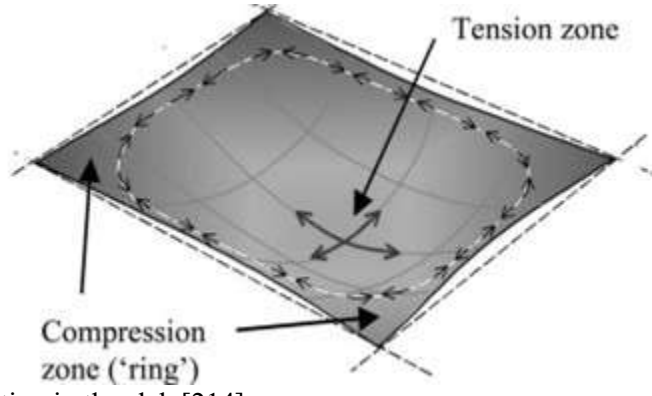


Fig. 4.15 Membrane action in the slab [214]

4.4.2.3 Ground conditions

Subsoil profile

In accordance with the literature review, laboratory experiments on ground-supported slabs typically employ only one type of subsoil (see Chapter 3.4.2 and Table B.1 in Appendix B). The application of multilayered solution would considerably complicate the construction and preparation of the testing setup, as well as subsequent analyses. Commonly adopted subbase materials include clay, sand, gravel, crushed stones, or materials simulating the natural aggregates such as cork planks and insulation boards. Furthermore, when designing the experimental campaign, both the common practices in industrial floor construction and the practical aspects related to preparation and compaction were taken into account. Based on these considerations, and the classification presented in Table 4.7, crushed stone was selected as the single layer subbase material for the large-scale slab tests. The moisture content of the aggregate was maintained at around 10%.

Table 4.7 Typical values of modulus of subgrade reaction k depending on the soil type [68]

| Soil type | k [MPa/m] | | |
|---------------------------------|-----------|--|--|
| Fine or slightly compacted sand | 15-30 | | |
| Well compacted sand | 50-100 | | |
| Very well compacted sand | 100-150 | | |
| Loam or clay (moist) | 30-60 | | |
| Loam or clay (moist) | 80-100 | | |
| Clay with sand | 80-100 | | |
| Crushed stone with sand | 100-150 | | |
| Coarse crushed stone | 200-250 | | |
| Well compacted crushed stone | 200-300 | | |

An additional aspect requiring consideration was the provision of uniform contact between the slab and the subgrade. To investigate this, two subsoil profile configurations were evaluated using two slabs of type 6, specifically specimens 6.1 and 6.3. The selection of this slab type was based on preliminary results from 3PBTs reported in [72], which demonstrated that among all tested concretes (PM_2, PM_3, PD_2, PD_3, and FF_2), the FF_2 mixture exhibited the highest flexural tensile strength and superior average residual flexural tensile strengths. Accordingly, type 6 slabs were considered appropriate for verifying subgrade preparation methods and for assessing expected cracking patterns, ultimate load levels, deflection magnitudes, the capacity of the test setup, and the accuracy of the measurement instrumentation. A detailed description of the analyzed subgrade profiles and their preparation procedures is provided in Table 4.8. In both variants, the soil was compacted in three primary layers. The first two layers

were compacted using a mechanical plate compactor, while the top layer was compacted manually with a hand rammer, followed by controlled water addition to enhance optimal compaction level. Subsequently, two approaches were evaluated to ensure uniform contact between the slab and the ground. In Variant I, the fourth layer consisted of crushed aggregates with smaller grain sizes, mixed with cement and water, and placed at a thickness of approximately 3 cm. This configuration was intended to simulate the behavior of lean concrete commonly employed beneath ground-supported slabs in practical applications. In Variant II, the fourth layer also comprised finely graded crushed aggregate, however, lime and water were used as binding agents instead of cement. The thickness of this layer was significantly reduced to approximately 0.5 cm, resulting in a less stiff interface compared to Variant I. The total compacted thickness of the subsoil profile in both configurations was approximately 43 cm. Finally, a plastic foil was placed to minimize friction and reduce water evaporation. To ensure proper settlement of the slab on the subgrade, the slab had to be positioned immediately after the preparation of the final soil layer.

The findings from the large-scale tests of slabs 6.1 and 6.3 led to the modification of Variant III and the development of Variant III for the subsoil profile, adopted for subsequent testing of slabs types 1-5. Specifically, in Variant III, the fourth layer consisted solely of crushed aggregates of smaller grain sizes, without the addition of water, cement, or lime, as detailed in Table 4.9. Consequently, the use of plastic foil was deemed unnecessary, as strict moisture control was not required for this variant. Moreover, since the last layer in Variant III exhibited low deformability and did not conform to the slab's underside geometry, resining from the plastic foil facilitated more accurate assessment of the slab-ground contact area. Prior to testing, at locations where inadequate contact was observed, additional crushed aggregates were introduced and properly compacted to ensure the intended support conditions.

It is important to emphasize that after each test, the third and fourth soil layer (Table 4.9) were removed, replaced, and recompacted to maintain a consistent level of subsoil compaction and stiffness. To optimize time efficiency and reduce labor intensity during the preparation of the setup before each test, loosening was limited to only upper soil layers. However, measurements of the subgrade reaction modulus k confirmed that repeatability of ground conditions was achieved despite partial soil replacement.

Finally, to verify the thesis of differing structural behavior, particularly in terms of load-bearing capacity and failure mechanisms, between SyFRC slabs unsupported and supported by the ground, slab 6.2 was tested. Specifically, slab 6.2 was supported exclusively on four steel supporting rollers, as illustrated in Fig. 4.16.

Table 4.8 Ground preparation procedure – Variant I and II $\,$

| Slab 6.1 – Variant I | Slab 6.3 – Variant II | | |
|---|--|--|--|
| Placement of the 1st layer of crushed aggregates | Placement of the 1st layer of crushed aggregates | | |
| into the box – thickness \approx 15 cm | into the box – thickness \approx 15 cm | | |
| Addition of ≈ 10 liters of water | Addition of ≈ 10 liters of water | | |
| Compaction of the 1 st soil layer by plate | Compaction of the 1 st soil layer by plate | | |
| compactor for $\approx 20 \text{ min}$ | compactor for $\approx 20 \text{ min}$ | | |
| | | | |
| Placement of the 2 nd layer of crushed aggregates | Placement of the 2 nd layer of crushed aggregates | | |
| into the box – thickness \approx 15 cm | into the box – thickness \approx 15 cm | | |
| Addition of ≈ 10.0 liters of water | Addition of ≈ 10.0 liters of water | | |
| Compaction of the 2 nd soil layer by plate | Compaction of the 2 nd soil layer by plate | | |
| compactor for ≈ 20 min | compactor for $\approx 20 \text{ min}$ | | |
| Placement of 3 rd layer of crushed aggregates into | Placement of the 3 rd layer of crushed aggregates | | |
| the box – thickness ≈ 10 cm | into the box – thickness \approx 13 cm | | |
| Addition of ≈ 6.5 liters of water | Addition of ≈ 8.5 liters of water | | |
| Compaction of the 3 rd soil layer by hand rammer | Compaction of the 3 rd soil layer by hand rammer | | |
| for ≈ 20 min | for $\approx 20 \text{ min}$ | | |
| Placement of the 4 th layer of crushed aggregates | Placement of the 4 th layer of crushed aggregates | | |
| of smaller grain sizes mixed with cement and | of smaller grain sizes mixed with lime and water | | |
| water (lean concrete) – thickness \approx 3 cm | – thickness ≈ 0.5 cm | | |
| | | | |
| Placement of the plastic foil | Placement of the plastic foil | | |
| Immediately placement of the slab | Immediate placement of the slab | | |
| | | | |

Table 4.9 Ground preparation procedure – variant III

Variant IIIPlacement of the 1st layer of crushed aggregates into the box – thickness \approx 15 cmAddition of \approx 10 liters of waterCompaction of the 1st soil layer by plate compactor for \approx 20 minPlacement of the 2nd layer of crushed aggregates into the box – thickness \approx 15 cmAddition of \approx 10.0 liters of waterCompaction of the 2nd soil layer by plate compactor for \approx 20 minPlacement of the 3rd layer of crushed aggregates into the box – thickness \approx 13 cmAddition of \approx 8.5 liters of waterCompaction of the 3rd soil layer by hand rammer for \approx 20 min



Placement of the 4th layer of crushed aggregates of smaller grain sizes in order to fil the empty spaces between the coarse grains of the last soil layer – thickness \approx **0.5 cm**





Fig. 4.16 Slab 6.2 after the test exclusively on four steel supporting rollers, without ground support

Modulus of subgrade reaction k

As previously indicated, the type of the subsoil and degree of its compaction significantly influence the structural response of ground-supported slab. Moreover, to ensure that slab fails due to punching shear, appropriate ground conditions had to be provided. Furthermore, to control repeatability in the degree of compaction, the modulus of subgrade reaction k needed to remain consistent throughout the experimental campaign. To monitor and assess the k value, two in-situ tests were conducted: the static plate load test using a VSS bearing plate and the dynamic plate load test using a Light Falling Weight Deflectometer (LFWD).

The static plate load test, performed in accordance with Appendix B of PN-S-02205:1998 standard [215], involved the measurement of vertical subgrade deformations under incremental static loading. The applied load was transmitted through a circular steel plate with a diameter of 300 mm. Moreover, the VSS testing apparatus consisted of a hydraulic jack with a manual pump, a dial gauges for settlement measurements, a gauge mounting stand, pipe extensions, and a spherical hinge (Fig. 4.17). It is worth mentioning that, instead of a vehicle typically used as a counterweight in field conditions, a rigid steel frame was employed. Following the setup of the apparatus, the subsoil was subjected to incremental loading, beginning at 0.05 MPa and increasing in 0.05 MPa steps up to a final pressure of 0.25 MPa, while settlement readings were continuously recorded. Subsequently, the unloading phase was conducted in 0.10 MPa decrements down to 0 MPa, again recording the corresponding settlements. Finally, a second loading cycle was performed using the same loading increments as in the initial cycle. Based on the pressure-settlement curve obtained from the static plate load test, the primary and secondary static deformation modulus E_{vl} and $E_{\nu 2}$, respectively, were determined.







Fig. 4.17 Static plate load test on the subsoil of slab 6.1 using a VSS bearing plate

The dynamic plate load test, described in ASTM E2835-11 [216] standard and German regulations TP BF-StB – Part B 8.3 [217], is typically used to assess the compaction quality of non-cohesive soils, including the crushed aggregates applied in this study. It should be noted that this method allows for the evaluation of only the uppermost subsoil layers, up to a depth of approximately 0.5 m, which was sufficient for the purposes of the experimental campaign conducted within this dissertation. The test procedure involved measuring the maximum displacement at the center of a 300 mm diameter, 20 mm thick plate (weighing 15 kg), caused by a 10 kg weight falling along a steel, vertical guide. Deflection sensors were mounted directly on the plate surface, and the readings were recorded using an electronic measurement device. The resulting vertical deformation was subsequently used to automatically calculate the dynamic deformation modulus E_{vd} . Representative photos of the test conducted on the subgrade beneath slab 3.1 are presented in Fig. 4.18.

One of the main advantages of LFWD is the short duration of the test with results available immediately. As such, the LFWD method is significantly more convenient and practical than the conventional VSS test, which requires careful apparatus arrangement and heavy equipment to provide counterweight for the hydraulic loading system. Consequently, it was decided to adopt the dynamic plate load test for further control of subgrade compaction after determining the correlation coefficient γ_2 between $E_{\nu 2}$ and E_{vd} . It is a common practice to derive such correlation factor, and several studies have demonstrated a satisfactory agreement between E_{v2} and E_{vd} [218]–[220]. On the other hand, the correlation between E_{vd} and the primary modulus E_{vl} is less frequently used and typically shows poorer agreement. This can be attributed to the fact that the loading conditions during the dynamic plate test more closely resemble those of the secondary load cycle in the VSS test, as the falling mass causes multiple rebounds, contributing to further compaction of the soil. Nonetheless, assuming a constant value of the deformation index I_0 due to the consistent compaction methodology employed, it is possible to derive the correlation coefficient γ_I between E_{vd} and E_{vI} using the approach described in equations (4.1)-(4.3).

$$I_0 = \frac{E_{v2}}{E_{v1}} \tag{4.1}$$

$$I_{0} = \frac{E_{v2}}{E_{v1}}$$

$$E_{v2} = \gamma_{2} \cdot E_{vd}; \ \gamma_{2} = \frac{E_{v2}}{E_{vd}}$$

$$(4.1)$$

$$E_{v1} = \frac{\gamma_2 \cdot E_{vd}}{I_0} = \gamma_1 \cdot E_{vd} \tag{4.3}$$

where:

 I_0 – deformation index [-],

 E_{vI} – primary static deformation modulus from static plate load test [N/mm²],

 E_{v2} – secondary static deformation modulus from static plate load test [N/mm²],

 E_{vd} – dynamic deformation modulus from dynamic plate load test [N/mm²],

 γ_1 , γ_2 – correlation coefficients [-].



Fig. 4.18 Dynamic plate load test on the subsoil of slab 4.2 using a LFWD

The literature provides several formulas for determining the modulus of subgrade reaction k, including those proposed by Eisenmann (based on Odemark's theory), Wilun (derived from Winkler's model), and other based on the OSŻD's approach. Additionally, equation (4.4), recommended in the design guidelines published by the Bekaert company [221] and aligned with the TR34 guideline [68], is also commonly referenced. As documented in [24], a comparison of k values obtained using these four approaches showed that the resulting differences are relatively minor. Therefore, in this dissertation, the modulus of subgrade reaction k was determined based on equation (4.4), which is also cited in Hajduk's book [24] dedicated particularly to the design of industrial ground-supported slabs.

$$k = \frac{E_{v1}}{550} \tag{4.4}$$

where:

k – modulus of subgrade reaction [N/mm³],

 E_{vI} – primary static deformation modulus from static plate load test [N/mm²].

Boundary conditions

The soil supporting the slab was placed directly on the laboratory's reinforced concrete strong floor with a thickness of 113 cm and was laterally confined by four concrete beams measuring 125 mm in thickness, 333 mm in height, and 1530 mm in length. Consequently, the resulting internal dimensions of the soil containment box were 377 x 995 x 995 mm. Given the limited dimensions of this box, undoubtedly the vertical stress distribution beneath the slab was influenced by the rigid boundary conditions imposed by the laboratory floor and surrounding concrete beams. As a consequence, the stiffness of the confined soil was higher than expected under actual in-situ conditions. According to the Boussinesq theory (see Fig. 4.19), for a slab with plan dimensions of 1200 x 1200 mm, a significantly larger soil containment box, approximately 2600 x 3600 x 3600 mm, would be required to ensure an undisturbed stress distribution extending to a level of 10% of the applied load. However, such dimensions of the testing setup were not feasible due to laboratory limitations, including available space, equipment, material, and financial considerations.

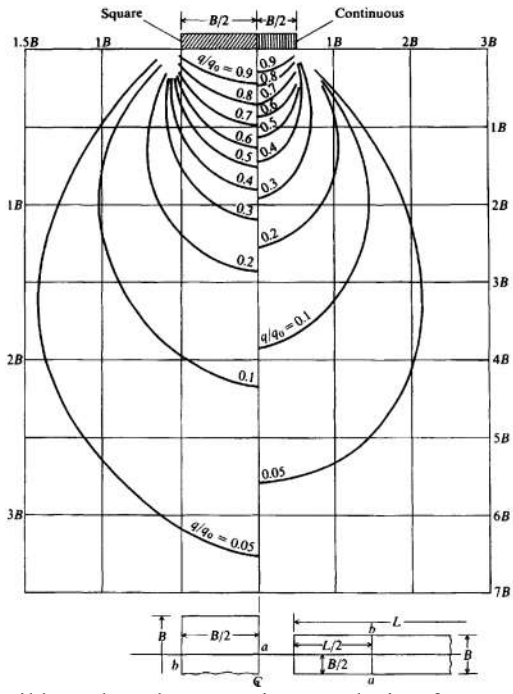


Fig. 4.19 Pressure isobars in soil based on the Boussinesq solution for square and continuous foundations [222]

In conclusion, the author acknowledges that the experimental program did not fully capture all phenomena and conditions associated with the concentrated loading of real ground-supported slabs, such as membrane action, slab dimensions, and actual subgrade conditions. Ideally, testing should be conducted in situ on full-scale slabs, concreted and supported on natural ground, to reflect real structural behavior most accurately.

Nevertheless, the carefully designed experimental campaign and specially designed testing setup adopted in this study are considered to provide reliable and meaningful results, enabling the formulation of important and practically relevant conclusions.

4.4.2.4 Measuring methods and testing setup

The schematic and photographic views of the testing setup used for large-scale tests on ground-supported slabs subjected to central concentrated loading are presented in Fig. 4.20 and Fig. 4.21. The load was applied at the center of a 1200 x 1200 mm slab with a thickness of 200 mm, placed on a soil containment box (internal dimensions: 430 x 995 x 995 mm) filled with compacted crushed stone aggregates. The soil was placed directly on a 1130 mm thick laboratory strong floor and laterally confined on all four sides by concrete beams measuring 125 mm in thickness, 333 mm in height, and 1530 mm in length. To reinforce the upper surface of the concrete beams and to slightly increase the thickness of the supporting soil layer, a 40 mm thick concrete screed was cast over the beam tops. The slab was supported nearly entirely on the prepared subgrade, with its edges supported by steel angle profiles (L 8 x 75 x 100 mm) of 1120 mm in length and aligned at ground level. To avoid interference at the corners, 50 mm segments were cut off from both ends of each angle. These profiles facilitated accurate positioning of the slab on supporting steel rollers (diameter: 40 mm and length: 1200 mm), which were placed in steel rails of 995 mm in length. The rollers were positioned near locations of expected zero bending moment, points where the slab begins to lose contact with the subgrade and were intended to allow slab rotation. Given the anticipated magnitude of the applied loads, the concrete beams were additionally restrained using steel boxes held by screw fasteners fixed to the laboratory floor. The gap between the box and the screw was eliminated by inserting pairs of steel wedges. In total, eight steel boxes were installed, with two located on each side of the containment box. Finally, to prevent deformation of the upper part of the soil box during testing, a steel clamping frame was installed around the perimeter of the concrete screed.

The test was conducted using a 970 kN hydraulic actuator, beneath which a load cell CT100 of class 1 was mounted via a hinged connection to record the applied load. The load cell had a capacity of $1000 \, \text{kN}$, with the measurement accuracy of $\pm 10 \, \text{kN}$ (accuracy class 1%). It is important to note that the actuator's maximum stroke was approximately 80 mm, which in some cases limited the continuation of the slab test. The concentrated force was transferred to the slab through a steel column ($100 \, \text{x} \, 100 \, \text{x} \, 150 \, \text{mm}$) positioned directly beneath the load cell, representing the geometry of a typical base of rack leg.

The slab was loaded monotonically, without incremental steps, using a manually operated electric pump with a pressure capacity of 100 MPa. Due to the limitations of the pump, produced by ENERPAC, model C6T17FZ81B, it was not possible to maintain either constant load or constant deflection control during the tests.

A review of relevant literature revealed that symmetrical, diagonal, or combined LVDT arrangements have been used, with corresponding observations of both symmetrical and diagonal crack patterns. However, based on yield line theory and findings from numerical analyses, diagonal crack morphology was predominantly anticipated. Accordingly, a symmetrical LVDT layout was adopted in the testing methodology to monitor the deflection of the slab, with the awareness that crack development could occur at sensor locations. A total of 12 LVDTs (type PJx20, referred to as LVDT20), manufactured by PELTRON, were installed on the slab surface. The measurement range and accuracy of the indications were equal to ± 10 mm and ± 0.05 mm, respectively (accuracy class 0.5%). The arrangement of the LVDTs is illustrated in Fig. 4.22 and Fig. 4.23. Notably, they were mounted on a dedicated steel footing frame supported externally, beyond the testing setup. Given the limited slab dimensions and the high density of measurement points, it was necessary to position the frame structure on the laboratory strong floor, independent of the concrete slab.

Additionally, four LVDTs (type PJx10, referred to as LVDT10), manufactured by PELTRON, were used. The measurement range and accuracy of the indications were equal to ± 5 mm and ± 0.025 mm, respectively (accuracy class 0.5%). The LVDT10s were mounted using special clamps and positioned in contact with one end of steel rods, socalled pushrods, which passed through the entire thickness of the slab via pre-drilled holes, as illustrated in Fig. 4.24. For the first series of tests (slabs 6.1, 6.2, and 6.3), the holes, with a diameter of 12 mm, were drilled along the symmetry axis of the slabs (Fig. 4.22, Variant I). In subsequent tests (slabs of types 1-5), the hole arrangement was revised, and the rods were installed along the diagonals of the slabs (Fig. 4.22, Variant II). The primary objective of this change was to align the sensors exclusively with punching shear cracks, thereby avoiding the influence of flexural cracks. Due to this, the pushrods were located along a circle at a radial distance of 100 mm from the edges of the steel loading column. This location corresponded to the critical control section position estimated to occur between 0.5d and 1.0d from the loaded area (Fig. 4.22). The function of these sensors was to measure the vertical displacements (LVDT10) caused by inclined shear cracking at angle θ . Then, using geometrical relationships, the resulting crack width opening w could have been determined (Fig. 4.25) in accordance with equation (4.5).

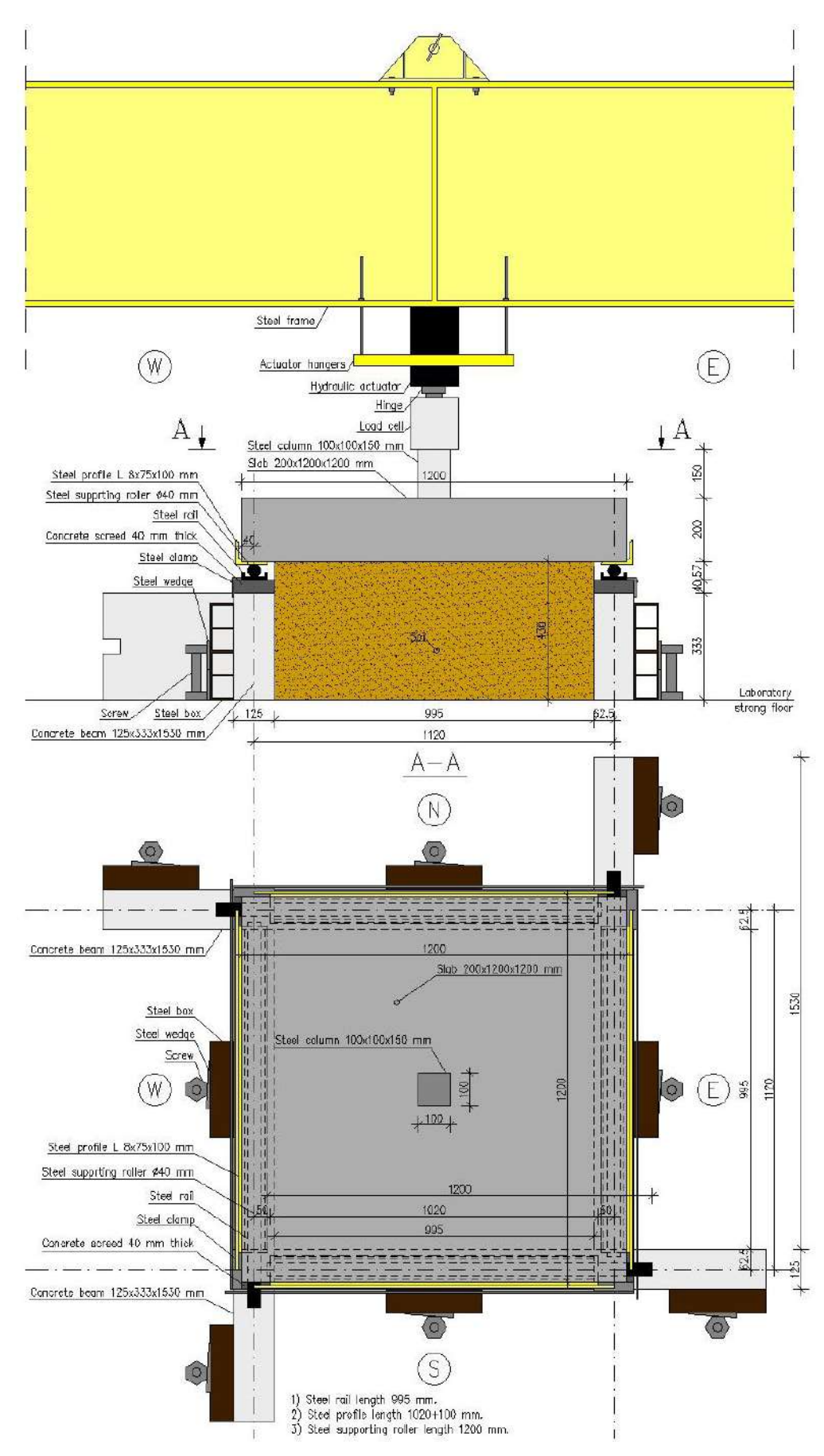


Fig. 4.20 Scheme of the testing setup for ground-supported slabs centrally loaded by a concentrated force



Fig. 4.21 Testing setup for ground-supported slabs centrally loaded by a concentrated force

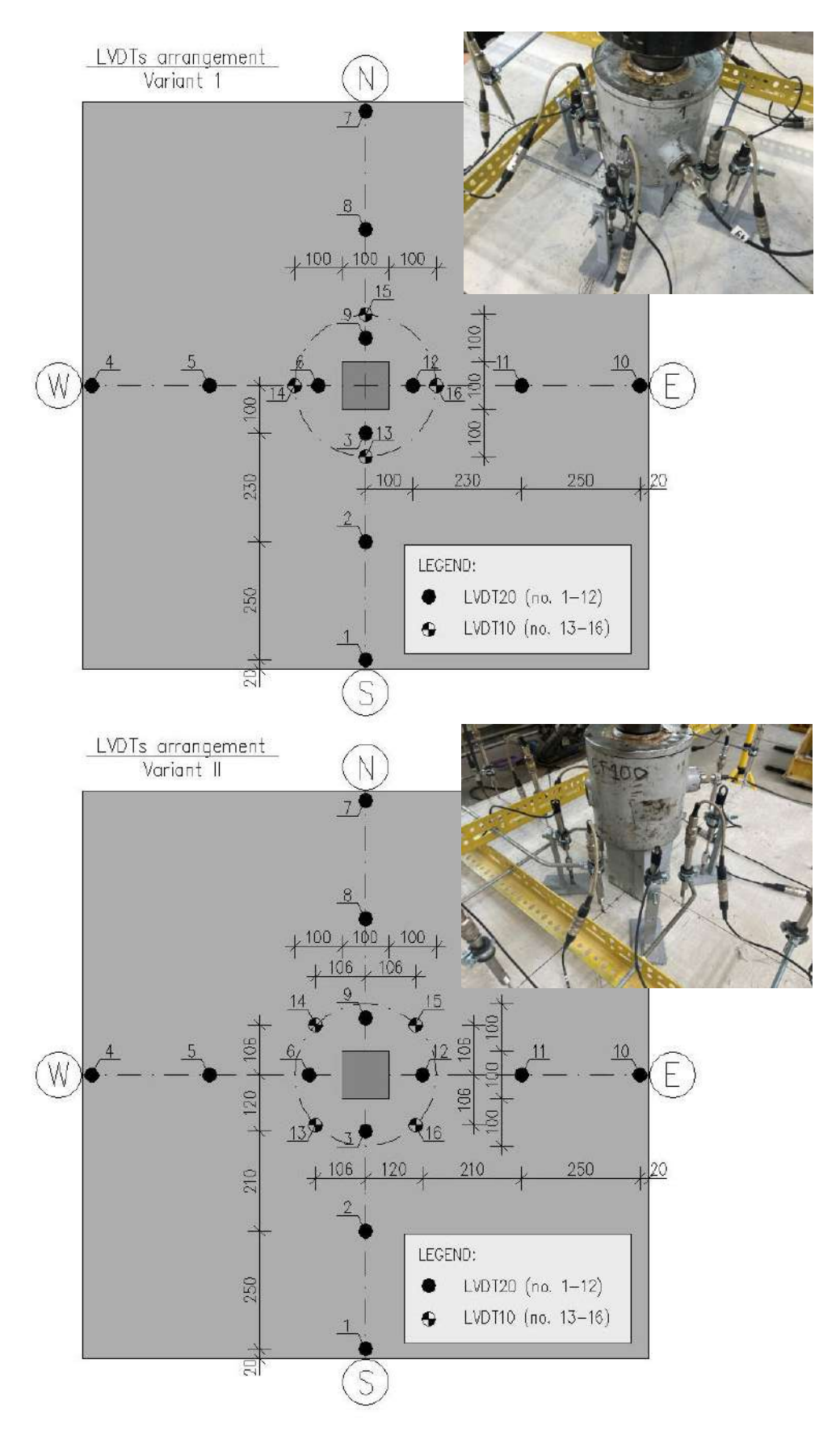


Fig. 4.22 Scheme of the LVDTs arrangement for Variant I (slabs of type 6) and Variant II (slabs of types 1-5)





Fig. 4.23 LVDTs arrangement for: a) Variant I (slabs of type 6), b) Variant II (slabs of types 1-5)



Fig. 4.24 Installation of the pushrod measurement devices on the slab top surface

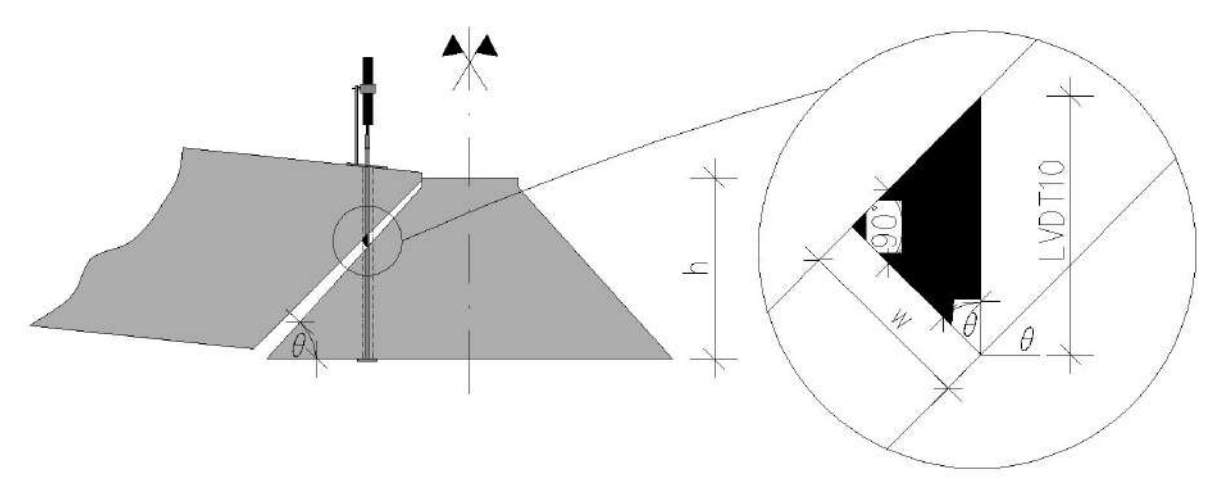


Fig. 4.25 Principles for determining crack width opening based on geometric relationships using pushrod measurement devices

$$w = \cos\theta \cdot LVDT10 \tag{4.5}$$

where:

w – crack width opening [mm],

 θ – inclination angle of the punching cone [rad],

LVDT10 – slab height increase measured by the pushrod [mm].

The applied concentrated load F and the corresponding deflections δ were measured at 12 locations on the slab throughout the test until its termination. The central deflection, denoted as $\delta_{central}$, was calculated as the median value of the readings from LVDTs no. 3, 6, 9, and 12. The use of the median was intended to mitigate the influence of non-uniform slab behavior, which occasionally led to significant deviations in individual LVDT readings. Specifically, the median is less sensitive to outliers and therefore more appropriate when extreme values are present. The test was interrupted for one of three reasons: 1) most commonly, due to a sudden drop in applied force accompanied by visible punching shear failure and large slab deformations; 2) in some cases, when deflections continued to increase significantly while the applied force remained nearly constant; 3) finally, due to equipment limitations, namely, when the majority of LVDTs exceeded their measurement range or the actuator approached its maximum stroke capacity.

The maximum punching shear force (F_p) was identified at the point of sudden force drop, accompanied by the abrupt punching of the steel column into the slab. However, prior to this, the appearance of flexural cracks at the slab edges was observed. Typically, bending occurred in two stages, hence, the loads corresponding to the initiation of these cracks, denoted as F_{cr1} and F_{cr2} , were determined at the first and second noticeable reductions in the slab's load-bearing capacity. These points were identified as turning points on the F- $\delta_{central}$ curve and were consistent with both visual observations and the timing of crack formation at the slab edges. The maximum load-bearing capacity (F_{max}) was defined as the peak force recorded during the test. For each slab type, the median values of the flexural forces $(F_{cr1}$ and $F_{cr2})$ and the punching shear force (F_p) were determined and used in subsequent analyses and comparisons.

To examine the punching shear cones, the tested slabs were placed on a steel ring with a diameter of 40 cm, and the cones were pushed out using a manual hydraulic jack, counteracted by a steel frame, as shown in Fig. 4.26. Subsequently, the inclination angles of the punching cone sidewalls (θ) were measured at six different locations around the cone perimeter using an angle finder ruler (Fig. 4.27). The average value of θ was calculated based on all individual measurements. The measurement locations were selected depending on the shape of the cone, with an effort to maintain approximately uniform spacing between them. Finally, for each slab type, the average θ value was determined and used in subsequent analyses and comparisons.





Fig. 4.26 Setup for punching shear cone removal from the tested slabs



Fig. 4.27 Measurement of punching shear cone inclination angles θ using an angle finder ruler

5. RESULTS

5.1. Material characteristics

5.1.1. Fresh concrete properties

The results from flow table tests are presented in Table 5.1 while the flow classes were assigned according to PN-EN 12350-5 [207]. Additionally, photographs taken during the tests are shown in Fig. 5.1. The results indicated that the workability of the concrete mixtures was not consistent and ranged from flow class F3 to F5. Only mixtures of type 1 and type 2 fulfilled the prescribed requirement of class F5. These discrepancies in concrete workability can be attributed to observed variability in weather conditions. Specifically, it was concluded that concreting conducted on rainy days, particularly when preceded by prolonged periods of unfavorable weather, resulted in higher flow classes. Conversely, during periods of dry and sunny weather, the tested mixtures exhibited lower workability. Since the aggregates used for concrete production were stored outdoors and thus exposed to atmospheric conditions, their humidity varied over time. As a result, adjustments to the mix design recipe, specifically, the amount of added water, were required. However, it is possible that the concrete batching plant did not properly modify the mix proportions to account for these changes. Moreover, the slab casting process was conducted over a six-month period, which may have resulted in the use of materials from different deliveries, potentially affecting the concrete properties. Another factor likely contributing to the variability in workability was the presence of SyFs. Namely, the inclusion of fibers increases the overall surface area that must be coated with cement paste. This corresponds with the reduced workability observed in mixtures with SyFs of types 3-6, in contrast to reference mix of type 1. Moreover, based on results of PM 2 and PM 3 mixtures, the increased dosage of SyFs might have also caused a decline in workability. To maintain adequate flow class, an increased volume of mortar would typically be required in FRC compared to PC. However, in this

experimental program, the concrete composition was consciously kept constant, regardless of the presence, type, or dosage of SyFs. It is worth noting that the use of a high flow class (F5) was specifically prescribed to compensate for the anticipated reduction in workability due to fiber addition. Ultimately, the observed variability in fresh concrete properties is expected to have an impact on its mechanical performance.

Table 5.1 Flow table test results with flow class classification according to PN-EN 12350-5 [207]

| Type | 1 (PC) | 2 (PM_2) | 3 (PM_3) | 4 (PD_2) | 5 (PD_3) | 6 (FF_2) |
|----------------------|--------|----------|----------|----------|----------|----------|
| E1 4-1-1 - 44 [1 | 580 | 610 | 470 | 500 | 510 | 520 |
| Flow table test [mm] | 570 | 590 | 460 | 490 | 510 | 542 |
| Average [mm] | 575 | 600 | 465 | 495 | 510 | 531 |
| Flow class | F5 | F5 | F3 | F4 | F4 | F4 |

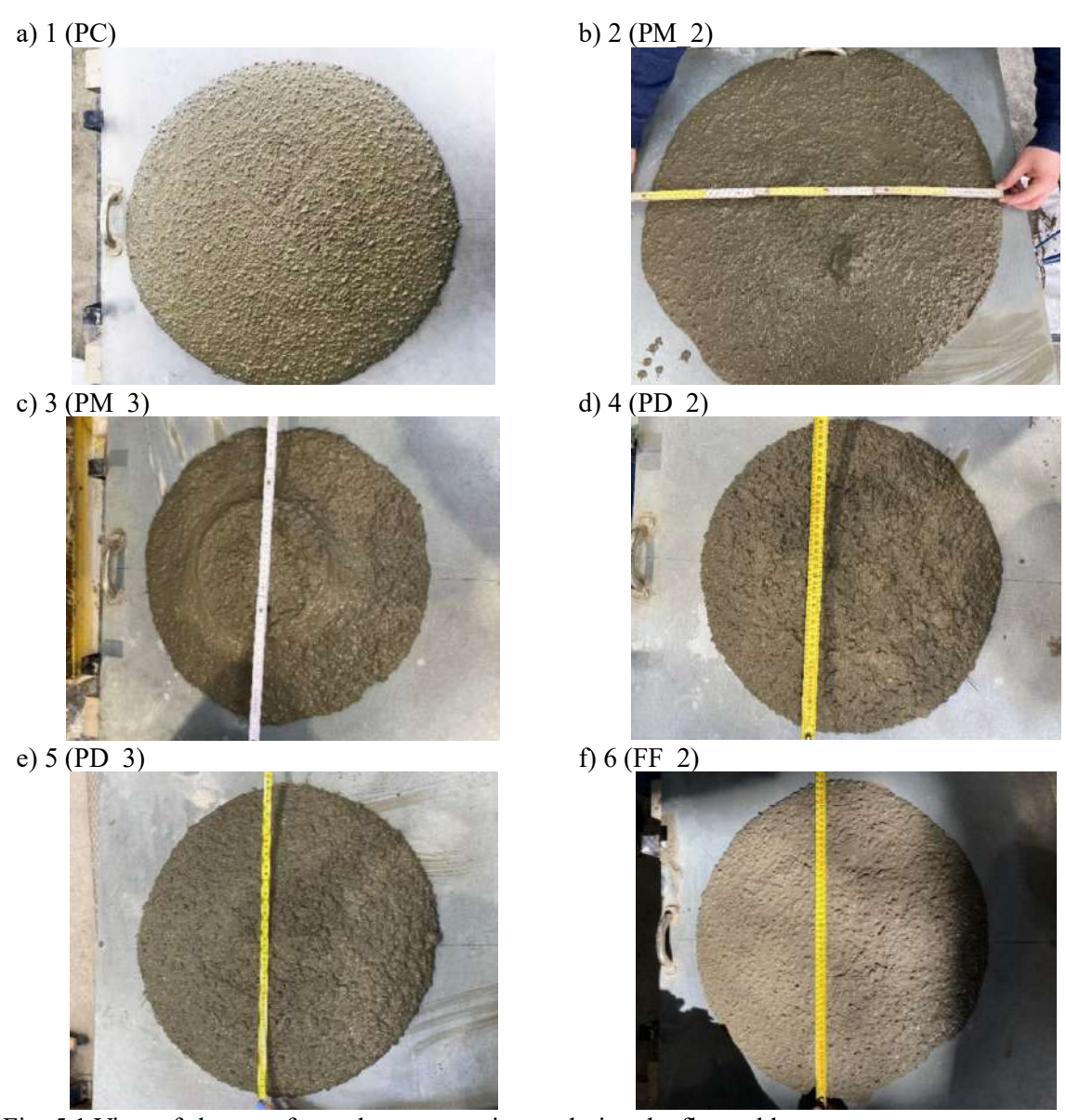


Fig. 5.1 View of slumps of tested concrete mixture during the flow table tests

5.1.2. Compressive strength tests

For each concrete type 1-6, six cubes $(150\pm1 \text{ x } 150\pm1 \text{ x } 150\pm1 \text{ mm})$ were tested to determine compressive strength, resulting in a total of 36 samples. The cubes, numbered from 1 to 6, were evaluated on the same day as the slab of corresponding concrete type. Prior to testing, each cube was individually measured and weighed. For each set of six cubes representing the same concrete type, the average weight and compressive strength $(f_{c,cube})$, as well as the corresponding standard deviation (SD) and coefficient of variation (COV), were calculated. The results of the weight measurements are presented in Table 5.2, while the compressive strength results are summarized in Table 5.3.

Table 5.2 Weight of cast cubes

| Type | 1 (PC) | 2 (PM_2) | 3 (PM_3) | 4 (PD_2) | 5 (PD_3) | 6 (FF_2) |
|--------------|--------|----------|-----------------|----------------|----------|----------|
| Sample no. | | A | At a time of sl | ab testing [kg | | |
| 1 | 7.224 | 7.564 | 6.915 | 7.559 | 7.566 | 7.482 |
| 2 | 7.414 | 7.439 | 6.908 | 7.528 | 7.617 | 7.504 |
| 3 | 7.324 | 7.493 | 6.961 | 7.448 | 7.560 | 7.470 |
| 4 | 7.302 | 7.338 | 6.895 | 7.445 | 7.476 | 7.473 |
| 5 | 7.357 | 7.475 | 6.945 | 7.505 | 7.657 | 7.476 |
| 6 | 7.265 | 7.502 | 6.917 | 7.486 | 7.506 | 7.548 |
| Average [kg] | 7.314 | 7.469 | 6.924 | 7.495 | 7.564 | 7.492 |
| SD [kg] | 0.067 | 0.076 | 0.025 | 0.045 | 0.067 | 0.030 |
| COV [%] | 0.92 | 1.02 | 0.36 | 0.60 | 0.89 | 0.40 |

Table 5.3 Compressive strength of cast cubes $f_{c,cube}$

| Type | 1 (PC) | 2 (PM_2) | 3 (PM_3) | 4 (PD_2) | 5 (PD_3) | 6 (FF_2) |
|---------------|--------|----------|-----------------|---------------|----------|----------|
| Sample no. | | At | t a time of sla | b testing [MP | 'a] | |
| 1 | 33.07 | 40.32 | 28.03 | 55.63 | 54.29 | 45.60 |
| 2 | 37.08 | 38.96 | 28.33 | 55.99 | 52.62 | 43.10 |
| 3 | 35.35 | 38.67 | 29.20 | 52.45 | 55.07 | 43.70 |
| 4 | 33.45 | 41.16 | 26.96 | 50.15 | 58.05 | 43.87 |
| 5 | 36.83 | 42.97 | 28.30 | 51.98 | 52.72 | 41.03 |
| 6 | 34.26 | 39.04 | 27.13 | 51.53 | 54.03 | 40.85 |
| fc,cube [MPa] | 35.01 | 40.19 | 27.99 | 52.95 | 54.46 | 43.03 |
| SD [MPa] | 1.70 | 1.66 | 0.83 | 2.34 | 2.00 | 1.82 |
| COV [%] | 4.87 | 4.14 | 2.98 | 4.43 | 3.66 | 4.22 |

As shown in Table 5.3, the compressive strengths of PM_2 and FF_2 at the time of slab testing were 40.19 MPa and 43.03 MPa, respectively, representing increases of approximately 15% and 23% compared to PC, which reached 35.01 MPa. In the case of PD_2 and PD_3 concretes, the enhancements in $f_{c,cube}$ exceeded 50% relative to PC specimens. However, the conclusion that the addition of SyFs significantly improved

the compressive strength must be approached with caution. As indicated in the literature review, macro SyFs generally have a negligible effect on $f_{c,cube}$, which depends primarily on the concrete matrix, including the quality of the cement paste and aggregates as well as w/c ratio. Moreover, it was established that increasing the PD fiber dosage had only a marginal influence on compressive strength, with $f_{c,cube}$ improvements of less than 3%. In contrast, samples containing 3 kg/m³ of PM fibers experienced a 20% reduction in strength relative to PC specimens. Overall, considerable variability in $f_{c,cube}$ was observed among concretes of types 1 to 6. This may be attributed to inconsistencies in concrete composition, particularly with respect to water content adjustments necessitated by changing aggregate humidity, as well as different concrete material properties or presence and excessive fiber content. These conclusions were also consistent with the previously discussed variations in fresh concrete consistency. Nonetheless, the effects of fiber addition became clearly evident upon reaching the $f_{c,cube}$, since PC specimens exhibited brittle failure, while the SyFRC samples demonstrated ductile behavior and maintained structural integrity after failure.

To verify whether the variation in $f_{c,cube}$ of concrete types 1-6 was also reflected in the slab specimens, compressive strength tests were conducted on cores drilled from the slabs. Additionally, the core compressive strength ($f_{c,core}$) was required for the elastic modulus tests in order to determine the upper and lower stress levels applied during cyclic loading, in accordance with the standard [90]. A total of 18 cores, one from each slab, were tested. The specimens had dimensions of ϕ 94±1 mm in diameter and 188±2 mm in height. Their number corresponds to the slab number (1-3) from which the core was extracted. Each core was weighed (Table 5.4) and measured prior to testing, which was performed within one month of the respective slab test. The results are summarized in Table 5.5, where the average compressive strength ($f_{c,core}$), standard deviation (SD), and coefficient of variation (COV) are reported. It is important to note that no correction factors were applied, as the length-to-diameter ratio of the cores was equal to 2 [223]. Selected core specimens after testing are shown in Fig. 5.2.

Table 5.4 Weight of drilled cores

| Type | 1 (PC) | 2 (PM_2) | 3 (PM_3) | 4 (PD_2) | 5 (PD_3) | 6 (FF_2) | |
|--------------|--------|---|----------|----------|----------|----------|--|
| Sample no. | | Within one month after testing slabs [kg] | | | | | |
| 1 | 2.7980 | 2.8517 | 2.6707 | 2.8772 | 2.8802 | 2.8815 | |
| 2 | 2.7688 | 2.8630 | 2.6493 | 2.8574 | 2.8937 | 2.8470 | |
| 3 | 2.7831 | 2.8919 | 2.6834 | 2.8561 | 2.9093 | 2.9189 | |
| Average [kg] | 2.7833 | 2.8689 | 2.6678 | 2.8636 | 2.8944 | 2.8825 | |
| SD [kg] | 0.0146 | 0.0207 | 0.0172 | 0.0118 | 0.0146 | 0.0360 | |
| COV [%] | 0.52 | 0.72 | 0.65 | 0.41 | 0.50 | 1.25 | |

Table 5.5 Compressive strength of drilled cores $f_{c,core}$

| Type | 1 (PC) | 2 (PM_2) | 3 (PM_3) | 4 (PD_2) | 5 (PD_3) | 6 (FF_2) | |
|---------------|--------|--|----------|----------|----------|----------|--|
| Sample no. | | Within one month after testing slabs [MPa] | | | | | |
| 1 | 23.90 | 26.81 | 22.52 | 33.08 | 32.95 | 30.12 | |
| 2 | 24.83 | 22.86 | 24.16 | 42.75 | 40.78 | 38.27 | |
| 3 | 26.30 | 31.67 | 23.85 | 32.64 | 41.95 | 23.90 | |
| fc,core [MPa] | 25.01 | 27.11 | 23.51 | 36.16 | 38.56 | 30.76 | |
| SD [MPa] | 1.21 | 4.41 | 0.87 | 5.71 | 4.89 | 7.21 | |
| COV [%] | 4.84 | 16.26 | 3.69 | 15.80 | 12.68 | 23.42 | |

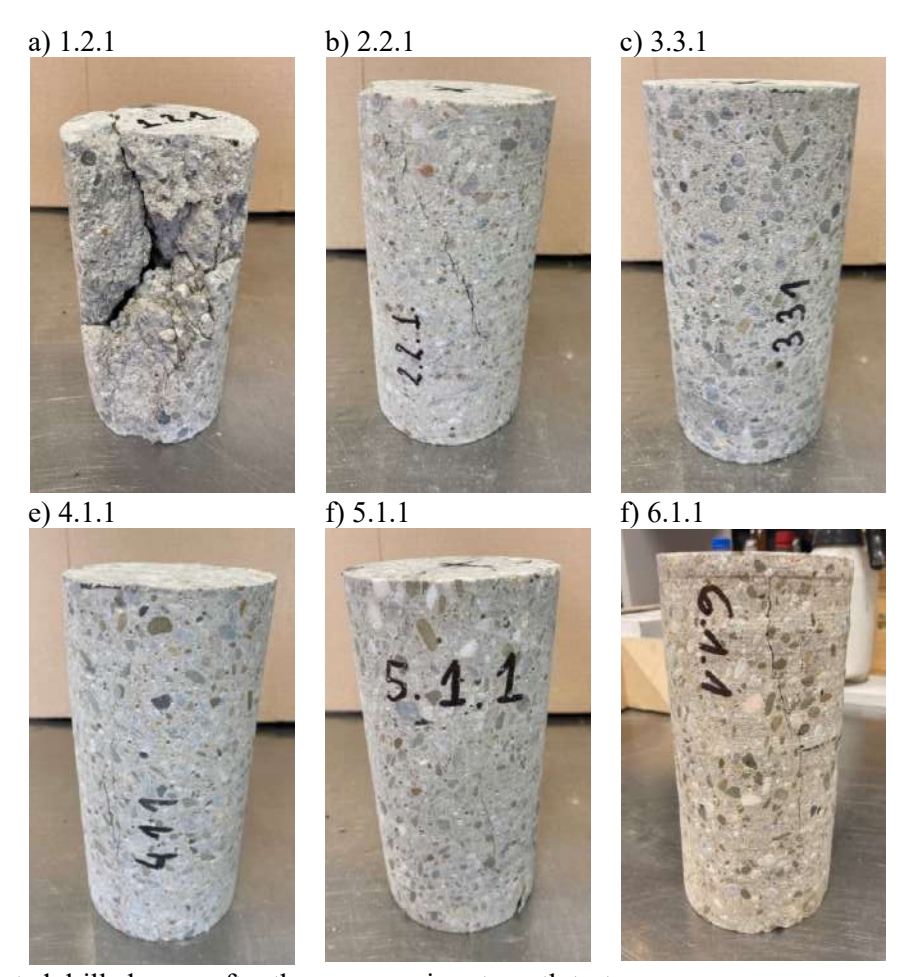


Fig. 5.2 Selected drilled cores after the compressive strength tests

As shown in Table 5.5, the $f_{c,core}$ of PM_2 and FF_2 was equal to 27.11 MPa and 30.76 MPa, representing an increase of 8% and 23%, respectively, compared to that of PC (25.01 MPa). For concretes PD_2 and PD_3, the increases in $f_{c,core}$ exceeded 44% and 54%, respectively, relative to the PC reference. However, as in the case of cast cube specimens, no definitive conclusion was drawn regarding the effect of fiber addition on compressive strength, due to the previously discussed factors. It was also observed that increasing the PD fiber dosage from 2 to 3 kg/m³ resulted in a 7% increase in $f_{c,core}$. Conversely, a 13% reduction in compressive strength was recorded for samples with

3 kg/m³ of PM fibers when compared to PM_2 specimens. These inconsistencies may have been influenced by variations in the workability of the mixtures. Moreover, in some cases, it was assessed as insufficient, potentially due to excessive fiber content or incorrect adjustment and differences in the concrete composition. Nevertheless, the influence of SyFs addition became clearly apparent after reaching $f_{c,core}$. Specifically, SyFRC core specimens exhibited ductile failure modes, maintaining structural integrity, whereas PC cores failed in a brittle manner, as illustrated in Fig. 5.2.

The compressive strength results from drilled cores and cast samples exhibited similar trends. Namely, the lowest $f_{c,core}$ values were recorded for type 3 samples, followed by types 1, 2, and 6, while types 4 and 5 showed the highest strengths. The discrepancies in strength between cores from PC and SyFRC slabs were comparable to or smaller than those observed for cast samples. Notably, $f_{c,core}$ values were consistently lower than $f_{c,cube}$ values, primarily due to inherent differences in specimen geometry, dimensions, and stress distribution patterns between cylindrical cores and cubic samples. No simple direct relationship exists between these strengths, and the ratio of cylinder strength to cube strength is known to increase significantly with higher concrete strength. Nevertheless, literature commonly cites a conversion factor of approximately 0.85 [223], [224]. Furthermore, various studies indicate that even under optimal conditions of concrete placement, compaction, and curing, core strength typically ranges from 70% to 85% of the strength of standard laboratory specimens [223]. The standard PN-EN 13791:2008 [225] similarly specifies the ratio of in-situ concrete strength to standardized specimen strength as 0.85. To enable comparison between cast cube and drilled core results, the average compressive strengths from Table 5.3 were multiplied by a factor of 0.85², accounting for both shape and extraction method differences. The obtained compressive strengths for concrete types 1-6 were 25.29, 29.04, 20.22, 38.26, 39.35, and 31.09 MPa, respectively, which align well with the core test results summarized in Table 5.5. The largest discrepancy was noted for type 3 samples, with a 14% underestimation, whereas overestimations for the other types remained below 7%.

5.1.3. Modulus of elasticity tests

The initial and stabilized modulus of elasticity of drilled cores ($E_{c0,core}$ and $E_{cs,core}$) was determined for all concrete types 1-6. The core compressive strength $f_{c,core}$, necessary for estimating the upper and lower stresses applied during the cycling loading procedure according to standard [90], was measured on separate samples to prevent damage to the steel frame (Table 5.5). A total of 18 cylindrical cores, each with nominal

dimensions of ϕ 94±1 mm diameter and 188±2 mm length, were extracted, one from each tested slab. Specimen identification corresponds to the respective slab number (1-3). Prior to testing, cores were precisely measured and weighed (Table 5.6). Testing was conducted within one month following slab testing. Summary statistics, including average values, standard deviations (SD), and coefficients of variation (COV) for $E_{c0,core}$ and $E_{cs,core}$, are presented in Table 5.7 and Table 5.8, respectively. Moreover, no dimensional correction factors were applied due to the core length-to-diameter ratio being equal to 2, what was consistent with recommendations in [223]. Finally, the $E_{cs,core}$ was adopted as the mean secant modulus of elasticity (E_{cm}) for use in subsequent analytical analysis according to [226].

Table 5.6 Weight of drilled cores

| Type | 1 (PC) | 2 (PM_2) | 3 (PM_3) | 4 (PD_2) | 5 (PD_3) | 6 (FF_2) | |
|--------------|--------|---|----------|----------|----------|----------|--|
| Sample no. | | Within one month after testing slabs [kg] | | | | | |
| 1 | 2.784 | 2.904 | 2.671 | 2.834 | 2.927 | 2.872 | |
| 2 | 2.780 | 2.852 | 2.648 | 2.887 | 2.909 | 2.859 | |
| 3 | 2.758 | 2.874 | 2.673 | 2.849 | 2.907 | 2.932 | |
| Average [kg] | 2.780 | 2.877 | 2.664 | 2.857 | 2.914 | 2.887 | |
| SD [kg] | 0.021 | 0.026 | 0.014 | 0.028 | 0.011 | 0.039 | |
| COV [%] | 0.77 | 0.91 | 0.52 | 0.96 | 0.38 | 1.35 | |

Table 5.7 Initial secant modulus of elasticity of drilled cores $E_{c0,core}$

| Type | 1 (PC) | 2 (PM_2) | 3 (PM_3) | 4 (PD_2) | 5 (PD_3) | 6 (FF_2) | |
|--------------------------|--------|--|----------|----------|----------|----------|--|
| Sample no. | | Within one month after testing slabs [MPa] | | | | | |
| 1 | 14.774 | 18.265 | 16.579 | 24.386 | 25.878 | 24.294 | |
| 2 | 16.943 | 19.295 | 15.147 | 23.590 | 25.450 | 23.214 | |
| 3 | 19.425 | 16.706 | 14.382 | 25.458 | 27.182 | 25.362 | |
| $E_{c\theta,core}$ [GPa] | 17.047 | 18.089 | 15.369 | 24.478 | 26.170 | 24.290 | |
| SD [GPa] | 2.327 | 1.303 | 1.115 | 0.937 | 0.902 | 1.074 | |
| COV [%] | 13.65 | 7.21 | 7.26 | 3.83 | 3.45 | 4.42 | |

Table 5.8 Stabilized secant modulus of elasticity of drilled cores $E_{cs,core}$

| Type | 1 (PC) | 2 (PM_2) | 3 (PM_3) | 4 (PD_2) | 5 (PD_3) | 6 (FF_2) |
|----------------|--------|----------|--------------|-----------------|----------|----------|
| Sample no. | | Within o | ne month aft | er testing slal | os [MPa] | |
| 1 | 17.419 | 22.036 | 18.406 | 27.014 | 29.321 | 27.062 |
| 2 | 20.165 | 21.801 | 18.392 | 26.473 | 29.654 | 25.968 |
| 3 | 21.659 | 20.421 | 17.263 | 27.960 | 30.728 | 27.171 |
| Ecs,core [GPa] | 19.748 | 21.419 | 18.020 | 27.149 | 29.901 | 26.734 |
| SD [GPa] | 2.151 | 0.873 | 0.656 | 0.753 | 0.735 | 0.665 |
| COV [%] | 10.89 | 4.07 | 3.64 | 2.77 | 2.46 | 2.49 |

As presented in Table 5.7 and Table 5.8, the $E_{c0,core}$ and $E_{cs,core}$ for PM 2 were 18.089 GPa and 21.419 GPa, representing increases of approximately 6% and 8%, respectively, relative to the values obtained for PC (17.047 GPa and 19.748 GPa). For concretes FF 2, PD 2, and PD 3, the enhancements in both $E_{c0,core}$ and $E_{cs,core}$ exceeded 42% and 35% compared to PC, respectively. Nevertheless, caution is warranted in attributing these increases solely to the addition of SyFs. As established in the literature, the modulus of elasticity is predominantly governed by factors such as compressive strength, cement paste quality, aggregate properties and proportions, porosity, and the incorporation of mineral admixtures [227]. Moreover, the stiffness of macro SyFs is substantially lower than that of hardened concrete, and their presence is generally expected to have a negligible effect on both $E_{c0,core}$ and $E_{cs,core}$. The results further indicated that increasing the dosage of PD and PM fibers from 2 to 3 kg/m³ provided a 7% and 10% improvement in $E_{c0,core}$ and $E_{cs,core}$, respectively, for PD fibers, but a 15% and 16% reduction for PM fibers. These inconsistent trends might have been attributed to variations in mixture workability, which was sometimes assessed insufficient due to excessive fiber content or improper adjustments and differences in the concrete mix composition. Additionally, the relatively low modulus values observed across all concrete types are likely influenced by the use of rounded river gravel aggregates with a maximum particle size of 8 mm, which may contribute to a weaker interfacial transition zone than expected. It should also be noted that concrete samples extracted from in-situ structures often show a compressive strength reduction of approximately 25-30% compared to standardized laboratory specimens, due to differences in placement, compaction, and curing conditions [223], which can also led to the decrease of the modulus of elasticity. Furthermore, minor damage sustained during core extraction may have contributed to lower than expected values of measured modulus. Finally, these findings align with prior research [228]–[230] highlighting significant discrepancies between experimentally determined moduli of elasticity and standard recommendations, with the measured values typically lower than those prescribed by relevant standards. In conclusion, the moduli of elasticity results were consistent with the compressive strength findings for both cast specimens and drilled cores, exhibiting analogous trends. The lowest values of initial $E_{c0,core}$ and stabilized $E_{cs,core}$ were observed for type 3 samples, followed sequentially by types 1, 2, and 6, whereas types 4 and 5 demonstrated the highest values. The initial modulus $E_{c0,core}$ corresponds to approximately 86%, 84%, 85%, 90%, 88%, and 91% of the stabilized modulus $E_{cs,core}$ for concrete types 1 through 6, respectively, which aligns well with previously reported results of [230], [231].

5.1.4. Splitting tensile tests

Samples for determining splitting tensile strength were obtained by halving the drilled cores previously tested for modulus of elasticity. For each concrete type, six cores ($94\pm1 \text{ x } 92\pm3 \text{ mm}$) were evaluated within one month following slab testing, resulting in a total of 36 specimens. Each specimen was weighed and measured prior to testing, and the results are summarized in Table 5.9. For concrete types 1-6, the average splitting tensile strength ($f_{spl,core}$), along with the corresponding standard deviation (SD) and coefficient of variation (COV), were calculated. Furthermore, the final row of Table 5.9 presents the axial tensile strength (f_{ct}) derived from $f_{spl,core}$ results using equation (3.3) specified in PN-EN 1992-1-1:2024-05 [33]. Fig. 5.3 illustrates selected failed specimens after the splitting tensile test, with specimen numbering indicating concrete type (1-6), slab number (1-3), and sample identifier (A or B).

Table 5.9 Splitting tensile strength of drilled cores $f_{spl,core}$

| Type | 1 (PC) | 2 (PM_2) | 3 (PM_3) | 4 (PD_2) | 5 (PD_3) | 6 (FF_2) |
|-----------------------------------|--------|----------|--------------|-----------------|-----------|----------|
| Sample no. | | Within | one month af | ter testing sla | abs [MPa] | |
| 1A | 2.23 | 2.44 | 2.12 | 2.68 | 3.63 | 2.45 |
| 1B | 2.27 | 2.52 | 1.94 | 2.83 | 3.31 | 2.90 |
| 2A | 2.19 | 2.30 | 2.25 | 3.20 | 2.89 | 2.57 |
| 2B | 1.86 | 2.18 | 2.17 | 3.34 | 3.17 | 2.58 |
| 3A | 2.08 | 1.88 | 1.54 | 3.34 | 2.72 | 2.76 |
| 3B | 2.10 | 1.97 | 2.24 | 2.64 | 3.35 | 3.01 |
| f _{spl,core} [MPa] | 2.12 | 2.22 | 2.04 | 3.00 | 3.18 | 2.71 |
| SD [MPa] | 0.15 | 0.26 | 0.27 | 0.33 | 0.33 | 0.22 |
| COV [%] | 7.01 | 11.58 | 13.23 | 10.85 | 10.33 | 7.97 |
| $f_{ct} = 0.9 f_{spl,core}$ [MPa] | 1.91 | 1.99 | 1.84 | 2.70 | 2.86 | 2.44 |

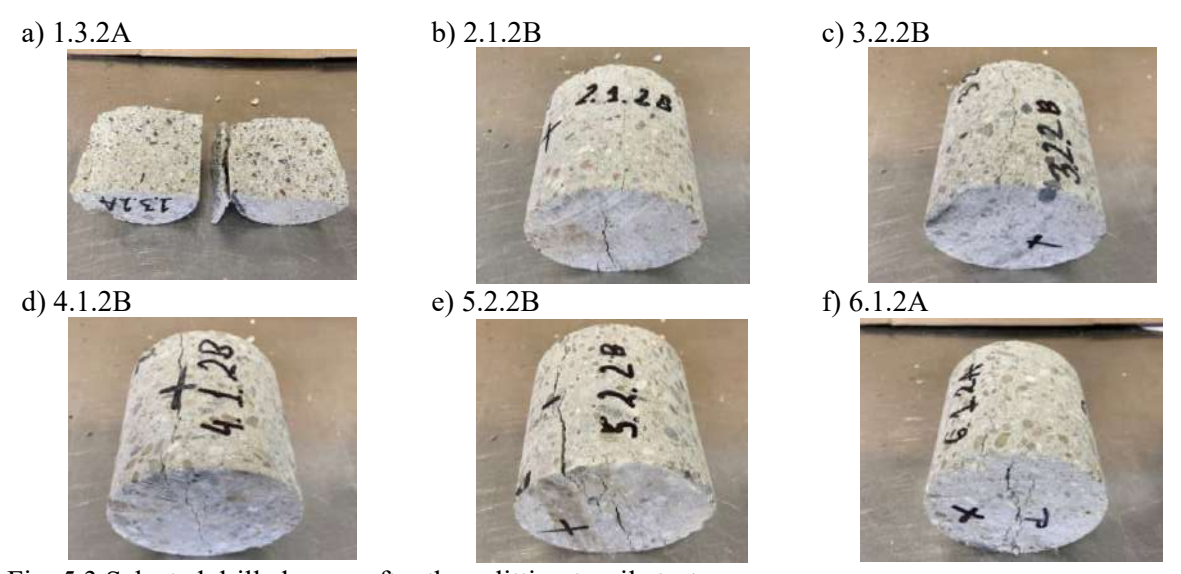


Fig. 5.3 Selected drilled cores after the splitting tensile tests

As presented in Table 5.9, the *f_{spl,core}* of PM_3 and FF_2 was 2.04 and 2.71 MPa, representing a 4% decrease and a 28% increase, respectively, relative to that of PC (2.12 MPa). For concretes PD 2 and PD 3, the improvements in f_{spl,core} exceeded 41% and 49%, respectively, compared to reference samples of type 1. Although the findings reported in literature indicate that the addition of macro SyFs increases the splitting tensile strength, improvements greater than 30% are more characteristic for SFRCs than SyFRCs. Overall, the observed variability in $f_{spl,core}$ values across concrete types was primarily attributed to differences in compressive strength. Furthermore, an increase in PD fiber dosage from 2 to 3 kg/m³ resulted in a 6% gain in $f_{spl,core}$, while the same dosage increase for PM fibers led to an 8% reduction. These inconsistent trends might have been attributed to variations in mixture workability, which was sometimes assessed insufficient due to excessive fiber content or improper adjustments and differences in the concrete mix composition. Finally, the $f_{spl,core}$ exhibited consistent trends with both compressive strength and moduli of elasticity results. Specifically, the lowest values were recorded for type 3 specimens, followed by types 1, 2, and 6, while types 4 and 5 showed the highest splitting tensile strength.

Furthermore, the calculated ratio of axial tensile strength f_{ct} to compressive strength $f_{c,core}$ ranged between 8% and 9%, depending on the concrete type, what was slightly below the expected 10% threshold. This discrepancy might have been explained by several factors. Firstly, testing was conducted on non-standardized specimens with a length-to-diameter ratio of 1. Then, concrete samples drilled from the construction typically exhibits a 25-30% reduction in strength relative to standard specimens due to differences in placement, compaction, and curing [223]. Finally, the drilled cores may have sustained minor damage during extraction or previously performed elasticity modulus testing, potentially reducing their splitting tensile strength.

5.1.5. Flexural tensile strength tests

For each concrete type, three beams with dimensions of 150 ± 1 x 150 ± 1 x 550 ± 2 mm were tested to evaluate the flexural tensile behavior, with specimens numbered from 1 to 3, resulting in a total of 18 samples. Prior to testing, each beam was measured and weighed (Table 5.10). The flexural tests were conducted within one month following slab testing of corresponding concrete type. Based on the *F-CMOD* curves, the $f_{R,j}$ -*CMOD* graphs were derived using equations (3.29) and (3.30) according to [29] (Chapter 3.3.2.3), as illustrated in Fig. 5.4. For each concrete type, the average $f_{R,j}$ -*CMOD* curve was derived and is presented in Fig. 5.5, labeled from 1 to 6 for

concrete types 1-6, respectively. The limit of proportionality $f_{ct,L}$ and residual flexural tensile strengths: $f_{R,1}$, $f_{R,2}$, $f_{R,3}$, $f_{R,4}$ obtained from the 3PBT for individual beams and from the averaged curves, are summarized in Table 5.11.

Table 5.10 Weight of cast beams

| Type | 1 (PC) | 2 (PM_2) | 3 (PM_3) | 4 (PD_2) | 5 (PD_3) | 6 (FF_2) | | |
|--------------|--------|---|----------|----------|----------|----------|--|--|
| Sample no. | | Within one month after testing slabs [kg] | | | | | | |
| 1 | 27.703 | 28.028 | 25.791 | 28.842 | 28.145 | 27.998 | | |
| 2 | 27.692 | 28.176 | 25.930 | 28.147 | 28.092 | 27.877 | | |
| 3 | 27.987 | 28.355 | 26.187 | 28.032 | 28.359 | 27.698 | | |
| Average [kg] | 27.794 | 28.186 | 25.969 | 28.340 | 28.199 | 27.858 | | |
| SD [kg] | 0.167 | 0.164 | 0.201 | 0.438 | 0.141 | 0.151 | | |
| COV [%] | 0.60 | 0.58 | 0.77 | 1.55 | 0.50 | 0.54 | | |

For the PC samples, the $f_{ct,L}$ was determined to be 3.499 MPa. The incorporation of 2 kg/m³ of PM fibers led to a 7.6% increase in $f_{ct,L}$ (Table 5.11). This finding was consistent with the author's previous research, which demonstrated a 5% improvement in flexural tensile strength, from 3.26 MPa to 3.42 MPa, due to the inclusion of the same fiber type and dosage [72]. Similarly, Rucka et al. [232] reported a 6.8% enhancement in $f_{ct,L}$ for concrete incorporating 2 kg/m³ of identical PM fibers. Moreover, Luna et al. [133] found that the addition of 2.7 kg/m³ of copolymer fibers ($l_f/d_f = 38/2.0 \times 0.5 \text{ mm}$) resulted in a 6.4% increase in $f_{ct,L}$. Consequently, these findings indicated a comparable magnitude of improvement in flexural tensile strength observed across several studies. Then, beams without fibers exhibited a brittle failure mode immediately upon reaching $f_{ct,L}$, thus precluding the determination of residual flexural tensile strengths (see Fig. 5.4a and Fig. 5.5). In contrast, all SyFRC beams were characterized by post-cracking strength, with a gradual reduction in load and increasing CMOD values, indicative of ductile softening behavior (see Fig. 5.4b-f and Fig. 5.5). Fig. 5.6a illustrates the complete separation of PC beams post-failure, while Fig. 5.6b-f shows the SyFRC specimens maintaining structural integrity after testing. These observations confirmed the significant enhancement in ductility typically associated with macro SyFs addition.

In the case of type 3 beams, no improvement in $f_{ct,L}$ was observed relative to PC samples, with results indicating an 11.2% reduction. This decrease was likely attributable to compromised workability due to excessive fiber dosage, resulting in non-uniform fiber distribution and poor matrix integrity (Table 5.11). In order to evaluate fiber distribution across the notch cross-section, the beams were bisected after the flexural tests (Fig. 5.7). As shown in Fig. 5.7c, the presence of fiber agglomerates was identified in samples 3.2 and 3.3, what undoubtedly led to the deterioration of the

mechanical performance of PM_3 samples. Furthermore, for type 4 and 5 specimens, an increase in PD fiber dosage from 2 kg/m³ to 3 kg/m³ did not result in any enhancing effect on $f_{ct,L}$. In fact, a 13% reduction was observed, with values decreasing from 6.303 MPa to 5.504 MPa (Table 5.11). These results were in agreement with the findings of [72], where a 1 kg/m³ increase in SyFs amount led to a 5% decrease in flexural tensile strength (from 3.63 MPa for PD_2 to 3.44 MPa for PD_3), most likely due to non-uniform fiber distribution. It should be noted that previous studies have also reported reductions in flexural tensile strength despite fiber addition or increased fiber dosage [111], [118], [189]. These findings emphasized that only quality-controlled, well-designed, well-mixed, and properly cured concrete can result in the mechanical benefits of fiber reinforcement [233], [234]. Otherwise, strength properties may deteriorate and the design requirements of the material will not be fulfilled.

The influence of fiber type was evident in the flexural performance of type 2 and type 6 beams, both containing a total fiber dosage of 2 kg/m³. Specifically, the hybrid blend used in type 6 beams, comprising 95% twisted multifilament and 5% fibrillated fibers, showed a nearly 31% higher $f_{ct,L}$ (Table 5.11) than the type 2 concrete containing 100% twisted multifilament fibers of comparable properties (Table 4.1). This improvement can be attributed to the fibrillated fibers, whose smaller diameter may have been more effective in bridging microcracks during the initial loading phase. Finally, the $f_{ct,L}$ results partially aligned with trends observed in compressive strength, splitting tensile strength, and modulus of elasticity results. Specifically, the lowest $f_{ct,L}$ was again recorded for type 3 samples, followed by types 1, 2, and 6. However, an atypical trend was observed for concretes types 4 and 5, with type 4 exhibiting the highest $f_{ct,L}$, in contrast to the corresponding results obtained from other strength and stiffness measurements.

A comparative analysis of the residual flexural tensile strengths ($f_{R,j}$) between PD_2 and PD_3 beams indicated that only in the case of $f_{R,l}$ did the specimens containing 2 kg/m³ of fibers outperformed those with 3 kg/m³, achieving an average increase of approximately 40%. For the subsequent residual strengths $f_{R,2}$, $f_{R,3}$, and $f_{R,4}$ higher values were recorded for the type 5 beams, with improvements of 89%, 85%, and 77%, respectively, relative to type 4 specimens. A similar pattern was observed in the study [72], where increasing the dosage of the same PD fibers from 2 kg/m³ to 3 kg/m³ resulted in a 41% reduction in $f_{R,l}$, but increases of 35%, 27%, and 28% in $f_{R,2}$, $f_{R,3}$, and $f_{R,4}$, respectively. These observations aligned with existing literature results [111], [118], [132], which confirmed that higher fiber dosage enhanced post-cracking performance, provided that the workability of the mixture remained adequate.

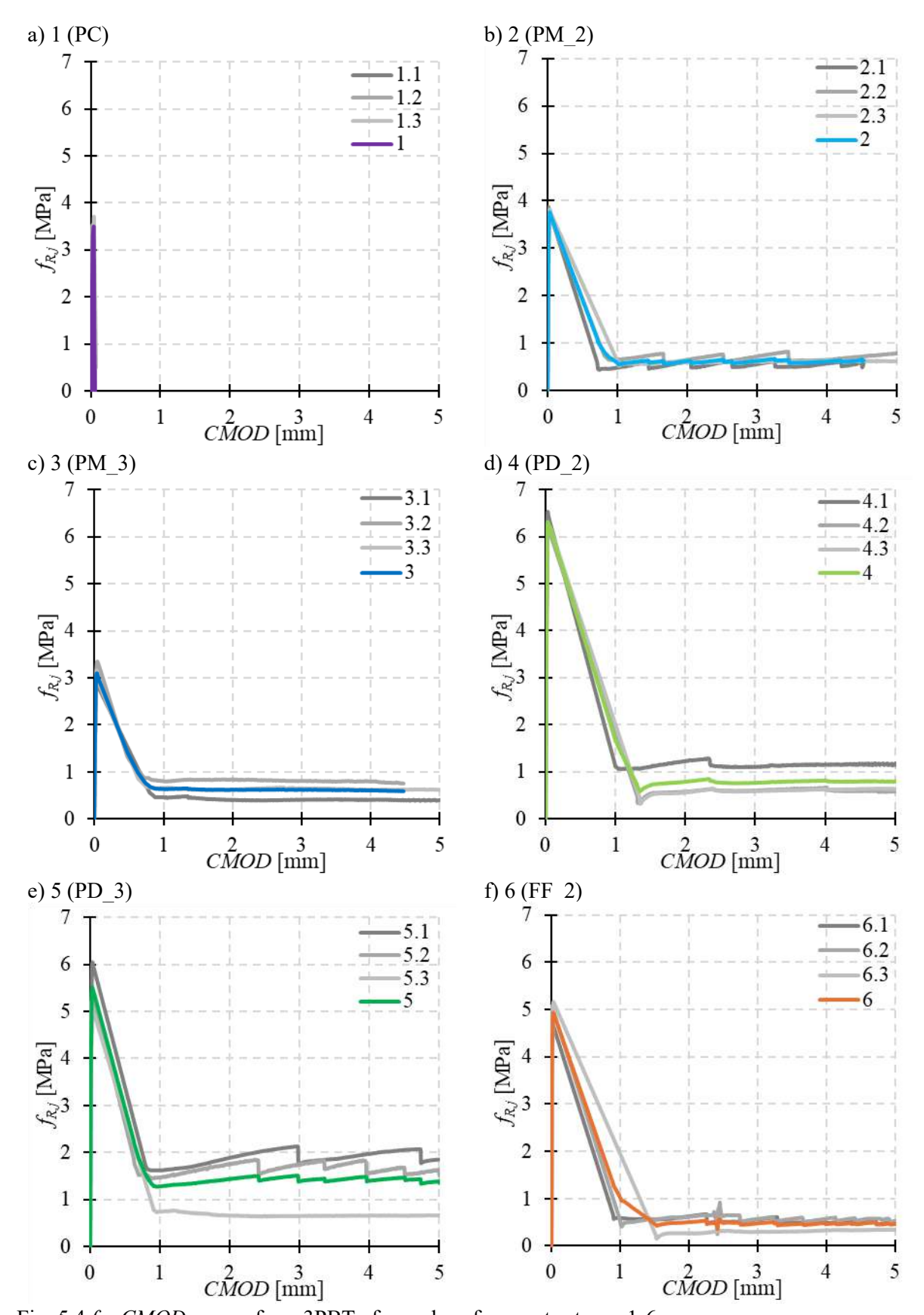


Fig. 5.4 $f_{R,j}$ -CMOD curves from 3PBT of samples of concretes types 1-6

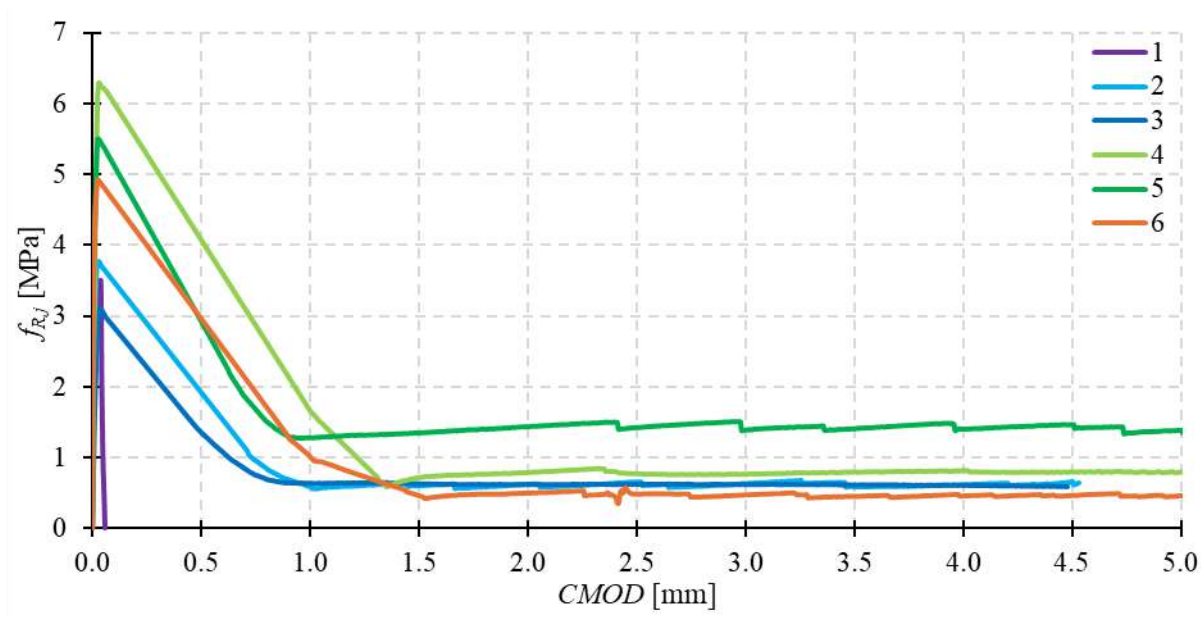


Fig. 5.5 Averaged $f_{R,j}$ -CMOD curves from 3PBT of concretes types 1-6

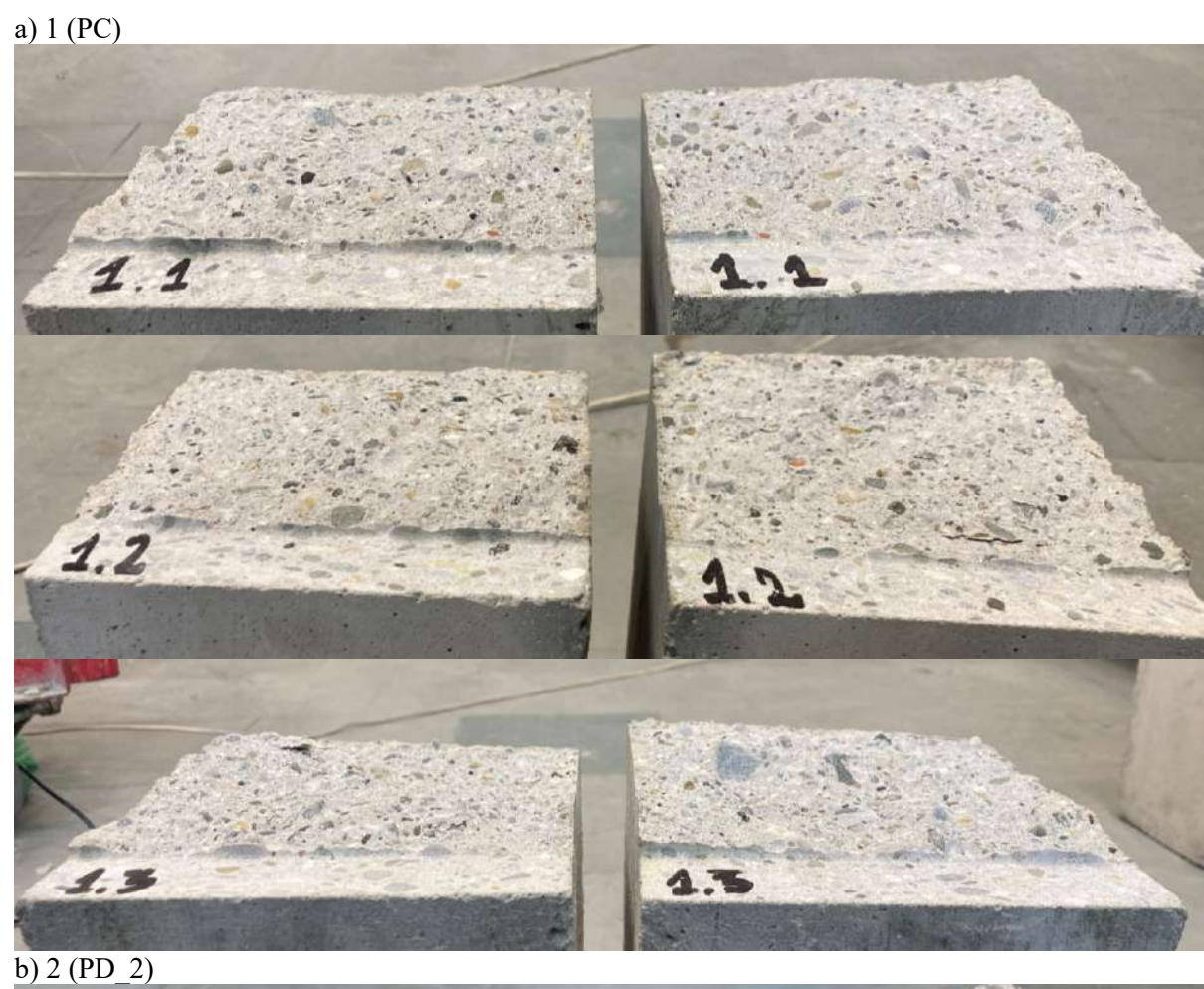
Table 5.11 Limit of proportionality $f_{ct,L}$ and residual flexural tensile strengths $f_{R,j}$ for samples of concretes types 1-6 and their average

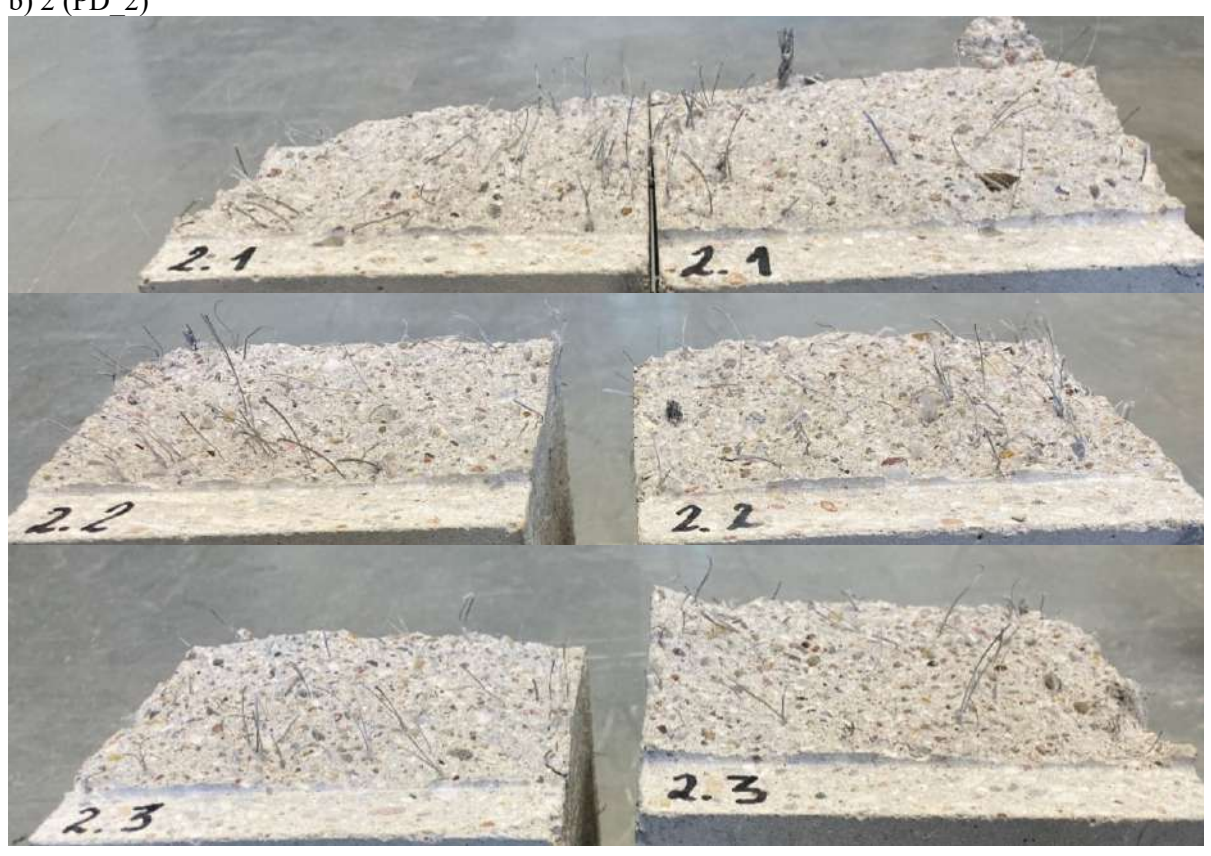
| Sample no. | f _{ct,L} [MPa] | $f_{R,1}$ [MPa] | $f_{R,2}$ [MPa] | $f_{R,3}$ [MPa] | $f_{R,4}$ [MPa] |
|------------|-------------------------|-----------------|-----------------|-----------------|-----------------|
| 1.1 | 3.484 | 0.000 | 0.000 | 0.000 | 0.000 |
| 1.2 | 3.530 | 0.000 | 0.000 | 0.000 | 0.000 |
| 1.3 | 3.689 | 0.000 | 0.000 | 0.000 | 0.000 |
| 1 | 3.499 | 0.000 | 0.000 | 0.000 | 0.000 |
| 2.1 | 3.873 | 1.573 | 0.478 | 0.589 | 0.504 |
| 2.2 | 3.715 | 1.923 | 0.744 | 0.754 | 0.623 |
| 2.3 | 3.816 | 2.249 | 0.567 | 0.597 | 0.618 |
| 2 | 3.765 | 1.915 | 0.596 | 0.646 | 0.582 |
| 3.1 | 2.931 | 1.473 | 0.440 | 0.395 | 0.412 |
| 3.2 | 3.342 | 1.271 | 0.829 | 0.813 | 0.787 |
| 3.3 | 3.153 | 1.334 | 0.617 | 0.652 | 0.633 |
| 3 | 3.107 | 1.359 | 0.629 | 0.620 | 0.611 |
| 4.1 | 6.525 | 3.884 | 1.103 | 1.113 | 1.138 |
| 4.2 | 6.161 | 4.108 | 0.532 | 0.603 | 0.635 |
| 4.3 | 6.239 | 4.250 | 0.500 | 0.587 | 0.605 |
| 4 | 6.303 | 4.081 | 0.711 | 0.768 | 0.793 |
| 5.1 | 6.046 | 3.377 | 1.713 | 2.037 | 1.860 |
| 5.2 | 5.438 | 2.617 | 1.612 | 1.583 | 1.696 |
| 5.3 | 5.195 | 2.776 | 0.712 | 0.646 | 0.654 |
| 5 | 5.504 | 2.923 | 1.346 | 1.422 | 1.403 |
| 6.1 | 4.687 | 2.477 | 0.548 | 0.502 | 0.486 |
| 6.2 | 5.063 | 2.811 | 0.545 | 0.618 | 0.563 |
| 6.3 | 5.162 | 3.600 | 0.277 | 0.309 | 0.295 |
| 6 | 4.926 | 2.962 | 0.457 | 0.476 | 0.448 |

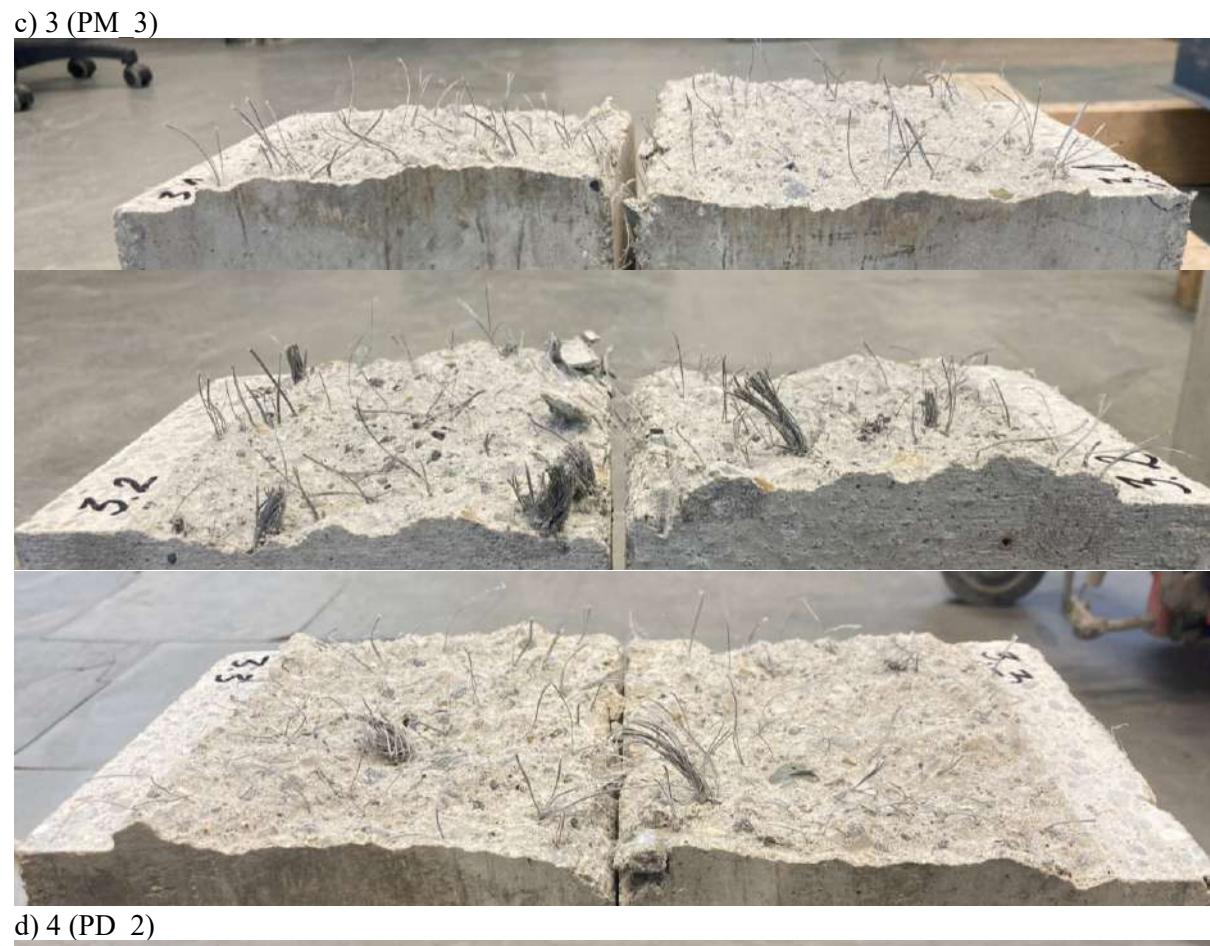


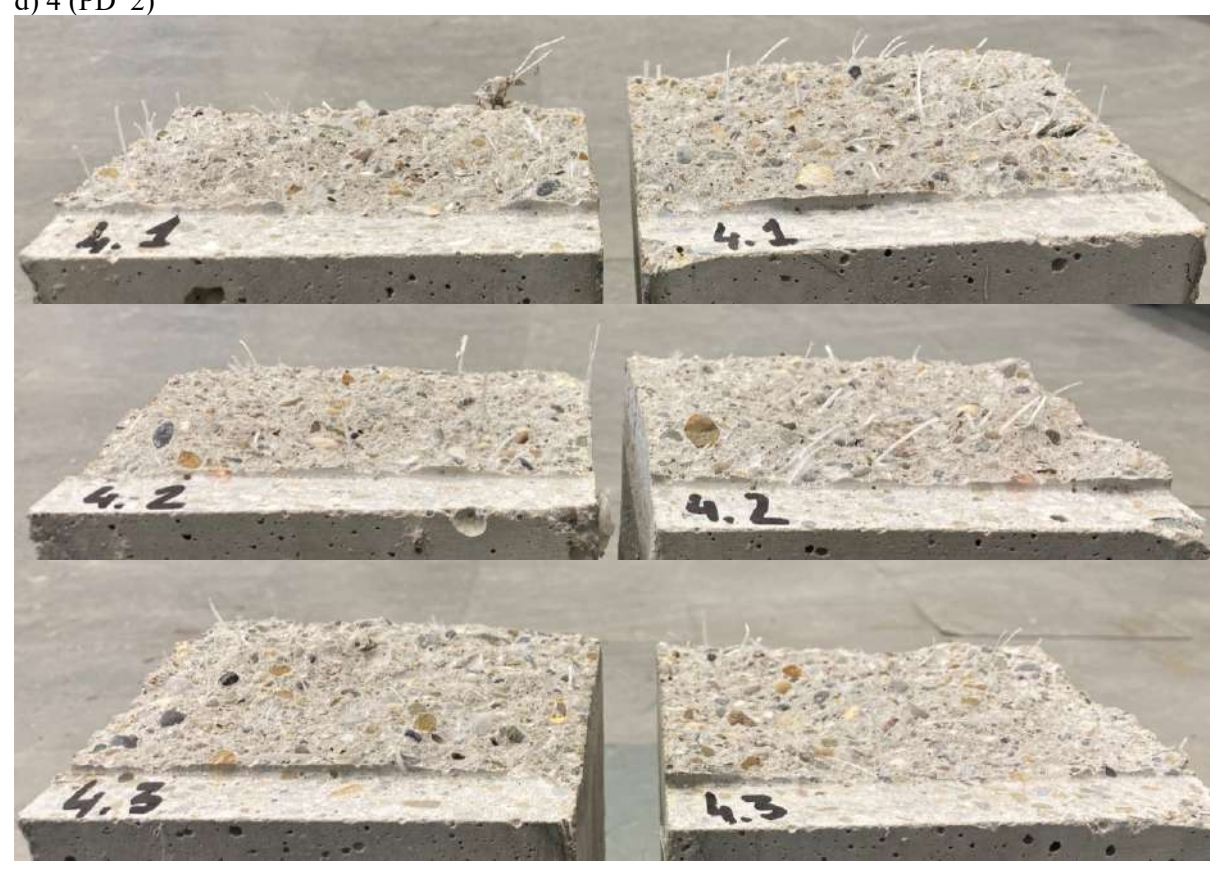
Fig. 5.6 Beam crack morphology after 3PBT with brittle and ductile type of failure for PC and SyFRCs, respectively (single crack formation at the tip of the notch and propagation upwards)

Concerning the influence of fiber type on residual flexural response, it was found that the addition of 2 kg/m³ of FF fiber blend was less effective than the same dosage of PM fibers. This difference could have been partially attributed to the lower content of macrofibers in type 6 beams (95% of 2 kg/m³, i.e., 1.9 kg/m³), compared to the 2 kg/m³ of macro SyFs in type 2 samples. Additionally, fiber distribution appeared to have played a role, since FF fibers exhibited a greater tendency to agglomerate and form clusters in type 6 specimens (Fig. 5.7f), as opposed to the more uniformly distributed PM fibers observed in type 2 beams (Fig. 5.7b). Notably, PD fibers were less prone to bundling than the other SyFs (Fig. 5.7d and Fig. 5.7e), which may have contributed to their superior post-cracking behavior.









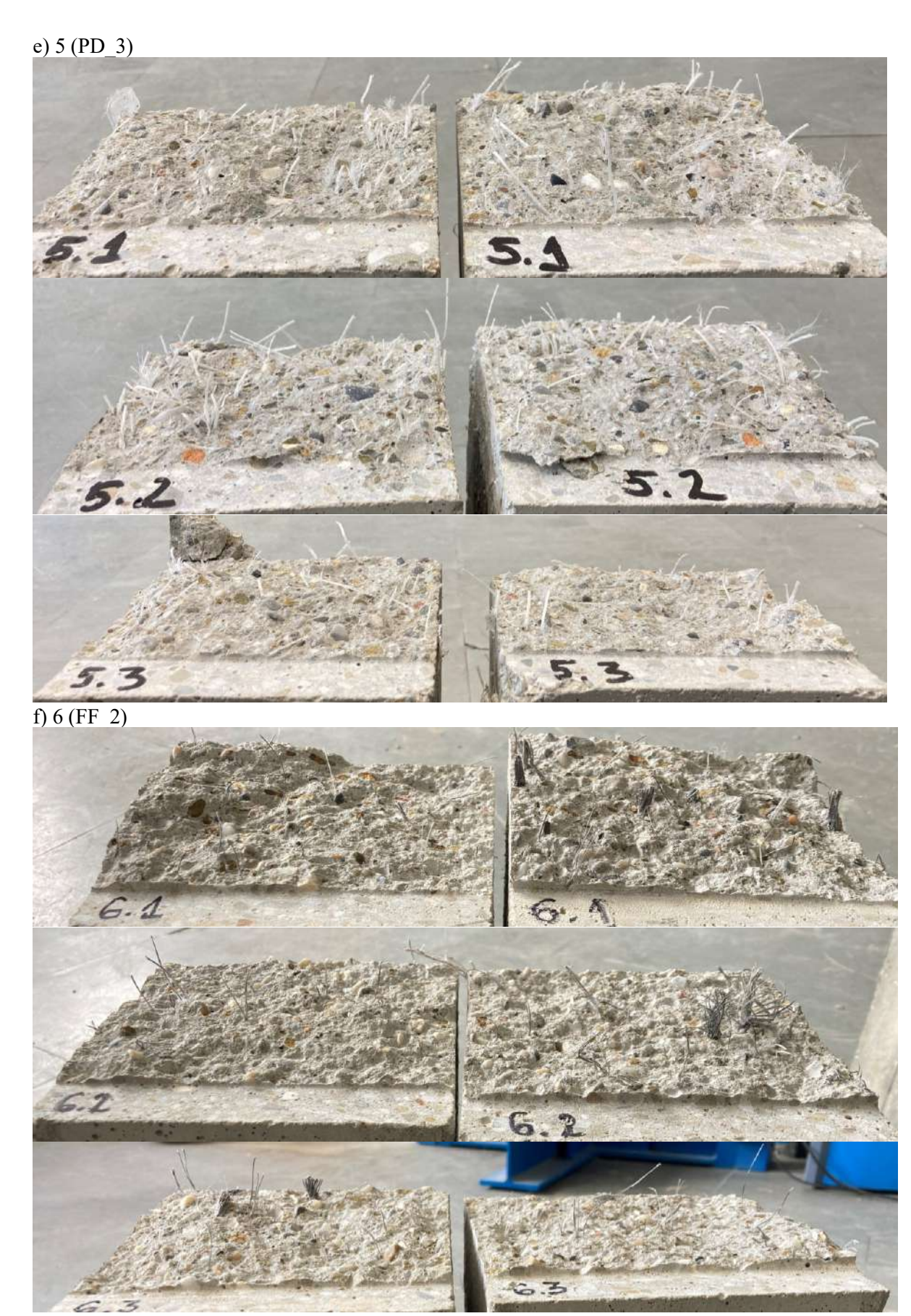


Fig. 5.7 Notch cross-section of broken beams after 3PBT (fiber distribution)

The significant variation in flexural tensile strengths observed across concrete types 1-6 required careful consideration. Specifically, these inconsistencies were likely attributable to variations in mixture workability, which was sometimes assessed insufficient due to excessive fiber content or improper adjustments and differences in the concrete mixture composition. Consequently, to enable a more objective comparison of flexural performance irrespective of strength discrepancies, standardized $f_{R,f}$ -CMOD curves were derived and are presented in Fig. 5.8. This approach allowed for the evaluation of flexural behavior trends across different concrete types. Namely, the standardized diagrams revealed that the increased fiber dosage generally improved post-cracking flexural behavior of beams. Among the concretes with a fiber volume fraction $V_f = 2 \text{ kg/m}^3$, the PM fibers exhibited the most favorable performance in terms of residual flexural tensile strength, followed by PD and FF fibers. Conversely, at a dosage of 3 kg/m³, PD fibers demonstrated superior effectiveness compared to PM fibers.

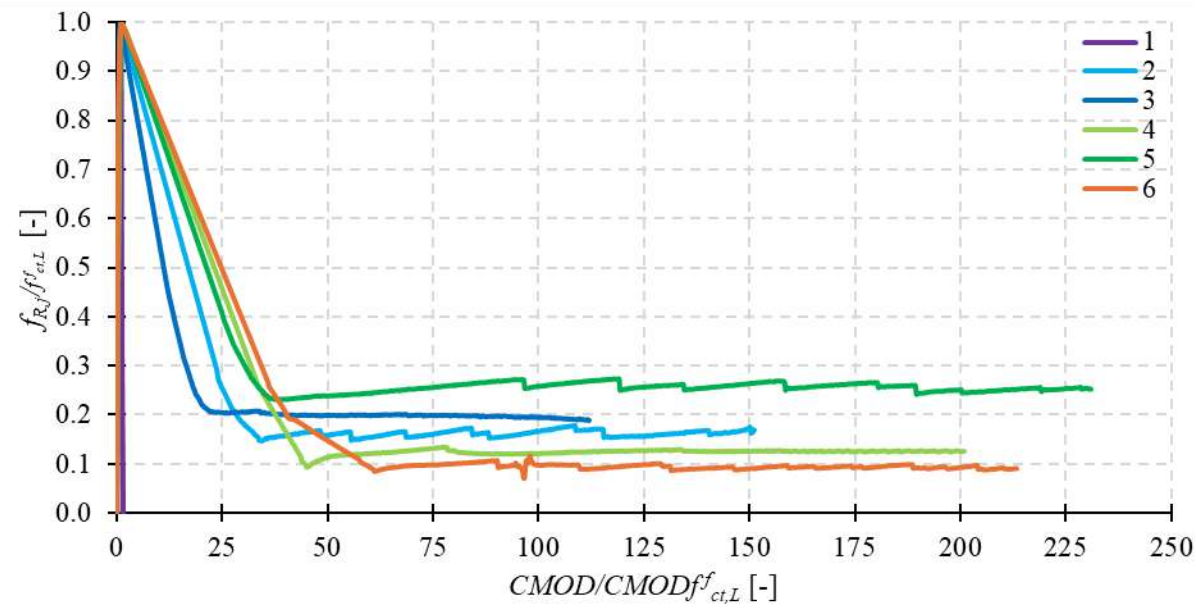


Fig. 5.8 Standardized averaged $f_{R,i}$ -CMOD curves from 3PBT of concretes types 1-6

The failure mechanism in all tested beams was governed by the development of a quasi-vertical crack initiating at the notch tip and propagating upwards (Fig. 5.6). As a result, deformations were consistently concentrated in the notch plane, while the remaining parts of the specimens exhibited minimal inelastic response. Experimental results also indicated the presence of abrupt vertical jumps in the $f_{R,j}$ -CMOD curves during the post-cracking stage in selected specimens, most notably beam types 2, 5, and 6 (Fig. 5.4). Although such discontinuities were frequently attributed in literature to fiber rupture or pull-out from the cementitious matrix, the present study identified a different cause. Detailed inspection revealed that the observed jumps resulted from the sudden

slippage of the beams over the steel supporting rollers. This issue was first detected during bending tests on beam types 6 (Fig. 5.4f) and type 2 (Fig. 5.4b). The sequence of 3PBTs followed the same order as the slab testing program: types 6, 2, 3, 1, 4, and 5. To resolve the slippage problem, the supports were lubricated with oil prior to testing the type 3 beams. As illustrated in Fig. 5.4c and Fig. 5.4d, this solution proved effective, resulting in smoother $f_{R,j}$ -CMOD curves for beam types 3 and 4. During testing of type 5 beams (Fig. 5.4e), re-lubrication of the rollers was necessary to ensure stable support conditions.

Fracture energy (G_F) is defined as an amount of work required to generate a unit crack area [235], [236]. It was calculated as the area under the F-CMOD curve up to CMOD = 3.5 mm divided by the ligament cross-sectional area (Fig. 5.9). The average G_F values for beams types 2, 3, 4, 5, and 6 were approximately 28, 25, 49, 53, and 34 times higher, respectively, than that of type 1. These results confirmed a significant improvement in fracture energy and ductility for SyFRCs compared to PC samples. The highest fracture energy value, 1090 N/m, was obtained for the SyFRC containing 3 kg/m³ of PD fibers (type 5), whereas the lowest value, 514 N/m, was recorded for type 3 beams with 3 kg/m³ of PM fibers.

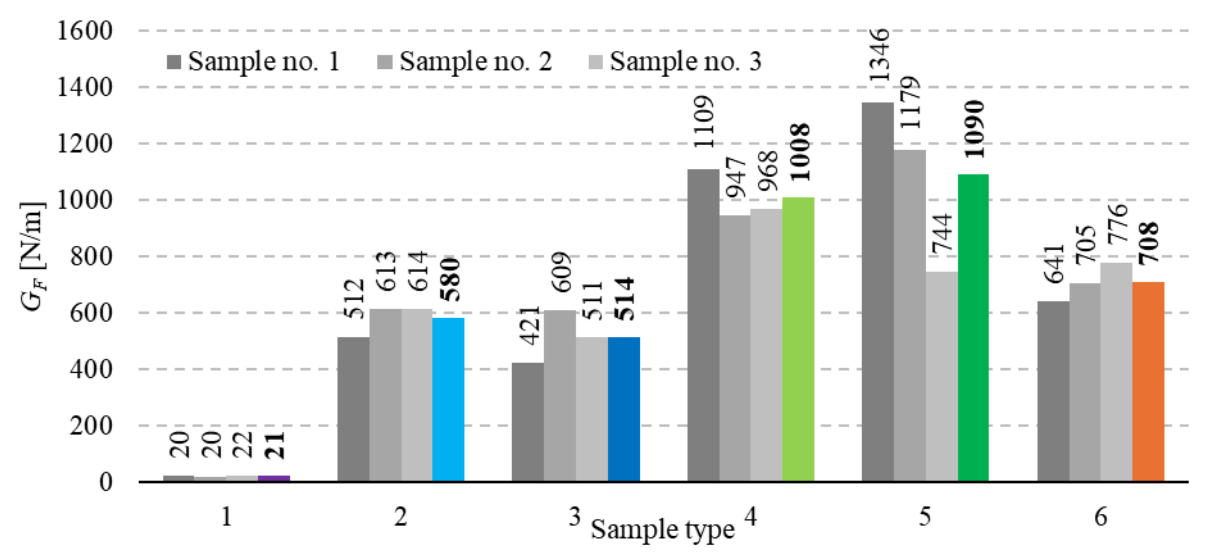


Fig. 5.9 Fracture energy G_F of samples of concretes types 1-6 and their average

Empirical equations for estimating the maximum flexural tensile strength of concrete with and without fibers, as presented in Chapter 3.4.1.7, were compared with the experimental results (Table 5.12). In the application of equation (3.41), a coefficient $\lambda = 0.35$ was assumed, and the cylindrical compressive strength (f_c) was calculated as 85% of the cubic compressive strength $f_{c,cube}$, based on the values provided in Table 5.3 [224]. Equations (3.42), (3.43), and (3.44), developed specifically for FRC, were applied

only to the specimens incorporating fibers. However, equations (3.43) and (3.44) required the knowledge of the flexural tensile strength of a reference PC, which could not be determined for beams types 4-6. In these cases, the compressive strengths differed too significantly from that of type 1 (Table 5.3), thereby precluding their use as a valid reference. Moreover, specimens of type 3 exhibited notable workability deterioration, which ultimately contributed to reduced compressive strength. Lastly, equation (3.40) from PN-EN 1992-1-1:2008 [30] was validated using the axial tensile strength f_{ct} obtained from splitting tensile tests performed on cores drilled from the tested slabs.

As shown in Table 5.12, the equation proposed by Blazy et al. [72] (equation (3.44)) provided an accurate estimation of the flexural tensile strength for type 2 concrete, closely aligning with the experimental results. In contrast, the formula by Swamy and Mangat [71] (equation (3.43)) showed less satisfactory predictions. The equation proposed by Glinicki [70] (equation (3.42)) generally underestimated the flexural tensile strength (f_{fl}) for most cases, however, for PM 3, the predicted value was 26% higher than the experimentally obtained $f_{ct,L}$. Despite certain concerns discussed in Chapter 3.3.2.3, the equation developed by Legeron and Paultre [69] (equation (3.41)) demonstrated good predictive accuracy for concretes with $f_{c,cube} \leq 40$ MPa, with a maximum deviation of 7%. For such concretes, this equation may be particularly useful when data regarding the flexural tensile strength of a reference PC and/or information about the type and dosage of SyFs are unavailable. However, for concretes with higher compressive strengths, equation (3.41) significantly underestimated f_{fl} . Finally, the use of equation (3.40) from PN-EN 1992-1-1:2008 [30] increasingly underestimated the f_{fl} as concrete compressive strength increased (with the exception of concrete type 5), resulting in unsatisfactory predictions of f_{fl} .

Table 5.12 Flexural tensile strength of tested samples of concretes types 1-6 calculated using selected empirical equations [MPa]

| Sample | Experimental | Acc. to eq. |
|----------|--------------|-------------|-------------|-------------|-------------|-------------|
| no. | $f_{ct,L}$ | (3.41) | (3.42) | (3.43) | (3.44) | (3.40) |
| 1 (DC) | 3.499 | 3.361 | | | | 2.817 |
| 1 (PC) | (100%) | (96%) | - | - | _ | (81%) |
| 2 (PM_2) | 3.765 | 3.685 | 2.858 | 4.287 | 3.676 | 2.935 |
| | (100%) | (98%) | (76%) | (114%) | (98%) | (78%) |
| 2 (DM 2) | 3.107 | 2.895 | 3.922 | | | 2.714 |
| 3 (PM_3) | (100%) | (93%) | (126%) | - | _ | (87%) |
| 4 (DD 2) | 6.303 | 4.429 | 2.149 | | | 3.983 |
| 4 (PD_2) | (100%) | (70%) | (34%) | - | _ | (63%) |
| 5 (DD 2) | 5.504 | 4.512 | 2.858 | | | 4.219 |
| 5 (PD_3) | (100%) | (82%) | (52%) | - | _ | (77%) |
| 6 (FE 2) | 4.926 | 3.857 | 2.858 | | | 3.599 |
| 6 (FF_2) | (100%) | (78%) | (58%) | _ | _ | (73%) |

5.1.6. Summary

Significant discrepancies in workability, compressive strength, splitting tensile strength, flexural tensile strength, and modulus of elasticity among concrete types 1-6 cannot be disregarded. As previously discussed, these inconsistencies may result from excessive fiber dosage, as well as variations in concrete composition caused by changing weather conditions affecting aggregate humidity and the use of materials from different deliveries, due to the extended concreting period. Consequently, direct comparison of results across all tested concrete types, both small-scale and large-scale slab specimens, was not considered methodologically valid. To assess the effect of optimal fiber addition on mechanical performance, concrete types 1 and 2 were compared. In contrast, the comparison between types 1 and 3 aimed to illustrate the adverse impact of excessive fiber content. The effect of fiber dosage was evaluated through a comparison of concretes types 4 and 5, while the influence of fiber type was examined by comparing types 2 and 6. The assumptions guiding the comparative analysis of material properties are summarized in Table 5.13. Furthermore, a complete overview of the tested mechanical properties for concrete types 1-6 is provided in Table 5.14.

Table 5.13 Assumptions for the further comparative analysis of cubes, cores, and beams

| Comparison object | Assessment subject | | |
|---|---------------------------------------|--|--|
| Samples type 1 (PC) vs. type 2 (PM_2) | Influence of optimal fiber addition | | |
| Samples type 1 (PC) vs. type 3 (PM_3) | Influence of excessive fiber addition | | |
| Samples type 4 (PD_2) vs. type 5 (PD_3) | Influence of fiber dosage | | |
| Samples type 2 (PM_2) vs. type 6 (FF_2) | Influence of fiber type | | |

Table 5.14 Mechanical properties of concretes types 1-6

| Property | 1 (PC) | 2 (PM_2) | 3 (PM_3) | 4 (PD_2) | 5 (PD_3) | 6 (FF_2) |
|-----------------------------|--------|----------|----------|----------|----------|----------|
| $f_{c,cube}$ [MPa] | 35.01 | 40.19 | 27.99 | 52.95 | 54.46 | 43.03 |
| $f_{c,core}$ [MPa] | 25.01 | 27.11 | 23.51 | 36.16 | 38.56 | 30.76 |
| $E_{c0,core}$ [GPa] | 17.047 | 18.089 | 15.369 | 24.478 | 26.170 | 24.290 |
| $E_{cs,core}$ [GPa] | 19.748 | 21.419 | 18.020 | 27.149 | 29.901 | 26.734 |
| f _{spl,core} [MPa] | 2.12 | 2.22 | 2.04 | 3.00 | 3.18 | 2.71 |
| f_{ct} [MPa] | 1.91 | 1.99 | 1.84 | 2.70 | 2.86 | 2.44 |
| $f_{ct,L}$ [MPa] | 3.499 | 3.765 | 3.107 | 6.303 | 5.504 | 4.926 |
| $f_{R,I}$ [MPa] | 0.000 | 1.915 | 1.359 | 4.081 | 2.923 | 2.962 |
| $f_{R,2}$ [MPa] | 0.000 | 0.596 | 0.629 | 0.711 | 1.346 | 0.457 |
| $f_{R,3}$ [MPa] | 0.000 | 0.646 | 0.620 | 0.768 | 1.422 | 0.476 |
| $f_{R,4}$ [MPa] | 0.000 | 0.582 | 0.611 | 0.793 | 1.403 | 0.448 |

5.1.6.1 Influence of fiber addition

The comparative analysis of type 1 and type 2 specimens demonstrated that the incorporation of 2 kg/m³ of macro SyFs led to an 8-15% increase in compressive strength, depending on the sample type. Notably, the beneficial effect of PM fiber addition was more pronounced in cast specimens than in core-drilled ones. The initial and stabilized modulus of elasticity for PM_2 increased by 6% and 8%, respectively, compared to PC. Furthermore, the addition of PM fibers enhanced the splitting tensile strength and flexural tensile strength by 4% and 8%, respectively. The influence of fiber reinforcement became particularly evident beyond the peak flexural load: PM_2 specimens exhibited a ductile failure mode with significant residual strength, whereas PC specimens failed in a brittle manner. These mechanical response differences were also reflected by the fracture energy results. In summary, the addition of 2 kg/m³ of PM fibers enhanced mechanical properties of concrete, improving both its strength and post-cracking ductility.

The excessive dosage of PM fibers significantly compromised the workability of the mixture, which consequently led to a decrease of selected mechanical properties of concrete. Specifically, specimens containing 3 kg/m³ of PM fibers exhibited a reduction in compressive strength of 6% for core-drilled samples and 20% for cast cubes, relative to the PC reference. In addition, the initial and stabilized modulus of elasticity for PM_3 was 10% and 9% lower, respectively, compared to samples without SyFs. The elevated fiber dosage also led to reductions in splitting tensile strength and flexural tensile strength by 4% and 11%, respectively. However, despite the reduction in peak strengths, the presence of fibers provided a ductile failure mode with the preservation of residual strength, in contrast to the brittle failure observed in PC specimens. This conclusion was also supported by the fracture energy results. In conclusion, while the incorporation of 3 kg/m³ of PM fibers led to a decrease of the selected peak strengths of concrete, it still enhanced post-cracking performance and residual strength when compared to concrete without fibers.

5.1.6.2 Influence of fiber dosage

The addition of 1 kg/m³ of PD fibers resulted in a negligible increase in the compressive strength of cast cubes (less than 3%), while core-drilled specimens exhibited a more pronounced improvement of approximately 7%. Increasing the PD fiber dosage from 2 to 3 kg/m³ led to enhancements of 7% and 10% in the initial and

stabilized modulus of elasticity, respectively. Furthermore, the higher fiber content in type 5 specimens improved the splitting tensile strength by 6% compared to type 4. However, the 1 kg/m³ increase in SyFs content did not lead to an improvement in the limit of proportionality, which was reduced by 13%. Nonetheless, higher PD fiber dosage contributed to increased residual flexural tensile strength. This observation was further supported by the fracture energy results. Furthermore, standardized bending test results confirmed that an increased fiber dosage enhanced the flexural tensile performance in the post-cracking phase. In summary, increasing the PD fiber content from 2 to 3 kg/m³ improved mechanical properties of concrete, particularly in terms of post-cracking behavior and ductility.

5.1.6.3 Influence of fiber type

The comparative analysis of PM and FF fibers revealed that the use of a hybrid fiber blend resulted in a 7% and 13% increase in compressive strength for cast and core-drilled specimens, respectively, relative to concrete type 2. The initial and stabilized modulus of elasticity for FF_2 was 34% and 25% higher, respectively, compared to PM_2. Furthermore, the replacement of PM fibers with FF fibers led to increases of 22% in splitting tensile strength and 31% in flexural tensile strength. However, the residual flexural strength of type 6 beams was slightly lower than that of type 2 beams. This observation was consistent with the standardized bending test results, which indicated that PM fibers were the most effective at a fiber volume dosage of $V_f = 2 \text{ kg/m}^3$, followed by PD and FF fibers. At $V_f = 3 \text{ kg/m}^3$, however, PD fibers demonstrated superior performance compared to PM fibers. In summary, the incorporation of FF fibers resulted in higher peak strength parameters but lower residual strength response relative to concrete reinforced with PM fibers.

5.2. Large-scale slab tests

The large-scale slab tests under centrally applied concentrated load were performed in accordance with the methodology described in Chapter 4.4.2, using a specially designed test setup. In total, 18 slabs with dimensions of 200 x 1200 x 1200 mm were tested. The preliminary phase comprised one unsupported slab and two ground-supported slabs of concrete type 6, prepared with different subsoil support

conditions. The purpose of these initial tests was to evaluate the influence of subgrade support and to identify the most appropriate subbase configuration for the subsequent testing of 15 slabs of types 1-5. To ensure repeatability of the experimental program, the degree of soil compaction, and consequently the modulus of subgrade reaction k had to remain consistent throughout all tests. For this reason, in-situ measurements were conducted to monitor and verify the k value. Two approaches were employed: static plate load tests with a VSS bearing plate, carried out in accordance with Appendix B of PN-S-02205:1998 [215], to determine the primary and secondary deformation moduli $(E_{v1}$ and E_{v2} , respectively), and dynamic plate load tests with a Light Falling Weight Deflectometer, performed according to ASTM E2835-11 [216] and TP BF-StB - Part B 8.3 [217], to determine the dynamic deformation modulus (E_{vd}) . On this basis, the correlation coefficients γ_1 and γ_2 between E_{v1} and E_{vd} as well as E_{v2} and E_{vd} , respectively were subsequently established. Specifically, both testing methods were applied to the subsoil beneath slab 6.3 (Table 5.15), and the coefficients γ_1 and γ_2 were calculated using equations (5.1)-(5.3), following the procedure described in Chapter 4.4.2.3. The value of y_2 was determined to be 3.443, and by assuming a constant deformation index of $I_0 = 1.80$, γ_I was calculated as 1.913. Since equation (4.4) for subgrade reaction modulus k relies on the E_{vI} value, determining the coefficient γ_I and relation between E_{vd} and E_{vl} was essential for further analytical analysis. A summary of the test results is presented in Table 5.15, where average values of E_{vd} and E_{vl} were calculated for slabs of the same type. Namely, the average E_{vI} for 16 tested ground-supported slabs (excluding 6.1 and 6.2) was 139 MPa, with a standard deviation (SD) of 5.67 MPa and a coefficient of variation (COV) of 4.09%, indicating low variability in subsoil compaction across the tested slabs.

$$I_0 = \frac{E_{v2}}{E_{v1}} = \frac{237.6}{132.0} = 1.80$$

$$\gamma_2 = \frac{E_{v2}}{E_{vd}} = \frac{237.6}{69.0} = 3.443$$
(5.1)

$$\gamma_2 = \frac{E_{v2}}{E_{vd}} = \frac{237.6}{69.0} = 3.443 \tag{5.2}$$

$$E_{v1} = \frac{\gamma_2 \cdot E_{vd}}{I_0} = \gamma_1 \cdot E_{vd} = 1.913 \cdot E_{vd}$$
 (5.3)

where:

 I_0 – deformation index [-],

 E_{vl} – primary static deformation modulus from static plate load test [N/mm²],

 E_{v2} – secondary static deformation modulus from static plate load test [N/mm²],

 E_{vd} – dynamic deformation modulus from dynamic plate load test [N/mm²],

 α , β – correlation coefficients [-].

Table 5.15 Results from static plate load tests (VSS bearing plate) and dynamic plate load tests (LFWD)

| Slab type | Static plate test | Dynamic plate load test | | | | |
|--|--|--|--|--|--|--|
| Siab type | PC | Dynamic plate toau test | | | | |
| 1.1 $E_{vl} = 140 \text{ MPa}$ $E_{vd} = 73.2 \text{ MPa}$ | | | | | | |
| 1.2 | $E_{vl} = 145 \text{ MPa}$ | $E_{vd} = 75.8 \text{ MPa}$ | | | | |
| 1.3 | $E_{vl} = 144 \text{ MPa}$ | $E_{vd} = 75.3 \text{ MPa}$ | | | | |
| Average | $E_{vI} = 143 \text{ MPa}$ | $E_{vd} = 74.8 \text{ MPa}$ | | | | |
| SD | 2.65 MPa | 1.38 MPa | | | | |
| COV | 1.85 % | 1.85 % | | | | |
| | PM_2 | | | | | |
| 2.1 | $E_{vl} = 134 \text{ MPa}$ | $E_{vd} = 70.1 \text{ MPa}$ | | | | |
| 2.2 | $E_{vI} = 124 \text{ MPa}$ | $E_{vd} = 64.9 \text{ MPa}$ | | | | |
| 2.3 | $E_{vI} = 145 \text{ MPa}$ | $E_{vd} = 75.8 \text{ MPa}$ | | | | |
| Average | $E_{vI} = 134 \text{ MPa}$ | $E_{vd} = 70.3 \text{ MPa}$ | | | | |
| SD | 10.5 MPa | 5.45 MPa | | | | |
| COV | 7.82 % | 7.76 % | | | | |
| 2.1 | PM_3 | T 70.0 \ FD | | | | |
| 3.1 | $E_{vl} = 138 \text{ MPa}$ | $E_{vd} = 72.2 \text{ MPa}$ | | | | |
| 3.2 | $E_{vI} = 136 \text{ MPa}$ | $E_{vd} = 71.1 \text{ MPa}$ | | | | |
| | $E_{vl} = 142 \text{ MPa}$ $E_{vl} = 139 \text{ MPa}$ | $E_{vd} = 74.3 \text{ MPa}$ | | | | |
| Average SD | 3.06 MPa | $E_{vd} = 72.5 \text{ MPa}$ 1.63 MPa | | | | |
| COV | 2.20 % | 2.24 % | | | | |
| COV | PD 2 | 2.24 /0 | | | | |
| 4.1 | $E_{vI} = 145 \text{ MPa}$ | $E_{vd} = 75.8 \text{ MPa}$ | | | | |
| 4.2 | $E_{vI} = 141 \text{ MPa}$ | $E_{vd} = 73.7 \text{ MPa}$ | | | | |
| 4.3 | $E_{vl} = 136 \text{ MPa}$ | $E_{vd} = 71.0 \text{ MPa}$ | | | | |
| Average | $E_{vI} = 141 \text{ MPa}$ | $E_{vd} = 73.5 \text{ MPa}$ | | | | |
| SD | 4.51 MPa | 2.41 MPa | | | | |
| COV | 3.21 % | 3.27 % | | | | |
| | PD_3 | | | | | |
| 5.1 | $E_{vl} = 139 \text{ MPa}$ | $E_{vd} = 72.6 \text{ MPa}$ | | | | |
| 5.2 | $E_{vI} = 135 \text{ MPa}$ | $E_{vd} = 70.6 \text{ MPa}$ | | | | |
| 5.3 | $E_{vl} = 141 \text{ MPa}$ | $E_{vd} = 73.5 \text{ MPa}$ | | | | |
| Average | $E_{vI} = 138 \text{ MPa}$ | $E_{vd} = 72.2 \text{ MPa}$ | | | | |
| SD | 3.06 MPa | 1.48 MPa | | | | |
| COV | 2.21 % | 2.05 % | | | | |
| (1 | FF 2 | | | | | |
| 6.1 | $E_{vl} = 107 \text{ MPa (with lean concrete)}$ | - | | | | |
| 6.2 | Ç | ound support | | | | |
| Average | $E_{vl} = 132.0 \text{ MPa}; E_{v2} = 237.6 \text{ MPa}$ $E_{vl} = 132 \text{ MPa}$ | $E_{vd} = 69.0 \text{ MPa}$ $E_{vd} = 69.0 \text{ MPa}$ | | | | |
| SD | $L_{VI} = 132$ WH a | <i>Lyd</i> – 07.0 WII a | | | | |
| COV | _ | | | | | |
| 201 | Summary for all tests | ed subbases | | | | |
| Average | $E_{vl} = 139 \text{ MPa}$ | $E_{vd} = 72.4 \text{ MPa}$ | | | | |
| SD | 5.67 MPa | 2.95 MPa | | | | |
| COV | 4.09 % | 4.07 % | | | | |
| | | 1 1 771 1 1 1 1 | | | | |

Note: The blue results are the ones experimentally obtained. The others are determined according to equation (5.3).

The subsequent Chapters present the results of the large-scale tests, with particular emphasis on the effects of fiber addition, dosage, and type on their structural behavior. The discussion specifically addresses load-deflection responses, crack initiation and propagation patterns, deflection profiles, and the characterization of the punching shear cones geometry of the centrally loaded slabs. Additionally, the influence of subgrade support and supporting conditions on overall slabs' performance is examined.

5.2.1. Slabs FF 2 - type 6

5.2.1.1 Load-deflection response

For slabs type 6 with 2 kg/m³ of FF fibers, three samples measuring 200 x 1200 x 1200 mm were subjected to central concentrated force testing. Slab 6.2 was supported only by steel rollers, while slabs 6.1 and 6.3 were additionally supported by the ground. Notably, the ground conditions for slabs 6.1 and 6.3 differed, as detailed in Chapter 4.4.2.3. The preliminary testing of three distinct support conditions aimed to identify the most suitable and effective option for subsequent studies, as well as to assess the influence of subsoil support. Fig. 5.10a shows the loading force F versus central deflection $\delta_{central}$ curves, derived as a median from LVDTs no. 3, 6, 9, and 12 positioned near the slab center. Fig. 5.10b presents the trend curves (standardized values), illustrating the relationship between the ratio of applied force to maximum observed force (F/F_{max}) and the ratio of central deflection corresponding to F to that corresponding to F_{max} ($\delta_{central}/\delta_{central,Fmax}$). Table 5.16 summarizes the flexural cracking forces (F_{cr1} and F_{cr2}) and punching shear forces (F_p) with associated central deflections.

The results indicated that deflection of the SyFRC slabs exhibited a nearly linear response to increasing load until the F_{crl} was reached. Initial nonlinearities of slabs 6.2 and 6.3 were attributed to setup adjustments and actuator bearing against the steel frame. Notably, the F- $\delta_{central}$ plot revealed no evidence of crack initiation prior to F_{crl} , what was also confirmed by visual observations during testing. However, monitoring of crack propagation on the slab's underside was not feasible due to ground support. Nevertheless, crack initiation on the slab bottom may be correlated with observable nonlinearities at load levels of 322 and 378 kN in sample 6.1. Slabs 6.1-6.3 experienced edge cracking at F_{crl} values of 403.45 kN (N, E, S, and W sides), 169.81 kN (W and E sides), and 171.94 kN (W and E sides), respectively. Post F_{crl} , load-bearing capacities decreased by 28%, 67%, and 37%, respectively.

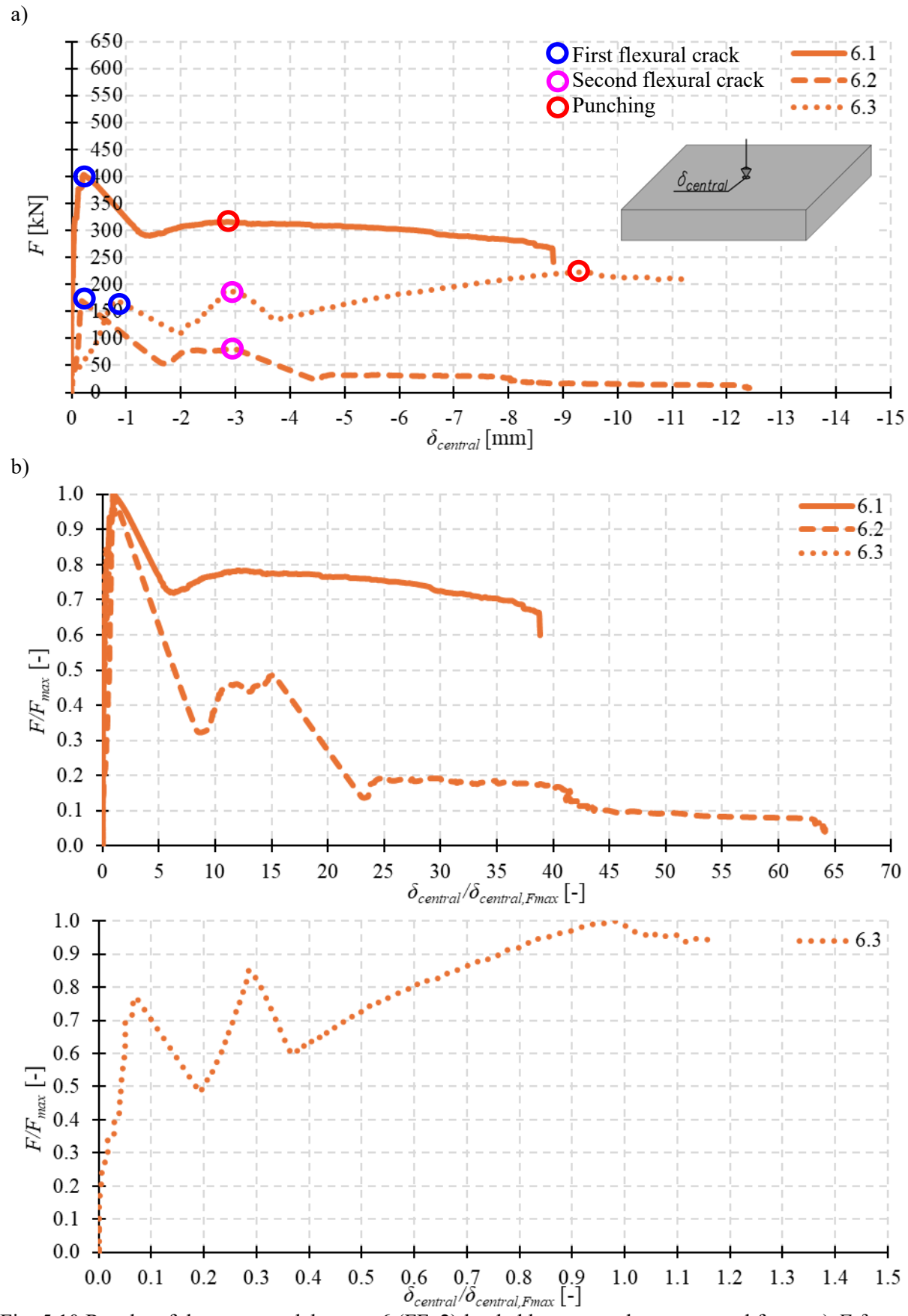


Fig. 5.10 Results of the tests on slabs type 6 (FF_2) loaded by a central concentrated force: a) F- $\delta_{central}$ curve, b) F/F_{max} - $\delta_{central}/\delta_{central,Fmax}$ curve

Table 5.16 Flexural cracking and punching shear forces with corresponding deflections for slabs type 6 (FF_2)

| Slab no. | F _{cr1} [kN] | δ _{central,Fcr1} [mm] | <i>F_{cr2}</i> [kN] | δ _{central,Fcr2} [mm] | F_p [kN] | δ _{central,Fp} [mm] | F _{max} [kN] | δ _{central,Fmax} [mm] |
|----------|------------------------|--------------------------------|-----------------------------|--------------------------------|------------|------------------------------|-----------------------|--------------------------------|
| 6.1 | 403.45 (N, E, S, W) | -0.228 | - | - | 316.29 | -2.706 | 403.45 | -0.228 |
| 6.2 | 169.81 (W, E) | -0.194 | 82.91 (N, S) | -2.939 | - | - | 169.81 | -0.194 |
| 6.3 | 171.94 (W, E) | -0.804 | 190.22 (N, S) | -2.829 | 222.82 | -9.424 | 222.82 | -9.424 |

The second flexural crack (F_{cr2}) for slabs 6.2 and 6.3 occurred at 82.91 kN (N and S sides) and 190.22 kN (N and S sides), resulting in force reductions of 71% and 30%, respectively. In contrast, slab 6.1 did not experience the secondary flexural cracking. Subsequently, load-bearing capacities of the slabs 6.1 and 6.3 increased with further deflection until reaching the punching shear failure force (F_p) equals to 316.29 kN and 222.82 kN, respectively. Slab 6.2 demonstrated a continuous decline in load-bearing capacity after reaching F_{cr2} without indications of punching shear failure. The mechanical behavior of slab 6.2 clearly differed from slabs 6.1 and 6.3 what was explained by a lack of ground support. On the other hand, the distinct load-deflection response of slab 6.1, in contrast to slab 6.3, was attributed to differing ground support conditions (variant I for slab 6.1 and variant II for slab 6.3). Specifically, the stiffness of the subsoil with a lean concrete as a top layer was significantly greater than that with compacted crushed aggregates necessitating a higher force to fracture slab 6.1 compared to slab 6.3. Ultimately, slab 6.3 experienced larger vertical deflections corresponding to punching shear force (-9.424 mm) compared to slab 6.1 (-2.706 mm). Testing terminated upon the observation of a sudden force drop in slab 6.1, significant increase of deflection accompanied by a non-growing force in slab 6.2, and severe surface punching at the load application area in slab 6.3. The failure mechanism for slabs 6.1 and 6.3 was identified as punching shear failure, whereas for slab 6.2 as a bending failure. Finally, it must be highlighted that the presence of 2 kg/m³ of FF fibers prevented brittle failure of the SyFRC slabs, thereby maintaining their structural integrity and facilitating intact lifting and inspection from below (Fig. 5.11).



Fig. 5.11 Synthetic fibers FF maintaining the structural integrity of the tested slab 6.3

5.2.1.2 Crack morphology

Fig. 5.12 illustrates the locations of the first and second flexural cracks on the edges of the tested slabs, associated with forces F_{cr1} and F_{cr2} , respectively. Fig. 5.13 presents the crack pattern on the top and bottom surface of the slabs with the sequence of crack formation. Additionally, the perimeters of the punching cones were marked at the bottom surfaces of the ground slabs.

The crack morphology of all slabs of type 6 was similar, dividing the slabs into four main segments with additional punching shear cracks in case of slabs 6.1 and 6.3. Observations indicated that flexural cracks initially formed on the bottom edge sides, propagating upwards to the top surface before extending toward the slab center. Slab 6.1 exhibited initial cracking simultaneously on all four edges, while slabs 6.2 and 6.3 cracked firstly on two opposite edges from W and E sides, followed by the cracks on the other two edges on N and S sides. Finally, the circumferential cracks resulting from the punching shear were observed at the bottom of the slabs 6.1 and 6.3 under the load application area. These cracks defined the base of the punching shear cones. It must be mentioned that no circumferential cracks were observed at the top of the slabs, indicating that the failure mechanism was not associated with exceeding the negative bending moment capacity.

The differing crack appearance sequence in slab 6.1 versus slab 6.3 can be attributed to a varied ground supporting conditions. Namely, the contact of the slab with the subsoil profile with lean concrete as a top layer was more uniform than the one with compacted crushed aggregates. This resulted in simultaneous flexural cracking at all four edges of slab 6.1. For slab 6.2, no punching shear cracks were observed as failure occurred upon reaching its flexural load capacity.

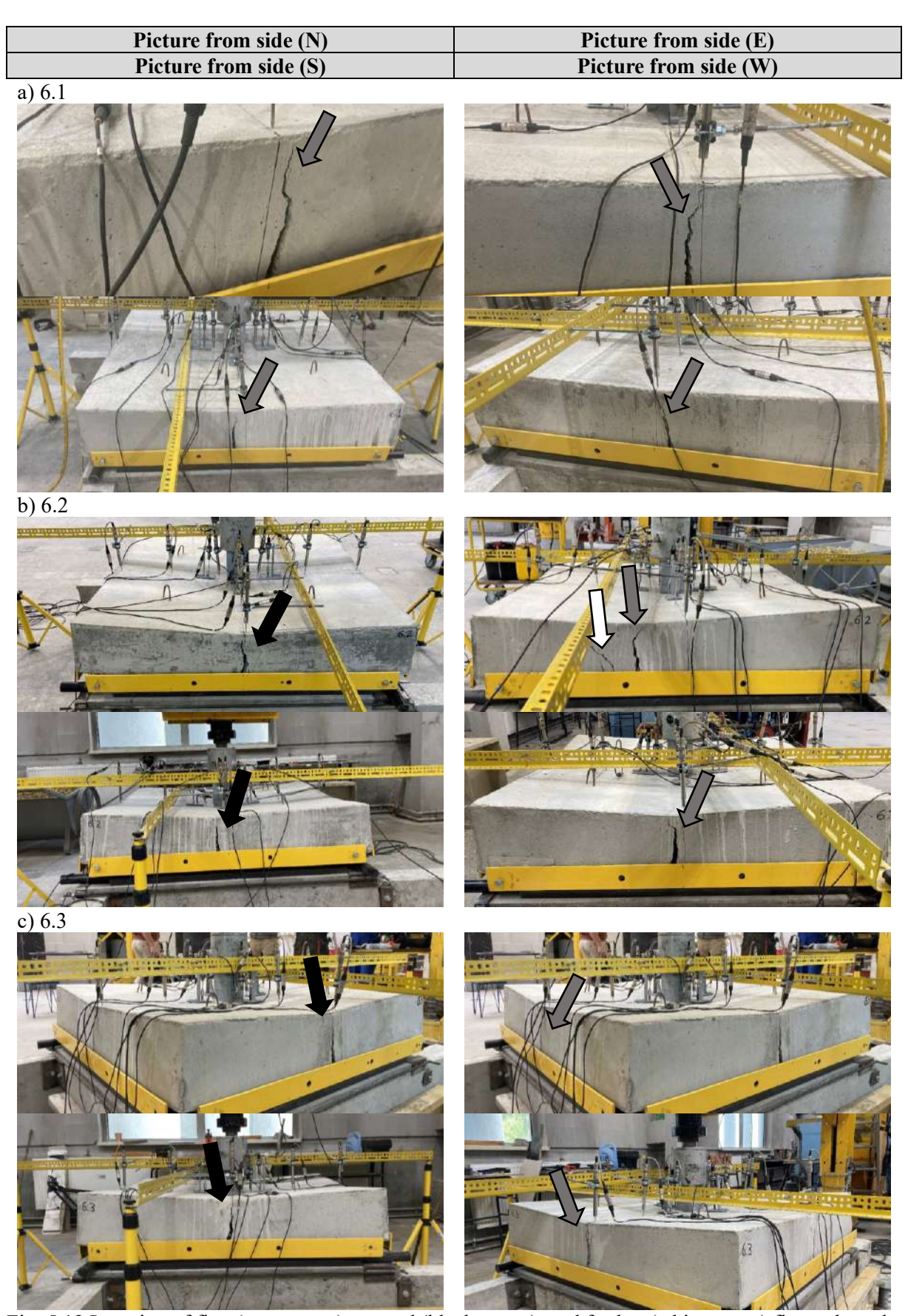


Fig. 5.12 Location of first (grey arrow), second (black arrow), and further (white arrow) flexural cracks of tested slabs of type 6 (FF_2)

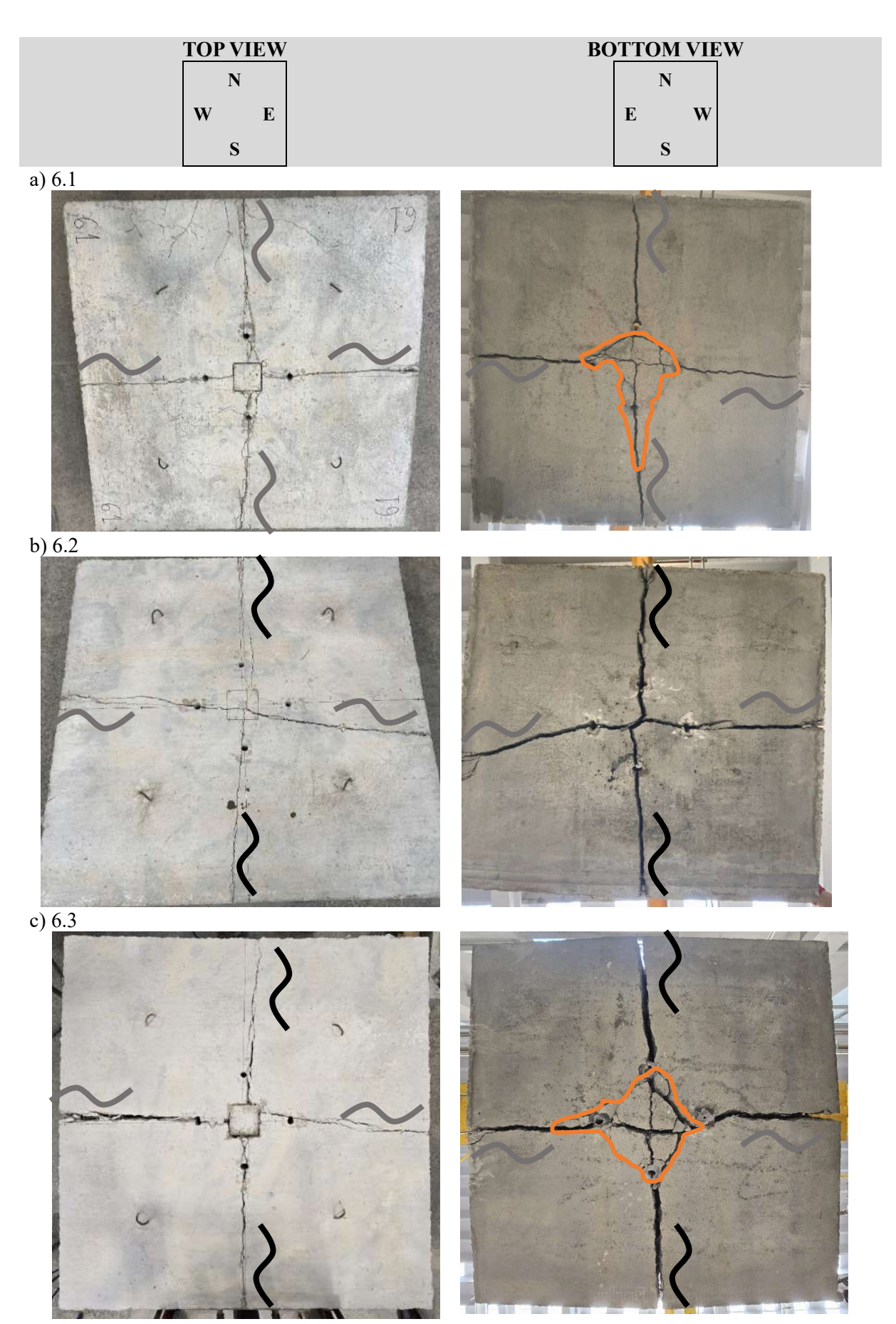


Fig. 5.13 Crack pattern of tested slabs of type 6 (FF_2): first (grey curve), and second (black curve) flexural cracks with marked perimeter of the punching cone

5.2.1.3 Deflection profiles

Fig. 5.14 presents the deflection profiles of type 6 slabs under a central concentrated force. The results indicated deflections associated with the first and second flexural cracking forces (F_{cr1} and F_{cr2}), punching shear force (F_p), and ultimate force (F_u) along the N-S and W-E axes. Notably, prior to the first flexural crack, certain parts of slab edges were not in contact with the underlying supporting steel rollers (Fig. 5.14). Specifically, the deflection profiles for F_{crl} show that LVDTs no. 1, 4, 10 of slab 6.1, no. 1, 4, 7 of slab 6.2, and no. 1, 4, 7, 10 of slab 6.3, exhibited deflections relative to their initial positions. However, in slab 6.1, the first adjustments were relatively small when compared to other slabs of type 6. In slab 6.2, the E edge was already in contact, while the S edge contacted the rollers prior to reaching F_{cr2} , as evidenced by the increase in LVDT no. 1 compared to the deflection profile at F_{crl} . The term 'edge contacted with the roller' refers to the contact between the slab's lower surface and the roller at the location corresponding to the LVDT measurement point. In slab 6.3, these parts of S and N edge made contact with the rollers during the load increment from F_{crl} to F_{cr2} , as indicated by the increase in LVDTs no. 1 and 7. Consequently, the parts of edges from the W and N sides for slab 6.2 as well as W and E sides for slab 6.3 maintained a lack of full contact with the rollers, recording even lower deflections at load level F_{cr2} . In conclusion, deflection profile analysis indicated that at the beginning of the tests, the slabs were not fully ground-supported or uniformly on all four rollers, but rather partially by the ground and/or one to four steel rollers. This applies mainly to slabs 6.2 and 6.3. Along with the continuation of the test, at the F_p , the edges of type 6 ground slabs typically lost contact with the rollers due to observed corner and edge uplift and as a result of slab rotation on the steel linear supports. Additionally, these contributed to partial loss of slab contact with the ground. This was more evidence in case of slab 6.1 compared to slab 6.3. However, determining the precise timing and magnitude of edge uplift, deflections, and the actual slab contact area with the subbase was challenging, as it remained unclear when the slab engaged the rollers, and which position of the LVDTs should be referred to. Nonetheless, Fig. 5.14 suggests that at F_p , type 6 ground slabs likely maintained contact with the subbase over the majority of the area defined by the soil containment box (995 x 995 mm). In case of slab 6.1, the uplift of external LVDTs was even more severe for the F_u compared to other slabs. The deflection profiles also indicated that higher load intensity led to non-uniform deflections, likely caused by uneven failure progression and load redistribution. It was particularly evident in the slab 6.2, where deflections along the W-E significantly exceeded those along the N-S axis.

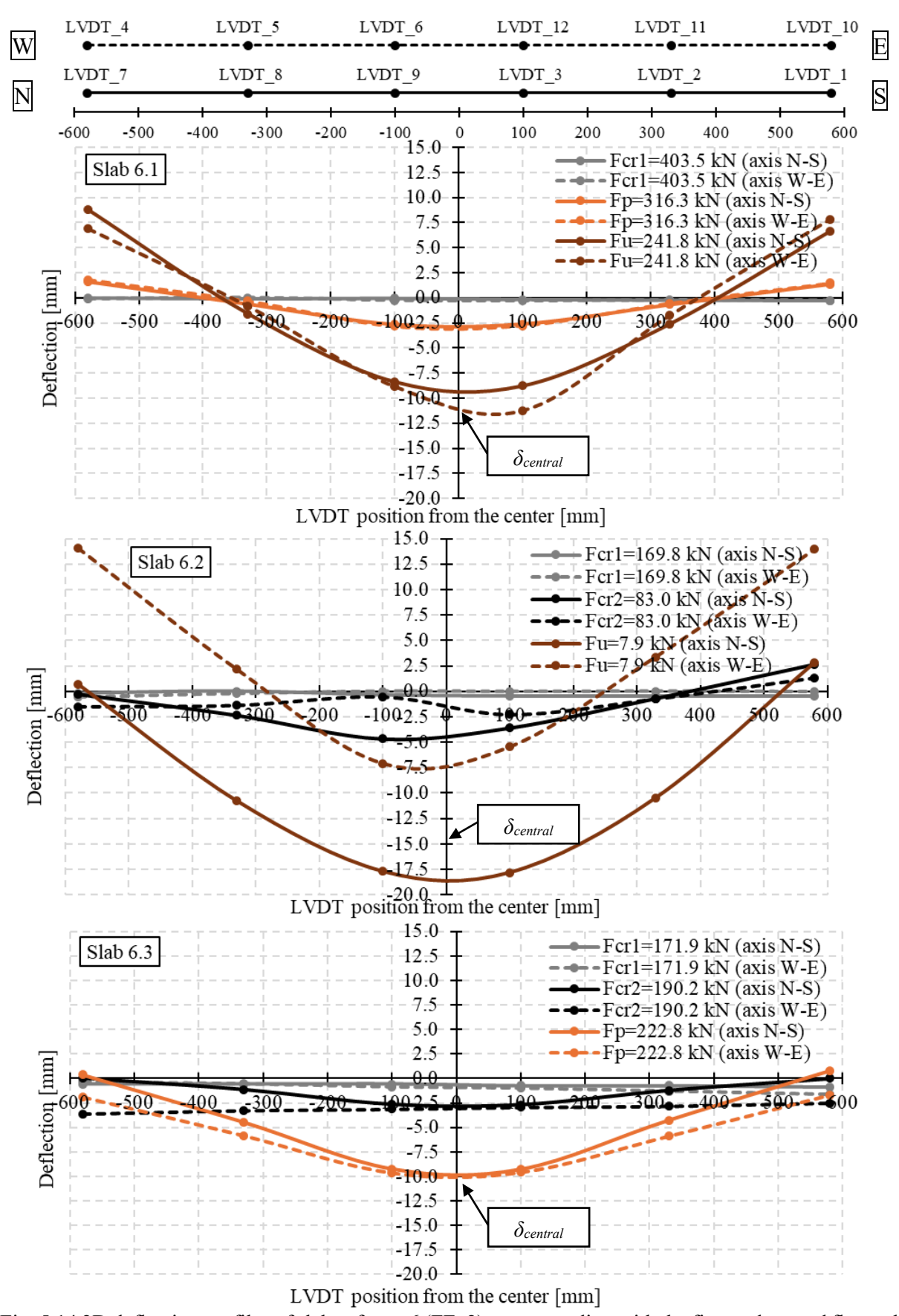


Fig. 5.14 2D deflection profiles of slabs of type 6 (FF_2) corresponding with the first and second flexural cracking force (F_{crl} and F_{cr2}), and punching shear force (F_p)

5.2.1.4 Punching cone characteristics

Fig. 5.15 illustrates the distinct displacement of the central punching shear cone on the load application surface relative to the surrounding portion of the slabs, which was equal to around 0.8 and 3.5 cm for slab 6.1 and 6.3, respectively. Slab 6.2 exhibited no signs of punching shear failure. To examine the punching cones, they were pushed out from slabs 6.1 and 6.3 using a manual hydraulic jack stabilized by a steel frame (Fig. 4.26 and Fig. 4.27). Fig. 5.16 presents the top and side views of the punching cones from slabs of type 6 (FF_2).



Fig. 5.15 Punching of the tested slabs of type 6 (FF_2) at the load application surface

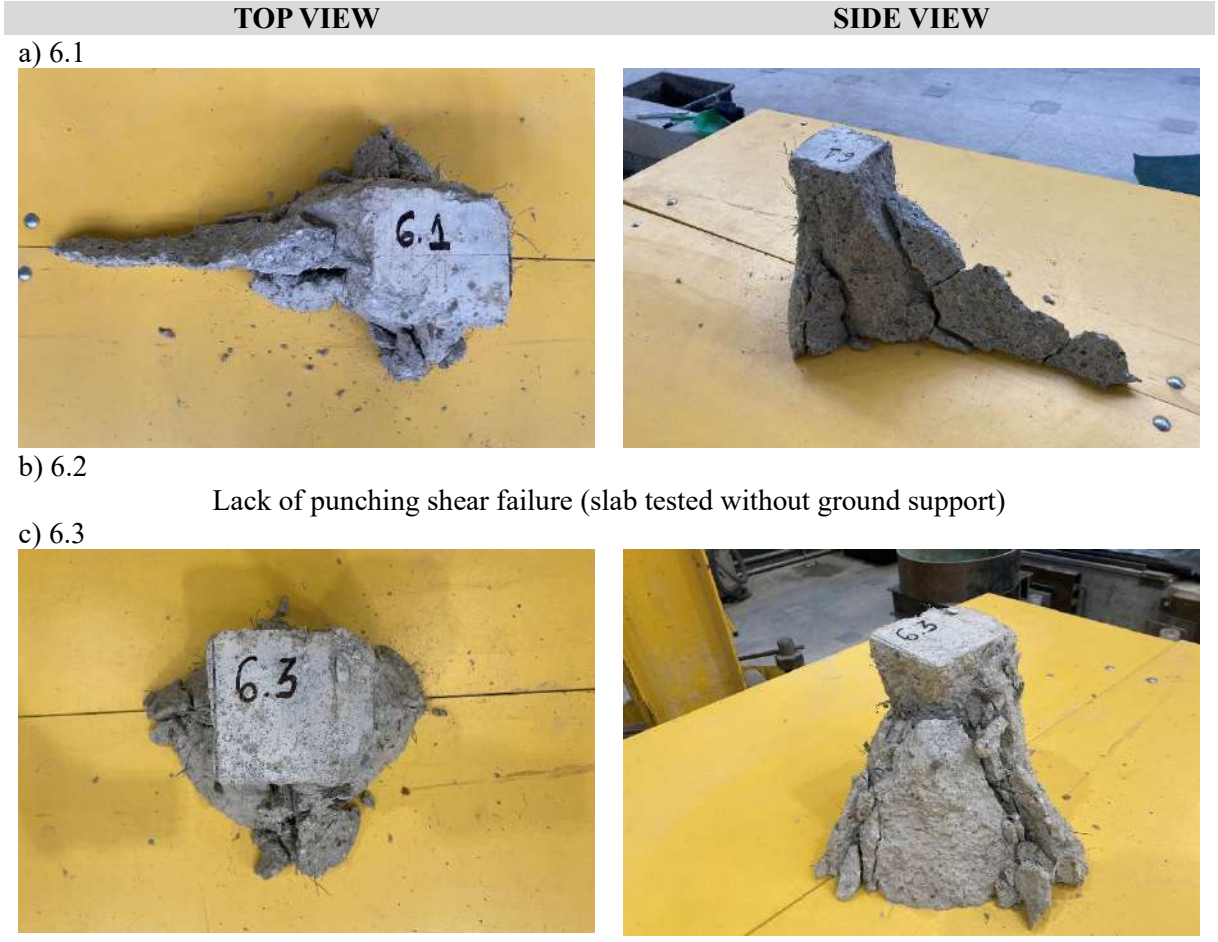


Fig. 5.16 Punching cones from tested slabs of type 6 (FF 2)

The inclination angles θ of the punching cones were measured in six distinct positions along the cone sidewalls using an angle finder ruler. The single and average values of θ are documented in Table 5.17. The inspection indicated that the punching cones had an irregular shape of truncated pyramid with an average θ of 69.7° and 72.7° for slab 6.1 and 6.3, respectively. Finally, due to presence of fibers the cones maintained their structural integrity, facilitating their movement and transport.

Table 5.17 Punching cone inclination angles θ for tested slabs of type 6 (FF 2)

| Slab no. | Punching cone inclination angles $	heta$ | Average θ |
|----------|--|-------------------------|
| 6.1 | 79°, 70°, 77°, 38°, 76°, 78° | $\theta = 69.7^{\circ}$ |
| 6.2 | Lack of punching shear cone (slab tested without ground su | pport) |
| 6.3 | 72°, 63°, 79°, 88°, 73°, 61° | $\theta = 72.7^{\circ}$ |

5.2.1.5 Influence of ground support

The results demonstrated a significant influence of subsoil support on the structural behavior, load-bearing capacity, deflections, and failure modes of slabs subjected to central concentrated loading. Specifically, unsupported slabs failed by reaching their flexural load-bearing capacity and did not exhibit punching shear failure, in contrast to slabs supported by the ground. This finding highlighted the necessity of conducting separate analyses for ground-supported and unsupported slabs. Furthermore, the consideration of punching shear capacity in ground-supported slabs was confirmed to be critical and must not be neglected in the design process. Additionally, the layering and preparation of the subsoil were found to substantially affect slab structural response under concentrated loads.

5.2.1.6 Provisions for further tests

Based on the conducted tests of slabs type 6, it was decided that the subsequent experimental campaign would proceed with slightly modified Variant II of ground preparation procedure described in Chapter 4.4.2.3, denoted as a Variant III. It is important to mention that in Variant I the lean concrete was gaining strength over time, thus requiring slab testing at consistent time intervals following their placement on the supporting ground. Considering the large number of experiments conducted in the Laboratory of Civil Engineering, the occupation of the laboratory workers, and potential unforeseen delays, it was anticipated that maintaining a strict time schedule would be challenging. In contrast, Variant III allowed slab placement on the testing setup

independently of the groundwork schedule, thereby facilitating more flexible test planning and execution. Furthermore, the high subsoil stiffness in Variant I necessitated approximately 400 kN for slab 6.1 to fail. Given that slabs type 4 and 5, containing PD_2 and PD_3 concretes of higher strength, were expected to require even greater forces, concerns arose regarding the capacity and stroke limits of the testing actuator, as well as the capacity of the testing setup. Additionally, deflection profiles showed that although Variant I ensured better slab-subsoil contact and more uniform crack propagation, the edge uplift was less pronounced in slab 6.3. Moreover, the punching cone in slab 6.3 exhibited a more regular geometry. Taking these factors into account, it was concluded that Variant III represented the optimal ground preparation method for testing slabs of types 1-5.

The positioning of the pushrods (LVDT10 sensors) was specifically determined to align with shear cracks resulting from punching, not with flexural cracks induced by bending. Namely, the primary objective of these measurement devices was to record vertical displacement associated with the development of shear cracks and, subsequently, to estimate shear crack widths, as described in Chapter 4.4.2.4. Expecting diagonal crack propagation, pushrods were initially placed along the symmetry axis during tests of type 6 slabs (Fig. 4.22, Variant I). However, all FF_2 slabs exhibited flexural cracking along the symmetry axis, coinciding with the pushrod locations, as shown in Fig. 5.17. Consequently, in subsequent tests, LVDT10s were positioned along the diagonals of slabs types 1-5 (Fig. 4.22, Variant II) to ensure exclusive indication of shear cracks. This adjustment also reduced the number of measurement devices along the symmetry axis.



Fig. 5.17 Bottom surface of the ground slabs type 6 (FF 2) after removal of the punching cone

5.2.2. Slabs PC – type 1

5.2.2.1 Load-deflection response

For ground slabs type 1 without fibers (PC), three samples measuring 200 x 1200 x 1200 mm were subjected to central concentrated force testing. Fig. 5.18a shows the loading force F versus central deflection $\delta_{central}$ curves, derived as a median from LVDTs no. 3, 6, 9, and 12 positioned near the slab center. Fig. 5.18b presents the trend curves (standardized values), illustrating the relationship between the ratio of applied force to maximum observed force (F/F_{max}) and the ratio of central deflection corresponding to F to that corresponding to F_{max} ($\delta_{central}/\delta_{central,F_{max}}$). Finally, Table 5.18 summarizes the flexural cracking forces (F_{cr1} and F_{cr2}) and punching shear forces (F_p) with associated central deflections for type 1 slabs.

The results indicated that deflection of the concrete slabs exhibited a nearly linear response to increasing load until the first flexural cracking force was reached. Initial nonlinearities were attributed to setup adjustments and actuator bearing against the steel frame. Notably, the F- $\delta_{central}$ plot revealed no evidence of crack initiation prior to F_{crl} , what was also confirmed by visual observations during testing. However, monitoring of crack propagation on the slab's underside was not feasible due to ground support. PC slabs 1.1, 1.2, and 1.3 experienced edge cracking at F_{crl} values of 144.01 kN (W and E sides), 219.82 kN (W, E, and S sides), and 112.04 kN (W and E sides), respectively. Post F_{crl} , load-carrying capacities decreased by 38%, 34%, and 63%, respectively. The second flexural crack (F_{cr2}) for slabs 1.1 and 1.3 occurred at 172.56 kN (S side) and 137.95 kN (S side), followed by force reductions of 31% and 38%, respectively. In contrast, slab 1.2 recorded an F_{cr2} value lower than F_{cr1} of 187.98 kN (E side), after which a 23% decrease in force was observed. Subsequently, load-bearing capacities of the slabs increased with further deflection until reaching the punching shear failure force (F_p) equals to 257.57 kN, 180.73 kN, and 255.91 kN for slabs 1.1, 1.2, and 1.3, respectively. Slabs 1.1 and 1.3 surpassed both F_{cr1} and F_{cr2} at the point of the punching shear force F_p , while slab 1.2 exhibited F_p lower than both flexural cracking forces. Ultimately, slabs 1.1 and 1.3 experienced larger vertical deflections corresponding to punching shear force (-6.469 mm and -9.478 mm) compared to slab 1.2 (-5.589 mm). Testing of PC slabs terminated upon the observation of a sudden force drop and significant surface punching at the load application area. The failure mechanism for slabs 1.1, 1.2, and 1.3 was identified as punching shear failure.

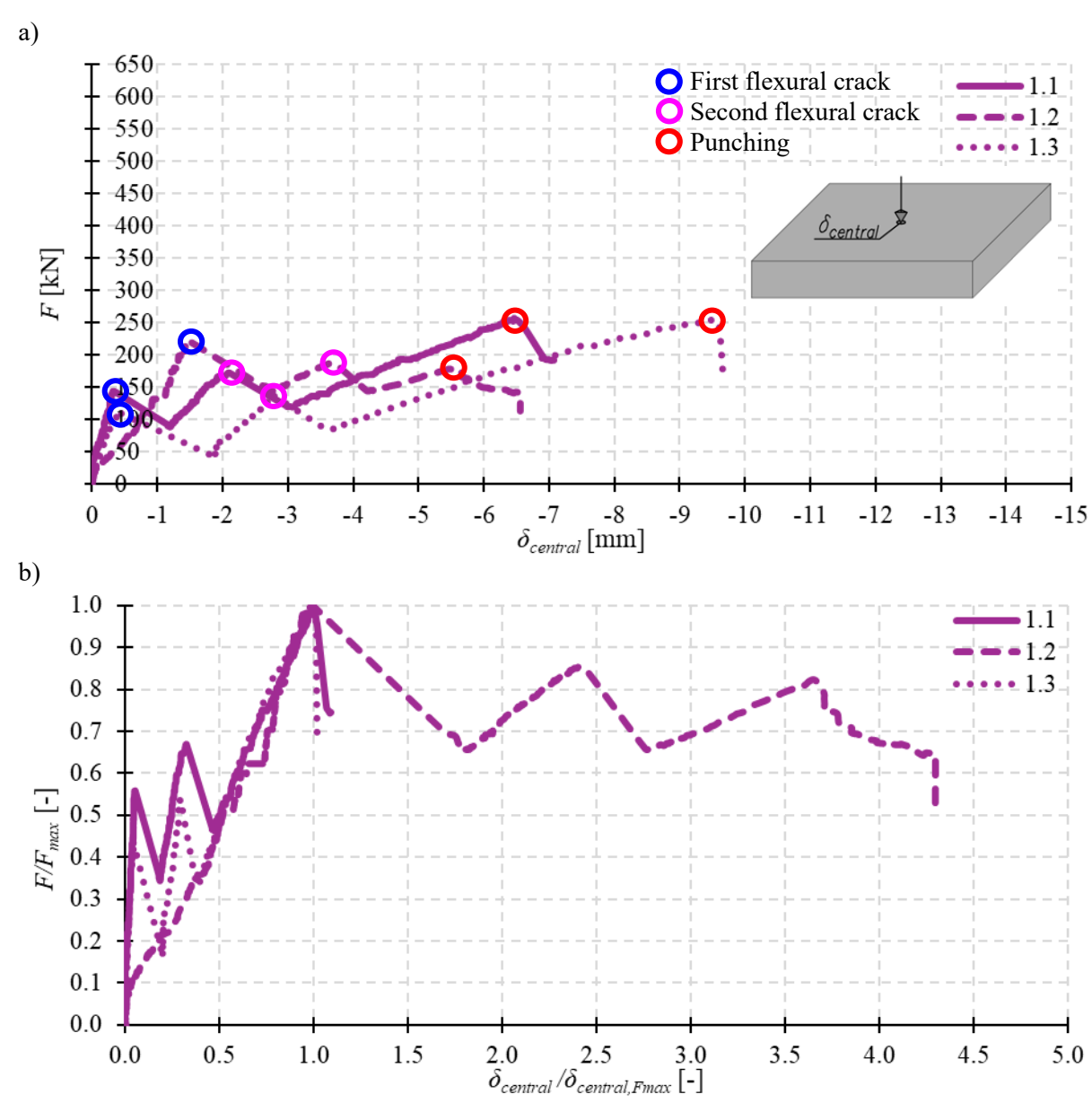


Fig. 5.18 Results of the tests on slabs type 1 (PC) loaded by a central concentrated force: a) F- $\delta_{central}$ curve, b) F/F_{max} - $\delta_{central}/\delta_{central,Fmax}$ curve

Table 5.18 Flexural cracking and punching shear forces with corresponding deflections for slabs type 1 (PC)

| Slab no. | F _{cr1} [kN] | δ _{central,Fcr1} [mm] | F _{cr2} [kN] | δ _{central,Fcr2} [mm] | F_p [kN] | δ _{central,Fp} [mm] | F _{max} [kN] | δ _{central,Fmax} [mm] |
|----------|-----------------------|--------------------------------|-----------------------|--------------------------------|------------|------------------------------|-----------------------|--------------------------------|
| 1.1 | 144.01 (W, E) | -0.343 | 172.56 (S) | -2.108 | 257.57 | -6.469 | 257.57 | -6.469 |
| 1.2 | 219.82 (W, E, S) | -1.527 | 187.98 (E) | -3.675 | 180.73 | -5.589 | 219.82 | -1.527 |
| 1.3 | 112.04 (W, E) | -0.413 | 137.95 (S) | -2.775 | 255.91 | -9.478 | 255.91 | -9.478 |

5.2.2.2 Crack morphology

Fig. 5.19 illustrates the locations of the first and second flexural cracks on the edges of the tested slabs, associated with forces F_{crl} and F_{cr2} , respectively. Moreover, Fig. 5.20 presents the crack pattern on the top surface of the slabs with the sequence of crack formation.

Observations indicated that flexural cracks initially formed on the bottom edge sides, propagating upwards to the top surface before extending toward the slab center. The distinct load-deflection response of slab 1.2, compared to slabs 1.1 and 1.3 (Fig. 5.18), can be attributed to the varying crack patterns observed. Specifically, slab 1.2 exhibited initial cracking simultaneously on three edges, whereas slabs 1.1 and 1.3 exhibited cracking on only two edges. Then, the further crack propagation led to the detachment of the N side of slabs 1.1 and 1.3 from the remainder, including the supporting steel column inducing the force. Consequently, only the S side of slabs 1.1 and 1.3 experienced loading until the punching shear force F_p was reached. In contrast, all four segments of slab 1.2 were uniformly loaded. The extensive cracking resulted in a complete brittle failure of the PC slabs, dividing samples 1.1 and 1.3 into three segments, whereas sample 1.2 into four sections along the diagonals. Consequently, the visual inspection of the bottom surfaces and assessment of flexural and punching failures from underneath was unfeasible. Finally, it must be mentioned that no circumferential cracks were observed at the top of the slabs, indicating that the failure mechanism was not associated with exceeding the negative bending moment capacity.



Fig. 5.19 Location of first (grey arrow), and second (black arrow) flexural cracks of tested slabs of type 1 (PC)

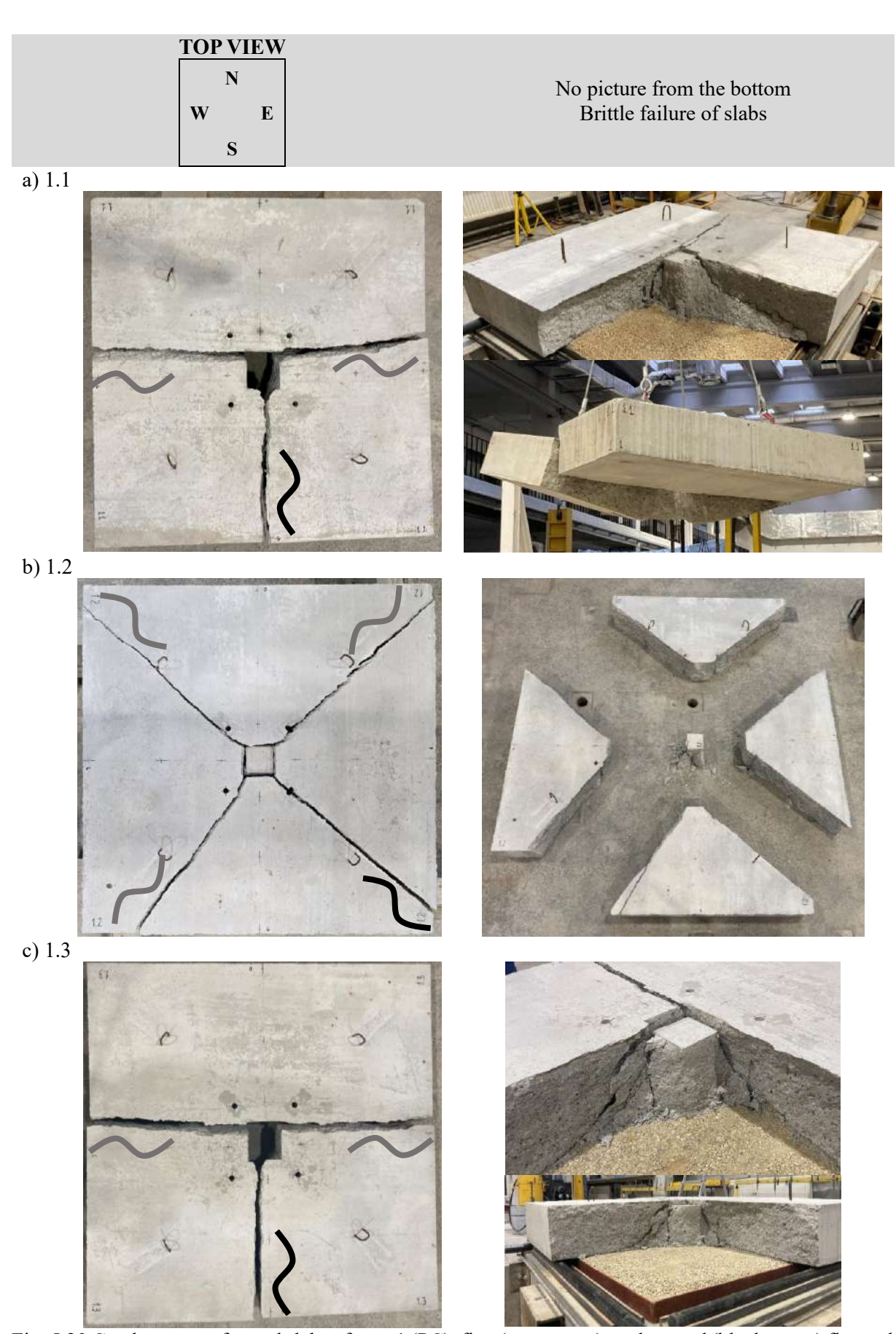


Fig. 5.20 Crack pattern of tested slabs of type 1 (PC): first (grey curve), and second (black curve) flexural cracks

5.2.2.3 Deflection profiles

Fig. 5.21 presents the deflection profiles of type 1 ground slabs under a central concentrated force. The results indicated deflections associated with the first and second flexural cracking forces (F_{cr1} and F_{cr2}) and the punching shear force (F_p) along the N-S and W-E axes. It must be mentioned that prior to the first flexural crack, certain parts of slab edges were not in contact with the underlying supporting steel rollers, as evidenced in Fig. 5.21. Specifically, the deflection profiles for F_{crl} show that LVDTs no. 4 and 10 of slab 1.1, and no. 1, 4, 7, and 10 of slabs 1.2 and 1.3, exhibited deflections relative to their initial positions. Places of LVDTs no. 4 and 10 of slab 1.1 maintained a lack of contact with the rollers on W and E sides, recording even lower deflections at load level F_{cr2} . In slab 1.2, all edges achieved contact with the rollers before reaching F_{cr2} , as indicated by an increase in marginal LVDT measurements compared to the deflection profile for F_{crl} . The term 'edge contacted with the roller' refers to the contact between the slab's lower surface and the roller at the location corresponding to the LVDT measurement point. Conversely, in slab 1.3, these parts of the S and N edges appeared to contact the rollers during the load increment from F_{cr1} to F_{cr2} as indicated by the increase in LVDTs no. 1 and 7, unlike the W and E edges, where LVDTs no. 4 and 10 continued to decrease relative to the F_{crl} profile. In conclusion, deflection profile analysis indicated that at the beginning of the tests, the slabs were not fully ground-supported or uniformly on all four rollers, but rather partially by the ground and/or one to four steel rollers. Along with the continuation of the test, at the punching shear load level F_p , the edges of type 1 slabs typically lost contact with the rollers due to observed corner and edge uplift and as a result of slab rotation on the steel linear supports. Additionally, these contributed to partial loss of slab contact with the ground support. However, determining the precise timing and magnitude of edge uplift, deflections, and the actual slab contact area with the subbase was challenging, as it remained unclear when the slab engaged the supporting rollers, and which position of the LVDTs should be referred to. Nonetheless, Fig. 5.21 suggests that at load level F_p , type 1 slabs likely maintained contact with the subbase over the majority of the area defined by the soil containment box (995 x 995 mm). The deflection profiles also indicated that increased load intensity resulted in non-uniform deflections, likely due to uneven slab failure progression and load redistribution.

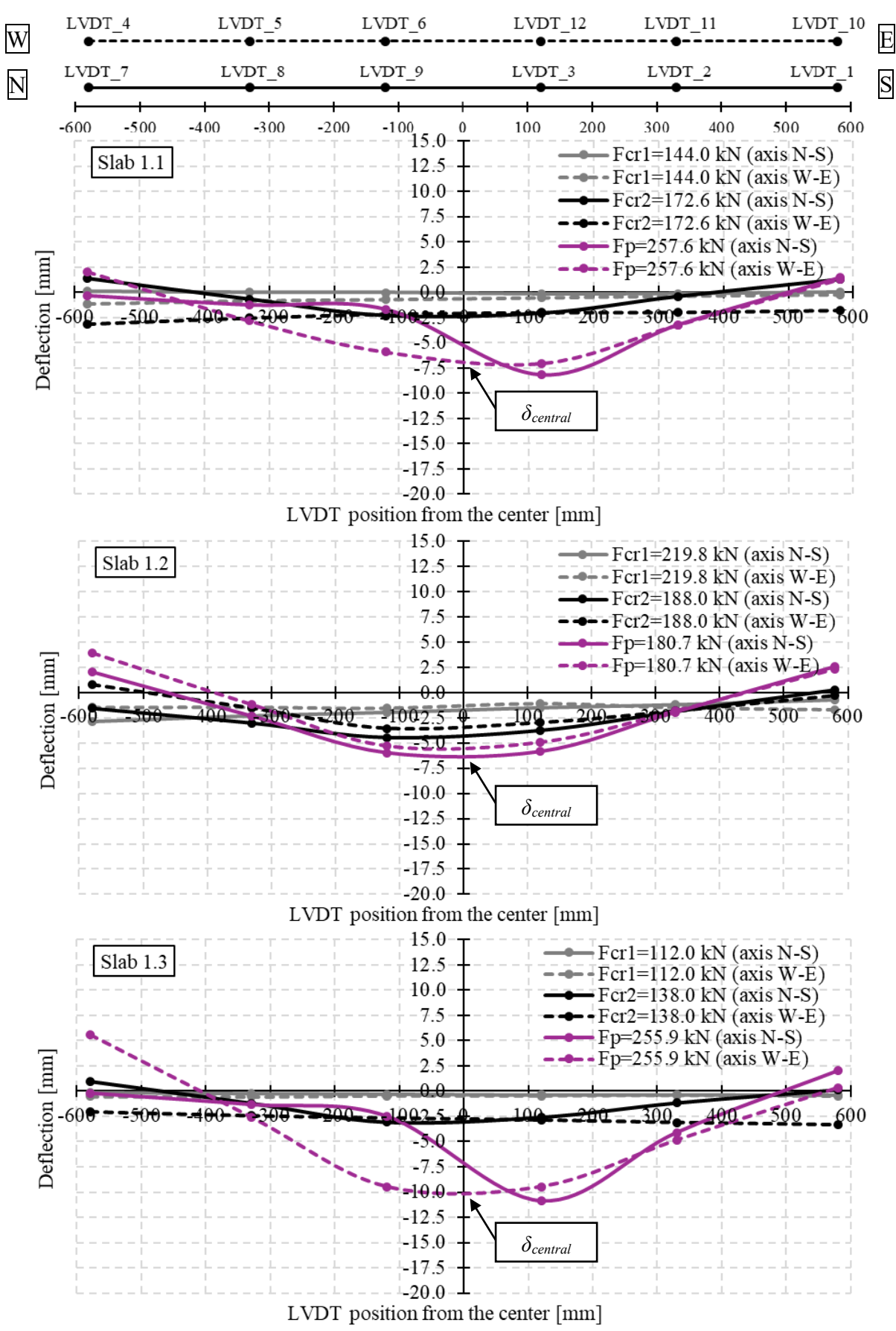


Fig. 5.21 2D deflection profiles of slabs of type 1 (PC) corresponding with the first and second flexural cracking force (F_{cr1} and F_{cr2}), and punching shear force (F_p)

5.2.2.4 Punching cone characteristics

Fig. 5.22 illustrates the distinct displacement of the central punching shear cone on the load application surface relative to the surrounding portion of the slabs, which was equal to around 1.7, 2.5, and 2.6 cm for slab 1.1, 1.2, and 1.3, respectively. To examine the punching cones, they were typically pushed out from the slabs using a manual hydraulic jack stabilized by a steel frame. However, in case of PC slabs, the cones had already detached as a result of testing and the brittle type of failure characteristic for concrete without fibers. Fig. 5.23 presents the top and side views of the punching cones from slabs of type 1 (PC). The inclination angles θ of the punching cones were measured in six distinct positions along the cone sidewalls using an angle finder ruler. For slab 1.1, measurements were taken around the cone limited by the red dashed line (see Fig. 5.23a), as the other section was affected by flexural cracking. The single and average values of θ are documented in Table 5.19. The inspection indicated that the punching cones were nearly vertical, with an average θ of 76.7°, 81.2°, and 79.3° for slab 1.1, 1.2, and 1.3, respectively. It is noteworthy that the cones exhibited brittleness, complicating their movement and transport due to disintegration of their parts.



Fig. 5.22 Punching of the tested slabs of type 1 (PC) at the load application surface

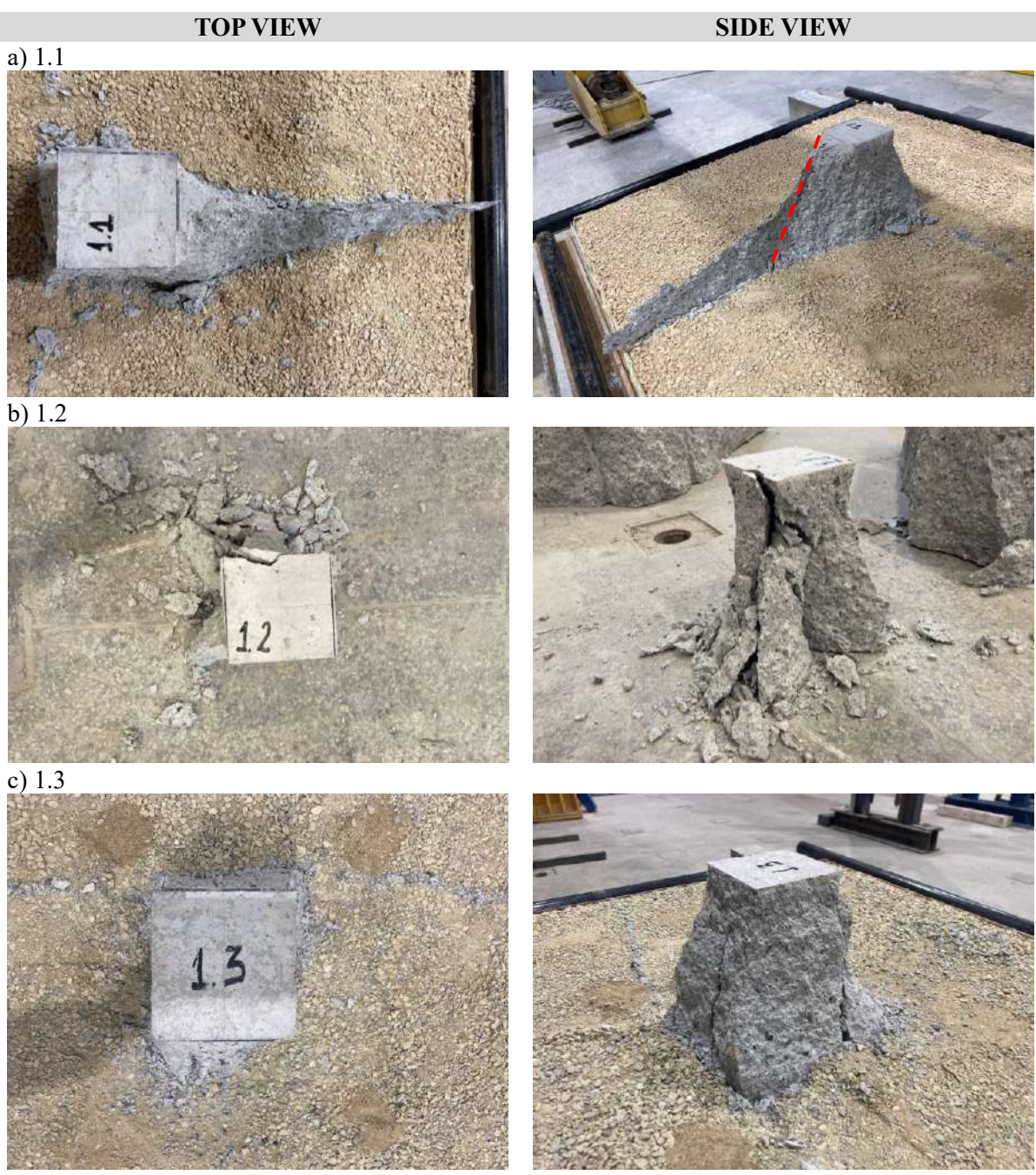


Fig. 5.23 Punching cones from tested slabs of type 1 (PC)

Table 5.19 Punching cone inclination angles θ for tested slabs of type 1 (PC)

| Slab no. | Punching cone inclination angles $	heta$ | Average θ |
|----------|--|-------------------------|
| 1.1 | 90°, 86°, 50°, 76°, 85°, 73° | θ = 76.7° |
| 1.2 | 85°, 75°, 90°, 75°, 91°, 71° | $\theta = 81.2^{\circ}$ |
| 1.3 | 75°, 68°, 74°, 89°, 93°, 77° | θ = 79.3° |

5.2.3. Slabs PM_2 – type 2

5.2.3.1 Load-deflection response

For ground slabs type 2 with 2 kg/m³ of PM fibers, three samples measuring 200 x 1200 x 1200 mm were subjected to central concentrated force testing. Fig. 5.24a shows the loading force F versus central deflection $\delta_{central}$ curves, derived as a median from LVDTs no. 3, 6, 9, and 12 positioned near the slab center. Fig. 5.24b presents the trend curves (standardized values), illustrating the relationship between the ratio of applied force to maximum observed force (F/F_{max}) and the ratio of central deflection corresponding to F to that corresponding to F_{max} ($\delta_{central}/\delta_{central,F_{max}}$). Finally, Table 5.20 summarizes the flexural cracking forces (F_{cr1} and F_{cr2}) and punching shear forces (F_p) with associated central deflections for type 2 slabs.

The results indicated that deflection of the SyFRC slabs exhibited a nearly linear response to increasing load until the first flexural cracking force was reached. Initial nonlinearities were attributed to setup adjustments and actuator bearing against the steel frame. Notably, the F- $\delta_{central}$ plot revealed no evidence of crack initiation prior to F_{crl} , what was also confirmed by visual observations during testing. However, monitoring of crack propagation on the slab's underside was not feasible due to ground support. PM 2 slabs 2.1, 2.2, and 2.3 experienced edge cracking at F_{crl} values of 166.99 kN (W and E sides), 108.69 kN (W and E sides), and 142.20 kN (W and E sides), respectively. Post F_{crl} , load-carrying capacities decreased by 34%, 41%, and 39%, respectively. The F_{cr2} for slabs 2.2 and 2.3 occurred at 186.54 kN (N and S sides) and 289.05 kN (N and S sides), followed by force reductions of 25% (after the plateau) and 16%, respectively. In contrast, slab 2.1 recorded an F_{cr2} value lower than F_{cr1} of 118.76 kN (N and S sides), after which a 16% decrease in force was observed. Subsequently, load-bearing capacities of the slabs increased with further deflection until reaching the punching shear failure force (F_p) equals to 296.31 kN, 395.13 kN, and 438.06 kN for slab 2.1, 2.2, and 2.3, respectively. It must be mentioned that all slabs surpassed both F_{cr1} and F_{cr2} at the point of the punching shear force F_p . Ultimately, slabs 2.1 and 2.2 experienced larger vertical deflections corresponding to F_p (-8.158 mm and -8.946 mm) compared to slab 1.3 (-6.897 mm). Testing of PM 2 slabs terminated upon the observation of a sudden force drop and significant surface punching at the load application area. The failure mechanism for slabs 2.1, 2.2, and 2.3 was identified as punching shear failure.

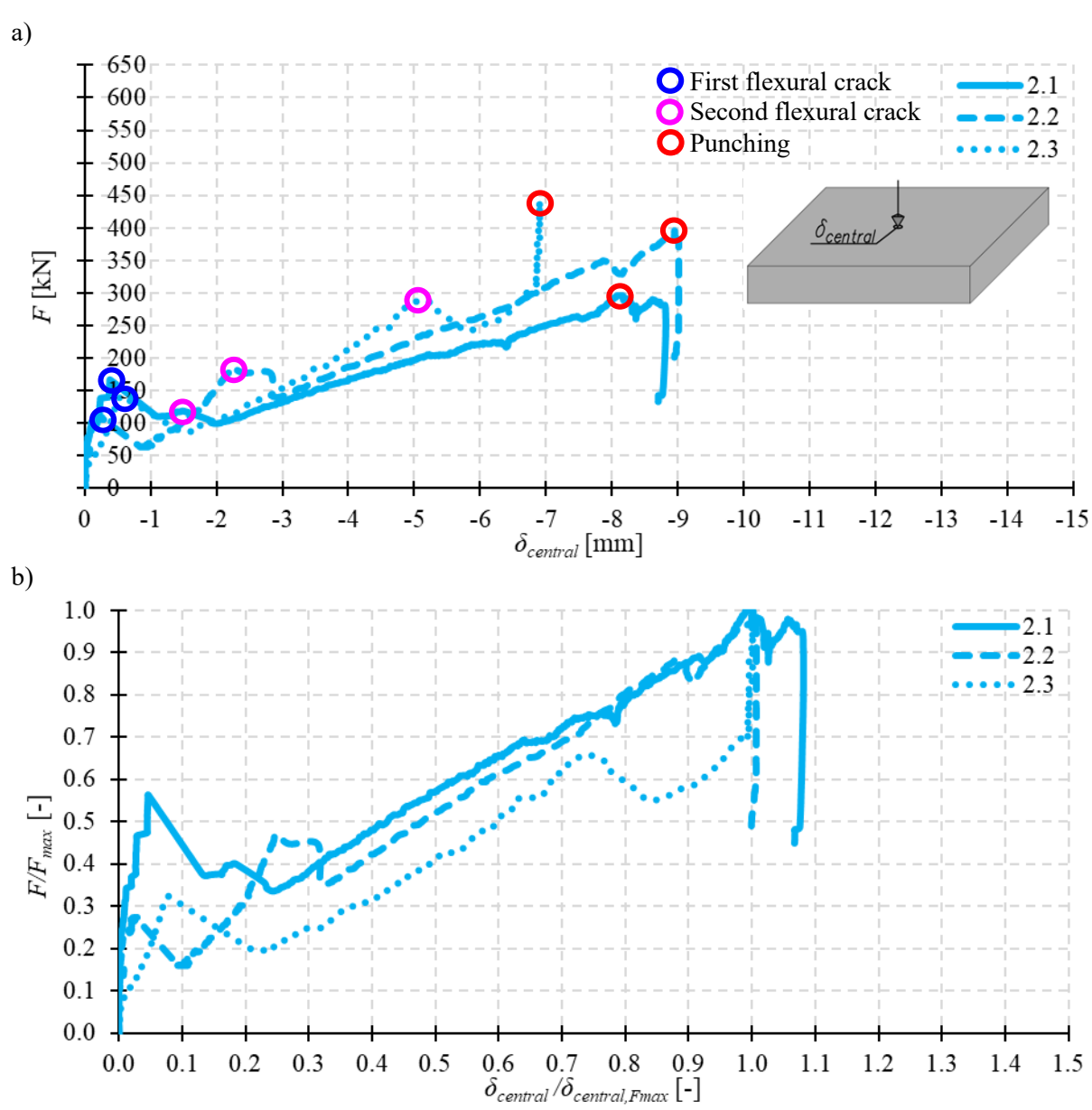


Fig. 5.24 Results of the tests on slabs type 2 (PM_2) loaded by a central concentrated force: a) F- $\delta_{central}$ curve, b) F/F_{max} - $\delta_{central}/\delta_{central,Fmax}$ curve

Table 5.20 Flexural cracking and punching shear forces with corresponding deflections for slabs type 2 (PM_2)

| Slab no. | F _{cr1} [kN] | δ _{central,Fcr1} [mm] | F _{cr2} [kN] | δ _{central,Fcr2} [mm] | F_p [kN] | $\delta_{central,Fp} \ [ext{mm}]$ | F _{max} [kN] | δ _{central,Fmax} [mm] |
|----------|-----------------------|--------------------------------|-----------------------|--------------------------------|------------|------------------------------------|-----------------------|--------------------------------|
| 2.1 | 166.99 (W, E) | -0.379 | 118.76 (N, S) | -1.505 | 296.31 | -8.158 | 296.31 | -8.158 |
| 2.2 | 108.69 (W, E) | -0.218 | 186.54 (N, S) | -2.237 | 395.13 | -8.946 | 395.13 | -8.946 |
| 2.3 | 142.20 (W, E) | -0.541 | 289.05 (N, S) | -5.111 | 438.06 | -6.897 | 438.06 | -6.897 |

Finally, it must be highlighted that the presence of 2 kg/m³ of PM fibers prevented brittle failure of the SyFRC slabs, thereby maintaining their structural integrity and facilitating intact lifting and inspection from below (Fig. 5.25).





Fig. 5.25 Synthetic fibers PM maintaining the structural integrity of the tested slab 2.2

5.2.3.2 Crack morphology

Fig. 5.26 illustrates the locations of the first and second flexural cracks on the edges of the tested slabs, associated with forces F_{cr1} and F_{cr2} , respectively. Fig. 5.27 shows the crack pattern on the slabs' top and bottom surfaces with the sequence of crack formation. The punching cone perimeters were also marked on the slabs' bottom surfaces.

The crack morphology of all slabs of type 2 was similar, dividing the slabs into four main segments with some subdivisions in case of slabs 2.2 and 2.3 (white curves in Fig. 5.27). Observations indicated that flexural cracks initially formed on the bottom edge sides, propagating upwards to the top surface before extending toward the slab center. All slabs exhibited initial cracking simultaneously on two opposite edges on W and E sides, followed by the cracks on the other two edges on N and S sides. Moreover, some additional cracks at the slab edges were observed unattributed to the achievement of a specific force. Finally, the circumferential cracks resulting from the punching shear were observed at the bottom of the slabs under the load application area. These cracks defined the base of the punching shear cones. No circumferential cracks were observed at the top of the slabs, indicating that the failure mechanism was not associated with exceeding the negative bending moment capacity.

The distinct load-deflection response of slab 2.1, compared to slabs 2.2 and 2.3, characterized by force F_{cr2} not exceeding F_{crl} (Fig. 5.24), can be attributed to a more significant stiffness reduction in slab 2.1 after first flexural cracking. This reduction might have been a result of a broader crack development range at F_{crl} . However, this conclusion remains uncertain as a visual inspection of the crack propagation on the slab's bottom surface was not feasible during testing. Another contributing factor may be the slightly different directions of the cracks in slab 2.1, which were oriented more diagonally compared to the crosswise crack orientation of slabs 2.2 and 2.3.

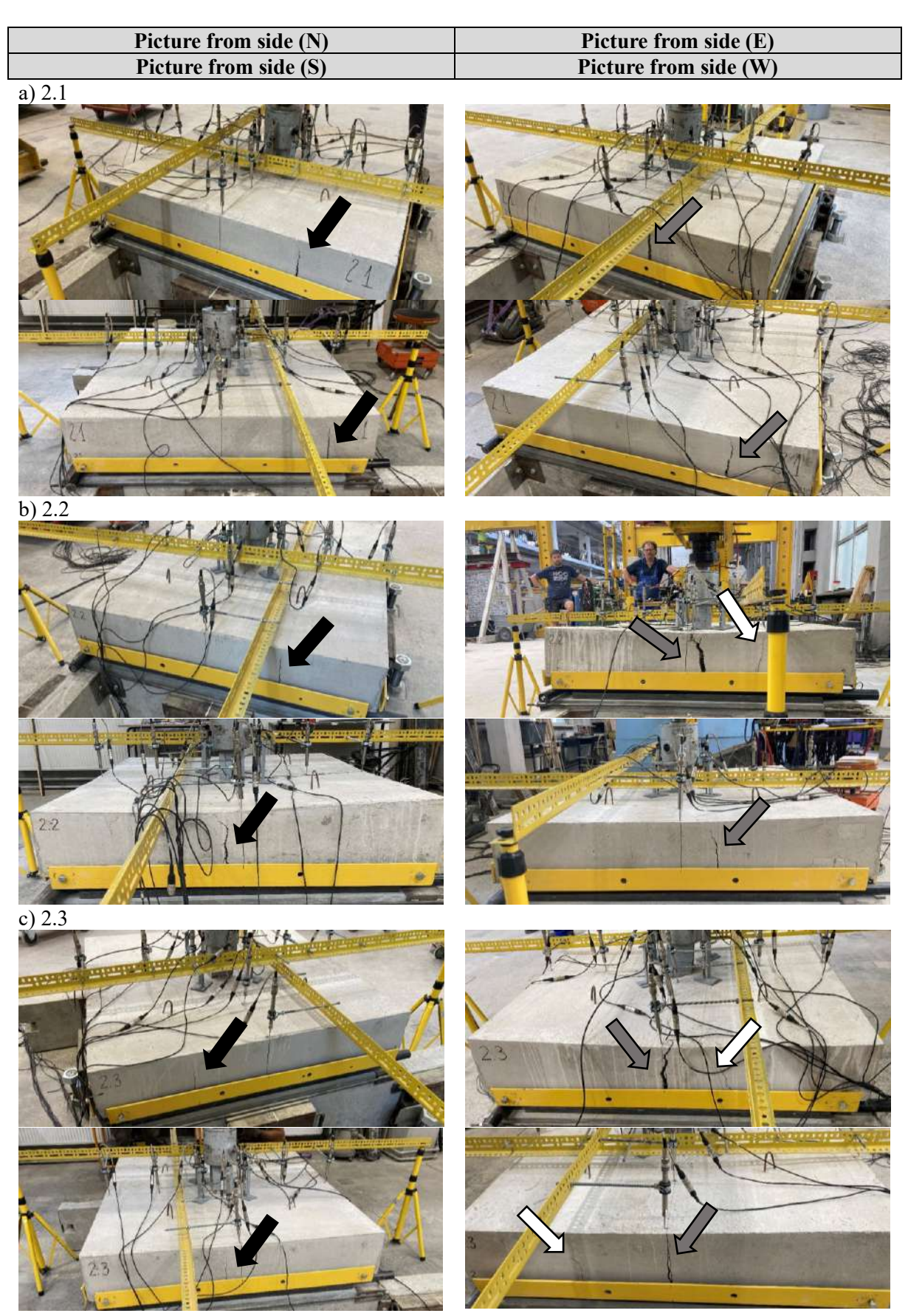


Fig. 5.26 Location of first (grey arrow), second (black arrow), and further (white arrow) flexural cracks of tested slabs of type 2 (PM_2)

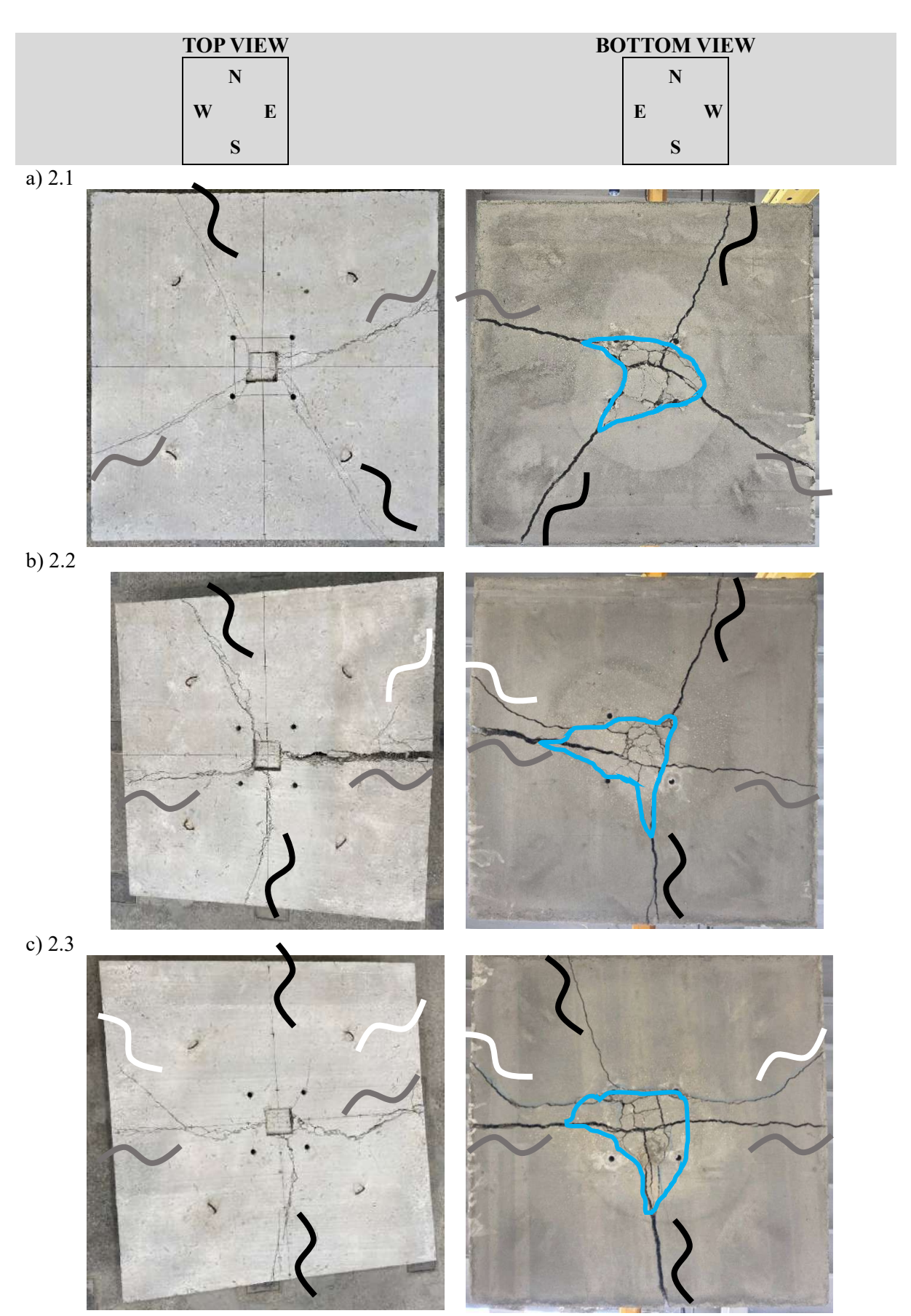


Fig. 5.27 Crack pattern of tested slabs of type 2 (PM_2): first (grey curve), second (black curve), and further (white curve) flexural cracks with marked punching cone perimeter

5.2.3.3 Deflection profiles

Fig. 5.28 presents the deflection profiles of type 2 ground slabs under a central concentrated force. The results indicated deflections associated with the first and second flexural cracking forces (F_{cr1} and F_{cr2}) and the punching shear force (F_p) along the N-S and W-E axes. It must be mentioned that prior to the first flexural crack, certain parts of slab edges were not in contact with the underlying supporting steel rollers, as evidenced in Fig. 5.28. Specifically, the deflection profiles for F_{crl} show that LVDTs no. 1, 4, 7, and 10 of slabs 2.1 and 2.3, and no. 4, 7, and 10 of slabs 2.2, exhibited deflections relative to their initial positions. In slab 2.1, both the S and N edges made contact with the rollers during the load increment from F_{cr1} to F_{cr2} , as indicated by the increase in LVDTs no. 1 and 7. The term 'edge contacted with the roller' refers to the contact between the slab's lower surface and the roller at the location corresponding to the LVDT measurement point. In slab 2.2, these parts of S edge were already in contact, and the N edge also contacted the rollers prior to reaching F_{cr2} , as evidenced by the increase in LVDT no. 7 compared to the deflection profile at F_{crl} . In slab 2.3, the LVDT measurement place only on the N edge contacted the rollers during the load increment from F_{cr1} to F_{cr2} (LVDT no. 7 increased), while on the S edge showed a continued decrease in LVDT no. 1 relative to the F_{crl} profile. Places corresponding with LVDTs no. 4 and 10 of all slabs maintained a lack of contact with the rollers on W and E sides, recording even lower deflections at load level F_{cr2} . In conclusion, deflection profile analysis indicated that at the beginning of the tests, the slabs were not fully ground-supported or uniformly on all four rollers, but rather partially by the ground and/or one to four steel rollers. Along with the continuation of the test, at the punching shear load level F_p , the edges of type 2 slabs typically lost contact with the rollers due to observed corner and edge uplift and as a result of slab rotation on the steel linear supports. Additionally, these contributed to partial loss of slab contact with the ground support. However, determining the precise timing and magnitude of edge uplift, deflections, and the actual slab contact area with the subbase was challenging, as it remained unclear when the slab engaged the supporting rollers, and which position of the LVDTs should be referred to. Nonetheless, Fig. 5.28 suggests that at load level F_p , type 2 slabs likely maintained contact with the subbase over the majority of the area defined by the soil containment box (995 x 995 mm). The deflection profiles also indicated that increased load intensity resulted in non-uniform deflections, likely due to uneven slab failure progression and load redistribution.

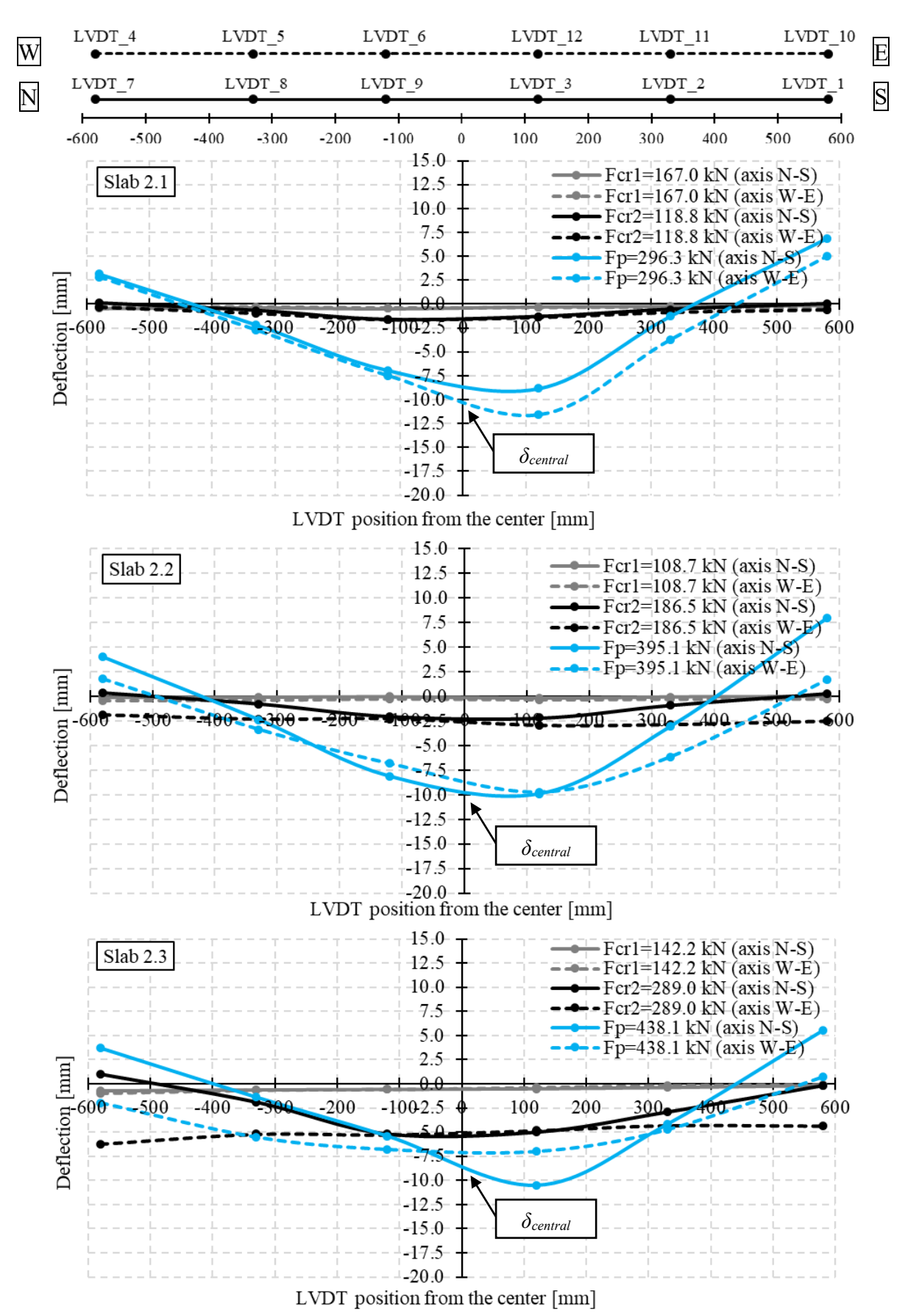


Fig. 5.28 2D deflection profiles of slabs of type 2 (PM_2) corresponding with the first and second flexural cracking force (F_{cr1} and F_{cr2}), and punching shear force (F_p)

5.2.3.4 Punching cone characteristics

Fig. 5.29 illustrates the distinct displacement of the central punching shear cone on the load application surface relative to the surrounding portion of the slabs, which was equal to around 6.0, 2.5, and 1.8 cm for slab 2.1, 2.2, and 2.3, respectively. To examine the punching cones, they were pushed out from the slabs using a manual hydraulic jack stabilized by a steel frame (Fig. 4.26 and Fig. 4.27). Fig. 5.30 presents the top and side views of the punching cones from slabs of type 2 (PM_2). The inclination angles θ of the punching cones were measured in six distinct positions along the cone sidewalls using an angle finder ruler. The single and average values of θ are documented in Table 5.21. The inspection indicated that the punching cones had an irregular shape of truncated pyramid with an average θ of 68.0°, 61.0°, and 65.7° for slab 3.1, 3.2, and 3.3, respectively. It is noteworthy that the cones maintained structural integrity, facilitating their movement and transport.



Fig. 5.29 Punching of the tested slabs of type 2 (PM_2) at the load application surface

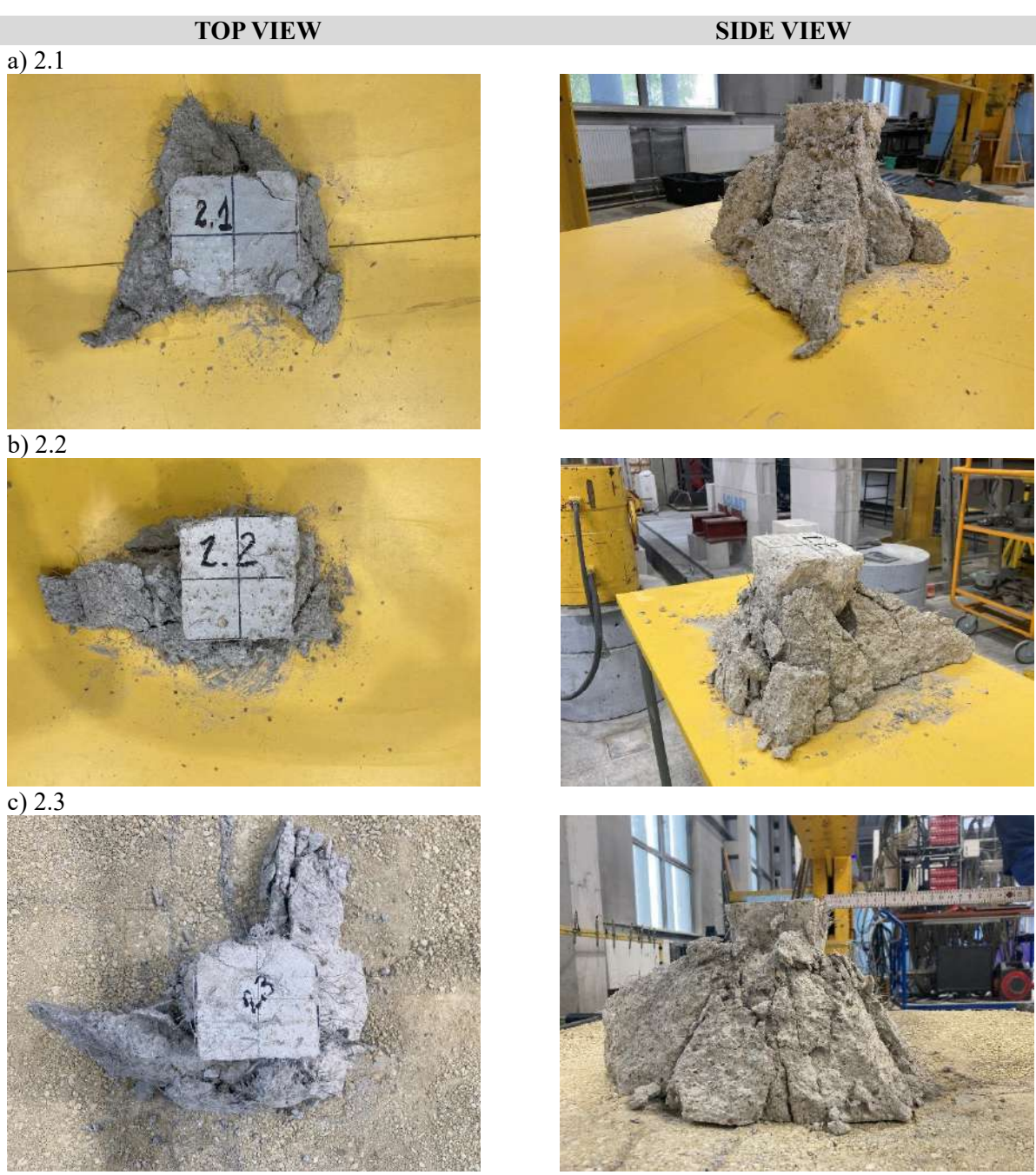


Fig. 5.30 Punching cones from tested slabs of type 2 (PM_2)

Table 5.21 Punching cone inclination angles θ for tested slabs of type 2 (PM_2)

| Slab no. | Punching cone inclination angles $	heta$ | Average $	heta$ |
|----------|--|-------------------------|
| 2.1 | 75°, 88°, 48°, 63°, 65°, 69° | $\theta = 68.0^{\circ}$ |
| 2.2 | 75°, 51°, 53, 45°, 78°, 64° | $\theta = 61.0^{\circ}$ |
| 2.3 | 45°, 58°, 67°, 60°, 76°, 88° | θ = 65.7° |

5.2.4. Slabs PM_3 – type 3

5.2.4.1 Load-deflection response

For ground slabs type 3 with 3 kg/m³ of PM fibers, three samples measuring 200 x 1200 x 1200 mm were subjected to central concentrated force testing. Fig. 5.31a shows the loading force F versus central deflection $\delta_{central}$ curves, derived as a median from LVDTs no. 3, 6, 9, and 12 positioned near the slab center. Fig. 5.31b presents the trend curves (standardized values), illustrating the relationship between the ratio of applied force to maximum observed force (F/F_{max}) and the ratio of central deflection corresponding to F to that corresponding to F_{max} ($\delta_{central}/\delta_{central,F_{max}}$). Finally, Table 5.22 summarizes the flexural cracking forces (F_{cr1} and F_{cr2}) and punching shear forces (F_p) with associated central deflections for type 3 slabs.

The results indicated that deflection of the SyFRC slabs exhibited a nearly linear response to increasing load until the first flexural cracking force was reached. Initial nonlinearities were attributed to setup adjustments and actuator bearing against the steel frame. Notably, the F- $\delta_{central}$ plot revealed no evidence of crack initiation prior to F_{crl} , what was also confirmed by visual observations during testing. However, monitoring of crack propagation on the slab's underside was not feasible due to ground support. PM 3 slabs 3.1, 3.2, and 3.3 experienced edge cracking at F_{crl} values of 148.73 kN (N and S sides), 96.91 kN (W and E sides), and 164.40 kN (N and S sides), respectively. Post F_{cr1} , load-carrying capacities decreased by 27%, 65%, and 31%, respectively. Additionally, the F- $\delta_{central}$ plot of slab 3.2 exhibited a notably nonlinear force increase compared to slabs 3.1 and 3.3. This may be attributed to the gradual increase in the contact area between the slab and both the supporting ground and the steel rollers as the applied force increased. The second flexural crack (F_{cr2}) for slabs 3.2 and 3.3 occurred at 132.98 kN (S side) and 226.86 kN (E side), followed by force reductions of 16% and 7%, respectively. Similarly to slab 2.1, slab 3.1 recorded an F_{cr2} value lower than F_{cr1} of 126.35 kN (N and E sides), after which a 28% decrease in force was observed. The F- $\delta_{central}$ plot also revealed the appearance of the third flexural crack on W side of slab 3.3 at load equal to 249.76 kN. Subsequently, load-bearing capacities of the slabs increased with further deflection until reaching the punching shear failure force (F_p) equals to 249.35 kN, 276.69 kN, and 381.67 for slab 3.1, 3.2, and 3.3, respectively. It must be mentioned that all slabs surpassed both F_{cr1} and F_{cr2} at the point of the punching shear force F_p . Ultimately, slabs 3.1 and 3.3 experienced almost twice lower vertical deflections corresponding to punching shear force (-6.337 mm and -7.817 mm)

compared to slab 3.2 (-12.990 mm). Testing of 3.1 and 3.3 slabs terminated upon the observation of a sudden force drop and significant surface punching at the load application area. In case of slab 3.2, the actuator was reaching a stroke close to its maximum thus the test had to be stopped. The failure mechanism for slabs 3.1, 3.2, and 3.3 was identified as punching shear failure. Finally, it must be highlighted that the presence of 3 kg/m³ of PM fibers prevented brittle failure of the SyFRC slabs, thereby maintaining their structural integrity and facilitating intact lifting and inspection from below (Fig. 5.32).

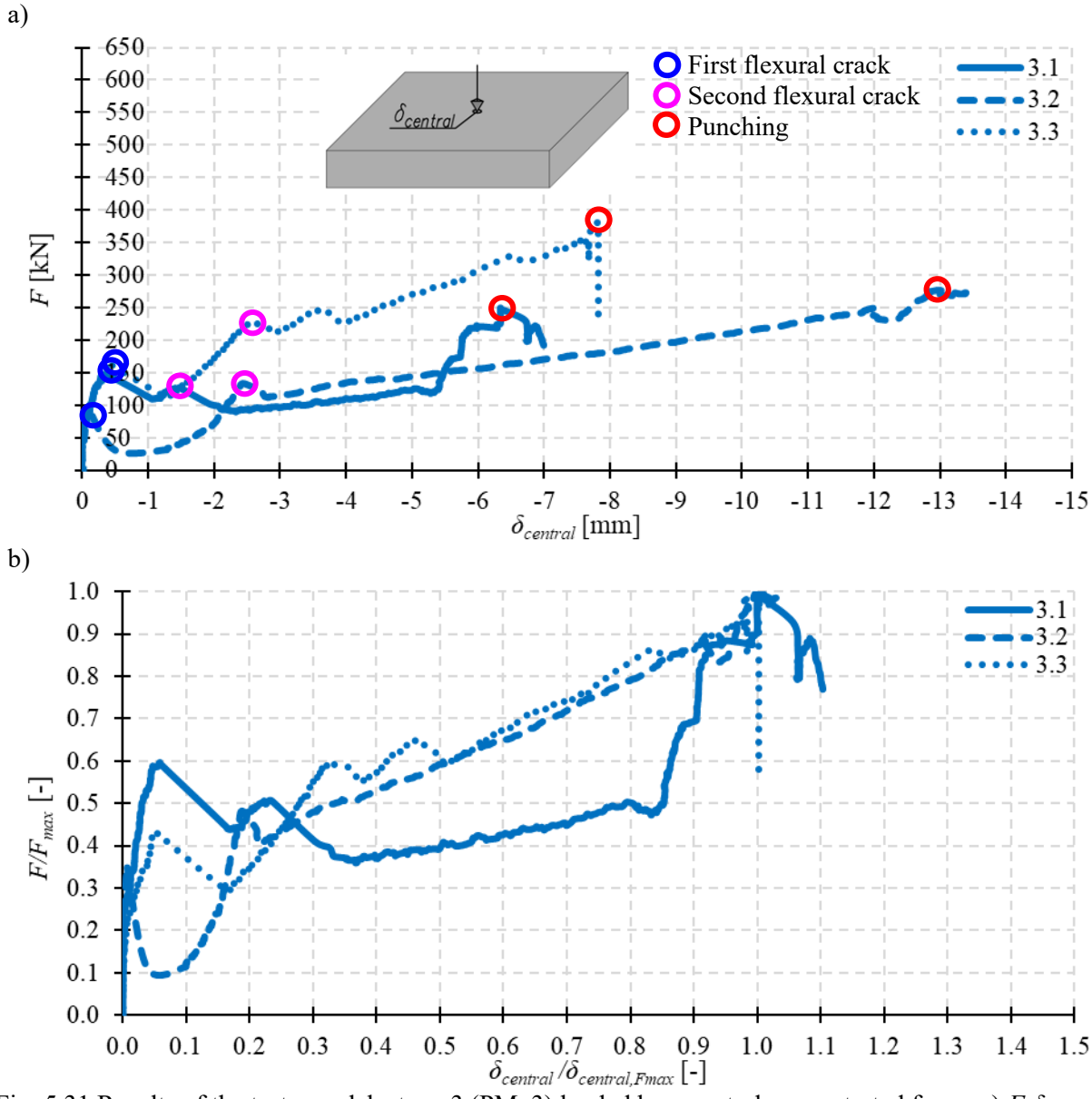


Fig. 5.31 Results of the tests on slabs type 3 (PM_3) loaded by a central concentrated force: a) F- $\delta_{central}$ curve, b) F/F_{max} - $\delta_{central}/\delta_{central,Fmax}$ curve

Table 5.22 Flexural cracking and punching shear forces with corresponding deflections for slabs type 3 (PM_3)

| Slab no. | F _{cr1} [kN] | δ _{central,Fcr1} [mm] | F _{cr2} [kN] | δ _{central,Fcr2} [mm] | F_p [kN] | δ _{central,Fp} [mm] | F _{max} [kN] | δ _{central,Fmax} [mm] |
|----------|-----------------------|--------------------------------|-----------------------|--------------------------------|------------|------------------------------|-----------------------|--------------------------------|
| 3.1 | 148.73 (N, S) | -0.372 | 126.35 (N, E) | -1.484 | 249.35 | -6.337 | 249.35 | -6.337 |
| 3.2 | 96.91 (W, E) | -0.085 | 132.98 (S) | -2.423 | 276.69 | -12.990 | 276.69 | -12.990 |
| 3.3 | 164.40 (N, S) | -0.429 | 226.86 (E) | -2.528 | 381.67 | -7.817 | 381.67 | -7.817 |



Fig. 5.32 Synthetic fibers PM maintaining the structural integrity of the tested slab 3.2

5.2.4.2 Crack morphology

Fig. 5.33 illustrates the locations of the first and second flexural cracks on the edges of the tested slabs, associated with forces F_{cr1} and F_{cr2} , respectively. Fig. 5.34 shows the crack pattern on the slabs' top and bottom surfaces with the sequence of crack formation. The punching cone perimeters were also marked on the slabs' bottom surfaces.

Observations indicated that flexural cracks initially formed on the bottom edge sides, propagating upwards to the top surface before extending toward the slab center. All slabs exhibited simultaneous initial cracking on two opposing edges: slabs 3.1 and 3.3 on the N and S edges, and slab 3.2 on the W and E edges. An increase in load to F_{cr2} resulted in an additional crack on the N edge and a new crack on the E side of slab 3.1. For slabs 3.2 and 3.3, only one crack formed on the S and E edges, respectively upon reaching the second flexural force F_{cr2} . Notably, slab 3.3 experienced a fourth crack on the W edge shortly after reaching F_{cr2} . Finally, the circumferential cracks resulting from the punching shear were observed at the bottom of the slabs under the load application area. These cracks defined the base of the punching shear cones. It must be mentioned that no circumferential cracks were observed at the top of the slabs, indicating that the failure mechanism was not associated with exceeding the negative bending moment capacity.



Fig. 5.33 Location of first (grey arrow), second (black arrow), and third (red arrow) flexural cracks of tested slabs of type $3 \, (PM_3)$

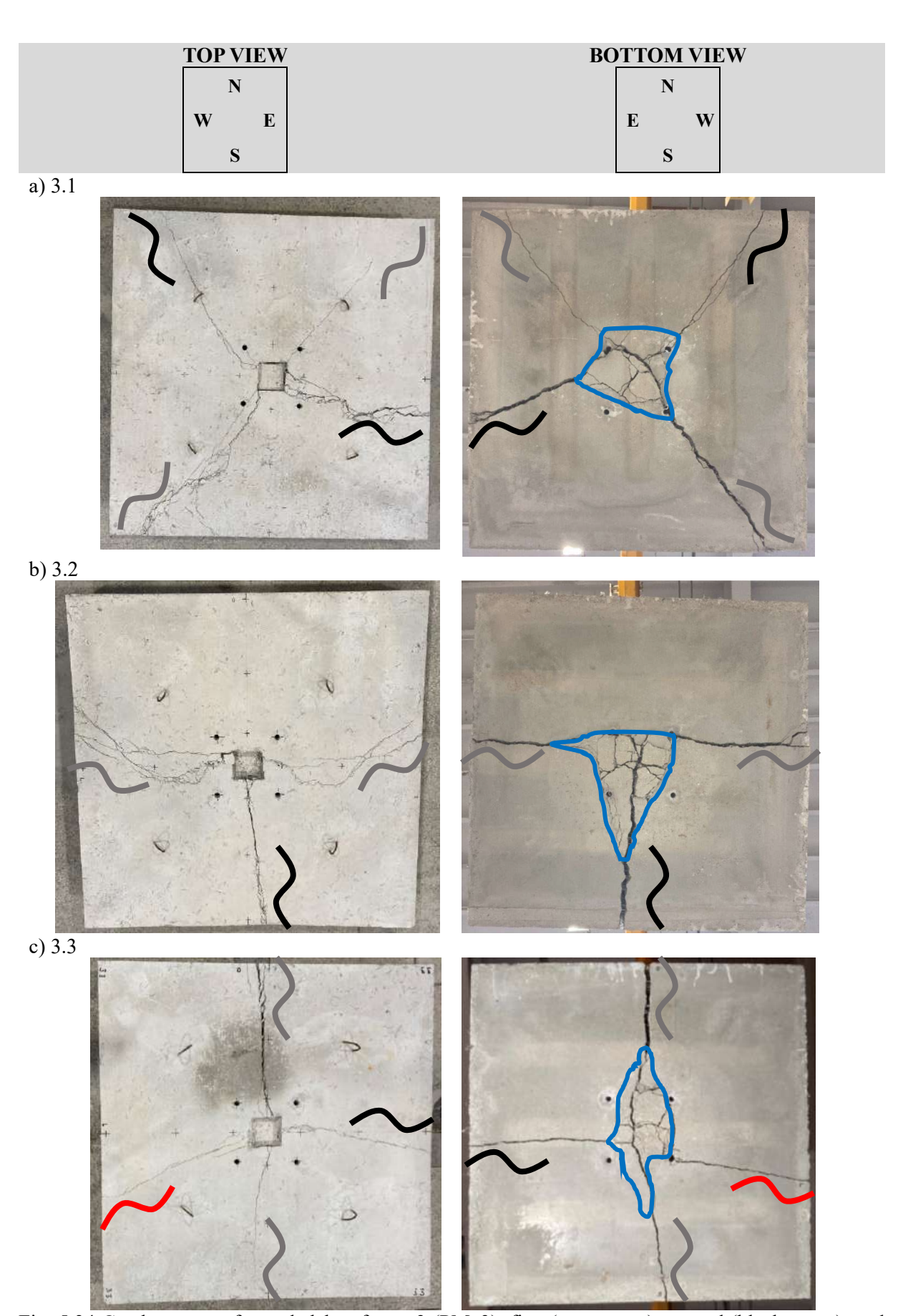


Fig. 5.34 Crack pattern of tested slabs of type 3 (PM_3): first (grey curve), second (black curve), and third (red curve) flexural cracks with marked punching cone perimeter

The crack morphology of slab 3.2, fractured into three sections, was similarly to that of slab 1.1 and 1.3, however, crack propagation did not result in slab division. Slabs 3.1 and 3.3 exhibited similar crack patterns, dividing the slabs into four segments. Notably, slab 3.1 displayed cracks oriented more diagonally, while slab 3.3 had crosswise crack orientations. Additionally, in case of sample 3.1 no visible cracks were present on the W edge, whereas two cracks were identified on the N side. These factors may explain the observed distinct load-deflection response of slab 3.1, which was characterized by force F_{cr2} not exceeding F_{cr1} (Fig. 5.31). This may also be attributed to a more significant reduction in stiffness in slab 3.1 following initial flexural cracking, potentially due to a broader range of crack development at F_{cr1} when comparing with slabs 3.2 and 3.3. However, this conclusion remains uncertain as a visual inspection of the crack propagation on the slab's bottom surface was not feasible during testing.

5.2.4.3 Deflection profiles

Fig. 5.35 presents the deflection profiles of type 3 ground slabs under a central concentrated force. The results indicated deflections associated with the first and second flexural cracking forces (F_{cr1} and F_{cr2}) and the punching shear force (F_p) along the N-S and W-E axes. It must be mentioned that prior to the first flexural crack, certain parts of slab edges were not in uniform contact with the underlying supporting steel rollers, as evidenced in Fig. 5.35. Specifically, the deflection profiles for F_{crl} show that LVDTs no. 1, 4, 7, and 10 of slabs 3.1, no. 1, 4, 10 of slab 3.2, and no. 1, 7, 10 of slab 3.3, exhibited deflections relative to their initial positions. In slab 3.1, the N, W, and E edges made contact with the rollers during the load increment from F_{cr1} to F_{cr2} , as indicated by the increase in LVDTs no. 4, 7, and 10. The term 'edge contacted with the roller' refers to the contact between the slab's lower surface and the roller at the location corresponding to the LVDT measurement point. In slab 3.2, the N edge was already in contact, and the opposite parts of the S edge also contacted the rollers prior to reaching F_{cr2} , as evidenced by the increase in LVDT no. 1 compared to the deflection profile at F_{crl} . In slab 3.3, the W edge was already in contact, while the opposite parts of E edge contacted the rollers during the load increment from F_{cr1} to F_{cr2} (LVDT no. 10 increased). Consequently, the LVDT measurement places at edges from the S side for slab 3.1, W and E side for slab 3.2, as well as N and S side for slab 3.3 maintained a lack of contact with the rollers, recording even lower deflections at load level F_{cr2} . In conclusion, deflection profile analysis indicated that initially, the slabs were not fully ground-supported or uniformly on all four rollers, but rather partially by the ground and/or one to four steel rollers.

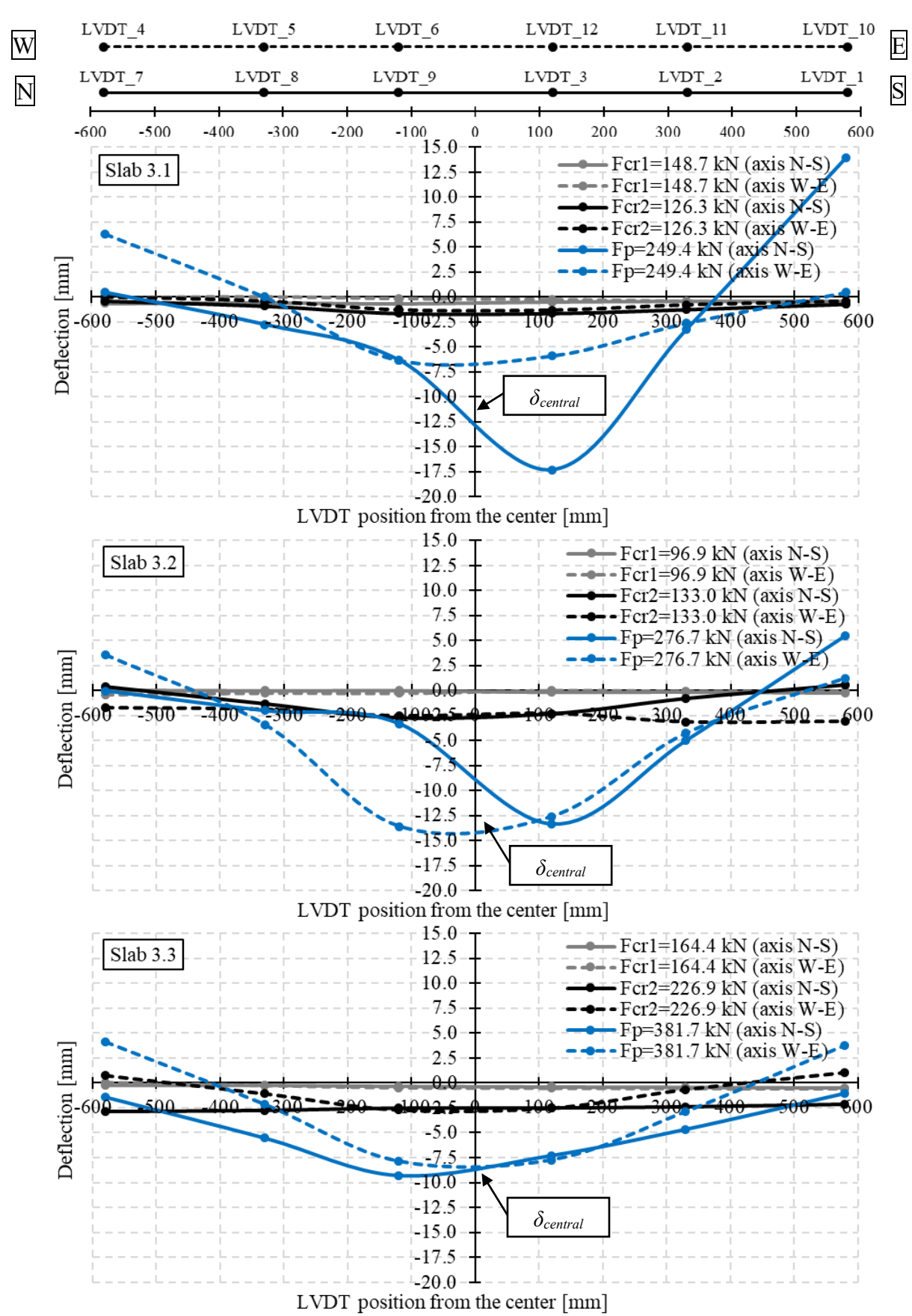


Fig. 5.35 2D deflection profiles of slabs of type 3 (PM_3) corresponding with the first and second flexural cracking force (F_{cr1} and F_{cr2}), and punching shear force (F_p)

Along with the continuation of the test, at the punching shear load level F_p , the edges of type 3 slabs typically lost contact with the rollers due to observed corner and edge uplift and as a result of slab rotation on the steel linear supports. Additionally, these contributed to partial loss of slab contact with the ground support. However, determining the precise timing and magnitude of edge uplift, deflections, and the actual slab contact area with the subbase was challenging, as it remained unclear when the slab engaged the supporting rollers, and which position of the LVDTs should be referred to. Nonetheless, Fig. 5.35 suggests that at load level F_p , type 3 slabs likely maintained contact with the subbase over the majority of the area defined by the soil containment box (995 x 995 mm). The deflection profiles also indicated that increased load intensity resulted in non-uniform deflections, likely due to uneven slab failure progression and load redistribution.

5.2.4.4 Punching cone characteristics

Fig. 5.36 illustrates the distinct displacement of the central punching shear cone on the load application surface relative to the surrounding portion of the slabs, which was equal to around 3.1, 4.5, and 3.5 cm for slab 3.1, 3.2, and 3.3, respectively. To examine the punching cones, they were pushed out from the slabs using a manual hydraulic jack stabilized by a steel frame (Fig. 4.26 and Fig. 4.27). Fig. 5.37 presents the top and side views of the punching cones from slabs of type 3 (PM_3). The inclination angles θ of the punching cones were measured in six distinct positions along the cone sidewalls using an angle finder ruler. The single and average values of θ are documented in Table 5.23. The inspection indicated that the punching cones had an irregular shape of truncated pyramid with an average θ of 66.0°, 63.2°, and 66.8° for slab 3.1, 3.2, and 3.3, respectively. It is noteworthy that the cones maintained structural integrity, facilitating their movement and transport.



Fig. 5.36 Punching of the tested slabs of type 3 (PM 3) at the load application surface

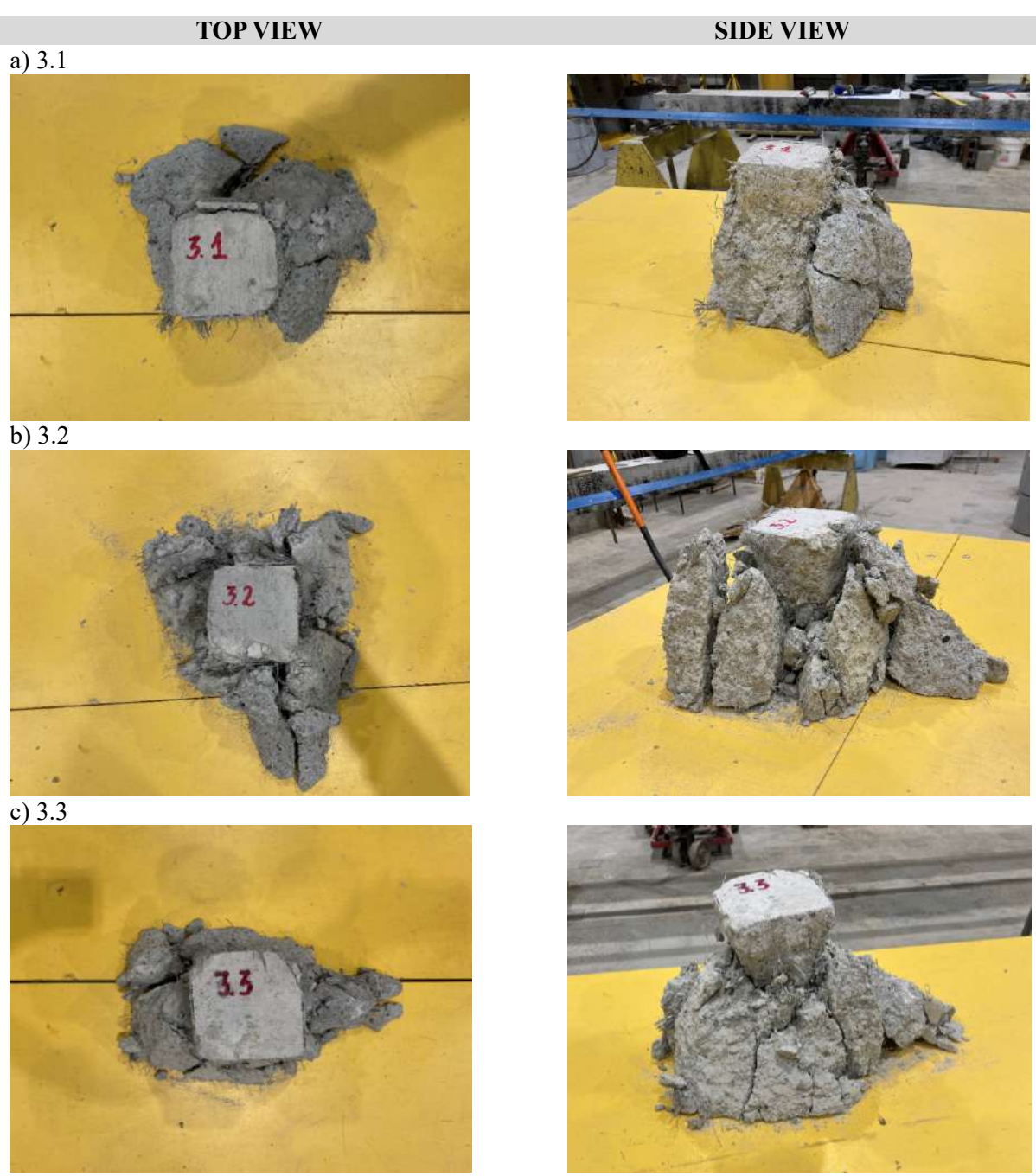


Fig. 5.37 Punching cones from tested slabs of type 3 (PM_3)

Table 5.23 Punching cone inclination angles θ for tested slabs of type 3 (PM_3)

| Slab no. | Punching cone inclination angles $	heta$ | Average $	heta$ |
|----------|--|------------------|
| 3.1 | 61°, 71°, 84°, 60°, 64°, 56° | θ = 66.0° |
| 3.2 | 59°, 49°, 68°, 73°, 67°, 63° | θ = 63.2° |
| 3.3 | 69°, 77°, 64°, 46°, 74°, 70° | θ = 66.8° |

5.2.5. Slabs PD_2 - type 4

5.2.5.1 Load-deflection response

For ground slabs type 4 with 2 kg/m³ of PD fibers, three samples measuring 200 x 1200 x 1200 mm were subjected to central concentrated force testing. Fig. 5.38a shows the loading force F versus central deflection $\delta_{central}$ curves, derived as a median from LVDTs no. 3, 6, 9, and 12 positioned near the slab center. Fig. 5.38b presents the trend curves (standardized values), illustrating the relationship between the ratio of applied force to maximum observed force (F/F_{max}) and the ratio of central deflection corresponding to F to that corresponding to F_{max} ($\delta_{central}/\delta_{central,F_{max}}$). Finally, Table 5.24 summarizes the flexural cracking forces (F_{cr1} and F_{cr2}) and punching shear forces (F_p) with associated central deflections for type 4 slabs.

The results indicated that deflection of the SyFRC slabs exhibited a nearly linear response to increasing load until the first flexural cracking force was reached. Initial nonlinearities were attributed to setup adjustments and actuator bearing against the steel frame. Notably, the F- $\delta_{central}$ plot revealed no evidence of crack initiation prior to F_{crl} , what was also confirmed by visual observations during testing. However, monitoring of crack propagation on the slab's underside was not feasible due to ground support. PD 2 slabs 4.1, 4.2, and 4.3 experienced edge cracking at F_{crl} values of 463.13 kN (N, S, and E sides), 198.48 kN (W and E sides), and 254.92 kN (N and S sides), respectively. Post F_{crl} , load-carrying capacities decreased by 21%, 44%, and 7%, respectively. The second flexural crack (F_{cr2}) for slabs 4.2 and 4.3 occurred at 405.47 kN (N and S sides) and 265.67 kN (W and E sides), followed by force reductions of 18% and 31%, respectively. In contrast, slab 4.1 recorded an F_{cr2} value lower than F_{cr1} of 439.38 kN (W side), after which a 7% decrease in force was observed. Subsequently, load-bearing capacities of the slabs increased with further deflection until reaching the punching shear failure force (F_p) equals to 462.37 kN, 468.97 kN, and 513.00 kN for slab 4.1, 4.2, and 4.3, respectively. Slabs 4.2 and 4.3 surpassed both F_{cr1} and F_{cr2} at the point of the punching shear force F_p , while slab 4.1 exhibited an F_p slightly lower than F_{crl} but higher than F_{cr2} . Ultimately, slabs 4.1 and 4.3 experienced larger vertical deflections corresponding to punching shear force (-8.486 mm and -7.911 mm) compared to slab 4.2 (-11.695 mm). Testing of PD 2 slabs terminated upon the observation of a sudden force drop and significant surface punching at the load application area. The failure mechanism for slabs 4.1, 4.2, and 4.3 was identified as punching shear failure.

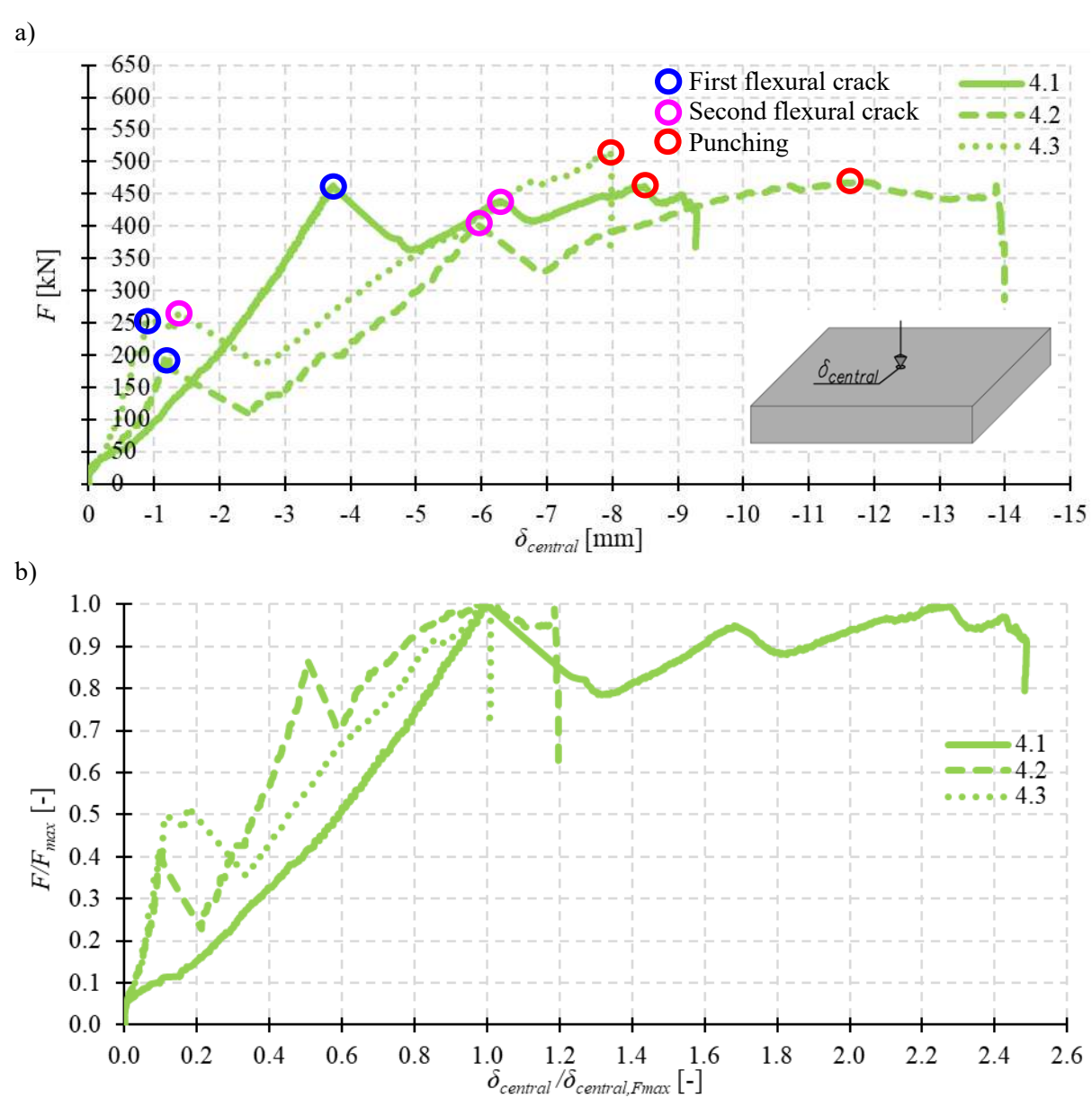


Fig. 5.38 Results of the tests on slabs type 4 (PD_2) loaded by a central concentrated force: a) F- $\delta_{central}$ curve, b) F/F_{max} - $\delta_{central}/\delta_{central,Fmax}$ curve

Table 5.24 Flexural cracking and punching shear forces with corresponding deflections for slabs type 4 (PD_2)

| Slab no. | F _{cr1} [kN] | δ _{central,Fcr1} [mm] | F _{cr2} [kN] | δ _{central,Fcr2} [mm] | F_p [kN] | δ _{central,Fp} [mm] | F _{max} [kN] | δ _{central,Fmax} [mm] |
|----------|-----------------------|--------------------------------|-----------------------|--------------------------------|------------|------------------------------|-----------------------|--------------------------------|
| 4.1 | 463.13 (N, S, E) | -3.731 | 439.38 (W) | -6.272 | 462.37 | -8.486 | 463.13 | -3.731 |
| 4.2 | 198.48 (W, E) | -1.242 | 405.47 (N, S) | -5.918 | 468.97 | -11.695 | 468.97 | -11.695 |
| 4.3 | 254.92 (N, S) | -0.887 | 265.67 (W, E) | -1.379 | 513.00 | -7.911 | 513.00 | -7.911 |

Finally, it must be highlighted that the presence of 2 kg/m³ of PD fibers prevented brittle failure of the SyFRC slabs, thereby maintaining their structural integrity and facilitating intact lifting and inspection from below (Fig. 5.39).



Fig. 5.39 Synthetic fibers PD maintaining the structural integrity of the tested slab 4.2

5.2.5.2 Crack morphology

Fig. 5.40 illustrates the locations of the first and second flexural cracks on the edges of the tested slabs, associated with forces F_{cr1} and F_{cr2} , respectively. Fig. 5.41 presents the crack pattern on the top and bottom surface of the slabs with the sequence of crack formation. Additionally, the perimeters of the punching cones were marked at the bottom surfaces of the slabs.

The crack morphology of all slabs of type 4 was similar, dividing the slabs into four segments. Observations indicated that flexural cracks initially formed on the bottom edge sides, propagating upwards to the top surface before extending toward the slab center. The distinct load-deflection response of slab 4.1, compared to slabs 4.2 and 4.3 (Fig. 5.38), can be attributed to the varying crack patterns observed. Specifically, slab 4.1 exhibited initial cracking simultaneously on three edges similarly to slab 1.2, whereas slabs 4.2 and 4.3 exhibited initial cracking on only two opposite edges. Differences in the behavior of slab 4.1, characterized by force F_{cr2} not exceeding F_{cr1} , may also be a consequence of a more significant stiffness reduction compared to slabs 4.2 and 4.3 after first flexural cracking. This reduction might have been a result of a broader crack development range at F_{crl} . However, this conclusion remains uncertain as a visual inspection of the crack propagation on the slab's bottom surface was not feasible during testing. Another contributing factor may be the slightly different directions of the cracks in slab 4.1, which were oriented more diagonally compared to the crosswise crack orientation of slabs 4.2 and 4.3. Finally, the circumferential cracks resulting from the punching shear were observed at the bottom of the slabs under the load application area. These cracks defined the base of the punching shear cones. It must be mentioned that no circumferential cracks were observed at the top of the slabs, indicating that the failure mechanism was not associated with exceeding the negative bending moment capacity.



Fig. 5.40 Location of first (grey arrow), and second (black arrow) flexural cracks of tested slabs of type 4 (PD_2)

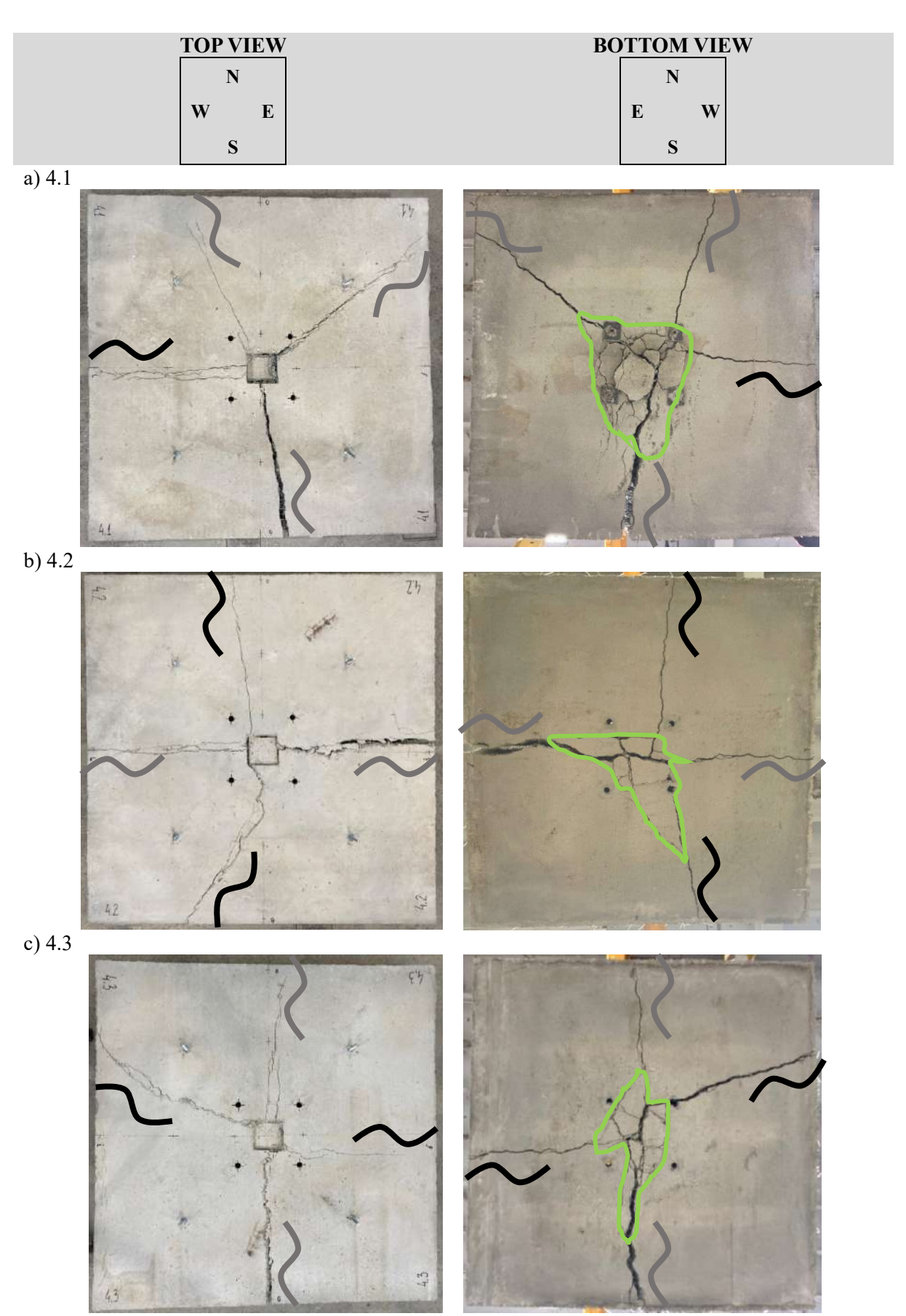


Fig. 5.41 Crack pattern of tested slabs of type 4 (PD_2): first (grey arrow), and second (black arrow) flexural cracks with marked perimeter of the punching cone

5.2.5.3 Deflection profiles

Fig. 5.42 presents the deflection profiles of type 4 ground slabs under a central concentrated force. The results indicated deflections associated with the first and second flexural cracking forces (F_{cr1} and F_{cr2}) and the punching shear force (F_p) along the N-S and W-E axes. It must be mentioned that prior to the first flexural crack, certain parts of slab edges were not in contact with the underlying supporting steel rollers, as evidenced in Fig. 5.42. Specifically, the deflection profiles for F_{crl} show that LVDTs no. 1, 4, 7, and 10 of all slabs exhibited deflections relative to their initial positions. In slab 4.1, the N, W, and E edges made contact with the rollers during the load increment from F_{crl} to F_{cr2} , as indicated by the increase in LVDTs no. 7, 4 and 10. The term 'edge contacted with the roller' refers to the contact between the slab's lower surface and the roller at the location corresponding to the LVDT measurement point. In slab 4.2, these parts of both S and N edge contacted the rollers prior to reaching F_{cr2} , as evidenced by the increase in LVDTs no. 1 and 7 compared to the deflection profile at F_{crl} . In slab 4.3, the places corresponding with the LVDT location on both W and E edge contacted the rollers during the load increment from F_{cr1} to F_{cr2} (LVDT no. 4 and 10 increased). Consequently, these parts of edges from the S side for slab 4.1, W and E side for slab 4.2, as well as N and S side for slab 4.3 maintained a lack of contact with the rollers, recording even lower deflections at load level F_{cr2} . In conclusion, deflection profile analysis indicated that at the beginning of the tests, the slabs were not fully ground-supported or uniformly on all four rollers, but rather partially by the ground and/or one to four steel rollers. Along with the continuation of the test, at the punching shear load level F_p , the edges of type 4 slabs typically lost contact with the rollers due to observed corner and edge uplift and as a result of slab rotation on the steel linear supports. Additionally, these contributed to partial loss of slab contact with the ground support. However, determining the precise timing and magnitude of edge uplift, deflections, and the actual slab contact area with the subbase was challenging, as it remained unclear when the slab engaged the supporting rollers, and which position of the LVDTs should be referred to. Nonetheless, Fig. 5.42 suggests that at load level F_p , type 4 slabs likely maintained contact with the subbase over the majority of the area defined by the soil containment box (995 x 995 mm). The deflection profiles also indicated that increased load intensity resulted in non-uniform deflections, likely due to uneven slab failure progression and load redistribution.

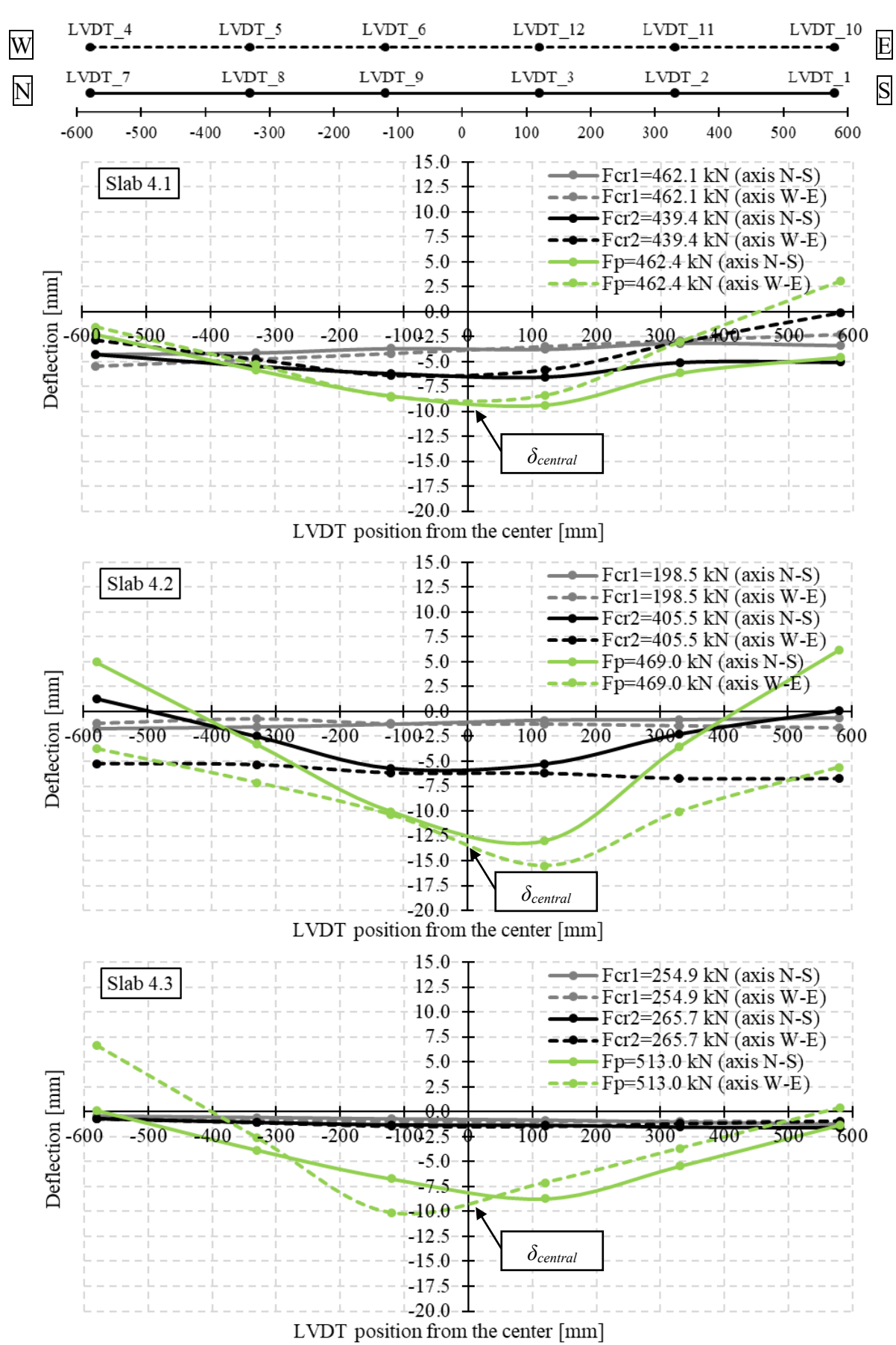


Fig. 5.42 2D deflection profiles of slabs of type 4 (PD_2) corresponding with the first and second flexural cracking force (F_{cr1} and F_{cr2}), and punching shear force (F_p)

5.2.5.4 Punching cone characteristics

Fig. 5.43 illustrates the distinct displacement of the central punching shear cone on the load application surface relative to the surrounding portion of the slabs, which was equal to around 5.0, 2.5, and 2.5 cm for slab 4.1, 4.2, and 4.3, respectively. To examine the punching cones, they were pushed out from the slabs using a manual hydraulic jack stabilized by a steel frame (Fig. 4.26 and Fig. 4.27). Fig. 5.44 presents the top and side views of the punching cones from slabs of type 4 (PD_2). The inclination angles θ of the punching cones were measured in six distinct positions along the cone sidewalls using an angle finder ruler. The single and average values of θ are documented in Table 5.25. The inspection indicated that the punching cones had an irregular shape of truncated pyramid with an average θ of 56.8°, 61.5°, and 71.7° for slab 4.1, 4.2, and 4.3, respectively. It is noteworthy that the cones maintained structural integrity, facilitating their movement and transport.



Fig. 5.43 Punching of the tested slabs of type 4 (PD 2) at the load application surface

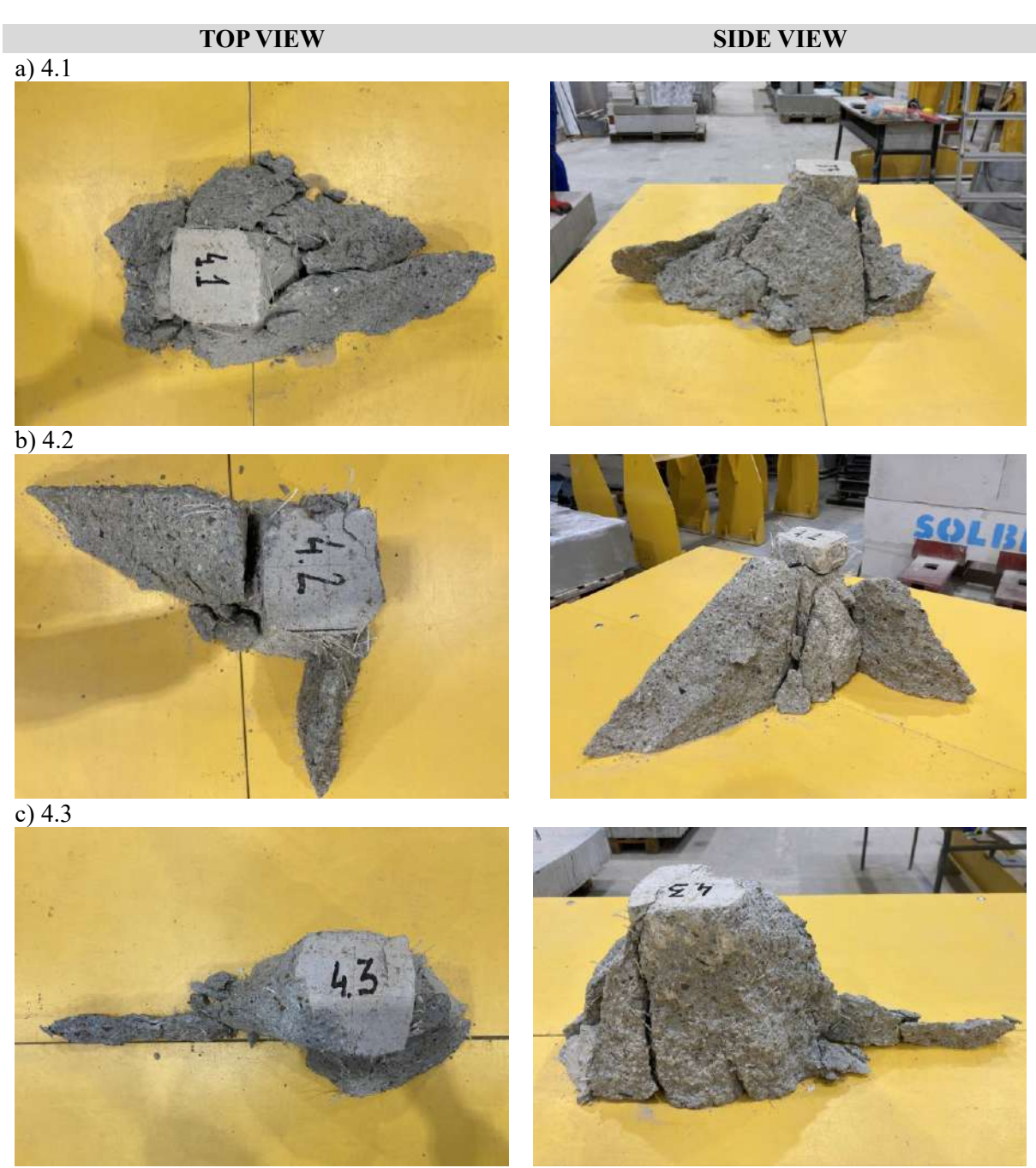


Fig. 5.44 Punching cones from tested slabs of type 4 (PD_2)

Table 5.25 Punching cone inclination angles θ for tested slabs of type 4 (PD_2)

| Slab no. | Punching cone inclination angles $	heta$ | Average θ |
|----------|--|-------------------------|
| 4.1 | 65°, 60°, 69°, 58°, 47°, 42° | θ = 56.8° |
| 4.2 | 76°, 36°, 63°, 83°, 69°, 42° | θ = 61.5° |
| 4.3 | 56°, 70°, 88°, 66°, 84°, 66° | $\theta = 71.7^{\circ}$ |

5.2.6. Slabs PD_3 – type 5

5.2.6.1 Load-deflection response

For ground slabs type 5 with 3 kg/m³ of PD fibers, three samples measuring 200 x 1200 x 1200 mm were subjected to central concentrated force testing. Fig. 5.45a shows the loading force F versus central deflection $\delta_{central}$ curves, derived as a median from LVDTs no. 3, 6, 9, and 12 positioned near the slab center. Fig. 5.45b presents the trend curves (standardized values), illustrating the relationship between the ratio of applied force to maximum observed force (F/F_{max}) and the ratio of central deflection corresponding to F to that corresponding to F_{max} ($\delta_{central}/\delta_{central,Fmax}$). Finally, Table 5.26 summarizes the flexural cracking forces (F_{cr1} and F_{cr2}) and punching shear forces (F_p) with associated central deflections for type 5 slabs. The results indicated that deflection of the SyFRC slabs exhibited a nearly linear response to increasing load until the first flexural cracking force was reached. Initial nonlinearities were attributed to setup adjustments and actuator bearing against the steel frame. Notably, the F- $\delta_{central}$ plot revealed no evidence of crack initiation prior to F_{crl} , what was also confirmed by visual observations during testing. However, monitoring of crack propagation on the slab's underside was not feasible due to ground support. PD 3 slabs 5.1, 5.2, and 5.3 experienced edge cracking at F_{cr1} values of 186.70 kN (N and S sides), 181.86 kN (N and S sides), and 178.37 kN (W and E sides), respectively. Post F_{crl} , load-carrying capacities decreased by 29%, 41%, and 46%, respectively. The second flexural crack (F_{cr2}) for slabs 5.1, 5.2, and 5.3 occurred at 240.50 kN (W and E sides), 327.22 kN (W and E sides), and 379.48 kN (N and S sides), followed by force reductions of 21%, 19%, and 13%, respectively. All slabs of type 5 recorded an F_{cr2} value greater than F_{cr1} . Subsequently, load-bearing capacities of the slabs increased with further deflection until reaching the punching shear failure force (F_p) equals to 563.71 kN, 528.91 kN, and 601.80 kN for slab 5.1, 5.2, and 5.3, respectively. Each slab surpassed both F_{cr1} and F_{cr2} at the point of the punching shear force F_p . Ultimately, slabs of type 5 experienced comparable vertical deflections corresponding to punching shear force varying from -7.251 to -9.176 mm. Testing of PD 3 slabs terminated upon the observation of a sudden force drop and significant surface punching at the load application area. The failure mechanism for slabs 5.1, 5.2, and 5.3 was identified as punching shear failure. Finally, it must be highlighted that the presence of 3 kg/m³ of PD fibers prevented brittle failure of the SyFRC slabs, thereby maintaining their structural integrity and facilitating intact lifting and inspection from below (Fig. 5.46).

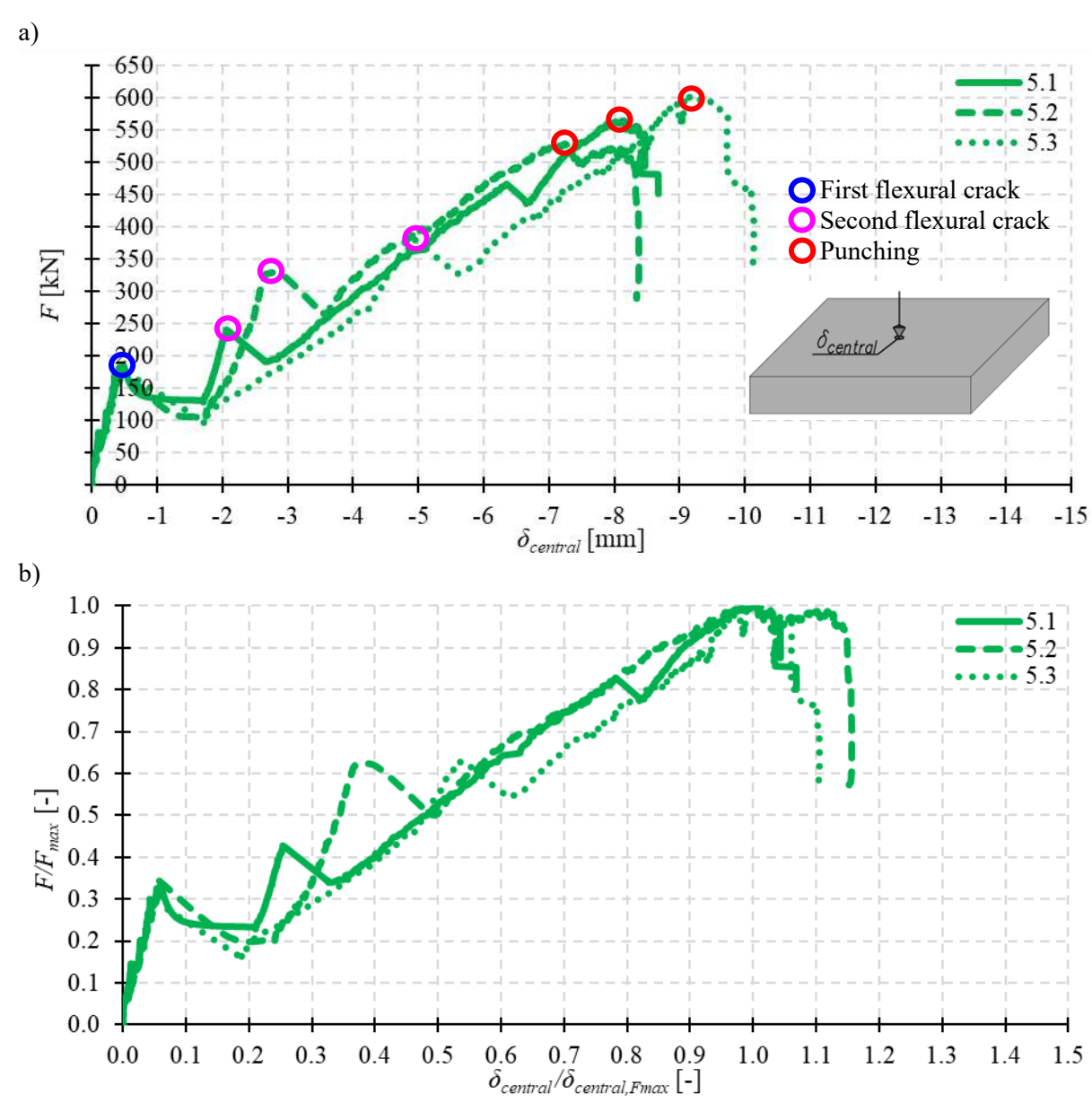


Fig. 5.45 Results of the tests on slabs type 5 (PD_3) loaded by a central concentrated force: a) F- $\delta_{central}$ curve, b) F/F_{max} - $\delta_{central}/\delta_{central,F_{max}}$ curve

Table 5.26 Flexural cracking and punching shear forces with corresponding deflections for slabs type 5 (PD_2)

| Slab no. | F _{cr1} [kN] | δ _{central,Fcr1} [mm] | <i>F_{cr2}</i> [kN] | δ _{central,Fcr2} [mm] | F_p [kN] | $\delta_{central,Fp} \ [ext{mm}]$ | F _{max} [kN] | δ _{central,Fmax} [mm] |
|----------|-----------------------|--------------------------------|-----------------------------|--------------------------------|------------|------------------------------------|-----------------------|-----------------------------------|
| 5.1 | 186.70 (N, S) | -0.475 | 240.50 (W, E) | -2.058 | 563.71 | -8.119 | 563.71 | -8.119 |
| 5.2 | 181.86 (N, S) | -0.418 | 327.22 (W, E) | -2.664 | 528.91 | -7.251 | 528.91 | -7.251 |
| 5.3 | 178.37 (W, E) | -0.446 | 379.48 (N, S) | -4.942 | 601.80 | -9.176 | 601.80 | -9.176 |



Fig. 5.46 Synthetic fibers PD maintaining the structural integrity of the tested slab 5.3

5.2.6.2 Crack morphology

Fig. 5.47 illustrates the locations of the first and second flexural cracks on the edges of the tested slabs, associated with forces F_{cr1} and F_{cr2} , respectively. Fig. 5.48 presents the crack pattern on the top and bottom surface of the slabs with the sequence of crack formation. Additionally, the perimeters of the punching cones were marked at the bottom surfaces of the slabs.

The crack morphology of all slabs of type 5 was similar, dividing the slabs into four main segments with some subdivisions in case of slabs 5.1 and 5.2. Observations indicated that flexural cracks initially formed on the bottom edge sides, propagating upwards to the top surface before extending toward the slab center. All slabs exhibited simultaneous initial cracking on two opposing edges: slabs 5.1 and 5.2 on the N and S edges, and slab 5.3 on the W and E edges. An increase in load to F_{cr2} resulted in a secondary flexural cracks on the remaining two edges W, E or S, N depending on the slab. Moreover, additional edge cracks at slabs 5.1 and 5.2 were observed unattributed to the achievement of a specific force, as in the case of slabs 2.2 and 2.3. Finally, the circumferential cracks resulting from the punching shear were observed at the bottom of the slabs under the load application area. These cracks defined the base of the punching shear cones. It must be mentioned that no circumferential cracks were observed at the top of the slabs, indicating that the failure mechanism was not associated with exceeding the negative bending moment capacity.

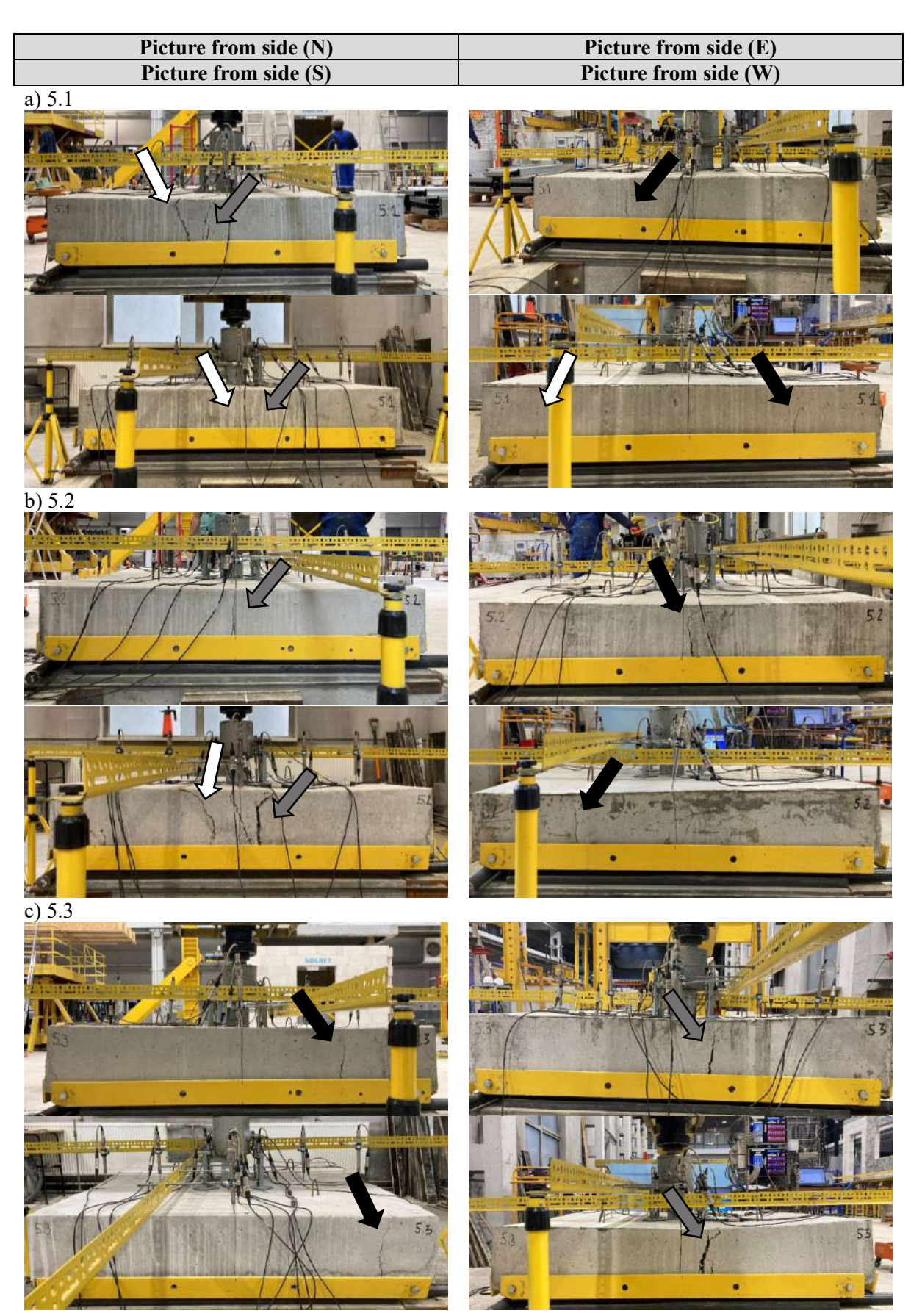


Fig. 5.47 Location of first (grey arrow), second (black arrow), and further (white arrow) flexural cracks of tested slabs of type 5 (PD_3)

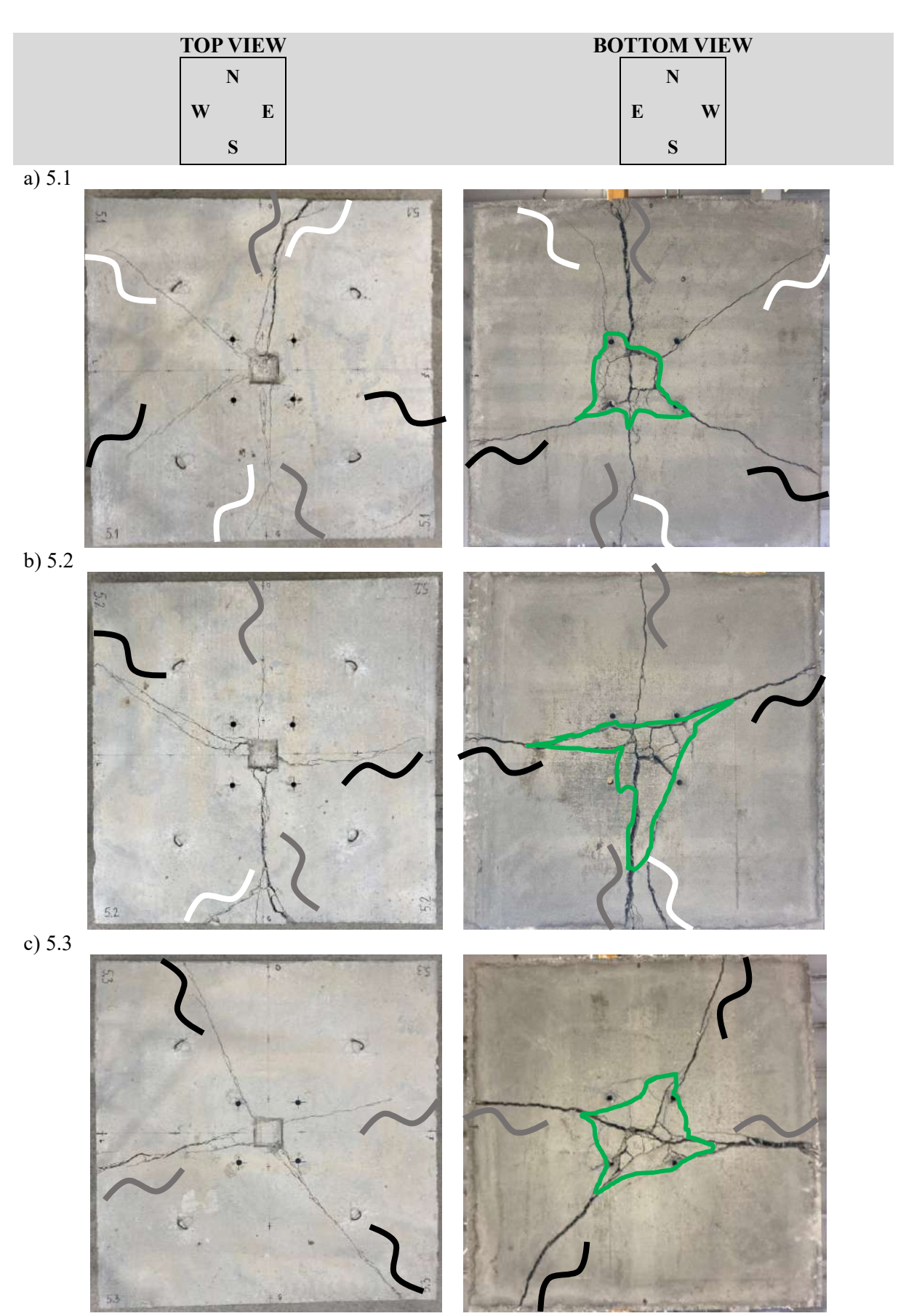


Fig. 5.48 Crack pattern of tested slabs of type 5 (PD_3): first (grey curve), second (black curve), and further (white curve) flexural cracks with marked perimeter of the punching cone

5.2.6.3 Deflection profiles

Fig. 5.49 presents the deflection profiles of type 5 ground slabs under a central concentrated force. The results indicated deflections associated with the first and second flexural cracking forces (F_{cr1} and F_{cr2}) and the punching shear force (F_p) along the N-S and W-E axes. It must be mentioned that prior to the first flexural crack, certain parts of slab edges were not in contact with the underlying supporting steel rollers, as evidenced in Fig. 5.42. Specifically, the deflection profiles for F_{crl} show that LVDTs no. 1, 4, 7, and 10 of all slabs exhibited deflections relative to their initial positions. In slab 5.1 and 5.2, the W and E edges made contact with the rollers during the load increment from F_{cr1} to F_{cr2} , as indicated by the increase in LVDTs no. 4 and 10. The term 'edge contacted with the roller' refers to the contact between the slab's lower surface and the roller at the location corresponding to the LVDT measurement point. In slab 5.3, these parts of both S and N edge contacted the rollers prior to reaching F_{cr2} , as evidenced by the increase in LVDTs no. 1 and 7 compared to the deflection profile at F_{crl} . Consequently, places corresponding with the LVDT location on the edges from the N and S side for slab 5.1 and 5.2 as well as from W and E side for slab 5.3 maintained a lack of contact with the rollers, recording even lower deflections at load level F_{cr2} . In conclusion, deflection profile analysis indicated that at the beginning of the tests, the slabs were not fully ground-supported or uniformly on all four rollers, but rather partially by the ground and/or one to four steel rollers. Along with the continuation of the test, at the punching shear load level F_p , the edges of type 5 slabs typically lost contact with the rollers due to observed corner and edge uplift and as a result of slab rotation on the steel linear supports. Additionally, these contributed to partial loss of slab contact with the ground support. However, determining the precise timing and magnitude of edge uplift, deflections, and the actual slab contact area with the subbase was challenging, as it remained unclear when the slab engaged the supporting rollers, and which position of the LVDTs should be referred to. Nonetheless, Fig. 5.49 suggests that at load level F_p , type 5 slabs likely maintained contact with the subbase over the majority of the area defined by the soil containment box (995 x 995 mm). The deflection profiles also indicated that increased load intensity resulted in non-uniform deflections, likely due to uneven slab failure progression and load redistribution.

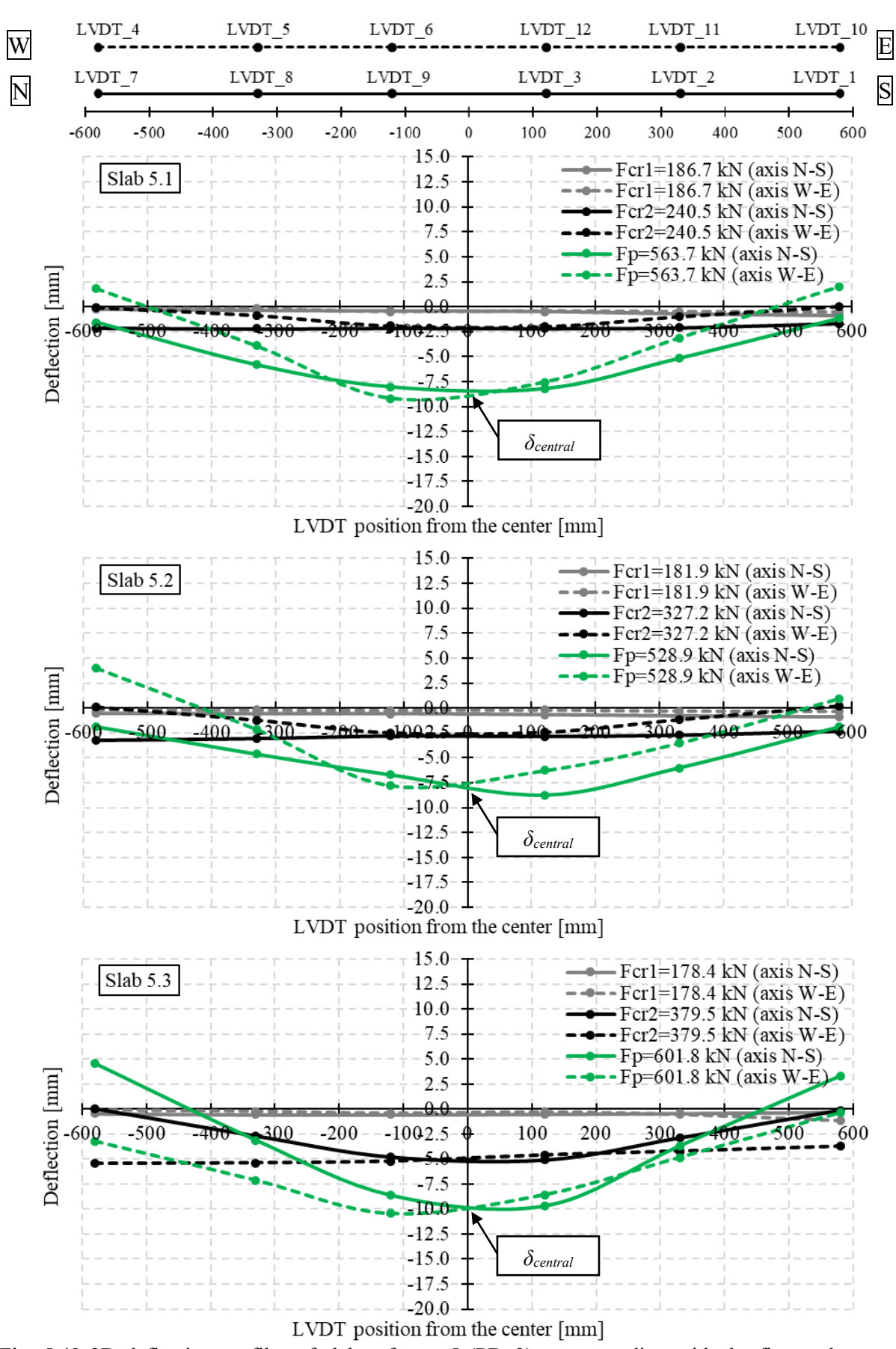


Fig. 5.49 2D deflection profiles of slabs of type 5 (PD_3) corresponding with the first and second flexural cracking force (F_{cr1} and F_{cr2}), and punching shear force (F_p)

5.2.6.4 Punching cone characteristics

Fig. 5.50 illustrates the distinct displacement of the central punching shear cone on the load application surface relative to the surrounding portion of the slabs, which was equal to around 3.2, 3.0, and 2.4 cm for slab 5.1, 5.2, and 5.3, respectively. To examine the punching cones, they were pushed out from the slabs using a manual hydraulic jack stabilized by a steel frame (Fig. 4.26 and Fig. 4.27). Fig. 5.51 presents the top and side views of the punching cones from slabs of type 5 (PD_3). The inclination angles θ of the punching cones were measured in six distinct positions along the cone sidewalls using an angle finder ruler. The single and average values of θ are documented in Table 5.27. The inspection indicated that the punching cones had an irregular shape of truncated pyramid with an average θ of 70.3°, 68.0°, and 60.0° for slab 5.1, 5.2, and 5.3, respectively. It is noteworthy that the cones maintained structural integrity, facilitating their movement and transport.



Fig. 5.50 Punching of the tested slabs of type 5 (PD 3) at the load application surface

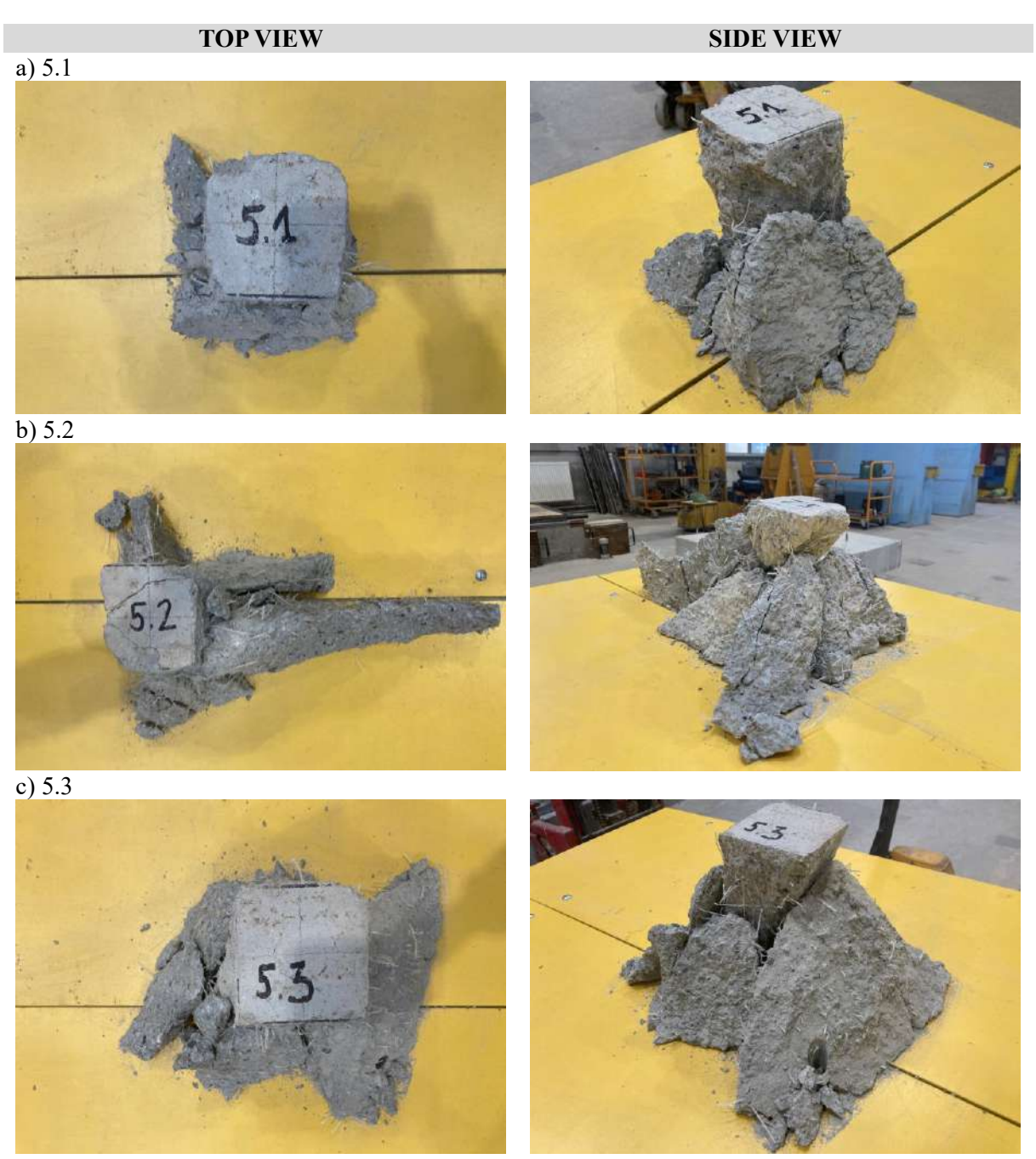


Fig. 5.51 Punching cones from tested slabs of type 5 (PD_3)

Table 5.27 Punching cone inclination angles θ for tested slabs of type 5 (PD_3)

| Slab no. | Punching cone inclination angles $	heta$ | Average $	heta$ |
|----------|--|-------------------------|
| 5.1 | 65°, 68°, 71°, 90°, 65°, 63° | θ = 70.3° |
| 5.2 | 65°, 79°, 55°, 86°, 59°, 64° | $\theta = 68.0^{\circ}$ |
| 5.3 | 57°, 51°, 64°, 51°, 60°, 77° | $\theta = 60.0^{\circ}$ |

5.2.7. Pushrod results

The positioning of the pushrods (LVDT10 sensors) was determined to align exclusively with shear cracks resulting from punching, not with flexural cracks induced

by bending. As a result, the LVDT10s were installed in position, where the critical control section for punching shear was anticipated. The primary objective of these sensors was to record vertical displacement associated with the development of shear cracks and, subsequently, to estimate shear crack widths, as described in Chapter 4.4.2.4. However, in some cases, flexural cracks intersected the pushrod locations, as illustrated in Fig. 5.52 for PC ground slabs and in Fig. 5.53 for SyFRC ground slabs. Additionally, the actual punching cones exhibited highly irregular geometries, and their perimeters did not consistently coincide with the pushrod locations (see Fig. 5.52 and Fig. 5.53), which limited the precision of shear crack width measurements.

Nevertheless, the deployment of pushrods cannot be considered entirely ineffective, as several LVDT10 positioned within the punching cone region provided measurable indications of shear crack development. This measurement approach showed potential, particularly if adjusted by reducing the distance between the pushrods and the load application area, thereby increasing the probability of intersecting shear cracks. Representative results for slabs 2.1, 3.2, 4.1, and 5.1 are presented in Fig. 5.54, while the corresponding positions of LVDT10 no. 13 and 16 in selected slabs are shown in Fig. 5.53. In slabs 2.1 and 3.2, shear crack initiation was observed to occur after the formation of the second flexural crack, with a rapid increase in crack width up to the punching shear load, followed by a noticeable reduction in the rate of crack widening. In contrast, for slabs 4.1 and 5.1, shear cracks formed only upon reaching the punching shear capacity, with crack widths increasing rapidly until a limiting value corresponding to the maximum LVDT10 measurement range.



Fig. 5.52 Fractured side surface of the ground slabs type 1 (PC)

However, based on the aforementioned observations, it was concluded that the intended objective of accurately measuring shear crack width was not achievable in the majority of cases. This was primarily due to the simultaneous presence of flexural cracks interfering with the measurements or the inability of the pushrods to detect the shear cracks. Consequently, it was determined that the data obtained from the LVDT10 measurement devices did not provide meaningful insights for the current stage of analysis and were therefore excluded from further consideration.

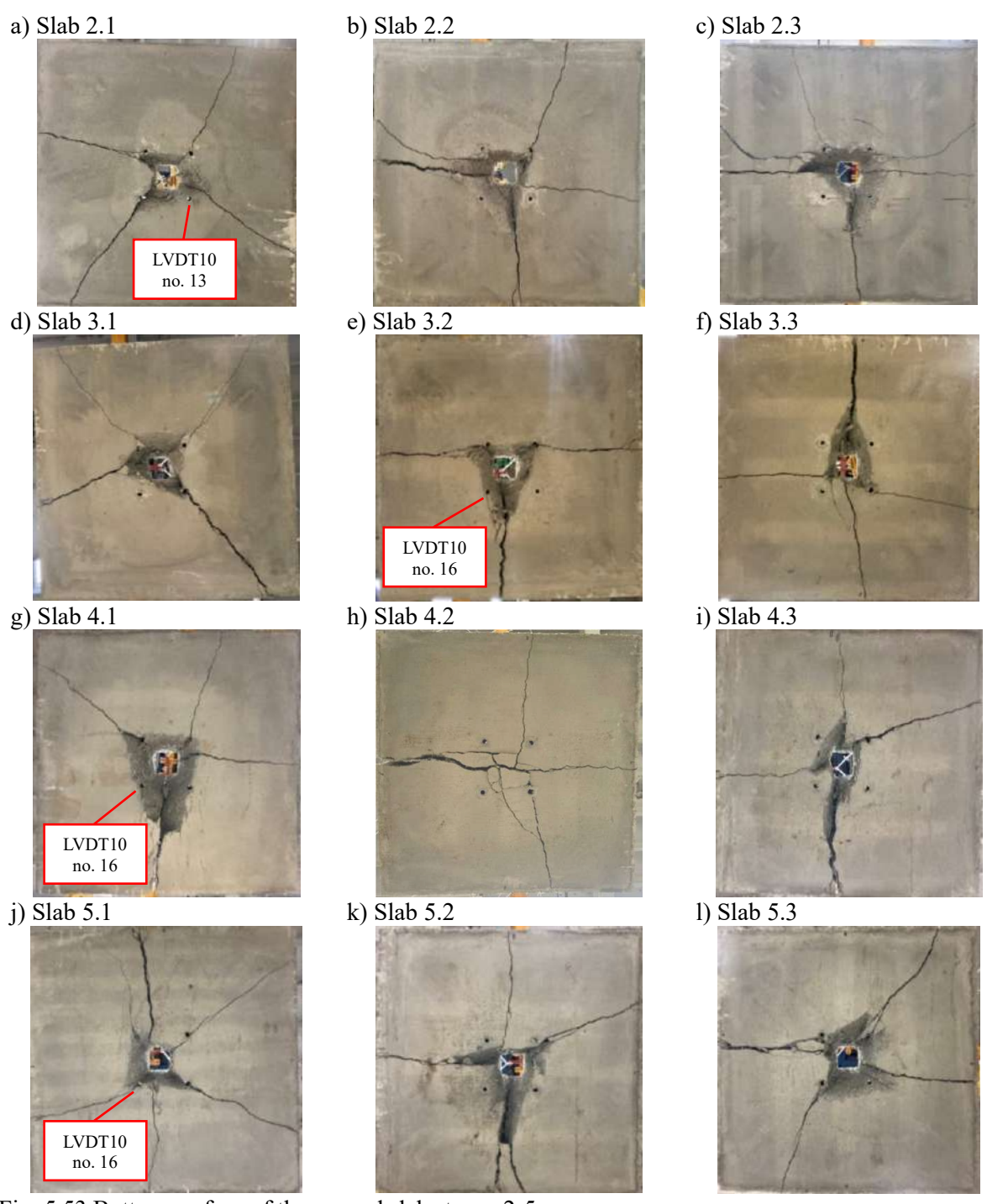


Fig. 5.53 Bottom surface of the ground slabs types 2-5

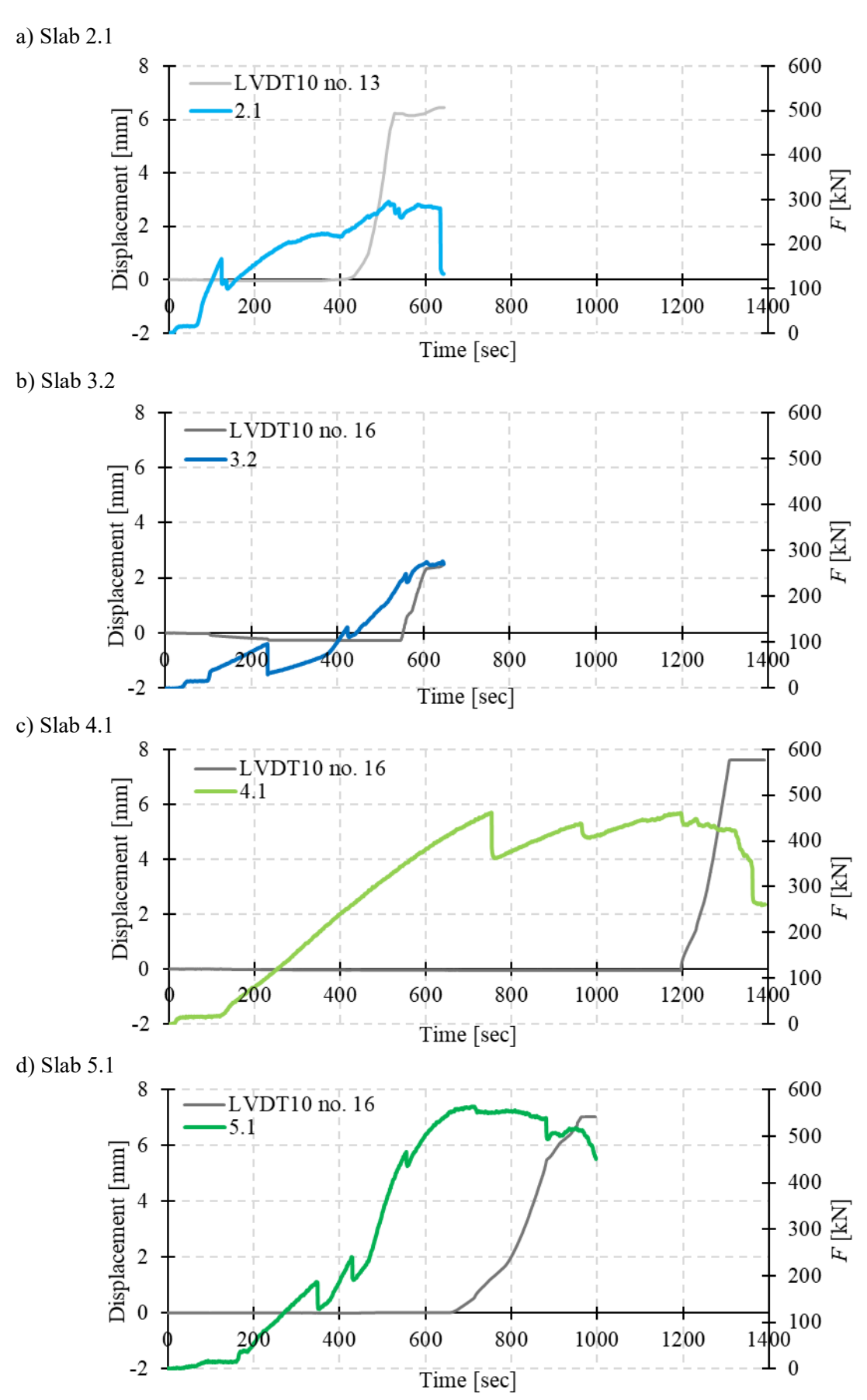


Fig. 5.54 Results from selected pushrods for slabs 2.1, 3.2, 4.1, and 5.1 showing the development of shear cracks

5.2.8. Summary

The comparative analysis of the tested ground slabs was conducted in accordance with the assumptions described in Table 5.28, which are consistent with those adopted in Table 5.13. A summary of flexural cracking (F_{crl} and F_{cr2}) and punching shear load-bearing capacities (F_p), along with the corresponding central deflections ($\delta_{central}$), for ground slabs of types 1-6 are provided in Table 5.29. Additionally, average values were calculated for each slab type to facilitate comparison. The load-deflection (F- $\delta_{central}$) response of the analyzed centrally loaded slabs is presented in Fig. 5.55a. To account for discrepancies and better illustrate the performance trends among the different concrete types, standardized curves are shown in Fig. 5.55b. Finally, Table 5.30 summarizes the measured inclination angles θ of the punching cones from tested ground slabs.

Table 5.28 Assumptions for the further comparative analysis of ground slabs

| Comparison object | Assessment subject |
|---------------------------------------|---------------------------------------|
| Slabs type 1 (PC) vs. type 2 (PM_2) | Influence of optimal fiber addition |
| Slabs type 1 (PC) vs. type 3 (PM_3) | Influence of excessive fiber addition |
| Slabs type 4 (PD_2) vs. type 5 (PD_3) | Influence of fiber dosage |
| Slabs type 2 (PM_2) vs. type 6 (FF_2) | Influence of fiber type |

Table 5.29 Summary of flexural cracking and punching shear forces with corresponding deflections for ground slabs types 1-6

| Sla | b no. | F_{cr1} [kN] | $\delta_{central,Fcr1}$ [mm] | F_{cr2} [kN] | $\delta_{central,Fcr2}$ [mm] | F_p [kN] | $\delta_{central,Fp}$ [mm] |
|-----|-------|-------------------|------------------------------|-------------------|------------------------------|------------|----------------------------|
| 1.1 | | 144.01 | -0.343 | 172.56 | -2.108 | 257.57 | -6.469 |
| 1.2 | Ŋ | 219.82 | -1.527 | 187.98 | -3.675 | 180.73 | -5.589 |
| 1.3 | PC | 112.04 | -0.413 | 137.95 | -2.775 | 255.91 | -9.478 |
| 1 | | 128.03 | -0.378 | 155.26 | -2.44 | 256.74 | -7.974 |
| 2.1 | | 166.99 | -0.379 | 118.76 | -1.505 | 296.31 | -8.158 |
| 2.2 | 1_2 | 108.69 | -0.218 | 186.54 | -2.237 | 395.13 | -8.946 |
| 2.3 | PM | 142.20 | -0.541 | 289.05 | -5.111 | 438.06 | -6.897 |
| 2 | | 139.29 | -0.379 | 198.12 | -2.951 | 376.50 | -8.000 |
| 3.1 | | 148.73 | -0.372 | 126.35 | -1.484 | 249.35 | -6.337 |
| 3.2 | PM_3 | 96.91 | -0.085 | 132.98 | -2.423 | 276.69 | -12.990 |
| 3.3 | | 164.40 | -0.429 | 226.86 | -2.528 | 381.67 | -7.817 |
| 3 | | 136.68 | -0.295 | 162.06 | -2.145 | 302.57 | -9.048 |
| 4.1 | | 463.13 | -3.731 | 439.38 | -6.272 | 462.37 | -8.486 |
| 4.2 | 2_ | 198.48 | -1.242 | 405.47 | -5.918 | 468.97 | -11.695 |
| 4.3 | PD | 254.92 | -0.887 | 265.67 | -1.379 | 513.00 | -7.911 |
| 4 | | 226.70 | -1.065 | 335.57 | -3.649 | 490.99 | -9.803 |
| 5.1 | PD_3 | 186.70 | -0.475 | 240.50 | -2.058 | 563.71 | -8.119 |
| 5.2 | | 181.86 | -0.418 | 327.22 | -2.664 | 528.91 | -7.251 |
| 5.3 | | 178.37 | -0.446 | 379.48 | -4.942 | 601.80 | -9.176 |
| 5 | | 182.31 | -0.446 | 315.73 | -3.221 | 564.81 | -8.182 |
| 6.3 | FF_2 | 171.94 | -0.804 | 190.22 | -2.829 | 222.82 | -9.424 |

Note: Slabs 1.2 and 4.1 were not considered in the comparative analysis, as their load-deflection responses deviated substantially from the other tested slabs.

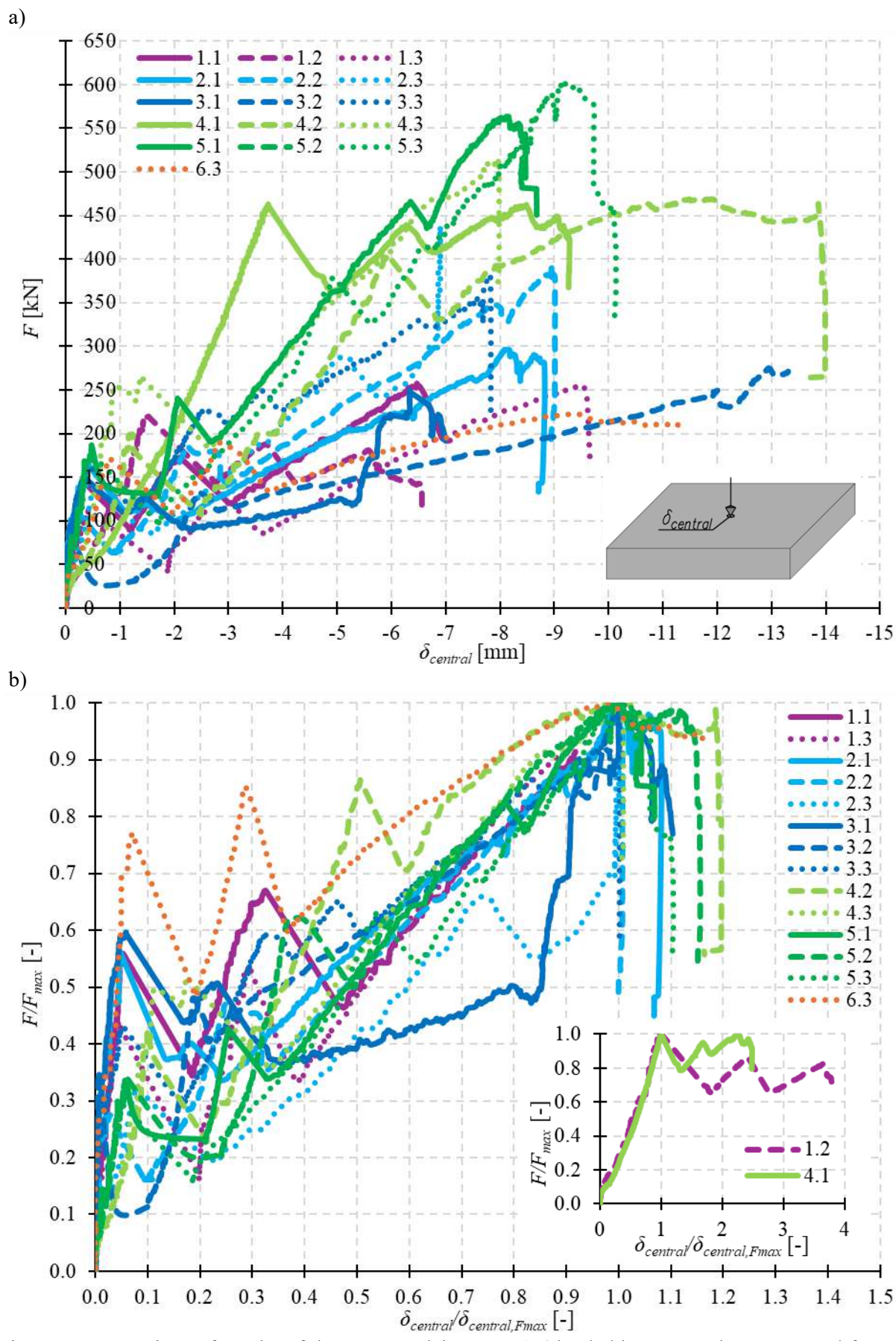


Fig. 5.55 Comparison of results of the tests on slabs types 1-6 loaded by a central concentrated force: a) F- $\delta_{central}$ curve, b) F/F_{max} - $\delta_{central}/\delta_{central,Fmax}$ curve

Table 5.30 Summary of the average punching cone inclination angles θ from ground slabs types 1-6

| Slab no. | | Average punching cone inclination angle $	heta$ |
|----------|-----------|---|
| 1.1 | | $\theta = 76.7^{\circ}$ |
| 1.2 | PC | $\theta = 81.2^{\circ}$ |
| 1.3 | Ь | <i>θ</i> = 79.3° |
| 1 | | <i>θ</i> = 79.1° |
| 2.1 | | $\theta = 68.0^{\circ}$ |
| 2.2 | PM_2 | $\theta = 61.0^{\circ}$ |
| 2.3 | PIV | θ = 65.7° |
| 2 | | $\theta = 64.9^{\circ}$ |
| 3.1 | | $\theta = 66.0^{\circ}$ |
| 3.2 | PM_3 | $\theta = 63.2^{\circ}$ |
| 3.3 | PIV | $\theta = 66.8^{\circ}$ |
| 3 | | $\theta = 65.3^{\circ}$ |
| 4.1 | | θ = 56.8° |
| 4.2 | PD_2 | θ = 61.5° |
| 4.3 | PD | $\theta = 71.7^{\circ}$ |
| 4 | | $\theta = 63.3^{\circ}$ |
| 5.1 | | θ = 70.3° |
| 5.2 | PD_{-3} | $\theta = 68.0^{\circ}$ |
| 5.3 | PD | θ = 60.0° |
| 5 | | $\theta = 66.1^{\circ}$ |
| 6.3 | FF_2 | $	heta=72.7^{\circ}$ |

The results presented in Table 5.30 indicated that the presence of fibers had a noticeable effect on the inclination angles θ of the punching cones. However, no consistent correlation was observed between concrete strength, fiber type, or fiber dosage and the θ values. This lack of a clear trend, combined with the irregular geometry of the punching cones, the limited number of measurement points (six), and the considerable variability in the recorded angles, questioned the adopted methodology. As a result, an alternative approach was introduced to determine the equivalent critical control perimeter of the punching cone (u_{eq}). Initially, the base perimeter of the punching cone (u_{base}) was measured using AutoCAD software. For PC slabs, this perimeter was identified from the top surface due to the brittle nature of failure, whereas for SyFRC slabs, it was determined from the underside, as illustrated in Fig. 5.56. All fragments detached from the inclined lateral surfaces were included within the punching shear perimeter, as they were attributed to shear failure. Subsequently, the equivalent perimeter at the effective slab depth (d = 0.75h = 150 mm) was calculated as proportional to the base perimeter of the punching cone ($u_{eq} = 0.75u_{base}$). An exception was made for slabs 1.2 and 1.3, where the punching cones exhibited a cuboid shape, and the perimeter at the effective slab depth was assumed to be equal to the base perimeter $(u_{eq} = u_{base})$. The corresponding distance of the critical control section from the column face a was then computed by transforming equation (5.4), assuming x = 100 mm and t = 0 mm.

Finally, the inclination angle θ was calculated using the expression $\theta = \arctan(d/a)$, as defined in Fig. 3.8. The detailed results of these calculations are presented in Table 5.31.

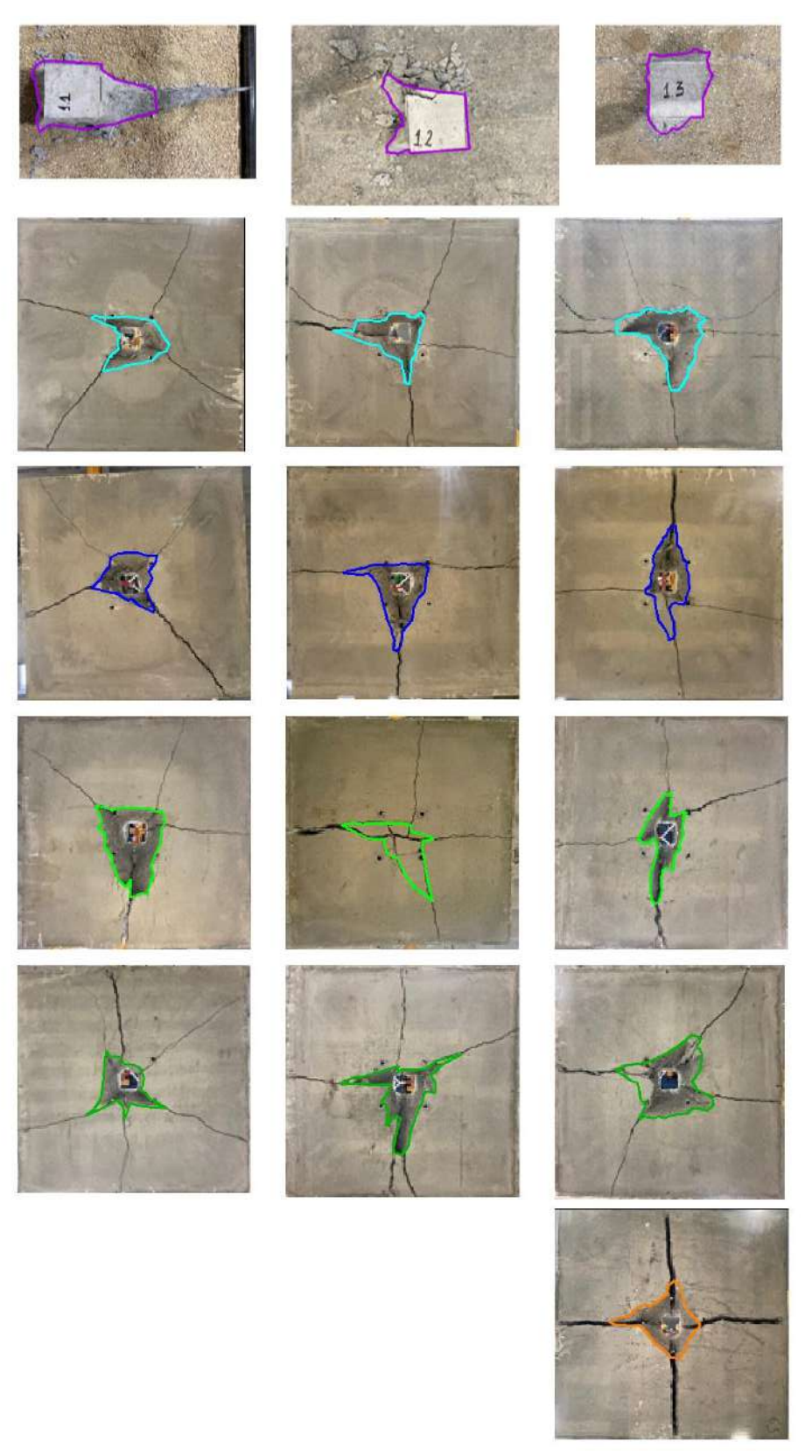


Fig. 5.56 Marked perimeters of punching cones of ground-supported slabs types 1-6 loaded by a central concentrated force

$$u_{eq} = 4(x+4t) + 2\pi a \tag{5.4}$$

where:

 u_{eq} – equivalent length of the critical control perimeter at a distance a from the loaded area [mm],

x – column dimensions [mm],

t – thickness of the baseplate [mm],

a – distance of the critical control section from the loading area [mm].

Table 5.31 Summary of equivalent critical control perimeters of punching cones u_{eq} with corresponding inclination angles θ and distances a for ground slabs types 1-6

| Slab no. | | Perimeter of punching cone base | Equivalent critical control perimeter of punching cone at effective slab depth | Distance of the critical control section from the loading area | Punching cone inclination |
|-------------|------|---------------------------------|--|--|---------------------------|
| | | u_{base} [mm] | u_{eq} [mm] | <i>a</i> [mm] | angle θ [°] |
| 1.1 | | 618 | 464 | a = 10 mm = 0.07d | $\theta = 86.1^{\circ}$ |
| 1.2 | PC | 563 | 563* | a = 26 mm = 0.17d | θ = 80.2° |
| 1.3 | Ь | 482 | 482* | a = 13 mm = 0.09d | $\theta = 85.1^{\circ}$ |
| 1 | | 554 | 503 | a = 16 mm = 0.11d | $\theta = 83.8^{\circ}$ |
| 2.1 | | 1264 | 948 | a = 87 mm = 0.58d | θ = 59.8° |
| 2.2 | PM_2 | 1435 | 1076 | a = 108 mm = 0.72d | θ = 54.3° |
| 2.3 | ΡΝ | 1518 | 1139 | a = 118 mm = 0.78d | $\theta = 51.9^{\circ}$ |
| 2 | | 1406 | 1054 | a = 104 mm = 0.69d | $\theta = 55.2^{\circ}$ |
| 3.1 | | 1109 | 832 | a = 69 mm = 0.46d | $\theta = 65.4^{\circ}$ |
| 3.2 | 1_3 | 1501 | 1125 | a = 115 mm = 0.77d | $\theta = 52.4^{\circ}$ |
| 3.3 | PM | 1416 | 1062 | a = 105 mm = 0.70d | $\theta = 54.9^{\circ}$ |
| 3 | | 1342 | 1007 | a = 97 mm = 0.64d | $\theta = 57.2^{\circ}$ |
| 4.1 | | 1514 | 1135 | a = 117 mm = 0.78d | θ = 52.0° |
| 4.2 | 2 | 1564 | 1173 | a = 123 mm = 0.82d | θ = 50.6° |
| 4.3 | PD | 1524 | 1143 | a = 118 mm = 0.79d | θ = 51.8° |
| 4 | | 1534 | 1150 | a = 119 mm = 0.80d | $\theta = 51.5^{\circ}$ |
| 5.1 | | 1409 | 1057 | a = 105 mm = 0.70d | θ = 55.1° |
| 5.2 | _3 | 2212 | 1659 | a = 200 mm = 1.34d | θ = 36.8° |
| 5.3 | PD | 1674 | 1255 | a = 136 mm = 0.91d | $\theta = 47.8^{\circ}$ |
| 5 | | 1765 | 1324 | a = 147 mm = 0.98d | $\theta = 45.6^{\circ}$ |
| 6.3 | FF_2 | 1347 | 1010 | a = 97 mm = 0.65d | $\theta = 57.1^{\circ}$ |

Note: * The punching cones from slab 1.2 and 1.3 exhibited a cuboidal shape, consequently the perimeter at the effective slab depth was assumed to be equal to the base perimeter of the punching cone.

5.2.8.1 Influence of fiber addition

Fig. 5.57 presents the load-central deflection (F- $\delta_{central}$) curves for slabs of types 1 (PC), 2 (PM_2), and 3 (PM_3). Slab 1.2 was excluded from the comparative analysis due to its substantially different load-deflection response compared to slabs 1.1 and 1.3, as discussed in Chapter 5.2.2 and illustrated in Fig. 5.55b.

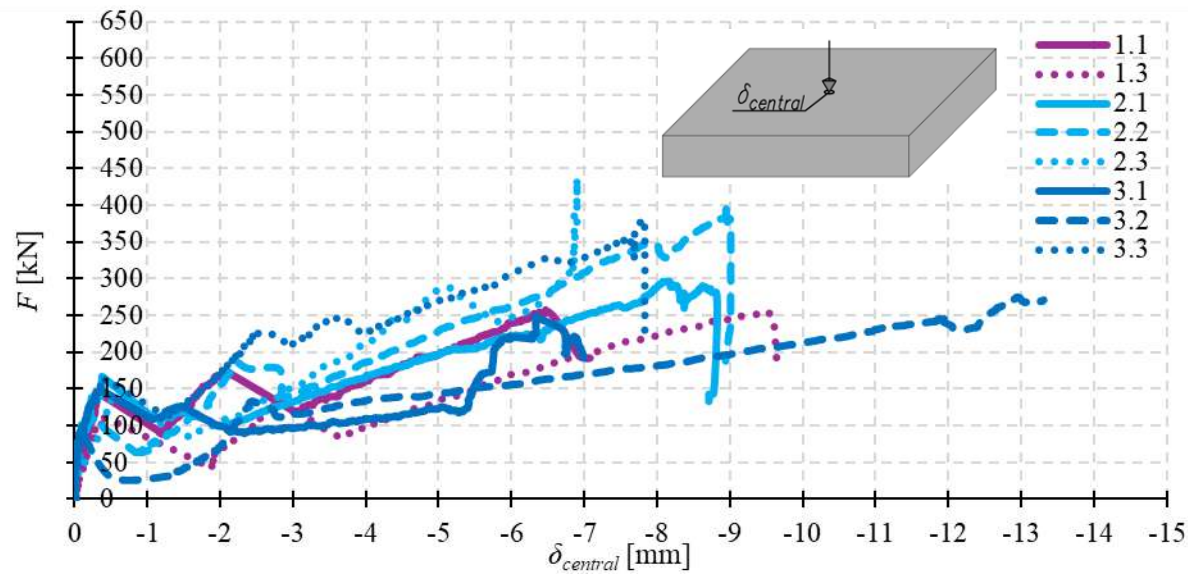


Fig. 5.57 Comparison of F- $\delta_{central}$ curves from the tests on slabs type 1 (PC), 2 (PM_2), and 3 (PM_3) loaded by a central concentrated force

The results demonstrated that all analyzed slabs exhibited an approximately linear response to increasing load until the first flexural cracking load (F_{crl}) , with initial nonlinearities attributed to setup adjustments. The average F_{cr1} for slabs with 2 kg/m³ and 3 kg/m³ of PM fibers (types 2 and 3) was 9% and 7% higher, respectively, than for the PC slabs (type 1). Specifically, F_{cr1} increased from 128.03 kN (PC) to 139.29 kN (PM 2) and 136.68 kN (PM 3), as presented in Table 5.29. A notable 28% increase in the average second flexural cracking load (F_{cr2}) was recorded for PM_2 slabs (198.12 kN) compared to PC slabs (155.26 kN). However, increasing the fiber dosage to 3 kg/m³ did not provide the expected further improvement, on the contrary, F_{cr2} decreased to 162.06 kN. Despite this reduction, the average F_{cr2} for PM 3 slabs remained 4% higher than that of PC. In addition, FRC slabs experienced smaller reductions in load following F_{cr1} and F_{cr2} than the PC slabs, indicating enhanced post-cracking behavior. The average punching shear capacity (F_p) of PM 2 slabs reached 376.50 kN, representing a 47% increase relative to PC slabs (256.74 kN). Similar to the flexural cracking loads, further increasing the fiber dosage did not improve the punching shear capacity. PM 3 slabs exhibited an average F_p of 302.57 kN, a 20% decrease relative to PM 2, but still an 18% improvement over PC slabs. Interestingly, the F_p results aligned with the fracture energy (G_F) trends from the 3PBT tests, in which PM_3 beams demonstrated an 11% lower G_F than PM_2 specimens. The average central deflection at the punching shear load level ($\delta_{central,Fp}$) was approximately -8 mm for both PC and PM 2 slabs, regardless of SyFs presence (Table 5.29). However for PM 3 slabs, a higher average $\delta_{central,Fp}$ of -9.048 mm was recorded, primarily due to slab 3.2, which exhibited substantially greater deflection at F_p , as shown in Fig. 5.57.

As a result, the PM_3 slabs showed a 13% greater average $\delta_{central,Fp}$ compared to PC and PM_2 slabs. For all analyzed slabs of types 1-3, the failure mechanism was identified as punching shear failure. Nevertheless, a key difference was observed in the post-peak behavior. Specifically, PC slabs failed in a brittle manner, fragmenting into multiple pieces, whereas both PM_2 and PM_3 slabs exhibited ductile behavior, maintaining structural integrity and enabling transportation as a single piece. This distinction in failure mode highlighted the beneficial influence of PM fiber addition on the structural integrity and ductility of ground slabs under concentrated loading.

The crack morphology observed in slabs 1.1, 1.3, and all slabs of type 2 revealed significant differences between PC and PM 2 slabs, with the former generally splitting into three primary segments and the latter into four (see Fig. 5.20 and Fig. 5.27). In all cases, initial cracking occurred simultaneously on two opposing edges at the F_{crl} load level. Then, as the load increased, secondary flexural cracks developed at force F_{cr2} . For PM 2 slabs, these appeared on the remaining two edges, resulting in the division into four primary segments. In contrast, the PC slabs exhibited cracking on only one of the remaining edges, as the detachment of the north side led to loading exclusively the south part of the slab. For PM 3 slabs, incorporating 3 kg/m³ of PM fibers, crack morphology varied. Namely, slab 3.2 exhibited a cracking pattern resembling that of the PC slabs, whereas slabs 3.1 and 3.3 experienced crack development similar to PM 2 slabs, characterized by division into four parts (Fig. 5.34). This discrepancy was attributed to non-uniform fiber distribution and a locally reduced fiber content in slab 3.2 relative to the other type 3 samples. Moreover, slabs 2.2 and 2.3 developed additional edge cracks, leading to further division of the specimens. Circumferential cracks associated with punching shear were observed exclusively at the bottom surfaces of slabs containing PM fibers. Such cracks were not identified in PC slabs due to the inability to conduct visual inspection from underneath. Furthermore, no circumferential cracks were observed on the top surfaces of any slabs, indicating that failure was not governed by exceeding the negative bending moment capacity.

Analysis of the deflection profiles (see Fig. 5.21, Fig. 5.28, and Fig. 5.35) indicated that at the initial stages of loading, slabs of types 1-3 were not fully supported by the ground nor uniformly resting on all four steel rollers, irrespective of fiber inclusion. Instead, partial contact was concluded, both with the ground or with one to four supporting rollers. By the time, the second flexural cracking load F_{cr2} was reached, the majority of slab edges had established contact with the supporting rollers. However, as the tests progressed, the edges of PC, PM_2, and PM_3 slabs gradually lost contact with both the rollers and the ground. This phenomenon was attributed to the uplift of slab

corners and edges, and partially as a consequence of slab rotation on the steel rollers. The deflection profiles further demonstrated that higher load levels led to increasingly non-uniform deflections. These irregularities were more evident in type 1 slabs compared to type 2, likely due to asymmetrical failure and crack development, as well as less efficient load redistribution in PC samples. Among the three considered slab types, type 3 exhibited the most noticeable deflection asymmetry, which was attributed to non-uniform fiber distribution within the concrete matrix.

The examination of the punching cones from slabs of types 2 and 3 revealed that all exhibited an irregular truncated pyramidal shape. In contrast, the cones formed in slabs without fibers were nearly vertical and more closely resembled a cuboid. The average values of the punching cone inclination angle θ and the corresponding distance of the critical control section from the loading area a were 55.2° and 0.69d for slabs with 2 kg/m³ of PM fibers, and 57.2° and 0.64d for slabs with 3 kg/m³ of PM fibers, as summarized in Table 5.31. In comparison, the PC slabs exhibited a significantly steeper average angle of θ = 83.8° and a much shorter distance of a = 0.11d. Consequently, the presence of SyFs not only affected the shape and inclination of the punching cones but also contributed to an increase in the length of the critical control perimeter. Furthermore, it is noteworthy that only the punching cones formed in FRC slabs maintained their structural integrity, facilitating their movement and transport.

In conclusion, the incorporation of 2 and 3 kg/m³ of PM fibers led to a moderate improvement in both the first and second flexural cracking loads and a significant enhancement in the punching shear capacity of the tested ground slabs, relative to slabs without fibers. However, increasing the PM fiber dosage from 2 to 3 kg/m³ did not provide the anticipated further gains in flexural or punching capacity. On the contrary, a reduction in these parameters of PM 3 samples was observed in comparison to the PM 2 slabs. This was attributed to the excessive fiber content, which may negatively influence the fiber distribution and consequently the mechanical properties of concrete type 3. Nevertheless, the presence of fibers resulted in a ductile failure mechanism in the PM 2 and PM 3 slabs, in contrast to the brittle behavior exhibited by the PC slabs. As a result, SyFRC ground slabs preserved their structural integrity even after failure, unlike the PC samples. In terms of crack morphology, the addition of PM fibers altered the mode of slab division and facilitated more effective load redistribution. The uniformity of deflections was improved in PM 2 slabs compared to PC slabs, while it deteriorated in PM 3 slabs, suggesting an uneven distribution of fibers. Finally, the incorporation of PM fibers contributed to a reduction in the punching cone inclination angle θ and an increase in the distance a from the loading area to the critical control section, transforming the shape of the cone from a cuboid to a truncated pyramid.

5.2.8.2 Influence of fiber dosage

Fig. 5.58 presents the F- $\delta_{central}$ curves for slabs of type 4 (PD_2) and type 5 (PD_3). It should be noted that slab 4.1 was excluded from the comparative analysis due to its substantially different load-deflection response compared to slabs 4.2 and 4.3, as discussed in Chapter 5.2.5 and illustrated in Fig. 5.55b.

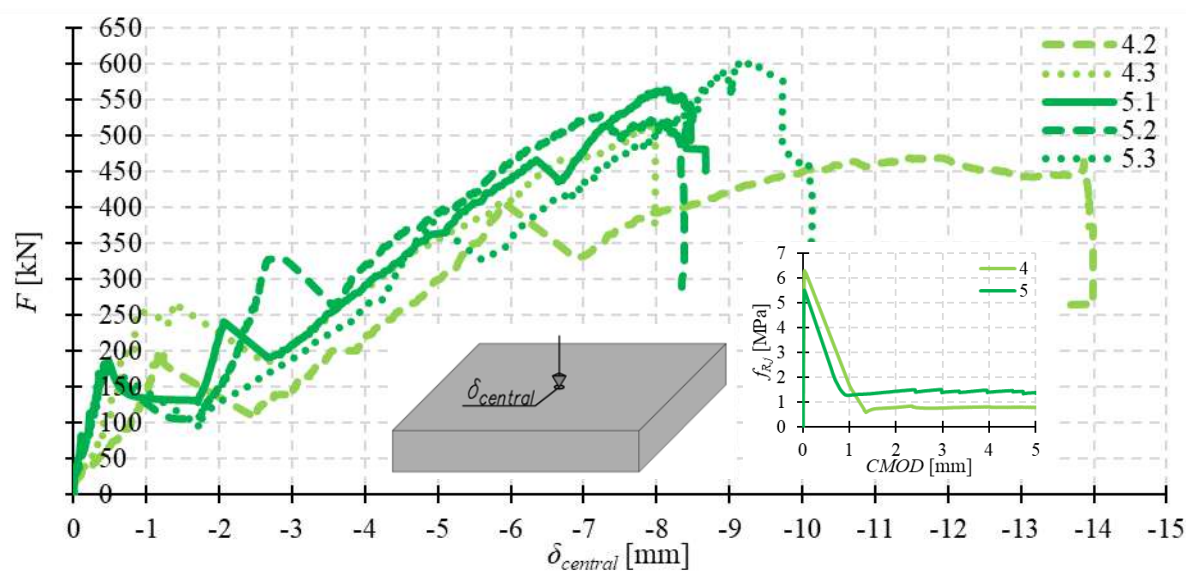


Fig. 5.58 Comparison of F- $\delta_{central}$ curves from the tests on slabs type 4 (PD_2) and 5 (PD_3) loaded by a central concentrated force

The results demonstrated that all analyzed slabs exhibited an approximately linear response to increasing load until F_{crl} , with initial nonlinearities attributed to setup adjustments. The average F_{crl} for type 5 slabs was found to be 20% lower than that of type 4 slabs, decreasing from 226.70 kN to 182.31 kN (Table 5.29). Similarly, the F_{cr2} decreased by 6%, from 335.57 kN for PD_2 slabs to 315.73 kN for PD_3 slabs. In contrast, slabs incorporating 3 kg/m³ of PD fibers achieved a significantly higher average F_p of 564.81 kN, representing a 15% increase over the 490.99 kN recorded for slabs containing 2 kg/m³ of PD fibers. Interestingly, the F_{crl} values obtained from the ground slab tests aligned with the 3PBT results, where the average limit of proportionality ($f_{ct,L}$) for PD_3 beams was 13% lower than that of PD_2 samples (Fig. 5.58). Conversely, the residual flexural tensile strengths ($f_{R,j}$) of PD_3 specimens significantly exceeded those of PD_2, and the G_F was 8% higher for PD_3 than for

PD_2 beams. These findings likely explain the superior punching shear performance observed in type 5 slabs compared to type 4. With regard to $\delta_{central,Fp}$, slab 4.2 exhibited a significantly greater central deflection at F_p compared to slab 4.3 and all slabs of type 5. As a result, the average $\delta_{central,Fp}$ for PD_2 slabs was - 9.803 mm, while for PD_3 slabs it was -8.182 mm, representing a 17% reduction with increased fiber dosage (Table 5.29). For all slabs of types 4 and 5, the governing failure mode was identified as punching shear. Moreover, regardless of fiber dosage, all slabs with PD fibers exhibited ductile behavior, maintaining structural integrity and facilitating their movement and transport.

The crack morphology of slabs 4.2, 4.3, and all slabs of type 5 revealed notable similarities, with each slab divided into four primary segments (see Fig. 5.41 and Fig. 5.48). Slabs reinforced with PD fibers exhibited simultaneous initial cracking at the F_{cr1} load level along two opposing edges. Further loading led to the formation of secondary flexural cracks at the force F_{cr2} along the remaining two edges. Additional edge cracks were observed in slabs 5.1 and 5.2, resulting in further subdivision of the slab samples. In contrast, slabs of type 4 exhibited only the primary flexural cracking pattern, without the presence of additional cracks. Finally, circumferential cracks attributed to punching shear were identified at the bottom surface of both PD_2 and PD_3 slabs beneath the point of load application. Furthermore, no circumferential cracks were observed at the top surfaces, indicating that the failure mechanism did not involve exceeding the negative bending moment capacity.

Deflection profile analysis (see Fig. 5.42 and Fig. 5.49) indicated that, at the initial stages of loading, slabs incorporating both 2 and 3 kg/m³ of PD fibers were not fully supported by the ground or uniformly by all four steel rollers. Instead, they exhibited partial contact with the ground and/or along one to four supporting rollers. By the time the F_{cr2} was reached, most slab edges had established contact with the rollers. However, as the tests progressed, the edges of PD_2 and PD_3 slabs gradually lost contact with both the rollers and the ground. This phenomenon was attributed to the uplift of slab corners and edges, and partially as a consequence of slab rotation on the steel rollers. The deflection profiles further demonstrated that higher load levels led to increasingly non-uniform deflections, which were more pronounced in slabs of type 4 than in those of type 5. This difference was likely due to more uneven progression of failure and the resulting load redistribution in the PD_2 slabs.

The examination of punching cones from slabs 4.1-4.3 and 5.1-5.3 revealed that all exhibited an irregular truncated pyramid shape. The average values of angle θ and the distances a were determined to be 51.5° and 0.80d for slabs with 2 kg/m³ of PD fibers, and 45.6° and 0.98d for slabs with 3 kg/m³ of PD fibers (Table 5.31). These results

suggested that the increased dosage of SyFs influenced both the cone inclination and geometry, resulting in a greater critical control perimeter length for slabs of type 5. All punching cones remained their structural integrity, thereby facilitating their movement and transport.

In conclusion, increasing the PD fiber dosage from 2 to 3 kg/m³ resulted in an improvement in the punching shear capacity of the tested ground slabs. However, this increase did not lead to enhancement in the resistance to either first or second flexural cracking. These findings were consistent with the results of three-point bending tests conducted on beams types 4 and 5, particularly in terms of the limit of proportionality and residual flexural tensile strength. Regarding the crack morphology, the higher fiber dosage contributed to a greater number of final cracks in the slabs containing 3 kg/m³ of PD fibers, indicating improved load redistribution. Moreover, deflection profiles revealed more uniform behavior in PD_3 slabs compared to PD_2 slabs. Finally, the increase in PD fiber content led to a reduction in the punching cone inclination angle θ and an increase in the distance a from the loading area to the critical control section.

5.2.8.3 Influence of fiber type

Fig. 5.59 illustrates the F- $\delta_{central}$ curves for type 2 (PM_2) slabs and slab 6.3 (FF_3). It should be noted that slabs 6.1 and 6.2 were excluded from the comparative analysis due to differing support conditions relative to slab 6.3, as discussed in Chapter 5.2.1.

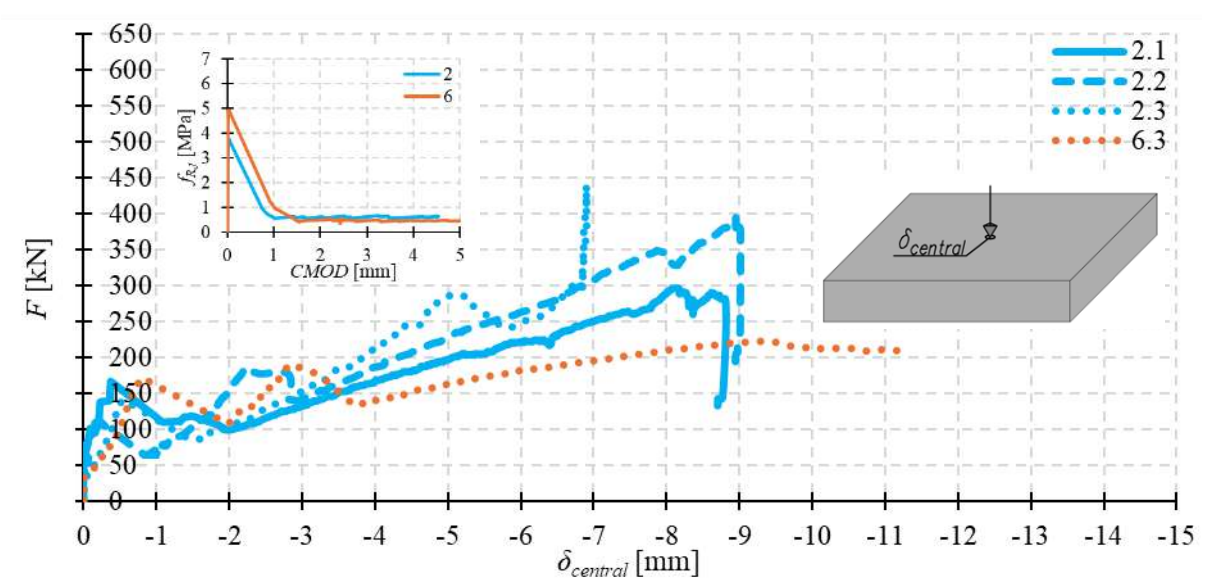


Fig. 5.59 Comparison of F- $\delta_{central}$ curves from the tests on slabs type 2 (PM_2) and slab 6.3 (FF_2) loaded by a central concentrated force

The results demonstrated that all analyzed slabs exhibited an approximately linear response to increasing load until F_{crl} , with initial nonlinearities attributed to setup adjustments. The average F_{cr1} for type 2 slabs was 19% lower than that of slab 6.3, decreasing from 171.94 kN to 139.29 kN (Table 5.29). Additionally, the average F_{cr2} for PM_2 slabs was only 4% higher than that of the FF_3 slab (198.12 kN vs. 190.22 kN). In contrast, the average F_p of PM_2 slabs reached 376.50 kN, representing a substantial 69% increase over the 222.82 kN recorded for slab 6.3. Interestingly, the F_{crl} values observed in ground slab tests aligned with the results of three-point bending tests, where the limit of proportionality $f_{ct,L}$ for PM_2 beams was 24% lower than that of FF_3 beams (see Fig. 5.59). However, the residual flexural tensile strength of type 2 specimens exceeded $f_{R,j}$ of type 6 specimens, which may explain the superior F_p values of PM_2 slabs. In contrast to previous comparisons between slabs 2 and 3 and slabs 4 and 5, the fracture energy results did not confirm this trend with G_F greater for FF 2 than for PD 2 concrete. With respect to $\delta_{central,Fp}$, slab 6.3 exhibited a larger deflection at F_p compared to type 2 slabs. Specifically, $\delta_{central,Fp}$ for slab 6.3 was -9.424 mm, while the average value for PM 2 slabs was -8.000 mm, corresponding to a 15% reduction for slabs reinforced with 2 kg/m³ of PM fibers (Table 5.29). For all slabs of types 2 and slab 6.3, the governing failure mode was identified as punching shear. Moreover, regardless of fiber type, all slabs exhibited ductile behavior, maintaining structural integrity and facilitating their movement and transport.

The crack morphology observed in slab 6.3 and all slabs of type 2 revealed notable similarities, with the slabs dividing into four primary segments (see Fig. 5.13 and Fig. 5.27). Slabs reinforced with 2 kg/m³ of either PM or FF fibers exhibited simultaneous initial cracking at the F_{crl} load level along two opposing edges. As the load increased, secondary flexural cracks developed at force F_{cr2} along the remaining two edges. Additional edge cracks were identified in slabs 2.2 and 2.3, resulting in further subdivision of the slab samples. In contrast, slab 6.3 exhibited only the primary flexural cracking pattern, without the presence of additional cracks. Finally, circumferential cracks attributed to punching shear were observed at the bottom surface of all PM_2 slabs and slab 6.3 beneath the point of load application. Furthermore, no circumferential cracking was observed at the top surfaces of the slabs, indicating that the failure mechanism did not involve exceeding the negative bending moment capacity.

Deflection profile analysis (see Fig. 5.14 and Fig. 5.28) revealed that, at the initial stages of loading, slabs incorporating both FF and PM fibers were not fully supported by the ground or uniformly by all four steel rollers. Instead, they exhibited partial contact

with the ground and/or along one to four supporting rollers. By the time the cracking load F_{cr2} was reached, most slab edges had established contact with the rollers. However, as the test progressed, the edges of the slabs, regardless of fiber type, gradually lost contact with both the supporting rollers and the ground. This behavior was attributed to the observed uplift of the corners and edges, and partially as a consequence of slab rotation on the steel rollers. The deflection profiles further demonstrated that higher load levels led to increasingly non-uniform deflections, which were more pronounced in slabs with PM fibers compared to slab 6.3. This difference was likely due to more uneven progression of failure and the resulting load redistribution in the PM 2 slabs.

The examination of punching cones from slabs 2.1-2.3 and slab 6.3 revealed that all exhibited an irregular truncated pyramid shape. The average values of angle θ and the distance a for slabs of type 2 were determined to be 55.2° and 0.69d, respectively. This showed no significant difference compared to slab 6.3, which exhibited an inclination angle θ of 57.1° and a distance a of 0.65d. All punching cones remained their structural integrity, thereby facilitating their movement and transport.

In conclusion, replacing FF fibers with PM fibers enhanced the punching shear capacity of the tested ground slabs. However, it did not improve resistance to the first flexural cracking and had no significant effect on the resistance to the second flexural cracking. The superior performance of FF fibers in resisting cracking forces can be attributed to the presence of fibrillated fibers with smaller diameters (constituting 5% of the FF hybrid blend in slab 6.3), which more effectively bridged microcracks during the initial loading phase. Conversely, the lower punching shear capacity observed in slab 6.3 may be explained by the reduced quantity of macrofibers (95% of the FF hybrid blend, equivalent to 1.9 kg/m³) compared to slabs of type 2 containing 2 kg/m³ of macro PM fibers. These observations corresponded well with the limit of proportionality and residual flexural tensile strength results obtained from three-point bending tests on beams types 2 and 6. Regarding crack morphology, the change from FF to PM fibers resulted in a higher final crack number for type 2 slabs, indicating greater load redistribution. Conversely, deflection uniformity was improved in the FF 2 slab compared to PM 2 slabs. Finally, no notable influence of fiber type on the punching cone inclination angle θ or on the distance of the critical control section from the loading area a was identified at this stage of the investigation. It is important to note, however, that only a single result from type 6 slabs was included in the comparative analysis, which may limit the generalizability of these conclusions.

5.3. Synthesis and conclusions of the research program

The research involved a comprehensive experimental program aimed at investigating the properties of concrete with particular emphasis on the influence of macro SyFs. Six concrete types were examined: one reference PC and five SyFRCs containing two different dosages of PM and PD fibers, 2 kg/m³ for PM 2, 3 kg/m³ for PM 3, 2 kg/m³ for PD 2, 3 kg/m³ for PD 3, and one dosage of FF fibers, 2 kg/m³ for FF 2. The experimental campaign included characterization of both fresh and hardened concrete properties. Firstly, the workability was assessed using flow table tests. Compressive strength tests were performed on cast cubes (150 mm sides) as well as on cores $(\phi 94 \times 188 \text{ mm})$ drilled from tested slabs. Additionally, both initial and stabilized moduli of elasticity were determined on the cores, which were subsequently halved (ϕ 94 x 94 mm) and used for splitting tensile strength tests to calculate the axial tensile strength. Finally, the flexural tensile strength was obtained by means of 3PBT on cast beams (150 x 150 x 550 mm), allowing for the determination of the limit of proportionality, residual flexural tensile strengths, and fracture energy. In terms of large-scale testing, three ground slabs of each concrete type (200 x 1200 x 1200 mm) were subjected to centrally applied concentrated loading. The investigations focused on the load-deflection response, flexural cracking forces (F_{cr1} , F_{cr2}), punching shear capacity (F_p) , deflection profiles, crack morphology, and punching cones' geometry.

Regarding the results of the experimental campaign, variability in the workability of fresh concrete was observed across the tested mixtures, ranging from consistency class F3 to F5. This was attributed to the incorporation of SyFs into the mixtures as well as changing weather conditions affecting aggregate humidity during casting and the use of materials from different deliveries. As anticipated, variability in concrete consistency influenced its hardened properties, including compressive strength, which ranged from 35.01 MPa for PC to 54.46 MPa for PD_3, based on tests of standardized cubes. While certain SyFRC types exhibited notably higher average compressive strength compared to PC, caution should have been taken against concluding its significant improvement due to macro SyFs addition, as it primarily depends on the concrete matrix and aggregate quality. Moreover, according to the findings reported in the literature, SyFs inclusion has generally a neutral effect on compressive strength. Nevertheless, a pronounced reduction in compressive strength was recorded in the case of an excessive PM fiber dosage of 3 kg/m³. These results underscore the importance of well-designed concrete mixture with optimized fiber

dosage, in which a compromise between workability and mechanical performance is achieved. The measured initial and stabilized moduli of elasticity followed trends similar to those observed in compressive strength. In general, SyFRCs incorporating PM, PD, and FF fibers showed improved modulus values relative to PC, except in the case of PM 3, where the excessive fiber content contributed to a deterioration in stiffness. These findings were not consistent with expectations, as macro SyFs typically exhibit lower stiffness than hardened concrete, and thus should only marginally affect the concrete modulus of elasticity. Nevertheless, given that the modulus is strongly correlated with compressive strength, the observed variability of the latter was also reflected in the elastic modulus results. It is worth noting that the obtained modulus values across all concrete types were lower than those predicted by standard design codes. This discrepancy was likely due to the use of rounded river gravel aggregates with small diameters, as well as the origin of the tested specimens, which were drilled as cores from previously loaded slabs. Then, it was concluded that the addition and the increased dosage of macro SyFs generally enhanced splitting tensile strength, however, improvements exceeding 30%, observed in SyFRC samples with PD fibers, are more typical for SFRC. These substantial differences in splitting tensile strength were primarily attributed to the previously discussed variability in compressive strength. Furthermore, while an excessive dosage of PM fibers resulted in reduced splitting tensile strength, an increase in PD fiber dosage led to improvements, confirming the benefits of optimally designed SyFRC. In flexural tensile strength tests, PC beams exhibited brittle failure upon reaching the limit of proportionality $f_{ct,L}$, with no residual flexural tensile strength. In contrast, all SyFRC beams, regardless of fiber type or dosage, demonstrated ductile failure, retaining structural integrity and carrying significant residual loads after cracking. Moreover, all FRC beams exhibited characteristic softening behavior. The addition of the optimal PM fiber content (2 kg/m³) showed a modest increase in $f_{ct,L}$ relative to PC, which was consistent with findings reported in the literature. However, increasing the PM and PD fiber dosage from 2 to 3 kg/m³ did not lead to further improvement in $f_{ct,L}$. In the case of PM 3 beams, this was likely due to the reduced workability and potential fiber clustering or their uneven distribution. For PD 3 beams, the decrease of $f_{ct,L}$ was counterbalanced by a substantial enhancement in residual flexural strength. These observations align with the general conclusion that the addition and higher fiber contents contribute most to the increase of concrete residual strength, provided that sufficient workability is maintained. At the same fiber dosage of 2 kg/m³, FF fibers were generally more effective in improving $f_{ct,L}$ than PM fibers. This was

attributed to the presence of microfibers in the FF hybrid blend, which contributed more effectively to microcrack bridging. Conversely, PM_2 beams demonstrated superior post-cracking behavior compared to FF_2 samples, primarily due to the higher macro SyFs content enhancing load transfer after cracking. These findings indicated that the type of SyFs had a significant influence on the obtained flexural performance of concrete beams.

Preliminary testing on type 6 slabs (FF_2) under varying ground support conditions was conducted to identify the most suitable and effective support configuration for subsequent investigations, as well as to assess the influence of subsoil support on slab behavior. The results demonstrated a substantial impact of ground on the structural response, load-bearing capacity, deflection behavior, and failure mechanisms of slabs subjected to central concentrated loading. Namely, the unsupported slab failed in bending and did not exhibit punching shear failure, unlike tested ground-supported slabs. These findings highlighted the importance of considering punching capacity in ground-supported slabs and the need for their distinct analyses from elevated slabs. Moreover, the tests revealed that the layering and preparation of the subbase had a significant effect on slab performance. Based on the insights gained from testing type 6 slabs, the supporting ground for subsequent tests on types 1-5 was assumed. Namely, the configuration with three layers of crushed aggregates, topped with a thin layer of finer aggregate material, were prepared for later tests.

The further comparative analysis of the ground-supported slabs aimed to investigate the influence of the addition, dosage, and type of SyFs on the structural response, including flexural cracking and punching shear load-bearing capacities, deflections, crack morphology, punching cone characteristics (inclination angle θ and distance a), and failure modes of SyFRC slabs subjected to centrally applied concentrated loading. One of the principal conclusions was that PC slabs exhibited brittle failure, breaking into segments defined by the crack pattern, whereas SyFRC slabs with PM, PD, or FF fibers demonstrated ductile behavior, preserving structural integrity and enabling load redistribution. These findings emphasized that even a small addition of SyFs to concrete elements can have a beneficial effect on structural safety compared to plain concrete. Moreover, for all tested ground-supported slabs, the governing failure mode was identified as punching shear failure, preceded by the formation of first and second flexural cracks. The detailed classification of failure mechanisms is presented in Fig. 5.60. Failure Mechanism I was identified in two SyFRC ground slabs and was characterized by the simultaneous initiation of cracks on three edges, followed by flexural cracking along the remaining direction, ultimately leading to punching shear failure. In this mechanism, the load corresponding to the first flexural cracking was the maximum recorded value, exceeding both the loads associated with the second flexural cracking and with punching shear failure. Failure Mechanisms II and III exhibited similar crack morphologies, as all slabs initially developed cracks on two opposite edges, followed by cracking on the remaining one or both edges, and eventually failed due to punching shear. The distinction between these mechanisms lies in the relationship between the loads corresponding to successive flexural cracks. In Failure Mechanism II, the first flexural cracks formed under a higher load than the second ones, whereas in Failure Mechanism III, the second flexural cracks developed under a higher load than the first. The latter behavior can be attributed to a more pronounced stiffness reduction in two slabs after the formation of the first flexural cracking. For both mechanisms, the maximum load attained corresponded to the punching shear capacity of the slab. It is noteworthy that the majority of the tested ground-supported slabs failed according to Failure Mechanism III.

The experimental campaign demonstrated that the behavior of ground-supported slabs is influenced by the inclusion, type, and dosage of macro SyFs within the concrete element. Namely, the addition of fibers (PM 2 vs. PC) moderately increased both the first and second flexural cracking loads, while a notable improvement was observed in punching shear capacity. Increasing the PM fiber dosage (PM 3 vs. PM 2) did not further enhance flexural cracking or punching shear capacity, in fact, both parameters decreased, what was attributed with excessive fiber amount. Nevertheless, PM 3 slabs still exhibited a slight advantage over PC slabs. In contrast, increasing the PD fiber dosage (PD 3 vs. PD 2) led to an improvement in punching shear capacity but did not enhance the resistance to first and second flexural cracking. This trend was consistent with the flexural tensile strength results obtained from beam tests, indicating that small-scale samples can provide valuable indications regarding the behavior of structural elements. Furthermore, a higher PD fiber dosage was associated with an increased final crack number, suggesting greater load redistribution capacity. A change in fiber type from FF to PM (PM 2 vs. FF 2) resulted in a substantial improvement in punching shear capacity. However, FF fibers were more effective in resisting the first flexural cracking load, whereas PM fibers were slightly more effective in resisting the second flexural cracking load. As before, these observations were generally consistent with the outcomes of the threepoint bending tests. However, it should be noted that results from only one slab of type 6 were included in this comparative analysis, which may limit the generality of above mentioned conclusions.

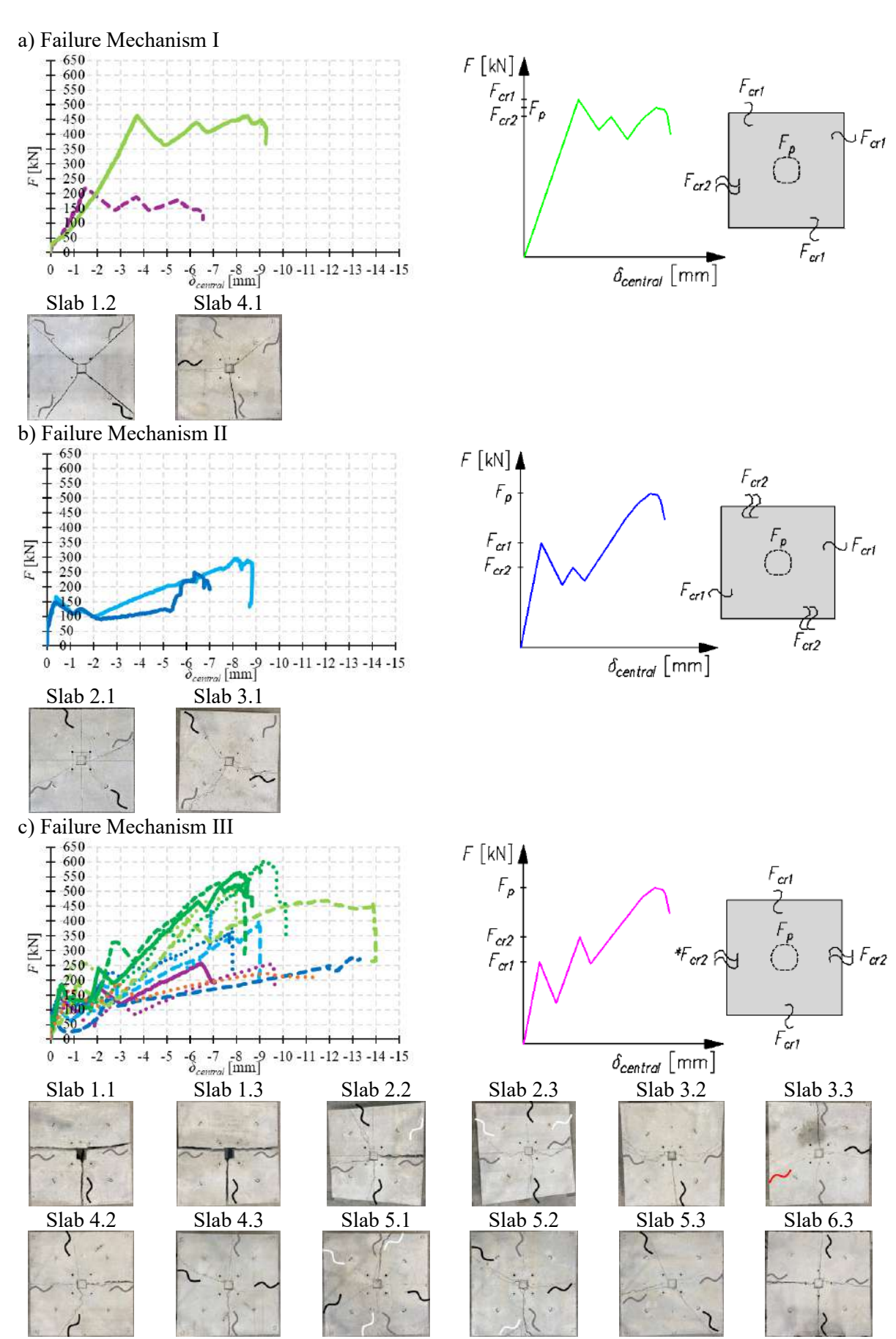


Fig. 5.60 Classification of Failure Mechanisms of ground-supported slabs centrally loaded by a concentrated force

The characterization of the punching cones of PC and SyFRC ground slabs was one of the principal objectives of the experimental program. The initial approach, involving the use of an angle finder ruler to assess the inclination of the extracted punching cones, proved to be unreliable. Consequently, an alternative method was implemented, based on calculating the equivalent critical control perimeter of the punching cone. The analysis revealed that central loading of PC slabs resulted in nearly vertical punching cones resembling cuboidal shapes, while for SyFRC slabs irregular, truncated pyramid shapes were observed (see Fig. 5.61). The addition of SyFs clearly influenced both the shape and inclination of the punching cones, resulting in an increased length of the critical control perimeter. Moreover, increasing the dosage of PD fibers from 2 to 3 kg/m³ was associated with a reduction in the punching cone inclination angle θ and an increase in the distance a of the critical control section from the loading area. In the case of cones from slabs of types 2 and 3, this trend was not observed, likely due to the reduced workability and decreased compressive strength attributed to the use of excessive dosage of 3 kg/m³ of PM fibers. Furthermore, replacing FF fibers with PM fibers did not produce a significant change in either θ or a, however, this conclusion must be treated with caution as it was derived from a comparison including only one FF 2 slab sample. The results also suggested that the inclination of punching cones may have been influenced by both compressive and tensile strengths of the concrete. Specifically, higher concrete strength appeared to correlate with a reduced inclination angle of the punching cone. The only exception was the cone from slab 6.3, which may again be explained by the limited amount of data, potentially limiting the reliability of the result. Finally, it is also noteworthy that **all punching cones** extracted from SyFRC slabs maintained their structural integrity, enabling easier movement and transport, in contrast to the brittle cones from PC slabs.

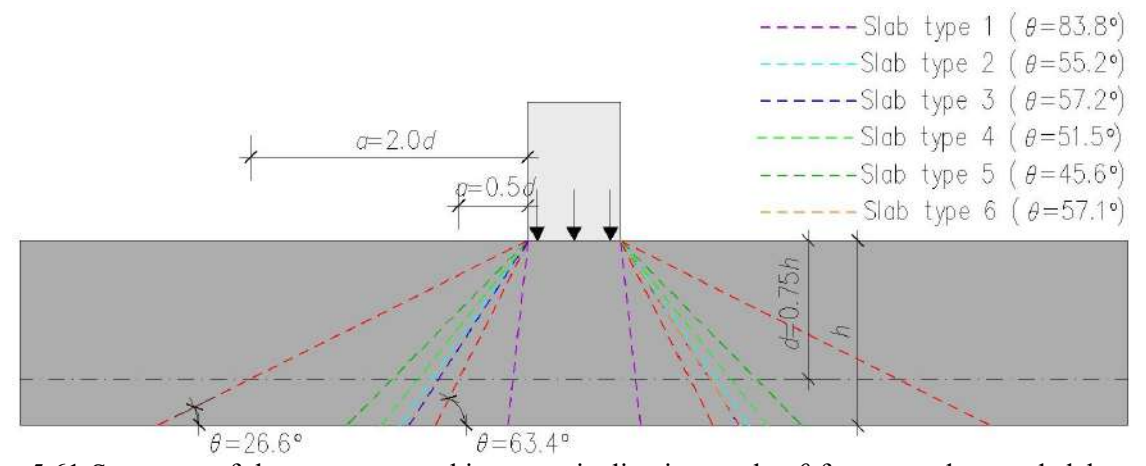


Fig. 5.61 Summary of the average punching cone inclination angles θ from tested ground slabs types 1-6 with $\theta = 63.4^{\circ}$ and 26.6° corresponding with a = 0.5d and 2.0d (red lines), respectively

6. ANALYTICAL ANALYSIS

6.1. Introduction

The initial methodology for designing slabs on ground was introduced by Westergaard, following on elasticity theory. In the 1960s, Meyerhof and Losberg developed a design model for reinforced concrete ground slabs based on yield line theory (plastic analysis). Comparative evaluation of this approach against alternatives proposed by Baumann and Weisgerber, as well as Rao and Singh, concluded that the Meyerhof-Losberg model was the most straightforward, leading to its adoption in the TR4 report [28]. Currently, TR34 is the most widely used guideline for the design and construction of concrete industrial ground floors. Furthermore, the design principles in TR34 are aligned with PN-EN 1992-1-1:2008 [30], particularly regarding punching shear design. In 1995 and 1997, novel methodologies based on Finite Element Models were introduced by Falkner et al. and Shentu et al., respectively.

In order to assess the experimentally obtained results, analytical calculations were performed following the approaches of Westergaard, Falkner et al., Shentu et al., and Meyerhof-Losberg. The latter were conducted in accordance with the TR34 [28] design procedures, including verification of punching shear capacity in compliance with PN-EN 1992-1-1:2008 [30]. It should be emphasized that primary focus was placed on the TR34 guideline [28], as it accounted for the majority of variables examined in this experimental campaign, including the influence of fibers, ground support conditions, and calculations of both flexural and punching shear load-bearing capacities. The objective of this chapter was to compare the experimental results of tested slabs with predictions from theoretical models. Furthermore, the influence of selected variables on flexural and punching shear capacities, as well as the contribution of individual components: concrete, fibers, and ground to punching shear capacity, was evaluated according to [28]. Given that the analytically derived punching shear capacity strongly depends on the equation applied for calculating the additional shear resistance provided

by the presence of fibers in concrete, several formulas proposed in selected standards were verified. To achieve satisfactory agreement between analytical and experimental results, supplementary analyses were conducted. Specifically, the analysis of crack morphology and deflection profiles indicated that, at the initial stages of testing, the slabs may not have been fully supported by the ground and/or uniformly along all four steel rollers located at the slab's edges. Consequently, calculations were performed for both simply supported slabs and ground-supported slabs with one to four edges supported. This analytical approach was undertaken to estimate the initial support conditions of the tested slabs, considering both experimental observations and analytical results. Finally, the procedure for validating the analytical models was presented.

For analytical calculations, concrete strength parameters were adopted from the material tests described in Chapter 5.1. The concrete modulus of elasticity, as well as compressive and tensile strengths obtained from tests on drilled cores, were utilized for concrete types 1-6, while flexural tensile strength was derived from beam tests. In cases where experimental results were unavailable, appropriate analytical relationships were applied. Additionally, for all analytical approaches, the modulus of subgrade reaction k obtained from equation (4.4) was used, based on performed modulus of deformation tests and established correlations.

6.2. Westergaard approach

Chapter 3.2.3.1 provides a detailed description of the Westergaard approach and its underlying assumptions. By rearranging equation (3.1), the formula for the interior cracking load of the ground slab was derived (equation (6.1)). It is important to emphasize that the Westergaard approach considers only the elastic behavior of the material, allowing for the calculation of the initial cracking load exclusively ($P_{cr,W}$). This method does not account for the post-cracking strength characteristic of SyFRCs. Consequently, the application of this model is expected to underestimate the load-bearing capacity of SyFRC ground slabs. Table 6.1 presents the calculation procedure and results for the experimentally tested ground slab of type 2, with Table 6.2 summarizes the results for all slabs of types 1-6.

$$P_{cr,W} = \frac{f_{ct,fl} \cdot h^2}{0.275 \cdot (1+v) \cdot \left[\log\left(\frac{E_c h^3}{k b_r^4}\right) - 0.436\right]}$$
(6.1)

where:

 $P_{cr,W}$ – cracking load-bearing capacity of the ground slab according to the Westergaard approach [N],

 $f_{ct,fl}$ – concrete flexural tensile strength [N/mm²],

h – slab thickness [mm],

v – Poisson's ratio [-],

 E_c – concrete modulus of elasticity [N/mm²],

k – modulus of subgrade reaction [N/mm³],

 b_r – equivalent radius of the pressure distribution according to equation (3.4) or (3.5) [mm].

Table 6.1 Determination of the cracking load-bearing capacity of tested ground slab type 2 according to the Westergaard approach

| | SLAD OF TVDE | 2 Wastangaard annyaaah | | | | |
|-------------------|--|---|--|--|--|--|
| Dotomino | SLAB OF TYPE 2 – Westergaard approach | | | | | |
| Determine | Determination of the cracking load-bearing capacity of SyFRC ground slab centrally loaded by a | | | | | |
| | concentrated force | | | | | |
| | Determination of data | | | | | |
| | Slab thickness | h = 200 mm | | | | |
| | | n = 200 mm | | | | |
| | Concrete parameters | v = 0.2 | | | | |
| DM EM | Poisson's ratio | v = 0.2 From test: | | | | |
| PN-EN 12390-13 | Modulus of elasticity | | | | | |
| [90] | | $E_c = 21419 \text{ MPa}$ | | | | |
| PN-EN | Flavural tancila strangth | From test: | | | | |
| 14651 [29] | 8 | | | | | |
| 14031 [29] | 1. 3.1) . | | | | | |
| | Ground parameters | | | | | |
| | Primary static modulus of | From test: | | | | |
| | deformation | $E_{v1} = 134 \text{ MPa}$ | | | | |
| Hajduk [24] | Modulus of subgrade reaction | $k = \frac{E_{v1}}{550} = \frac{134}{550} = 0.244 \text{ MPa/mm}$ | | | | |
| | Load characterization | | | | | |
| | Column side dimension | x = 100 mm | | | | |
| | Baseplate thickness | t = 0 mm (absence of a baseplate) | | | | |
| | Determination of the equivalent | nt radius of the pressure distribution | | | | |
| | Equivalent radius of contact area | a of the load | | | | |
| | $a_r = \sqrt{\frac{(x+4t)^2}{\pi}} = \sqrt{\frac{(100+4\cdot0)^2}{\pi}} = 56 \text{ mm}$ | | | | | |
| | Equivalent radius of the pressure | e distribution | | | | |
| | for $a_r < 1.724h$ (56 mm < 345 m | m) | | | | |
| | $b_r = \sqrt{1.6a_r^2 + h^2} - 0.675h =$ | $= \sqrt{1.6 \cdot 56^2 + 200^2} - 0.675 \cdot 200 = 77 \text{ mm}$ | | | | |
| | Determination of the cracking | | | | | |
| | Cracking load-bearing capacity | | | | | |

$$P_{cr,W} = \frac{f_{ct,fl} \cdot h^2}{0.275 \cdot (1+v) \cdot \left[\log\left(\frac{E_c h^3}{k b_r^4}\right) - 0.436 \right]}$$

$$= \frac{3.765 \cdot 200^2}{0.275 \cdot (1+0.2) \cdot \left[\log\left(\frac{21419 \cdot 200^3}{0.244 \cdot 77^4}\right) - 0.436 \right]} = \mathbf{118.31 \, kN}$$

Table 6.2 Determination of the cracking load-bearing capacity of tested ground slabs types 1-6 according to the Westergaard approach

| Slab type | 1 | 2 | 3 | 4 | 5 | 6.3 |
|------------------------|---|----------------|----------------|---------------|---------------|--------|
| | | Deter | mination of da | ata_ | | |
| | | | Slab | | | |
| | | h = 200 mm; | x = 100 mm; | t = 0 mm | | |
| | | Conc | rete paramete | ers | | |
| v [-] | 0.2 | 0.2 | 0.2 | 0.2 | 0.2 | 0.2 |
| E_c [MPa] | 19748 | 21419 | 18020 | 27149 | 29901 | 26734 |
| $f_{ct,fl}$ [MPa] | 3.499 | 3.765 | 3.107 | 6.303 | 5.504 | 4.926 |
| | | Grou | ınd paramete | rs | | |
| E_{vl} [MPa] | 143 | 134 | 139 | 141 | 138 | 132 |
| k [MPa/mm] | 0.260 | 0.244 | 0.253 | 0.256 | 0.251 | 0.240 |
| D | etermination | of the equiva | lent radius of | the pressure | distribution | |
| a_r [mm] | 56 | 56 | 56 | 56 | 56 | 56 |
| b_r [mm] | 77 | 77 | 77 | 77 | 77 | 77 |
| | Determ | ination of the | cracking load | d-bearing cap | acit <u>y</u> | |
| $P_{cr,W}[kN]$ | 111.79 | 118.31 | 99.99 | 194.00 | 167.23 | 150.78 |
| Experimental results | | | | | | |
| F_{crl} [kN] | 128.03 | 139.29 | 136.68 | 226.70 | 182.31 | 171.94 |
| | Comparison of experimental and analytical results | | | | | |
| $F_{crl}/P_{cr,W}$ [-] | 1.15 | 1.18 | 1.37 | 1.17 | 1.09 | 1.14 |

6.3. Falkner et al. approach

Chapter 3.2.3.2 provides a detailed description of the Falkner et al. approach and its underlying assumptions. This model employs plastic theory and addresses two critical conditions: the initial cracking load ($P_{cr,W}$), which corresponds to the Westergaard load, and the ultimate load-bearing capacity ($P_{u,F}$). Based on equation (3.6), the capacity of a centrally loaded ground slab is computed using equations (6.2) and (6.3). As discussed in Chapter 3.3.2.3, the incorporation of the fracture toughness index R_e enables assessment of the post-cracking strength of FRC and the resulting additional load-bearing capacity due to fiber addition. However, R_e is referenced in earlier guidelines for FRC design, such as the third edition of TR34 [68]. Currently, reliance on residual flexural tensile strengths obtained from 3PBT is more common. Consequently, equation (6.2) has been reformulated into equation (6.3). It is noteworthy that the ultimate load capacity is significantly influenced by the additional strength attributed to

fiber incorporation. Table 6.3 presents the calculation procedure and results for the experimentally tested type 2 ground slab, while Table 6.4 summarizes the results for all slabs of types 1-6.

$$P_{u,F} = P_{cr,W} \cdot \left[1 + \left(\frac{k}{E_c h^3} \right)^{0.25} \cdot W \cdot \frac{\sqrt{A}}{h} \right] \cdot \left[1 + \frac{R_{e,3}}{100} \right]$$

$$P_{u,F} = P_{cr,W} \cdot \left[1 + \left(\frac{k}{E_c h^3} \right)^{0.25} \cdot W \cdot \frac{\sqrt{A}}{h} \right] \cdot \left[1 + \frac{f_{Ftu}}{f_{ct,fl}} \right]$$
(6.2)

$$P_{u,F} = P_{cr,W} \cdot \left[1 + \left(\frac{k}{E_c h^3} \right)^{0.25} \cdot W \cdot \frac{\sqrt{A}}{h} \right] \cdot \left[1 + \frac{f_{Ftu}}{f_{ct,fl}} \right]$$
(6.3)

where:

 $P_{u,F}$ – ultimate load-bearing capacity of the ground slab according to the Falkner et al. approach [N],

 $P_{cr,W}$ – cracking load-bearing capacity of the ground slab according to the Westergaard approach [N],

W – slab width [mm],

 $A - \text{load area } [\text{mm}^2],$

k – modulus of subgrade reaction [N/mm²],

 E_c – concrete modulus of elasticity [N/mm³],

h – slab thickness [mm],

 $R_{e,3}$ – fracture toughness index [%],

 f_{Ftu} – concrete residual tensile strength based on the rigid-plastic model [N/mm²],

 $f_{ct,fl}$ – concrete flexural tensile strength [N/mm²].

Fig. 6.1 presents a comparison between the experimentally obtained first and second flexural cracking forces and punching shear forces, and the analytically calculated load-bearing capacities for tested slabs of types 1-6 according to the Falkner et al. approach, aiming to assess the accuracy of the analytical model. For the majority of slab types (excluding slabs 2.2 and 3.2), $P_{cr,W}$ was lower than the experimentally measured F_{crl} , indicating that Falkner's model tends to underestimate the initial cracking force. This discrepancy was particularly pronounced for slabs 1.2 and 4.1, where F_{crl} significantly exceeded the calculated values. Excluding four slabs (2.2, 3.2, 1.2, and 4.1) from the evaluation, the Falkner et al. approach predicted the initial cracking force with an average safety margin of approximately 23%. Furthermore, the predicted ultimate load $P_{u,F}$ exceeded the experimentally measured F_{cr2} in more than half of the tested slabs, while remaining lower than F_p in nearly all cases, except for slabs 1.2 and 6.3.

Table 6.3 Determination of the load-bearing capacity of tested slab type 2 according to the Falkner et al. approach

| | SLAB OF TYPE | 2 – Falkner et al. approach | | | |
|------------------|---|---|--|--|--|
| Deter | | pacity of SyFRC ground slab centrally loaded by a | | | |
| | concentrated force | | | | |
| | Determination of data | ž | | | |
| | Slab | | | | |
| | Slab thickness | h = 200 mm | | | |
| | Slab width | W = 1120 mm | | | |
| | | assumed as a distance between axis of the steel supporting rollers | | | |
| | Concrete parameters | | | | |
| PN-EN | Modulus of elasticity | From test: | | | |
| 12390-13 [90] | | $E_c = 21419 \text{ MPa}$ | | | |
| PN-EN | Flexural tensile strength | From test: | | | |
| 14651 [29] | $f_{ct,fl} = 3.765 \mathrm{MPa}$ | | | | |
| PN-EN | Residual tensile strength | $f_{Ftu} = \kappa_0 \cdot \kappa_G \cdot 0.33 \cdot f_{R,3} = 1.0 \cdot 1.0 \cdot 0.33 \cdot 0.646$ | | | |
| 1992-1- | | $= 0.213 \mathrm{MPa}$ | | | |
| 1:2024 [33] | | where: $\kappa_O = 1.0$, $\kappa_G = 1.0$, and $f_{R,3} = 0.646$ MPa | | | |
| | Ground parameters | | | | |
| | Primary static modulus of | From test: | | | |
| | deformation | $E_{v1} = 134 \text{ MPa}$ | | | |
| Hajduk [24] | Modulus of subgrade reaction | $E_{v1} = 134 \text{ MPa}$ $k = \frac{E_{v1}}{550} = \frac{134}{550} = 0.244 \text{ MPa/mm}$ | | | |
| | Load characterization | | | | |
| | Column side dimension | x = 100 mm | | | |
| | Load area | $A = x^2 = 10000 \text{ mm}^2$ | | | |
| | Baseplate thickness | t = 0 mm (absence of a baseplate) | | | |
| | Determination of the load-bea | ring capacity | | | |
| | Load-bearing capacity | | | | |
| | $\mathbf{P_{u,F}} = P_{cr,W} \cdot \left[1 + \left(\frac{k}{E_c h^3} \right)^{0.25} \cdot W \cdot \frac{\sqrt{A}}{h} \right] \cdot \left[1 + \frac{f_{eq}}{f_{ct,fl}} \right]$ | | | | |
| | L L | $-\left(\frac{0.244}{21419 \cdot 200^3}\right)^{0.25} \cdot 1120 \cdot \frac{\sqrt{10000}}{200} \cdot \left[1 + \frac{0.213}{3.765}\right]$ | | | |
| | = 190.66 + 10 | .80 = 201.46 kN | | | |

Table 6.4 Determination of the load-bearing capacity of tested ground slabs types 1-6 according to the Falkner et al. approach

| Slab type | 1 | 2 | 3 | 4 | 5 | 6.3 |
|------------------|-------------------|--------------|----------------------|-------------------------|-----------|-------|
| | | Deter | mination of d | ata_ | | |
| | | | Slab | | | |
| | h = 200 mm; | W = 995 mm; | x = 100 mm; 200 mm | $A = 1000 \text{ mm}^2$ | t = 0 mm | |
| | | Conc | rete paramete | ers | | |
| E_c [MPa] | 19748 | 21419 | 18020 | 27149 | 29901 | 26734 |
| $f_{ct,fl}[MPa]$ | 3.499 | 3.765 | 3.107 | 6.303 | 5.504 | 4.926 |
| $f_{R,3}$ [MPa] | 0.000 | 0.646 | 0.620 | 0.768 | 1.422 | 0.476 |
| $f_{Ftu}[MPa]$ | 0.000 | 0.213 | 0.205 | 0.253 | 0.469 | 0.157 |
| | Ground parameters | | | | | |
| E_{vl} [MPa] | 143 | 134 | 139 | 141 | 138 | 132 |

| k [MPa/mm] | 0.260 | 0.244 | 0.253 | 0.256 | 0.251 | 0.240 | |
|---|---|---------------|----------------|---------------|--------|--------|--|
| | Determination of the cracking load capacity | | | | | | |
| $P_{cr,W}[kN]$ | 111.79 | 118.31 | 99.99 | 194.00 | 167.23 | 150.78 | |
| | Det | termination o | f the load-bea | ring capacity | | | |
| $P_{u,F}[kN]$ | 182.70 | 201.46 | 175.25 | 319.59 | 284.34 | 245.26 | |
| $P_{u,F}[kN]$ * not accounting for SyFs influence | 182.70 | 190.66 | 164.43 | 307.24 | 262.01 | 237.68 | |
| | | Expe | rimental resu | <u>lts</u> | | | |
| F_{crl} [kN] | 128.03 | 139.29 | 136.68 | 226.70 | 182.31 | 171.94 | |
| F_{cr2} [kN] | 155.26 | 198.12 | 162.06 | 335.57 | 315.73 | 190.22 | |
| F_p [kN] | 256.74 | 376.50 | 302.57 | 490.99 | 564.81 | 222.82 | |
| Comparison of experimental and analytical results | | | | | | | |
| $F_{crl}/P_{u,F}$ [-] | 0.70 | 0.69 | 0.78 | 0.71 | 0.64 | 0.70 | |
| $F_{cr2}/P_{u,F}$ [-] | 0.85 | 0.98 | 0.92 | 1.05 | 1.11 | 0.78 | |
| $F_p/P_{u,F}$ [-] | 1.41 | 1.87 | 1.73 | 1.54 | 1.99 | 0.91 | |

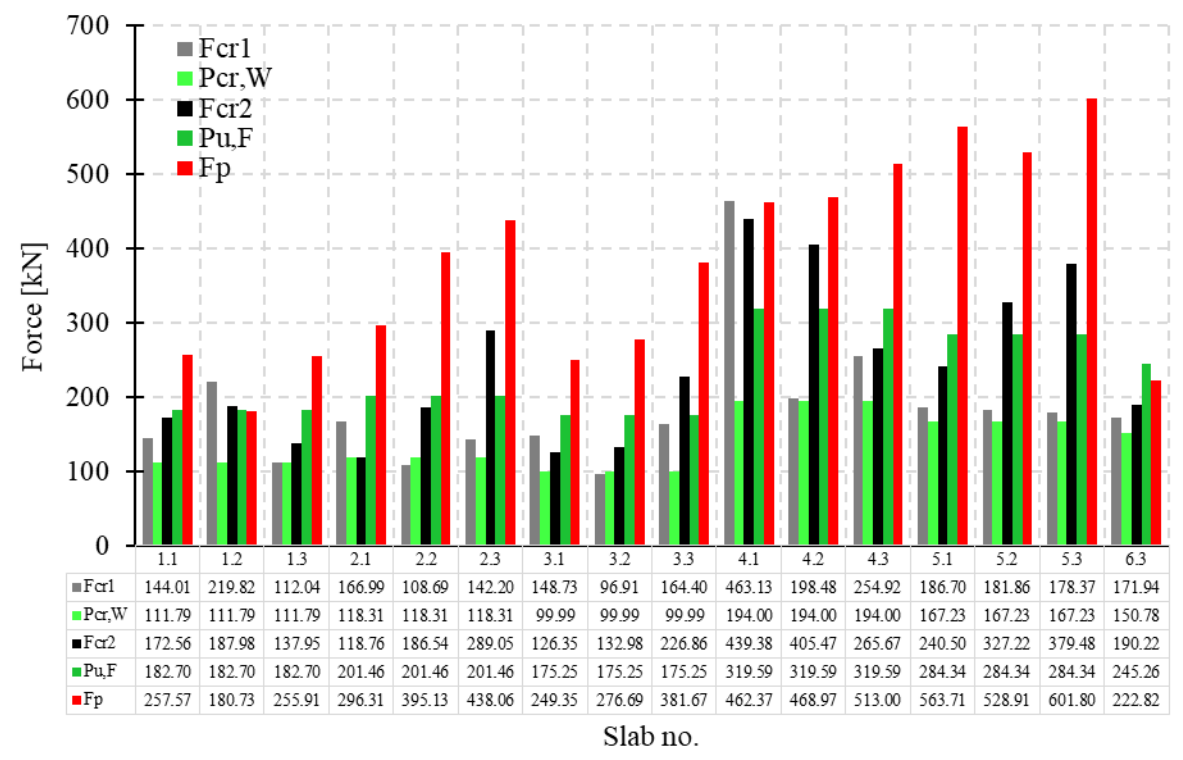


Fig. 6.1 Comparison of the experimentally obtained first and second flexural cracking force (F_{cr1} and F_{cr2}) and punching shear force (F_p) with analytically calculated load-bearing capacities for tested ground slabs types 1-6 centrally loaded by concentrated force according to the Westergaard ($P_{cr,W}$) and Falkner et al. ($P_{u,F}$) approaches

6.4. Shentu et al. approach

Chapter 3.2.3.3 provides a detailed description of the Shentu et al. approach and its underlying assumptions. Based on the equation (3.7), the formula for the load-bearing capacity of a single centrally loaded slab ($P_{u,S}$) was computed (equation (6.4)). Table 6.5

presents the calculation procedure and results for an experimentally tested ground slab of type 2, while Table 6.6 summarizes the results for all slabs of types 1-6. Notably, the ultimate load capacity is significantly influenced by the radius of loaded area as well as concrete modulus of elasticity and modulus of subgrade reaction.

$$P_{u,S} = 1.72 \cdot \left[\left(\frac{ka_r}{E_c} \right) \cdot 10^4 + 3.6 \right] \cdot f_{ct} \cdot h^2$$
 (6.4)

where:

 $P_{u,S}$ – ultimate load-bearing capacity of the ground slab according to the Shentu et al. approach [N],

k – modulus of subgrade reaction [N/mm³],

 a_r – radius of loaded area [mm],

 E_c – concrete modulus of elasticity [N/mm²],

 f_{ct} – concrete uniaxial tensile strength [N/mm²],

h – slab thickness [mm].

Undoubtedly, the results obtained using the Shentu et al. approach were several times greater than those calculated by the Westergaard and Falkner et al. methods. Similar observations were reported by other researchers, who noted that failure loads predicted by the Shentu et al. model significantly exceed those obtained from alternative analytical approaches [26], [88], [186]. Moreover, the experimentally measured values were considerably lower than the Shentu et al. predictions. This discrepancy may be attributed to the consideration of in-plane compressive forces generating horizontal thrust, commonly referred to as membrane action, in the Shentu et al. model. In the case of the tested slabs, this effect was not present due to the limited dimensions of the samples and the lack of lateral restraint (see Chapter 4.4.2.2).

Table 6.5 Determination of the load-bearing capacity of tested slab type 2 according to the Shentu et al. approach

| | SLAB OF TYPE 2 – Shentu et al. approach | | | | |
|----------|---|---|--|--|--|
| Dete | rmination of the load-bearing | capacity of SyFRC ground slab centrally loaded by a | | | |
| | | concentrated force | | | |
| | Determination of data | | | | |
| | Slab | | | | |
| | Slab thickness | h = 200 mm | | | |
| | Concrete parameters | | | | |
| PN-EN | Modulus of elasticity | From test: | | | |
| 12390-13 | | $E_c = 21419 \text{ MPa}$ | | | |
| [90] | | | | | |

| PN-EN | Uniaxial tensile strength | From test: | | |
|----------------|---|---|--|--|
| 12390-6 | | $f_{ct} = 1.99 \text{ MPa}$ | | |
| [49] | | | | |
| | Ground parameters | | | |
| | Primary static modulus of | From test: | | |
| | deformation | $E_{v1} = 134 \text{ MPa}$ | | |
| Hajduk [24] | Modulus of subgrade reaction | $k = \frac{E_{v1}}{550} = \frac{134}{550} = 0.244 \text{ MPa/mm}$ | | |
| | Load characterization | | | |
| | Column side dimension | x = 100 mm | | |
| | Baseplate thickness | t = 0 mm (absence of a baseplate) | | |
| | Determination of the equivalent radius of contact area of the load | | | |
| | Equivalent radius of contact area | a of the load | | |
| | $a_r = \sqrt{\frac{(x+4t)^2}{\pi}} = \sqrt{\frac{(100+4)^2}{\pi}}$ | $\frac{(\cdot \cdot 0)^2}{} = 56 \text{ mm}$ | | |
| | Determination of the load-bea | ring capacity | | |
| | Load-bearing capacity | | | |
| | $P_{u,S} = 1.72 \cdot \left[\left(\frac{ka_r}{E_c} \right) \cdot 10^4 + 3. \right]$ | $6 ight] \cdot f_{ct} \cdot h^2$ | | |
| | $= 1.72 \cdot \left[\left(\frac{0.24}{21} \right) \right]$ | $\left(\frac{4\cdot 56}{419}\right) \cdot 10^4 + 3.6 \cdot 1.99 \cdot 200^2 = 1371.52 \text{ kN}$ | | |

Table 6.6 Determination of the load-bearing capacity of tested ground slabs types 1-6 according to the Shentu et al. approach

| Slab type | 1 | 2 | 3 | 4 | 5 | 6.3 |
|-----------------------|---|---------------|----------------|----------------|-------------|---------|
| | Determination of data | | | | | |
| | | | Slab | | | |
| | | h = 200 mm; | x = 100 mm; | t = 0 mm | | |
| | | Conc | rete paramete | ers | | |
| E_c [MPa] | 19748 | 21419 | 18020 | 27149 | 29901 | 26734 |
| f_{ct} [MPa] | 1.91 | 1.99 | 1.84 | 2.70 | 2.86 | 2.44 |
| | | Grou | ınd paramete | rs | | |
| E_{vl} [MPa] | 143 | 134 | 139 | 141 | 138 | 132 |
| k [MPa/mm] | 0.260 | 0.244 | 0.253 | 0.256 | 0.251 | 0.240 |
| I | Determination | of the equiva | lent radius of | f contact area | of the load | |
| a_r [mm] | 56 | 56 | 56 | 56 | 56 | 56 |
| | Det | termination o | f the load-bea | ring capacity | | |
| $P_{u,S}[kN]$ | 1449.18 | 1371.52 | 1457.41 | 1658.38 | 1639.92 | 1454.60 |
| | | Expe | rimental resu | <u>lts</u> | | |
| F_{crl} [kN] | 128.03 | 139.29 | 136.68 | 226.70 | 182.31 | 171.94 |
| F_{cr2} [kN] | 155.26 | 198.12 | 162.06 | 335.57 | 315.73 | 190.22 |
| F_p [kN] | 256.74 | 376.50 | 302.57 | 490.99 | 564.81 | 222.82 |
| | Comparison of experimental and analytical results | | | | | |
| $F_{crl}/P_{u,F}$ [-] | 0.09 | 0.10 | 0.09 | 0.14 | 0.11 | 0.12 |
| $F_{cr2}/P_{u,F}$ [-] | 0.11 | 0.14 | 0.11 | 0.20 | 0.19 | 0.13 |
| $F_p/P_{u,F}$ [-] | 0.18 | 0.27 | 0.21 | 0.30 | 0.34 | 0.15 |

6.5. Technical Report 34 – Meyerhof-Losberg approach and Eurocode 2

6.5.1. Moment and punching shear capacity calculations

Analytical calculations of the tested ground slabs were conducted in accordance with the TR34 guideline [28]. The Meyerhof-Losberg approach, along with its underlying assumptions for determining the moment capacity of centrally loaded ground slabs, is described in detail in Chapter 3.2.3.4. Furthermore, Chapters 3.3.5.1 and 3.3.5.3 present design methodology based the punching shear on provisions PN-EN 1992-1-1:2008 [30]. In TR34 [28], bending failure is assumed to occur when the negative moment reaches the negative moment capacity, and circumferential cracks appear on the slab surface, as the design criterion aims to avoid cracks at the slab top. This stage is preceded by the formation of radial cracks at the bottom of the slab, corresponding to reaching the positive moment capacity. Regarding punching shear failure, it may develop either at the perimeter of the loaded area or at the critical control perimeter. The distance of the critical control section from the loading area was assumed as a = 2d, following recommendations of TR34 [28], and alternatively as the value a obtained from experimental slab tests (see Table 5.31). Table 6.7 illustrates the calculation procedure applied to evaluate the load-bearing capacity and failure mode of the experimentally tested ground slab of type 2, while Table 6.8 summarizes the results for all slabs of types 1-6.

Table 6.7 Determination of the load-bearing capacity of tested ground slab type 2 according to the calculation procedure of Technical Report 34 [28]

| | SLAB OF TYPE 2 – supported by the ground | | | | |
|-----------|---|---|--|--|--|
| Deter | Determination of the load-bearing capacity of SyFRC ground slab centrally loaded by a | | | | |
| | con | ncentrated force | | | |
| | Determination of data | | | | |
| | Slab | | | | |
| | Slab thickness | h = 200 mm | | | |
| TR34 [28] | Slab effective depth | $d = 0.75h = 0.75 \cdot 200 = 150 \text{ mm}$ | | | |
| p. 6.4 | | 0.70.70.70.70.70.70.70.70.70.70.70.70.70 | | | |
| | Concrete parameters | | | | |
| TR34 [28] | Poisson's ratio | v = 0.2 | | | |
| p. 7.5 | | 0.2 | | | |
| PN-EN | Compressive strength | From test: | | | |
| 12390-3 | | $f_c = f_{c,core} = 27.11 \text{ MPa}$ | | | |
| [23] | | | | | |
| PN-EN | Modulus of elasticity | From test: | | | |
| 12390-13 | | $E_c = 21419 \text{ MPa}$ | | | |
| [90] | | | | | |

| PN-EN | Uniaxial tensile strength | From test: | | |
|------------------|--|--|--|--|
| 12390-6 | Omaziai tenshe strength | $f_{ct} = 1.99 \text{ MPa}$ | | |
| [49] | | | | |
| PN-EN | Flexural tensile strength | From test: | | |
| 14651 [29] | | $f_{ct,fl} = 3.765 \mathrm{MPa}$ | | |
| PN-EN | Residual flexural tensile | From test: | | |
| 14651 [29] | strength at <i>CMOD</i> =0.5, 1.5, | $f_{R,1} = 1.915 \text{ MPa}; f_{R,2} = 0.596 \text{ MPa};$ | | |
| 11031 [25] | 2.5, and 3.5 mm, respectively | $f_{R,3} = 0.646 \text{ MPa}; f_{R,4} = 0.582 \text{ MPa}$ | | |
| TD 24 [20] | | $J_{R,3} = 0.040 \text{ MI a}, J_{R,4} = 0.302 \text{ MI a}$ | | |
| TR34 [28] | Mean axial tensile strength at the tip of the crack | $\sigma_{r1} = 0.45 f_{R,1} = 0.45 \cdot 1.915 = 0.862 \text{ MPa}$ | | |
| p. 6.3.4 TR34 | 1 | | | |
| | Mean axial tensile strength at | $\sigma = 0.27f = 0.27 \cdot 0.592 = 0.215 \text{ MP}_2$ | | |
| p. 6.3.4 | the crack) | $\sigma_{r4} = 0.37 f_{R,4} = 0.37 \cdot 0.582 = 0.215 \text{ MPa}$ | | |
| TD 24 [20] | Additional shear strength | 0.015 (6 + 6 + 6 + 6) | | |
| TR34 [28] | resulting from the presence of | $v_f = 0.015 \cdot \left(f_{R,1} + f_{R,2} + f_{R,3} + f_{R,4} \right)$ | | |
| eq. (14) | fibers in concrete | = 0.015 | | |
| | libers in concrete | $\cdot (1.915 + 0.596 + 0.646 + 0.582)$ | | |
| | | = 0.056 MPa | | |
| | Ground parameters | | | |
| | Primary static modulus of | From test: | | |
| | deformation | $E_{v1} = 134 \text{ MPa}$ $k = \frac{E_{v1}}{550} = \frac{134}{550} = 0.244 \text{ MPa/mm}$ | | |
| Hajduk | Modulus of subgrade reaction | $k = \frac{E_{v1}}{E_{v1}} = \frac{134}{E_{v1}} = 0.244 \text{ MPa/mm}$ | | |
| [24] | | 550 550 550 | | |
| | Load characterization | | | |
| | Column side dimension | x = 100 mm | | |
| | Baseplate thickness $t = 0 \text{ mm}$ (absence of a baseplate) | | | |
| | Determination of the indicator of contact area a/l | | | |
| | Radius of relative stiffness | | | |
| TR34 [28] | $l = \left(\frac{E_c \cdot h^3}{12 \cdot (1 - v^2) \cdot k}\right)^{0.25} = \left(\frac{21419 \cdot 200^3}{12 \cdot (1 - 0.2^2) \cdot 0.244}\right)^{0.25} = 497 \text{ mm}$ | | | |
| eq. (20) | $l = (\frac{12 \cdot (1 - v^2) \cdot k}{12 \cdot (1 - v^2) \cdot k}) = (\frac{1}{2})$ | $\frac{12 \cdot (1 - 0.2^2) \cdot 0.244}{12 \cdot (1 - 0.2^2) \cdot 0.244} = 497 \text{ mm}$ | | |
| | Equivalent radius of contact area | | | |
| TR34 [28] | Equivalent radius of contact area of the load | | | |
| Fig. 7.4 | $(x+4t)^2$ $(100+4)^2$ | $(\cdot \cdot 0)^2$ | | |
| 115. 7.1 | $a_r = \sqrt{\frac{(x+4t)^2}{\pi}} = \sqrt{\frac{(100+4)^2}{\pi}}$ | = 56 mm | | |
| | Indicator of contact area | | | |
| TR34 [28] | | | | |
| p. 7.6 | $\frac{a_r}{l} = \frac{56}{497} = 0.114$ | | | |
| p. 7.0 | Determination of the moment | canacity | | |
| | Negative moment capacity | Capacity | | |
| TR34 [28] | | 2 | | |
| | $M_{un} = \frac{f_{ct,fl}}{\gamma_c} \cdot \frac{h^2}{6} = \frac{3.765}{1.0} \cdot \frac{200}{6}$ | - = 25.100 kNm/m | | |
| eq. (2) | | | | |
| ED 0 4 5007 | Positive moment capacity | 222 | | |
| TR34 [28] | $M = \frac{h^2}{m} (0.29\sigma + 0.16\sigma)$ | $=\frac{200^2}{1} \cdot (0.29 \cdot 0.215 + 0.16 \cdot 0.862)$ | | |
| eq. (6) | $M_{up} = \frac{h^2}{\gamma_{fc}} (0.29\sigma_{r4} + 0.16\sigma_{r1}) = \frac{200^2}{1.0} \cdot (0.29 \cdot 0.215 + 0.16 \cdot 0.862)$ | | | |
| | = 8.013 kNm/r | m | | |
| | For an internal load: | | | |
| | for $a_r/l=0$ | | | |
| TR34 [28] | | - (25 100 + 0.012) - 200 0 (l N | | |
| eq. (21) | $F_{u,0,i} = 2\pi \cdot (M_{un} + M_{up}) = 2\pi$ | $\tau \cdot (25.100 + 8.013) = 208.06 \mathrm{kN}$ | | |
| * ` / | for $a_r/l=0.2$ | | | |
| TR34 [28] | $M_{nn} + M_{nn}$ | 25.100 + 8.013 | | |
| eq. (22) | $ P_{u,0.2,i} = 4\pi \cdot \frac{ar}{1} \cdot \frac{ar}{a_r} = 4\pi$ | $\frac{25.100 + 8.013}{1 - \frac{1}{2} \cdot 0.2} = 445.83 \text{ kN}$ | | |
| Cq. (22) | | | | |

| | T . 1 .: C . // 0.102 |
|--------------------|--|
| | Interpolation for $a_r/l=0.103$ |
| | $P_{u,i} = \frac{P_{u,0,2,i} - P_{u,0,i}}{0.2 - 0} \cdot \frac{a_r}{l} + P_{u,0,i} = \frac{445.83 - 208.06}{0.2 - 0} \cdot 0.114 + 208.06$ |
| | $\begin{array}{cccccccccccccccccccccccccccccccccccc$ |
| | Determination of the punching shear capacity |
| | Strength reduction factor for concrete cracked in shear |
| EC2 [30] | |
| p. 6.2.2(6) | $k_2 = 0.6 \cdot \left(1 - \frac{f_c}{250}\right) = 0.6 \cdot \left(1 - \frac{27.11}{250}\right) = 0.535$ |
| 1 - (-) | Maximum shear strength of concrete at the face of the loaded area |
| EC2 [30] | - |
| p. 6.4.5(3) | $v_{max} = 0.5 \cdot k_2 \cdot f_c = 0.5 \cdot 0.535 \cdot 27.11 = 7.251 \text{ MPa}$ |
| | Length of the perimeter of the loaded area |
| | $u_0 = 4 \cdot (x + 4t) = 4 \cdot (100 + 4 \cdot 0) = 400 \text{ mm}$ |
| | Punching shear capacity at the face of the loaded area |
| TR34 [28] eq. (11) | $P_{p,max} = v_{max} \cdot u_0 \cdot d = 7.251 \cdot 400 \cdot 150 = 435.06 \text{ kN}$ |
| | Coefficient taking into consideration size effect |
| EC2 [30] | $(200)^{0.5}$ $(200)^{0.5}$ |
| p. 6.4.4(1) | $k_{s} = min \left\{ 1 + \left(\frac{200}{d} \right)^{0.5} = min \left\{ 1 + \left(\frac{200}{150} \right)^{0.5} = 2.155 = 2.0 \right\} \right\}$ |
| | ` 2.0 |
| | Concrete minimum shear strength at a distance $a=2d$ from the loaded area (assumed in |
| | TR34) |
| TR34 [28] | $v_{R,c,min,2d} = 0.035 \cdot k_s^{1.5} \cdot f_c^{0.5} \cdot \frac{2d}{2d} = 0.035 \cdot 2.0^{1.5} \cdot 27.11^{0.5} \cdot \frac{2 \cdot 150}{2 \cdot 150} = 0.515 \text{ MPa}$ |
| eq. (12) | |
| | Concrete minimum shear strength at a distance $a=0.69d$ from the loaded area |
| TD 24 [29] | (experimentally determined) |
| TR34 [28] eq. (12) | $v_{R,c,min,acrit} = 0.035 \cdot k_s^{1.5} \cdot f_c^{0.5} \cdot \frac{2d}{0.69d} = 0.035 \cdot 2.0^{1.5} \cdot 27.11^{0.5} \cdot \frac{2 \cdot 150}{0.69 \cdot 150}$ |
| eq. (12) | = 1.494 MPa |
| | Length of the critical control perimeter for $a=2d$ |
| | $u_{1,2d} = 4 \cdot (x + 4t) + 2 \cdot 2d \cdot \pi = 4 \cdot (100 + 4 \cdot 0) + 4 \cdot 150 \cdot \pi = 2285 \text{ mm}$ |
| | Length of the critical control perimeter for $a=0.69d$ |
| | $u_{1,a} = 4 \cdot (x + 4t) + 2 \cdot 0.69d \cdot \pi = 4 \cdot (100 + 4 \cdot 0) + 2 \cdot 0.69 \cdot 150 \cdot \pi = 1050 \text{ mm}$ |
| | Punching shear capacity at a distance $a=2d$ from the loaded area |
| TR34 [28] | $P_{p,c,2d} = v_{R,c,min,2d} \cdot u_{1,2d} \cdot d = 0.515 \cdot 2285 \cdot 150 = 176.66 \text{ kN}$ |
| eq. (13) | |
| | Punching shear capacity at a distance $a=0.69d$ from the loaded area |
| TR34 [28] eq. (13) | $P_{p,c,a} = v_{R,c,min,a} \cdot u_{1,a} \cdot d = 1.494 \cdot 1050 \cdot 150 = 235.38 \text{ kN}$ |
| | Determination of the additional punching shear capacity resulting from the |
| | presence of fibers in concrete |
| | At a distance $a=2d$ from the loaded area |
| | $P_{p,f,2d} = v_f \cdot u_{1,2d} \cdot d = 0.056 \cdot 2285 \cdot 150 = 19.22 \text{ kN}$ |
| | At a distance $a=0.69d$ from the loaded area |
| | $P_{p,f,a} = v_f \cdot u_{1,a} \cdot d = 0.056 \cdot 1050 \cdot 150 = 8.84 \text{ kN}$ |
| | Determination of the punching shear capacity with additional shear strength |
| | resulting from the presence of fibers in concrete |
| TD 2/1 [20] | At a distance <i>a</i> =2 <i>d</i> from the loaded area |
| TR34 [28] eq. (15) | $P_{p,cf,2d} = (v_{R,c,min,2d} + v_f) \cdot u_{1,2d} \cdot d = (0.515 + 0.056) \cdot 2285 \cdot 150 = 195.89 \text{ kN}$ |
| -q. (1 <i>3)</i> | At a distance $a=0.69d$ from the loaded area |
| TR34 [28] | |
| eq. (15) | $P_{p,cf,a} = (v_{R,c,min,a} + v_f) \cdot u_{1,a} \cdot d = (1.494 + 0.056) \cdot 1050 \cdot 150 = 244.22 \text{ kN}$ |
| | |

| | Determination of the additional punching shear capacity resulting from the ground |
|----------------------|---|
| | support |
| | Equation intended only for point load applied through a stiff bearing, where $a/l < 0$ – condition fulfilled |
| | At a distance $a=2d$ from the loaded area |
| TR34 [28] | |
| eq. (31) | $R_{p,c,2d} = 1.4 \cdot \left(\frac{d}{l}\right)^2 \cdot P_{p,c,2d} + 0.47 \cdot (x_b + y_b) \cdot \frac{d \cdot P_{p,c,2d}}{l^2}$ |
| | $= 1.4 \cdot \left(\frac{150}{497}\right)^2 \cdot 176.66 + 0.47 \cdot (100 + 100) \cdot \frac{150 \cdot 176.66}{497^2}$ |
| | = 32.68 kN |
| | where x_b and y_b are dimensions of the bearing plate: $x_b = y_b = x = 100 \text{ mm}$ |
| | At a distance $a=2d$ from the loaded area including presence of fibers in concrete |
| TR34 [28] eq. (31) | $R_{p,cf,2d} = 1.4 \cdot \left(\frac{d}{l}\right)^2 \cdot P_{p,cf,2d} + 0.47 \cdot (x_b + y_b) \cdot \frac{d \cdot P_{p,cf,2d}}{l^2}$ |
| | $= 1.4 \cdot \left(\frac{150}{497}\right)^2 \cdot 195.89 + 0.47 \cdot (100 + 100) \cdot \frac{150 \cdot 195.89}{497^2}$ |
| | = 36.24 kN |
| | At a distance $a=0.69d$ from the loaded area |
| TR34 [28] App. F | $R_{p,c,a} = \frac{0.106 \cdot P_{p,c,a}}{l^2} \cdot \pi \cdot (0.69d)^2 + \frac{1}{3} \cdot \pi \cdot (0.69d)^2 \cdot (0.125 - 0.106) \cdot \frac{P_{p,c,a}}{l^2}$ |
| eq. (F3) and (F5) | $+ 0.93 \cdot (2 \cdot x_b \cdot 0.69d + 2 \cdot y_b \cdot 0.69d) \cdot \frac{0.125 \cdot P_{p,c,a}}{l^2}$ |
| | $= \frac{0.106 \cdot 235.38}{497^2} \cdot \pi \cdot (0.69 \cdot 150)^2 + \frac{1}{3} \cdot \pi \cdot (0.69 \cdot 150)^2$ |
| | $\cdot (0.125 - 0.106) \cdot \frac{235.38}{497^2} + 0.93$ |
| | $\cdot (2 \cdot 100 \cdot 0.69 \cdot 150 + 2 \cdot 100 \cdot 0.69 \cdot 150) \cdot \frac{0.125 \cdot 235.38}{497^2}$ |
| | = 8.19 kN |
| | At a distance $a=0.69d$ from the loaded area including presence of fibers in concrete |
| TR34 [28] App. F | $R_{p,cf,ac} = \frac{0.106 \cdot P_{p,cf,a}}{l^2} \cdot \pi \cdot (0.69d)^2 + \frac{1}{3} \cdot \pi \cdot (0.69d)^2 \cdot (0.125 - 0.106) \cdot \frac{P_{p,cf,a}}{l^2}$ |
| eq. (F3) and (F5) | $+0.93 \cdot (2 \cdot x_b \cdot 0.69d + 2 \cdot y_b \cdot 0.69d) \cdot \frac{0.125 \cdot P_{p,cf,a}}{l^2}$ |
| | $= \frac{0.106 \cdot 244.22}{497^2} \cdot \pi \cdot (0.69 \cdot 150)^2 + \frac{1}{3} \cdot \pi \cdot (0.69 \cdot 150)^2$ |
| | $(0.125 - 0.106) \cdot \frac{244.22}{497^2} + 0.93$ |
| | $\cdot (2 \cdot 100 \cdot 0.69 \cdot 150 + 2 \cdot 100 \cdot 0.69 \cdot 150) \cdot \frac{0.125 \cdot 244.22}{497^2}$ |
| | = 8.49 KN |
| | Determination of the punching shear capacity resulting from the ground support |
| | At a distance $a=2d$ from the loaded area |
| | $P_{p,cR,2d} = P_{p,c,2d} + R_{p,c,2d} = 176.66 \text{ kN} + 32.68 \text{ kN} = 209.35 \text{ kN}$ |
| | At a distance $a=0.69d$ from the loaded area |
| | $P_{p,cR,a} = P_{p,c,a} + R_{p,c,a} = 235.38 \text{ kN} + 8.19 \text{ kN} = 243.57 \text{ kN}$ |
| | Determination of the total punching shear capacity resulting from the ground |
| | support and presence of fibers in concrete |
| | At a distance $a=2d$ from the loaded area |
| | $P_{p,cfR,2d} = P_{p,cf,2d} + R_{p,cf,2d} = 195.89 \text{ kN} + 36.24 \text{ kN} = 232.13 \text{ kN}$ |
| | At a distance $a=0.69d$ from the loaded area |
| | $P_{p,cfR,a} = P_{p,cf,a} + R_{p,cf,a} = 244.22 \text{ kN} + 8.49 \text{ kN} = 252.71 \text{ kN}$ |
| | Determination of the critical condition |

```
At a distance a=2d from the loaded area  \begin{cases} P_{p,cfR,2d} < P_{p,max} \\ P_{p,cfR,2d} < P_{u,i} \end{cases} = \begin{cases} 232.13 \text{ kN} < 435.06 \text{ kN} \\ 232.13 \text{ kN} < 343.00 \text{ kN} \end{cases}  At a distance a=0.69d from the loaded area  \begin{cases} P_{p,cfR,a} < P_{p,max} \\ P_{p,cfR,a} < P_{u,i} \end{cases} = \begin{cases} 252.71 \text{ kN} < 435.06 \text{ kN} \\ 252.71 \text{ kN} < 343.00 \text{ kN} \end{cases}  CONCLUSION: Punching shear failure at the critical control perimeter
```

Table 6.8 Determination of the load-bearing capacity of tested ground slabs types 1-6 according to the calculation procedure of Technical Report 34 [28]

| Slab type | 1 | 2 | 3 | 4 | 5 | 6.3 |
|-------------------------|---------------|----------------------|----------------|----------------------|---------------|---------------|
| | | <u>Detern</u> | nination of da | <u>ıta</u> | | |
| | | | Slab | | | |
| | h = 20 | 0 mm; d = 150 | 0 mm; x = 100 | 0 mm; $t = 0$ m | m | |
| | | | ete paramete | | | |
| v [-] | 0.20 | 0.20 | 0.20 | 0.20 | 0.20 | 0.20 |
| f_c [MPa] | 25.01 | 27.11 | 23.51 | 36.16 | 38.56 | 30.76 |
| E_c [GPa] | 19748 | 21419 | 18020 | 27149 | 29901 | 26734 |
| f_{ct} [MPa] | 1.91 | 1.99 | 1.84 | 2.70 | 2.86 | 2.44 |
| $f_{ct,fl}$ [MPa] | 3.499 | 3.765 | 3.107 | 6.303 | 5.504 | 4.926 |
| $f_{R,1}$ [MPa] | 0.000 | 1.915 | 1.359 | 4.081 | 2.923 | 2.962 |
| $f_{R,2}$ [MPa] | 0.000 | 0.596 | 0.629 | 0.711 | 1.346 | 0.457 |
| $f_{R,3}$ [MPa] | 0.000 | 0.646 | 0.620 | 0.768 | 1.422 | 0.476 |
| $f_{R,4}$ [MPa] | 0.000 | 0.582 | 0.611 | 0.793 | 1.403 | 0.448 |
| σ_{rl} [MPa] | 0.000 | 0.862 | 0.612 | 1.836 | 1.315 | 1.333 |
| σ_{r4} [MPa] | 0.000 | 0.215 | 0.226 | 0.293 | 0.519 | 0.166 |
| $v_f[MPa]$ | 0.000 | 0.056 | 0.048 | 0.095 | 0.106 | 0.065 |
| | | | nd parameter | ·s | | |
| E_{vl} [MPa] | 143 | 134 | 139 | 141 | 138 | 132 |
| k [MPa/mm] | 0.260 | 0.244 | 0.253 | 0.256 | 0.251 | 0.240 |
| | Determ | ination of th | e indicator of | contact area | | |
| a_r [mm] | 56 | 56 | 56 | 56 | 56 | 56 |
| <i>l</i> [mm] | 479 | 497 | 472 | 521 | 536 | 527 |
| a_r/l [-] | 0.118 | 0.114 | 0.120 | 0.108 | 0.105 | 0.107 |
| | <u>D</u> | <u>etermination</u> | of the momen | nt capacity | | |
| M_{un} [kNm/m] | 23.327 | 25.100 | 20.713 | 42.020 | 36.693 | 32.840 |
| M_{up} [kNm/m] | 0.000 | 8.013 | 6.536 | 15.157 | 14.440 | 10.453 |
| $P_{u,i}[kN]$ | 245.17 | 343.00 | 288.23 | 581.66 | 514.40 | 438.31 |
| | | <u>mination of t</u> | he punching | <u>shear capacit</u> | | |
| u_0 [mm] | 400 | 400 | 400 | 400 | 400 | 400 |
| $P_{p,max}$ [kN] | 405.14 | 435.06 | 383.38 | 556.74 | 587.03 | 485.56 |
| $u_{1,2d}[\mathrm{mm}]$ | 2285 | 2285 | 2285 | 2285 | 2285 | 2285 |
| $P_{p,f,2d}[kN]$ | 0.00 | 19.22 | 16.55 | 32.66 | 36.47 | 22.33 |
| $P_{p,c,2d}[kN]$ | 169.68 | 176.66 | 164.52 | 204.03 | 210.69 | 188.18 |
| $P_{p,cf,2d}[kN]$ | 169.68 | 195.89 | 181.07 | 236.69 | 247.17 | 210.51 |
| $R_{p,c,2d}[kN]$ | 33.77 | 32.68 | 33.80 | 34.39 | 33.48 | 30.93 |
| $P_{p,cR,2d}[kN]$ | 203.46 | 209.35 | 198.31 | 238.42 | 244.17 | 219.11 |
| $R_{p,cf,2d}[kN]$ | 33.77 | 36.24 | 37.20 | 39.90 | 39.27 | 34.60 |
| $P_{p,cfR,2d}$ [kN] | 203.46 | 232.13 | 218.26 | 276.59 | 286.44 | 245.11 |
| a [mm] | 0.11 <i>d</i> | 0.69 <i>d</i> | 0.64 <i>d</i> | 0.80d | 0.98 <i>d</i> | 0.65 <i>d</i> |
| $u_{l,a}[\mathrm{mm}]$ | 176 | 1050 | 1003 | 1154 | 1324 | 1013 |
| $P_{p,f,a}[kN]$ | 0.000 | 8.84 | 7.27 | 16.50 | 21.13 | 9.90 |

| $P_{p,c,a}[kN]$ | 237.53 | 235.38 | 225.72 | 257.61 | 249.08 | 256.60 |
|--------------------------|----------|----------|----------|----------|----------|----------|
| $P_{p,cf,a}[kN]$ | 237.53 | 244.22 | 232.98 | 274.10 | 270.21 | 266.50 |
| $R_{p,c,a}[kN]$ | 0.000 | 8.19 | 7.83 | 10.13 | 12.52 | 7.28 |
| $P_{p,cR,a}[kN]$ | 237.53 | 243.57 | 233.54 | 267.74 | 261.60 | 263.88 |
| $R_{p,cf,a}[kN]$ | 0.000 | 8.49 | 8.08 | 10.78 | 13.58 | 7.56 |
| $P_{p,cfR,a}$ [kN] | 237.53 | 252.71 | 241.06 | 284.88 | 283.79 | 274.05 |
| For <i>a</i> =2 <i>d</i> | Punching | Punching | Punching | Punching | Punching | Punching |
| For a from tests | Punching | Punching | Punching | Punching | Punching | Punching |

From Table 6.8, it can be concluded that, assuming the TR34 [28] recommended distance of the critical control section a = 2d from the loaded area, punching shear capacity was the governing failure criterion for all slab types. These calculations also aimed to provide a preliminary prediction of expected slab failure modes prior to testing Specifically, they confirmed the validity of the experimental research design and methodology, which were aimed at punching shear analysis. When considering the experimentally determined values of a, it was revealed that again punching shear failure at the critical control section would occur before bending failure. It must be mentioned that in the case of PC ground slabs 1.1 and 1.3, crack propagation led to the sequential detachment of the northern portion of the slab, followed by the division of the southern segment along the N-S axis (Fig. 5.20). Consequently, only one quarter of the slab remained subjected to loading until the punching shear capacity was reached. Therefore, the assessment of punching capacity was performed under the assumption of corner loading, with no contribution from subgrade support considered. As shown in Table 6.8, regardless of whether calculations were carried out using the critical perimeter location recommended by TR34 [28] at a = 2d, or the experimentally determined a value, the predicted failure modes remained consistent and in agreement with experimental observations. Nevertheless, the punching shear load-bearing capacity was generally higher when the actual a value was applied, which more accurately reflected the experimental results and enhanced the predictivity of the analytical calculations. It should be noted, however, that the static scheme of the tested slabs only approximately corresponded to the model assumptions presented in TR34 [28], which may have contributed to the differences between the experimental and analytical results.

For further discussion, Table 6.9 summarizes the contribution of each mechanism to the punching shear load-bearing capacity according to the TR34 calculation procedure [28]. For PC ground slabs, when the critical control perimeter is defined at a distance of a = 2d, approximately 83.4% of the punching load is transferred by the concrete, with the remaining portion carried by the subgrade. When a = 0.11d, the entire punching load is assumed to be transferred exclusively by concrete. It is further shown that, for SyFRC

ground slabs, the average contributions of concrete, fibers, and subgrade to the total punching shear capacity are 75.1%, 9.9%, and 15.0%, respectively, when the critical control perimeter is defined at a distance of 2d from the loading area. For the perimeter established based on experimental results, the majority of the load is transferred by concrete (91.7%), while fibers and subgrade contribute only 4.7% and 3.6%, respectively, to the total punching shear capacity. This can be explained by the significantly reduced length of the critical control perimeter for smaller values of a. Nevertheless, it should be noted that the calculated contributions of fibers and ground in load transfer appear to be underestimated.

Table 6.9 Contribution of each component in punching shear load-bearing capacity of tested slabs types 1-6 according to the calculation procedure of Technical Report 34 [28]

| Component | Concrete | | Fibers | | Ground | | Total | |
|-----------------------------|-------------------|-------------------|-------------------|------------------|--------------------|-------------------|---------------------|--------------------|
| Component capacity | $P_{p,c,2d}$ [kN] | $P_{p,c,a}$ [kN] | $P_{p,f,2d}$ [kN] | $P_{p,f,a}$ [kN] | $R_{p,cf,2d}$ [kN] | $R_{p,cf,a}$ [kN] | $P_{p,cfR,2d}$ [kN] | $P_{p,cfR,a}$ [kN] |
| Slab type 1 | 169.68 | 237.53 | 0.00 | 0.00 | 33.77 | 0.00 | 203.46 | 237.53 |
| (PC) Slab type 2 | (83.4%) 176.66 | (100%) 235.38 | (0.0%) 19.22 | (0.0%) 8.84 | (16.6%) 36.24 | (0.0%) 8.49 | (100%) 232.13 | (100%) 252.71 |
| (PM_2) Slab type 3 | (76.1%) 164.52 | (93.1%) 225.72 | (8.3%) | 7.27 | (15.6%) 37.20 | (3.4%) 8.08 | (100%) | (100%) 241.06 |
| (PM_3) | (75.4%) | (93.6%) | (7.6%) | (3.0%) | (17.0%) | (3.4%) | (100%) | (100%) |
| Slab type 4 (PD 2) | 204.03 (73.8%) | 257.61 (90.4%) | 32.66 (11.8%) | 16.50 (5.8%) | 39.90 (14.4%) | (3.8%) | 276.59 (100%) | 284.88 (100%) |
| Slab type 5 | 210.69 | 249.08 | 36.47 | 21.13 | 39.27 | 13.58 | 286.44 | 283.79 |
| (PD_3) Slab type 6.3 | (73.6%) 188.18 | (87.8%) 256.60 | (12.7%) 22.33 | 9.90 | (13.7%) | (4.8%) 7.56 | (100%) 245.11 | (100%) 274.05 |
| (FF_2) | (76.8%) | (93.6%) | (9.1%) | (3.6%) | 14.1%) | 2.8%) | (100%) | (100%) |
| Average for SyFRC slabs 2-6 | 75.1% | 91.7% | 9.9% | 4.7% | 15.0% | 3.6% | 100% | 100% |

Note: The percentage values were calculated as the ratio of the load-bearing capacity provided by concrete $(P_{p,c})$, fibers $(P_{p,f})$, or ground $(R_{p,cf})$ to the total punching shear load-bearing capacity $(P_{p,cfR})$.

Firstly, the experimental campaign demonstrated that the addition of macro SyFs significantly enhanced the punching load-bearing capacity of the tested ground slabs, which was not reflected in the analytical results. Specifically, the inclusion of 2 and 3 kg/m^3 of PM fibers resulted in improvements of 47% and 18%, respectively, compared to ground slabs without fibers. Consequently, even in samples with reduced concrete strength, the contribution of fibers to structural performance was clearly evident and should not be overlooked. This phenomenon can be explained by the fact that in TR34 [28], the equation adopted for the additional (residual) shear strength resulting from the presence of fibers in concrete, v_f (equation (3.89)), was approached with considerable caution due to the limited number of supporting experimental studies, which may have

led to a significant underestimation of this value. Secondly, the procedure outlined in TR34 [28] for calculating the contribution of ground support in transferring punching shear incorporates several simplifications and conservative assumptions that may lead to an underestimation of the results. For instance, it is considered that the bearing pressure at the critical control perimeter is equivalent to 85% of the peak bearing pressure. However, based on the experimental results, it was concluded that the critical control section was situated significantly closer than at the recommended distance a = 2d, what can result in higher bearing pressure along the critical control section, however with a reduced perimeter length. Furthermore, in [28], the contribution of ground pressure directly beneath the bearing plate (column, racking leg) is neglected to avoid the potentially unconservative approach of that the peak pressure at the perimeter of the stiff bearing equals to that directly under the concentrated load. Consequently, this further limits the area of ground upward pressure that can contribute to transferring the punching shear force.

6.5.2. Contribution of fibers and ground in transferring punching shear load

The punching shear capacity of PC ground-supported slabs subjected to a centrally applied concentrated load calculated according to the TR34 [28] provisions (237.53 kN) was 8% and 9% lower than the experimental results for slabs 1.1 (257.57 kN) and 1.3 (255.91 kN), respectively, but 31% higher in the case of slab 1.2 (180.73 kN). Considering that slab 1.2 exhibited a distinct failure mode (Fig. 5.60) which may account for deviations in the results, a strong correlation was observed between the experimental data and the analytical predictions for PC slabs. However, based on Table 6.8, it was concluded that only limited agreement was achieved between the analytical and experimental results for SyFRC slabs types 2-6 with respect to punching shear capacity. Moreover, the analytical analysis indicated a rather low contribution of fibers in transferring punching shear load (Table 6.9). This could have been explained by the previously discussed conservative assumption in TR34 [17] regarding the equation (3.89) for v_f , justified by the limited number of supporting experimental studies. To address this issue, alternative equations for calculating the residual shear strength v_f were examined, as proposed in other standards (Fig. 6.2). Specifically, the formulas suggested in RILEM TC 162-TDF [66] (Chapter 3.3.3.1, equation (3.45), PN-EN 1992-1-1:2024 [33] (Chapter 3.3.3.3, equation (3.68)), and MC2010 [80] (Chapter 3.3.5.4, equation (3.90)) were applied to determine new values of punching shear capacities (Table 6.10).

TR34 [28]
$$v_{f} = \frac{0.12 \cdot \left(\frac{f_{R,1} + f_{R,2} + f_{R,3} + f_{R,4}}{4}\right)}{2}$$
RILEM TC 162-TDF [66]
$$v_{f} = 0.12 \cdot f_{R,4}$$
PN-EN 1992-1-1:2024 [33]
$$v_{f} = \kappa_{0} \cdot \kappa_{G} \cdot 0.33 \cdot f_{R,3}$$
where: $\kappa_{0} = 1.0$ and $\kappa_{G} = 1.0$

$$v_{f} = f_{Fts} - \frac{w_{u}}{CMOD_{3}} (f_{Fts} - 0.5f_{R,3} + 0.2f_{R,1})$$
where: $f_{Fts} = 0.45f_{R,I}$; $w_{u} = 1.5$ mm, and $f_{th} = 0.5$ mm

Fig. 6.2 Formulas proposed in selected standard for calculating the additional shear strength resulting from the presence of fibers in concrete

Table 6.10 Punching shear load-bearing capacity of tested slabs types 2-6 calculated according to the Technical report 34 [28] dependent on the applied formula for v_f calculations

| Slab type | 2 | 3 | 4 | 5 | 6.3 | | | |
|-----------------------------|--------|------------------|---------------------|--------|--------|--|--|--|
| | - | Experiment | al results | - | - | | | |
| F_p [kN] | 376.50 | 302.57 | 490.99 | 564.81 | 222.82 | | | |
| Concrete contribution | | | | | | | | |
| $P_{p,c,a}[kN]$ | 235.38 | 225.72 | 257.61 | 249.08 | 256.60 | | | |
| | | Technical Rep | ort 34 [28] | | - | | | |
| $v_f[MPa]$ | 0.056 | 0.048 | 0.095 | 0.106 | 0.065 | | | |
| $P_{p,f,a}$ [kN] | 8.84 | 7.27 | 16.50 | 21.13 | 9.90 | | | |
| $R_{p,cf,a}$ [kN] | 8.49 | 8.08 | 10.78 | 13.58 | 7.56 | | | |
| $P_{p,cfR,a}$ [kN] | 252.71 | 241.06 | 284.88 | 283.79 | 274.05 | | | |
| | | rison with the e | | | | | | |
| $F_p/P_{p,cfR,a}$ [-] | 1.49 | 1.26 | 1.72 | 1.99 | 0.81 | | | |
| | | RILEM TC 16 | 2-TDF [66] | | | | | |
| $v_f[MPa]$ | 0.070 | 0.073 | 0.095 | 0.168 | 0.054 | | | |
| $P_{p,f,a}$ [kN] | 11.00 | 11.03 | 16.48 | 33.43 | 8.17 | | | |
| $R_{p,cf,a}$ [kN] | 8.57 | 8.21 | 10.78 | 14.20 | 7.51 | | | |
| $P_{p,cfR,a}$ [kN] | 254.95 | 244.96 | 284.86 | 296.71 | 272.28 | | | |
| | | rison with the e | | | | | | |
| $F_p/P_{p,cfR,a}$ [-] | 1.48 | 1.24 | 1.72 | 1.90 | 0.82 | | | |
| | | PN-EN 1992-1- | -1:2024 [33] | | | | | |
| $v_f[MPa]$ | 0.213 | 0.205 | 0.253 | 0.469 | 0.157 | | | |
| $P_{p,f,a}$ [kN] | 33.59 | 30.79 | 43.87 | 93.17 | 23.86 | | | |
| $R_{p,cf,a}$ [kN] | 9.35 | 8.90 | 11.85 | 17.21 | 7.96 | | | |
| $P_{p,cfR,a}$ [kN] | 278.32 | 265.40 | 313.33 | 359.46 | 288.41 | | | |
| | | rison with the e | | | | | | |
| $F_p/P_{p,cfR,a}$ [-] | 1.35 | 1.14 | 1.57 | 1.57 | 0.77 | | | |
| Model Code 2010 [80] | | | | | | | | |
| $v_f[MPa]$ | 0.309 | 0.268 | 0.475 | 0.602 | 0.321 | | | |
| $P_{p,f,a}$ [kN] | 48.64 | 40.26 | 82.27 | 119.52 | 48.68 | | | |
| $R_{p,cf,a}$ [kN] | 9.88 | 9.22 | 13.36 | 18.53 | 8.66 | | | |
| $P_{p,cfR,a}$ [kN] | 293.89 | 275.20 | 353.24 | 387.13 | 313.49 | | | |
| | | rison with the e | _ | | T | | | |
| $F_p/P_{p,cfR,a}$ [-] | 1.28 | 1.10 | 1.39 | 1.46 | 0.71 | | | |

From Table 6.10, it can be concluded that the greatest contribution of fibers in resisting punching shear was obtained using equation (3.90) from MC2010 [80], with $P_{p,f,a}$ at least 4.9 times greater than the values resulting from equation (3.89) adopted in

TR34 [28]. Then, the capacities derived from equation (3.68) from PN-EN 1992-1-1:2024 [33] were lower by 22-51%, depending on the slab type, compared to those from MC2010 [80], however still considerable higher than the values obtained using equation (3.89) according to TR34 [28]. Finally, the equation (3.45) from RILEM TC 162-TDF [66] provided $P_{p,f,a}$ values usually closely aligned with those derived from TR34's equation (3.89).

In further analysis, the adjustments to the punching shear load-bearing capacity calculations also addressed the corrected ground's contribution in resisting the punching shear force, denoted as $P_{p,g,a}$. Specifically, to obtain a more accurate assessment of the ground support role in transferring the concentrated force, several modifications were introduced to equation (6.5), leading to the formulation of equation (6.6).

$$R_{p,cf,a} = \frac{0.106 \cdot P_{p,cf,a}}{l^2} \cdot \pi \cdot a^2 + \frac{1}{3} \cdot \pi \cdot a^2 \cdot (0.125 - 0.106) \cdot \frac{P_{p,cf,a}}{l^2} + 0.93$$
$$\cdot (2 \cdot x_b \cdot a + 2 \cdot y_b \cdot a) \cdot \frac{0.125 \cdot P_{p,cf,a}}{l^2}$$
(6.5)

$$P_{p,g,a} = \left(1 - \frac{a}{b}\right) \cdot \frac{0.125 \cdot P_{p,cf,a}}{l^2} \cdot \pi \cdot a^2 + \frac{1}{3} \cdot \pi \cdot a^2 \cdot \frac{a}{b} \cdot \frac{0.125 \cdot P_{p,cf,a}}{l^2} + 0.93$$

$$\cdot \left(2 \cdot x_b \cdot a + 2 \cdot y_b \cdot a\right) \cdot \frac{0.125 \cdot P_{p,cf,a}}{l^2} + \left(x_b \cdot y_b\right)$$

$$\cdot \frac{0.125 \cdot P_{p,cf,a}}{l^2}$$

$$(6.6)$$

where:

 $R_{p,cf,a}$ – ground reaction resulting from an internal point load applied through a stiff bearing, where $a_r/l < 0.2$ according to Appendix F of TR34 [28] [N],

 $P_{p,g,a}$ – corrected ground reaction resulting from an internal point load applied through a stiff bearing, where $a_r/l < 0.2$ [N],

a – distance of the critical control section from the loading area [mm],

b – distance from the load application point to zero ground bearing pressure assumed to be 2.75l (see Fig. 6.3a) [mm],

l – radius of relative stiffness according to equation (3.15) [mm],

 $P_{p,cf,a}$ – concrete punching shear load-bearing capacity including the additional capacity resulting from the presence of fibers in concrete at the critical control section [N], x_b and y_b – effective dimensions of a stiff bearing plate [mm].

Following Appendix F of TR34 [28], a simplified inverted cone model of ground pressure distribution was adopted, in which the pressure decreases linearly from its peak

at the load application point to zero at a distance b, assumed to be 2.75l (Fig. 6.3a). Consequently, the actual bearing pressure at the experimentally determined critical control section, located at a distance a from the loading area, was calculated without applying the TR34 assumption that the bearing pressure at the perimeter equals 85% of the peak value. The peak pressure was determined using the Westergaard expression, multiplied by the modulus of subgrade reaction k [237]. Specifically, it was taken as $0.125P/l^2$, resulting in a critical control section bearing pressure of $(1-a/b)(0.125P/l^2)$, where P is the concentrated load. In addition, following equation (6.5), the increased length of the critical control perimeter due to force application through the stiff bearing was also considered in equation (6.6). Furthermore, the ground pressure directly beneath the racking leg was included, assuming that the pressure under the perimeter of the loading area equals that beneath the concentrated load (Fig. 6.3b). In equation (6.6), the highlighted components of ground reaction correspond to the adequate volumes of ground pressure distribution illustrated in Fig. 6.3b. Table 6.11 presents the corrected ground reaction values $P_{p,g,a}$ for all selected formulas used to calculate the additional punching shear strength v_f resulting from the presence of fibers in concrete.

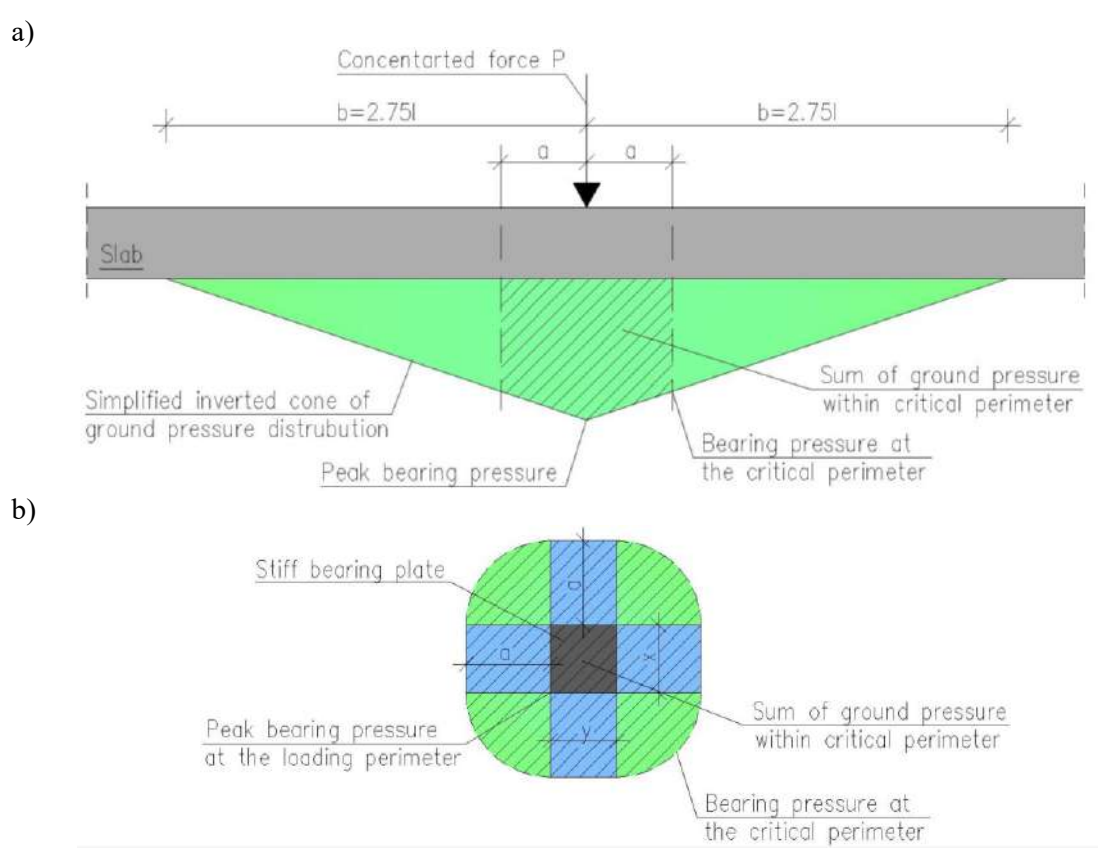


Fig. 6.3 a) Simplified ground pressure distribution under a central concentrated force, b) increased length of critical control perimeter with modified shape of ground pressure distribution for load applied through a stiff bearing

Table 6.11 Contribution of each component in punching shear load-bearing capacity of experimentally tested slabs calculated according to Technical Report 34 [28] dependent on the applied formula for v_f calculations and including corrections for ground contribution

| Slab type | 2 | 3 | 4 | 5 | 6.3 |
|--------------------------------------|--------------|---------------|---------------------|--------------|--------------|
| × • | ! | Technical Rep | ort 34 [28] | ! | - |
| D [1-N] | 235.38 | 225.72 | 257.61 | 249.08 | 256.60 |
| $P_{p,c,a}[\mathrm{kN}]$ | (92.6%) | (93.1%) | (89.9%) | (87.3%) | (93.2%) |
| D [1-N]] | 8.84 | 7.27 | 16.50 | 21.13 | 9.90 |
| $P_{p,f,a}$ [kN] | (3.5%) | (3.0%) | (5.8% | (7.4%) | (3.6%) |
| $P_{p,g,a}[kN]$ | 9.94 | 9.59 | 12.30 | 15.04 | 8.96 |
| 1 p,g,a [KIN] | (3.9%) | (4.0%) | (4.3%) | (5.3%)) | (3.3%) |
| $P_{p,cfg,a}\left[\mathrm{kN} ight]$ | 254.16 | 242.57 | 286.40 | 285.25 | 275.45 |
| 1 p,cjg,a [Ki v] | (100%) | (100%) | (100%) | (100%) | (100%) |
| | | RILEM TC 16 | 2-TDF [66] | | |
| $P_{p,c,a}[\mathrm{kN}]$ | 235.38 | 225.72 | 257.61 | 249.08 | 256.60 |
| 1 p,c,a [K1N] | (91.8%) | (91.6%) | (90.0%) | (83.5%) | (93.8%) |
| $P_{p,f,a}$ [kN] | 11.00 | 11.03 | 16.47 | 33.43 | 8.17 |
| 1 p,j,a [KIV] | (4.3%) | (4.5%) | (5.8%) | (11.2%) | (3.0%) |
| $P_{p,g,a}[kN]$ | 10.03 | 9.74 | 12.30 | 15.72 | 8.90 |
| 1 p,g,a [KIV] | (3.9%) | (4.0%) | (4.3%) | (5.3%) | (3.3%) |
| $P_{p,cfg,a}$ [kN] | 256.41 | 246.49 | 286.38 | 298.23 | 273.67 |
| 1 p,cjg,a [Ki v] | (100%) | (100%) | (100%) | (100%) | (100%) |
| | | PN-EN 1992-1 | -1:2024 [33] | | |
| $P_{p,c,a}[kN]$ | 235.38 | 225.72 | 257.61 | 249.08 | 256.60 |
| 1 p,c,a [K1N] | (84.1%) | (84.5%) | (81.8%) | (68.9%) | (88.5%) |
| $P_{p,f,a}$ [kN] | 33.59 | 30.79 | 43.87 | 93.17 | 23.86 |
| I p,f,a [KIV] | (12.0%) | (11.5%) | (13.9%) | (25.8%) | (8.2%) |
| $P_{p,g,a}[kN]$ | 10.95 | 10.55 | 13.53 | 19.04 | 9.43 |
| 1 p,g,a [KIV] | (3.9%) | (4.0%) | (4.3%) | (5.3%) | (3.3%) |
| $P_{p,cfg,a}$ [kN] | 279.91 | 267.06 | 315.01 | 361.30 | 289.89 |
| 1 p,cjg,a [Ki v] | (100%) | (100%) | (100%) | (100%) | (100%) |
| | | Model Code | 2010 [80] | | |
| $P_{p,c,a}[\mathrm{kN}]$ | 235.38 | 225.72 | 257.61 | 249.08 | 256.60 |
| 1 p,c,a [K1N] | (79.6%) | (81.5%) | (72.5%) | (64.0%) | (81.3%) |
| $P_{p,f,a}$ [kN] | 48.64 | 40.26 | 82.27 | 119.52 | 48.68 |
| 1 p,j,a [K1N] | (16.5%) | (14.5%) | (23.2%) | (30.7% | (15.4%) |
| $P_{p,g,a}[kN]$ | 11.56 | 10.94 | 15.25 | 20.51 | 10.26 |
| 1 p,g,a [K1N] | (3.9%) | (4.0%) | (4.3%) | (5.3%) | (3.3%) |
| $P_{p,cfg,a}$ [kN] | 295.57 | 276.92 | 355.12 | 389.11 | 315.55 |
| I p,cfg,a [KIN] | (100%) | (100%) | (100%) | (100%) | (100%) |

Note: The percentage values were calculated as the ratio of the load-bearing capacity provided by concrete $(P_{p,c,a})$, fibers $(P_{p,f,a})$, or ground $(P_{p,g,a})$ to the total punching shear load-bearing capacity $(P_{p,cfg,a})$.

Table 6.11 presents a summary of the contributions of each component to the punching shear load-bearing capacity of the experimentally tested slabs, calculated according to TR34 [28], depending on the formula adopted for v_f determination and including the corrections for ground contribution. Firstly, the results indicated that the ground accounts for 3.9, 4.0, 4.3, 5.3, and 3.3% of the total $P_{p,cfg,a}$ for slabs types 2-6, respectively, irrespective of the v_f equation applied. Consequently, it was concluded that

the corrections to the ground reaction, based on a detailed and more accurate analysis of ground pressure distribution beneath the point load, did not lead to a substantial increase in $P_{p,g,a}$. On average, this contribution rose only from 3.6% to 4.1% when equation (6.6) was used instead of equation (6.5). This finding suggests that the simplified approach to calculating ground pressure within the critical control perimeter, as proposed in TR34 [28], provides sufficiently accurate results. The analysis also demonstrated that the distance of the critical control section from the loading area a had a significant influence on the contribution of the ground in resisting punching shear. Specifically, with increasing a, the ground's participation in load transfer became more pronounced, indicating an enhanced interaction between the slab and its subgrade support. In terms of fiber contribution, the highest values of $P_{p,f,a}$, ranging from 14.5% to 30.7%, were obtained when v_f was calculated according to MC2010 [80]. Then, the application of the PN-EN 1992-1-1:2024 [33] v_f equation resulted in an approximately 15% increase in punching shear capacity, similar to that observed in tested slabs types 4 and 5. MC2010 [80] predicted a slightly lower increase of about 10%. In contrast, analytical calculations based on TR34 [28] and RILEM TC 162-TDF [66] formulas indicated either negligible increases or even slight decreases in $P_{p,cfg,a}$, which did not align with the experimental observations. The greatest discrepancy between punching shear capacities of slabs types 2 and 3 was again identified using MC2010 [80], predicting a 6% reduction, whereas experimental testing showed a substantially larger decrease of approximately 20%. The calculations according to other standards provided even smaller predicted deterioration of $P_{p,cfg,a}$. Finally, considering that the experimental results showed increases in punching shear capacity of 47% and 18% with the inclusion of 2 and 3 kg/m^3 of PM fibers, respectively, it can be concluded that SyFs have a substantial influence on the overall slab capacity, which should be appropriately reflected in design provisions. Therefore, the equations from PN-EN 1992-1-1:2024 [33] and MC2010 [80] appear to provide a more accurate estimation of the fiber contribution to punching shear transfer. It is also worth noting that only the TR34 [28] formula for v_f failed to reflect the obtained in tests capacities, while the approaches from [33], [66], [80] followed the experimentally observed ranking of capacities, where the highest was obtained by type 5, followed by type 4, 2, and 3 slabs. Moreover, none of the analytically calculated results for slab 6.3 reflected the values observed during testing, regardless of the equation applied for the additional shear strength v_f . This discrepancy may be attributed to the fact that only a single slab with this specific fiber type, dosage, and ground conditions was tested. The obtained results may represent outliers, potentially due to a lower actual FF fiber content in the slab or an uneven fiber distribution within the

concrete matrix. It is likely that testing three specimens, as was done for the other slabs types 1-5, would have resulted in higher punching shear capacities. Nevertheless, caution must be taken when drawing far-reaching conclusions based on such limited data, and further experimental investigations are required to verify these observations.

In conclusion, despite employing more precise and comprehensive analytical analysis, an ideal agreement with the experimental results was generally not achieved for SyFRC ground-supported slabs loaded by central concentrated force (Fig. 6.4). On average, the predicted punching shear load-bearing capacities were underestimated by 60%, 57%, 43%, and 33% for nearly all slabs when the fiber contribution v_f was calculated according to TR34 [28], RILEM TC 162-TDF [66], PN-EN 1992-1-1:2024 [33], and MC2010 [80], respectively.

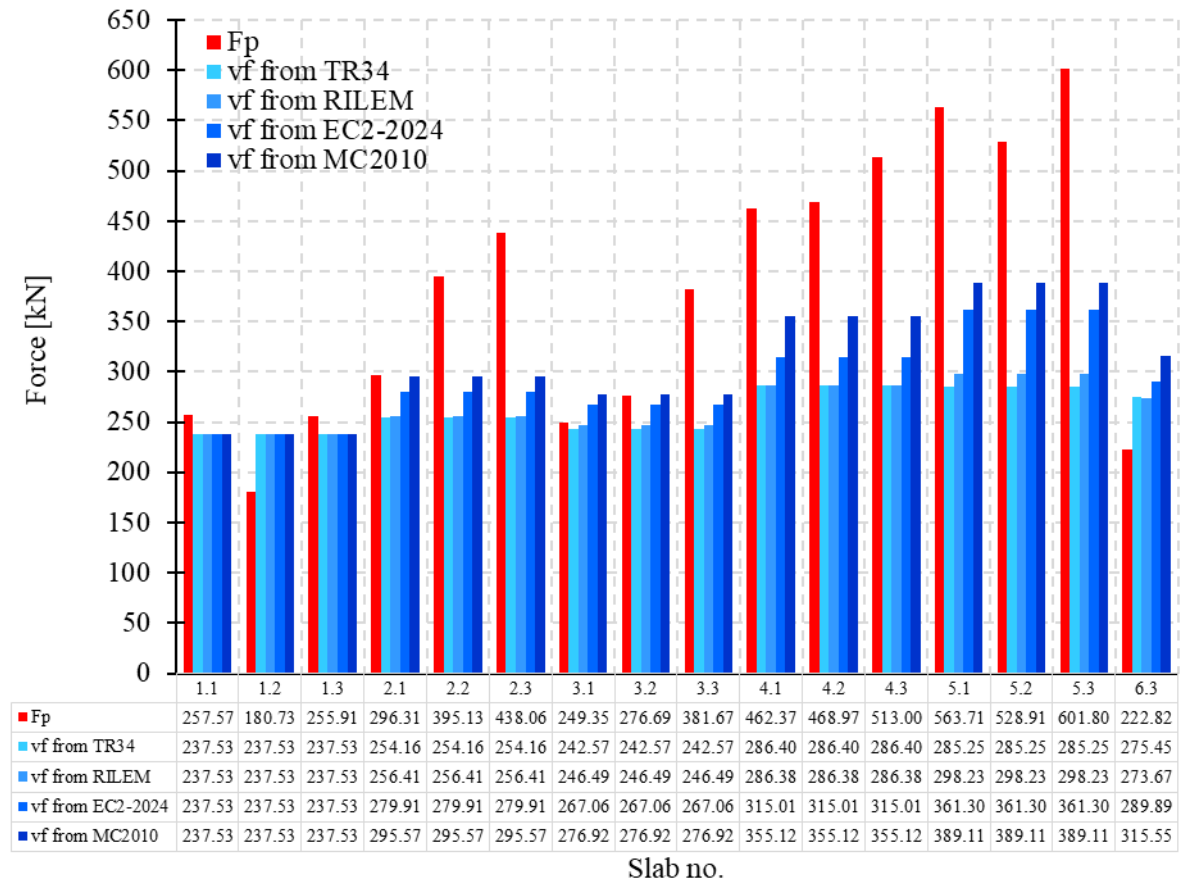


Fig. 6.4 Comparison of the experimentally obtained punching shear forces (F_p) with analytically calculated punching shear load-bearing capacities according to the Technical Report 34 [28] for tested ground slabs types 1-6 dependent on the applied formula for v_f calculations and including corrections for ground contribution

The only notable exceptions were slab 6.3, whose punching capacity was consistently overestimated regardless of the v_f formula applied, and slab 3.1, which also exhibited overestimations when a higher fiber contribution to punching shear capacity

was assumed. A possible explanation for the observed discrepancies between experimental and analytical results lies in the limited dimensions of the tested slabs and the soil confinement provided by the concrete beams of the containment box, which may have altered the distribution of ground pressure. In particular, the distance *b* from the point of load application to the location of zero ground bearing pressure was restricted, potentially resulting in an increased peak bearing pressure. Moreover, the enhanced stiffness of the subgrade could have contributed to a higher punching shear capacity of tested slabs. Consequently, the discrepancies between the experimental and analytical results may be attributed with the fact that the performed laboratory tests only approximately reflected the model assumptions presented in TR34 [28]. Nevertheless, it can be concluded that the applied analytical models, accounting for the actual location of the critical control section, the increased ground contribution, and the greater role of fibers in load transfer, provided reasonably accurate predictions of punching shear load-bearing capacity of SyFRC slabs, maintaining a safety margin.

6.6. Simply supported slab

Based on the calculations and analyses performed, it was concluded that the SyFRC ground slabs should have initially experienced punching shear failure. However, the experimental campaign revealed that flexural cracks appeared prior to punching failure. Consequently, the load-bearing capacity of simply supported slabs was calculated to investigate the hypothesis that the slabs were not uniformly supported by the subgrade and along all edges at the initial stage of the tests. Notably, since the first cracks typically appeared on opposite edges of the slabs, it was speculated that cylindrical bending might have occurred. As a result, the first selected method predicted the load-bearing capacity of a cylindrically bent slab ($P_{fl,2edges}$), followed by calculations of the capacity of slabs supported on four edges and centrally loaded by a concentrated force, based on equations from Starosolski [238] ($P_{fl,4edges}$), Timoshenko et al. [239] ($P_{fl,4edges}$), and Niezgodziński et al. [209] ($P_{fl,4edges}$) (see Fig. 6.5).

In the analysis of the slabs under cylindrical bending and according to [238] and [239] proposal, the acting bending moment m (equation (6.7)) was compared to the critical bending moment m_{cr} (equation (6.8)) to determine the concentrated load P that reaches the slab's moment capacity, using equation (6.9). Moreover, the Starosolski method [238] was based on reading the required coefficient α from a chart presented in

Fig. 6.5a, depended on the loading area and slab dimensions, which then was used to calculate the slab's load-bearing capacity. In the case of the Timoshenko et al. proposal [239], the coefficient α was provided directly for square slabs loaded as illustrated in Fig. 6.5b. In case of Niezgodziński et al. method [209], the maximum acting stress σ_{max} was replaced by the concrete flexural tensile strength $f_{ct,fl}$ and by rearrangement of the equation from Fig. 6.5c, the maximum force P was calculated. Table 6.12 presents the calculated flexural load-bearing capacities of type 2 slabs simply supported on two or four edges and subjected to a central concentrated load, according to the four selected methods. The calculated capacities for slabs types 1-6 are summarized in Table 6.13 with the experimentally obtained average loads corresponding to the first flexural cracking load F_{crl} (Table 5.29), with a graphical comparison provided in Fig. 6.6 for each slab.

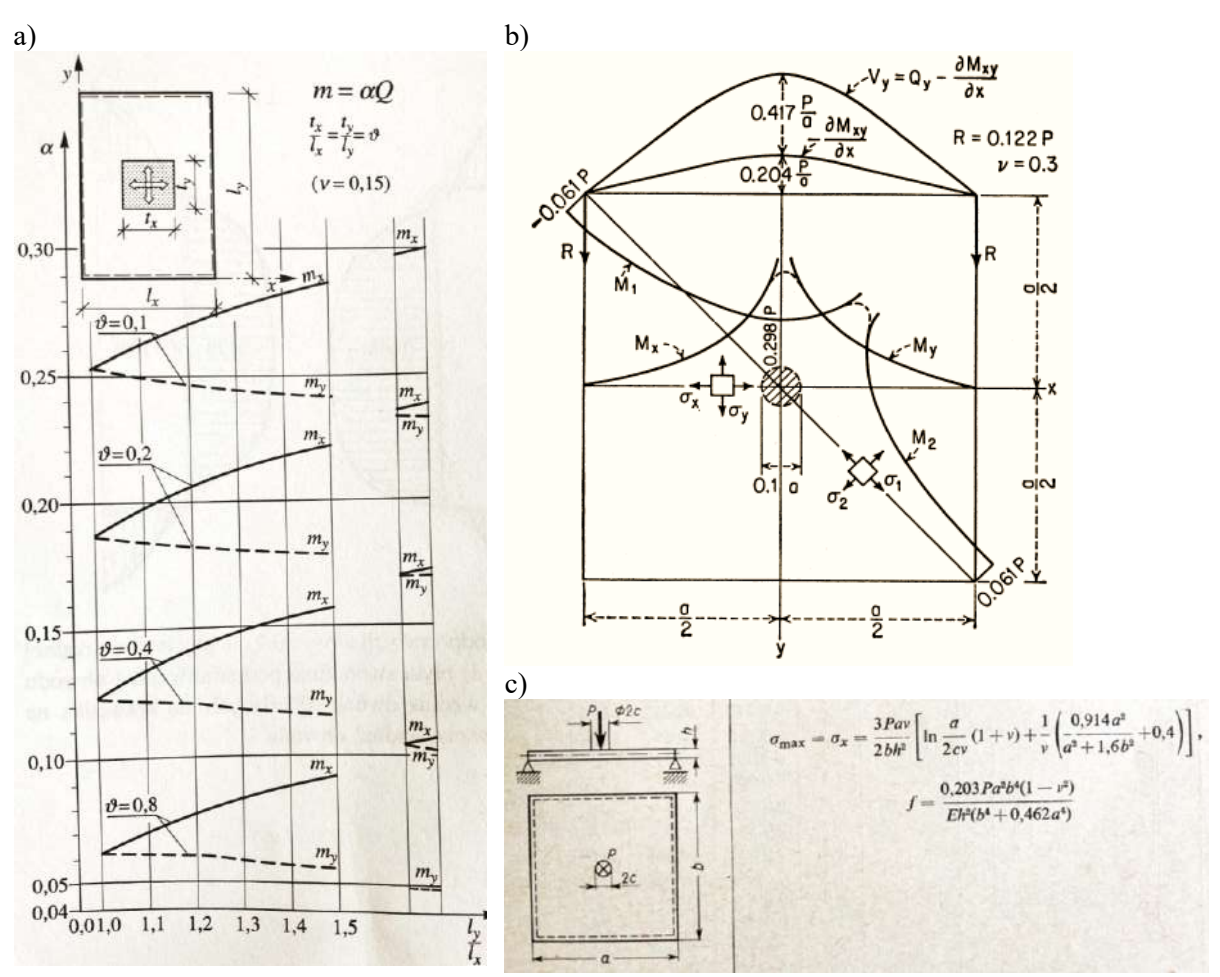


Fig. 6.5 Selected methods for calculating the flexural load-bearing capacity of slabs simply supported on four edges centrally loaded by a concentrated force according to: a) Starosolski [238], b) Timoshenko et al. [239], c) Niezgodziński et al. proposal [209]

$$m = \alpha Pl \tag{6.7}$$

$$m_{cr} = f_{ct,fl} \cdot W_{el} = f_{ct,fl} \cdot \frac{bh^2}{6}$$

$$\tag{6.8}$$

$$m_{cr} = f_{ct,fl} \cdot W_{el} = f_{ct,fl} \cdot \frac{bh^2}{6}$$

$$m = m_{cr}, \qquad \alpha Pl = f_{ct,fl} \cdot \frac{bh^2}{6}, \qquad P = \frac{f_{ct,fl} \cdot h^2 \cdot b}{6 \cdot \alpha \cdot l}$$

$$(6.8)$$

where:

m – acting bending moment [Nmm],

 α – parameter [-],

P – concentrated force [N],

l – slab span (distance between axis of the steel supporting rollers) [mm],

 m_{cr} – critical bending moment [Nmm],

 $f_{ct,fl}$ – concrete flexural tensile strength [N/mm²],

 W_{el} – elastic section modulus, for rectangular section = $bh^2/6$ [mm³],

b – slab width [mm],

h – slab thickness [mm].

Firstly, it is important to note that all three formulas predicted lower allowable central concentrated forces for slabs simply supported on four edges compared to those supported on only two edges (Table 6.13). This outcome is inconsistent, as an increased number of slab supports would typically be expected to enhance, rather than reduce, the load-bearing capacity. Such a contradiction indicates a potential limitation or oversimplification in the formulas presented in [209], [238], [239]. Based on the data presented in Table 6.13 and Fig. 6.6, it can also be concluded that all analytical methods produced results lower than the experimentally observed forces F_{crl} corresponding to the first flexural cracking. Specifically, for slabs of types 1, 2, 3, 4, 5, and 6.3, the calculated values of $P_{fl,2edges}$, $P_{fl,4edges}^S$, $P_{fl,4edges}^T$, and $P_{fl,4edges}^N$ represented, on average, 73%, 72%, 61%, and 43%, respectively, of the experimental cracking load F_{crl} . The associated standard deviations for the four equations were 7%, 7%, 6%, and 4%, respectively, indicating a consistent level of underestimation for each analytical method, regardless of slab type. Furthermore, the calculations and analyses suggested that, during the initial stage of testing, the slabs had partial contact with the supporting soil, as evidenced by their ability to resist higher concentrated loads than would be expected under simply supported conditions. However, a comparison between two type 6 slabs, slab 6.2 (unsupported by the ground) and slab 6.3 (ground-supported), revealed that their F_{cr1} were nearly identical (169.81 kN and 171.94 kN, respectively). This finding implied that, at the beginning of the tests, the ground support may have engaged only a limited

area of the slab's underside. In conclusion, the initial cracking in the tested slabs was attributed to the exceedance of their flexural capacity, resulting from non-uniform support conditions.

Table 6.12 Determination of the flexural load-bearing capacity of tested slab type 2 assuming simple support on two or four edges according to the selected methods

| | ÇI A | AB OF TYPE 2 | | | | | | |
|------------|---|---|--|--|--|--|--|--|
| Dotomning | | | | | | | | |
| Determinat | | rapacity of SyFRC slab simply supported on two or four aded by a concentrated force | | | | | | |
| | Determination of data | adea by a concentrated force | | | | | | |
| | Slab | | | | | | | |
| | Slab thickness | h = 200 mm | | | | | | |
| | Slab dimensions (between axis | | | | | | | |
| | of supporting rollers) | b = B = 1120 mm | | | | | | |
| | Load characterization | D-D-1120 Hilli | | | | | | |
| Table 6.7 | | $a_r = 56 \text{ mm}$ | | | | | | |
| 14016 0.7 | area of the load | $ a_r - 30 $ mm | | | | | | |
| | Concrete parameters | | | | | | | |
| | Poisson's ratio | v = 0.2 | | | | | | |
| PN-EN | Flexural tensile strength | From test: | | | | | | |
| 14651 [29] | Flexural tensile strength | | | | | | | |
| 14031 [27] | Cylindrical banding (two adge | $f_{ct,fl} = 3.765 \text{ MPa}$ | | | | | | |
| | Cylindrical bending (two edge | (F 2002 1120 | | | | | | |
| | $P_{fl,2edges} = \frac{f_{ct,fl} \cdot h^2 \cdot B}{6 \cdot A \cdot \alpha} = \frac{3.7}{6}$ | $\frac{65 \cdot 200^{-1120}}{1120} = 100.40 \text{ kN}$ | | | | | | |
| | $6 \cdot A \cdot \alpha$ 6 | · 1120 · 0.250 | | | | | | |
| | where $\alpha = 0.250$ | | | | | | | |
| | According to Starosolski (four edges) [238] | | | | | | | |
| | $P_{fl,4edges}^S = \frac{f_{ct,fl} \cdot h^2 \cdot B}{6 \cdot A \cdot \alpha} = \frac{3.765 \cdot 200^2 \cdot 1120}{6 \cdot 1120 \cdot 0.253} = 99.21 \text{ kN}$ | | | | | | | |
| | | | | | | | | |
| | where $\alpha = 0.253$ assumed according to Fig. 6.5a from [238] for $\vartheta = \frac{x}{A} = \frac{x}{B} = \frac{100}{1120} = 0.000$ | | | | | | | |
| | 0.089 ≈ 0.1 | | | | | | | |
| | According to Timoshenko et al. (4 edges) [239] | | | | | | | |
| | $P_{fl,4edges}^{T} = \frac{f_{ct,fl} \cdot h^2 \cdot B}{6 \cdot A \cdot \alpha} = \frac{3.765 \cdot 200^2 \cdot 1120}{6 \cdot 1120 \cdot 0.298} = 84.23 \text{ kN}$ | | | | | | | |
| | fl , $4eages = 6 \cdot A \cdot \alpha = 6 \cdot 1120 \cdot 0.298 = 0.4.23 \text{ KeV}$ | | | | | | | |
| | where $\alpha = 0.293$ assumed according to Fig. 6.5b from [239] | | | | | | | |
| | According to Niezgodziński et al. (4 edges) [209] | | | | | | | |
| | P_{i}^{N} — $2 \cdot f$ | $c_{ct,fl} \cdot h^2 \cdot B$ | | | | | | |
| | $P_{fl,4edges}^{N} = \frac{2 \cdot f_{ct,fl} \cdot h^{2} \cdot B}{3Av \cdot \left(\ln \frac{A}{2av} \cdot (1+v) + \frac{1}{v} \cdot \left(\frac{0.914A^{2}}{A^{2} + 1.6B^{2}} + 0.4 \right) \right)}$ | | | | | | | |
| | $2 \cdot 3.765 \cdot 200^2 \cdot 1120$ | | | | | | | |
| | $= {3 \cdot 1120 \cdot 0.2 \cdot \left(\ln \frac{1120}{2 \cdot 56 \cdot 0.2} \cdot (1 + 0.2) + \frac{1}{0.2} \cdot \left(\frac{0.914 \cdot 1120^2}{1120^2 + 1.6 \cdot 1120^2} + 0.4 \right) \right)}$ | | | | | | | |
| | = 59.46 kN | , | | | | | | |
| | Summary | | | | | | | |
| | $P_{fl,2edges} = 100.40 \text{ kN}$ | | | | | | | |
| | $P_{fl,4ed,ges}^{S} = 99.21 \text{ kN}$ | | | | | | | |
| | $P_{fl,4edges}^{T} = 84.23 \text{ kN}$ | | | | | | | |
| | | | | | | | | |
| | $P_{fl,4edges}^{N} = 59.46 \text{ kN}$ | | | | | | | |

Table 6.13 Determination of the flexural load-bearing capacity of tested ground slabs types 1-6 simply supported on two or four edges according to the selected methods

| Slab type | 1 | 2 | 3 | 4 | 5 | 6.3 | | | | |
|--------------------------|--------------------------------------|----------------------|-----------------|----------------|---------------|---------|--|--|--|--|
| | Determination of data | | | | | | | | | |
| | | | Slab | | | | | | | |
| | | h = 200 mm; 200 mm | A = B = 1120 m | nm; x = 100 mr | n | | | | | |
| | | Lo | ad characteriz | ation | | | | | | |
| | | | a = 56 mm | | | | | | | |
| | | Co | ncrete param | eters | | | | | | |
| | | | v = 0.2 | | | | | | | |
| $f_{ct,fl}$ [MPa] | 3.499 | 3.765 | 3.107 | 6.303 | 5.504 | 4.926 | | | | |
| | Det | ermination of | the flexural lo | ad-bearing ca | <u>pacity</u> | | | | | |
| $P_{\mathit{fl,2edges}}$ | 93.31 | 100.40 | 82.85 | 168.08 | 146.77 | 131.36 | | | | |
| [kN] | (72.9%) | (72.1%) | (60.6%) | (74.1%) | (80.5%) | (76.4%) | | | | |
| $P_{fl,4edges}^{S}$ | 92.20 | 99.21 | 81.87 | 166.09 | 145.03 | 129.80 | | | | |
| [kN] | (72.0%) | (71.2%) | (59.9%) | (73.3%) | (79.6%) | (75.5%) | | | | |
| $P^{T}_{fl,4edges}$ | 78.28 | 84.23 | 69.51 | 141.01 | 123.13 | 110.20 | | | | |
| [kN] | (61.1%) | (60.5%) | (50.9%) | (62.2%) | (67.5%) | (64.1%) | | | | |
| $P^{N}_{fl,4edges}$ | 55.26 | 59.46 | 49.07 | 99.54 | 86.92 | 77.79 | | | | |
| [kN] | (43.2%) | (42.7%) | (35.9%) | (43.9%) | (47.7%) | (45.2%) | | | | |
| | Experimental flexural cracking force | | | | | | | | | |
| F_{crl} [kN] | 128.03 | 139.29 | 136.68 | 226.70 | 182.31 | 171.94 | | | | |
| r'crl [Kin] | (100%) | (100%) | (100%) | (100%) | (100%) | (100%) | | | | |

Note: The percentage values were calculated as the ratio of the analytically calculated results ($P_{fl,2edges}$, $P_{fl,4edges}^S$, or $P_{fl,4edges}^N$) to the experimentally obtained flexural cracking load (F_{crl}).

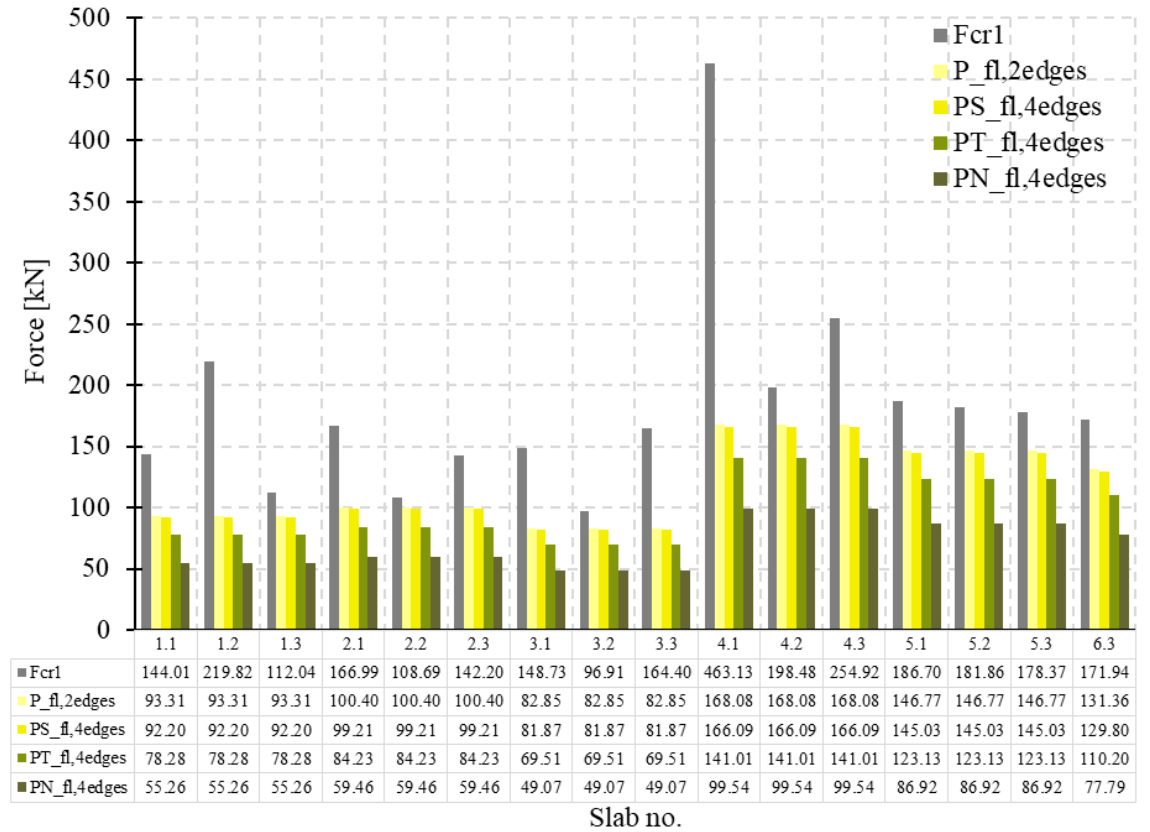


Fig. 6.6 Comparison of the experimentally obtained first flexural cracking forces (F_{crl}) with analytically calculated flexural load-bearing capacities for tested ground slabs types 1-6 simply supported on two ($P_{fl,2edges}$) or four edges ($P_{fl,4edges}^S$, $P_{fl,4edges}^T$, and $P_{fl,4edges}^N$) according to the selected methods

6.7. Ground-supported slab with linear edge support

The existing literature does not provide analytical solutions for slabs simultaneously supported by the subgrade and along their edges. Consequently, a dedicated analytical approach was developed, resulting in simplified engineering models for estimating the load-bearing capacity of ground-supported slabs subjected to a centrally applied concentrated load, with additional support provided along two, three, or four edges (Fig. 6.7). In the ABC Plate software, a square slab with dimensions 1200 x 1200 mm and a thickness of 200 mm was modeled. The slab was subjected to a unit concentrated load P = 1 kN, uniformly distributed over an area of 100 x 100 mm. The support conditions consisted of a Winkler elastic subgrade combined with various edge support configurations: all four edges (Model 1), two opposite edges (Model 2), three edges (Model 3), and two adjacent edges (Model 4). The Winkler subgrade modulus k was determined using equation (4.4), with the E_{vI} values taken from Table 5.15. These models were used to determine the dimensionless parameters α and β , which enable the calculation of bending moments m_x and m_y in accordance with equations (6.10) and (6.11), respectively. The computed bending moments m_x and m_y were compared with the critical bending moment m_{cr} , as defined by equation (6.12), to determine the corresponding concentrated loads P^x and P^y that would induce failure in the x and y directions, respectively (equations (6.13) and (6.14)). For subsequent analyses, the lower of these two values, $min(P^x, P^y)$, was adopted as the governing flexural load-bearing capacity and compared with F_{crl} . It should be noted that, since F_{cr2} corresponded to the nonlinear phase of the slab response, its correlation with $\max(P^x, P^y)$ was not considered. Table 6.14 presents the calculation procedure of the load-bearing capacities of ground slab type 2, centrally loaded by a concentrated force, for various edge-support configurations (Fig. 6.7). The capacities were determined for the slab supported on four edges (P^{1}_{4edges}), two opposite edges ($P^{2}_{2edges,o}$), three edges (P^3_{3edges}) , and two adjacent edges $(P^4_{2edges,a})$. Table 6.15 summarizes the results for slabs types 1-6, including experimentally obtained average loads F_{crl} (Table 5.29), with a graphical representation of results in Fig. 6.8 for each tested slab. For slab 6.2, tested without ground support, the k value was assumed to be 0 MPa/m.

$$m_x = \alpha Pl$$
 (6.10)

$$m_y = \beta Pl$$
 (6.11)

$$m_{\nu} = \beta P l \tag{6.11}$$

$$m_{cr} = f_{ct,fl} \cdot W_{el} = f_{ct,fl} \cdot \frac{bh^2}{6}$$

$$\tag{6.12}$$

$$m_{x} = m_{cr}, \qquad \alpha P^{x} l = f_{ct,fl} \cdot \frac{bh^{2}}{6}, \qquad P^{x} = \frac{f_{ct,fl} \cdot h^{2} \cdot b}{6 \cdot \alpha \cdot l}$$

$$m_{y} = m_{cr}, \qquad \beta P^{y} l = f_{ct,fl} \cdot \frac{bh^{2}}{6}, \qquad P^{y} = \frac{f_{ct,fl} \cdot h^{2} \cdot b}{6 \cdot \beta \cdot l}$$

$$(6.13)$$

$$m_y = m_{cr}, \qquad \beta P^y l = f_{ct,fl} \cdot \frac{bh^2}{6}, \qquad P^y = \frac{f_{ct,fl} \cdot h^2 \cdot b}{6 \cdot \beta \cdot l}$$
 (6.14)

where:

 m_x and m_y – acting bending moments in x and y direction, respectively [Nmm], α and β – parameters [-],

P – concentrated force [N],

l – slab span (distance between axis of the steel supporting rollers) [mm],

 m_{cr} – critical bending moment [Nmm],

 $f_{ct,fl}$ – concrete flexural tensile strength [N/mm²].

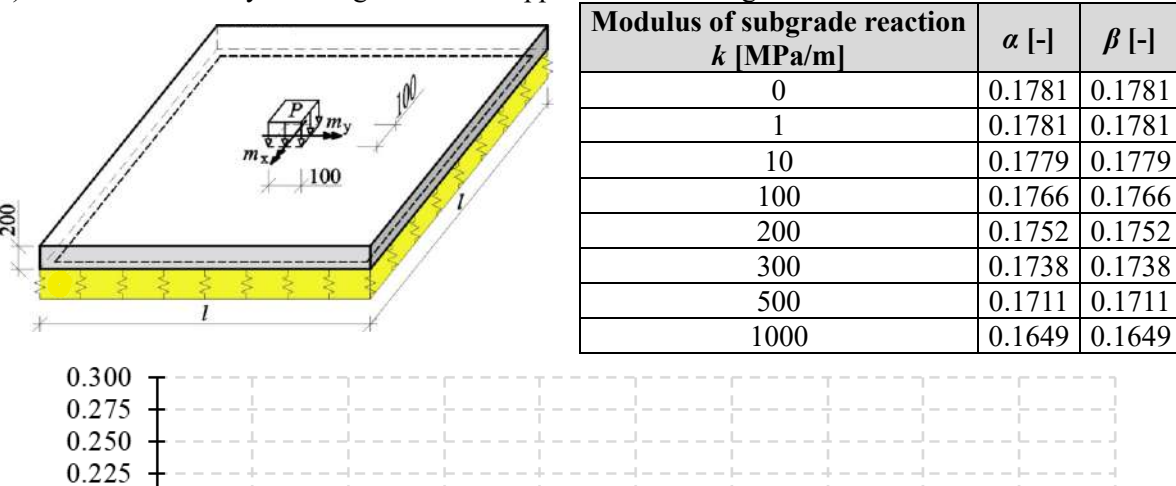
 W_{el} – elastic section modulus, for rectangular section = $bh^2/6$ [mm³],

b – slab width [mm],

h – slab thickness [mm].

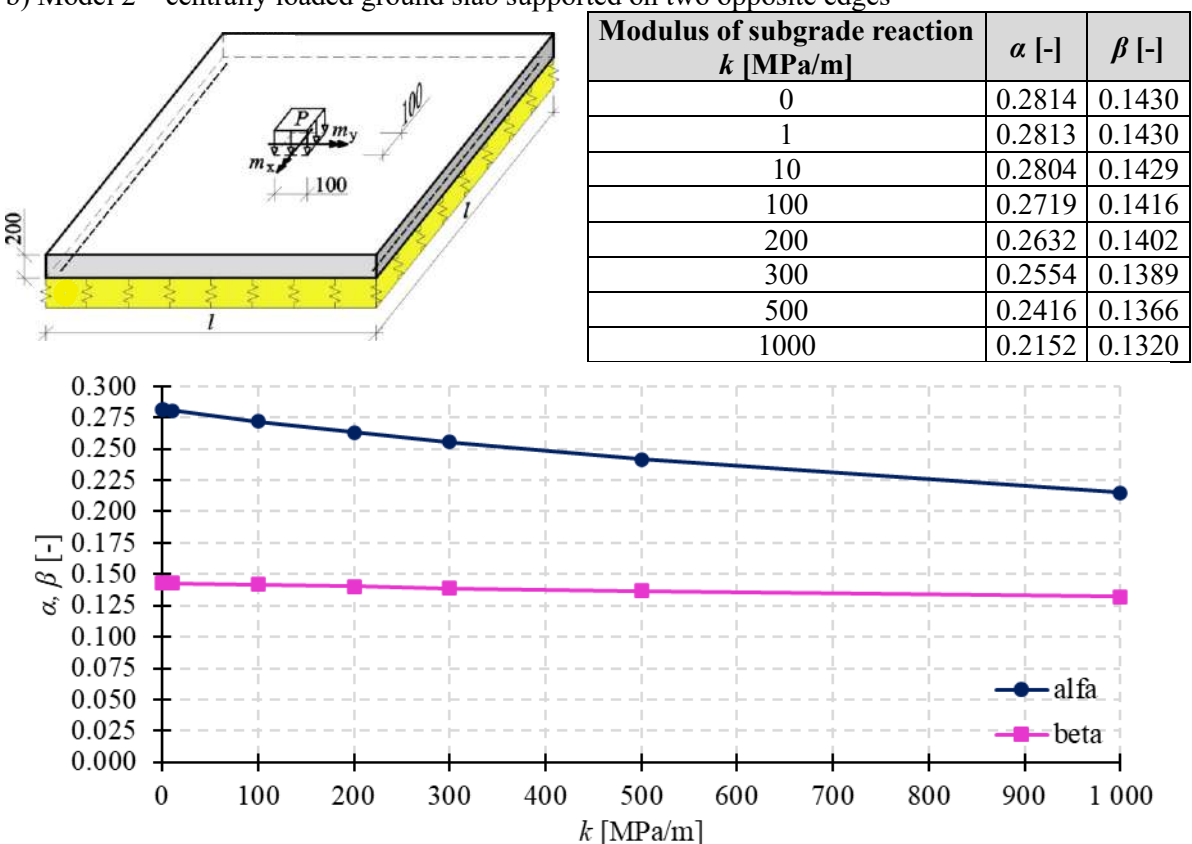
Based on Table 6.15 and Fig. 6.8, it was revealed that Model 1 exhibited the highest analytically determined capacity. This result is consistent with expectations, as a greater number of supported edges provides stiffer boundary conditions, thereby increasing resistance to cracking. In contrast, Model 2 showed the lowest capacity values, corresponding to the weakest support configuration. Models 3 and 4 produced intermediate results, with the three edge support configuration performing worse than that with two adjacently supported edges. A comparison between slabs 6.2 (unsupported by the ground) and 6.3 (ground-supported) highlighted the significant influence of subgrade support in Models 1-4. Specifically, the presence of the ground led to the increase of the load-bearing capacity by 3.65, 9.57, 6.84, and 22.27 kN in Models 1-4, respectively. Furthermore, Fig. 6.9 demonstrates that the addition of ground support to a slab simply supported on four edges, following the Starosolski method [238], resulted in a 45% increase in the calculated maximum allowable concentrated load. Even greater improvements were observed when comparing P^{I}_{4edges} with $P^{T}_{fl,4edges}$ and $P^{N}_{fl,4edges}$, calculated using formulas of Timoshenko et al. [239] and Niezgodziński et al. [209], respectively. Regarding cylindrical bending, it was noted that the calculated values of $P^{2}_{2edges,o}$ were lower than those of $P_{fl,2edges}$, despite the additional subgrade support. This indicates that the capacity of slabs simply supported along two opposite edges was overestimated in Chapter 6.6. This aligns with the previously observed inconsistency whereby the capacity of cylindrically bent slabs exceeded that of slabs supported on four edges, regardless of the analytical model selected from Fig. 6.5 [209], [238], [239].

a) Model 1 – centrally loaded ground slab supported on four edges



0.225 0.200 ± 0.175 $\overline{\approx}$ 0.150 ⊌ 0.125 0.100 0.075 **→** alpha 0.050 ---beta 0.025 0.000 100 200 300 400 500 600 700 1 000 800 900 $k \, [MPa/m]$

b) Model 2 – centrally loaded ground slab supported on two opposite edges



c) Model 3 – centrally loaded ground slab supported on three edges Modulus of subgrade reaction α [-] β [-] k [MPa/m]0.2216 0.1633 0 0.2216 0.1633 1 10 0.2212 | 0.1631 100 0.2173 0.1616 200 0.2133 | 0.1600 0.2096 | 0.1585 300 0.2027 500 0.1556 1000 0.1883 | 0.1495 0.300 0.275 0.250 0.225 0.200 $\stackrel{\textstyle \longrightarrow}{\simeq} 0.175 \\ \stackrel{\textstyle \bigcirc}{\simeq} 0.150$ € 0.125 0.1000.075 📤 alfa 0.050

-beta

0.025

100

200

300

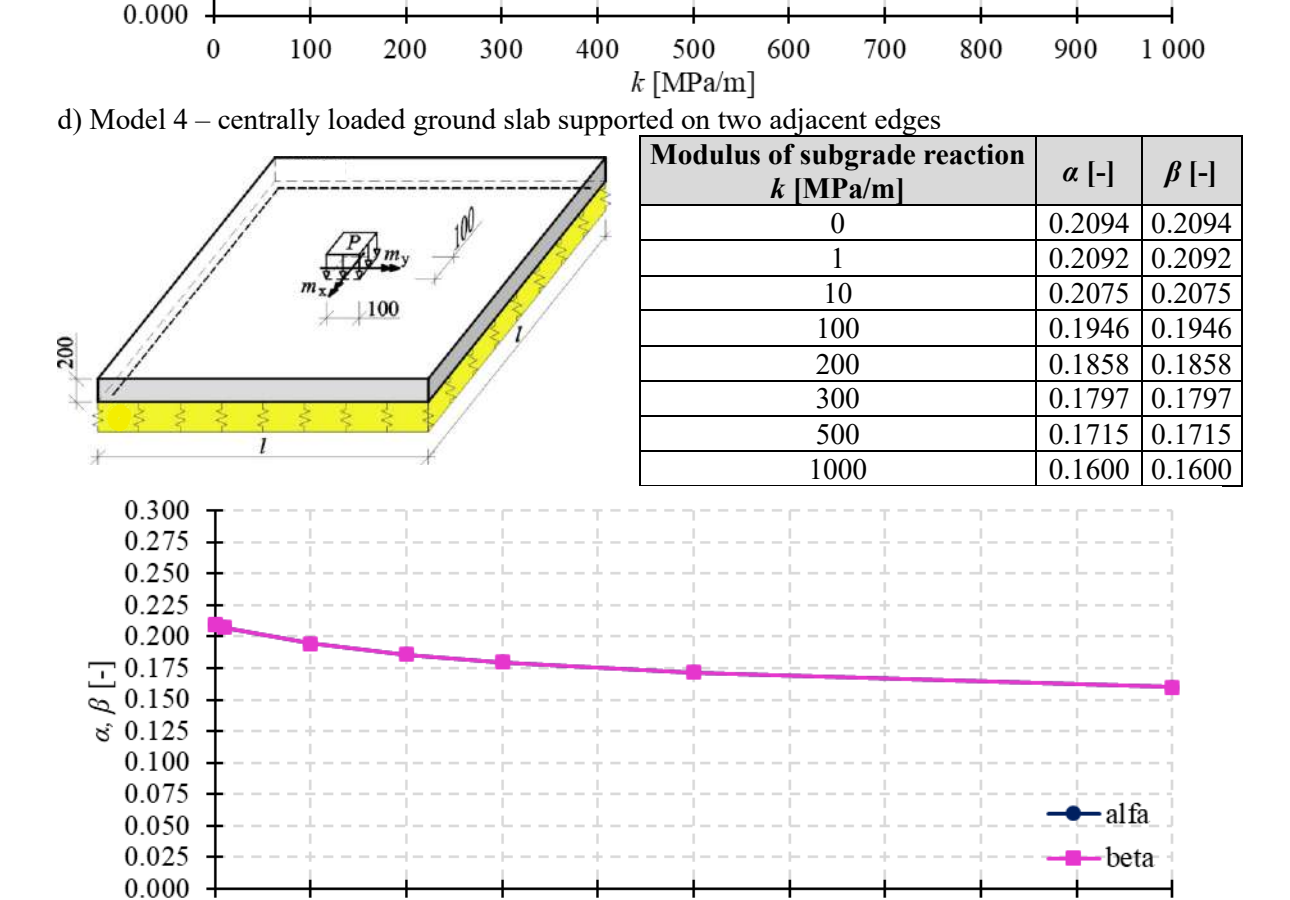


Fig. 6.7 Values of parameters α and β for various modulus of subgrade reactions k and edge support configurations of centrally loaded ground slabs

500

k [MPa/m]

600

700

800

900

1 000

400

Table 6.14 Determination of the load-bearing capacity of tested ground slab type 2 assuming various edge support configurations of Models 1-4

| | SLA | AB OF TYPE 2 | | | | | |
|------------|---|--|--|--|--|--|--|
| Determina | tion of the load-bearing capacity | of SyFRC ground slab assuming various edge support | | | | | |
| | | centrally loaded by a concentrated force | | | | | |
| | Determination of data | | | | | | |
| | Slab | | | | | | |
| | Slab thickness | h = 200 mm | | | | | |
| | Slab dimensions (between axis | | | | | | |
| | | b = B = 1120 mm | | | | | |
| | Concrete parameters | | | | | | |
| PN-EN | Flexural tensile strength | From test: | | | | | |
| 14651 [29] | | $f_{ct,fl} = 3.765 \mathrm{MPa}$ | | | | | |
| | Ground parameters | | | | | | |
| | Primary static modulus of | From test: | | | | | |
| TT '1 1 | deformation | $E_{v1} = 134 \text{ MPa}$ | | | | | |
| Hajduk | Modulus of subgrade reaction | $E_{v1} = 134 \text{ MPa}$ $k = \frac{E_{v1}}{550} = \frac{134}{550} = 0.244 \frac{\text{MPa}}{\text{mm}} = 244 \frac{\text{MPa}}{\text{m}}$ | | | | | |
| [24] | Model 1 – ground slab support | l 550 550 mm m | | | | | |
| | $f = h^2 \cdot R = 2.765$ | 5.200 ² .1120 | | | | | |
| | $P_{4edges}^{1x,y} = \frac{f_{ct,fl} \cdot h^2 \cdot B}{6 \cdot A \cdot \alpha} = \frac{3.765}{6 \cdot 1}$ where $\alpha = \beta = 0.1746$ assumed | $\frac{3.200 \cdot 1120}{120.01746} = 143.77 \text{ kN}$ | | | | | |
| | where $\alpha = \beta = 0.1746$ assumed | d according to Fig. 6.7a | | | | | |
| | Model 2 – ground slab support | ted on two opposite edges | | | | | |
| | $\begin{cases} f_{-1} & \text{s. } h^2 \cdot R \\ \end{cases}$ | 3 765 · 200 ² · 1120 | | | | | |
| | $P_{2edges,o}^{2x} = \frac{f_{ct,fl} + h + b}{f_{ct,fl}} = \frac{3.763 \cdot 200 \cdot 1120}{6.1120 \cdot 0.3500} = 96.61 \text{ kN}$ | | | | | | |
| | $min \left\{ \begin{array}{c} 0 + h^2 \\ f \cdot g \cdot h^2 \cdot R \end{array} \right.$ | $3.765 \cdot 200^2 \cdot 1120$ = 96.61 kN | | | | | |
| | $min \begin{cases} P_{2edges,o}^{2x} = \frac{f_{ct,fl} \cdot h^2 \cdot B}{6 \cdot A \cdot \alpha} = \frac{3.765 \cdot 200^2 \cdot 1120}{6 \cdot 1120 \cdot 0.2598} = 96.61 \text{ kN} \\ P_{2edges,o}^{2y} = \frac{f_{ct,fl} \cdot h^2 \cdot B}{6 \cdot A \cdot \beta} = \frac{3.765 \cdot 200^2 \cdot 1120}{6 \cdot 1120 \cdot 0.1396} = 179.76 \text{ kN} \end{cases} = 96.61 \text{ kN}$ | | | | | | |
| | where $\alpha = 0.2599$ and $\beta = 0.11$ | 206 assumed according to Fig. 6.7h | | | | | |
| | where $\alpha = 0.2598$ and $\beta = 0.1396$ assumed according to Fig. 6.7b Model 3 – ground slab supported on three edges) | | | | | | |
| | $min \begin{cases} P_{3edges}^{3x} = \frac{f_{ct,fl} \cdot h^2 \cdot B}{6 \cdot A \cdot \alpha} = \frac{3.765 \cdot 200^2 \cdot 1120}{6 \cdot 1120 \cdot 0.2117} = 118.57 \text{ kN} \\ P_{3edges}^{3y} = \frac{f_{ct,fl} \cdot h^2 \cdot B}{6 \cdot A \cdot \beta} = \frac{3.765 \cdot 200^2 \cdot 1120}{6 \cdot 1120 \cdot 0.1593} = 157.52 \text{ kN} \end{cases} = 118.57 \text{ kN}$ | | | | | | |
| | $P_{3edges}^{3x} = \frac{J_{ct,fl} \cdot h \cdot b}{c} =$ | $=\frac{3.763 \cdot 200 \cdot 1120}{6.4420 \cdot 0.2447} = 118.57 \text{ kN}$ | | | | | |
| | $min \left\{ \begin{array}{c} 6 \cdot A \cdot \alpha \\ f + h^2 \cdot B \end{array} \right.$ | $6 \cdot 1120 \cdot 0.211$ / 2.765 200 ² 1120 = 118.57 kN | | | | | |
| | $P_{2adaes}^{3y} = \frac{J_{ct,fl} \cdot h \cdot b}{f} =$ | $=\frac{3.763 \cdot 200 \cdot 1120}{6.1120 \cdot 1120} = 157.52 \text{ kN}$ | | | | | |
| | $6 \cdot A \cdot \beta$ | 6 · 1120 · 0.1593 | | | | | |
| | | 593 assumed according to Fig. 6.7c | | | | | |
| | Model 4 – ground slab support | | | | | | |
| | $P_{2edges,a}^{4x,y} = \frac{f_{ct,fl} \cdot h^2 \cdot B}{6 \cdot A \cdot \alpha} = \frac{3.76}{6}$ | $\frac{65 \cdot 200^2 \cdot 1120}{1120 \cdot 0.1831} = 137.06 \text{ kN}$ | | | | | |
| | where $\alpha = \beta = 0.1831$ assumed | d according to Fig. 6.7d | | | | | |
| | Summary | | | | | | |
| | $P_{4edges}^{1x,y} = 143.77 \text{ kN}$ | | | | | | |
| | $P_{2edges,o}^{2x} = 96.61 \text{ kN}$ | | | | | | |
| | $P_{3edges}^{3x} = 118.57 \text{ kN}$ | | | | | | |
| | $P_{2edges,a}^{4x,y} = 137.06 \text{ kN}$ | | | | | | |

Table 6.16 presents the ratio of experimentally obtained first flexural cracking forces F_{crl} to analytically calculated load-bearing capacities for tested slabs of types 1-6, assuming various edge support configurations according to Models 1-4. The objective of this analysis was to identify the Model that most accurately correlates with the

 F_{crl} and to assess its consistency with the observed crack morphology during testing. For seven of the tested ground slabs, the experimental F_{crl} exceeded the predictions of all analytical Models, indicating that these slabs were most likely uniformly supported along all four edges during testing. Exceptions include slabs 1.3, 4.2, 5.1, 5.2, 5.3, and 6.3, as well as slabs 2.2 and 3.2, for which analytical results suggested that the initial support was limited to two adjacent or two opposite edges, respectively, with only partial support along a third edge. Slabs 2.3 and 6.2 were most likely supported by two adjacent steel rollers, with ununiform support along the remaining edges. However, these analytical conclusions were not fully aligned with experimental observations, which indicated that most slabs were initially supported along two opposite edges. This finding was based on the fact that cracking was first observed along the W-E or S-N axis of the slabs, suggesting higher bending stresses in these directions due to the lack of initial support. In conclusion, despite extensive analyses employing various analytical models, unambiguous determination of the initial support conditions of the tested ground slabs remains highly challenging, particularly in the absence of detailed information regarding crack morphology on the slab undersides. Future research should incorporate nonlinear analyses to improve the accuracy of predictive calculations.

Table 6.15 Determination of the load-bearing capacity of tested slabs types 1-6 assuming various edge support configurations of Models 1-4

| Slab type | 1 | 2 | 3 | 4 | 5 | 6.3 | *6.2 | | |
|----------------------------|--------|------------|---------------|---------------|-----------------|--------|--------|--|--|
| | | Ī | Determinatio | on of data | | | | | |
| Slab | | | | | | | | | |
| | | h = 20 | 0 mm; $l = A$ | = B = 1120 r | nm | | | | |
| | | (| Concrete pa | rameters | | | | | |
| $f_{ct,fl}[MPa]$ | 3.499 | 3.765 | 3.107 | 6.303 | 5.504 | 4.926 | 4.926 | | |
| | | | Ground par | rameters | | | | | |
| E_{vl} [MPa] | 143 | 134 | 139 | 141 | 138 | 132 | 0 | | |
| k [MPa/m] | 260 | 244 | 253 | 256 | 251 | 240 | 0 | | |
| | | Determinat | ion of the lo | ad-bearing | <u>capacity</u> | | | | |
| $\alpha = \beta$ [-] | 0.1744 | 0.1746 | 0.1745 | 0.1744 | 0.1745 | 0.1746 | 0.1781 | | |
| $P^{lx,y}_{4edges}$ [kN] | 133.79 | 143.77 | 118.73 | 240.93 | 210.29 | 188.04 | 184.39 | | |
| α[-] | 0.2585 | 0.2598 | 0.2591 | 0.2588 | 0.2592 | 0.2601 | 0.2814 | | |
| β [-] | 0.1394 | 0.1396 | 0.1395 | 0.1395 | 0.1395 | 0.1397 | 0.1430 | | |
| $P^{2x}_{2edges,o}$ [kN] | 90.23 | 96.61 | 79.95 | 162.36 | 141.55 | 126.27 | 116.70 | | |
| $P^{2y}_{2edges,o}$ [kN] | 167.31 | 179.76 | 148.47 | 301.29 | 262.96 | 235.11 | 229.65 | | |
| α [-] | 0.2111 | 0.2117 | 0.2113 | 0.2112 | 0.2114 | 0.2118 | 0.2216 | | |
| β [-] | 0.1591 | 0.1593 | 0.1592 | 0.1592 | 0.1592 | 0.1594 | 0.1633 | | |
| P^{3x}_{3edges} [kN] | 110.51 | 118.57 | 98.01 | 198.95 | 173.56 | 155.04 | 148.20 | | |
| P^{3y}_{3edges} [kN] | 146.62 | 157.52 | 130.10 | 264.02 | 230.43 | 206.02 | 201.10 | | |
| $\alpha = \beta$ [-] | 0.1821 | 0.1831 | 0.1826 | 0.1824 | 0.1827 | 0.1834 | 0.2094 | | |
| $P^{4x,y}_{2edges,a}$ [kN] | 128.07 | 137.06 | 113.45 | 230.42 | 200.85 | 179.10 | 156.83 | | |
| | | Experim | ental flexur | al cracking | <u>force</u> | | | | |
| F_{crl} [kN] | 128.03 | 139.29 | 136.68 | 226.70 | 182.31 | 171.94 | 169.81 | | |

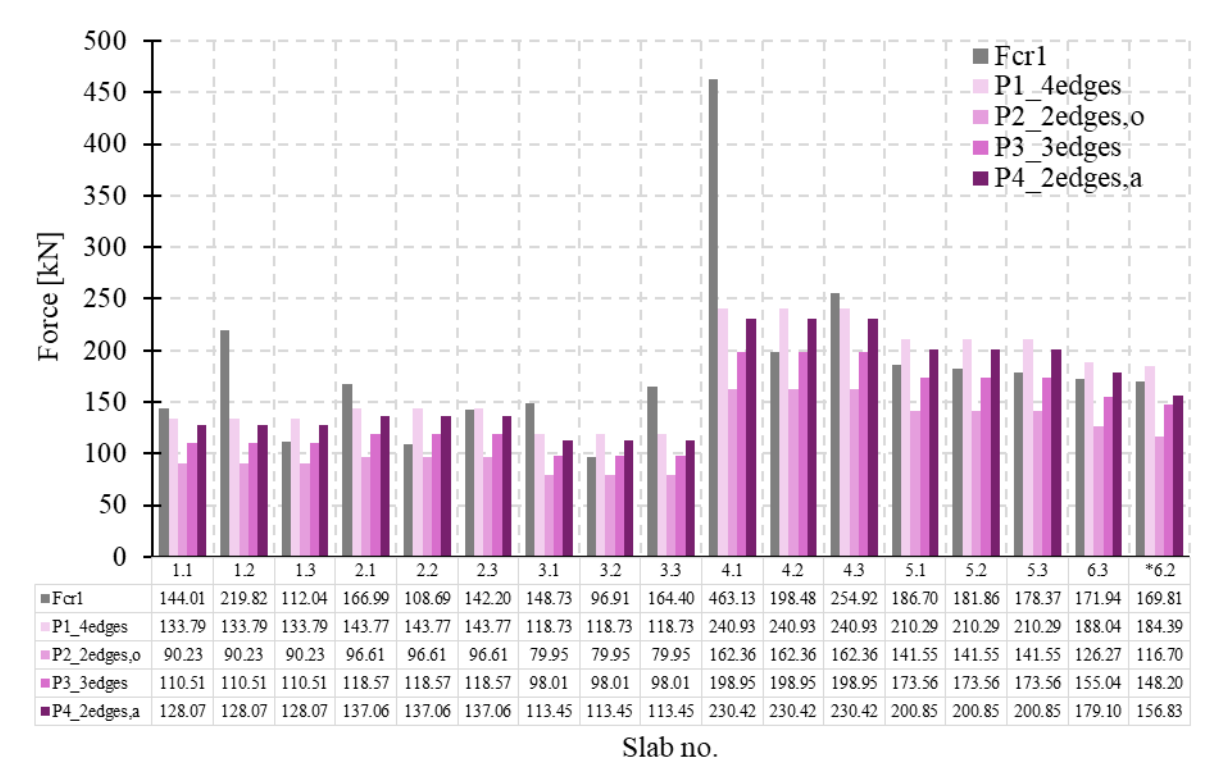


Fig. 6.8 Comparison of the experimentally obtained first flexural cracking forces (F_{crl}) with analytically calculated load-bearing capacities for tested slabs types 1-6 assuming various edge support configurations of Models 1-4 (P^{l}_{4edges} , $P^{2}_{2edges,o}$, P^{3}_{3edges} , $P^{4}_{2edges,a}$)

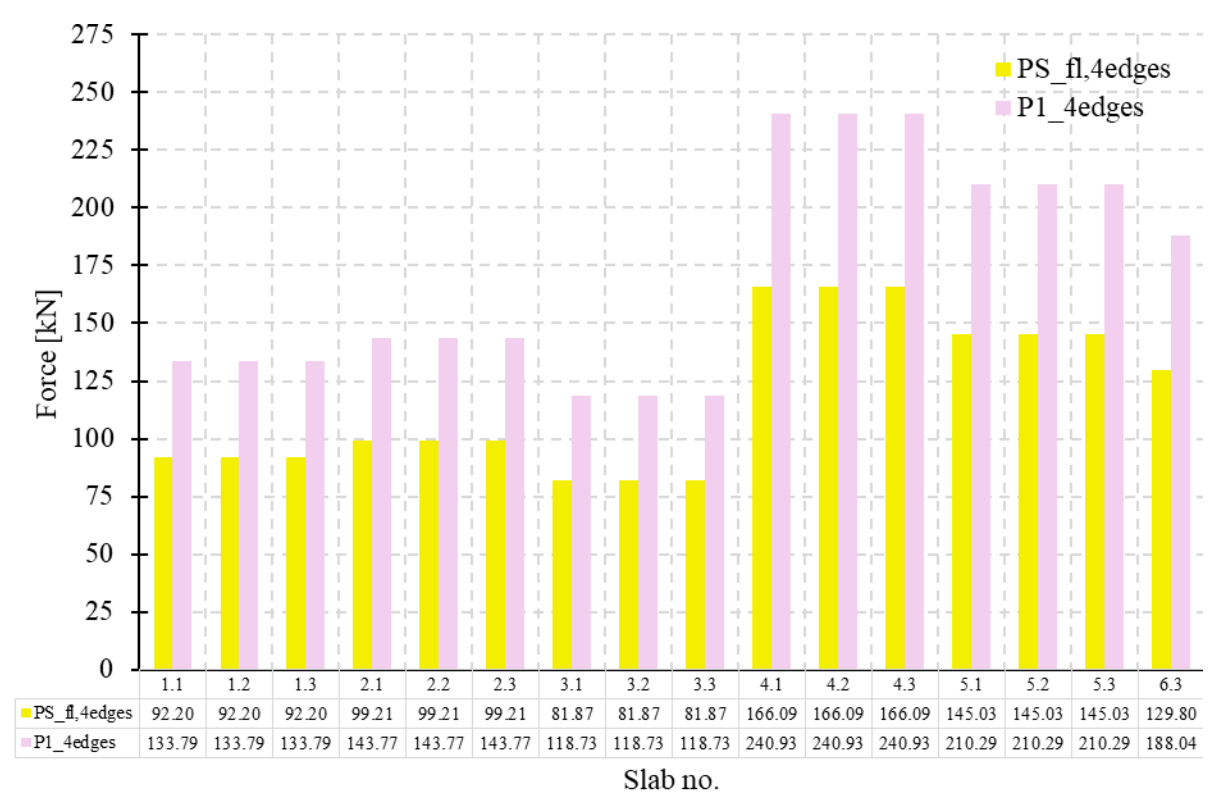


Fig. 6.9 Comparison of analytically calculated load-bearing capacities for tested ground slabs types 1-6 simply supported slab on four edges according to the Starosolski [238] approach ($P^{S}_{fl,4edges}$) with capacities for ground slabs additionally supported on four edges according to Model 1 (P^{I}_{4edges})

Table 6.16 Ratio of the experimentally obtained first flexural cracking forces with analytically calculated load-bearing capacities for tested slabs types 1-6 for various edge support configurations of Models 1-4

| Slab type | F_{cr1}/P^{1}_{4edges} | $F_{cr1}/P^2_{2edges,o}$ | F_{cr1}/P^3_{3edges} | $F_{cr1}/P^4_{2edges,a}$ | First flexural cracking |
|-----------|--------------------------|--------------------------|------------------------|--------------------------|-------------------------|
| 1.1 | 1.08 | 1.60 | 1.30 | 1.12 | 2 opposite edges W-E |
| 1.2 | 1.64 | 2.44 | 1.99 | 1.72 | 3 cracks on edges S-W-E |
| 1.3 | 0.84 | 1.24 | 1.01 | 0.87 | 2 opposite edges W-E |
| 2.1 | 1.16 | 1.73 | 1.41 | 1.22 | 2 opposite edges W-E |
| 2.2 | 0.76 | 1.12 | 0.92 | 0.79 | 2 opposite edges W-E |
| 2.3 | 0.99 | 1.47 | 1.20 | 1.04 | 2 opposite edges W-E |
| 3.1 | 1.25 | 1.86 | 1.52 | 1.31 | 2 opposite edges N-S |
| 3.2 | 0.82 | 1.21 | 0.99 | 0.85 | 2 opposite edges W-E |
| 3.3 | 1.38 | 2.06 | 1.68 | 1.45 | 2 opposite edges N-S |
| 4.1 | 1.92 | 2.85 | 2.33 | 2.01 | 3 cracks on edges N-E-S |
| 4.2 | 0.82 | 1.22 | 1.00 | 0.86 | 2 opposite edges W-E |
| 4.3 | 1.06 | 1.57 | 1.28 | 1.11 | 2 opposite edges N-S |
| 5.1 | 0.89 | 1.32 | 1.08 | 0.93 | 2 opposite edges N-S |
| 5.2 | 0.86 | 1.28 | 1.05 | 0.91 | 2 opposite edges N-S |
| 5.3 | 0.85 | 1.26 | 1.03 | 0.89 | 2 opposite edges W-E |
| 6.3 | 0.91 | 1.36 | 1.11 | 0.96 | 2 opposite edges N-S |
| *6.2 | 0.92 | 1.46 | 1.15 | 1.083 | 2 opposite edges W-E |

6.8. Analytical model validation

The analytical models considered in this study, including those of Westergaard, Falkner et al., Shentu et al., Meyerhof-Losberg, the punching shear model proposed in TR34 [28], and Models 1-4 developed in ABC Slab, can be subjected to validation. The validation may account for discrepancies between the analytically assumed and actual testing conditions, including variations in slab support and geometry, as well as uncertainties in force measurement and material properties. Models 1-4 from ABC Slab were specifically selected for the validation, as their assumptions most closely reflect the experimental conditions, particularly with respect to slab geometry and support configuration (ground + edge support). All four models were validated, given that the actual support conditions at the beginning of testing could not be unambiguously determined. Moreover, the validation was limited to slabs of type 5, as these exhibited the lowest coefficient of variation (COV = 2.3%).

First, for slabs 5.1-5.3, the average ratio between the experimentally obtained first cracking force (F_{crl}) and the calculated load-bearing capacity ($P^{cal} = P^{l}_{4edges}$, $P^{2}_{2edges,o}$, P^{3}_{3edges} , or $P^{4}_{2edges,a}$ depending on Model 1, 2, 3, or 4, respectively) was determined. Subsequently, the empirical validation coefficients, defining the confidence interval, were calculated according to equation (6.15). The procedures and results of the model

validation are summarized in Table 6.17, where the selected empirical coefficients are underlined and then applied to calculate $P^{cal,val}$.

$$P\left(\overline{\left(\frac{F_{cr1}}{P^{cal}}\right)} - t_{1-\alpha/2} \frac{SD}{\sqrt{n}} < \overline{\left(\frac{F_{cr1}}{P^{cal}}\right)} < \overline{\left(\frac{F_{cr1}}{P^{cal}}\right)} + t_{1-\alpha/2} \frac{SD}{\sqrt{n}}\right) = \alpha \tag{6.15}$$

where:

 $\overline{(F_{cr1}/P^{cal})}$ – average ratio F_{crl}/P^{cal} [-],

 F_{crl} – experimentally obtained first flexural cracking force [kN],

P^{cal} – calculated load-bearing capacity based on Models 1-4 (see Fig. 6.7) [kN],

 $t_{1-\alpha/0.2}$ – Student's t-distribution for n-1 degrees of freedom [-],

 α – confidence level, assumed as 0.80 [-],

n – number of results [-],

SD – sample standard deviation [-].

Based on the data presented in Table 6.17, the validated load-bearing capacity $P^{cal,val}$ for Models 1-4 was determined to be 175.26 kN. Consequently, the initially calculated capacities P^{cal} for Models 1 and 4 had to be reduced by the empirical coefficients of 0.833 and 0.873, respectively to achieve validation of the analytical models. In contrast, for Models 2 and 3, the empirical coefficients of 1.238 and 1.010 provided an increase of P^{cal}. Additionally, it is worth mentioning that validation was not feasible for slabs of types 1 and 4, as the load-deflection response of samples 1.2 and 4.1 deviated significantly from other slabs of the same type. Consequently, only two results could be considered, which was assessed to be insufficient for reliable validation. Specifically, with one degree of freedom, the Student's t-distribution value was 6.314, leading to empirical validation coefficients for Model 1 of 0.203 and 0.201 for slabs of type 1 and 4, respectively. Accordingly, the computed $P^{cal,val}$ values were considerably lower than both the experimentally obtained F_{crl} and the analytically determined capacity $P^{cal} = P^{l}_{4edges}$, indicating a notable discrepancy between validated model predictions and experimental observations. For slabs of types 2 and 3, with COV of 21% and 26%, the empirical coefficients for Model 1 were 0.626 and 0.650, respectively, which again led to a substantial reduction in $P^{cal,val}$. In summary, the validation procedure proved effective only when a sufficient number of specimens was available and the variability of the results was limited. It is therefore assumed that reliable model validation requires at least three results and a coefficient of variation not exceeding 15%.

Table 6.17 Validation of the Models 1-4 for slabs of type 5

| | Tests Before validation | | After validation | | | |
|---------|---|---|--|-----------------------|---------------------------|---------------------------|
| | Slab type | $F_{cr1}[kN]$ | P ^{cal} [kN] | F_{cr1}/P^{cal} [-] | P ^{cal,val} [kN] | $F_{crl}/P^{cal,val}$ [-] |
| | 5.1 | 186.70 | 210.29 | 0.888 | 175.26 | 1.07 |
| Model 1 | 5.2 | 181.86 | 210.29 | 0.865 | 175.26 | 1.04 |
| | 5.3 | 178.37 | 210.29 | 0.848 | 175.26 | 1.02 |
| | | Average [-] | | 0.867 | | _ |
| | SD [-] | | | 0.02 | | |
| | COV [%] | | | 2.3 | | |
| | Number of results n [-] | | | 3 | | |
| | Degrees of freedom n-1 [-] | | | 2 | | |
| | Student's t-distribution $t_{1-\alpha/2}$ for $\alpha = 0.80$ [-] | | | 2.920 | | |
| | Validation coefficient $\overline{\left(rac{F_{cr1}}{p^{cal}} ight)} - t_{1-lpha/2} rac{SD}{\sqrt{n}}$ [-] | | | 0.833 | | |
| | Validation coefficient $\frac{\overline{\left(\frac{F_{cr1}}{p_{cal}}\right)}}{\left(\frac{F_{cr1}}{p_{cal}}\right)} + t_{1-\alpha/2} \frac{SD}{\sqrt{n}}$ [-] | | | 0.900 | | |
| | 5.1 | 186.70 | 141.55 | 1.319 | 175.26 | 1.07 |
| | 5.2 | 181.86 | 141.55 | 1.285 | 175.26 | 1.04 |
| | 5.3 | 178.37 | 141.55 | 1.260 | 175.26 | 1.02 |
| | | Average [-] | | 1.288 | | |
| 2 | | SD [-] | | 0.03 | 1 | |
| Model 2 | | COV [%] | | 2.3 | _ | |
| Mo | | ber of results n | | 3 | _ | |
| | | es of freedom n | | 2 | _ | |
| | Student's t-dis | tribution <u>t_{1-a/2}</u> fo | or $\alpha = 0.80$ [-] | 2.920 | _ | |
| | Validation coefficient $\frac{\left(\frac{F_{cr1}}{pcal}\right)}{\left(\frac{pcal}{pcal}\right)} - t_{1-\alpha/2} \frac{SD}{\sqrt{n}}$ [-] | | | 1.238 | - | |
| | Validation co | efficient $\frac{\overline{\left(\frac{F_{cr1}}{P^{cal}}\right)}}{+}$ | $-t_{1-\alpha/2}\frac{SD}{\sqrt{n}}\left[-\right]$ | 1.338 | | |
| | 5.1 | 186.70 | 173.56 | 1.076 | 175.26 | 1.07 |
| | 5.2 | 181.86 | 173.56 | 1.048 | 175.26 | 1.04 |
| | 5.3 | 178.37 | 173.56 | 1.028 | 175.26 | 1.02 |
| | Average [-] | | | 1.050 | | |
| 3 | SD [-] | | | 0.02 | | |
| Model 3 | COV [%] | | | 2.3 | | |
| Ao(| Number of results n [-] | | | 3 | | |
| | Degrees of freedom n-1 [-] | | | 2 | | |
| | Student's t-distribution $t_{1-\alpha/2}$ for $\alpha = 0.80$ [-] | | | 2.920 | | |
| | Validation coefficient $\left(rac{F_{cr1}}{pcal} ight) - t_{1-lpha/2}rac{SD}{\sqrt{n}}$ [-] | | | <u>1.010</u> | | |
| | Validation coefficient $\overline{\left(\frac{F_{cr1}}{p^{cal}}\right)} + t_{1-\alpha/2} \frac{SD}{\sqrt{n}}$ [-] | | | 1.091 | | |
| | 5.1 | 186.70 | 200.85 | 0.930 | 175.26 | 1.07 |
| | 5.2 | 181.86 | 200.85 | 0.905 | 175.26 | 1.04 |
| | 5.3 | 178.37 | 200.85 | 0.888 | 175.26 | 1.02 |
| | Average [-] | | | 0.908 | 1 | |
| 4 | SD [-] | | | 0.02 | _ | |
| del | COV [%] | | | 2.3 | _ | |
| Model 4 | Number of results n [-] | | | 3 | 4 | |
| | Degrees of freedom n-1 [-] | | | 2 2 2 2 2 2 | 4 | |
| | Student's t-distribution $t_{1-\alpha/2}$ for $\alpha = 0.80$ [-] | | | 2.920 | - | |
| | Validation coefficient $\frac{\overline{\left(\frac{F_{cr1}}{p^{cal}}\right)}}{\overline{\left(\frac{F_{cr1}}{p^{cal}}\right)}} - t_{1-\alpha/2} \frac{SD}{\sqrt{n}} [-]$ | | | 0.873 | | |
| | Validation co | efficient $\overline{\left(\frac{F_{cr1}}{p_{cal}}\right)}$ + | $-t_{1-\alpha/2}\frac{SD}{\sqrt{n}}\left[-\right]$ | 0.943 | | |

6.9. Synthesis and conclusions of the analytical analysis

The comprehensive analytical study of SyFRC ground slabs and simply supported slabs aimed to compare experimental results with various theoretical models to evaluate their accuracy in terms of load-bearing capacity, understand the influence of support conditions, and verify failure mechanisms. Flexural cracking forces and punching shear capacities were calculated using methodologies developed by Westergaard, Falkner et al., Shentu et al., and the Technical Report 34, which integrates Meyerhof-Losberg and Eurocode 2 principles (Fig. 6.10). Additionally, the contributions of concrete, fibers, and ground support to the overall slab capacity were examined. The analysis highlighted limitations of available analytical models and proposed potential modifications to improve the prediction of structural behavior of ground slabs. Finally, calculations for simply supported slabs were performed, and simplified engineering models were developed to estimate the initial support conditions of ground slabs based on calculated load-bearing capacities (Fig. 6.11).

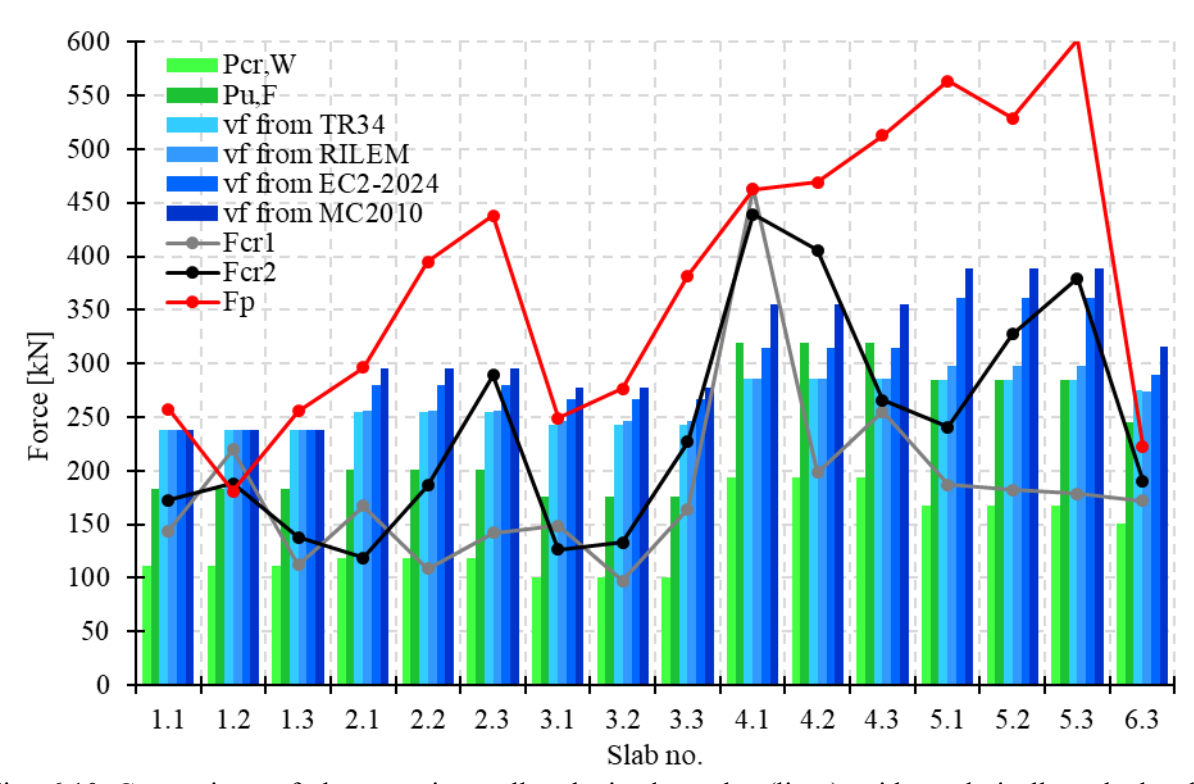


Fig. 6.10 Comparison of the experimentally obtained results (lines) with analytically calculated load-bearing capacities according to the Westergaard and Shentu et al. approaches (green columns) and punching shear load-bearing capacities according to the Technical Report 34 (blue columns) depending on the applied formula for v_f calculations and including corrections for ground contribution for tested slabs types 1-6

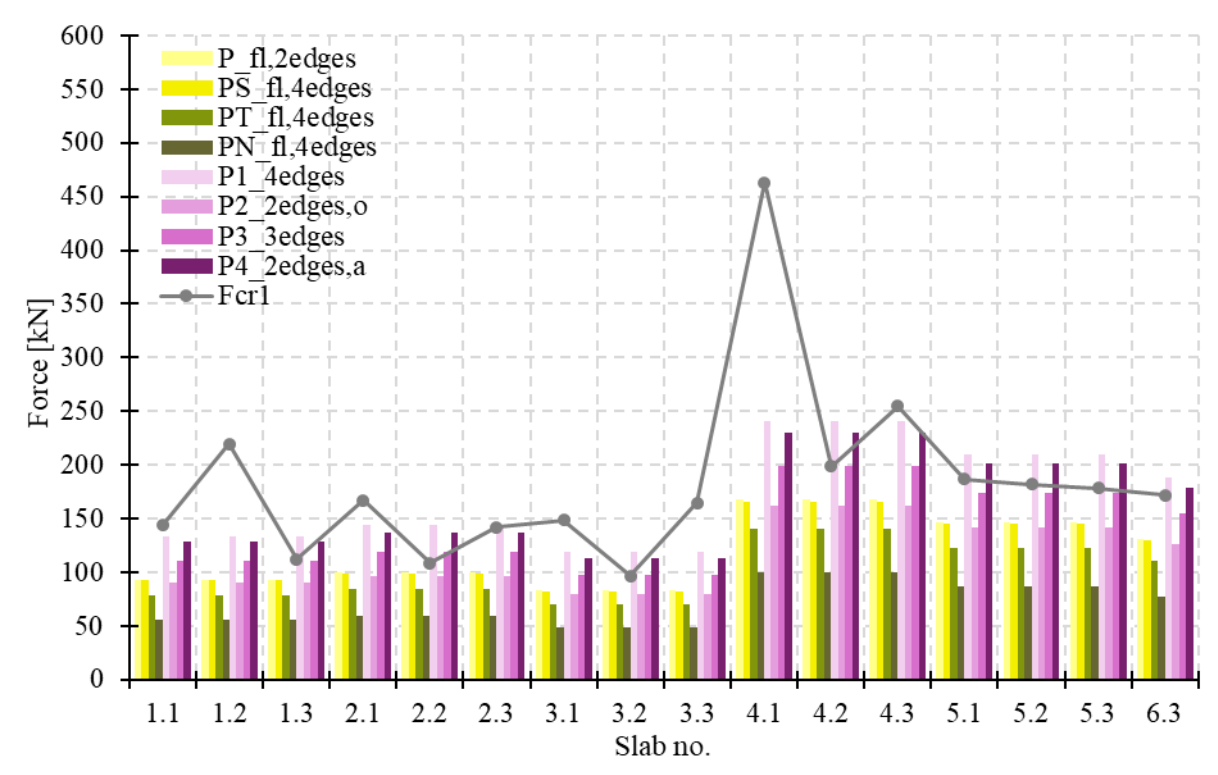


Fig. 6.11 Comparison of the experimentally obtained first flexural cracking forces (grey line) with analytically calculated load-bearing capacities assuming simply supported conditions on two or four edges (yellow columns) and ground support with additional edge support configuration dependent on the assumed Models 1-4 (purple columns) for tested ground slabs types 1-6

Firstly, the Westergaard approach allowed for a reasonable estimation of the initial cracking load of ground slabs, with an average safety margin of 23% when compared to the experimentally obtained F_{crl} values (Fig. 6.10). However, experimental observations indicated that the slabs were not initially uniformly supported by the underlying ground or along all edges, necessitating a more detailed analysis. As a result, further analytical methods, assuming simply supported slabs (Starosolski, Timoshenko et al., Niezgodziński et al.), predicted flexural load-bearing capacities lower than the experimentally observed F_{crl} (Fig. 6.11). This suggested that the slabs had some contact with the supporting soil at the beginning of testing. Subsequently, four models for ground-supported slabs with different edge support configurations were evaluated to determine whether the ground slabs were initially supported on all four edges (Model 1), two opposite edges (Model 2), three edges (Model 3), or two adjacent edges (Model 4) (Fig. 6.11). For seven of the tested ground slabs, the experimentally measured F_{cr1} values exceeded the predictions of all analytical models, indicating that these slabs were most likely uniformly supported along all four edges during testing. Notable exceptions included six slabs whose analytical results suggested initial support limited to two adjacent or two opposite edges, with only partial contact along a third edge. Additionally, two slabs were most likely supported by two

adjacent steel rollers, with non-uniform support along the remaining edges. Concluding, approximately half of the tested ground slabs were likely uniformly supported along all four edges, while the remainder experienced partial support, often limited to two or three edges according to analytical Models 1-8. Nonetheless, these findings were not fully aligned with experimental observations and the sequence of crack **development.** In conclusion, while various analytical models provided valuable insights into different slab support conditions, accurately predicting the complex interaction between the slab, subgrade, and linear supports remains challenging, particularly in the absence of detailed information on crack morphology on the underside of the slabs. Future research should incorporate nonlinear analyses and model calibration to improve the accuracy of predictive calculations. Nonetheless, Models 1-4 confirmed that the presence of subgrade support contributes to increased load-bearing capacity. For instance, adding ground support to a slab simply supported on four edges (acc. to Starosolski approach) resulted in a 45% increase in the calculated maximum allowable central concentrated load (Fig. 6.11). Then, correlation with the experimentally observed secondary flexural cracking force F_{cr2} remained challenging, as F_{cr2} corresponded to the nonlinear phase of slab structural response. Specifically, the predicted ultimate load based on Falkner et al.'s approach generally exceeded F_{cr2} in more than half of the tested slabs, while remaining lower than the punching shear load F_p in nearly all cases (Fig. 6.10). Regarding Shentu et al.'s approach, the calculated failure loads were significantly higher than those predicted by Westergaard and Falkner et al. methods, as well as the experimentally obtained results. This discrepancy may be attributed to the consideration of horizontal thrust in Shentu et al.'s model, an effect absent in the tested slabs due to their limited dimensions and lack of lateral restraint.

Technical Report 34 proved to be the most promising approach for predicting failure loads, as it provides explicit formulas for calculating both flexural and punching shear capacities of ground slabs subjected to a centrally applied concentrated load. Moreover, it accounts for the contributions of macro SyFs and subgrade support. Preliminary calculations were performed for the critical control perimeter located at a = 2d, following TR34 recommendations, to estimate potential failure mechanisms prior to experimental testing. It was confirmed that punching shear was the governing failure mode across all slab types, thereby validating the adopted research program design. For experimentally determined critical control section distances a, also punching shear failure was expected to occur prior to bending failure for all ground slabs. In conclusion, the predicted failure mode was consistent for both the assumed a = 2d and experimentally determined a values, nevertheless, using the actual location of the

critical control section resulted in higher punching shear capacities, which better corresponded to the test results. Furthermore, analytical calculations for a = 2dindicated that the average contributions to the total punching shear load-bearing capacity were 75.1% from concrete, 9.9% from fibers, and 15.0% from the subgrade. However, when using experimentally determined a, the concrete contribution increased significantly to 91.7%, while the contributions from fibers and ground support decreased to 4.7% and 3.6%, respectively. This change was primarily attributed to the significantly reduced length of the critical control perimeter. Nevertheless, a relatively low contribution of SyFs to punching shear capacity was revealed, which did not align with the experimental findings. This underestimation was explained by the conservative approach of the TR34 equation used to calculate the additional shear strength provided by the presence of fibers in concrete v_f . Consequently, alternative formulations for v_f were evaluated (Fig. 6.10). Specifically, the v_f equation proposed in Model Code 2010 provided the greatest fiber contribution to punching shear capacity, at least 4.9 times higher than the TR34 formula. The equation from PN-EN 1992-1-1:2024 resulted in fiber contributions that were 22% to 51% lower than those calculated using the Model Code 2010 formula, but still more than 2.4 times higher than those obtained from TR34. The application of the equation proposed by RILEM TC 162-TDF produced contributions generally closely aligned with those from TR34. It is noteworthy that only the equations from standards RILEM TC 162-TDF, PN-EN 1992-1-1:2024, and Model Code 2010 reflected the same punching shear capacity ranking among the SyFRC slabs as observed experimentally, with type 5 slabs exhibiting the highest punching capacity, followed sequentially by types 4, 2, and 3. Analytical results for slab 6.3 exhibited notable inconsistency with experimental observations, which may be attributed to the limited experimental data (as only a single test sample was considered) and/or potential variations in fiber content or distribution. Further experimental investigations are necessary to verify these assumptions. In conclusion, the equations for v_f from PN-EN 1992-1-1:2024 and Model Code 2010 provided more accurate estimations of the SyFs contribution to punching shear capacity, demonstrating better agreement with experimental punching shear forces than the formulations from TR34 and RILEM TC 162-TDF. The conducted analytical analyses highlighted the significant, but often underestimated, role of fibers in punching shear capacity and emphasized the need for adequate analytical models that fully capture and benefit from the SyFs addition to concrete. Regarding the calculation of ground contribution, the TR34 procedure incorporates simplifications and conservative assumptions, which may

lead to its underestimation. However, the modifications to the ground reaction values provided only a minor increase in ground contribution (from an average of 3.6% to 4.1%), suggesting that the simplified methods in TR34 for calculating ground pressure are sufficiently accurate. Finally, despite implementing more precise and comprehensive analytical analyses, ideal agreement between analytical predictions and experimental results was generally not achieved. Specifically, predicted punching shear load-bearing capacities were underestimated on average by 60%, 57%, 39%, and 29%, after excluding slab 6.3 results, when the fiber contribution v_f was calculated according to TR34, RILEM TC 162-TDF, PN-EN 1992-1-1:2024, and Model Code 2010, respectively. The discrepancy between experimental and analytical results reported in this dissertation may be attributed to the limited dimensions of the tested slabs and soil confinement, which might have altered the ground pressure distribution and increased subgrade stiffness. Specifically, the testing methodology of ground slabs only approximately corresponded to the model assumptions presented in TR34, which may have contributed to the differences between the experimental and analytical results. Nevertheless, the analytical model following the TR34 guideline provided a reasonably accurate prediction of the failure mode and punching shear load-bearing capacity, especially when considering the actual location of the critical control section, increased ground contribution, and a greater role of SyFs in load transfer.

Finally, the **procedure for validating the analytical models** was presented and discussed. The validation may account for discrepancies between the analytically assumed and actual testing conditions, as well as uncertainties in force measurements and material properties. Models 1-4 from ABC Slab software were specifically selected for validation, as their assumptions most closely represent the experimental conditions, particularly with respect to slab geometry and support configuration (ground + edge support). In conclusion, the validation procedure proved effective when a sufficient number of specimens was available and the variability of results was limited. It is therefore assumed that **reliable model validation requires at least three results and a coefficient of variation not exceeding 15%**. **For slabs of type 5, the empirical validation coefficients ranged from 0.833 to 1.238, depending on Models 1-4.**

7. DISCUSSION

The scope of this dissertation covered a comprehensive literature review, laboratory testing of material properties and large-scale samples of ground-supported slabs as well as analytical calculations, which required comparative evaluation and discussion. Firstly, the ground slab tests confirmed the conclusions drawn from the beam tests, specifically that SyFRC demonstrates significantly improved ductility and post-cracking performance compared to brittle response of PC samples. Excluding SyFRC type 6 from the analysis, given that only one specimen was available for this type, it was observed that the results for flexural cracking forces F_{cr1} and F_{cr2} of ground slabs corresponded well with residual flexural tensile strength $f_{R,I}$ obtained from 3PBT, as both follow the same trend for types 1-5 in the order: 1, 3, 2, 5, 4. Therefore, it appears reasonable that calculations of the positive bending moment largely depend on the $f_{R,1}$ value. For the slabs' punching shear load, F_p values showed good agreement with $f_{R,3}$ results from the bending tests of beams, where the highest average value was recorded for SyFRC samples type 5, followed by 4, 2, 3, and the lowest F_p for PC type 1. These findings suggest that the equations for the additional punching shear strength v_f provided in PN-EN 1992-1-1:2024 [33] and Model Code 2010 [80] are the most suitable for estimating the SyFs contribution in punching shear capacity, as they primarily depend on the $f_{R,3}$ value. These approaches appear to be notably more accurate than those of TR34 [28] and RILEM TC 162-TDF [66], which either rely equally on all residual flexural tensile strength values $(f_{R,1}-f_{R,4})$ or solely on $f_{R,4}$, respectively. It can therefore be concluded that the results of small-scale beam samples from 3PBT provide an indicative prediction for structural behavior of SyFRC ground-supported slabs, even though they do not account for soil-structure interaction. Similar conclusions were reported by Bischoff et al. [192], who stated that slab load-bearing capacity depends primarily on the concrete post-cracking strength and that beam test results provide a reliable indication of the slab performance. Nonetheless, these conclusions require further

investigation. Following the work and recommendations of Gaedicke et al. [240], it is suggested that beams with the same depth as the slab thickness, supported on soil foundations, should be tested to more accurately predict the structural behavior of ground-supported slabs.

The experimental results demonstrated a substantial impact of ground on the structural response of slabs subjected to central concentrated loading, which was confirmed by the considered analytical models. Specifically, the calculations of simply supported slabs and ground slabs additionally supported along the edges, according to Models 1-4, concluded that the presence of subgrade support contributes to increased load-bearing capacity. This finding highlighted the necessity of conducting separate analyses for ground-supported and unsupported slabs, with particular emphasis on identifying the governing failure mode. Namely, the tests revealed that unsupported slabs failed by reaching their flexural load-bearing capacity and did not exhibit punching shear failure, in contrast to slabs supported by the ground.

In alignment with the literature review, based on the Westergaard approach the calculated load-bearing capacities of ground-supported slabs showed values that were 1.62 to 2.30 times lower for PC slabs and 2.38 to 3.82 times lower for SyFRC slabs than those recorded in the experimental campaign (excluding slabs type 6). Similarly, calculations based on the method proposed by Falkner et al. resulted in underestimated capacities by factors of 0.99-1.41 for PC slabs and 1.42-2.18 for SyFRC slabs type 2-5, again relative to experimental results. These discrepancies between analytical predictions and experimental results are most likely attributable to the differing assumptions, regarding the ground, slab geometry, and boundary conditions, and excessive simplifications of the theoretical models, as well as the divergence between the experimentally observed failure mode (punching shear) and the predicted flexural failure assumed in the analyses. Nevertheless, the Falkner et al. approach proved effective in predicting the initial cracking force, corresponding to the Westergaard load, while maintaining a reasonable safety margin for calculated ultimate load-bearing capacity for the majority of tested slabs. Regarding Shentu et al.'s approach, the calculated failure loads were significantly higher than those predicted by Westergaard and Falkner et al. methods, as well as the **experimentally obtained results**. This was explained by the consideration of horizontal thrust in Shentu et al.'s model, an effect absent in the tested slabs due to their limited dimensions and lack of lateral restraint. It should be noted that the analytical models considered in this study can be subjected to validation, which may account for the aforementioned discrepancies between the analytically assumed and actual testing

conditions. A validation procedure for these models, based on Models 1-4 developed in the ABC Slab software, was presented and discussed within the scope of this dissertation, and was shown to be effective when a sufficient number of specimens was available and the variability of results was limited.

Analytical estimations of punching shear capacity, when based on the TR34 guideline and assuming a predefined critical control section location at a distance a = 2d, underestimated the capacity by an average of 68% for SyFRC ground slabs of types 2-5. These findings are consistent with previous conducted studies [186]–[188], [241], which also concluded that the experimental punching shear load-bearing capacity of FRC ground slabs was often greater than the one predicted from analytical calculations. Assumption of the experimentally obtained location of the critical control section led to increased punching shear capacity by an average of 7% for SyFRC, resulting in improved alignment with F_p and a reduced average safety margin of 61% for slabs of types 2-5. Calculation accuracy further increased when the fiber contribution in shear resistance v_f was determined according to other formulas, while additionally accounting for the corrected effect of ground support. Specifically, the application of v_f equations from TR34 [28], RILEM TC 162-TDF [66], PN-EN 1992-1-1:2024 [33], and Model Code 2010 [80] resulted in predicted punching shear capacities that were underestimated by average 60%, 57%, 39%, and 29%, respectively, considering all tested slabs except slab 6.3. These results highlight the importance of accurately representing the fiber contribution in punching shear capacity, as it is crucial for the optimized design of FRC ground-supported slabs. Design guidelines often rely on conservative simplifications, suggesting that the effectiveness of SyFs in stress transfer is negligible or significantly lower than that of SFs. As a result, they typically do not allow for the inclusion of additional shear capacity provided by SyFs in punching shear calculations, what is contradicted by experimental results presented in this dissertation and other previously performed studies. Namely, the experimental research confirmed that the addition and increased SyFs dosage enhanced the punching shear capacity. Additionally, the accurate determination of the critical control section location improves the accuracy of failure load predictions. The commonly used assumption of a = 2d was shown to be usually too conservative, given that the experimentally observed ranged from 0.64d to 0.98d depending on the fiber dosage and type. Therefore, the recent revision in PN-EN 1992-1-1:2024-05 [33], which specifies the distance as a = 0.5d, appears more justified and consistent with the presented findings. Interestingly, with the inclusion and increased fiber amount the shape of the punching cone changes from cuboidal

shape (PC slabs) into truncated pyramid shape (SyFRC slabs) what is associated with a reduction in the punching cone inclination angle θ and an increase in the distance a of the critical control section from the loading area.

The failure mode observed in all tested ground-supported slabs was identified as punching shear failure, typically preceded by the formation of first and second flexural cracks. In most cases, the second flexural crack developed under a higher applied load than the first, with the maximum load corresponding to the punching shear capacity of the slab. This failure pattern aligns with observations reported by Bischoff et al. [192], who noted that flexural cracking in orthogonal directions often precedes punching shear failure in FRC ground slabs. Similarly, Roesler et al. [189], [190] documented the occurrence of primary and secondary flexural cracks, followed by a sudden drop in load-carrying capacity, leading to either punching or bending failure. The previously discussed non-uniform support conditions, resulting from partial contact between the slab, ground, and steel rollers, may have influenced the observed crack morphology. Nonetheless, the literature reports various crack patterns, including usually combination of 'x'-shaped and '+'-shaped cracking morphology [242] (Fig. 7.1). Moreover, the obtained crack patterns and failure mechanisms are consistent with those described in the guide for the design and construction of FRC structures [243]. As shown in Table 7.1 both ground-supported and simply supported slabs tend to develop cracks along the axis of symmetry. For future studies, it is recommended to cast slab specimens directly on natural ground to ensure more uniform and realistic support conditions, thereby improving the validity and applicability of the experimental findings.

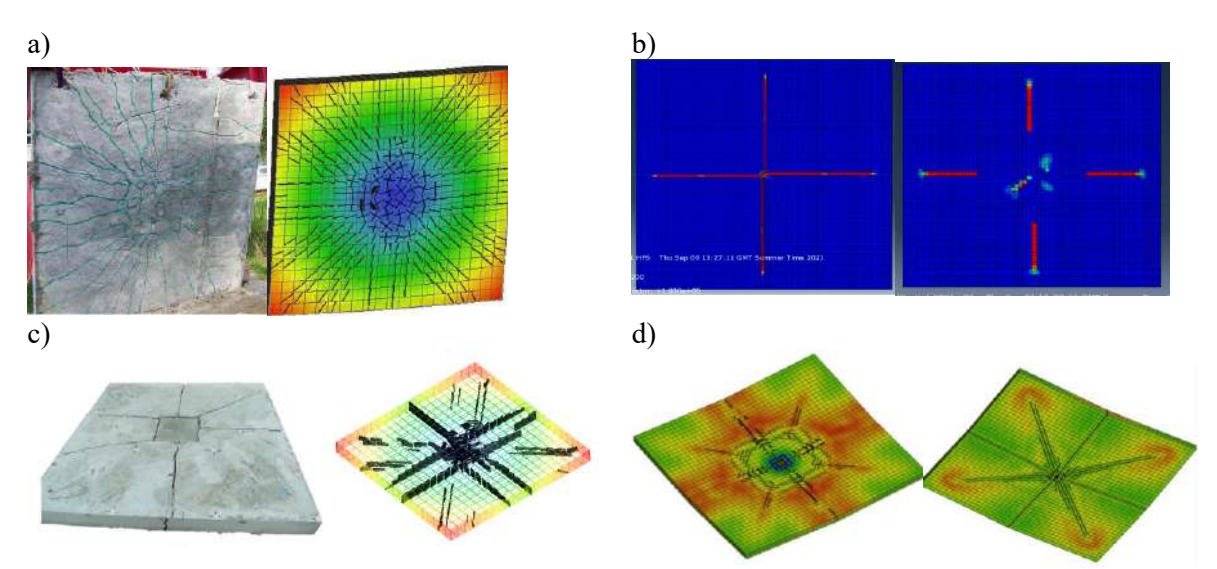


Fig. 7.1 Crack morphology from numerical analysis of ground slabs: a) reinforced with steel wire mesh [244], b) PC [242], c) PC [245], d) material not specified [246]

Table 7.1 Crack morphology of slabs with different supporting conditions according to CNR-DT 204/2006 [243]

| Simply supported slab subjected to bending | Clamped slab subjected to bending | Ground-supported slab |
|--|--------------------------------------|-----------------------|
| a los=h | losi=h/2 | los=h + a |

Critical assessment

This dissertation makes a significant contribution to the limited knowledge on the punching shear behavior of FRC ground-supported slabs. It particularly focuses on the influence of SyFs on both material characterization and the structural performance of large-scale specimens. To the best of the author's knowledge, this study is the first to analyze the effect of SyFs inclusion, dosage, and type on the geometry of punching shear cones and the location of the critical control section. Although some research has been conducted on the use of SyFs in ground slabs, studies examining their influence on load-bearing capacity, crack propagation, deformations, and failure mechanisms still remain limited. A significant advantage of this study is its systematic compilation and discussion of previously fragmented information into a single comprehensive work, providing one of the most thorough literature reviews available in this specific field. The review revealed that no unified standard currently exists for the design of SyFRC ground-supported slabs, while the available guidelines for PC and SFRC slabs vary significantly in their methodologies, often leading to confusion and inconsistent design provisions and results. In this context, the findings of this research offer a valuable foundation for future analytical model calibrations and the development of standardized design recommendations for SyFRC ground-supported slabs. Furthermore, one of the key contributions of this dissertation is the design and implementation of a novel testing set-up and a dedicated experimental methodology. Additionally, testing three large-scale specimens per concrete type undoubtedly improved the credibility of the conclusions. Since studies involving multiple large-scale specimens of a single concrete type are rare in the existing literature, the present work offers valuable and more consistent insights within the considered topic.

However, despite the recognized research significance, this study also exhibits certain limitations and areas for further development. Upon completion of the research, several aspects were identified that could have been modified or approached differently to improve the accuracy and completeness of the results and analyses. Notably, the

excessive fiber dosage in some mixes, particularly for SyFRC type 3, resulted in a significant reduction in workability. This led to non-uniform fiber distribution and a deterioration in SyFRC mechanical properties. In addition, variations in concrete composition, caused by changing weather conditions affecting aggregate humidity and the use of materials from different deliveries due to an extended concreting timeframe, introduced inconsistencies in the material characterization. These factors complicated the direct comparison of results across concrete types, limiting the completeness and clarity of conclusions regarding the influence of SyFs inclusion, dosage, and fiber type. For future research, it is recommended to implement a more rigorous procedure for controlling concrete composition, including careful monitoring of water content, superplasticizer dosage, and aggregate humidity. This study once again confirmed that optimizing the fiber dosage is a crucial factor in maintaining consistent workability and achieving uniform matrix quality across all FRC batches. Investigating methods to improve fiber uniform distribution and reduce bundling, particularly for SyFs types prone to clustering, is also advised. Finally, testing only one slab of SyFRC type 6 under specific ground conditions did not ensure statistically valid findings, leading to limited creditability of the conclusions about the influence of fiber type.

The limited accuracy in reflecting the actual behavior of ground-supported slabs under concentrated loads also arose from constraints associated with the construction of the testing setup and the fact that the tests were conducted under laboratory conditions. Specifically, in industrial floor, the ground slab is typically supported by a complex, heterogeneous, and infinite subgrade. Replicating such ground conditions within the laboratory environment was infeasible due to restrictions on the maximum achievable thickness and dimensions of the soil containment box supporting the slab, as well as the presence of the high-strength concrete laboratory floor. Furthermore, the supporting soil was confined laterally by concrete beams forming a rigid box structure. It is important to acknowledge that both the reduction in subbase area and thickness as well as the lateral confinement have influenced the distribution of ground pressure under tested slabs. Additionally, limitations in testing space and laboratory infrastructure necessitated the use of samples with relatively small dimensions compared to in situ ground-supported slabs. This scale reduction inherently limited the ability to realistically simulate field conditions, particularly regarding membrane action, and contributed to the pronounced uplift of slab corners and edges observed during testing. Nevertheless, unlike flexural behavior analysis, the characterization of punching shear failure in ground-supported slabs predominantly requires investigation of the slab region within the radius of relative stiffness. Analytical calculations confirmed that the dimensions of the tested slabs adequately satisfy this criterion. To simulate regions of zero bending moment, steel rollers were installed to support the slab along their edges. However, testing prefabricated slabs introduced additional challenge of uneven support conditions. Namely, despite meticulous preparation of the subgrade and controlled concrete casting and curing procedures, ideal ground support conditions and uniform contact between the slab and steel rollers were typically not achieved. Consequently, the slabs were often only partially supported by the subgrade and/or one to four steel rollers. The uncertainties in support conditions complicated the interpretation of deflection measurements, particularly during the initial loading stages. For future investigations, it is recommended to cast slabs directly on natural ground to ensure more uniform and realistic support conditions. Additionally, eliminating the edge line supports could potentially enhance slab-to-subgrade contact, particularly considering the observed edge uplift, which diminished the effectiveness of support provided by the steel rollers. Limitations associated with the testing equipment and measurement methodology were also identified. Firstly, the maximum actuator stroke of 80 mm occasionally restricted the continuation of testing beyond certain deflection levels. Moreover, the use of a manually operated electric pump constrained the ability to apply a constant load or deflection rate increase, thereby reducing the precision and repeatability of the loading process. Additionally, deflection profile analyses indicated that LVDTs should be mounted on a raft supported directly on the concrete slab, rather than on the laboratory's strong floor. This modification would allow for the measurement of solely slab deflections, excluding any potential influence from setup deformations or imperfections in the test rig. Then, visual observation of crack propagation on the bottom surface of the ground-supported slabs during testing was not feasible. Therefore, alternative techniques for monitoring crack initiation and development on the underside of the slab should be explored. One potential solution involves the use of fiber optic sensors, however, the implementation of such systems is associated with significant costs. Furthermore, the pushrod measurement devices, intended to record shear crack widths, were found to be usually ineffective. This was attributed to their coinciding with flexural cracks and/or improper positioning relative to the shear cracks locations. Nevertheless, this measurement technique appears promising, particularly with adjustments of the pushrod location based on expected shear crack angle. Finally, it was determined that the initial method for measuring the inclination of the punching shear cones, using an angle finder ruler, was unreliable due to their irregular shape and the limited number of measurement points. Nevertheless, further adapted methodology proved to be effective. Although the experimental campaign was subjected to certain limitations, its strengths

must also be acknowledged. Notably, the study covered a broad range of tests, enabling comprehensive characterization of the material, from fresh to hardened properties, as well as investigation of unsupported and ground-supported slabs. In total, 36 cubes, 18 beams, 36 drilled cores, and 18 slabs were tested. This extensive experimental scope facilitated a holistic understanding of the effects of SyFs on both the mechanical properties of concrete and the structural behavior of ground slabs. The large-scale testing of SyFRC samples represents a significant contribution, providing valuable insights into their response under simulated loading conditions. Furthermore, the experimental campaign included a systematic comparative analysis, supported by detailed visual inspections of crack propagation patterns and the geometry of punching shear cones.

Regarding the limitations of the analytical analyses, only selected theoretical models were considered. These models were likely developed based on historical test data for PC and conventionally reinforced concrete slabs and therefore may not be appropriately calibrated for SyFRC. It is likely that alternative and more advanced analytical models could have shown more accurate predictions of the structural response and capacity of SyFRC ground-supported slabs subjected to concentrated load. Furthermore, the performed analytical calculations typically employed a simplified Winkler foundation model for ground support. The assumption of a nonlinear soil behavior model, accounting for significant slab deformations and partial loss of contact between the slab and the supporting soil, as observed during the experimental campaign, would likely show more consistent results with the testing findings. Additionally, the scope of the analytical analysis was limited to the verification of cracking loads, ultimate loadbearing capacities, and estimation of initial supporting conditions as well as the contribution of individual components in the punching shear capacity. Incorporating an iterative or graphical method to determine the location of the critical control section for punching failure and comparing its position with experimental observations would undoubtedly enhance the credibility and validity of the analysis. Finally, the absence of numerical models for the tested ground slabs, supported by inverse analysis of SyFRC beams, prevented the validation and confirmation of the experimentally observed results. The development of Finite Element Method (FEM) would provide a valuable tool for extending the applicability of the findings.

8. FINAL CONCLUSIONS AND RECOMMENDATIONS

This doctoral dissertation presents an extensive review of existing standards, theories, analytical models, testing methods, and previously conducted studies on SyFs, SyFRC, and ground-supported slabs. The literature review revealed a significant knowledge gap concerning the influence of SyFs on the punching shear capacity of ground slabs. As a result, their contribution to shear resistance is frequently underestimated or omitted in structural design, which limits the broader acceptance of SyFRC in engineering practice. To address this research gap, the present study was guided by specific objectives (Table 8.1) and achieved within the scope of the dissertation.

Table 8.1 Objectives of the doctoral dissertation

| No. | Objectives | | |
|-----|---|----------|--|
| 1. | Comprehensive review and critical analysis of selected theoretical and analytical models, existing standards, and guidelines as well as performed experimental investigations on the effect of SyFs inclusion in concrete, testing and design methods of SyFRC focusing particularly on ground slabs and punching shear capacity. | | |
| 2. | Execution of an experimental campaign on small-scale specimens to determine the influence of SyFs addition, type, and dosage on selected physical and mechanical properties of concrete, including workability, modulus of elasticity, compressive, flexural, and splitting tensile strength as well as fracture energy. | √ | |
| 3. | Development and design of a testing setup and adequate experimental methodology to investigate the punching shear behavior of semi-full scale ground slab samples. | √ | |
| 4. | Assessment of structural behavior differences between centrally loaded unsupported slabs and ground-supported slabs. | √ | |
| 5. | Comparative analysis of flexural cracking loads, punching shear load capacity, crack morphology, deflections, and location of the critical control section of PC and SyFRC ground slabs, considering various SyFs types and dosages. Identification and characterization of failure stages and mechanisms of SyFRC ground-supported slabs under concentrated central loads. | ✓ | |
| 6. | Validation of the accuracy and predictivity of selected analytical models through comparison with experimental results. Conducting analytical analyses to quantify the contribution of SyFs to punching shear load-bearing capacity and support conditions to flexural cracking loads. | √ | |
| 7. | Formulation of practical design recommendations, including methods to incorporate SyFs contribution in punching shear capacity calculations and determination of critical control section location for SyFRC ground-supported slabs. | ✓ | |

A comprehensive experimental program was developed to investigate the punching shear behavior of SyFRC ground-supported slabs subjected to centrally applied concentrated load. The study detailed the experimental methodologies and results related to both the characterization of concrete mechanical properties and structural performance of slabs in large-scale testing. The influence of SyFs inclusion, fiber type, dosage, and ground conditions on load-bearing capacity, deflection, crack morphology, failure modes, and particularly the location of the critical control section was systematically examined. Finally, the experimental results were compared against selected theoretical models proposed by Westergaard, Falkner et al., Shentu et al., and Meyerhof-Losberg to assess their predictive accuracy and validity. Furthermore, calculations based on the Technical Report 34 guideline were conducted to, among other objectives, identify the governing failure mode and evaluate the individual contributions of concrete, fibers, and ground support in punching shear capacity.

Based on extensive experimental testing, analytical evaluation, and critical comparisons with existing literature, the following key conclusions have been drawn:

• Influence of macro SyFs addition, dosage, and type

- The addition of macro SyFs to concrete significantly enhanced the limit of proportionality, residual flexural tensile strengths, and energy absorption of beam specimens. In the case of ground-supported slabs, moderate improvements were observed in flexural cracking capacity, while post-cracking behavior, and punching load-bearing capacity enhanced significantly. Depending on the type of SyFRC, flexural cracking and punching load capacities increased by approximately 4-28% and 18-47%, respectively, compared to reference PC slabs. Furthermore, load reductions following flexural cracking were less pronounced in SyFRC slabs than in PC slabs. The addition of SyFs also altered the failure mode from brittle to more ductile behavior in both small-scale and large-scale samples.
- An increased dosage of SyFs led to an improved residual flexural tensile strength and energy absorption in beam specimens, as well as to the punching load-bearing capacity of ground-supported slabs. Specifically, increasing the fiber dosage from 2 kg/m³ to 3 kg/m³ resulted in an average capacity increase of approximately 15%. A higher fiber dosage also led to a greater number of final cracks in slabs, indicating improved load redistribution.
- o SyFRC with higher fiber dosages requires careful mix design, as

excessively high fiber content reduces workability, leads to non-uniform fiber distribution and consequently deteriorates concrete mechanical properties. Failure to comply with this principle precluded a comprehensive evaluation of the effects of increased fiber content on the mechanical properties and structural performance of SyFRC ground-supported slabs.

- Achieving consistent concrete quality requires strict control over mixture composition and design. Non-compliance with these requirements resulted in significant variability in concrete mechanical properties, which prevented a systematic assessment of the influence of fiber type on small-scale samples and SyFRC ground slabs performance.
- o In order to increase the validity of the derived conclusions, three slab specimens of each concrete type were usually tested. Nevertheless, discrepancies in the results were occasionally observed. This highlights the importance of sufficient specimen numbers in FRC testing, where the non-uniform distribution of fibers within the matrix may significantly influence structural performance. For this reason, the results obtained for slab 6.3 were interpreted with particular caution.

• Structural response and failure mode of SyFRC slabs

- The presence of ground support had a significant influence on the mechanical response of SyFRC slabs, resulting in increased load-bearing capacity and additional punching shear cracking compared to unsupported slabs. Ultimately, the unsupported slab failed in bending, while tested ground-supported slabs exhibited punching shear failure. This highlights the necessity of conducting distinct analyses for ground-supported and unsupported slabs.
- Variability in subsoil support conditions had a notable effect on the load-deflection response of ground-supported slabs.
- All tested SyFRC ground-supported slabs failed due to punching, which was preceded by the formation of first and secondary flexural cracks.
- Three distinct Failure Mechanisms were identified, depending on the relative magnitudes of the flexural cracking forces and the punching shear force. Most of the tested ground slabs exhibited Failure Mechanism III, characterized by the development of the secondary flexural cracks at a higher load level than the first, with the maximum load corresponding to the punching shear capacity.

O The residual flexural tensile strength results obtained from small-scale beam specimens in three-point bending tests provided an indicative prediction for the structural behavior of SyFRC ground-supported slabs. In particular, the value of $f_{R,1}$ correlated with the flexural cracking loads, while $f_{R,3}$ corresponded to the punching shear capacity.

• Punching shear cone characteristics

- The addition and increased dosage of SyFs resulted in a decrease of the punching shear cone inclination angle θ and an increase in the distance of the critical control section a from the loading area. These changes contributed to an enhanced punching shear load-bearing capacity. Moreover, the inclusion of SyFs altered the punching cone geometry from the nearly cuboid shape observed in PC slabs to an irregular truncated pyramid shape in SyFRC slabs, underscoring the influence of fibers on stress distribution and crack propagation.
- Experimentally observed values of the critical control section location a for SyFRC ground-supported slabs ranged from 0.64d to 0.98d depending on the fiber dosage and type, while for PC slabs a = 0.11d.

Analytical analysis

- Theoretical approaches of Westergaard and Falkner et al. underestimated by at least 2.3 and 1.4 times, respectively the load-bearing capacities of tested SyFRC ground-supported slabs subjected to centrally applied concentrated load.
- The Westergaard approach allowed for a reasonable estimation of the initial cracking load of centrally loaded ground-supported slabs, with an average safety margin of 23% when compared to the experimentally obtained first cracking loads.
- The predicted ultimate loads based on Falkner et al.'s approach exceeded secondary flexural cracking loads in more than half of the tested slabs, while remained lower than the punching shear load in nearly all cases.
- According to the Shentu et al. approach, the calculated failure loads were significantly higher than those predicted by Westergaard and Falkner et al. methods, as well as the experimentally obtained results. This discrepancy was attributed to the consideration of horizontal thrust in Shentu et al.'s model, an effect absent in the tested slabs due to their limited dimensions and lack of lateral restraint.
- o The failure modes predicted according to the Technical Report 34

- guideline for ground-supported slabs centrally loaded by a concentrated force were consistent with the punching shear failure modes observed during the experimental campaign.
- The common assumption of a predefined critical control section location at a distance of a=2d from the loading area resulted in an average underestimation of the punching shear capacity by approximately 68% for most of the tested SyFRC ground-supported slabs. In contrast, using the experimentally determined length of the critical control perimeter increased by average 7% the punching shear capacities predicted according to Technical Report 34, improving their alignment with experimental results.
- The accuracy of punching shear load-bearing capacity predictions improved when the fiber contribution to shear resistance v_f was calculated using formulas provided in Technical Report 34, RILEM TC 162-TDF, PN-EN 1992-1-1:2024, and Model Code 2010, while additionally incorporating the corrected contribution of ground support. These methods led to average underestimations of punching shear capacities by approximately 60%, 57%, 39%, and 29%, respectively, when considering all tested slabs except slab 6.3. Moreover, the equations for v_f from RILEM TC 162-TDF, PN-EN 1992-1-1:2024, and Model Code 2010 reflected the same punching shear capacity ranking among the SyFRC slabs as observed experimentally.
- The experimental observations and analytical calculations confirmed that at the initial stage of loading the tested slabs were likely not fully supported by the ground and/or edge supports.
- The proposed validation procedure proved effective when a sufficient number of specimens was available and the variability of results was limited. It is therefore assumed that reliable model validation requires at least three results and a coefficient of variation not exceeding 15%. For slabs of type 5, the empirical validation coefficients ranged from 0.833 to 1.238, depending on Models 1-4 developed in ABC Slab software.

The findings of this study have led to the formulation of several practical recommendations for designing ground-supported slabs.

• It is recommended to incorporate macro SyFs into ground-supported slabs when enhanced flexural cracking capacity, post-cracking behavior, and/or punching shear capacity is required. The addition of 2 kg/m³ of macro SyFs

already results in improved mechanical performance and structural safety, maintaining integrity and facilitating load redistribution. Higher fiber dosages require carefully designed mixtures to optimize mechanical properties without compromising workability.

- The consideration of punching shear load-bearing capacity in ground-supported slabs subjected to concentrated loading is of a great importance and must not be overlooked in the design process.
- The Technical Report 34, based on the Meyerhof-Losberg approach for flexural load capacity and PN-EN 1992-1-1:2008 for punching shear capacity calculations, is identified as the most promising design guideline for SyFRC ground-supported slabs subjected to concentrated loads. It accounts for both fiber reinforcement and ground support contributions in load-bearing capacity.
- The recent revision in PN-EN 1992-1-1:2024-05, which specifies the distance of the critical control section from the loading area as a = 0.5d, appears more justified and consistent for SyFRC ground-supported slabs than the usually proposed a = 2d, i.e., in the Technical Report 34 guideline.
- The role of fibers in enhancing the load-bearing capacity of structural elements should be properly acknowledged. As a result, the equations for calculation of the macro SyFs contribution to shear resistance v_f provided in PN-EN 1992-1-1:2024 and Model Code 2010 are recommended in the punching shear load-bearing capacity design of SyFRC (Fig. 8.1).

```
PN-EN 1992-1-1:2024 [33] v_f = \kappa_0 \cdot \kappa_G \cdot 0.33 \cdot f_{R,3}

Model Code 2010 [80] v_f = f_{Fts} - \frac{w_u}{CMOD_3} (f_{Fts} - 0.5f_{R,3} + 0.2f_{R,1})
```

Fig. 8.1 Formulas proposed for calculating the additional shear strength resulting from the presence of macro SyFs in concrete

Finally, the conducted research and analyses addressed the thesis summarized in Table 8.2. It must be mentioned that due to the complexity of SyFRC ground-supported slabs' behavior and the limitations of the scope of the study, some theses cannot be confirmed unambiguously. For instance, Thesis 1 was only partially confirmed and further investigation is required, as significant variability in workability and mechanical properties among different concrete types compromised the generalizability of the withdrawn conclusions. Additionally, a notable limitation is that the standardized flexural tensile tests do not account for the soil-sample interaction. Thesis 2 was positively verified based on both experimental and analytical results obtained for unsupported and ground-supported slabs. Theses 3 and 4 were also confirmed for the

tested macro SyFs types and optimal fiber dosage. However, Thesis 5 requires further research due to notable discrepancies in mechanical performance of both small- and large-scale specimens with different macro SyFs types. Moreover, the limited number of slab specimens for one of the fiber types prevented a reliable and statistically valid comparative analysis.

Table 8.2 Theses of the doctoral dissertation

| No. | Theses | | | |
|-----|---|----------|--|--|
| 1. | The structural response of SyFRC ground-supported slabs under concentrated loading | | | |
| | can be reliably predicted based on the results obtained from small-scale beam specimens. | 2 | | |
| 2. | The structural behavior of SyFRC ground-supported slabs under concentrated loading | | | |
| | differs substantially from that of unsupported slabs, particularly in terms of load-bearing | | | |
| | capacity and failure mechanisms. | | | |
| 3. | The addition of SyFs improves the post-cracking behavior and results in more ductile | | | |
| | failure modes in slabs compared to PC ground-supported slabs. | • | | |
| 4. | The inclusion and increased dosage of SyFs enhance the punching shear load-bearing | | | |
| | capacity of the ground-supported slabs and increase the critical control perimeter. | | | |
| 5. | The type of SyFs has influence on both the punching shear load-bearing capacity and the | | | |
| | length of the critical control perimeter of the ground-supported slabs. | ≈ | | |

9. FURTHER RESEARCH AREAS

Despite the comprehensive literature review and the extensive experimental and analytical investigations conducted within this dissertation, the scope of the study remains still limited to specific test conditions, materials, and samples' geometry. As a result, several important aspects remain unaddressed. These limitations highlight promising directions for future research that could significantly enhance both the theoretical understanding and the practical application of SyFRC in ground-supported slabs.

• Advanced numerical analysis using the Finite Element Method (FEM)

The application of FEM could be employed to simulate the structural response of the experimentally tested PC and SyFRC slabs, both unsupported and ground-supported, while accurately calibrating the boundary and loading conditions observed during testing. Notably, despite careful subgrade preparation (compaction, leveling) and sample concreting and curing, perfect support conditions and full contact between the slab and ground were not achieved. In reality, slabs were likely only partially supported by the subgrade and/or by one to four steel rollers, which undoubtedly influenced their mechanical response. FEM simulations could be used to examine the impact of this partial support, as well as to investigate differences between PC and various SyFRCs (in terms of fiber type and dosage) in relation to cracking load, punching shear capacity, deformation behavior, and crack morphology. Moreover, numerical modeling could allow examination of flexural and circumferential cracks on the slab's bottom surface, which was not accessible during experimental testing. Furthermore, investigating the influence of corner and edge uplift on the effective ground support area of the slab could enable for more accurate analytical calculations. Concluding, validated numerical models would offer deeper insight into the punching shear behavior of tested ground-supported slabs.

• Expanded material study on SyFRC

Future studies should investigate a broader range of macro SyFs types, also including hybrid reinforcement systems (e.g., macro + micro SyFs, or SyFs combined with SFs), alongside with varying fiber dosages, concrete compositions, and strengths. Such investigations would be particularly valuable for validating the findings of this study, especially regarding fiber contribution to the punching shear capacity and influence on the critical control section location. Additionally, comparative studies involving SFRC slabs and slabs reinforced with traditional reinforcement (e.g., wire mesh) would provide meaningful data on the influence of reinforcement type on punching shear behavior.

• Behavior under diverse loading conditions

Research on the structural response of SyFRC slabs subjected to non-central loadings (e.g., edge and corner loads), varied load distributions (e.g., multiple point loads, line loads, or uniformly distributed loads), different loading areas, and load types (e.g., dynamic or fatigue loading) would allow for a broader perspective and more comprehensive conclusions. Given that industrial slabs are often exposed to repetitive and dynamic actions, resulting from forklift traffic and impact from dropped goods, and that SyFs significantly improve concrete fracture energy, such tests would be especially valuable.

• Influence of subgrade conditions

Investigating the effect of different modulus of subgrade reaction, soil types, subgrade thicknesses, and layering on the structural response of ground-supported slabs would contribute significantly to enhance the understanding of slab-subsoil interaction. In particular, studying slabs subjected to non-uniform support conditions, such as partial support by compacted and loose soils, is of high practical relevance, as such conditions are frequently encountered in situ applications and can critically affect slab's capacity.

• Larger-scale testing on natural subbases

Testing slabs with dimensions closer to in situ applications, placed on natural subbase, would enable the analysis of size effects and ground pressure distribution on load-deflection response, crack morphology, failure modes, and punching cone characteristics. Such large-scale tastings are essential for validating laboratory-scale results.

• Improved measurement and monitoring techniques

Future experimental campaigns should incorporate advanced measurement systems, such as acoustic emission sensors, strain gauges, Digital Image Correlation, or fiber optic sensing to enhance the monitoring of cracking loads, deformations, and crack propagation. These technologies would allow for more accurate and continuous tracking of the slabs' structural response during testing.

In conclusion, while the findings presented in this dissertation provide a valuable foundation for understanding the structural behavior of SyFRC ground-supported slabs, extending the research along the above directions would enable the validation and generalization of drawn conclusions. This, in turn, would support the development of universally applicable design guidelines and standards for SyFRC ground slab construction.

10. BIBLIOGRAPHY

- [1] B. Nowogońska and M. Mielczarek, "Renovation management method in neglected buildings," *Sustainability*, vol. 13, no. 2, pp. 1–20, 2021, doi: 10.3390/su13020929.
- [2] B. Nowogońska, "Influence of the Rate of Aging Hazards of Components on the Building Degradation Process," in *2nd International Conference on Durability, Repair and Maintanance of Structures*, 2025, pp. 3–14, doi: 10.1007/978-3-031-96476-3 1.
- [3] A. Thomsen, F. Schultmann, and N. Kohler, "Deconstruction, demolition and destruction," *Building Research and Information*, vol. 39, no. 4, pp. 327–332, 2011, doi: 10.1080/09613218.2011.585785.
- [4] J. Blazy, Ł. Drobiec, and P. Wolka, "Projektowanie fibrobetonowych posadzek na guncie," in *XXXVIII Ogólnopolskie Warsztaty Pracy Projektanta Konstrukcji, Wisła, 9-12 kwietnia 2024*, 2024, pp. 543–548.
- [5] B. Sadowska-Buraczewska and I. Skrzypczak, "Reinforced Concrete Beams Made of High-Performance Recycled Aggregate with Use Steel Fibre," *IOP Conference Series: Materials Science and Engineering*, vol. 471, no. 5, p. 052021, 2019, doi: 10.1088/1757-899X/471/5/052021.
- [6] N. Randl, T. Mészöly, and P. Harsányi, "Load Bearing Behaviour of slender UHPC Beam Members in Shear," in *Proceedings of Hipermat 2016 4th International Symposium on Ultra-High Performance Concrete and High Performance Construction Materials Kassel*, 2016, pp. 1–8.
- [7] A. H. A. Raheem, M. Mahdy, and A. A. Mashaly, "Mechanical and fracture mechanics properties of ultra-high-performance concrete," *Construction and Building Materials*, vol. 213, pp. 561–566, 2019, doi: 10.1016/j.conbuildmat.2019.03.298.
- [8] S. Fröhlich, J. Wurst, and B. Middendorf, "Influence of Compaction on the Position Stability of Fibres in flowable UHPC," in *Proceedings of Hipermat 2016 4th International Symposium on Ultra-High Performance Concrete and High Performance Construction Materials Kassel*, 2016, pp. 1–8.
- [9] M. A. Glinicki, "Beton ze zbrojeniem strukturalnym," in XXV Ogólnopolskie Warsztaty Pracy Projektanta Konstrukcji, Szczyrk, 10-13 marca 2010, 2010, pp. 279–308.
- [10] T. Ponikiewski and J. Gołaszewski, "Wpływ zawartości włókien stalowych na ich rozkład w elementach z fibrobetonu samozagęszczalnego," in *Monografie technologii betonu: VII Konferencja Dni Betonu, Wisła, 8-10 października 2012*,

- 2012, pp. 1–9.
- [11] J. Blazy and Ł. Drobiec, "Punching Shear Behavior of FRC Ground Slabs," in *BEFIB 2024: Supplementary Conference Proceedings Book*, 2024, pp. 267–275.
- [12] Z. Bonić, E. Zlatanović, N. Davidović, N. Romić, and N. Marinković, "Proposal of modification of Eurocode 2 in terms of calculation of the punching shear capacity of RC column footings," *Facta Universitatis. Architecture and Civil Engineering*, vol. 19, no. 2, pp. 141–153, 2021, doi: 10.2298/FUACE211130011B.
- [13] A. El-said, A. F. Deifalla, S. E. A. S. Yousef, T. A. El-Sayed, M. Tawfik, and N. M. Ayash, "Code provisions evaluation for the punching shear capacity of R.C footings without reinforcement for punching shear," *Case Studies in Construction Materials*, vol. 18, p. e02182, 2023, doi: 10.1016/j.cscm.2023.e02182.
- [14] I. Löfgren, "Fibre-reinforced Concrete for Industrial Construction a fracture mechanics approach to material testing and structural analysis," Chalmers University of Technology, Göteborg, 2005.
- [15] FIB, "Model Code for Concrete Structures 2010, Volume 1." 2010, doi: 10.1002/9783433604090.
- [16] A. Hillerborg, "Analysis of fracture by means of the fictitious crack model, particularly for fibre reinforced concrete," *International Journal of Cement Composites*, vol. 2, no. 4, pp. 177–184, 1980.
- [17] A. Hillerborg, M. Modéer, and P.-E. Petersson, "Analysis of crack formation and crack growth in concrete by means of fracture mechanics and finite elements," *Cement and Concrete Research*, vol. 6, no. 6, pp. 773–781, 1976, doi: 10.1016/0008-8846(76)90007-7.
- [18] Z. P. Bažant and B. H. Oh, "Crack band theory for fracture of concrete," *Materials and Structures*, vol. 16, pp. 155–177, 1983, doi: 10.1007/BF02486267.
- [19] O. Sucharda, M. Pająk, T. Ponikiewski, and P. Konecny, "Identification of mechanical and fracture properties of self-compacting concrete beams with different types of steel fibres using inverse analysis," *Construction and Building Materials*, vol. 138, pp. 263–275, May 2017, doi: 10.1016/j.conbuildmat.2017.01.077.
- [20] J. Skoček and H. Stang, "Inverse analysis of the wedge-splitting test," *Engineering Fracture Mechanics*, vol. 75, no. 10, pp. 3173–3188, 2008, doi: 10.1016/j.engfracmech.2007.12.003.
- [21] S. J. Stephen, B. Raphael, R. Gettu, and S. Jose, "Determination of the tensile constitutive relations of fiber reinforced concrete using inverse analysis," *Construction and Building Materials*, vol. 195, pp. 405–414, 2019, doi: 10.1016/j.conbuildmat.2018.11.014.
- [22] P. K. Juhasz, "The effect of synthetic fibre reinforcement on the fracture energy of the concrete," Budapest University of Technology and Economics, Budapest, 2018.
- [23] H. M. Westergaard, "Stresses in Concrete Pavements Computed by Theoretical Analysis," *Public Road*, vol. 7, no. 2, pp. 25–35, 1926.
- [24] P. Hajduk, *Projektowanie i ocena techniczna betonowych podłóg przemysłowych*, 2nd ed. Warszawa: Państwowe Wydawnictwo Naukowe, 2018.
- [25] JSCE-SF4, "Methods of tests for flexural strength and flexural toughness of fiber

- reinforced concrete." 1984.
- [26] W. A. Elsaigh, "Steel Fiber Reinforced Concrete Ground Slabs. A comparative evaluation of plain and steel fiber reinforced concrete ground slabs," University of Pretoria, Pretoria, 2001.
- [27] L. Shentu, D. Jiang, and C.-T. T. Hsu, "Load-Carrying Capacity for Concrete Slabs on Grade," *Journal of Structural Engineering*, vol. 123, no. 1, pp. 95–103, Jan. 1997, doi: 10.1061/(ASCE)0733-9445(1997)123:1(95).
- [28] The Concrete Society, "Technical Report 34. Concrete industrial ground floors. A guide to design and construction." 2016.
- [29] PN-EN 14651+A1:2007, "Test method for metallic fibre concrete Measuring the flexural tensile strength (limit of proportionality (LOP), residual)." 2007.
- [30] PN-EN 1992-1-1:2008, "Eurocode 2: Design of concrete structures Part 1-1: General rules and rules for buildings." 2008.
- [31] M. Gołdyn, "O propozycji zmian dotyczących obliczania fundamentów na przebicie, wynikającej z prac nad drugą generacją norm europejskich," *Inżynieria i Budownictwo*, no. 5, pp. 1–10, 2018.
- [32] PN-B-03264:2002, "Konstrukcje betonowe, żelbetowe i sprężone Obliczenia statyczne i projektowanie." 2002.
- [33] PN-EN 1992-1-1:2024-05, "Eurocode 2 Design of concrete structures Part 1-1: General rules and rules for buildings, bridges and civil engineering structures." 2024.
- [34] K. Nepelski, "Wyznaczanie krytycznego obwodu kontrolnego w obliczeniach przebicia stopy fundamentowej wg EC2," *Materiały Budowlane*, vol. 3, no. 511, pp. 58–60, 2015, doi: 10.15199/33.2015.03.18.
- [35] M. A. Knauff and P. Knyziak, "Prosta metoda sprawdzania fundamentów ze względu na przebicie," *Przegląd Budowlany*, vol. 84, no. 12, pp. 19–23, 2013.
- [36] O. Sucharda, M. Smirakova, J. Vaskova, P. Mateckova, J. Kubosek, and R. Cajka, "Punching Shear Failure of Concrete Ground Supported Slab," *International Journal of Concrete Structures and Materials*, vol. 12, no. 1, p. 36, 2018, doi: 10.1186/s40069-018-0263-6.
- [37] European Concrete Platform ASBL., *Eurocode 2 Commentary*. Brussels: European Concrete Platform ASBL, 2017.
- [38] PN-EN 206+A2:2021-08, "Concrete Specification, performance, production and conformity." 2021.
- [39] PN-EN 12390-3:2019-07, "Testing hardened concrete Part 3: Compressive strength of test specimens." 2019.
- [40] T. Urban, M. Gołdyn, and Ł. Krawczyk, "Badanie wytrzymałości na rozciąganie fibrobetonu z mikrozbrojeniem," *Materiały Budowlane*, vol. 613, no. 9, pp. 1–4, 2023, doi: 10.15199/33.2023.09.01.
- [41] Discrete construction. Civil Engineering Portal, "Comparative stress-strain curve of Steel Fiber Reinforced Concrete versus plain concrete." https://discreteconstruction.com/steel-fiber-reinforced-concrete-properties/ (accessed Jul. 06, 2025).
- [42] Japan Society of Civil Engineers, "Recommendations for Design and Construction of High Performance Fiber Reinforced Cement Composites with Multiple Fine Cracks (HPFRCC)." 2008.

- [43] G. Park, G. Park, J. Park, N. Lee, and S. Kim, "Residual Tensile Properties and Explosive Spalling of High-Performance Fiber-Reinforced Cementitious Composites Exposed to Thermal Damage," *Materials*, vol. 14, p. 1608, 2021, doi: doi.org/10.3390/ma14071608.
- [44] D. Wang, X. Wang, L. Qiu, H. Ye, N. Maimaitituersun, and B. Han, "Effect of nickel-coated carbon nanotubes on the tensile behaviors of ultra-high performance concrete (UHPC): insights from experiments and molecular dynamic simulations," *Journal of Materials Science*, vol. 58, no. 45, pp. 17225–17240, 2023, doi: 10.1007/s10853-023-09105-y.
- [45] J. Nilimaa and R. Nilforoush, "A Direct Tensile Strength Testing Method for Concrete from Existing Structures," *CivilEng*, vol. 4, no. 1, pp. 333–344, 2023, doi: 10.3390/civileng4010019.
- [46] GB/T 50081-2019, "Standard for test methods of concrete physical and mechanical properties." 2019.
- [47] CECS 13-2009, "Standard test methods for fiber reinforced concrete." 2009.
- [48] ASTM C496-96, "Standard test method for splitting tensile strength of cylindrical concrete specimens." 1996.
- [49] PN-EN 12390-6:2024-04, "Testing hardened concrete Part 6: Splitting tensile strength of test specimens." 2024.
- [50] Geotechnical equipment, "Splitting tensile device." https://geotechnical-equipment.com/product/splitting-tensile-device/ (accessed Oct. 29, 2024).
- [51] Geo engineer, "Splitting Tensile Strength Test (Brazilian)." https://www.geoengineer.org/education/laboratory-testing/splitting-tensile-strength-test-brazilian (accessed Oct. 29, 2024).
- [52] E. Brühwiler and F. H. Wittmann, "The wedge splitting test, a new method of performing stable fracture mechanics tests," *Engineering Fracture Mechanics*, vol. 35, no. 1–3, pp. 117–125, 1990, doi: 10.1016/0013-7944(90)90189-N.
- [53] I. Löfgren, "The wedge splitting test a test method for assessment of fracture parameters of FRC?," in *Fracture Mechanics of Concrete Structures FraMCoS-5, Vail, USA*, 2004, pp. 1155–1162.
- [54] L. Østergaard, "Early-Age Fracture Mechanics And Cracking of Concrete," Technical University of Denmark, 2003.
- [55] L. Segura-Castillo, R. Monte, and A. D. de Figueiredo, "Characterisation of the tensile constitutive behaviour of fibre-reinforced concrete: A new configuration for the Wedge Splitting Test," *Construction and Building Materials*, vol. 192, pp. 731–741, 2018, doi: 10.1016/j.conbuildmat.2018.10.101.
- [56] L. Segura-Castillo, R. Monte, and A. D. de Figueiredo, "New Test for the Characterization of the Tensile Constitutive Behaviour of FRC," in *High Tech Concrete: Where Technology and Engineering Meet*, D. Hordijk and M. Luković, Eds. Cham: Springer International Publishing, 2018, pp. 382–389.
- [57] J. Blazy and Ł. Drobiec, "Digital image correlation technique versus traditional measurement methods on the example of fiber reinforced concrete tests," *Inżynieria i Budownictwo*, no. 9–10, pp. 504–511, 2023, doi: 10.5604/01.3001.0053.8876.
- [58] J. Blazy, K. Grzyb, and Ł. Drobiec, "Comparative study of results from clip gauges, LVDTs, and DIC technique for PFRC three-point bending and splitting

- tensile test," in Next generation of concrete engineering for post-pandemic Europe. Conference proceedings, M. Salamak, Ed. nbi media, 2022, pp. 477–590.
- [59] J. Blazy, K. Grzyb, and J. Zając, "Comparative study of uniaxial, flexural, and splitting tensile behaviour of polymer fiber-reinforced concrete," in *Proceedings for the 6th fib International Congress 2022, Oslo, Norway, June 12-16, 2022*, S. Stokkeland and H. Braarud, Eds. Oslo: Novus Press, 2022, pp. 414–423.
- [60] J. Blazy and Ł. Drobiec, "Charakterystyka porównawcza wytrzymałości betonu z dodatkiem włókien polimerowych," *Materiały Budowlane*, vol. 1, no. 9, pp. 46–50, Sep. 2022, doi: 10.15199/33.2022.09.02.
- [61] I. Löfgren, H. Stang, and J. F. Olesen, "The WST method, a fracture mechanics test method for FRC," *Materials and Structures*, vol. 41, no. 1, pp. 197–211, 2008, doi: 10.1617/s11527-007-9231-3.
- [62] M. Prisco, M. G. L. Lamperti, and S. Lapolla, "Double-edge wedge splitting test: preliminary results," *Fracture Mechanics of Concrete and Concrete Structures*, pp. 1579–1586, 2010.
- [63] S. Nunes, M. Pimentel, F. Ribeiro, P. Milheiro-Oliveira, and A. Carvalho, "Estimation of the tensile strength of UHPFRC layers based on non-destructive assessment of the fibre content and orientation," *Cement and Concrete Composites*, vol. 83, pp. 222–238, 2017, doi: 10.1016/j.cemconcomp.2017.07.019.
- [64] PN-EN 12390-05:2019-08, "Testing hardened concrete Part 5: Flexural strength of test specimens." 2019.
- [65] CONTROLS, "High Stiffness Flexural Frame." https://controls-group.com/product/high-stiffness-flexural-frame-200-kn-cap-simplex/ (accessed Oct. 28, 2024).
- [66] RILEM TC 162-TDF, "Test and design methods for steel fibre reinforced concrete. σ-ε-design method. Final Recommendation," *Materials and Structures*, vol. 36, no. 262. pp. 560–567, 2003, doi: 10.1617/14007.
- [67] RILEM TC 162-TDF, "Test and design methods for steel fibre reinforced concrete, final recommendations," *Materials and Structures*, vol. 35, no. 9, pp. 579–582, 2002.
- [68] The Concrete Society, "Technical Report 34. Concrete industrial ground floors. A guide to design and construction." 2003.
- [69] F. Legeron and P. Paultre, "Prediction of Modulus of Rupture of Concrete," *ACI Materials Journal*, vol. 97, no. 2, pp. 193–200, 2000, doi: 10.14359/823.
- [70] M. A. Glinicki, "Ocena i projektowanie fibrobetonów na podstawie wytrzymałości równoważnej," *Drogi i Mosty*, no. 3, pp. 5–36, 2002.
- [71] R. N. Swamy and P. S. Mangat, "Influence of fiber geometry on the properties of steel fiber reinforced concrete," *Cement and Concrete Research*, vol. 4, no. 3, pp. 451–465, May 1974, doi: 10.1016/0008-8846(74)90110-0.
- [72] J. Blazy, Ł. Drobiec, and P. Wolka, "Flexural tensile strength of concrete with synthetic fibers," *Materials*, vol. 14, no. 16, p. 4428, 2021, doi: 10.3390/ma14164428.
- [73] A. Ilc and Z. Cotič, "Experimentally supported concrete pavement design," in *BEFIB 2024: Supplementary Conference Proceedings Book*, 2024, pp. 174–180.
- [74] J. Blazy and Ł. Drobiec, "Kształtowanie fibrobetonowych płyt na gruncie,"

- *Przegląd Budowlany*, vol. 96, no. 4, pp. 65–70, Aug. 2025, doi: 10.5604/01.3001.0055.2418.
- [75] J. Blazy and Ł. Drobiec, "Kształtowanie fibrobetonowych płyt na guncie," in *X Konferencja Naukowo-Techniczna "Kształtowanie konstrukcji i budowli"*, *Rzeszów, 4-6 czerwca 2025*, 2025, pp. 12–13.
- [76] Britpave. The British Cementitious Paving Association, "Concrete Hardstanding Design Guidance. Guidelines for the design of concrete hardstandings." 2023.
- [77] Interpave. The precast concrete paving and kerb association, "Heavy Duty Pavements. The structural design of heavy duty pavements for ports and other industries." 2007.
- [78] ACI 360R-10, "Design of Slabs-on-Ground." 2010.
- [79] M. Hallgren, S. Kinnunen, and B. Nylander, "Punching shear tests on column footings," *Nordic Concrete Research*, vol. 21, no. 1, pp. 1–22, 1998.
- [80] FIB, "Model Code for Concrete Structures 2010, Volume 2." 2010, doi: 10.1002/9783433604090.
- [81] M. Goldyn, "Application of the Critical Shear Crack Theory for calculation of the punching shear capacity of lightweight aggregate concrete slabs," *Archives of Civil Engineering*, vol. 69, no. 1, pp. 55–70, 2023, doi: 10.24425/ace.2023.144159.
- [82] FIB, "Bulletin 105. Fibre Reinforced Concrete. State of the art report." 2022, doi: 10.35789/fib.BULL.0105.
- [83] FIB, "Model Code for Concrete Structures 2020." 2020.
- [84] ASTM C1018-94, "Standard Test Method for Flexural Toughness and First-Crack Strength of Fiber-Reinforced Concrete (Using Beam With Third-Point Loading)." 1994.
- [85] ASTM C1609-05, "Standard Test Method for Flexural Performance of Fiber-Reinforced Concrete (Using Beam With Third-Point Loading)." 2005.
- [86] ASTM C1550-20, "Standard Test Method for Flexural Toughness of Fiber Reinforced Concrete (Using Centrally Loaded Round Panel)." 2020.
- [87] PN-EN 14488-5:2008, "Testing sprayed concrete. Determination of energy absorption capacity of fibre reinforced slab specimens." 2008.
- [88] S. Chen, "Strength of steel fibre reinforced concrete ground slabs," in *Proceedings* of the Institution of Civil Engineers Structures and Buildings, 2004, vol. 157, no. 2, pp. 157–163, doi: 10.1680/stbu.2004.157.2.157.
- [89] J. Blazy and Ł. Drobiec, "Wpływ położenia krytycznego obwodu kontrolnego oraz włókien na nośność na przebicie posadzek przemysłowych," *Materiały Budowlane*, vol. 10, no. 626, pp. 145–148, 2024.
- [90] PN-EN 12390-13:2021-12, "Testing hardened concrete Part 13: Determination of secant modulus of elasticity in compression." 2021.
- [91] ACI 318-19, "Building Code Requirements for Structural Concrete." 2019.
- [92] BS 8110-1: 1997, "Structural use of concrete Part 1: Code of practice for design and construction." 1997.
- [93] J. Gołaszewski, "Technologia betonu za progiem XXI wieku," *Budownictwo. Technologie. Architektura*, pp. 54–60, 2020.
- [94] R. Geryło and B. Nowogońska, "Wymogi zrównoważonego rozwoju a renowacja obiektów zabytkowych," *Przegląd Budowlany*, vol. 95, no. 1–2, pp. 24–27, 2024,

- doi: 10.5604/01.3001.0054.3600.
- [95] I. Skrzypczak, W. Radwański, and T. Pytlowany, "Durability vs technical the usage properties of road pavements," *E3S Web of Conferences*, vol. 45, p. 00082, 2018, doi: 10.1051/e3sconf/20184500082.
- [96] Ł. Drobiec and J. Blazy, "Współczesne niemetaliczne zbrojenia rozproszone stosowane w konstrukcjach betonowych," *Izolacje*, vol. 25, no. 5, pp. 70–84, 2020.
- [97] J. Blazy and Ł. Drobiec, "Wpływ włókien polipropylenowych na ściskanie i rozciąganie betonu w świetle norm PN-EN 206-1 i PN-EN 14651," *Inżynieria i Budownictwo*, vol. 8, pp. 391–396, 2021.
- [98] J. Blazy and Ł. Drobiec, "Badanie właściwości mechanicznych betonu ze zbrojeniem rozproszonym z włókien syntetycznych cz.2," *Izolacje*, vol. 6, pp. 78–83, 2021.
- [99] J. Blazy and Ł. Drobiec, "Analiza wyników badań fibrobetonu z włóknami polimerowymi," *Inżynieria i Budownictwo*, vol. 9–10, pp. 477–481, 2021.
- [100] S. Yin, R. Tuladhar, F. Shi, M. Combe, T. Collister, and N. Sivakugan, "Use of macro plastic fibres in concrete: A review," *Construction and Building Materials*, vol. 93, pp. 180–188, 2015, doi: 10.1016/j.conbuildmat.2015.05.105.
- [101] T. Zych and W. Krasodomski, "Włókna poliolefinowe stosowane w kompozytach cementowych metody wytwarzania, właściwości i zastosowanie," *Czasopismo Techniczne. Budownictwo.*, vol. 3, pp. 155–178, 2016, doi: 10.4467/2353737XCT.16.223.5972.
- [102] A. Mohajerani *et al.*, "Amazing types, properties, and applications of fibres in construction materials," *Materials*, vol. 12, no. 16, p. 2513, 2019, doi: 10.3390/ma12162513.
- [103] S. M. Hejazi, M. Sheikhzadeh, S. M. Abtahi, and A. Zadhoush, "A simple review of soil reinforcement by using natural and synthetic fibers," *Construction and Building Materials*, vol. 30, pp. 100–116, 2012, doi: 10.1016/j.conbuildmat.2011.11.045.
- [104] PN-EN 14889-2:2007, "Fibres for concrete Part 2: Polymer fibres Definitions, specifications and conformity." 2007.
- [105] M. H. Wan Ibrahim *et al.*, "Compressive and flexural strength of concrete containing palm oil biomass clinker and polypropylene fibres," *IOP Conference Series: Materials Science and Engineering*, vol. 271, no. 1, p. 012011, 2017, doi: 10.1088/1757-899X/271/1/012011.
- [106] Z. Hongbo, Z. Haiyun, and G. Hongxiang, "Characteristics of ductility enhancement of concrete by a macro polypropylene fiber," *Results in Materials*, p. 100087, 2020, doi: 10.1016/j.rinma.2020.100087.
- [107] A. El-Newihy, P. Azarsa, R. Gupta, and A. Biparva, "Effect of Polypropylene Fibers on Self-Healing and Dynamic Modulus of Elasticity Recovery of Fiber Reinforced Concrete," *Fibers*, vol. 6, no. 1, p. 9, Feb. 2018, doi: 10.3390/fib6010009.
- [108] V. M. Sounthararajan, "Effect of Accelerated Curing on the Furnace Slag Based Polypropylene Fiber Reinforced Concrete," *Advanced Materials Research*, vol. 1150, no. 11, pp. 91–102, 2018, doi: 10.4028/www.scientific.net/AMR.1150.91.
- [109] V. Afroughsabet, L. Biolzi, and T. Ozbakkaloglu, "High-performance fiber-reinforced concrete: a review," *Journal of Materials Science*, vol. 51, no. 14, pp.

- 6517–6551, 2016, doi: 10.1007/s10853-016-9917-4.
- [110] L. Domagała, "Modification of properties of structural lightweight concrete with steel fibres," *Journal of Civil Engineering and Management*, vol. 17, no. 1, pp. 36–44, 2011, doi: 10.3846/13923730.2011.553923.
- [111] F. Shi, T. M. Pham, H. Hao, and Y. Hao, "Post-cracking behaviour of basalt and macro polypropylene hybrid fibre reinforced concrete with different compressive strengths," *Construction and Building Materials*, vol. 262, p. 120108, 2020, doi: 10.1016/j.conbuildmat.2020.120108.
- [112] N. Buratti, C. Mazzotti, and M. Savoia, "Post-cracking behaviour of steel and macro-synthetic fibre-reinforced concretes," *Construction and Building Materials*, vol. 25, no. 5, pp. 2713–2722, 2011, doi: 10.1016/j.conbuildmat.2010.12.022.
- [113] M. N. Soutsos, T. T. Le, and A. P. Lampropoulos, "Flexural performance of fibre reinforced concrete made with steel and synthetic fibres," *Construction and Building Materials*, vol. 36, pp. 704–710, 2012, doi: 10.1016/j.conbuildmat.2012.06.042.
- [114] S. Kakooei, H. M. Akil, M. Jamshidi, and J. Rouhi, "The effects of polypropylene fibers on the properties of reinforced concrete structures," *Construction and Building Materials*, vol. 27, no. 1, pp. 73–77, 2012, doi: 10.1016/j.conbuildmat.2011.08.015.
- [115] M. Pająk and T. Ponikiewski, "Effect of the shape of steel fibers on the mechanical properties of reinforced self-compacting concrete," *Cement, Wapno, Beton*, no. 6, pp. 335–342, 2013, [Online]. Available: https://www.scopus.com/inward/record.uri?eid=2-s2.0-84903526450&partnerID=40&md5=2d2e1daf4375bcefdd7b51e3ec5f657c.
- [116] R. V. Balendran, F. P. Zhou, A. Nadeem, and A. Y. T. Leung, "Influence of steel fibres on strength and ductility of normal and lightweight high strength concrete," *Building and Environment*, vol. 37, no. 12, pp. 1361–1367, 2002, doi: 10.1016/S0360-1323(01)00109-3.
- [117] I. Markovic, "High-Performance Hybrid-Fibre Concrete. Development and Utilisation," Technische Universiteit Delft, Delft, 2006.
- [118] D. Altalabani, D. K. H. Bzeni, and S. Linsel, "Mechanical properties and load deflection relationship of polypropylene fiber reinforced self-compacting lightweight concrete," *Construction and Building Materials*, vol. 252, p. 119084, 2020, doi: 10.1016/j.conbuildmat.2020.119084.
- [119] O. Gencel, C. Ozel, W. Brostow, and G. Martínez-Barrera, "Mechanical properties of self-compacting concrete reinforced with polypropylene fibres," *Materials Research Innovations*, vol. 15, no. 3, pp. 216–225, 2011, doi: 10.1179/143307511X13018917925900.
- [120] J. Yang, R. Wang, and Y. Zhang, "Influence of dually mixing with latex powder and polypropylene fiber on toughness and shrinkage performance of overlay repair mortar," *Construction and Building Materials*, vol. 261, p. 120521, 2020, doi: 10.1016/j.conbuildmat.2020.120521.
- [121] Bautech, "Bautech. Industrial. Systems & products. Hardened concrete floors. Reinforcing fibres. Baucon," 2020. http://www.bautech.eu/en/products/concrete-floor/baucon.html (accessed Sep. 18, 2020).
- [122] S. Fallah and M. Nematzadeh, "Mechanical properties and durability of high-

- strength concrete containing macro-polymeric and polypropylene fibers with nano-silica and silica fume," *Construction and Building Materials*, vol. 132, pp. 170–187, 2017, doi: 10.1016/j.conbuildmat.2016.11.100.
- [123] R. V. Velasco, R. D. T. Filho, E. M. R. Fairbairn, P. R. L. Lima, and R. Neumann, "Spalling and stress-strain behaviour of polypropylene fibre reinforced hpc after exposure to high temperatures," in *6th RILEM Symposium on Fibre-Reinforced Concretes BEFIB2004*, 2004, pp. 699–708.
- [124] Ł. Drobiec and J. Blazy, "Właściwości fibrobetonu określane w badaniach normowych test wytrzymałości na ściskanie oraz test trzypunktowego zginania," *Materiały Budowlane*, vol. 9, no. 613, pp. 5–8, 2023, doi: 10.15199/33.2023.09.02.
- [125] J. Blazy and Ł. Drobiec, "Badanie właściwości mechanicznych betonu ze zbrojeniem rozproszonym z włókien syntetycznych cz.1," *Izolacje*, vol. 4, pp. 74–78, 2021.
- [126] K. Behfarnia and A. Behravan, "Application of high performance polypropylene fibers in concrete lining of water tunnels," *Materials and Design*, vol. 55, pp. 274–279, 2014, doi: 10.1016/j.matdes.2013.09.075.
- [127] R. Pol, V. Kumar, C. Kumar, A. Prakash, and P. V. V. S. S. R. Krishna, "Strength Characteristics of Fibrous Self Curing Concrete Using Super Absorbent Polymer," in *National Conference on Recent Advances in Civil Engineering*, 2019, pp. 5–9.
- [128] M. G. Chorzepa and M. Masud, "Performance of multiscale, including nanoscale, fibres in concrete," *Emerging Materials Research*, vol. 6, no. 1, pp. 198–209, 2017, doi: 10.1680/jemmr.16.00020.
- [129] H. Mashhadban, S. Soleimani, and M. Ali, "Prediction and modeling of mechanical properties in fiber reinforced self-compacting concrete using particle swarm optimization algorithm and artificial neural network," *Construction and Building Materials*, vol. 119, pp. 277–287, 2016, doi: 10.1016/j.conbuildmat.2016.05.034.
- [130] V. M. Sounthararajan, S. Thirumurugan, and A. Sivakumar, "Reinforcing Efficiency of Crimped Profile of Polypropylene Fibres on the Cementitious Matrix," *Research Journal of Applied Sciences, Engineering and Technology*, vol. 6, no. 14, pp. 2662–2667, 2013.
- [131] S. Ismail and M. Ramli, "Effects of Adding Fibre on Strength and Permeability of Recycled Aggregate Concrete Containing Treated Coarse RCA," *International Journal of Civil and Environmental Engineering*, vol. 8, no. 8, pp. 918–924, 2014.
- [132] J. Li, J. Niu, C. Wan, X. Liu, and Z. Jin, "Comparison of flexural property between high performance polypropylene fiber reinforced lightweight aggregate concrete and steel fiber reinforced lightweight aggregate concrete," *Construction and Building Materials*, vol. 157, pp. 729–736, 2017, doi: 10.1016/j.conbuildmat.2017.09.149.
- [133] A. M. de Luna *et al.*, "Experimental mechanical characterization of steel and polypropylene fiber reinforced concrete," *Revista Técnica de la Facultad de Ingeniería Universidad del Zulia*, vol. 37, no. 2, pp. 106–115, 2014.
- [134] A. Richardson and K. Coventry, "Dovetailed and hybrid synthetic fibre concrete-Impact, toughness and strength performance," *Construction and Building Materials*, vol. 78, pp. 439–449, 2015, doi: 10.1016/j.conbuildmat.2015.01.003.

- [135] M. Pająk and T. Ponikiewski, "The laboratory investigation on the influence of the polypropylene fibres on selected mechanical properties of hardened self-compacting concrete," *Architecture Civil Engineering Environment*, vol. 8, no. 3, pp. 69–78, 2015.
- [136] M. Pająk and T. Ponikiewski, "Flexural behavior of self-compacting concrete reinforced with different types of steel fibers," *Construction and Building Materials*, vol. 47, pp. 397–408, Oct. 2013, doi: 10.1016/j.conbuildmat.2013.05.072.
- [137] J. Blazy, Ł. Drobiec, and P. Wolka, "Mechanical properties of polymer fibre reinforced concrete in the light of various standards," *Archives of Civil Engineering*, no. 2, pp. 323–342, 2024, doi: 10.24425/ace.2024.149866.
- [138] Ł. Drobiec and J. Blazy, "Badanie właściwości mechanicznych betonu ze zbrojeniem rozproszonym z włókien syntetycznych cz.3," *Izolacje*, vol. 7/8, pp. 102–106, 2021.
- [139] J. Jeon, W. Kim, C. Jeon, and J. Kim, "Processing and Mechanical Properties of Macro Polyamide Fiber Reinforced Concrete," *Materials*, vol. 7, no. 12, pp. 7634–7652, 2014, doi: 10.3390/ma7127634.
- [140] F. S. Khalid, J. M. Irwan, M. H. Wan Ibrahim, N. Othman, and S. Shahidan, "Splitting tensile and pullout behavior of synthetic wastes as fiber-reinforced concrete," *Construction and Building Materials*, vol. 171, pp. 54–64, 2018, doi: 10.1016/j.conbuildmat.2018.03.122.
- [141] M. J. Hasan, M. Afroz, and H. M. I. Mahmud, "An Experimental Investigation on Mechanical Behavior of Macro Synthetic Fiber Reinforced Concrete," *International Journal of Civil & Environmental Engineering*, vol. 11, no. 3, pp. 18–23, 2011.
- [142] S. Y. Ghanem, J. Bowling, and Z. Sun, "Mechanical Properties of Hybrid Synthetic Fiber Reinforced Self-Consolidating Concrete," *Composites Part C: Open Access*, vol. 5, p. 100154, 2021, doi: 10.1016/j.jcomc.2021.100154.
- [143] I. Sadrinejad, R. Madandoust, and M. M. Ranjbar, "The mechanical and durability properties of concrete containing hybrid synthetic fibers," *Construction and Building Materials*, vol. 178, pp. 72–82, 2018, doi: 10.1016/j.conbuildmat.2018.05.145.
- [144] M. Saidani, D. Saraireh, and M. Gerges, "Behaviour of different types of fibre reinforced concrete without admixture," *Engineering Structures*, vol. 113, pp. 328–334, 2016, doi: 10.1016/j.engstruct.2016.01.041.
- [145] M. Hsie, C. Tu, and P. S. Song, "Mechanical properties of polypropylene hybrid fiber-reinforced concrete," *Materials Science and Engineering A*, vol. 494, no. 1–2, pp. 153–157, 2008, doi: 10.1016/j.msea.2008.05.037.
- [146] M. A. Othuman Mydin *et al.*, "Mechanical, durability and thermal properties of foamed concrete reinforced with synthetic twisted bundle macro-fibers," *Frontiers in Materials*, vol. 10, pp. 1–13, Mar. 2023, doi: 10.3389/fmats.2023.1158675.
- [147] J. J. Kim, C. Park, S.-W. Lee, S. Lee, and J. Won, "Effects of the geometry of recycled PET fiber reinforcement on shrinkage cracking of cement-based composites," *Composites Part B: Engineering*, vol. 39, no. 3, pp. 442–450, 2008, doi: 10.1016/j.compositesb.2007.05.001.

- [148] I. M. G. Bertelsen, L. M. Ottosen, and G. Fischer, "Influence of fibre characteristics on plastic shrinkage cracking in cement-based materials: A review," *Construction and Building Materials*, vol. 230, p. 116769, 2020, doi: 10.1016/j.conbuildmat.2019.116769.
- [149] P. Soroushian, J. Plasencia, and S. Ravanbakhsh, "Assessment of Reinforcing Effects of Recycled Plastic and Paper in Concrete," *ACI Materials Journal*, vol. 100, no. 3, pp. 203–207, 2003, doi: 10.14359/12620.
- [150] N. Yousefieh, A. Joshaghani, E. Hajibandeh, and M. Shekarchi, "Influence of fibers on drying shrinkage in restrained concrete," *Construction and Building Materials*, vol. 148, pp. 833–845, 2017, doi: 10.1016/j.conbuildmat.2017.05.093.
- [151] N. Banthia, P. Gupta, and C. Yan, "Impact resistance of fiber reinforced wet-mix shotcrete Part 1: Beam tests," *Materials and Structures/Materiaux et Constructions*, vol. 32, no. 8, pp. 563–570, 1999, doi: 10.1007/bf02480490.
- [152] N. Banthia, P. Gupta, and C. Yan, "Impact resistance of fiber reinforced wet-mix shotcrete Part 2: Plate tests," *Materials and Structures/Materiaux et Constructions*, vol. 32, no. 9, pp. 643–650, 1999, doi: 10.1007/bf02481702.
- [153] S. Mindess, N. Banthia, and C. Yan, "The fracture toughness of concrete under impact loading," *Cement and Concrete Research*, vol. 17, no. 2, pp. 231–241, 1987, doi: 10.1016/0008-8846(87)90106-2.
- [154] A. Arslan, "Mixed-mode fracture performance of fibre reinforced concrete under impact loading," *Materials and Structures*, vol. 28, no. 8, pp. 473–478, 1995, doi: 10.1007/BF02473167.
- [155] R. Jain, R. Gupta, M. G. Khare, and A. A. Dharmadhikari, "Use of polypropylene fibre reinforced concrete as a construction material for rigid pavements," *Indian Concrete Journal*, vol. 85, no. 3, pp. 45–53, 2011.
- [156] E. Najaf and H. Abbasi, "Impact resistance and mechanical properties of fiber-reinforced concrete using string and fibrillated polypropylene fibers in a hybrid form," *Structural Concrete*, vol. 24, no. 1, pp. 1282–1295, 2023, doi: 10.1002/suco.202200019.
- [157] D. Y. Yoo and N. Banthia, "Impact resistance of fiber-reinforced concrete A review," *Cement and Concrete Composites*, vol. 104, p. 103389, 2019, doi: 10.1016/j.cemconcomp.2019.103389.
- [158] X. Niu, Q. Zhao, and Y. Nie, "Effect of polypropylene macro-fiber on properties of high-strength concrete at elevated temperatures," *Key Engineering Materials*, vol. 629–630, pp. 284–290, 2015, doi: 10.4028/www.scientific.net/KEM.629-630.284.
- [159] A. Abdelalim, G. Abdelaziz, M. El-Mohr, and G. Salama, "Effect of Aggregate Type on the Fire Resistance of Normal and Self-Compacting Concretes," *Engineering Research Journal*, vol. 122, no. 6, pp. 47–62, 2009.
- [160] É. Lublóy, "The Influence of Concrete Strength on the Effect of Synthetic Fibres on Fire Resistance," *Periodica Polytechnica Civil Engineering*, vol. 62, no. 1, pp. 136–142, Jun. 2017, doi: 10.3311/PPci.10775.
- [161] H.-S. So, "Spalling Prevention of High Performance Concrete at High Temperatures," in *High Performance Concrete Technology and Applications*, H. Özmen and S. Yilmaz, Eds. Rijeka: IntechOpen, 2016, pp. 25–41.
- [162] P. Mehrabi, U. Dackermann, R. Siddique, and M. Rashidi, "A Review on the

- Effect of Synthetic Fibres, Including Macro Fibres, on the Thermal Behaviour of Fibre-Reinforced Concrete," *Buildings*, vol. 14, no. 12, p. 4006, 2024, doi: 10.3390/buildings14124006.
- [163] S. Hun, S. H. Lee, and S. Sugahara, "Spalling prevention measures of high performance concrete," *Magazine of the Korea Concrete Institute*, vol. 17, no. 3, pp. 33–39, 2005.
- [164] M. da S. Magalhães, R. D. Toledo Filho, and E. de M. R. Fairbairn, "Thermal stability of PVA fiber strain hardening cement-based composites," *Construction and Building Materials*, vol. 94, pp. 437–447, 2015, doi: 10.1016/j.conbuildmat.2015.07.039.
- [165] H. Bolat, O. Şimşek, M. Çullu, G. Durmuş, and Ö. Can, "The effects of macro synthetic fiber reinforcement use on physical and mechanical properties of concrete," *Composites Part B: Engineering*, vol. 61, pp. 191–198, 2014, doi: 10.1016/j.compositesb.2014.01.043.
- [166] A. Pietrzak and M. Ulewicz, "The effect of the addition of polypropylene fibres on improvement on concrete quality," *MATEC Web of Conferences*, vol. 183, p. 02011, 2018, doi: 10.1051/matecconf/201818302011.
- [167] Y. Chen, M. S. Waheed, S. Iqbal, M. Rizwan, and S. Room, "Durability Properties of Macro-Polypropylene Fiber Reinforced Self-Compacting Concrete," *Materials*, vol. 17, no. 2, p. 284, 2024, doi: 10.3390/ma17020284.
- [168] Z. Yuan, Y. Jia, and J. Xu, "Study on the Improvement Effect of Polypropylene Fiber on the Mechanical Properties and Freeze-Thaw Degradation Performance of High Fly Ash Content Alkali-Activated Fly Ash Slag Concrete," *Polymers*, vol. 17, no. 2, p. 175, 2025, doi: 10.3390/polym17020175.
- [169] K. E. Ridgley, A. A. Abouhussien, A. A. A. Hassan, and B. Colbourne, "Assessing abrasion performance of self-consolidating concrete containing synthetic fibers using acoustic emission analysis," *Materials and Structures*, vol. 51, no. 5, p. 119, 2018, doi: 10.1617/s11527-018-1247-3.
- [170] S. Etli, S. Cemalgil, and O. Onat, "Properties of Self-Compacting Mortars with Different Contents of Synthetic Macro Fiber," in *6th International Symposium on Innovative Technologies in Engineering and Science*, 2018, pp. 593–602.
- [171] R. Alyousef, "Sustainable Use of Waste Polypropylene Fibres to Enhance the Abrasion and Skid Resistance of Two-Stage Concrete," *Sustainability*, vol. 13, no. 9, p. 5200, 2021, doi: 10.3390/su13095200.
- [172] S.-J. Lee, H. Shin, H. Lee, S.-H. Park, H. Kim, and C. Park, "Effect of Waste PET Fiber on the Mechanical Properties and Chloride Ion Penetration of Emergency Repair Concrete for Road Pavement," *Materials*, vol. 17, no. 21, p. 5352, 2024, doi: 10.3390/ma17215352.
- [173] D. Li and S. Liu, "Macro polypropylene fiber influences on crack geometry and water permeability of concrete," *Construction and Building Materials*, vol. 231, p. 117128, 2020, doi: 10.1016/j.conbuildmat.2019.117128.
- [174] D. M. Carlesso, S. Cavalaro, and A. de la Fuente, "Flexural fatigue of pre-cracked plastic fibre reinforced concrete: Experimental study and numerical modeling," *Cement and Concrete Composites*, vol. 115, p. 103850, 2021, doi: 10.1016/j.cemconcomp.2020.103850.
- [175] P. Kumar Mehta and R. W. Burrows, "Building durable structures in the 21st

- century," Indian Concrete Journal, vol. 75, no. 7, pp. 437–443, 2001.
- [176] P. J. M. Monteiro, S. A. Miller, and A. Horvath, "Towards sustainable concrete," *Nature Materials*, vol. 16, no. 7, pp. 698–699, 2017, doi: 10.1038/nmat4930.
- [177] O. Ozturk and N. Ozyurt, "Effects of Polypropylene Macro Fibers on the Structural Requirements, Cost and Environmental Impact of Concrete Pavements," *Engineering proceedings*, vol. 17, no. 32, pp. 3–4, 2022, doi: doi.org/10.3390/engproc2022017032.
- [178] Rimsa, "Environmental Impact of Polymer-Fiber Reinforced Concrete," 2025. https://rimsa.com/environmental-impact-of-polymer-fiber-reinforced-concrete (accessed Jun. 26, 2025).
- [179] B. Ali, L. A. Qureshi, and R. Kurda, "Environmental and economic benefits of steel, glass, and polypropylene fiber reinforced cement composite application in jointed plain concrete pavement," *Composites Communications*, vol. 22, no. 7, p. 100437, 2020, doi: 10.1016/j.coco.2020.100437.
- [180] I. Hussain, B. Ali, T. Akhtar, M. S. Jameel, and S. S. Raza, "Comparison of mechanical properties of concrete and design thickness of pavement with different types of fiber-reinforcements (steel, glass, and polypropylene)," *Case Studies in Construction Materials*, vol. 13, p. e00429, 2020, doi: 10.1016/j.cscm.2020.e00429.
- [181] M. Małek, M. Jackowski, W. Łasica, and M. Kadela, "Characteristics of Recycled Polypropylene Fibers as an Addition to Concrete Fabrication Based on Portland Cement," *Materials*, vol. 13, no. 8, p. 1827, 2020, doi: 10.3390/ma13081827.
- [182] H. Mohammadhosseini *et al.*, "Durability and thermal properties of prepacked aggregate concrete reinforced with waste polypropylene fibers," *Journal of Building Engineering*, vol. 32, p. 101723, 2020, doi: 10.1016/j.jobe.2020.101723.
- [183] J. Blazy, R. Blazy, and Ł. Drobiec, "Glass Fiber Reinforced Concrete as a Durable and Enhanced Material for Structural and Architectural Elements in Smart City A Review," *Materials*, vol. 15, no. 8, p. 2754, 2022, doi: 10.3390/ma15082754.
- [184] J. Blazy and Ł. Drobiec, "Wpływ zbrojenia rozproszonego na pracę posadzek na gruncie," *Izolacje*, no. 1, pp. 2–9, 2024.
- [185] J. Blazy and Ł. Drobiec, "Praca fibrobetonowych posadzek na gruncie wpływ włókien," *Izolacje*, no. 10, pp. 50–57, 2024.
- [186] M. Aboutalebi, A. M. Alani, J. Rizzuto, and D. Beckett, "Structural behaviour and deformation patterns in loaded plain concrete ground-supported slabs," *Structural Concrete*, vol. 15, no. 1, pp. 81–93, 2014, doi: 10.1002/suco.201300043.
- [187] A. Alani, D. Beckett, and F. Khosrowshahi, "Mechanical behaviour of a steel fibre reinforced concrete ground slab," *Magazine of Concrete Research*, vol. 64, no. 7, pp. 593–604, 2012, doi: doi.org/10.1680/macr.11.00077.
- [188] A. M. Alani and D. Beckett, "Mechanical properties of a large scale synthetic fibre reinforced concrete ground slab," *Construction and Building Materials*, vol. 41, pp. 335–344, 2013, doi: 10.1016/j.conbuildmat.2012.11.043.
- [189] J. R. Roesler, D. A. Lange, S. A. Altoubat, K. A. Rieder, and G. R. Ulreich, "Fracture of plain and fiber-reinforced concrete slabs under monotonic loading," *Journal of Materials in Civil Engineering*, vol. 1561, pp. 452–460, 2004, doi: 10.1061/(ASCE)0899-1561(2004)16.
- [190] J. R. Roesler, S. A. Altoubat, D. A. Lange, K. Rieder, and G. R. Ulreich, "Effect

- of Synthetic Fibers on Structural Behavior of Concrete Slabs-on-Ground," *ACI Materials Journal*, vol. 103, no. 1, pp. 3–10, 2006, doi: 10.14359/15121.
- [191] J. Roesler, "Effect of Macrofibers on Behavior and Performance of Concrete Slabs and Overlays," Illinois, 2018.
- [192] P. H. Bischoff, A. J. Valsangkar, and J. Irving, "Use of Fibers and Welded-Wire Reinforcement in Construction of Slabs on Ground," *Practice Periodical On Structural Design And Construction*, pp. 41–46, 2003, doi: 10.1061/(ASCE)1084-0680(2003)8:1(41).
- [193] F. Shi, T. M. Pham, R. Tuladhar, Z. Deng, S. Yin, and H. Hao, "Comparative performance analysis of ground slabs and beams reinforced with macro polypropylene fibre, steel fibre, and steel mesh," *Structures*, vol. 56, p. 104920, 2023, doi: 10.1016/j.istruc.2023.104920.
- [194] P. Manfredi, F. D. A. Silva, D. Carlos, and T. Cardoso, "On Punching Shear Strength of Steel Fiber-Reinforced Concrete Slabs-on-Ground," *ACI Structural Journal*, vol. 119, no. 4, pp. 185–196, 2022, doi: 10.14359/51734520.
- [195] J. Blazy and R. Blazy, "Polypropylene fiber reinforced concrete and its application in creating architectural forms of public spaces," *Case Studies in Construction Materials*, vol. 14, p. e00549, 2021, doi: 10.1016/j.cscm.2021.e00549.
- [196] J. Blazy, D. Łukasz, and R. Blazy, "Zastosowanie fibrobetonu z włóknami polipropylenowymi w przestrzeniach publicznych," *Izolacje*, vol. 27, no. 6, pp. 128–131, 2022.
- [197] F. Szmatuła and J. Blazy, "Shaping a decorative concrete face for the renovation and modernization of buildings," *Materiały Budowlane*, vol. 1, no. 11, pp. 153–160, 2024, doi: 10.15199/33.2024.11.18.
- [198] J. Blazy, S. Nunes, C. Sousa, and M. Pimentel, "Development of an HPFRC for use in flat slabs," in *Concrete: Improvements and Innovations. RILEM-fib International Symposium on FRC (BEFIB) in 2020*, P. Serna, J. R. Martí-Vargas, A. Llano-Torre, and J. Navarro-Gregori, Eds. Springer, 2021, pp. 209–220.
- [199] J. Blazy, Ł. Drobiec, and R. Blazy, "Zastosowanie betonu zbrojonego włóknami szklanymi do tworzenia elementów konstrukcyjnych oraz form architektonicznych," *Przegląd Budowlany*, no. 5–6, pp. 27–33, 2022.
- [200] M. Musiał and D. Styś, "Posadzki przemysłowe ze zbrojeniem zwykłym lub/i rozproszonym," *Materiały Budowlane*, vol. 6, no. 502, pp. 60–61, 2014.
- [201] W. Drozd and M. Kowalik, "Współczesne posadzki przemysłowe," *Przegląd Budowlany*, vol. 7–8, pp. 34–39, 2014.
- [202] Z. Pająk and M. Wieczorek, "Posadzki przemysłowe," *Nauka i Budownictwo*, vol. 12, pp. 84–89, 2016.
- [203] Z. Pająk and Ł. Drobiec, "Uszkodzenia i naprawy betonowych podkładów posadzek przemysłowych," in XXIII Ogólnopolskie Warsztaty Pracy Projektanta Konstrukcji, Szczyrk, 5-8 marca 2008, 2008, pp. 1–58.
- [204] P. Hajduk, "Przyczyny powstawania wad i uszkodzeń w podłogach przemysłowych," *Przegląd Budowlany*, vol. 12, pp. 42–48, 2015.
- [205] PN-EN 13242:2004+A1:2010, "Aggregates for unbound and hydraulically bound materials for use in civil engineering work and road construction." 2010.
- [206] PN-EN 13043:2004, "Aggregates for bituminous mixtures and surface treatments

- for roads, airfields and other trafficked areas." 2004.
- [207] PN-EN 12350-5:2019, "Testing fresh concrete Part 5: Flow table test." 2019.
- [208] Poradnik Inżyniera. Paweł Wrochna, "Metoda stolika rozpływowego," 2022. https://poradnikinzyniera.pl/metoda-stolika-rozplywowego/ (accessed Nov. 22, 2024).
- [209] M. Niezgodziński and T. Niezgodziński, *Wzory, wykresy i tablice wytrzymałościowe*. Warszawa: Państwowe Wydawnictwo Naukowe, 1973.
- [210] T. Urban, J. Krakowski, M. Gołdyn, and Ł. Krawczyk, "Przebicie żelbetowych płyt krępych," Łódź, 2013. doi: 10.34658/kbb.2013.19.
- [211] J. R. Roesler and E. J. Barenberg, "Effect of Static and Fatigue Cracking on Concrete Strain Measurements," *Transportation Research Record: Journal of the Transportation Research Board*, vol. 1684, no. 1, pp. 51–60, Jan. 1999, doi: 10.3141/1684-07.
- [212] R. Cajka, Z. Marcalikova, M. Kozielova, P. Mateckova, and O. Sucharda, "Experiments on Fiber Concrete Foundation Slabs in Interaction with the Subsoil," *Sustainability*, vol. 12, no. 9, p. 3939, 2020, doi: 10.3390/su12093939.
- [213] J. Einpaul, M. Fernández Ruiz, and A. Muttoni, "Influence of moment redistribution and compressive membrane action on punching strength of flat slabs," *Engineering Structures*, vol. 86, pp. 43–57, 2015, doi: 10.1016/j.engstruct.2014.12.032.
- [214] C. G. Bailey, "Membrane action of slab/beam composite floor systems in fire," *Engineering Structures*, vol. 26, no. 12, pp. 1691–1703, 2004, doi: 10.1016/j.engstruct.2004.06.006.
- [215]PN-S-02205:1998, "Drogi samochodowe. Roboty ziemne. Wymagania i badania." 1998.
- [216] ASTM E2835-11, "Standard Test Method for Measuring Deflections using a Portable Impulse Plate Load." 2011, doi: 10.1520/E2835.
- [217] Road and Transportation Research Association, "TP BF-StB Part B 8.3: Technical testing regulations for soil and rock in road construction. Dynamic Plate Load Testing with the Light Drop-Weight Tester." 2012.
- [218] M. Wyroślak, "Korelacje parametrów gruntu w badaniach stanu zagęszczenia nasypu kontrolowanego," *Inżynieria Morska i Geotechnika*, no. 1, pp. 21–26, 2017.
- [219] S. Syma, "Analiza zależności modułów odkształcenia konstrukcji drogowych w metodach statycznej i dynamicznej," Politechnika Śląska, Gliwice, 2023.
- [220] Instytut badawczy dróg i mostów. Laboratorium geotechniki, "Badanie i ustalenie zależności korelacyjnych dla oceny stanu zagęszczenia i nośności gruntów niespoistych płytą dynamiczną," Warszawa, 2005.
- [221] Bekeart, "Steel fiber reinforced concrete industrial floor designed in accordane with the Concrete Society TR34." 1996.
- [222] J. Bowles, Foundation analysis and design. Peoria: The McGraw-Hill Companies, 1988.
- [223] A. M. Neville, *Właściwości betonu*, 4th ed. Kraków: Polski Cement Sp. z o.o., 2000.
- [224] V. Cervenka, L. Jendele, and J. Cervenka, *ATENA Program Documentation Part 1: Theory*. Prague: Cervenka Consulting Ltd., 2011.

- [225] PN-EN 13791:2008, "Assessment of in-situ compressive strength in structures and precast concrete components." 2008.
- [226] J. Michałek, "Wyznaczanie modułu sprężystości betonu przy ściskaniu," *Materiały Budowlane*, vol. 1, no. 6, pp. 66–67, 2015, doi: 10.15199/33.2015.06.23.
- [227] S. Narayanan, "Elastic modulus of concrete," *Civil Engineering & Construction Review*, vol. 34, no. 07, pp. 1–7, 2021.
- [228] Z. Marcalikova, V. Bilek, O. Sucharda, and R. Cajka, "Analysis of Fiber-Reinforced Concrete Slabs under Centric and Eccentric Load," *Materials*, vol. 14, no. 23, p. 7152, 2021, doi: 10.3390/ma14237152.
- [229] L. G. Sorelli, A. Meda, and G. A. Plizzari, "Steel Fiber Concrete Slabs on Ground: A Structural Matter," *ACI Structural Journal*, vol. 103, no. 4, pp. 551–558, 2006, doi: 10.14359/16431.
- [230] J. Krząkała, P. Łaziński, M. Gerges, Ł. Pyrzowski, and G. Grządziela, "Influence of Actual Curing Conditions on Mechanical Properties of Concrete in Bridge Superstructures," *Materials*, vol. 16, no. 1, 2023, doi: 10.3390/ma16010054.
- [231] L. Domagała, "A study on the influence of concrete type and strength on the relationship between initial and stabilized secant moduli of elasticity," *Solid State Phenomena*, vol. 258, pp. 566–569, 2017, doi: 10.4028/www.scientific.net/SSP.258.566.
- [232] M. Rucka, E. Wojtczak, M. Knak, and M. Kurpińska, "Characterization of fracture process in polyolefin fibre-reinforced concrete using ultrasonic waves and digital image correlation," *Construction and Building Materials*, vol. 280, 2021, doi: 10.1016/j.conbuildmat.2021.122522.
- [233] I. Skrzypczak, "Statistical Quality Inspection Methodology in Production of Precast Concrete Elements," *Materials*, vol. 16, no. 1, p. 431, 2023, doi: 10.3390/ma16010431.
- [234] I. Skrzypczak, W. Kokoszka, T. Pytlowany, and W. Radwański, "Control charts monitoring for quality concrete pavements," *Scientific Journal of Silesian University of Technology. Series Transport*, vol. 106, pp. 153–163, 2020, doi: 10.20858/sjsutst.2020.106.13.
- [235] M. O. Kim and A. Bordelon, "Determination of total fracture energy for fiber-reinforced concrete," 2016.
- [236] M. Xu and K. Wille, "Fracture energy of UHP-FRC under direct tensile loading applied at low strain rates," *Composites Part B: Engineering*, vol. 80, pp. 116–125, Oct. 2015, doi: 10.1016/j.compositesb.2015.05.031.
- [237] H. M. Westergaard, "Computation of stresses in concrete roads," in *Proceedings* of the fifth annual meeting of the Highway Research Board, 1925, pp. 90–112.
- [238] W. Starosolski, *Konstrukcje żelbetowe według Eurokodu 2 i norm związanych. Tom 2*, 15th ed. Warszawa: Państwowe Wydawnictwo Naukowe, 2016.
- [239] S. Timoshenko, *Theory of plates and shells*. New York: The McGraw-Hill Companies, 1959.
- [240] C. Gaedicke and J. Roesler, *Fracture-based method to determine the flexural load capacity of concrete slabs*. Illinois, 2009.
- [241] J. Øverli, "Experimental and Numerical Investigation of Slabs on Ground Subjected to Concentrated Loads," *Central European Journal of Engineering*

- Experimental, 2014, doi: 10.2478/s13531-013-0159-9.
- [242] M. Shahiduzzaman and M. S. Hossain, "The effect on punching shear failure in centrally loaded ground-supported concrete slabs for different aspects like slab thickness, size and the position of reinforcement bar, and the strength of concrete using a validated FE model," *Heliyon*, vol. 10, no. 4, p. e26057, 2024, doi: 10.1016/j.heliyon.2024.e26057.
- [243] CNR-DT 204/2006, "Guide for the Design and Construction of Fiber-Reinforced Concrete Structures." 2006.
- [244] M. Kozielova, M. Smirakova, P. Mateckova, and Z. Marcalikova, "Numerical modelling and analysis of reinforced concrete slab with subsoil," in *International Conference of Numerical Analysis and Applied Mathematics ICNAAM 2019*, 2020, vol. 130015, pp. 1–4, doi: 10.1063/5.0030879.
- [245] R. Cajka, Z. Marcalikova, V. Bilek, and O. Sucharda, "Numerical Modeling and Analysis of Concrete Slabs in Interaction with Subsoil," *Sustainability*, vol. 12, no. 23, p. 9868, 2020, doi: 10.3390/su12239868.
- [246] P. K. Juhasz and P. Schaul, "Design of Industrial Floors TR34 and Finite Element Analysis (Part 2)," *Journal of Civil Engineering and Architecture*, vol. 13, no. 8, pp. 512–522, 2019, doi: 10.17265/1934-7359/2019.08.005.
- [247] M. A. Glinicki, "Badania właściwości fibrobetonu z makrowłóknami syntetycznymi, przeznaczonego na podłogi przemysłowe," *Cement Wapno Beton*, vol. 13/75, no. 4, pp. 184–195, 2008.
- [248] C. Camille, D. Kahagala, O. Mirza, F. Mashiri, B. Kirkland, and T. Clarke, "Performance behaviour of macro-synthetic fibre reinforced concrete subjected to static and dynamic loadings for sleeper applications," *Construction and Building Materials*, vol. 270, p. 121469, 2021, doi: 10.1016/j.conbuildmat.2020.121469.
- [249] O. Sucharda, V. Bilek, M. Smirakova, J. Kubosek, and R. Cajka, "Comparative Evaluation of Mechanical Properties of Fibre-Reinforced Concrete and Approach to Modelling of Bearing Capacity Ground Slab," *Periodica Polytechnica Civil Engineering*, vol. 61, no. 4, pp. 972–986, 2017, doi: 10.3311/PPci.10688.
- [250] J. A. O. Barros and J. A. Figueiras, "Experimental behaviour of fibre concrete slabs on soil," *Mechanics of cohesive-frictional Materials*, vol. 3, no. 3, pp. 277–290, 1998, doi: 10.1002/(SICI)1099-1484(199807)3:3<277::AID-CFM52>3.0.CO;2-N.

APPENDIX A. Literature review on the influence of macro SyFs

Table A.1 Literature review on the influence of macro SyFs on selected concrete properties

| Ref. | V. | E_f | f o | l_f/d_f | Slump | E_c | f | f. | fa | W_0 |
|-------|--------------|------------|--------------------------|-----------------|--------------|----------|---------------------------|---------------------------|--------------------------|---------------------------|
| [-] | V_f [%] | [GPa] | f _{ft} [MPa] | | [mm] | [GPa] | f c [MPa] | f _{spl} [MPa] | f _{fl} [MPa] | [Nm] |
| [-] | 0.00 | - [GI a] | - [1 VII a] | | 230 | NT | 58.05 | NT | 3.26 | 0.64 |
| | 0.00 | NS | 600 | 54/0.45 | 160 | NT | 60.64 | NT | 3.44 | 10.28 |
| | 0.22 | NS | 600 | 54/0.45 | 130 | NT | 58.06 | NT | 3.42 | 13.96 |
| [72] | 0.33 | NS | 575 | 48/0.60 | 140 | NT | 61.31 | NT | 3.63 | 11.79 |
| | 0.22 | NS | 575 | 48/0.60 | 140 | NT | 59.44 | NT | 3.44 | 12.44 |
| | 0.33 | NS | 689 | 52/0.45 | 65 | NT | 60.87 | NT | 3.69 | 11.88 |
| | 0.00 | - | - | 32/0.43 | 20 | NT | 27.23 | NT | 2.13 | NT |
| | 0.00 | 7.3 | 425 | 55/0.85 | 15 | NT | 27.23 | NT | 2.13 | NT |
| [105] | 0.20 | 7.3 | 425 | 55/0.85 | 12 | NT | 27.71 | NT | 2.30 | NT |
| | 0.60 | 7.3 | 425 | 55/0.85 | 10 | NT | 26.61 | NT | 2.25 | NT |
| | 0.00 | - | - | - | NT | NT | 45.50 | NT | 5.40 | 0.09 |
| | 0.50 | 7-10 | ≈595 | =30 | NT | NT | 39.75 | NT | 4.60 | 0.05 |
| | 0.50 | 7-10 | ≈595 | =38 | NT | NT | 38.50 | NT | 4.70 | 0.43 |
| [106] | 0.50 | 7-10 | ≈595 | =43 | NT | NT | 35.50 | NT | 4.10 | 0.52 |
| [100] | 0.80 | 7-10 | ≈595 ≈595 | =30 | NT | NT | 34.25 | NT | 4.90 | 0.65 |
| | 0.80 | 7-10 | ≈595 ≈595 | =38 | NT | NT | 34.23 | NT | 4.20 | 0.03 |
| | 0.80 | 7-10 | ≈595 ≈595 | =43 | NT | NT | 33.75 | NT | 4.40 | 0.77 |
| | 0.10 | NS | 450 | 48/0.6 | NT | NT | 45.80 | 7.03 | 8.40 | NT |
| [108] | 0.10 | NS | 450 | 48/0.6 | NT | NT | 59.90 | 9.61 | 9.06 | NT |
| | 0.10 | NS | 450 | 48/0.6 | NT | NT | 42.70 | 8.18 | 7.60 | NT |
| [108] | 0.10 | NS | 450 | 48/0.6 | NT | NT | 51.10 | 7.67 | 9.40 | NT |
| | | 110 | 430 | 46/0.0 | ≈218 | NT | ≈30.6 | NT | | NT |
| | 0.00 0.30 | 12.0 | 640 | 60/0.58 | ~218 ≈185 | NT NT | ~30.6 ≈33.6 | NT NT | 3.09 2.94 | NT NT |
| [111] | 0.30 | 12.0 | 640 | 60/0.58 | ≈183 ≈140 | NT | ≈33.0 ≈32.4 | NT | 3.44 | NT |
| | 1.00 | 12.0 | 640 | 60/0.58 | ≈140 ≈115 | NT | ≈32.4 ≈32.4 | NT | 3.44 | NT |
| | 0.00 | | | - | ≈113 ≈185 | NT | ≈54.8 | NT | 3.79 | NT |
| | 0.00 | 12.0 | 640 | 60/0.58 | ≈183 ≈150 | NT | ~34.8 ≈57.8 | NT | 3.48 | NT |
| [111] | 0.30 | 12.0 | 640 | 60/0.58 | ≈130 ≈125 | NT | ≈60.8 | NT | 4.11 | NT |
| | 1.00 | 12.0 | 640 | 60/0.58 | ~123 ≈80 | NT | ≈57.5 | NT | 4.11 | NT |
| | 0.22 | NS | NS | 54/0.34 | 190 | 37.20 | 50.20 | NT | ≈4.75 | ≈3.0 |
| | 0.22 | NS NS | NS NS | 54/0.34 | 175 | 30.40 | 42.80 | NT | ≈4.73 ≈4.25 | ~3.0 ≈6.0 |
| | 0.33 | 11.3 | NS NS | 40/0.83 | 150 | 31.30 | 40.90 | NT | ≈4.23 ≈4.00 | ~6.0 ≈4.0 |
| [112] | | 11.3 | NS NS | 40/0.83 | 150 | 32.20 | | NT | | ~ 4 .0 ≈5.5 |
| | 0.74 0.22 | 9.5 | NS NS | 40/0.83 | 150 | 32.20 | 42.10 41.40 | NT NT | ≈4.50 ≈4.10 | ≈3.5 ≈3.5 |
| | 0.22 | 9.5 9.5 | NS NS | 40/0.44 | 130 | 31.20 | 44.60 | NT NT | ~4.10 ≈4.15 | ~3.3 ≈7.0 |
| | 0.00 | | | 40/0.44 | NT | NT | 32.50 | NT | 4.20 | 4.0 |
| [112] | 0.00 | - NC | - NS | - 40/3.0x0.2 | NT NT | NT NT | | NT NT | 4.20 ≈4.40 | 2.0 ≈33.0 |
| [113] | | NS NC | NS NS | | NT NT | | ≈34.50 ≈35.50 | | | |
| | 0.59 | NS | | 40/3.0x0.2 | | NT 24.11 | ≈35.50 | NT | ≈4.45 ≈7.50 | 48.0 |
| [1107 | 0.00 | 2.6 | 470 | - 20/0.79 | 820* 700* | 24.11 | 61.20 | 4.36 | | 0.00 |
| [118] | 0.44 | 3.6 | 470 | 39/0.78 | 790* 778* | 24.43 | 59.57 57.20 | 4.08 | ≈5.80 ≈6.05 | 17.84 |
| | 0.67 | 3.6 | 470 | 39/0.78 | | 24.34 | 57.29 | 4.00 | ≈6.05 | 19.76 |
| | 0.00 | 5.0 | 220 | - 45/1 0 | 730* | 29.00 | 36.80 | 2.95 | 3.30 | NT NT |
| [110] | 0.33 | 5.9 5.0 | 320 | 45/1.0 | 685* 623* | 27.96 | 38.29 | 3.58 | 5.23 | NT NT |
| [119] | 0.67 | 5.9 | 320 | 45/1.0 | 623* 596* | 32.51 | 41.49 | 4.03 | 6.63 | NT |
| | 1.00 | 5.9 | 320 | 45/1.0 | 586* 550* | 31.73 | 44.82 | 4.17 | 7.45 | NT NT |
| | 1.33 | 5.9 | 320 | 45/1.0 | 550* 750* | 33.26 | 43.19 | 3.95 | 8.29 | NT |
| [119] | 0.00 | - 5 0 | 220 | 45/1 0 | 750* | 36.00 | 55.10 | 3.96 | 4.21 | NT |
| ' ' | 0.33 | 5.9 | 320 | 45/1.0 | 715* | 36.00 | 57.58 | 4.15 | 6.96 | NT |

| Ref. | V_f | E_f | f_{ft} | l_f/d_f | Slump | E_c | f_c | f_{spl} | f_{fl} | W_0 |
|-------|-------|-------|----------|------------|----------------|-------|--------|-----------|----------|-------|
| [-] | [%] | [GPa] | [MPa] | [mm/mm] | [mm] | [GPa] | [MPa] | [MPa] | [MPa] | [Nm] |
| | 0.67 | 5.9 | 320 | 45/1.0 | 680* | 37.91 | 59.83 | 4.99 | 7.64 | NT |
| | 1.00 | 5.9 | 320 | 45/1.0 | 615* | 36.97 | 62.40 | 5.84 | 8.49 | NT |
| | 1.33 | 5.9 | 320 | 45/1.0 | 580* | 37.91 | 59.50 | 5.28 | 9.52 | NT |
| | 0.00 | - | - | - | 170 | 46.00 | 58.80 | 5.68 | NT | NT |
| | 0.25 | 3.6 | 500 | 39/0.78 | 170 | 47.30 | 63.50 | 6.14 | NT | NT |
| [122] | 0.50 | 3.6 | 500 | 39/0.78 | 170 | 48.00 | 61.30 | 6.16 | NT | NT |
| | 0.75 | 3.6 | 500 | 39/0.78 | 170 | 49.00 | 60.70 | 6.24 | NT | NT |
| | 1.00 | 3.6 | 500 | 39/0.78 | 170 | 49.60 | 59.40 | 6.74 | NT | NT |
| | 1.25 | 3.6 | 500 | 39/0.78 | 170 | 49.80 | 56.40 | 7.24 | NT | NT |
| | 0.00 | - | - | - | NT | 32.25 | 64.15 | NT | NT | NT |
| [123] | 0.25 | 3.5 | NS | 40/NS | NT | 34.93 | 68.06 | NT | NT | NT |
| | 0.50 | 3.5 | NS | 40/NS | NT | 32.48 | 70.46 | NT | NT | NT |
| | 0.00 | - | - | - | NT | 35.68 | 82.59 | NT | NT | NT |
| [123] | 0.25 | 3.5 | NS | 40/NS | NT | 35.75 | 80.44 | NT | NT | NT |
| | 0.50 | 3.5 | NS | 40/NS | NT | 32.61 | 77.50 | NT | NT | NT |
| | 0.00 | - | - | - | 120 | NT | 33.66 | 2.56 | 5.06 | NT |
| [126] | 0.80 | 10.0 | 550 | 48/NS | 80 | NT | 34.77 | 2.82 | 5.93 | NT |
| [120] | 0.60 | 10.0 | 550 | 48/NS | 99 | NT | 34.62 | 2.81 | 5.23 | NT |
| | 0.40 | 10.0 | 550 | 48/NS | 105 | NT | 34.59 | 2.69 | 5.09 | NT |
| | 0.00 | - | - | - | ≈ 740 * | NT | ≈64.0 | ≈4.20 | ≈5.10 | ≈0.3 |
| | 0.10 | 35.0 | NS | 50/0.8 | ≈ 744 * | NT | ≈64.2 | ≈4.50 | ≈6.30 | ≈0.4 |
| [129] | 0.20 | 35.0 | NS | 50/0.8 | ≈71 4* | NT | ≈65.7 | ≈4.72 | ≈6.50 | ≈0.6 |
| | 0.30 | 35.0 | NS | 50/0.8 | ≈762 * | NT | ≈66.6 | ≈5.05 | ≈6.60 | ≈0.4 |
| | 0.40 | 35.0 | NS | 50/0.8 | ≈744* | NT | ≈67.2 | ≈5.28 | ≈7.20 | ≈0.5 |
| | 0.00 | - | - | - | NT | NT | 32.43 | 3.39 | 5.04 | NT |
| | 0.10 | NS | 450 | 48/1.1x0.6 | NT | NT | 32.67 | 3.42 | 5.83 | NT |
| [130] | 0.20 | NS | 450 | 48/1.1x0.6 | NT | NT | 34.12 | 3.50 | 6.56 | NT |
| [130] | 0.30 | NS | 450 | 48/1.1x0.6 | NT | NT | 34.98 | 3.65 | 7.92 | NT |
| | 0.40 | NS | 450 | 48/1.1x0.6 | NT | NT | 30.12 | 3.15 | 5.98 | NT |
| | 0.50 | NS | 450 | 48/1.1x0.6 | NT | NT | 27.15 | 2.84 | 4.34 | NT |
| | 0.00 | - | - | - | NT | NT | 52.17 | NT | 4.78 | NT |
| | 0.60 | 10.0 | 640 | 27/0.52 | NT | NT | 51.23 | NT | 6.07 | NT |
| [131] | 0.90 | 10.0 | 640 | 27/0.52 | NT | NT | 59.22 | NT | 5.75 | NT |
| [131] | 1.20 | 10.0 | 640 | 27/0.52 | NT | NT | 59.69 | NT | 6.67 | NT |
| | 1.50 | 10.0 | 640 | 27/0.52 | NT | NT | 53.58 | NT | 5.34 | NT |
| | 1.80 | 10.0 | 640 | 27/0.52 | NT | NT | 54.52 | NT | 4.78 | NT |
| | 0.00 | - | - | - | ≈145 | NT | ≈37.50 | NT | ≈3.25 | 0.00 |
| | 0.50 | NS | 530 | 38/0.91 | ≈135 | NT | ≈38.50 | NT | ≈3.70 | 13.88 |
| [132] | 0.70 | NS | 530 | 38/0.91 | ≈120 | NT | ≈39.50 | NT | ≈4.15 | 16.60 |
| | 0.90 | NS | 530 | 38/0.91 | ≈110 | NT | ≈35.50 | NT | ≈3.60 | 18.13 |
| | 1.10 | NS | 530 | 38/0.91 | ≈95 | NT | ≈38.50 | NT | ≈4.15 | 23.26 |
| | 1.30 | NS | 530 | 38/0.91 | ≈85 | NT | ≈37.00 | NT | ≈3.05 | 18.27 |
| | 0.00 | - | - | - | NT | 48.07 | 30.62 | NT | 4.36 | NT |
| [133] | 0.33 | 4.0 | 586 | 50/1.5x0.5 | NT | 48.66 | 30.50 | NT | 4.35 | NT |
| [133] | 0.30 | 4.3 | 637 | 38/2.0x0.5 | NT | 46.82 | 32.64 | NT | 4.64 | NT |
| | 0.33 | 9.5 | 625 | 50/0.66 | NT | 48.31 | 31.35 | NT | 4.54 | NT |
| | 0.00 | - | - | - | NT | NT | 58.90 | NT | 6.00 | NT |
| [134] | 2.22 | 3.5 | ≈500 | 60/2.0 | NT | NT | 58.90 | NT | 5.50 | NT |
| [124] | 0.78 | 5.0 | ≈500 | 50/0.941 | NT | NT | 54.30 | NT | 4.70 | NT |
| | 0.78 | 3.5 | ≈500 | 50/1.183 | NT | NT | 57.70 | NT | 4.27 | NT |
| [139] | 0.78 | 3.0 | 650 | 30/0.47 | 120 | NT | 50.40 | NT | 5.39 | 24.98 |
| | 0.89 | 3.0 | 650 | 30/0.47 | 115 | NT | 51.00 | NT | 5.54 | 25.11 |

| Ref. | V_f | E_f | f _{ft} | l_f/d_f | Slump | E_c | f_c | <i>f</i> _{spl} | f_{fl} | W_0 |
|---------|--------------|--------------|------------------------|----------------|--------------|----------|----------|-------------------------|--------------|----------|
| [-] | [%] | [GPa] | [MPa] | [mm/mm] | [mm] | [GPa] | [MPa] | [MPa] | [MPa] | [Nm] |
| | 1.00 | 3.0 | 650 | 30/0.47 | 120 | NT | 52.50 | NT | 5.59 | 22.98 |
| | 0.78 | 3.0 | 650 | 30/0.47 | 115 | NT | 48.90 | NT | 4.65 | 23.02 |
| [139] | 0.89 | 3.0 | 650 | 30/0.47 | 110 | NT | 49.80 | NT | 4.28 | 23.05 |
| [139] | 1.00 | 3.0 | 650 | 30/0.47 | 120 | NT | 50.00 | NT | 5.10 | 28.57 |
| | 1.11 | 3.0 | 650 | 30/0.47 | 110 | NT | 49.50 | NT | 4.97 | 34.40 |
| [144] | 0.00 | - | - | - | 93 | NT | 58.40 | 3.42 | NT | NT |
| [177] | 4.00 | NS | 250 | 50/1.0 | 20 | NT | 55.30 | 5.63 | NT | NT |
| | 0.00 | - | - | - | 165 | NT | 27.97 | 2.40 | 4.58 | NT |
| [145] | 0.33 | 5.9 | 320 | 60/1.0 | 154 | NT | 29.28 | 2.43 | 4.87 | NT |
| | 0.67 | 5.9 | 320 | 60/1.0 | 142 | NT | 30.53 | 2.46 | 5.23 | NT |
| | 1.00 | 5.9 | 320 | 60/1.0 | 131 | NT | 31.68 | 2.60 | 5.50 | NT |
| [159] | 0.00 | - | - | - | NT | NT | 34.81 | 3.53 | NT | NT |
| [137] | 0.50 | NS | NS | NS | NT | NT | 34.81 | 4.51 | NT | NT |
| [159] | 0.00 | - | - | - | NT | NT | 38.25 | 4.02 | NT | NT |
| [137] | 0.50 | NS | NS | NS | NT | NT | 38.34 | 4.81 | NT | NT |
| [159] | 0.00 | - | - | - | NT | NT | 35.30 | 3.82 | NT | NT |
| [157] | 0.50 | NS | NS | NS | NT | NT | 35.30 | 4.61 | NT | NT |
| [159] | 0.00 | - | - | - | NT | NT | 38.83 | 4.02 | NT | NT |
| [157] | 0.50 | NS | NS | NS | NT | NT | 38.74 | 4.81 | NT | NT |
| [159] | 0.00 | - | - | - | NT | NT | 35.01 | 3.73 | NT | NT |
| [159] | 0.50 | NS | NS | NS | NT | NT | 35.01 | 4.51 | NT | NT |
| | 0.00 | - | - | - | NT | NT | 38.64 | 4.12 | NT | NT |
| | 0.50 | NS | NS | NS | NT | NT | 38.64 | 4.81 | NT | NT |
| | 0.00 | - | - | - | 13 | NT | 31.07 | NT | NT | NT |
| [165] | 0.43 | 1.7 | ≈600 | 30/1x0.60 | 7 | NT | 31.60 | NT | NT | NT |
| | 0.43 | 3.8 | ≈675 | 30/1x0.35 | 12 | NT | 29.23 | NT | NT | NT |
| | 0.00 | - | - | - | 40 | NT | 44.20 | NT | 3.95 | NT |
| [247] | 0.22 | 5.0 | 650 | 50/1.0 | 40 | NT | 41.10 | NT | 3.77 | NT |
| | 0.33 | 5.0 | 650 | 50/1.0 | 40 | NT | 35.30 | NT | 3.94 | NT |
| | 0.43 | 5.0 | 650 | 50/1.0 | 40 | NT | 27.80 | NT | 3.88 | NT |
| F1.7.43 | 0.56 | NS | NS | 48/NS | 95 | 37.10 | 64.50 | NT | 5.21 | NT |
| [174] | 1.11 | NS | NS | 48/NS | 120 | 37.00 | 63.80 | NT | 5.39 | NT |
| | 1.11 | NS | NS | 60/NS | 30 | 38.10 | 53.60 | NT | 5.14 | NT |
| F1001 | 0.00 | - 0.5 | | - | 200 | NT | 41.10 | NT | 4.73 | NT |
| [189] | 0.32 | 9.5 | 540 | 40/1.4x0.1 | 150 | NT | 36.10 | NT | 4.69 | NT |
| | 0.48 | 9.5 | 540 | 40/1.4x0.1 | 115 | NT | 31.80 | NT | 4.82 | NT |
| | 0.00 | 12.0 | 640 | - 40/NIC | 740* 575* | NT | NT | 5.10 | 5.00 | NT |
| | 0.20 0.40 | 12.0 12.0 | 640 640 | 48/NS 48/NS | 575* 675* | NT NT | NT NT | 6.70 7.20 | 4.60 5.00 | NT NT |
| | | | 640 | | 620* | | | | | NT |
| | 0.60 | 12.0 | | 48/NS | | NT | NT NT | 7.40 | 5.60 | |
| | 0.80 | 12.0 | 640 | 48/NS | 410* 400* | NT NT | NT NT | 7.20 | 5.00 | NT NT |
| | 1.00 1.50 | 12.0 | 640 640 | 48/NS 48/NS | 400** 190 | NT NT | NT NT | 7.40 9.20 | 5.10 5.70 | NT NT |
| [2/10] | 2.00 | 12.0 12.0 | 640 | 48/NS 48/NS | 75 | NT NT | NT NT | 9.20 | 3.70 4.70 | NT NT |
| [248] | 0.20 | 10.0 | NS NS | 46/NS 55/NS | 390* | NT NT | NT | 5.90 | 4.70 | NT |
| | 0.20 | 10.0 | NS NS | 55/NS | 420* | NT NT | NT NT | 6.20 | 4.80 | NT NT |
| | 0.40 | 10.0 | NS NS | 55/NS | 475* | NT NT | NT | 6.60 | 5.60 | NT |
| | 0.80 | 10.0 | NS NS | 55/NS | 280* | NT NT | NT | 7.20 | 5.00 | NT |
| | 1.00 | 10.0 | NS NS | 55/NS | 190* | NT NT | NT | 7.50 | 4.90 | NT |
| | 1.50 | 10.0 | NS NS | 55/NS | 90 | NT NT | NT | 7.30 | 5.30 | NT NT |
| | 2.00 | 10.0 | NS NS | 55/NS | 53 | NT NT | NT NT | 7.70 | 4.70 | NT |
| Nata N | | | | ot tested * – | | | | 7.00 | 7.70 | 111 |

Note: NS – not specified, NT – not tested, * – slump flow (spread).

Table A.2 Literature review on the influence of macro SyFs on concrete water absorption, porosity, and air content

| Ref. | V_f | E_f | f _{fi} | l_f/d_f | Absorption | Porosity | Air content |
|--------|--------------|------------|-----------------|------------------|------------|-----------|--------------|
| [-] | [%] | [GPa] | [MPa] | [mm/mm] | [%] NT | [%] NT | [%] |
| | 0.00 0.33 | - 5.9 | 320 | 45/1.0 | NT NT | NT NT | 1.80 1.98 |
| [110] | 0.33 | 5.9 | 320 | | NT NT | NT NT | 2.13 |
| [119] | 1.00 | 5.9 5.9 | 320 | 45/1.0 45/1.0 | NT NT | NT NT | 2.13 |
| | 1.33 | 5.9 | 320 | | | | 2.55 |
| | | | | 45/1.0 | NT | NT | |
| | 0.00 | - 5.0 | 220 | 45/1.0 | NT | NT | 1.80 |
| F1101 | 0.33 | 5.9 | 320 | 45/1.0 | NT | NT | 1.98 |
| [119] | 0.67 | 5.9 | 320 | 45/1.0 | NT | NT | 2.19 |
| | 1.00 | 5.9 | 320 | 45/1.0 | NT | NT | 2.40 |
| | 1.33 | 5.9 | 320 | 45/1.0 | NT | NT | 2.52 |
| | 0.00 | - | - | 20/0.70 | 3.33 | 7.96 | NT |
| | 0.25 | 3.6 | 500 | 39/0.78 | 3.15 | 7.54 | NT |
| [122] | 0.50 | 3.6 | 500 | 39/0.78 | 2.80 | 7.51 | NT |
| | 0.75 | 3.6 | 500 | 39/0.78 | 2.69 | 7.43 | NT |
| | 1.00 | 3.6 | 500 | 39/0.78 | 2.66 | 8.15 | NT |
| | 1.25 | 3.6 | 500 | 39/0.78 | 2.60 | 8.23 | NT |
| | 0.00 | - | _ | - | NT | 7.72 | NT |
| [123] | 0.25 | 3.5 | NS | 40/NS | NT | 7.51 | NT |
| | 0.50 | 3.5 | NS | 40/NS | NT | 7.42 | NT |
| | 0.00 | - | - | - | NT | 6.82 | NT |
| [123] | 0.25 | 3.5 | NS | 40/NS | NT | 6.59 | NT |
| | 0.50 | 3.5 | NS | 40/NS | NT | 6.66 | NT |
| | 0.00 | - | - | - | 2.48 | NT | NT |
| [126] | 0.40 | 10.0 | 550 | 48/NS | 1.37 | NT | NT |
| [120] | 0.60 | 10.0 | 550 | 48/NS | 1.75 | NT | NT |
| | 0.80 | 10.0 | 550 | 48/NS | 1.42 | NT | NT |
| | 0.00 | - | - | - | ≈1.85 | NT | NT |
| | 0.10 | 35.0 | NS | 50/0.8 | ≈1.91 | NT | NT |
| [129] | 0.20 | 35.0 | NS | 50/0.8 | ≈2.07 | NT | NT |
| | 0.30 | 35.0 | NS | 50/0.8 | ≈2.10 | NT | NT |
| | 0.40 | 35.0 | NS | 50/0.8 | ≈2.14 | NT | NT |
| | 0.00 | - | - | - | ≈3.00 | ≈12.16 | NT |
| | 0.60 | 10.0 | 640 | 27/0.52 | ≈2.70 | ≈11.01 | NT |
| Г1217 | 0.90 | 10.0 | 640 | 27/0.52 | ≈2.55 | ≈9.47 | NT |
| [131] | 1.20 | 10.0 | 640 | 27/0.52 | ≈2.77 | ≈9.86 | NT |
| | 1.50 | 10.0 | 640 | 27/0.52 | ≈2.62 | ≈10.24 | NT |
| | 1.80 | 10.0 | 640 | 27/0.52 | ≈2.70 | ≈11.01 | NT |
| | 0.00 | - | - | - | NT | NT | 2.80 |
| [165] | 0.43 | 1.7 | ≈600 | 30/1x0.60 | NT | NT | 3.70 |
| | 0.43 | 3.8 | ≈675 | 30/1x0.35 | NT | NT | 3.40 |
| | 0.00 | - | - | - | NT | NT | 3.30 |
| [0.47] | 0.22 | 5.0 | 650 | 50/1.0 | NT | NT | 3.60 |
| [247] | 0.33 | 5.0 | 650 | 50/1.0 | NT | NT | 2.80 |
| | 0.43 | 5.0 | 650 | 50/1.0 | NT | NT | 3.40 |
| | 0.56 | NS | NS | 48/NS | NT | NT | 2.20 |
| [174] | 1.11 | NS | NS | 48/NS | NT | NT | 2.10 |
| [-,.] | 1.11 | NS | NS | 60/NS | NT | NT | 3.00 |
| | | 1,~ | 1,2 | 50/110 | 111 | 1,1 | |

Note: NS – not specified, NT – not tested.

APPENDIX B. Literature review on large-scale ground slab testing

Table B.1 Literature review on large-scale ground-supported slabs subjected to a concentrated load

| Ref. | Slab characteristics | Subbase | Loading plate | Ultimate load [kN] |
|------------------------|---|--|-------------------------|--|
| | | characteristics | dimensions and position | – failure mode |
| | Casted in situ | Natural subbase, | 100x100 mm | |
| al. | 150x6000x6000 mm | in situ | | |
| Alanie et al. [186] | Plain concrete | <i>k</i> =0.05 MPa/mm | Central | 479 – punching shear |
| nie 18 | | | Edge 150 mm | 407 – punching shear |
| | | | Edge 300 mm | 443 – punching shear |
| 1 | | | Corner 150 mm | 192 – punching shear |
| | C + 1: ' | NT (1 11 | Corner 300 mm | 262 – punching shear |
| | Casted in situ 150x6000x6000 mm | Natural subbase, in situ | 100x100 mm | |
| Alanie et al. | 40 kg/m ³ SFs | k=0.05 MPa/mm | Central | 480 – punching shear |
| e et | $(l_f = 60 \text{ mm})$ | K-0.03 MIF a/IIIII | Edge 150 mm | 351 – punching shear |
| anie 118 | (ij - 00 mm) | | Edge 300 mm | 443 – punching shear |
| Alg | | | Corner 150 mm | 187 – punching shear |
| | | | Corner 300 mm | 310 – punching shear |
| | Casted in situ | Natural subbase, | 100x100 mm | 510 panering silear |
| l: | 150x6000x6000 mm | in situ | 100/1100 11111 | |
| , ta_ | 7 kg/m ³ SyFs | k=0.05 MPa/mm | Central | 490 – punching shear |
| ie et | $(l_f = 48 \text{ mm})$ | ., ., ., ., ., ., ., ., ., ., ., ., ., . | Edge 150 mm | 427 – punching shear |
| Alanie et al. [188] | | | Edge 300 mm | 500 – punching shear |
| A | | | Corner 150 mm | 240 – punching shear |
| | | | Corner 300 mm | 373 – punching shear |
| | Casted in situ | Natural | 100x100 mm | |
| | 150x2500x2500 mm | compacted | _ | |
| | Plain concrete | subbase, in situ | Central | ? – flexural cracks |
| | 10.01 / 3.07 | k=0.075 MPa/mm | | and punching shear |
| | $10.0 \text{ kg/m}^3 \text{ SFs}$ | | Central | ? – flexural cracks |
| | $(l_f/d_f = 60/0.8 \text{ mm})$ | | C 1 | and punching shear |
|)2] | $30.0 \text{ kg/m}^3 \text{ SFs}$ | | Central | ? – flexural cracks |
| [15 | $(l_f/d_f = 60/0.8 \text{ mm})$ 0.9 kg/m ³ PPFs | | Central | and punching shear ? – flexural cracks |
| et al. [192] | $(l_f = 51 \text{ mm})$ | | Central | and punching shear |
| et | $3.6 \text{ kg/m}^3 \text{ PPFs}$ | | Central | ? – flexural cracks |
| Bischoff | $(l_f = 51 \text{ mm})$ | | Centrar | and punching shear |
| scł | Steel mesh | | Central | ? – flexural cracks |
| Bi | (1 at the top) | | Contrar | and punching shear |
| | Steel mesh | | Central | ? – flexural cracks |
| | (1 at the top+1 at the bottom) | | | and punching shear |
| | $10.0 \text{ kg/m}^3 \text{ SFs}$ | Natural loose | Central | ? – flexural cracks |
| | $(l_f/d_f = 60/0.8 \text{ mm})$ | subbase, in situ | | and punching shear |
| | $30.0 \text{ kg/m}^3 \text{ SFs}$ | <i>k</i> =0.015 MPa/mm | Central | ? – flexural cracks |
| | $(l_f/d_f = 60/0.8 \text{ mm})$ | | | and punching shear |
| da 61 | Casted in situ | 300 mm of gravel | 200x200 mm | |
| narda .[36] | | layer + 5000 mm | | |
| Sucharda et al.[36] | Steel mesh | natural loess loam, | Central | 344 – punching shear |
| - FA 10 | (1 at the bottom) | in situ | I | I |

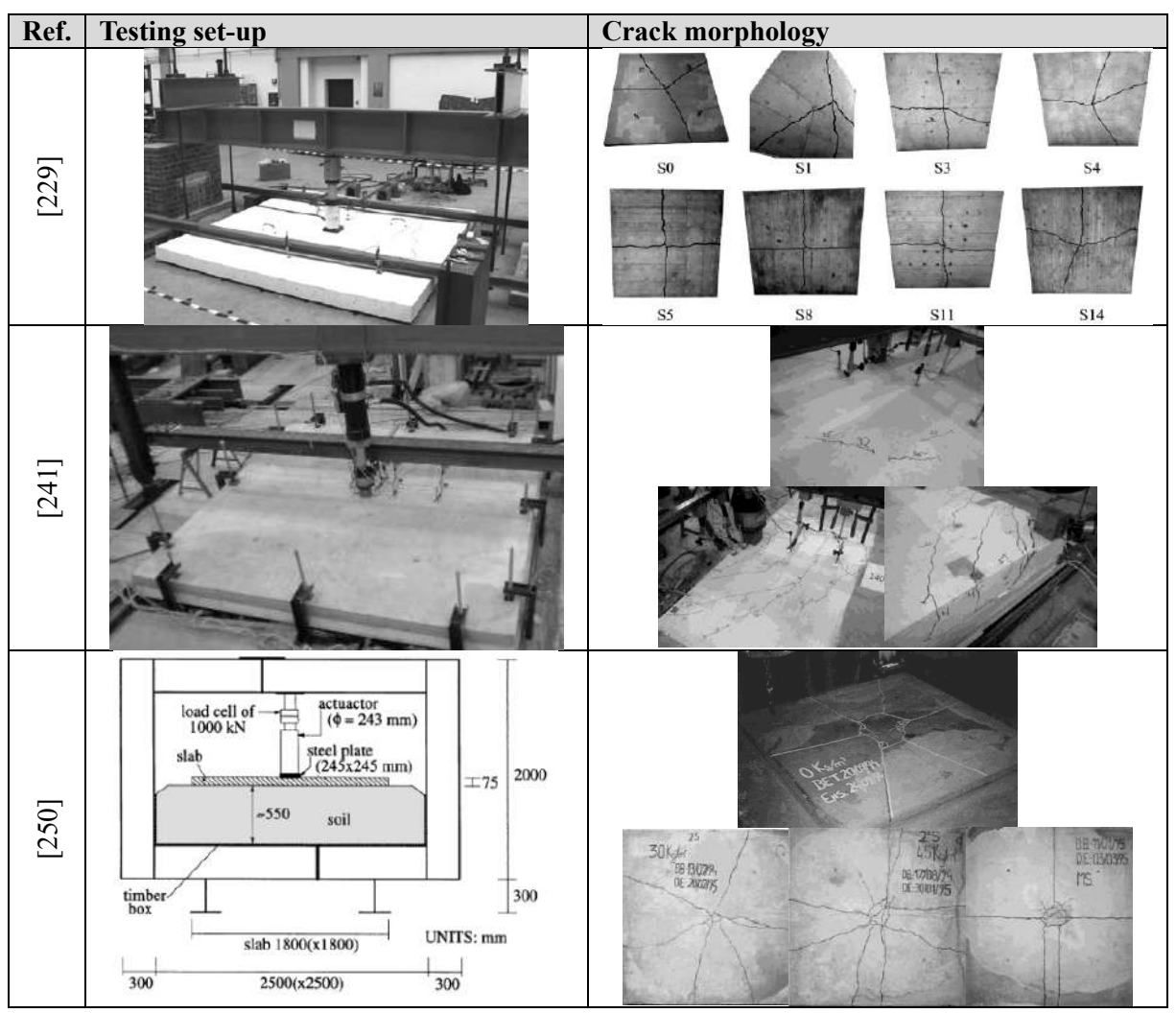
| Marcalikova et al. [228] | Casted in situ 150x2000x2000 mm $25 \text{ kg/m}^3 \text{ SFs}$ $(l//d_f = 60/0.9 \text{ mm})$ | Natural clayey sand subbase, in situ | 400x400 mm Central Eccentric | 499 – ? 478 – ? |
|--|--|--|-------------------------------|--|
| | Casted in situ | Natural clay | 400x400 mm | |
| 212] [249] | | subbase, in situ | Central | 345 – ? concrete |
| t al. [2 r et al. | 25 kg/m ³ SFs | | Central | crushing 542 – ? radial cracks, concrete crushing |
| Cajka et al. [212] 124 set al. [24] | $(l_f/d_f = 60/0.9 \text{ mm})$ 50 kg/m ³ SFs $(l_f/d_f = 60/0.9 \text{ mm})$ 75 kg/m ³ SFs | | Central | 640 – punching shear |
|) Su | 75 kg/m ³ SFs ($l_f/d_f = 60/0.9$ mm) | | Central | 752 – punching shear |
| | Precast | 200 mm of low- | 25x203x203 mm | |
| | 127x2200x2200 mm Plain concrete | plasticity clay subbase + ? k=0.103 MPa/mm | Central | 135 – flexural cracks and punching shear or circumferential |
| | | | Edge | cracks at the top 96 – flexural cracks and punching shear or circumferential |
| [190] | $3.0 \text{ kg/m}^3 \text{ SyFs}$ $(l_f/d_f = 40/0.44 \text{ mm})$ | | Central | cracks at the top 174 – flexural cracks and punching shear or circumferential |
| Roesler et al.[189], [190] | 4.4 kg/m ³ SyFs $(l_f/d_f = 40/0.44 \text{ mm})$ | | Central | cracks at the top 195 – flexural cracks and punching shear or circumferential |
| Roesler | | | Edge | cracks at the top 131 – flexural cracks and punching shear or circumferential |
| | 27.3 kg/m ³ SFs $(l/d_f = 60/0.92 \text{ mm})$ | | Central | cracks at the top 228 – flexural cracks and punching shear |
| | 39.0 kg/m ³ SFs $(l/d_f = 65/1.3 \text{ mm})$ | | Central | or circumferential cracks at the top 220 – flexural cracks and punching shear or circumferential |
| | | | | cracks at the top |
| | Precast 120x2000x2000 mm | 60 mm of cork plank +? | ? | |
| [88] | Plain concrete 20 kg/m ³ SFs | k=0.044 MPa/mm | Central Central | 227 – crushing 289 – punching shear |
| Chen [88] | $(l_f/d_f = 65/1.08 \text{ mm})$ 30 kg/m ³ SFs $(l_f/d_f = 65/1.08 \text{ mm})$ | | Central | 288 – punching shear |
| | 30 kg/m ³ SFs $(l_f/d_f = 32/1.0 \text{ mm})$ | | Central | 241 – punching shear and crushing |

| | Precast | 25 mm XPS | 20x100x100 mm | |
|-----------------------|--|---------------------------------|----------------------------|---|
| | 120x2000x2000 mm | insulation boards | | 110 |
| Manfredi et al. [194] | $20.0 \text{ kg/m}^3 \text{ SFs}$ | + concrete floor | Central | 142 – radial cracks at |
| | $(l_f/d_f = 60/0.75 \text{ mm})$ | | | the bottom, punching shear |
| et a | $30.0 \text{ kg/m}^3 \text{ SFs}$ | | Central | 155 – radial cracks at |
| :be | $(l/d_f = 60/0.75 \text{ mm})$ | | Contract | the bottom, punching |
| nfr | | | | shear |
| Ma | $40.0 \text{ kg/m}^3 \text{ SFs}$ | | Central | 175 – radial cracks at |
| | $(l_f/d_f = 60/0.75 \text{ mm})$ | | | the bottom, punching |
| | Precast | 150 mm of foamed | 50x100x100 mm | shear |
| | 150x3000x3000 mm | concrete layer + | 30x100x100 mm | |
| | Plain concrete | 1000 mm of | Central | 731 – punching shear |
| [97] | | concrete floor | Edge | 513 – punching shear |
| Elsaigh [26] | | <i>k</i> =0.25 MPa/mm | Corner 150 mm | 438 – punching shear |
| Saig | | | Corner 300 mm | 598 – bending |
| Els | 15 kg/m ³ SFs | | Central | 657 – punching shear |
| | $(l_f/d_f = 80/1.33 \text{ mm})$ | | Edge Corner 150 mm | 538 – punching shear |
| | | | Corner 300 mm | 413 – punching shear 568 – bending |
| | Precast | 400 mm of sand + | 15x100x100 mm | 300 - belianig |
| | 120x2000x2000 mm | concrete floor | 15X100X100 IIIII | |
| | Plain concrete | <i>k</i> =0.05 MPa/mm | Central | 68 – punching shear |
| 3 | 6.0 kg/m³ PPFs | | Central | 87 – punching shear |
| [19 | $(l_f/d_f = 50/0.6 \text{ mm})$ | | | and circumferential |
| al. | 20.01 / 3.05 | | G 1 | cracks at the top |
| Shi et al. [193] | 30.0 kg/m ³ SFs ($l_f/d_f = 50/0.3 \text{ mm}$) | | Central | 100 – punching shear and circumferential |
| Shi | $(ij ij - 30/0.3 \mathrm{Him})$ | | | cracks at the top |
| | Steel mesh | | Central | 122 – punching shear |
| | (1 at the bottom) | | | and circumferential |
| | | | | cracks at the top |
| | Precast | 100 mm XPS | 100x100 mm | |
| | 120x3500x3500 mm | insulation + | Control | 200 |
| | Steel mesh (1 at the top+1 at the bottom) | concrete floor k=0.15 MPa/mm | Central Edge | 390 – punching shear 153 – bending and |
| 14. | (1 at the top+1 at the bottom) | κ=0.13 IVII a/IIIIII | Edge | punching shear |
| 1 :1 | | | Edge | 140 – bending and |
| Øverli [241] | | | | punching shear |
| Ó | | | Corner | 70 – anchoring and |
| | | | ~ | punching shear |
| | | | Corner | 52 – anchoring and |
| | Precast | 5 mm cement | 245x245 mm | punching shear |
| | 75x1800x1800 mm | 5 mm cement mortar + 550 mm | 2 1 33243 IIIII | |
| [0] | Plain concrete (2 samples) | well graded silty | Central | 153, 163 – punching |
| [25 | () | sand subbase | | shear |
| Barros et al. [250] | 30 kg/m ³ SFs (2 samples) | | Central | 211, 260 – ? radial |
| s et | $(l_f/d_f = 60/0.75 \text{ mm})$ | | | cracks at the bottom |
| TTO | $45 \text{ kg/m}^3 \text{ SFs } (2 \text{ samples})$ | | Central | 257, 248 – ? radial |
| Bê | $(l_f/d_f = 60/0.75 \text{ mm})$ Steel mesh (2 samples) | | Central | cracks at the bottom 245, 274 – ? radial |
| | (1 at the bottom) | | Contrat | cracks at the bottom |
| L | (1 at the obttom) | l | | cracks at the bottom |

| | Precast | Steel spring | Squared | |
|----------|---|------------------------|---------|-----------------------|
| | 150x3000x3000 mm | supports | • | |
| | Plain concrete | <i>k</i> =0.079 MPa/mm | Central | 177 – ? radial cracks |
| | $\approx 3.4 \text{ kg/m}^3 \text{ SFs}$ | | Central | 265 – ? radial cracks |
| | $(l_f/d_f = 30/0.6 \text{ mm})$ | | | |
| 9] | $\approx 3.4 \text{ kg/m}^3 + 1.7 \text{ kg/m}^3 \text{ SFs}$ | | Central | 275 – ? radial cracks |
| [229] | $(l_f/d_f = 50/1.0 + 12/0.18 \text{ mm})$ | | | |
| TE | $\approx 3.4 \text{ kg/m}^3 \text{ SFs}$ | | Central | 239 – ? radial cracks |
| et al. | $(l_f/d_f = 50/1.0 \text{ mm})$ | | | |
| Sorelli | $\approx 3.4 \text{ kg/m}^3 \text{ SFs}$ | | Central | 252 – ? radial cracks |
| ore | $(l_f/d_f = 30/0.6 \text{ mm})$ | | | |
| ∞ | $\approx 3.4 \text{ kg/m}^3 \text{ SFs}$ | | Central | 246 – ? radial cracks |
| | $(l_f/d_f = 50/1.0 \text{ mm})$ | | | |
| | $\approx 5.1 \text{ kg/m}^3 \text{ SFs}$ | | Central | 232 – ? radial cracks |
| | $(l_f/d_f = 50/1.0 \text{ mm})$ | | | |
| | $\approx 3.4 \text{ kg/m}^3 + 1.7 \text{ kg/m}^3 \text{ SFs}$ | | Central | 273 – ? radial cracks |
| | $(l_f/d_f = 50/1.0 + 20/0.4 \text{ mm})$ | | | |

Note: Question mark (?) means that the authors did not provide clearly specified information.

Table B.2 Testing setups and crack morphologies of centrally loaded ground-supported slabs from selected studies [229], [241], [250]



SYNTHETIC FRC GROUND SLABS SUBJECTED TO A CENTRAL CONCENTRATED FORCE

Abstract

Fiber reinforced concrete (FRC) is increasingly used in industrial ground slabs due to its potential for crack control, post-cracking strength, and improved durability. However, synthetic fibers (SyFs), despite their growing popularity, remain underrepresented in design standards, which limits their broader acceptance in an engineering practice. Specifically, due to the limited number of studies, existing guidelines often apply very conservative assumptions to synthetic FRC (SyFRC), leading to a potential underestimation of its capacity. Moreover, a significant knowledge gap regarding the contributions of SyFs, particularly their addition, type, and dosage on punching shear capacity in ground-supported slabs has been identified. This study aimed to address these existing research gaps through a comprehensive experimental and analytical investigation of SyFRC ground-supported slabs subjected to centrally applied concentrated loading, with a particular focus on punching shear behavior.

The research was conducted in two stages. In the first stage, small-scale specimens were tested to determine the effects of macro SyFs addition, type, and dosage on key mechanical properties, including modulus of elasticity, compressive, flexural, and splitting tensile strength, as well as fracture energy. Five types of SyFRCs, differing in added fiber type (PM, PD, FF) and their dosage (2 and 3 kg/m³), were evaluated and compared with a reference plain concrete (PC). The results demonstrated that SyFRC significantly enhances post-cracking behavior, including ductility, fracture energy, and residual flexural tensile strengths. The second phase of the experimental campaign consisted of large-scale tests on ground-supported slabs of dimensions 200 x 1200 x 1200 mm aimed to characterize their load-deflection response, crack morphology, deflection profiles, failure mode, and punching cone geometry. A testing setup was designed to simulate subgrade support with 43 cm thick layer of compacted crushed aggregates and racking leg base by centrally applied concentrated static loading of area 100 x 100 mm. The obtained results confirmed that SyFRC slabs exhibit higher flexural cracking and punching shear capacity, more ductile failure mode, and improved load redistribution compared to PC slabs. Notably, increased fiber dosage resulted in longer critical control perimeters and reduced punching shear cone inclination angle. Furthermore, the inclusion of SyFs altered the punching cone geometry from the nearly cuboid shape observed in PC slabs to an irregular truncated pyramid shape in SyFRC slabs, underscoring the influence of fibers on stress distribution and crack propagation. It was also concluded that the presence of ground support had a significant influence on the mechanical response of SyFRC slabs, resulting in increased load-bearing capacity and additional punching shear cracking, leading to change of the failure mode from flexural to punching, compared to unsupported slabs. This highlights the necessity of conducting distinct analyses for unsupported and ground-supported slabs. The study also included a review and comparison of selected theoretical models, including the Westergaard, Falkner et al., Shentu et al., and provisions of Technical Report 34 (TR34), based on Meyerhof-Losberg approach and Eurocode 2 recommendations, to evaluate their applicability to SyFRC ground-supported slabs. The findings indicated usually significant discrepancies between analytical predictions and observed results, particularly in terms of calculated load-bearing capacities, highlighting the need for analytical model validation. These discrepancies were most likely due to the exclusion or underestimation of enhancing effect of post-cracking strength and fiber contribution while designing according to these models. Moreover, the static scheme of the tested slabs only approximately corresponded to the selected models' assumptions, which may have contributed to the differences between the experimental and analytical results. Nevertheless, among the available standards, the TR34 was identified as the most promising guideline for designing the SyFRC ground-supported slabs, as it accounts for fiber and ground support contributions in the calculations of the load-bearing capacity. Namely, TR34 provided a reasonably accurate prediction of the punching capacity and failure mode, especially when considering the actual location of the critical control section, increased ground contribution, and a greater role of SyFs in load transfer. Ultimately, the dissertation proposed modified recommendations for calculating punching shear capacity, particularly regarding the assumption of the critical control section location and SyFs contribution in load transfer.

While the research provided significant insights, limitations of the dissertation were also acknowledged. The experimental campaign focused on only a few SyFs types and dosages, specified slab geometry, and one loading scenario. Future research should explore broader ranges of SyFs, different loading types, and numerical modeling, complementing the experimental findings. Nevertheless, this study significantly advanced the understanding of SyFs influence of on the behavior of ground-supported slabs and may serve as a basis for future modifications to existing standards as well as the development of practical design guidelines.

PŁYTY NA GRUNCIE Z BETONU ZBROJONEGO WŁÓKNAMI SYNTETYCZNYMI PODDANE CENTRALNEMU OBCIĄŻANIU SIŁĄ SKUPIONA

Streszczenie

Fibrobeton (FRC) coraz częściej znajduje zastosowanie w konstrukcjach przemysłowych płyt posadzkowych, dzięki swojej zwiększonej zdolności kontrolowania zarysowań, przenoszenia obciążeń po zarysowaniu oraz wyższej trwałości. Mimo rosnącego zainteresowania włóknami syntetycznymi (SyFs), ich praktyczne wykorzystanie jest jednak wciąż dość ograniczone ze względu na niewystarczające regulacje normowe. Obecne wytyczne, oparte na nielicznych badaniach, często przyjmują bardzo konserwatywne założenia dla betonu z włóknami syntetycznymi (SyFRC), co skutkuje zaniżaniem jego rzeczywistej nośności. Ponadto istnieje wyraźna luka badawcza dotycząca wpływu dodatku, rodzaju oraz ilości SyFs na nośność na ścinanie przez przebicie w płytach podpartych na gruncie. Celem niniejszej pracy było uzupełnienie stanu wiedzy poprzez przeprowadzenie obszernego programu badawczego i rozbudowanych analiz analitycznych SyFRC płyt na gruncie, obciążonych centralną siłą skupioną, koncentrując się na ich zachowaniu przy przebiciu.

Badania przeprowadzono w dwóch etapach. W pierwszym etapie poddano badaniom małe próbki, aby ocenić wpływ dodatku, rodzaju oraz ilości makrowłókien SyFs na kluczowe właściwości mechaniczne betonu, takie jak moduł sprężystości, wytrzymałość na ściskanie, rozciąganie przy zginaniu i rozłupywaniu oraz energię pękania. Przebadano pięć wariantów SyFRC, różniących się typem dodanych włókien (PM, PF, FF) oraz ich dawką (2 i 3 kg/m³), porównując je z betonem referencyjnym bez włókien (PC). Wyniki jednoznacznie wskazały, że dodatek SyFs znacząco poprawia zachowanie betonu po zarysowaniu, zwiększając jego plastyczność, energię pękania oraz resztkowa wytrzymałości na rozciąganie przy zginaniu. Drugi etap programu badawczego obejmował testy elementów płytowych podpartych na gruncie o wymiarach 200 x 1200 x 1200 mm, których celem była analiza zależności między obciążeniem skupionym a ugięciem płyty, morfologii zarysowań, ugięć, mechanizmów zniszczenia oraz geometrii stożka przebicia. Do badań wykorzystano specjalnie zaprojektowane stanowisko badawcze imitujące podparcie gruntowe warstwą 43 cm zagęszczonego kruszywa oraz nacisk podstawy nogi regału, zadany poprzez statyczne obciążenie środka płyty siłą skupioną o powierzchni 100 x 100 mm. Uzyskane wyniki potwierdziły, że SyFRC płyty na gruncie charakteryzują się wyższą nośnością zarówno na zarysowanie przy zginaniu, jak i na ścinanie przez przebicie, a także bardziej plastycznym sposobem zniszczenia i lepszą redystrybucją obciążeń w porównaniu do płyt PC. Zwiększenie ilości włókien spowodowało wydłużenie krytycznego obwodu kontrolnego oraz zmniejszenie kata nachylenia stożka przebicia. Co więcej, dodatek SyFs zmienił geometrię stożka ze zbliżonej do prostopadłościanu w przypadku płyt PC na nieregularny, ścięty ostrosłup w płytach SyFRC, podkreślając wpływ włókien na rozkład naprężeń i sposób propagacji zarysowań. Zaobserwowano również, iż obecność podparcia gruntowego znacząco wpłynęła na zachowanie płyty, zwiększając jej nośność oraz powodując powstawanie dodatkowych rys związanych z przebiciem, co doprowadziło do zmiany modelu zniszczenia z uwagi na zginanie na zniszczenie przez przebicie, w porównaniu do płyt niepodpartych. Wynik ten podkreśla konieczność odrębnej analizy płyt niepodpartych i podpartych gruntem. W pracy dokonano również przegladu i porównania wybranych modeli teoretycznych m.in. Westergaarda, Falknera i in., Shentu i in. oraz procedur projektowych Raportu Technicznego 34 (TR34), bazującego na teorii Meyerhof'a-Losberg'a i wytycznych Eurokodu 2, w kontekście ich zastosowania do obliczeń SyFRC płyt na gruncie. Wykazano występowanie zazwyczaj istotnych rozbieżności między wynikami obliczeń a wynikami badań, szczególnie w zakresie obliczonych nośności, co wskazuje na konieczność walidacji modeli analitycznych. Różnice te wynikały najprawdopodobniej z braku uwzględniania lub niedoszacowania korzystnego wpływu resztkowej wytrzymałości SyFRC oraz udziału SyFs w przenoszeniu obciążeń podczas projektowania zgodnie z tymi modelami. Ponadto schemat statyczny badanych płyt jedynie w przybliżeniu odpowiadał założeniom wybranych modeli, co mogło dodatkowo przyczynić się do różnic pomiędzy wynikami eksperymentalnymi i analitycznymi. Niemniej jednak, spośród dostępnych norm za najbardziej adekwatny przewodnik projektowy dla SyFRC płyt podpartych na gruncie uznano TR34, który uwzględnia zarówno korzystny wpływ włókien, jak i warunków podparcia gruntowego podczas określania nośności płyty. Obliczenia według TR34 pozwoliły na stosunkowo dokładne określenie nośności na przebicie oraz modelu zniszczenia, zwłaszcza przy uwzględnieniu rzeczywistego położenia krytycznego przekroju kontrolnego, zwiększonego udziału podłoża oraz SyFs w przenoszeniu obciążeń. Na koniec, w ramach rozprawy doktorskiej, sformułowano zalecenia dotyczące obliczania nośności z uwagi na przebicie, ze szczególnym uwzględnieniem lokalizacji krytycznego przekroju kontrolnego oraz określenia udziału SyFs w przenoszeniu obciążeń.

Mimo iż przeprowadzone badania dostarczyły wiele cennych wniosków, wskazano również na ograniczenia pracy doktorskiej. Testy obejmowały bowiem wąską liczbę

typów i dozowań SyFs, płyty o określonej geometrii oraz pojedynczy rodzaj obciążenia. W przyszłych badaniach należałoby rozszerzyć zakres analiz o inne rodzaje włókien i schematy obciążeń, a także modelowanie numeryczne, uzupełniające badania eksperymentalne. Niemniej jednak, praca ta znacząco pogłębia wiedzę w temacie wpływu SyFs na pracę płyt na gruncie oraz może stanowić podstawę do przyszłych modyfikacji obowiązujących norm oraz rozwoju praktycznych wytycznych dla projektantów.

PŁYTY NA GRUNCIE Z BETONU ZBROJONEGO WŁÓKNAMI SYNTETYCZNYMI PODDANE CENTRALNEMU OBCIĄŻANIU SIŁĄ SKUPIONA

Poszerzone streszczenie

Tematyka niniejszej rozprawy doktorskiej wpisuje się w aktualne kierunki rozwoju konstrukcji betonowych, w których coraz większy nacisk kładzie się na nowoczesne rozwiązania materiałowe zgodne z idea zrównoważonego budownictwa. Rozwiązania charakteryzują się m.in. zwiększoną trwałością, obniżonymi kosztami eksploatacyjnymi oraz ograniczonym negatywnym oddziaływaniem na środowisko naturalne, przy jednoczesnym zachowaniu wymaganych właściwości mechanicznych elementu. Materiałem, który może spełniać powyższe kryteria, jest fibrobeton (FRC z ang. fiber reinforced concrete). Jednak pomimo rosnacego zainteresowania ta technologia, zdecydowana większość dotychczasowych badań, norm i wytycznych projektowych koncentruje się na fibrobetonach zawierających włókna stalowe (SFRC z ang. steel fiber reinforced concrete). Tym samym, zastosowanie włókien syntetycznych (SyFs z ang. synthetic fibers) w elementach konstrukcyjnych nadal pozostaje ograniczone, spotykając się ze sceptycyzmem i brakiem zaufania ze strony projektantów. Największym obszarem zastosowań SyFs są płyty na gruncie, najczęściej stosowane w halach przemysłowych. Mimo to, obowiązujące normy i przewodniki projektowe w sposób bardzo konserwatywny uwzględniają korzystny wpływ SyFs na nośność tych elementów, tłumacząc to ograniczoną ilością badań w tym temacie. Skutkiem jest często znaczne niedoszacowanie rzeczywistej nośności elementu, co ogranicza efektywność projektowania. Dodatkowo, nadal niedostatecznie rozpoznanym zagadnieniem w literaturze pozostaje problem przebicia płyt na gruncie pod wpływem działania obciążeń skupionych, pochodzących m.in. od kół wózków widłowych, nóg regałów wysokiego składowania czy maszyn, zwłaszcza gdy płyty te wykonane są z betonu z SyFs (SyFRC z ang. synthetic fiber reinforced concrete). W szczególności, wciąż brakuje spójnych i zweryfikowanych wytycznych projektowych określających położenie krytycznego przekroju kontrolnego względem krawędzi pola obciążenia a. Aktualnie obowiązujące normy oraz wytyczne sugerują rozbieżne wartości odległości a wahające się od 0,5d do 2d (gdzie d oznacza użyteczną wysokość płyty), a niektóre proponują integracyjny sposób wyznaczenia tej lokalizacji. Różnice występują również w sposobie obliczania wartości v_f , czyli dodatkowej wytrzymałości na ścinanie przy przebiciu, wynikającej z dodania do betonu włókien. W konsekwencji, istnieje wyraźna luka badawcza dotycząca wpływu dodatku, ilości i rodzaju SyFs na nośność na przebicie płyt podpartych na gruncie. Uzupełnienie tej luki stanowiło jeden z głównych celów rozprawy doktorskiej.

W ramach pracy sformułowano pięć tez naukowych oraz siedem szczegółowych celów badawczych. Jednym z nich było przeprowadzenie kompleksowego przeglądu literatury, który obejmował wybrane modele teoretyczne i analityczne, normy dotyczące badań oraz projektowania elementów z SyFRC, jak również wyniki dotychczasowych badań eksperymentalnych wpływu SyFs na właściwości betonu i pracę płyt na gruncie. Głównym celem rozprawy było jednak uzupełnienie aktualnego stanu wiedzy poprzez realizację kompleksowego programu badawczego, obejmującego zarówno testy laboratoryjne małych próbek, jak i badania płyt podpartych na gruncie, poddanych działaniu centralnej siły skupionej. Szczególny nacisk położono na analizę ich zachowania przy przebiciu i wpływu dodatku, ilości i rodzaju SyFs. Jednym z kluczowych wyzwań było opracowanie i wdrożenie odpowiedniej metodologii badawczej, w tym zaprojektowanie i wykonanie dedykowanego stanowiska badawczego do testów elementów płytowych. Równocześnie ważną częścią pracy było porównanie wyników badań z wynikami obliczeń wybranych modeli analitycznych, takich jak modele Westergaarda, Shentu i in., Falknera i in. oraz procedur projektowych Technicznego 34 (TR34),bazującego na teorii linii załomów Raportu Meyerhof'a-Losberg'a i wytycznych Eurokodu 2. Celem była ocena ich przydatności do oszacowania nośności i modelu zniszczenia SyFRC płyt podpartych na gruncie oraz opracowanie praktycznych wskazówek projektowych. Tezy rozprawy przedstawione w Tabela 1 dotyczyły: możliwości oszacowania odpowiedzi konstrukcyjnej SyFRC płyt na podstawie wyników badań wytrzymałości na rozciąganie przy zginaniu próbek belkowych; wpływu dodatku, ilości i rodzaju SyFs na nośność z uwagi na przebicie i położenie krytycznego obwodu kontrolnego stożka przebicia; oraz znaczenia warunków podparcia płyt dla pracy elementu, jego nośności i mechanizmu zniszczenia.

Metodologia badań obejmowała sześć wariantów mieszanek betonowych, w tym pięć rodzajów SyFRC, różniących się typem zastosowanego SyFs (PM, PD, FF) oraz ich dozowaniem (2 i 3 kg/m³), a także beton referencyjny niezbrojony włóknami (PC). Zamówiono beton klasy C40/50 z 400 kg/m³ cementu portlandzkiego CEM I 42,5R, przy współczynniku wodno-cementowym (w/c) równym 0,50. Jako kruszywo drobne zastosowano 670 kg/m³ piasku o uziarnieniu 0/2 mm, natomiast kruszywem grubym był żwir o maksymalnym uziarnieniu 8 mm w ilości 1012 kg/m³. W celu zapewnienia wymaganej urabialności, zastosowano dwa typy domieszek chemicznych: 2,12 kg/m³ Masterglenium Sky 591 oraz 3,20 kg/m³ Masterpozzolith 501 HE. Skład wszystkich

mieszanek betonowych był stały, a jedynym parametrem zmiennym była zawartość i rodzaj włókien: PC (0 kg/m³ – typ 1), PM_2 (2 kg/m³ włókien typu PM – typ 2), PM_3 (3 kg/m³ włókien typu PM – typ 3), PD_2 (2 kg/m³ włókien typu PD – typ 4), PD_3 (3 kg/m³ włókien typu PD – typ 5), FF_2 (2 kg/m³ włókien typu FF – typ 6). Charakterystyka użytych włókien zestawiona jest w Tabela 2 i uwzględniono w niej następujące parametry: długość włókna l_f , średnica włókna d_f , smukłość włókna l_f/d_f , wytrzymałość włókna na rozciąganie f_{ft} , i moduł Young'a włókna E_f .

Tabela 1 Tezy naukowe rozprawy doktorskiej

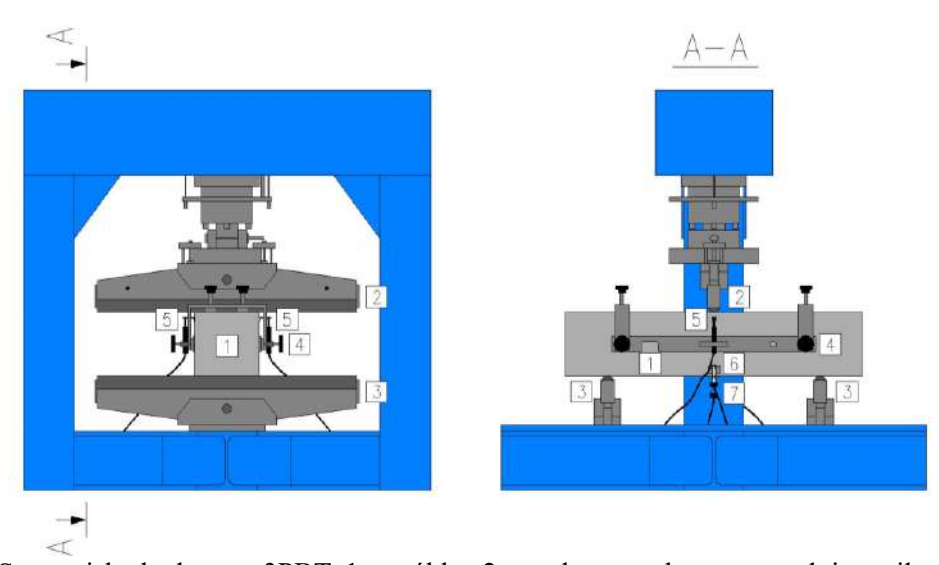
| Lp. | Tezy naukowe |
|-----|---|
| 1. | Odpowiedź konstrukcyjną betonowych płyt na gruncie zbrojonych włóknami syntetycznymi, |
| | obciążonych centralną siłą skupioną, można wiarygodnie przewidzieć na podstawie wyników |
| | uzyskanych z badań próbek belkowych poddanych rozciąganiu przy zginaniu. |
| 2. | Odpowiedź konstrukcyjna betonowych płyt na gruncie zbrojonych włóknami syntetycznymi, |
| | obciążonych centralną siłą skupioną, różni się znacząco od zachowania płyt niepodpartych, |
| | szczególnie pod względem nośności i modelu zniszczenia. |
| 3. | Dodatek włókien syntetycznych korzystnie wpływa na pracę betonowych płyt na gruncie po |
| | ich zarysowaniu oraz prowadzi do bardziej plastycznego modelu zniszczenia w porównaniu do |
| | płyt bez dodatku włókien. |
| 4. | Zastosowanie oraz zwiększenie ilości włókien syntetycznych zwiększa nośność z uwagi na |
| | przebicie oraz wydłuża krytyczny obwód kontrolny płyt na gruncie. |
| 5. | Rodzaj zastosowanych włókien syntetycznych ma wpływ zarówno na nośność z uwagi na |
| | przebicie, jak i na długość krytycznego obwodu kontrolnego płyt na gruncie. |

Tabela 2 Charakterystyka użytych SyFs

| Cecha | PM | PD | FF | | |
|-----------|---|--------------------------------|---|--|--|
| l_f | 54 mm | 48 mm | 54 mm/54 mm | | |
| d_f | 0,45 mm | 0,60 mm | 0,45 mm/brak danych | | |
| l_f/d_f | 120 | 80 | 120/brak danych | | |
| f_{ft} | 550-650 MPa | 500-580 MPa | 620-758 MPa | | |
| E_f | 4,8-5,9 GPa | > 10 GPa | brak danych | | |
| Forma | wytłaczane, skręcane, multifilamentowe | wytłaczane, monofilamentowe | hybrydowe: 95% skręcane, multifilamentowe/5% fibrylowane | | |
| Materiał | kopolimer | polimer | kopolimer/polipropylen | | |
| Тур | makrowłókna | makrowłókna | makrowłókna/mikrowłókna | | |
| Zdjęcie | | | | | |

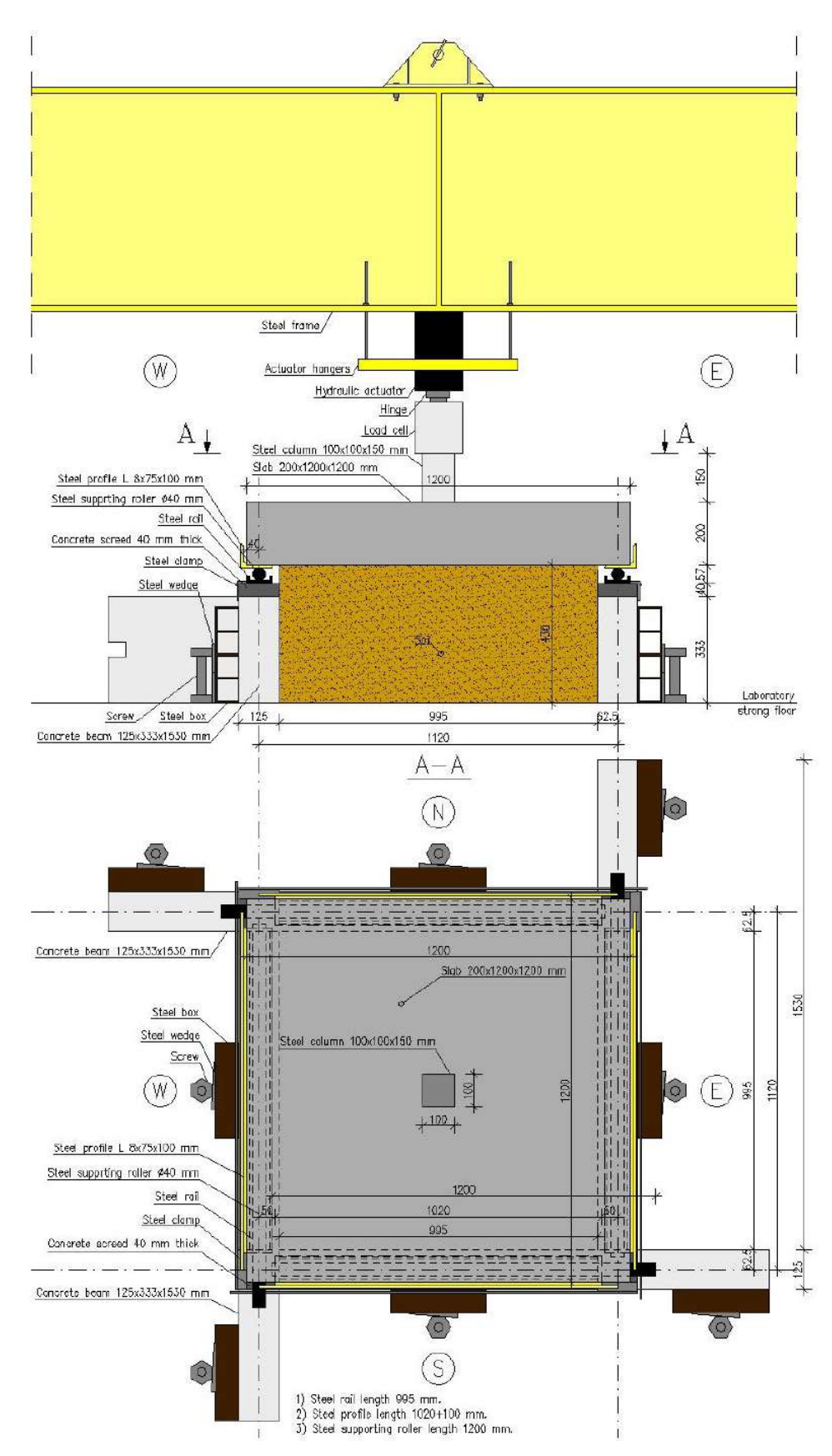
Badania został podzielony na dwa główne etapy: badania materiałowe oraz badania elementów płytowych. W pierwszym etapie określono podstawowe właściwości mechaniczne badanych betonów. Obejmowały one: moduł sprężystości (rdzenie o wymiarach \$\phi94\$ x 188 mm), wytrzymałość na ściskanie (próbki formowane o wymiarach \$150\$ x 150 mm + rdzenie o wymiarach \$\phi94\$ x 188 mm), wytrzymałość

na rozciąganie przy rozłupywaniu (rdzenie o wymiarach ϕ 94 x 94 mm) oraz wytrzymałość na rozciąganie przy zginaniu (belki formowane o wymiarach 150 x 150 x 550 mm). Badania trzy-punktowego zginania (3PBT) przeprowadzono zgodnie z normą PN-EN 14651 w celu obliczenia granicy proporcjonalności $f_{ct,L}$, wytrzymałości resztkowej $f_{R,j}$ oraz energii pękania Testy wykonano przy użyciu stanowiska badawczego, którego schemat przedstawiono na Rysunek 1.



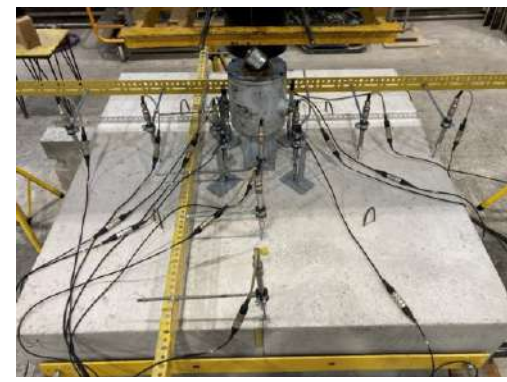
Rysunek 1 Stanowisko badawcze 3PBT: 1 – próbka, 2 – podpora ruchoma wywołująca siłę, 3 – podpora nieruchoma, 4 – stalowa, sztywna rama do instalacji czujników LVDT, 5 – czujnik LVDT do pomiaru ugięć, 6 – miernik zaciskowy do pomiaru *CTOD* (szerokość rozwarcia czubka rysy z ang. *crack tip opening displacement*), 7 – miernik zaciskowy do pomiaru *CMOD* (szerokość rozwarcia rysy z ang. *crack mouth opening displacement*)

W drugim etapie przeprowadzono badania doświadczalne osiemnastu płyt (po trzy próbki dla każdego wariantu betonu 1-6), o wymiarach 200 x 1200 x 1200 mm. Celem testów było określenie zależności pomiędzy obciążeniem skupionym a ugięciem płyty, analiza morfologii zarysowań, ugięć, mechanizmu zniszczenia oraz geometrii stożka przebicia. Grubość płyty została dobrana tak, aby odpowiadała rzeczywistym wymiarom stosowanym w konstrukcjach płyt na gruncie w magazynach czy parkingach o średnim poziomie obciążenia. Natomiast jej długość i szerokość ograniczono na podstawie analizy promienia względnej sztywności płyty *l*. Podobne podejście zaobserwowano w innych badaniach płyt na gruncie, a przegląd literatury wskazał, że płyty o nieskończonych wymiarach obciążone w środku można zastąpić fragmentami płyt o długości boków odpowiadających odległości między punktami zerowymi przemieszczeń, szczególnie kiedy przedmiotem analiz jest nośność z uwagi na przebicie. Do realizacji badań wykorzystano specjalnie zaprojektowane stanowisko badawcze, którego celem było jak najlepsze odwzorowanie warunków pracy obciążanej punktowo płyty na gruncie (Rysunek 2 i Rysunek 3).



Rysunek 2 Projekt stanowiska badawczego dla testów płyt podpartych na gruncie obciążonych centralną siłą skupioną





Rysunek 3 Widok stanowiska badawczego dla testów płyt podpartych na gruncie obciążonych centralną siłą skupioną

Podparcie gruntowe symulowano za pomocą 43-centymetrowej warstwy zagęszczonego kruszywa, natomiast obciążenie skupione przez statyczne oddziaływanie stalowego stempla o wymiarach podstawy 100 x 100 mm, imitując nacisk podstawy nogi regału. Grunt został umieszczony w skrzyni o wymiarach 377 x 995 x 995 mm, ograniczonej z czterech stron betonowymi burtami, a podstawę stanowiła płyta wielkich sił laboratorium. Należy również zaznaczyć, że zagęszczenie gruntu kontrolowano przed każdym badaniem, zapewniając powtarzalność warunków podparcia. Średnia wartość pierwotnego modułu odkształcenia podłoża E_{vl} wynosiła 139 MPa, przy odchyleniu standardowym równym 5,67 MPa i współczynniku zmienności 4,09%. Rejestrację przemieszczeń płyty umożliwiał wielopunktowy system pomiarowy, składający się z dwunastu czujników LVDT (z ang. Linear Variable Differential Transformer), rozmieszczonych wzdłuż osi symetrii płyty. Płyty badano zazwyczaj do momentu wystąpienia nagłego spadku przenoszonej siły, któremu towarzyszyło przebicie oraz znaczne deformacje płyty. W przypadku braku jednoznacznego załamania wykresu siła-ugięcie, test kontynuowano do momentu, w którym zaobserwowano istotny przyrost ugięcia przy niezmiennej wartości siły. Czasami ograniczeniem okazywało się również przekroczenie zakresu pomiaru przemieszczeń czujników LVDT lub wysięgu siłownika.

Wyniki badań materiałowych zestawiono w Tabela 3. Stwierdzono, że urabialność mieszanek, oceniana metodą rozpływu stożka, nie była stała i wahała się w zakresie klas konsystencji od F3 do F5. Tylko mieszanki typu 1 (PC) oraz 2 (PM_2) spełniły wymagania zakładanej klasy F5. W pozostałych typach dodatek SyFs wpłynął negatywnie na urabialność mieszanki betonowej. Wytrzymałość na ściskanie badanych próbek formowanych $f_{c,cube}$ oraz wywierconych rdzeni $f_{c,core}$ charakteryzowała się znacznym rozrzutem wartości pomiędzy typami 1-6, odpowiednio od 27,99 do 54,46 MPa oraz od 23,51 do 38,56 MPa. Zgodnie z przeglądem literatury, wpływ dodatku SyFs na wytrzymałość na ściskanie nie powinien być tak znaczący. Jej wartość

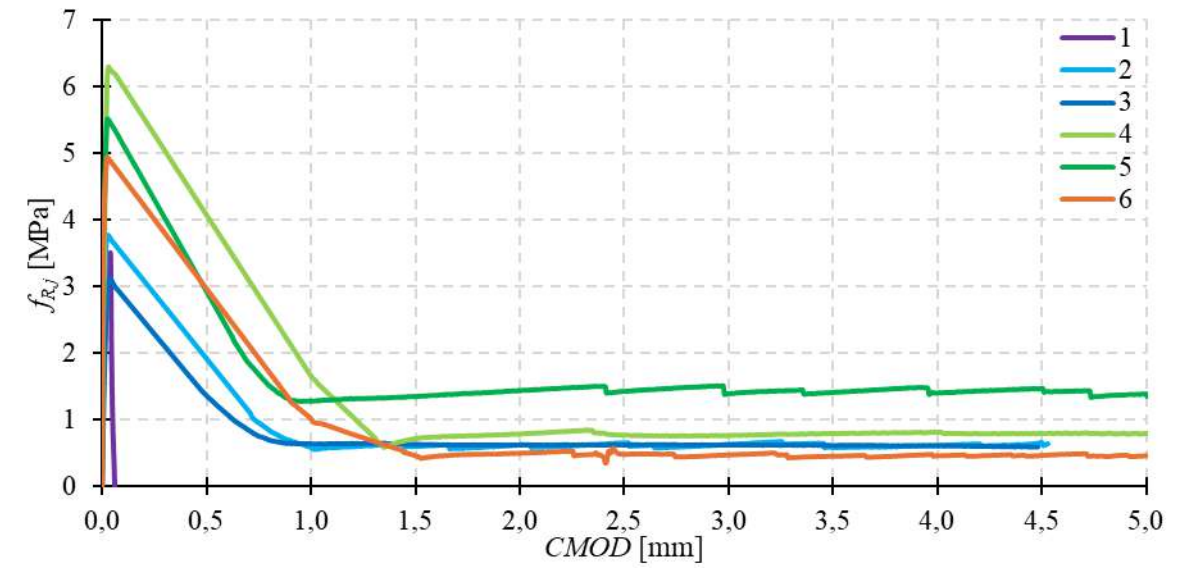
zależy bowiem przede wszystkim od jakości matrycy betonowej, którą determinuje m.in. rodzaj i ilość cementu oraz kruszywa, a także stosunek w/c. Na obserwowane wyniki istotny wpływ miała zróżnicowana urabialność mieszanek oraz niezamierzony zmienny skład betonów, różniący się pomiędzy poszczególnymi typami. W szczególności, mieszanki betonowe charakteryzowały się różną zawartością wody, co było konsekwencją zmiennej wilgotności kruszywa przechowywanego na otwartej przestrzeni i poddanego działaniu czynników atmosferycznych. Ponadto, proces betonowania płyt odbywał się na przełomie sześciu miesięcy, co wiązało się z wykorzystaniem materiałów pochodzących z różnych dostaw, a w konsekwencji mogło wpłynąć na zmienność właściwości betonu. Analogiczne spostrzeżenia dotyczą pierwotnego i ustabilizowanego modułu sprężystości oznaczonych odpowiednio jako $E_{c0,core}$ oraz $E_{cs,core}$. Warto również zauważyć, że zbadane wartości modułów sprężystości wszystkich betonów typu 1-6 były niższe od wartości przewidywanych na podstawie obowiązujących norm. Różnice te mogły wynikać zarówno z rodzaju zastosowanego kruszywa, jak i z faktu, że próbki rdzeniowe były pobierane z płyt wcześniej obciążonych. Podsumowując, znacząca zmienność właściwości materiałów wsadowych mieszanki skutkowała rozbieżnościami we właściwościach mechanicznych betonu, co uniemożliwiło bezpośrednie porównanie wszystkich badanych typów betonów zarówno w przypadku próbek normowych, jak i elementów płytowych. W związku z tym, aby ocenić wpływ dodatku optymalnej ilości SyFs, skoncentrowano się na porównaniu betonów typu 1 i 2. Dla zobrazowania efektu nadmiernej ilości SyFs przeanalizowano różnice pomiędzy próbkami betonów typu 1 i 3. Natomiast analiza porównawcza betonów typu 4 i 5 umożliwiła ocenę wpływu zwiększonej ilości dozowanych SyFs przy zachowaniu odpowiedniej urabialności. Wreszcie porównanie próbek typu 2 i 6 miało na celu określenie wpływu rodzaju SyFs.

Zgodnie z przyjętymi założeniami stwierdzono, że zarówno sam dodatek, jak i zwiększona zawartość SyFs korzystnie wpłynęły na wytrzymałość betonu na rozciąganie przy rozłupywaniu f_{ct} w porównaniu z betonem niezbrojonym. W teście 3PBT (Rysunek 4) próbki PC ulegały typowemu, kruchemu zniszczeniu bezpośrednio po osiągnięciu granicy proporcjonalności $f_{ct,L}$, nie wykazując jakiejkolwiek resztkowej wytrzymałości na rozciąganie przy zginaniu $f_{R,j}$. Z kolei próbki SyFRC, niezależnie od rodzaju i ilości włókien, wykazywały zdolność do przenoszenia obciążeń po zarysowaniu, charakteryzując się plastycznym mechanizmem zniszczenia i zachowując integralność strukturalną, nawet po zakończeniu badania. Dodatek włókien skutkował również wzrostem wartości $f_{ct,L}$ oraz $f_{R,j}$, a także energii pękania SyFRC typu 2 w porównaniu do betonu typu 1. Zwiększenie dawki włókien PM oraz PD z 2 do 3 kg/m³

nie przyniósł jednak spodziewanego wzrostu $f_{ct,L}$. W przypadku próbek typu 3 mogło to wynikać z pogorszonej urabialności mieszanki oraz nierównomiernego rozmieszczenia włókien w matrycy betonowej. Natomiast w przypadku próbek typu 5, zwiększona ilość SyFs korzystnie wpłynęła na $f_{R,j}$, wskazując na poprawę wytrzymałości dopiero po zarysowaniu. Porównując belki typu 2 i 6, zaobserwowano, że fibrobeton z włóknami FF osiągnął wyższe wytrzymałości f_{ct} i $f_{ct,L}$. Prawdopodobnie wynikało to z obecności w próbkach FF_2 mikrowłókien, które skuteczniej mostkowały mikropęknięcia w początkowej fazie obciążenia. Z drugiej strony, próbki typu 6 charakteryzowały się niższą wytrzymałością $f_{R,j}$ w porównaniu z betonem typu 2, co można przypisać mniejszej zawartości włókien makro, które odgrywają kluczową rolę w fazie po zarysowaniu.

Tabela 3 Wyniki badań urabialności i właściwości mechanicznych betonów typu 1-6

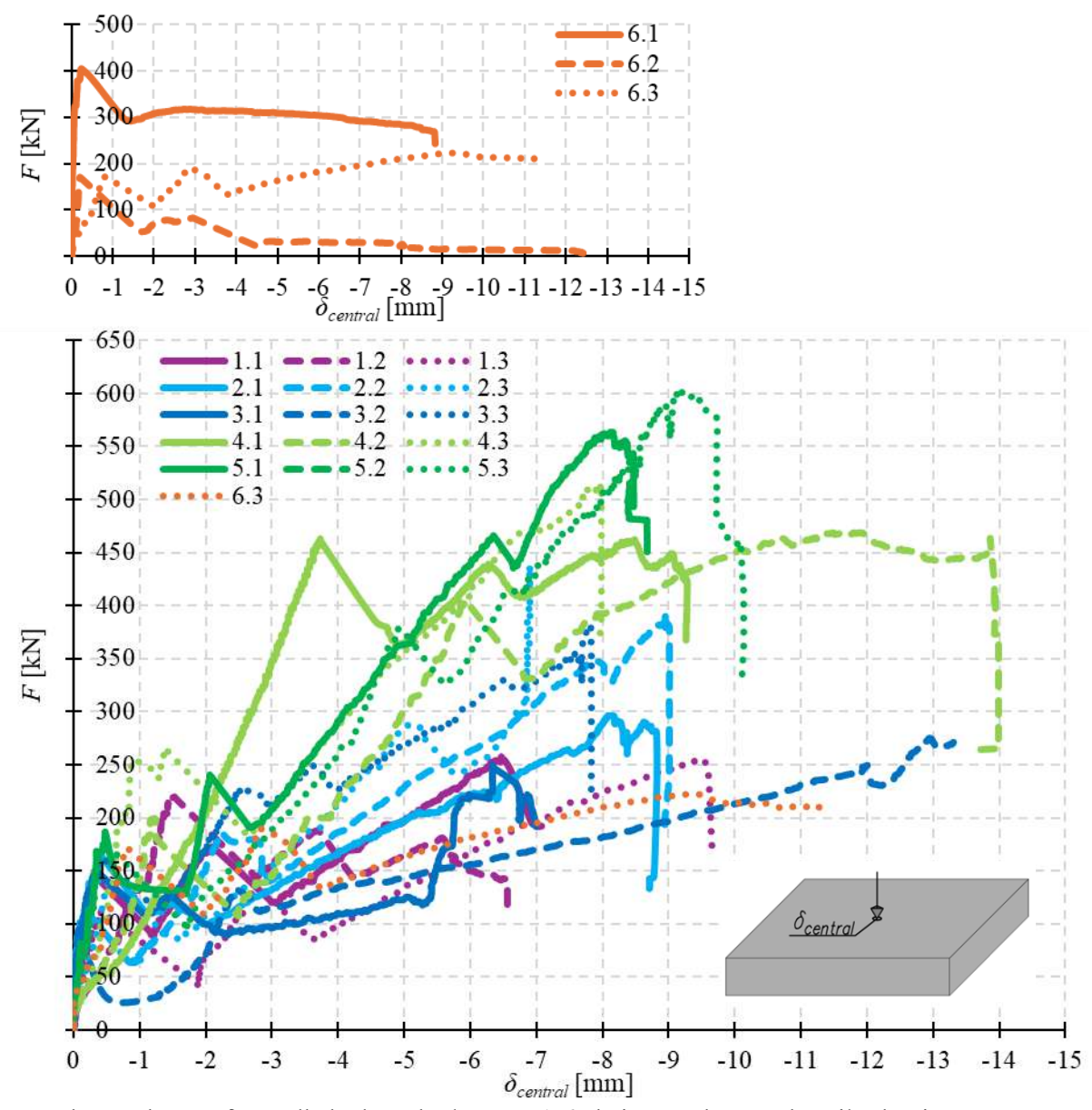
| Właściwość | 1 (PC) | 2 (PM_2) | 3 (PM_3) | 4 (PD_2) | 5 (PD_3) | 6 (FF_2) |
|----------------------|--------|----------|----------|----------|----------|----------|
| Urabialność [mm] | 575 | 600 | 465 | 495 | 510 | 531 |
| (klasa konsystencji) | (F5) | (F5) | (F3) | (F4) | (F4) | (F4) |
| $f_{c,cube}$ [MPa] | 35,01 | 40,19 | 27,99 | 52,95 | 54,46 | 43,03 |
| $f_{c,core}$ [MPa] | 25,01 | 27,11 | 23,51 | 36,16 | 38,56 | 30,76 |
| $E_{c0,core}$ [GPa] | 17,047 | 18,089 | 15,369 | 24,478 | 26,170 | 24,290 |
| $E_{cs,core}$ [GPa] | 19,748 | 21,419 | 18,020 | 27,149 | 29,901 | 26,734 |
| $f_{spl,core}$ [MPa] | 2,12 | 2,22 | 2,04 | 3,00 | 3,18 | 2,71 |
| f_{ct} [MPa] | 1,91 | 1,99 | 1,84 | 2,70 | 2,86 | 2,44 |
| $f_{ct,L}$ [MPa] | 3,499 | 3,765 | 3,107 | 6,303 | 5,504 | 4,926 |
| $f_{R,I}$ [MPa] | 0,000 | 1,915 | 1,359 | 4,081 | 2,923 | 2,962 |
| $f_{R,2}$ [MPa] | 0,000 | 0,596 | 0,629 | 0,711 | 1,346 | 0,457 |
| $f_{R,3}$ [MPa] | 0,000 | 0,646 | 0,620 | 0,768 | 1,422 | 0,476 |
| $f_{R,4}$ [MPa] | 0,000 | 0,582 | 0,611 | 0,793 | 1,403 | 0,448 |



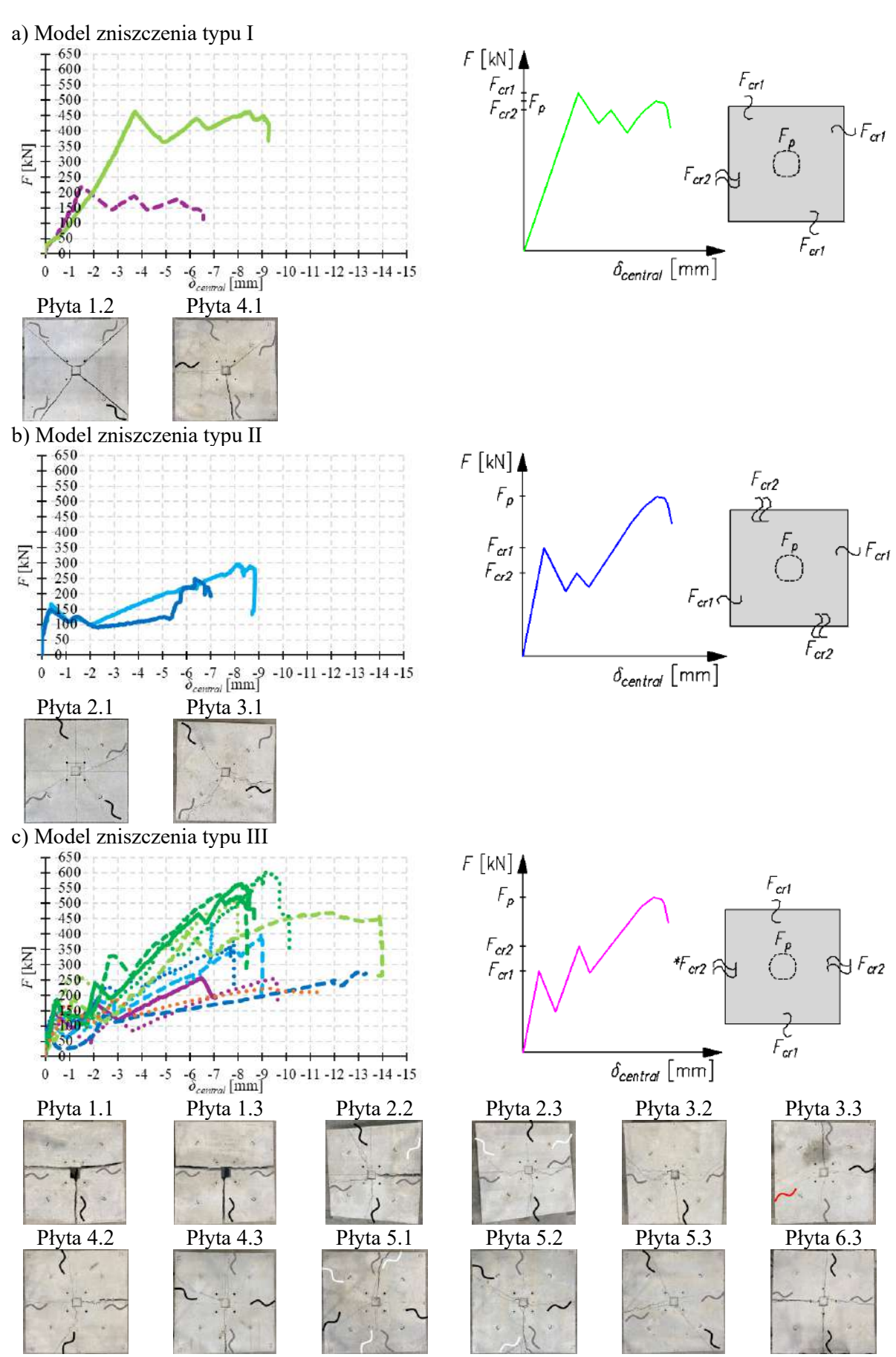
Rysunek 4 Wykresy uśrednionych $f_{R,i}$ -CMOD dla betonów typu 1-6 badanych w 3PBT

W celu oceny wpływu sposobu uwarstwienia podłoża gruntowego na pracę elementu płytowego oraz porównania odpowiedzi konstrukcyjnej płyty podpartej i niepodpartej na gruncie przeprowadzono wstępne badania trzech płyt typu 6 (Rysunek 5). Płyta 6.2, oparta wyłącznie wzdłuż krawędzi na stalowych wałkach (bez kontaktu z podłożem gruntowym), wykazała istotnie niższą nośność oraz uległa zniszczeniu z uwagi na zginanie, bez widocznych rys ścinających charakterystycznych przy przebiciu. W przeciwieństwie do niej, płyty 6.1 i 6.3, podparte na zagęszczonym podłożu gruntowym, wykazywały wyraźne oznaki zniszczenia przez przebicie, o czym świadczyło m.in. pojawienie się stożka przebicia. Na podstawie tych obserwacji stwierdzono, że w procesie projektowania płyt na gruncie nie można pominąć sprawdzenia warunku przebicia. Konieczne jest również prowadzenie odrębnych analiz płyt niepodpartych oraz podpartych na podłożu gruntowym, ze względu na różnice w ich zachowaniu konstrukcyjnym i zidentyfikowanych mechanizmach zniszczenia. Ponadto, badania płyt 6.1 i 6.3 wykazały, że sposób przygotowania i uwarstwienia podłoża gruntowego ma znaczący wpływ na pracę elementu płytowego. Dodatkowo, na podstawie wniosków z badań wstępnych przyjęto sposób przygotowania i uwarstwienia podłoża dla badań pozostałych płyt typu 1-5. Mianowicie, podłoże składało się z trzech warstw kruszywa łamanego, z wierzchnią, cienką warstwą kruszywa o drobniejszym uziarnieniu, która miała zapewnić równomierny kontakt płyty z podłożem. W oparciu o wyniki z badania płyt określono zależności pomiędzy obciążeniem skupionym F a ugięciem w środku płyty $\delta_{central}$ (Rysunek 5). Stwierdzono, że przebieg zależności F- $\delta_{central}$ był dość podobny dla każdej z badanych płyt na gruncie, ponieważ we wszystkich przypadkach zniszczenie następowało w wyniku przebicia, gdzie siła odpowiadająca przekroczeniu nośności na przebicie oznaczona została jako F_p . Przedtem jednak obserwowano pojawienie się rys giętnych w dwóch etapach, widocznych na bocznych krawędziach płyty, którym odpowiadały siły F_{cr1} i F_{cr2} . Po ich osiągnięciu następował znaczny spadek przenoszonego obciążenia. Na Rysunek 6 przedstawiono klasyfikację modeli zniszczenia badanych płyt podpartych na gruncie, obciążanych centralną siłą skupioną. Model zniszczenia typu I został zidentyfikowany w dwóch przypadkach i charakteryzował się jednoczesnym pojawieniem się rys giętnych wzdłuż trzech krawędzi płyty przy sile F_{crl} , a następnie powstaniem rysy na pozostałej krawędzi przy F_{cr2} , a ostatecznie do zniszczenia płyty przez przebicie. W tym modelu wartość F_{cr1} przewyższała zarówno F_{cr2} , jak i F_p . W przypadku modeli zniszczenia typu II i III, morfologia zarysowań była bardzo podobna, ponieważ pierwsze zarysowania pojawiały się na dwóch przeciwległych krawędziach płyty przy sile F_{crl} , po czym przy F_{cr2} dochodziło do zarysowania jednej lub obu pozostałych krawędzi.

Zniszczenie płyty wynikało z jej przebicia. Różnica pomiędzy tymi dwoma modelami dotyczyła relacji między siłami inicjującymi kolejne etapy zarysowania. W modelu II: $F_{crl} > F_{cr2}$, a w modelu III: $F_{cr2} > F_{crl}$. Prawdopodobne jest, że płyty 2.1 i 3.1 po pierwszym zarysowaniu charakteryzowały się większym spadkiem sztywności, co mogło wpłynąć na dalszy rozwój zarysowań i nośność próbek. Niezależnie od przyjętego modelu zniszczenia II lub III, maksymalna osiągnięta siła odpowiadała nośności na przebicie F_p . Większość badanych płyt wykazywała III model zniszczenia. Rysunek 6 przedstawia także morfologię rys na górnej powierzchni płyt oraz obserwowaną kolejność ich pojawiania się: kolorem szarym oznaczono zarysowanie odpowiadające pierwszej rysie przy F_{crl} , kolorem czarnym drugiej przy F_{cr2} , a kolorem białym lub czerwonym kolejnych rys.



Rysunek 5 Wykres F- $\delta_{central}$ dla badanych płyt typu 1-6 obciążonych centralną siłą skupioną



Rysunek 6 Klasyfikacja modeli zniszczenia płyt podpartych na gruncie, obciążonych centralną siłą skupioną

Tabela 4 zestawia siły odpowiadające zarysowaniom przy zginaniu (F_{cr1} oraz F_{cr2}) i nośności na przebicie (F_p), wraz z odpowiadającymi im ugięciami w środku płyty ($\delta_{central}$). Dla każdego typu płyty 1-6 obliczono również wartości średnie. Ze względu na znacząco odmienny model zniszczenia, płyty 1.2 i 4.1 nie zostały uwzględnione ani przy obliczaniu średnich, ani w analizie porównawczej płyt.

Tabela 4 Zestawienie sił odpowiadających zarysowaniu przy zginaniu i przebiciu wraz z odpowiadającymi ugięciami w środku płyty dla badanych płyt typu 1-6 podpartych na gruncie, obciążonych centralną siłą skupioną

| Pły | ta nr | F_{cr1} [kN] | $\delta_{central,Fcr1}$ [mm] | F_{cr2} [kN] | $\delta_{central,Fcr2}$ [mm] | F_p [kN] | $\delta_{central,Fp}$ [mm] |
|-----|-------|-------------------|------------------------------|-------------------|------------------------------|------------|----------------------------|
| 1.1 | | 144,01 | -0,343 | 172,56 | -2,108 | 257,57 | -6,469 |
| 1.2 | PC | 219,82 | -1,527 | 187,98 | -3,675 | 180,73 | -5,589 |
| 1.3 | P | 112,04 | -0,413 | 137,95 | -2,775 | 255,91 | -9,478 |
| 1 | | 128,03 | -0,378 | 155,26 | -2,44 | 256,74 | -7,974 |
| 2.1 | | 166,99 | -0,379 | 118,76 | -1,505 | 296,31 | -8,158 |
| 2.2 | 1_2 | 108,69 | -0,218 | 186,54 | -2,237 | 395,13 | -8,946 |
| 2.3 | PM | 142,20 | -0,541 | 289,05 | -5,111 | 438,06 | -6,897 |
| 2 | | 139,29 | -0,379 | 198,12 | -2,951 | 376,50 | -8,000 |
| 3.1 | | 148,73 | -0,372 | 126,35 | -1,484 | 249,35 | -6,337 |
| 3.2 | [_3 | 96,91 | -0,085 | 132,98 | -2,423 | 276,69 | -12,990 |
| 3.3 | PM | 164,40 | -0,429 | 226,86 | -2,528 | 381,67 | -7,817 |
| 3 | | 136,68 | -0,295 | 162,06 | -2,145 | 302,57 | -9,048 |
| 4.1 | | 463,13 | -3,731 | 439,38 | -6,272 | 462,37 | -8,486 |
| 4.2 | 2_ | 198,48 | -1,242 | 405,47 | -5,918 | 468,97 | -11,695 |
| 4.3 | PD | 254,92 | -0,887 | 265,67 | -1,379 | 513,00 | -7,911 |
| 4 | | 226,70 | -1,065 | 335,57 | -3,649 | 490,99 | -9,803 |
| 5.1 | | 186,70 | -0,475 | 240,50 | -2,058 | 563,71 | -8,119 |
| 5.2 | _3 | 181,86 | -0,418 | 327,22 | -2,664 | 528,91 | -7,251 |
| 5.3 | PD | 178,37 | -0,446 | 379,48 | -4,942 | 601,80 | -9,176 |
| 5 | | 182,31 | -0,446 | 315,73 | -3,221 | 564,81 | -8,182 |
| 6.3 | FF_2 | 171,94 | -0,804 | 190,22 | -2,829 | 222,82 | -9,424 |

Uwaga: Płyty 1.2 i 4.1 nie zostały uwzględnione w analizie porównawczej, ponieważ ich odpowiedź konstrukcyjna znacząco różniła się od pozostałych płyt (Rysunek 6).

Stwierdzono, że dodatek włókien PM w ilości 2 kg/m^3 spowodował wzrost średnich wartości sił F_{cr1} oraz F_{cr2} odpowiednio o 9% i 28%. Ponadto, zaobserwowano istotne, 47% zwiększenie średniej wartości siły F_p płyt typu 2 w porównaniu z płytami typu 1. Zwiększenie dozowania włókien PM do 3 kg/m^3 nie przyniosło jednak oczekiwanego dalszego wzrostu nośności na zginanie i przebicie względem płyt typu 2. Niemniej jednak, płyty typu 3 charakteryzowały się nadal wyższymi średnimi wartościami sił: F_{cr1} o 7%, F_{cr2} o 4%, oraz F_p o 18% względem płyt PC. Z kolei zwiększenie ilości włókien PD z 2 do 3 kg/m^3 , przy zachowanej odpowiedniej urabialności, przyczyniło się do wzrostu F_p o 15%, jednak nie wpłynęło korzystnie na wartości F_{cr1} oraz F_{cr2} w porównaniu do płyt typu 4. Wyniki te znajdują odzwierciedlenie w wynikach 3PBT belek typu 4 i 5. Granica proporcjonalności $f_{ct,L}$ próbek PD_3 była bowiem o 13% niższa

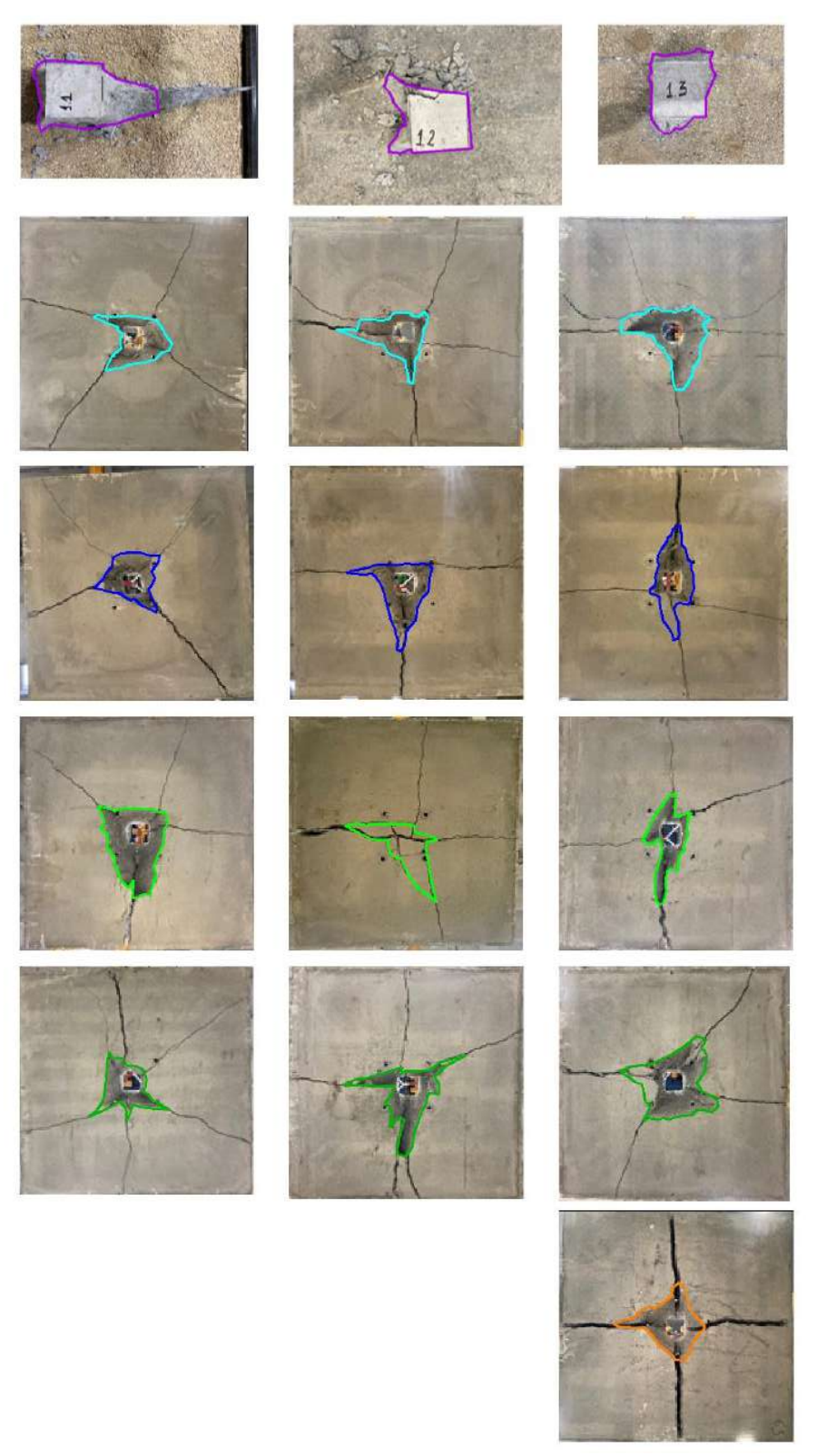
niż dla PD 2, natomiast belki typu 5 charakteryzowała większa wytrzymałość resztkowa $f_{R,i}$ niż belki typu 4. Istotny wydaje się również rodzaj zastosowanych włókien na odpowiedź konstrukcyjną płyt. Zmiana z włókien FF na PM doprowadziła do zwiększenia średniej siły F_p aż o 69%. Jednocześnie, fibrobeton typu 6 osiągnął o 23% wyższe wartości F_{crl} , natomiast o 4% niższe wartości F_{cr2} w porównaniu do płyty typu 2. Zależności te częściowo znajdują potwierdzenie w wynikach 3PBT, gdzie wartość $f_{ct,L}$ dla belek FF 2 była o 31% wyższa niż dla PM 2, natomiast wytrzymałość resztkowa $f_{R,i}$ dla próbek typu 2 zazwyczaj przewyższała wartość $f_{R,i}$ próbek typu 6. Może to tłumaczyć niższe wartości F_{crl} , ale wyższe F_p dla płyt PM 2 względem płyt FF 2. Należy jednak zaznaczyć, że w analizie porównawczej uwzględniono jedynie wyniki płyty 6.3, co może ograniczać ogólność powyższych wniosków. Jednym z kluczowych spostrzeżeń był również fakt, że wszystkie badane płyty PC ulegały kruchemu zniszczeniu, dzieląc się na trzy lub cztery segmenty wyznaczone przez rysy. W przeciwieństwie do nich, płyty SyFRC zachowały swoją integralność strukturalną nawet przy znacznej rozwartości rys. Wykazywały one również większą zdolność redystrybucji obciążeń oraz ich przenoszenia po zarysowaniu. Przykładowo, płyty 2.2, 2.3, 5.1 i 5.2 charakteryzowały się zwiększoną liczbą rys promieniowych (Rysunek 6).

Analizy porównawcze objęły również charakterystykę geometrii stożków przebicia, które uzyskano poprzez ich wypchnięcie z płyt typów 1-6 za pomocą ręcznego podnośnika hydraulicznego zapartego o stalową ramę. Wstępna metoda wyznaczania kąta nachylenia stożka θ przy użyciu kątomierza okazała się niewystarczająco precyzyjna. Głównymi przyczynami były: znaczna nieregularność kształtu stożków (Rysunek 7), duże rozbieżności pomiędzy pojedynczymi pomiarami kątów oraz ograniczona liczba wykonanych pomiarów w nierównomiernych odstępach. W związku z tym zastosowano alternatywną metodologię, polegającą na wyznaczeniu zastępczej długości krytycznego obwodu kontrolnego stożka przebicia ueg. Na początku, przy wykorzystaniu oprogramowania AutoCAD (Rysunek 8), określono długość obwodu podstawy stożka przebicia ubase odpowiednio z widoku z góry dla płyt PC, ze względu na ich kruchy charakter zniszczenia, oraz z widoku od dołu dla płyt SyFRC, w których obecność włókien umożliwiła inwentaryzację powierzchni dolnej płyty. Następnie, przy założeniu, że użyteczna wysokość płyty wynosi d = 0.75h (gdzie h to grubość płyty), obliczono odpowiadającą długość obwodu kontrolnego stożka na tej wysokości $(u_{eq} = 0.75 u_{base})$. Na podstawie wartości u_{eq} określono odpowiadającą mu odległość a oraz kat θ . Wyniki tych obliczeń zestawiono w Tabela 5, natomiast na Rysunek 9 przedstawiono średnie wartości kata nachylenia stożków przebicia θ poszczególnych typów płyt 1-6. Położenia krytycznego przekroju kontrolnego a płyt SyFRC mieściły

się w zakresie od 0,64d do 0,98d, w zależności od rodzaju i dawki włókien, podczas gdy dla płyt PC a = 0.11d. Przeprowadzona analiza wykazała, że obciążenie siłą skupioną płyt PC doprowadziło do powstawania niemal pionowych stożków przebicia o kształcie zbliżonym do prostopadłościanu. Natomiast w przypadku płyt SyFRC obserwowano stożki o nieregularnym kształcie ściętego ostrosłupa. Dodatek SyFs skutkował zatem zmniejszeniem kąta nachylenia stożka przebicia θ oraz zwiększeniem odległości krytycznego obwodu kontrolnego od powierzchni obciążenia a. Podobną tendencję zaobserwowano w przypadku płyt typu 5, zawierających zwiększoną ilość włókien PD (3 kg/m³), w porównaniu do płyt typu 4 (2 kg/m³), gdzie również stwierdzono spadek wartości kąta θ oraz wzrost odległości a. Natomiast w przypadku stożków przebicia z płyt typu 2 i 3, zawierających włókna PM, nie zaobserwowano wyraźnego wpływu zwiększenia dozowania SyFs na geometrię stożków. Prawdopodobną przyczyną była tutaj obniżona wytrzymałość na ściskanie oraz nierównomierne rozmieszczenie włókien w betonie typu 3, wynikające z pogorszonej urabialności mieszanki. Pomimo tego stwierdzono, że zarówno dodatek, jak i ilość SyFs mają wpływ na przebieg rys ścinających, a tym samym na kształt stożka przebicia oraz długość krytycznego obwodu kontrolnego. Z drugiej strony, zmiana typu włókien z PM na FF nie wpłynęła istotnie ani na wartość kąta θ , ani na odległość a. Ponownie należy jednak podkreślić, że w analizie tej uwzględniono jedynie stożek przebicia z jednej płyty typu 6, co ogranicza możliwość formułowania jednoznacznych wniosków. Warto również zaznaczyć, że wszystkie stożki przebicia z płyt SyFRC zachowały integralność strukturalną, co znacząco ułatwiało ich transport, podczas gdy stożki z płyt PC, ulegały kruchemu zniszczeniu i rozpadały się na fragmenty przy próbie ich przeniesienia.



Rysunek 7 Wybrane stożki przebicia badanych płyt 1-6 podpartych na gruncie, obciążonych centralną siła skupioną

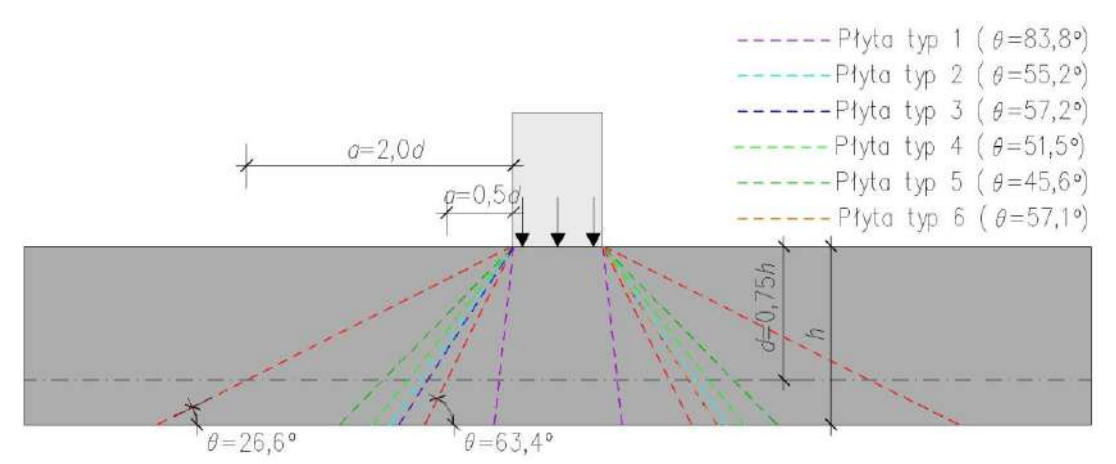


Rysunek 8 Obrys obwodów podstaw stożków przebicia badanych płyt typu 1-6 podpartych na gruncie, obciążonych centralną siłą skupioną

Tabela 5 Zestawienie długości zastępczych krytycznych obwodów kontrolnych stożków przebicia u_{eq} wraz z odpowiadającymi im kątami θ i odległościami a dla badanych płyt typu 1-6 podpartych na gruncie, obciążonych centralną siłą skupioną

| Plyta nr | | Obwód | Zastępczy krytyczny | Odległość krytycznego | Kąt |
|-------------|--------|------------------------|---|--|-------------------------|
| | | podstawy stożka | obwód kontrolny stożka przebicia na użytecznej | przekroju kontrolnego od powierzchni | nachylenia stożka |
| | | przebicia | wysokości płyty | obciążenia | przebicia |
| | | u _{base} [mm] | u_{eq} [mm] | a [mm] | |
| 1.1 | | 618 | 464 | a = 10 mm = 0.07d | θ = 86,1° |
| 1.2 | PC | 563 | 563* | a = 10 mm = 0.07d a = 26 mm = 0.17d | $\theta = 80,2^{\circ}$ |
| 1.3 | | 482 | 482* | a = 20 mm = 0.77a a = 13 mm = 0.09d | $\theta = 85,1^{\circ}$ |
| 1.3 | | | 503 | ŕ | $\theta = 83.8^{\circ}$ |
| | | 554 | | <i>a</i> = 16 mm = 0,11 <i>d</i> | |
| 2.1 | PM_2 | 1264 | 948 | a = 87 mm = 0.58d | $\theta = 59.8^{\circ}$ |
| 2.2 | | 1435 | 1076 | a = 108 mm = 0.72d | $\theta = 54,3^{\circ}$ |
| 2.3 | | 1518 | 1139 | a = 118 mm = 0.78d | θ = 51,9° |
| 2 | | 1406 | 1054 | a = 104 mm = 0.69d | $\theta = 55,2^{\circ}$ |
| 3.1 | | 1109 | 832 | a = 69 mm = 0.46d | $\theta = 65,4^{\circ}$ |
| 3.2 | 1_3 | 1501 | 1125 | a = 115 mm = 0,77d | $\theta = 52,4^{\circ}$ |
| 3.3 | PM_ | 1416 | 1062 | a = 105 mm = 0.70d | $\theta = 54.9^{\circ}$ |
| 3 | | 1342 | 1007 | a = 97 mm = 0.64d | $\theta = 57,2^{\circ}$ |
| 4.1 | | 1514 | 1135 | a = 117 mm = 0.78d | $\theta = 52,0^{\circ}$ |
| 4.2 | _2 | 1564 | 1173 | a = 123 mm = 0.82d | $\theta = 50.6^{\circ}$ |
| 4.3 | PD | 1524 | 1143 | a = 118 mm = 0.79d | $\theta = 51.8^{\circ}$ |
| 4 | | 1534 | 1150 | a = 119 mm = 0.80d | $\theta = 51,5^{\circ}$ |
| 5.1 | | 1409 | 1057 | a = 105 mm = 0.70d | $\theta = 55,1^{\circ}$ |
| 5.2 | _3 | 2212 | 1659 | a = 200 mm = 1,34d | $\theta = 36.8^{\circ}$ |
| 5.3 | PD | 1674 | 1255 | a = 136 mm = 0.91d | $\theta = 47.8^{\circ}$ |
| 5 | | 1765 | 1324 | a = 147 mm = 0.98d | $\theta = 45.6^{\circ}$ |
| 6.3 | FF_2 | 1347 | 1010 | a = 97 mm = 0.65d | $\theta = 57,1^{\circ}$ |

Uwaga: * Stożki przebicia z płyt 1.2 i 1.3 miały kształt prostopadłościanu, dlatego przyjęto, że obwód na użytecznej wysokości płyty u_{eq} jest równy obwodowi podstawy stożka przebicia u_{base} .

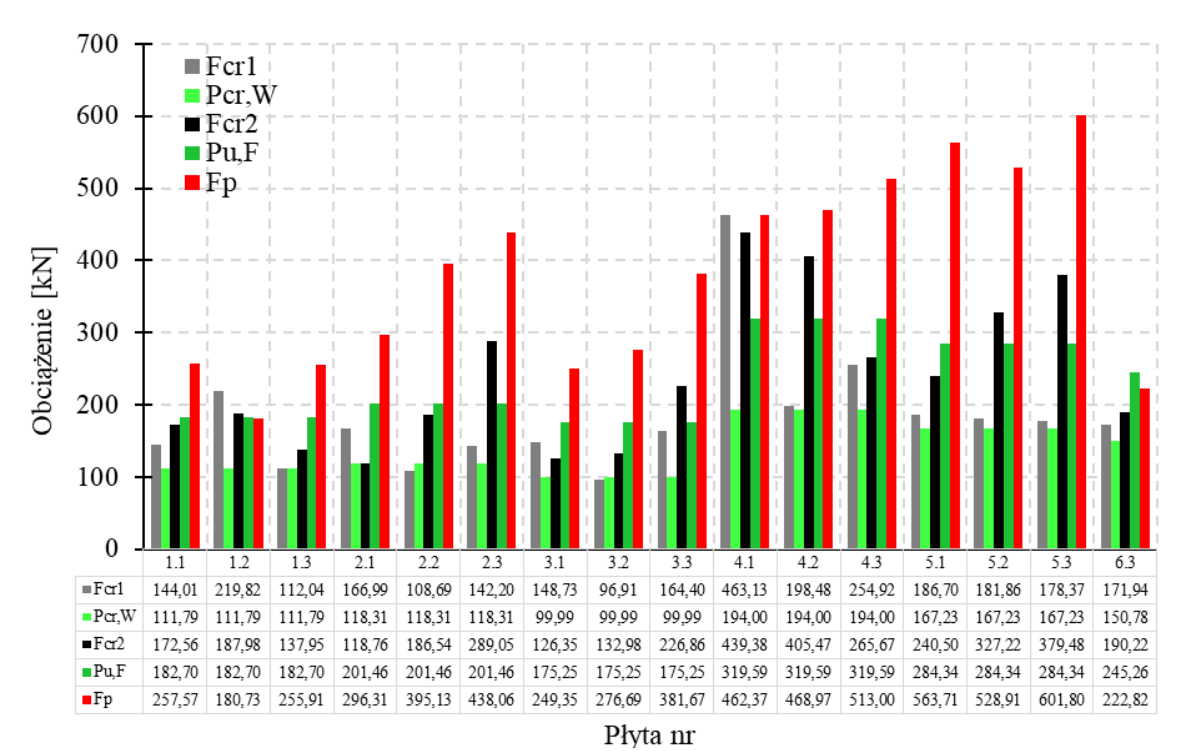


Rysunek 9 Zestawienie średnich kątów nachylenia stożków przebicia θ z badanych płyt typu 1-6 podpartych na gruncie, obciążonych centralą siłą skupioną, gdzie wartości kątów $\theta = 63.4^{\circ}$ i 26.6° odpowiadają odległościom a = 0.5d i 2.0d (czerwone linie)

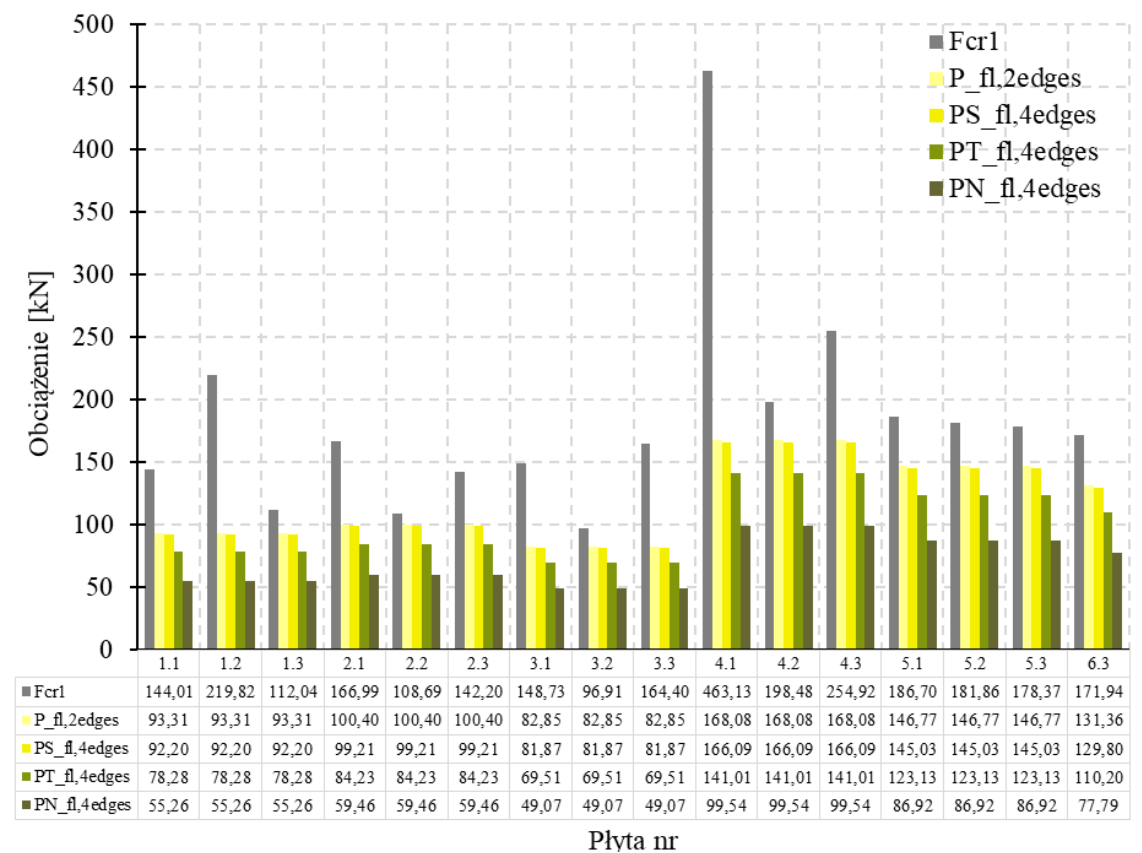
Rysunek 10 przedstawia porównanie eksperymentalnie wyznaczonych sił odpowiadających pierwszemu i drugiemu zarysowaniu przy zginaniu (F_{cr1} i F_{cr2}) oraz nośności na przebicie (F_p) z analitycznie obliczonymi nośnościami płyt typu 1-6,

podpartymi na gruncie i obciążonymi centralną siłą skupioną. Obliczenia przeprowadzono według modeli Westergaarda ($P_{cr,W}$) oraz Falknera i in. ($P_{u,F}$). Z analizy wynika, że model Westergaarda pozwala na stosunkowo trafne oszacowanie obciążenia rysującego F_{crl} . Tylko w przypadku płyt 2.2 i 3.2 wartości F_{crl} były niższe od $P_{cr,W}$ o maksymalnie 9%. Z drugiej strony, dla płyt 1.2 i 4.1 siła F_{crl} wyniosła około dwukrotność wartości $P_{cr,W}$. Po wykluczeniu tych czterech płyt, obserwowane w badaniach F_{cr1} było o średnio 23% mniejsze niż przewidywane analitycznie $P_{cr,W}$. Stwierdzono ponadto, że nośność obliczona według modelu Falknera i in. $(P_{u,F})$ w ponad połowie przypadków przewyższała siłę F_{cr2} . Jednocześnie wartość $P_{u,F}$ była niższa niż F_p w niemal wszystkich przypadkach, a wyjątek stanowiła jedynie płyta 1.2. Korelacja wartości F_{cr2} z wynikami analitycznymi okazała się niemożliwa, ponieważ drugie zarysowanie występowało już w fazie nieliniowej pracy płyty, nieuwzględnionej w analizowanych modelach obliczeniowych. Ponadto, podejścia teoretyczne Westergaarda oraz Falknera i in. zaniżały co najmniej 2,3- i 1,4-krotnie, odpowiednio nośności F_p badanych płyt SyFRC. Natomiast, w przypadku modelu Shentu i in., obliczone nośności $(P_{u,S})$ mieściły się w zakresie od 1372 kN do 1658 kN, a więc były kilkukrotnie wyższe od wartości uzyskanych zarówno według modelu Westergaarda, jak i Falknera i in. Dodatkowo, znacznie przewyższały wartości sił F_{crl} , F_{cr2} i F_p uzyskanych eksperymentalnie. Tak istotna rozbieżność mogła wynikać z faktu, że model Shentu i in. uwzględnia efekt membranowy, który nie występował w badanych płytach ze względu na ich mniejsze wymiary oraz brak bocznego ograniczenia krawędzi.

W związku z obserwacjami morfologii zarysowań oraz ugięć podczas badań, które sugerowały, że w początkowej fazie obciążania płyty nie były równomiernie podparte na podłożu gruntowym i/lub wzdłuż wszystkich krawędzi na stalowych wałkach, przeprowadzono dodatkowe obliczenia analityczne. Uwzględniono w nich zarówno przypadek jedynie swobodnego podparcia płyty, jak i podparcia gruntowego z dodatkowym oparciem wzdłuż od dwóch do czterech krawędzi. Celem tych analiz było oszacowanie rzeczywistych, początkowych warunków podparcia każdej z badanych płyt. Wszystkie rozważane metody analityczne dla płyt swobodnie podpartych i obciążonych centralną siłą skupioną, zarówno na dwóch krawędziach ($P_{fl,2edges}$), jak i na czterech krawędziach, według wzorów zaproponowanych przez kolejno: Starosolskiego ($P_{fl,4edges}^S$), Timoshenkę i in. ($P_{fl,4edges}^T$) oraz Niezgodzińskiego i in. ($P_{fl,4edges}^N$), przewidywały niższe nośności niż eksperymentalnie uzyskane siły F_{crl} (Rysunek 11). Dla płyt typu 1-6 obliczone wartości $P_{fl,2edges}$, $P_{fl,4edges}^S$ i $P_{fl,4edges}^N$ stanowiły średnio odpowiednio 73%, 72%, 61% i 43% siły F_{crl} . Wyniki te wskazują, że w początkowej fazie badania, płyty były co najmniej częściowo podparte przez grunt.



Rysunek 10 Porównanie eksperymentalnie uzyskanych sił odpowiadających pierwszemu i drugiemu zarysowaniu przy zginaniu (F_{cr1} i F_{cr2}) oraz nośności na przebicie (F_p) z analitycznie obliczonymi nośnościami badanych płyt typu 1-6, podpartymi na gruncie i obciążonymi centralną siłą skupioną, według modeli Westergaarda ($P_{cr,W}$) oraz Falknera i in. ($P_{u,F}$)



Rysunek 11 Porównanie eksperymentalnie uzyskanych sił odpowiadających pierwszemu zarysowaniu przy zginaniu (F_{crl}) z analitycznie obliczonymi nośnościami badanych płyt typu 1-6, podpartymi swobodnie na dwóch ($P_{fl,2edges}$) lub czterech krawędziach ($P_{fl,4edges}^S$, $P_{fl,4edges}^T$, $P_{fl,4edges}^N$) i obciążonymi centralną siłą skupioną według wybranych metod

W związku z faktem, że dostępna literatura nie dostarcza rozwiązań analitycznych dla przypadków płyt jednocześnie podpartych na gruncie oraz wzdłuż ich krawędzi, konieczne było opracowanie autorskiego podejścia analitycznego. W tym celu, w programie ABC Płyta, utworzono cztery uproszczone modele inżynierskie umożliwiające obliczenie nośności płyt na gruncie obciążonych centralną siłą skupioną, z dodatkowym podparciem wzdłuż czterech (Model 1), dwóch naprzeciwległych (Model 2), trzech (Model 3) i dwóch sąsiadujących (Model 4) krawędzi Obliczone wartości sił oznaczono odpowiednio jako P^{1}_{4edges} , $P^{2}_{2edges,o}$, P^{3}_{3edges} oraz $P^{4}_{2edges,a}$ i odpowiadały one wartości $min(P^x, P^y)$, które wyznaczano zgodnie z założeniami przedstawionymi na Rysunek 12. Na podstawie wyników obliczeń (Rysunek 13) stwierdzono, że Model 1 generował najwyższe wartości sił niszczących P^{l}_{4edges} , co było zgodne z oczekiwaniami, ponieważ większa liczba podpartych krawędzi zapewnia sztywniejsze warunki brzegowe, prowadząc do wyższej nośności płyty. Z kolei Model 2, uwzględniający podparcie jedynie na dwóch przeciwległych krawędziach, wykazywał najniższe wartości sił $P^2_{2edges,o}$, co potwierdza jego najmniejszą sztywność spośród wszystkich analizowanych modeli. Modele 3 i 4 dały wyniki pośrednie, przy czym nieoczekiwanie szacowana nośność płyt z trzema podpartymi krawędziami (Model $3 - P^3_{3edges}$) okazała się niższa niż w przypadku płyt podpartych na dwóch sąsiednich krawędziach (Model $4 - P^4_{2edges,a}$). Może to wynikać z ograniczeń przyjętego modelu liniowego, jak również ze sposobu uśredniania momentów zginających na odcinku 30 cm (szerokość stempla + 2 x 0,5 x grubość płyty), który mógł obejmować obszar poza ekstremami momentów. Niemniej jednak, dla 7 z 16 badanych płyt podpartych na gruncie wartości sił powodujących pierwsze zarysowanie F_{crl} przewyższały wartości obliczone w ramach wszystkich czterech modeli. Może to wskazywać na fakt, że badane płyty były równomiernie podparte wzdłuż wszystkich krawędzi. Wyjątek stanowiły płyty 1.3, 4.2, 5.1, 5.2, 5.3 oraz 6.3, jak również płyty 2.2 i 3.2, dla których obliczenia sugerowały ograniczone podparcie, odpowiednio do dwóch sąsiadujących lub przeciwległych krawędzi, z częściowym podparciem wzdłuż trzeciej. Płyta 2.3 oraz niepodparta gruntowo płyta 6.2 były najprawdopodobniej oparte na dwóch sąsiadujących stalowych wałkach i nierównomiernie na pozostałych krawędziach. Należy jednak zaznaczyć, że wyniki analiz nie pokrywają się w pełni z obserwacjami poczynionymi podczas badań. Morfologia oraz kolejność pojawiania się rys sugerowały bowiem, że większość płyt była początkowo podparta wzdłuż dwóch przeciwległych krawędzi. Wobec tego, mimo przeprowadzonych analiz oraz zastosowania różnych modeli obliczeniowych, jednoznaczne określenie warunków podparcia badanych płyt w początkowej fazie obciążania pozostaje niemożliwe.

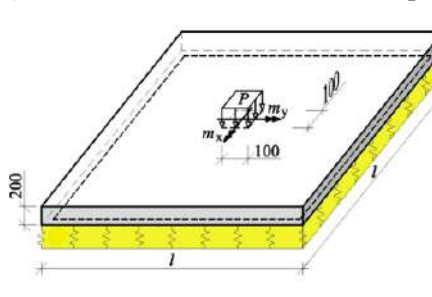
W dalszych pracach zaleca się wykonanie analiz nieliniowych, co umożliwi zwiększenie dokładności oraz wiarygodności uzyskiwanych wyników analitycznych.

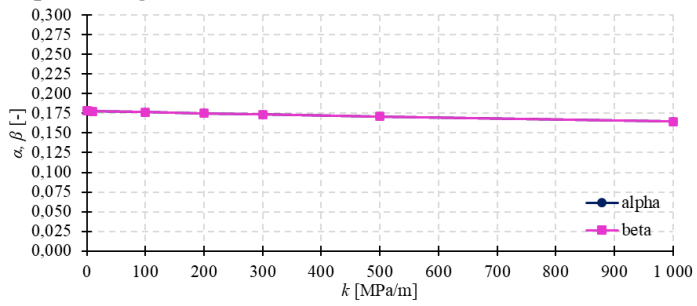
$$min \begin{cases} P^{x} = \frac{f_{ct,fl} \cdot h^{2} \cdot b}{6 \cdot \alpha \cdot l} \\ P^{y} = \frac{f_{ct,fl} \cdot h^{2} \cdot b}{6 \cdot \beta \cdot l} \end{cases}$$

 $\begin{cases} P^x = \frac{f_{ct,fl} \cdot h^2 \cdot b}{6 \cdot \alpha \cdot l} & \begin{cases} P^x \text{ i } P^y - \text{centralna siła skupiona na kierunku } x \text{ i } y, \text{ odpowiednio [N],} \\ P^y = \frac{f_{ct,fl} \cdot h^2 \cdot b}{6 \cdot \beta \cdot l} & \begin{cases} h - \text{grubość betonu na rozciąganie przy zginaniu [N/mm}^2],} \\ h - \text{grubość płyty [mm],} \end{cases} \\ b \text{ i } l - \text{szerokość i rozpiętość płyty między wałkami, odpowiednio [mm],} \end{cases}$

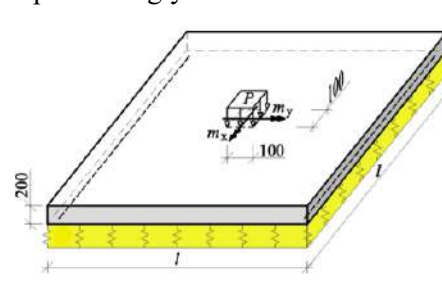
 α i β – parametr odpowiadający kierunkowi x i y, odpowiednio [-].

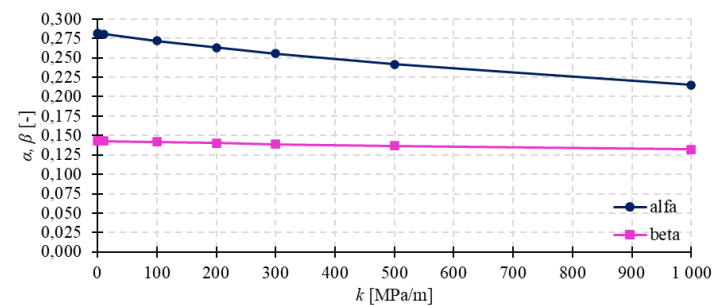
a) Model 1 – centralnie obciążona płyta podparta na gruncie i dodatkowo wzdłuż 4 krawędzi



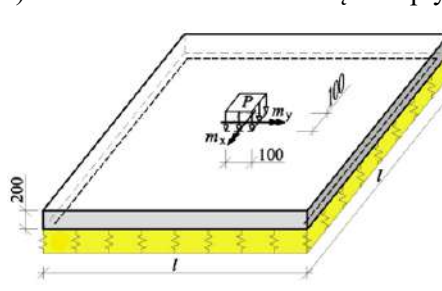


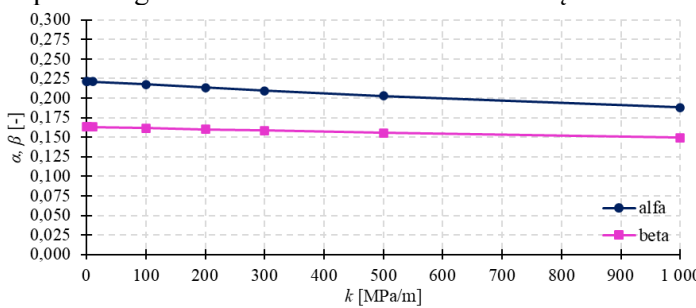
b) Model 2 – centralnie obciążona płyta podparta na gruncie i dodatkowo wzdłuż 2 krawędzi



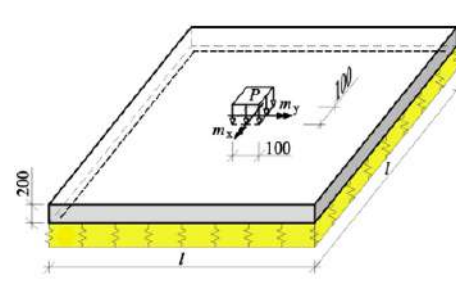


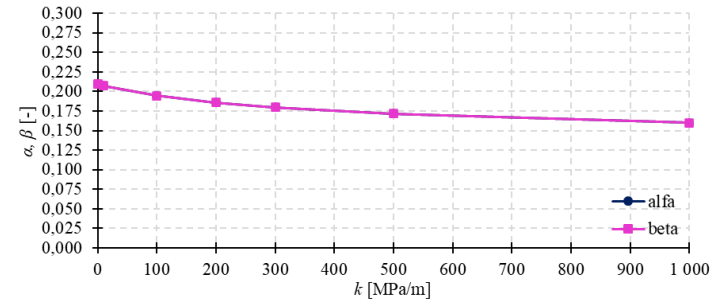
c) Model 3 – centralnie obciążona płyta podparta na gruncie i dodatkowo wzdłuż 3 krawędzi



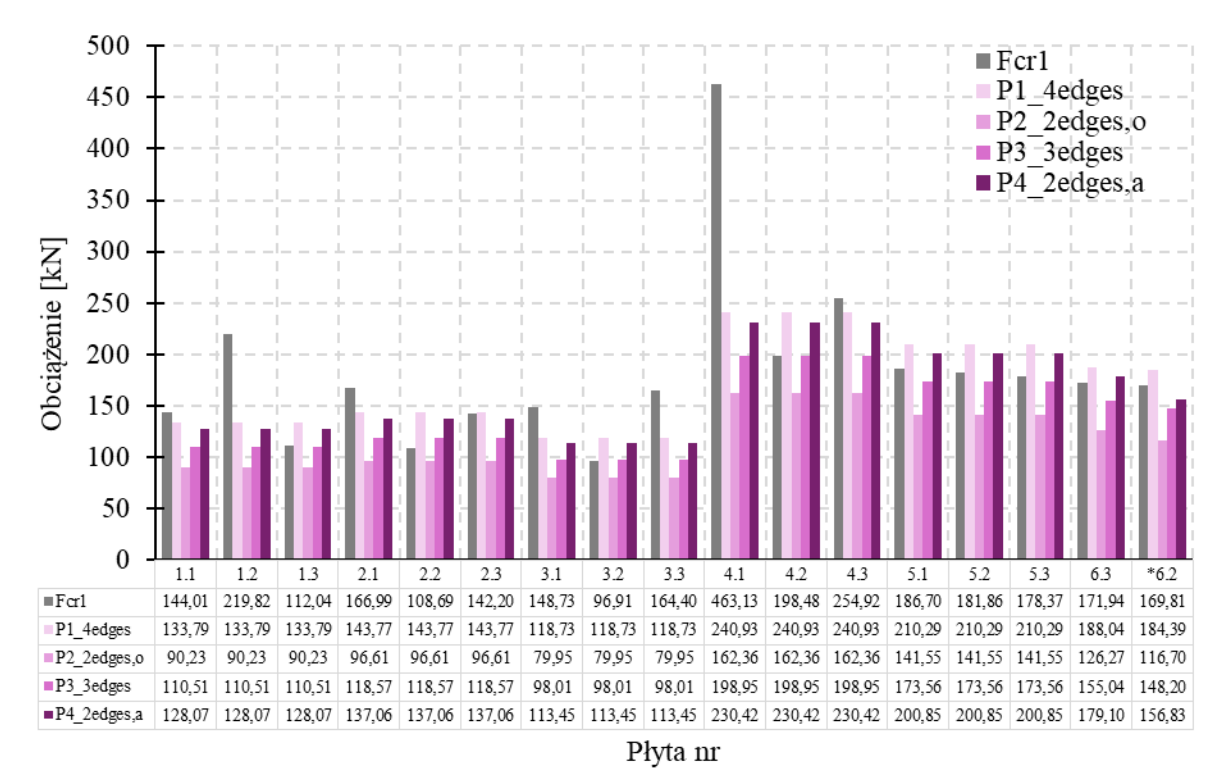


d) Model 4 – centralnie obciążona płyta podparta na gruncie i dodatkowo wzdłuż 2 krawędzi sąsiadujących





Rysunek 12 Wartości parametrów α i β w zależności od modułu reakcji podłoża k oraz warunków podparcia krawędziowego płyt podpartych na gruncie, obciążonych centralną siłą skupioną



Rysunek 13 Porównanie eksperymentalnie uzyskanych sił odpowiadających pierwszemu zarysowaniu przy zginaniu (F_{crl}) z analitycznie obliczonymi nośnościami badanych płyt typu 1-6, podpartymi na gruncie i dodatkowo wzdłuż krawędzi według Modeli 1-4 (P^{I}_{4edges} , $P^{2}_{2edges,o}$, P^{3}_{3edges} , $P^{4}_{2edges,a}$), obciążonych centralną siłą skupioną

Na podstawie Modeli 1-4 przedstawiono i umówiono również procedurę walidacji modeli analitycznych, gdyż ich założenia najlepiej odzwierciedlały warunki eksperymentalne, w szczególności geometrię płyt oraz sposób ich podparcia (podłoże + podpory krawędziowe). Taka walidacja może uwzględniać rozbieżności pomiędzy założeniami przyjętymi w modelu analitycznym a rzeczywistą metodologią badań oraz niepewności pomiarowe i zmienność właściwości materiałowych. Zaproponowana procedura walidacji okazała się skuteczna, gdy dostępna była wystarczająca liczba próbek o niedużym zróżnicowaniu wyników. Przyjęto, że wiarygodna walidacja modeli analitycznych wymaga co najmniej trzech wyników oraz współczynnika zmienności nieprzekraczającego 15%. W przypadku płyt typu 5 empiryczne współczynniki walidacyjne mieściły się w zakresie od 0,833 do 1,238, w zależności od rozważanego Modelu 1-4. Przedstawioną metodę walidacji można w analogiczny sposób zastosować do innych modeli analitycznych.

Najwięcej uwagi w części analitycznej poświęcono jednak wytycznym TR34, dedykowanym projektowaniu płyt podpartych na gruncie. Wstępne obliczenia nośności na przebicie przeprowadzono dla krytycznego przekroju kontrolnego zlokalizowanego w odległości a = 2d od krawędzi powierzchni obciążenia, zgodnie z wytycznymi TR34. Celem tych analiz było między innymi oszacowanie możliwego mechanizmu

zniszczenia jeszcze przed rozpoczęciem badań eksperymentalnych. Wyniki testów elementów płytowych potwierdziły wnioski z obliczeń, ponieważ we wszystkich przypadkach odnotowano zniszczenie z uwagi na przebicie. W dalszej kolejności wykonano obliczenia dla odległości a wyznaczonych eksperymentalnie. Także w tym przypadku, niezależnie od rodzaju materiału (SyFRC lub PC), obliczenia jednoznacznie wskazywały na mechanizm zniszczenia przez przebicie. Należy jednak zaznaczyć, że zastosowanie rzeczywistego położenia przekroju kontrolnego skutkowało wzrostem obliczonych wartości nośności na przebicie o średnio 7%, odpowiednio z 203 do 238 kN, 232 do 253 kN, 218 do 241 kN, 277 do 285 kN, 245 do 274 kN dla płyt typu 1, 2, 3, 4 i 6. Tylko w przypadku płyt typu 5 zaobserwowano niewielki spadek przewidywanej nośności z 286 do 284 kN, gdy obliczenia wykonano dla odległości a uzyskanej z badań. Dla płyt typu 2-5, wartości te były bliższe wynikom uzyskanym w badaniach eksperymentalnych, choć nadal stanowiły średnio jedynie około 61% rzeczywistej nośności. Niemniej jednak należy zauważyć, że schemat statyczny badanych płyt przybliżeniu odzwierciedlał założenia modelu obliczeniowego przedstawionego w TR34, co mogło przyczynić się do różnic pomiędzy wynikami eksperymentalnymi a analitycznymi. W dalszej części analiz oszacowano udział betonu, SyFs oraz podparcia gruntowego w całkowitej nośności płyt na przebicie. Dla przypadku a = 2d, średni udział betonu, włókien i gruntu wynosił odpowiednio 75,1%, 9,9% oraz 15,0%. Natomiast przy zastosowaniu eksperymentalnie wyznaczonych odległości a, udział betonu wzrósł istotnie do 91,7%, podczas gdy włókna oraz grunt były odpowiedzialne za przenoszenie jedynie średnio 4,7% oraz 3,6% obciążenia skupionego, odpowiednio. Zmiana ta wynikała głównie ze znacznego zmniejszenie odległości a od krawędzi powierzchni obciążenia, co bezpośrednio wpłynęło na zwiększenie minimalnej wytrzymałości betonu na ścinanie i jego udziału w nośności płyty. Z drugiej strony skrócenia długości krytycznego obwodu kontrolnego skutkowało mniejszym udziałem SyFs i odporu gruntu. Stwierdzono również, że pomimo obecności SyFs, ich wpływ na nośność na przebicie okazał się relatywnie niewielki według obliczeń opartych na TR34, co nie pokrywało się z wynikami badań eksperymentalnych. Niedoszacowanie to wyjaśniono bardzo konserwatywnym podejściem do obliczania dodatkowej wytrzymałości na ścinanie wynikającej z dodania do betonu włókien (v_f) przyjętym w TR34. Raport tłumaczy to bardzo małą ilością wiarygodnych badań dotyczących wpływu makrowłókien SyFs na wytrzymałość na ścinanie. W związku z powyższym przeprowadzono analizę alternatywnych wzorów do wyznaczania v_f proponowanych w innych normach (Rysunek 14).

TR34

$$v_{f} = \frac{0.12 \cdot \left(\frac{f_{R,1} + f_{R,2} + f_{R,3} + f_{R,4}}{4}\right)}{2}$$
RILEM TC 162-TDF

$$v_{f} = 0.12 \cdot f_{R,4}$$

$$v_{f} = \kappa_{O} \cdot \kappa_{G} \cdot 0.33 \cdot f_{R,3}$$

$$\text{gdzie: } \kappa_{O} = 1.0 \text{ and } \kappa_{G} = 1.0$$

$$v_{f} = f_{Fts} - \frac{w_{u}}{CMOD_{3}} (f_{Fts} - 0.5f_{R,3} + 0.2f_{R,1})$$

$$\text{gdzie: } f_{Fts} = 0.45f_{R,1}; w_{u} = 1.5 \text{ mm, and } CMOD_{3} = 2.5 \text{ mm}$$

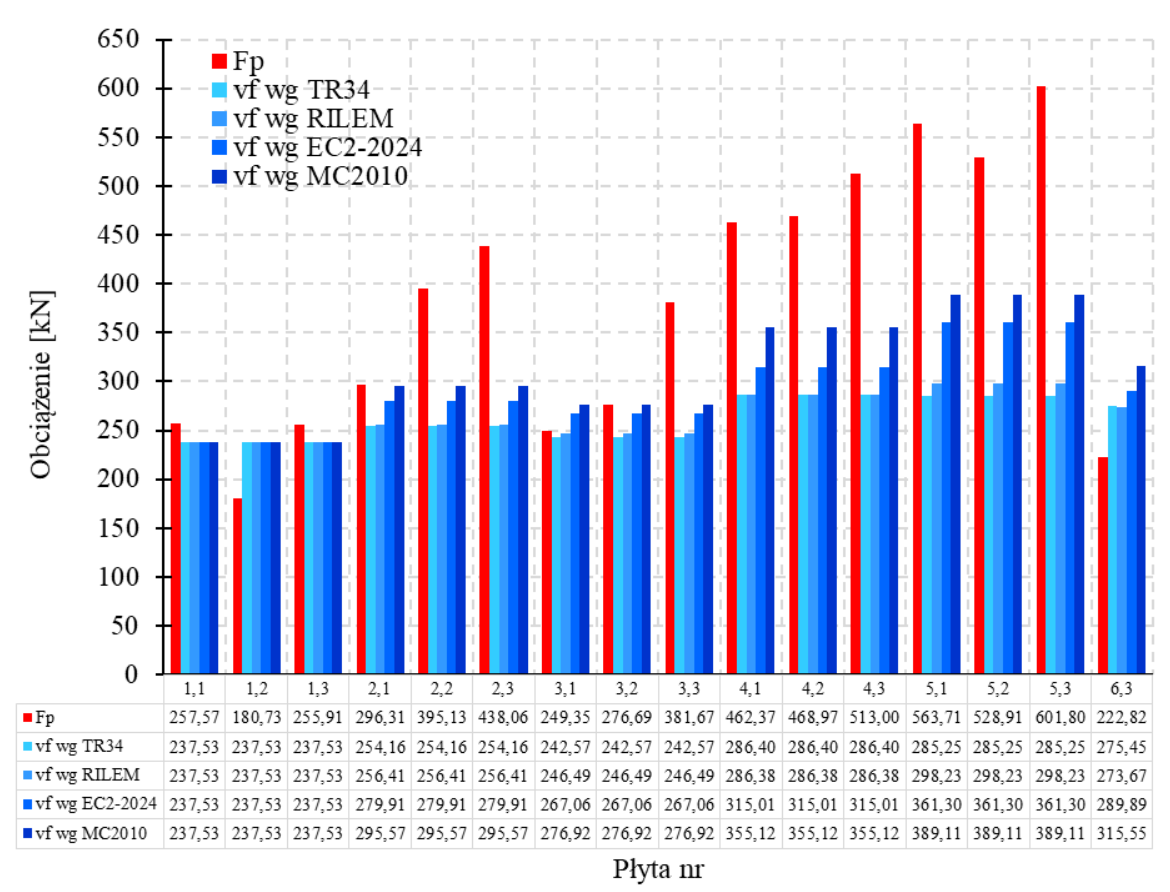
Rysunek 14 Wzory zaproponowane w wybranych normach do obliczania dodatkowej wytrzymałości na ścinanie wynikającej z obecności włókien w betonie v_f

Spośród porównywanych, wzór na v_f zawarty w Model Code 2010 (MC2010) wskazywał na największy udział SyFs w przenoszeniu siły skupionej, a wartość ta była co najmniej 4,9-krotnie wyższa niż uzyskana na podstawie wzoru z TR34 (Tabela 6). Obliczenia przeprowadzone zgodnie z normą PN-EN 1992-1-1:2024 generowały wartości niższe od MC2010 o 22% do 51%, lecz wciąż ponad 2,4-krotnie przewyższały wyniki według TR34. Z kolei zastosowanie równania w RILEM TC 162-TDF prowadziło zazwyczaj do wytrzymałości v_f bardzo zbliżonych do TR34. Warto również podkreślić, że jedynie wyniki v_f według wzorów MC2010, RILEM TC 162-TDF oraz PN-EN 1992-1-1:2024 odzwierciedlały ten sam trend pomiędzy poszczególnymi nośnościami na przebicie płyt SyFRC, jaki zaobserwowano w badaniach eksperymentalnych. Mianowicie, najwyższą wytrzymałość v_f i nośność F_p uzyskano dla płyty typu 5, a następnie odpowiednio dla typów 4, 2 i 3. Wyniki analityczne dla płyty 6.3 były natomiast niespójne z doświadczalnymi, co można przypisać ograniczonej, do jednej, liczbie próbek dla tego typu płyty. Podsumowując, spośród rozważanych wzorów analitycznych, najbardziej odpowiednie do obliczania udziału SyFs w nośności z uwagi na przebicie wydają się wzory zawarte w PN-EN 1992-1-1:2024 oraz MC2010. Ich przewagę potwierdza fakt, że równania te w dużym stopniu opierają się na wartości wytrzymałości resztkowej $f_{R,3}$ z 3PBT belek, która zgodnie z wynikami badań eksperymentalnych płyt koreluje z siłą odpowiadającą przebiciu F_p .

Tabela 6 Dodatkowa wytrzymałość na ścinanie wynikająca z dodania do betonu SyFs badanych płyt typu 2-6, podpartych na gruncie i obciążonych centralną siłą skupioną, według procedur Raportu Technicznego 34 w zależności od zastosowanego wzoru na obliczenie v_f

| Typ płyty | 2 | 3 | 4 | 5 | 6.3 |
|---|-------|-------|-------|-------|-------|
| v_f wg TR34 [MPa] | 0,056 | 0,048 | 0,095 | 0,106 | 0,065 |
| v _f wg RILEM TC 162-TDF [MPa] | 0,070 | 0,073 | 0,095 | 0,168 | 0,054 |
| <i>v_f</i> wg PN-EN 1992-1-1:2024 [MPa] | 0,213 | 0,205 | 0,253 | 0,469 | 0,157 |
| v _f wg Model Code 2010 [MPa] | 0,309 | 0,268 | 0,475 | 0,602 | 0,321 |

Rysunek 15 przedstawia porównanie uzyskanych eksperymentalnie sił F_p z obliczonymi wartościami nośności na przebicie badanych płyt. Obliczenia te wykonano zgodnie z procedurą TR34 przy zastosowaniu wybranych wzorów do wyznaczenia v_f oraz uwzględnieniu skorygowanego udziału podłoża gruntowego w przenoszeniu obciążenia skupionego.



Rysunek 15 Porównanie eksperymentalnie uzyskanych sił odpowiadających przebiciu (F_p) z analitycznie obliczonymi nośnościami na przebicie badanych płyt typu 2-6, podpartych na gruncie i obciążonych centralną siłą skupioną, według procedury Raportu Technicznego 34 w zależności od wybranego wzoru na obliczenie v_f i uwzględnieniem skorygowanego udziału podłoża w przenoszeniu obciążeń

Na początku należy zaznaczyć, że w wyniku bardziej szczegółowych obliczeń reakcji podłoża, udział gruntu w całkowitej nośności na przebicie wzrósł nieznacznie, średnio z 3,6% do 4,1%. Dodatkowo, nie uzyskano pełnej zgodności wyników analitycznych z wynikami eksperymentalnymi. Średnie niedoszacowanie nośności z uwagi na przebicie, po wykluczeniu z analizy wyników z płyty 6.3, wynosiło odpowiednio: 60% (v_f wg TR34), 57% (v_f wg RILEM TC 162-TDF), 39% (v_f wg PN-EN 1992-1-1:2024) oraz 29% (v_f wg MC2010). Rozbieżności te można tłumaczyć innymi warunkami pracy badanych elementów płytowych i rzeczywistych płyt podpartych na gruncie, których dotyczą założenia TR34. Mowa tutaj o m.in. mniejszych

wymiarach badanych płyt, ograniczonej możliwości przemieszczeń bocznych gruntu i obecności płyty wielkich sił, skutkujących zwiększoną sztywnością podłoża gruntowego i innym rozkładem naprężeń w gruncie. Niemniej jednak, obliczenia analityczne według TR34 umożliwiły trafną ocenę mechanizmu zniszczenia oraz oszacowanie wartości nośności badanych płyt z uwagi na przebicie, z zachowaniem marginesu bezpieczeństwa. Kluczowe okazało się jednak uwzględnienie rzeczywistego położenia krytycznego przekroju kontrolnego oraz mniej konserwatywne oszacowanie udziału gruntu i SyFs w przenoszeniu obciążenia skupionego.

Podsumowując, rola SyFs w przenoszeniu obciążeń jest często pomijana lub przyjęta w sposób bardzo konserwatywny, a zastosowanie SyFs ogranicza się jedynie do przeciwdziałania zarysowaniom. Przeprowadzone badania i analizy wskazały jednak na istotny udział SyFs w nośności na przebicie płyt podpartych na gruncie obciążonych centralną siłą skupioną. Dodatkowo, sprawdzenie warunku przebicia w tego typu elementach okazała się niezbędne i absolutnie nie może być pomijane w procesie projektowania płyt na gruncie. Spośród dostępnych norm i przewodników projektowych, TR34 okazał się najbardziej adekwatną pozycją literaturową do obliczania nośności płyt SyFRC podpartych na gruncie. Wytyczne te zawierają procedury analityczne zarówno do obliczania nośności na zginanie, jak i z uwagi na przebicie, uwzględniające jednocześnie udział włókien oraz odpór podłoża gruntowego w przenoszeniu obciążeń skupionych. Na podstawie przeprowadzonych badań oraz sformułowanych wniosków zaproponowano również praktyczne wskazówki projektowe dotyczące sposobu uwzględniania udziału SyFs w obliczeniach nośności na przebicie oraz przyjmowania położenia krytycznego przekroju kontrolnego. Potwierdzenie uzyskały tezy 2, 3 i 4 rozprawy doktorskiej. Natomiast, tezy 1 i 5 zostały potwierdzone jedynie częściowo, co wynikało z ograniczonego zakresu badań oraz złożoności rozważanego zagadnienia. W związku z tym konieczne są dalsze prace badawcze, w szczególności uwzględniające: szerszy zakres rodzajów i dozowań SyFs, różnorodne warunki podparcia (m.in. inne rodzaje gruntu, jego uwarstwienia i zagęszczenia), zróżnicowane typy obciążeń (np. wielopunktowe, liniowe, równomiernie rozłożone, zlokalizowane przy krawędzi lub w narożu), inną geometrię elementów badawczych oraz zastosowanie zaawansowanych technik pomiarowych. Istotne byłoby również uzupełnienie programu badawczego o modelowanie numeryczne w celu weryfikacji wyników i wniosków z badań eksperymentalnych. Ponadto, niektóre założenia i rozwiązania przyjęte w pracy mogą podlegać krytycznej ocenie. Między innymi znaczące różnice we właściwościach mechanicznych betonów typu 1-6, utrudniły bezpośrednią ocenę wpływu dodatku, ilości i rodzaju SyFs na prace płyt podpartych na gruncie. W celu zwiększenia wiarygodności

formułowanych wniosków zazwyczaj badano trzy płyty dla każdego rodzaju betonu. Mimo to obserwowano rozbieżności w wynikach, co podkreśla znaczenie odpowiedniej liczby próbek w badaniach SyFRC, w których nierównomierny rozkład włókien w matrycy może istotnie wpływać na zachowanie obciążonego elementu. Z tego względu wyniki uzyskane dla płyty 6.3 interpretowano ze szczególną ostrożnością. Trudność w analizie wyników stanowiła także prefabrykacja płyt, skutkująca nierównomiernym oparciem płyt na podłożu gruntowym. Udoskonalenia wymagałoby również stanowisko badawcze oraz metody pomiarowe. Wskazane ograniczenia rozprawy otwierają jednak przestrzeń do dalszych usprawnień, weryfikacji oraz rozwoju tematyki. Niewątpliwie, przedstawiona praca wnosi istotny wkład w rozwój wiedzy w zakresie projektowania SyFRC płyt na gruncie. Jej kompleksowy zakres, obejmujący poszerzony przegląd literaturowy, badania doświadczalne oraz analizy analityczne, pozwolił na pełniejsze zrozumienie wpływu SyFs zarówno na właściwości mechaniczne betonu, jak i na zachowanie przy przebiciu elementów płytowych. Zgodnie z wiedzą autora, są to pierwsze badania, które analizują wpływ dodatku, ilości i typu SyFs na geometrię stożków przebicia oraz lokalizację krytycznego przekroju kontrolnego w płytach SyFRC podpartych na gruncie. Praca ta może stanowić podstawę do przyszłych modyfikacji obowiązujących norm oraz rozwoju praktycznych wytycznych dla projektantów.